Transactions of the ASME, Journal of Heat Transfer (ISSN 0022-1481) is published bi-monthly (Feb., Apr., June, Aug., Oct., Dec.) by The American Society of Mechanical Engineers, Three Park Avenue, New York, NY 10016. Periodicals postage paid at New York, NY and additional mailing offices. POSTMASTER: Send address changes to Transactions of the ASME, Journal of Heat Transfer, c/o THE AMERICAN SOCIETY OF MECHANICAL ENGINEERS, 22 Law Drive, Box 2300, Fairfield, NJ 07007-2300.
CHANGES OF ADDRESS must be received at Society headquarters seven weeks before they are to be effective. Please send old label and new address.
STATEMENT from By-Laws. The Society shall not be responsible for statements or opinions advanced in papers or ... printed in its publications (B7.1, Para. 3), **COPYRIGHT © 2004** by The American Society of Mechanical Engineers. For authorization to photocopy material for internal or personal use under those circumstances not falling within the fair use provisions of the Copyright Act, contact the Copyright Clearance Center (CCC), 222 Rosewood Drive, Danvers, MA 01923, tel: 978-750-8400, *www.copyright.com*. Request for special permission or bulk copying should be addressed to Reprints/Permission Department. **INDEXED** by Applied Mechanics Reviews and Engineering Information, Inc. Canadian Goods & Services Tax Registration #126148048.

Journal of Heat Transfer

Published Bimonthly by ASME

VOLUME 126 • NUMBER 2 • APRIL 2004

TECHNICAL PAPERS

(**Contents continued on inside back cover**)

This journal is printed on acid-free paper, which exceeds the ANSI Z39.48-1992 specification for permanence of paper and library materials. ♾™
♻ 85% recycled content, including 10% post-consumer fibers.

Journal of Heat Transfer Volume 126, Number 2 APRIL 2004

The ASME Journal of Heat Transfer is abstracted and indexed in the following:

Applied Science and Technology Index, AMR Abstracts Database, Chemical Abstracts, Chemical Engineering and Biotechnology Abstracts (Electronic equivalent of Process and Chemical Engineering), Civil Engineering Abstracts, Compendex (The electronic equivalent of Engineering Index), Corrosion Abstracts, Current Contents, E & P Health, Safety, and Environment, Ei EncompassLit, Engineered Materials Abstracts, Engineering Index, Enviroline (The electronic equivalent of Environment Abstracts), Environment Abstracts, Environmental Engineering Abstracts, Environmental Science and Pollution Management, Fluidex, Fuel and Energy Abstracts, Index to Scientific Reviews, INSPEC, International Building Services Abstracts, Mechanical & Transportation Engineering Abstracts, Mechanical Engineering Abstracts, METADEX (The electronic equivalent of Metals Abstracts and Alloys Index), Petroleum Abstracts, Process and Chemical Engineering, Referativnyi Zhurnal, Science Citation Index, SciSearch (The electronic equivalent of Science Citation Index), Theoretical Chemical Engineering

Transient Heat Transfer Between a Semi-Infinite Hot Plate and a Flowing Cooling Liquid Film

Abram Dorfman
e-mail: abram_dorfman@hotmail.com
Visiting professor,
Department of Electrical Engineering and Computer Science,
University of Michigan Ann Arbor,
Ann Arbor, MI 48109-2122

Heat transfer between a hot, semi-infinite plate and thin liquid film flowing over its surface is considered. As the plate is semi-infinite, the finite cooled portion of the plate and the temperature at the moving film front are time variable. The heat transfer is transient, as opposed to the usual quasi-steady process that exists when the plate is infinite. To investigate the transient heat transfer, solutions describing the temperature fields of the wet and dry portions of the plate are conjugated at the moving film front. The basic characteristics of transient cooling process are found to be governed by a dimensionless parameter named the Leidenfrost number, which is the ratio of the Biot number and the square of the Peclet number. The plate temperatures at the moving front, the film velocity, and the time required to reach the wetting temperature are calculated. [DOI: 10.1115/1.1650389]

Keywords: Analytical, Conjugate, Film Cooling, Heat Transfer, Modeling, Transient

1 Introduction

An understanding of the heat transfer between a hot surface and an adjacent flowing cooling liquid film is important for many applications. Common examples include the controlled rewetting in nuclear water reactors during emergency loss of coolant, thermal control of electronic systems, the quenching of heated surfaces, and space station thermal control.

A number of experimental and theoretical investigations related to this problem have been performed for plates, rods, and tubes. Reviews of studies in this field can be found in several articles, [1–4]. The standard theoretical model is based on two main assumptions: (1) the plate, rod, or tube is infinite; and (2) the velocity of the wet front is constant with time. Under these assumptions, the unsteady heat conduction equation can be transformed into a quasi-steady form by using a coordinate system that moves with the film front. As a result, the temperature of the solid at the moving film front is a constant as well. Solutions of the one- and two-dimensional equations based on the quasi-steady model have been obtained for smooth and grooved surfaces, for adiabatic and heated unwetted regions, for single and composite bodies. Approximate analytical solutions [1,5–10] and numerical solutions using the finite difference method [11], control-volume approach [12], and numerical Fourier inversion [4] have been considered.

Here, this problem is reconsidered with a semi-infinite flat plate. There are some challenges in developing such a model compared with the situation when the plate is infinite. The length of the wet portion of the plate becomes time dependent. Thus, the heat transfer is a transient process, and the temperature of the plate at the moving film front is an unknown function of time. This temperature can be determined by conjugating the solutions describing the temperature fields in the wet and dry plate portions. However, to obtain these solutions, a boundary condition at the film front that is the same as the unknown temperature of the plate at the film front is required.

To transform the variable length of the wet portion to a constant one, a dimensionless variable is used instead of the longitudinal coordinate. To determine the unknown temperature at the moving front, the superposition method as a series is applied. By so doing, the solution of a differential equation with unknown boundary condition reduces to a system of differential equations with known boundary conditions. With this approach, the velocity of the moving film front and the plate temperature at this point are obtained as functions of time. The onset time that is required to reach the wetting temperature at the moving front is calculated as well.

2 Mathematical Development

As shown in Fig. 1, consider a one-dimensional model of a semi-infinite plate of thickness δ. The upper surface of the plate is covered by a moving liquid film of thickness δ_f, the lower surface is adiabatic. The usual basic assumptions in the studies of this topic are as follows [1]: (a) the properties of the plate and the liquid, and the heat transfer coefficient between the plate and the liquid film, h, are constant, (b) heat losses to the surroundings are negligible, and (c) the liquid film is supplied at constant velocity, U.

2.1 Governing Equation. In a moving coordinate frame with the origin at the front of the film, the one-dimensional conduction equation for the plate is

$$k\frac{\partial^2 T}{\partial x^2}-\frac{h}{\delta}(T-T_f)=\rho c\frac{\partial T}{\partial t} \tag{1}$$

Noting that the length of the wet portion at time t is equal to Ut, and that the heat fluxes at the edges of the plate are negligible (assumption b above), the initial and boundary conditions for wet and dry regions are

$$\text{wet:}\quad T(x,t=0)=T_i,\quad T(x=0,t>0)=T_w(t),\quad \frac{\partial T}{\partial x}(x=-Ut,t>0)=0 \tag{2}$$

$$\text{dry:}\quad T(x,t=0)=T_i,\quad T(x=0,t>0)=T_w(t)\quad T(x\to\infty,t>0)=T_i \tag{3}$$

To convert the time dependent length, x, to a constant one, and reduce the number of parameters in Eq. (1), we introduce the dimensionless variables for the wet region

$$\eta=\frac{x}{Ut},\quad z=\frac{h}{c\rho\delta}t,\quad \Theta=\frac{T-T_f}{T_i-T_f},\quad \Theta_w=\frac{T_w-T_f}{T_i-T_f} \tag{4}$$

Contributed by the Heat Transfer Division for publication in the JOURNAL OF HEAT TRANSFER. Manuscript received by the Heat Transfer Division November 20, 2002; revision received November 19, 2003. Associate Editor: G. S. Dulikravich.

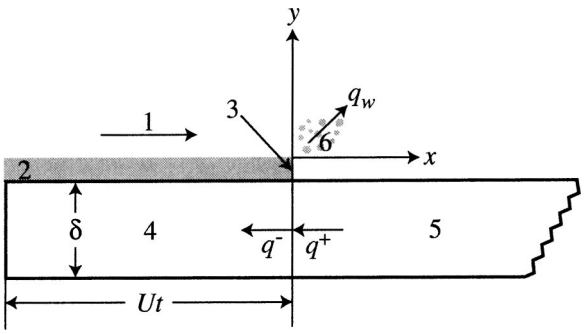

Fig. 1 Scheme of problem: 1-flow direction; 2-liquid film; 3-moving film front; x=0; 4-wet plate region; 5-dry plate region; and 6-sputtering

Applying the dimensionless variables to Eqs. (1) and (2), one gets a governing equation, and initial, and boundary conditions that depend on only one parameter, $\mathrm{Bi}/\mathrm{Pe}^2$.

As shown below, this ratio determines the rate of the transient cooling process. The greater this ratio, the shorter the dimensionless time z required to cool the plate to a given dimensionless temperature. Since cooling by a moving thin film proceeds in boiling transitional state, it seems right to name the ratio $\mathrm{Bi}/\mathrm{Pe}^2$ the Leidenfrost number, Ls, similar to the Leidenfrost point on the boiling curve. Then, Eqs. (1) and (2) become

$$\mathrm{Ls}\frac{\partial^2\Theta}{\partial\eta^2}+z\,\eta\frac{\partial\Theta}{\partial\eta}-z^2\frac{\partial\Theta}{\partial z}-z^2\Theta=0 \tag{5}$$

$$\mathrm{Ls}=\frac{\mathrm{Bi}}{\mathrm{Pe}^2}=\frac{kh}{\rho^2c^2U^2\delta} \tag{6}$$

$$\Theta(\eta,z=0)=1,\quad \Theta(\eta=0,z>0)=\Theta_w(z),$$

$$\frac{\partial\Theta}{\partial\eta}(\eta=-1,z>0)=0 \tag{7}$$

For the dry region where $h=0$, we use Eqs. (1) and (3) in the form

$$\frac{\partial^2\theta}{\partial\xi^2}-\frac{\partial\theta}{\partial z}=0 \tag{8}$$

$$\theta(\xi,z=0)=0,\quad \theta(\xi=0,z>0)=\theta_w(z),\quad \theta(\xi\to\infty,z>0)=0 \tag{9}$$

where $\xi=x(h/k\delta)^{1/2}$, $\theta=(T-T_i)/(T_f-T_i)$, and $\theta_w=(T_w-T_i)/(T_f-T_i)$.

The conjugate boundary condition at the moving front can be derived from an energy balance, as shown in Fig. 1. The heat $q^+(t)$ conducted from the dry region of the plate is slightly absorbed by the evaporation and sputtering $q_w(t)$ at the moving film front, while the majority of the heat $q^-(t)$ is transferred to the wet region of the plate

$$\text{at } x=0,\quad q^+(t)=q^-(t)+q_w(t) \tag{10}$$

The heat absorbed by evaporation and sputtering, $q_w(t)$, is usually neglected. Peng et al. [3] suggest that such an assumption is acceptable only if the plate temperature is lower than the wetting temperature. Consistent with this suggestion, we assume that the heat absorbed by evaporation and sputtering is proportional to the difference between the plate temperature at the moving film front and the wetting temperature

$$q_w(t)=h_w(T_w-T_{\mathrm{wet}}) \tag{11}$$

2.2 Analysis. It follows from Eqs. (5)–(7) and Eqs. (8) and (9), respectively, that $\Theta=f_1(z,\eta,\mathrm{Ls},\Theta_w)$ and $\theta=f_2(z,\xi,\theta_w)$. Consequently,

$$q^-=-k\left(\frac{\partial T}{\partial x}\right)_{x\to0^-}=-k\,\frac{T_i-T_f}{Ut}\left(\frac{\partial f_1}{\partial\eta}\right)_{\eta=0} \tag{12}$$

$$q^+=-k\left(\frac{\partial T}{\partial x}\right)_{x\to0^+}=k(T_f-T_i)\left(\frac{h}{k\delta}\right)^{1/2}\left(\frac{\partial f_2}{\partial\xi}\right)_{\xi=0} \tag{13}$$

If the heat of evaporation and sputtering is neglected, the energy balance, Eq. (10), gives

$$f_2'(z,\theta_w)=\frac{\mathrm{Ls}^{1/2}}{z}f_1'(z,\Theta_w,\mathrm{Ls}) \tag{14}$$

As $\theta_w=1-\Theta_w$, this result indicates that the function $\Theta_w(z)$ depends only on the Leidenfrost number, Ls. In the other case, when the heat absorbed by evaporation and sputtering is significant, Eq. (10) takes the form

$$f_2'(z,\theta_w)=\frac{\mathrm{Ls}^{1/2}}{z}f_1'(z,\Theta_w,\mathrm{Ls})+(h_w/h)\mathrm{Bi}^{1/2}(\Theta_w-\Theta_{\mathrm{wet}}) \tag{15}$$

In this case, Ls and two additional parameters, $(h_w/h)\mathrm{Bi}^{1/2}$ and Θ_{wet}, define $\Theta_w(z)$.

3 Solution of Conjugate Problem

As the boundary conditions given by Eqs. (7) and (9) contain the unknown functions $\Theta_w(t)$ and $\theta_w(t)$, the solutions of Eqs. (5) and (8) are coupled. To decompose this conjugate problem, we use the superposition method in the form of series [13,14]. By using this technique, the conjugate problem with unknown and time dependent boundary conditions reduces to an infinite system of equations with known and constant boundary conditions. This method has been used in the analysis of non-isothermal and conjugate heat transfer problems [15,16].

3.1 Reduction to a System of Independent Equations. The solution of Eqs. (5) and (8) are presented in the form of series

$$\Theta=G_0(\eta,z)\Theta_w+G_1(\eta,z)\frac{d\Theta_w}{dz}+G_2(\eta,z)\frac{d^2\Theta_w}{dz^2}+\ldots$$

$$+G_n(\eta,z)\frac{d^n\Theta_w}{dz^n}+\ldots \tag{16}$$

$$\theta=H_0(\xi,z)\theta_w+H_1(\xi,z)\frac{d\theta_w}{dz}+H_2(\xi,z)\frac{d^2\theta_w}{dz^2}+\ldots$$

$$+H_n(\xi,z)\frac{d^n\theta_w}{dz^n}+\ldots \tag{17}$$

Substituting Eqs. (16) and (17) into Eqs. (5) and (8) yields two infinite systems of equations with constant initial and boundary conditions, given by

$$\mathrm{Ls}\frac{\partial^2G_n}{\partial\eta^2}+\eta z\frac{\partial G_n}{\partial\eta}-z^2\frac{\partial G_n}{\partial z}-z^2G_n-z^2G_{n-1}=0,\quad G_{-1}=0$$

$$G_0(\eta,z=0)=1,\quad G_n(\eta,z=0)=0,\quad G_0(\eta=0,z)=1, \tag{18}$$

$$G_n(\eta=0,z)=0,\quad \frac{\partial G_n}{\partial\eta}(\eta=-1,z)=0$$

$$\frac{\partial^2H_n}{\partial\xi^2}-\frac{\partial H_n}{\partial z}-H_{n-1}=0,\quad H_{-1}=0$$

$$H_0(\xi,z=0)=0,\quad H_n(\xi,z=0)=0,\quad H_0(\xi=0,z)=1, \tag{19}$$

$$H_n(\xi=0,z)=0, \quad H_n(\xi\to\infty,z)=0$$

In formulating the initial conditions, we assume that at time $t=0$, the front of the film is at the edge of the semi-infinite plate.

3.2 Solution of Eqs. (18) and (19). The solutions of Eq. (19), which is linear, are given by the error functions [13]. The first two solutions ($n=0$, $n=1$) are

$$H_0(\xi,z)=1-\mathrm{erf}\left(\frac{\xi}{2z^{1/2}}\right)=\mathrm{erfc}\left(\frac{\xi}{2z^{1/2}}\right) \tag{20}$$

$$H_1(\xi,z)=\frac{\xi^2}{2}\mathrm{erfc}\left(\frac{\xi}{2z^{1/2}}\right)-\xi\left(\frac{z}{\pi}\right)^{1/2}\exp\left(-\frac{\xi^2}{4z}\right) \tag{21}$$

For $n>1$, the solution are [13]

$$H_n=\sum_{i=0}^{n}\frac{(-z)^{n-i}}{(n-i)!}S_i, \quad S_i(\xi,z=0)=0,$$

$$S_i(\xi=0,z)=\frac{z^i}{i!}, \quad S_i(\xi\to\infty,z)=0 \tag{22}$$

where $S_i(\xi,z)$ are functions satisfying Eq. (19) for $n=0$, $H_{-1}=0$, and Eqs. (22).

Equation (18), which is linear and has variable coefficients, is solved with the approximate integral method [14]. The appropriate forms of the solutions that satisfy the initial and boundary conditions given by Eqs. (18) are

$$G_0(\eta,z)=1+\lfloor(\eta^2/2)+\eta\rfloor A_0(z)+\lfloor(\eta^3/3)-\eta\rfloor B_0(z),$$
$$A_0(0)=B_0(0)=0 \tag{23}$$

$$G_n(\eta,z)=\lfloor(\eta^2/2)+\eta\rfloor A_n(z)+\lfloor(\eta^3/3)-\eta\rfloor B_n(z),$$
$$A_n(0)=B_n(0)=0 \tag{24}$$

To determine the unknown functions $A_0(z)$ and $B_0(z)$, the two integral forms of Eq. (18) are used. Denoting the left side of Eq. (18) as $F_n(\eta,z)$, one gets these forms as

$$\int_{-1}^{0}F_0(\eta,z)d\eta=0 \qquad \int_{-1}^{0}F_1(\eta,z)\eta d\eta=0 \tag{25}$$

Substituting Eq. (23) into Eq. (18) and then into Eq. (25) for $F_0(\eta,z)$ yields two ordinary differential equations, which after solving for derivatives, lead to the system

$$\frac{dA_0}{dz}=A_0(z)\left(-\frac{28\mathrm{Ls}}{z^2}+\frac{14}{3z}-1\right)+B_0(z)\frac{16}{3}\left(\frac{\mathrm{Ls}}{z^2}-\frac{1}{z}\right)+28$$
$$\frac{dB_0}{dz}=A_0(z)10\left(-\frac{2\mathrm{Ls}}{z^2}+\frac{1}{3z}\right)-B_0(z)\left(\frac{20\mathrm{Ls}}{z^2}+\frac{11}{3z}+1\right)+20 \tag{26}$$

Applying the same procedure for $G_1(\eta,z)$, (i.e., substituting Eq. (24) with $n=1$ into Eq. (18) and then into Eq. (25) for $F_1(\eta,z)$) yields the same system given by Eqs. (26), but with additional terms $28z$ and $20z$ for dA_1/dz and dB_1/dz, respectively.

The system given by Eq. (26) with the conditions given by Eq. (23) was solved numerically by the Runga-Kutta method. Because of the singularity at $z=0$, the Taylor series expansions were employed for small z. The coefficients are

$$a_k=-\frac{1}{12\mathrm{Ls}}[(k-3)a_{k-1}+a_{k-2}]+\frac{1}{15\mathrm{Ls}}[(k-4)b_{k-1}+b_{k-2}]$$
$$b_k=\frac{1}{4\mathrm{Ls}}[(k-1)a_{k-1}+a_{k-2}]-\frac{1}{20\mathrm{Ls}}[(7k-8)b_{k-1}+7b_{k-2}] \tag{27}$$

These formulas are used for $n\geq 4$. For Eq. (18), the first coefficients are: $a_1=a_3=b_1=b_2=0$, $a_2=1/\mathrm{Ls}$, $b_3=1/2\mathrm{Ls}^2$. They also are of use for $A_1(z)$ and $B_1(z)$, where $a_3=1/\mathrm{Ls}$.

Similar computations give $A_n(z)$ and $B_n(z)$ for $n\geq 2$ by solving integral equation

$$\int_{-1}^{0}F_n(\eta,z)\eta^n d\eta=0 \tag{28}$$

3.3 Conjugating the Solutions at the Moving Front. Differentiating Eqs. (16) and (17), and setting $\eta=0$ in the first result and $\xi=0$ in the second one, gives the heat fluxes

$$q^-(t)=-\frac{k(T_i-T_f)}{Ut}\left[\left(\frac{\partial G_0}{\partial\eta}\right)_{\eta=0}\Theta_w+\left(\frac{\partial G_1}{\partial\eta}\right)_{\eta=0}\frac{d\Theta_w}{dz}+\left(\frac{\partial G_2}{\partial\eta}\right)_{\eta=0}\frac{d^2\Theta_w}{dz^2}+\ldots\right] \tag{29}$$

$$q^+(t)=k(T_f-T_i)\left(\frac{h}{k\delta}\right)^{1/2}\left[\left(\frac{\partial H_0}{\partial\xi}\right)_{\xi=0}\theta_w+\left(\frac{\partial H_1}{\partial\xi}\right)_{\xi=0}\frac{d\theta_w}{dz}+\left(\frac{\partial H_2}{\partial\xi}\right)_{\xi=0}\frac{d^2\theta_w}{dz^2}+\ldots\right] \tag{30}$$

Considering the first two terms, and applying Eqs. (4), (20), (21), (23), and (24) yields

$$q^-(t)=\frac{k(T_i-T_f)}{Ut}\left[g_0\Theta_w+(g_1-g_0)z\frac{d\Theta_w}{dz}\right] \tag{31}$$

$$q^+(t)=k(T_i-T_f)\left(\frac{h}{k\delta}\right)^{1/2}\left[\frac{\theta_w}{(\pi z)^{1/2}}-\left(\frac{z}{\pi}\right)^{1/2}\frac{d\theta_w}{dz}\right] \tag{32}$$

where $g_0(z)=A_0(z)-B_0(z)$ and $g_1(z)=[A_1(z)-B_1(z)]/z$.

Substituting the components of the heat balance into Eq. (10), one obtains an ordinary differential equation, which determines the plate temperature at the moving front

$$[z+(g_1-g_0)(z\pi\mathrm{Ls})^{1/2}]\frac{d\Theta_w}{dz}+\Theta_w\left[1+g_0\left(\frac{\pi\mathrm{Ls}}{z}\right)^{1/2}+\frac{h_w}{h}(z\pi\mathrm{Bi})^{1/2}\right]-\left[1+\frac{h_w}{h}(z\pi\mathrm{Bi})^{1/2}\Theta_{\mathrm{wet}}\right]=0 \tag{33}$$

The solution of Eq. (33) must satisfy the boundary condition at the beginning of the cooling

$$\Theta_w(z=0)=1 \tag{34}$$

If the first term on the left side of Eq. (33) is assumed to be relatively small, the fist approximation to the solution can be derived as

$$\Theta_w=\frac{1+(h_w/h)(z\pi\mathrm{Bi})^{1/2}\Theta_{\mathrm{wet}}}{1+g_0(\pi\mathrm{Ls}/z)^{1/2}+(h_w/h)(z\pi\mathrm{Bi})^{1/2}} \tag{35}$$

3.4 Onset Time and Film Front Velocity. Setting in Eq. (35) $\Theta_w=\Theta_{\mathrm{wet}}$, one gets the onset time, z_{wet}, defining the dimensionless time required to cool the plate at the film front to the wetting temperature

$$\Theta_{\mathrm{wet}}=\frac{1}{1+g_0(z_{\mathrm{wet}})(\pi\mathrm{Ls}/z_{\mathrm{wet}})^{1/2}} \tag{36}$$

This result matches with Eq. (35) for $h_w=0$. Hence, the onset time depends on the dimensionless wetting temperature Θ_{wet} and the Leidenfrost number $Ls=\mathrm{Bi}/\mathrm{Pe}^2$, but does not depend on the ratio (h_w/h). Thus, Eq. (36) is of use whether the heat absorbed by evaporation and sputtering is taken into account or not.

Due to the evaporation and sputtering, the film front velocity U_w is less than the supplying velocity U. In a time Δt, the film advances by a length that is $\Delta x=(U-U_w)\Delta t$ shorter than it would be without evaporation and sputtering. The average amount

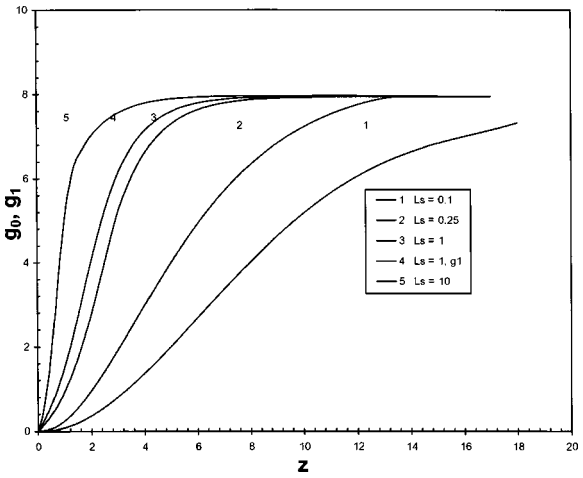

Fig. 2 Functions $g_0(z)$ and $g_1(z)$

of heat absorbed per second is $\delta_f \rho_f h_L(\Delta x/\Delta t) = \delta_f \rho_f h_L(U - U_w)$. Equation (11) corresponds to this heat transfer. Thus, we have

$$\delta_f \rho_f h_L(U - U_w) = \frac{h_w \delta}{z} \int_0^z (T_w - T_{\text{wet}}) \tag{37}$$

Noting that $m = \delta_f \rho_f U$ is the fluid flow rate, we obtain

$$\frac{U - U_w}{U} = \frac{h_w \delta}{m h_L}(T_i - T_f)\left(\frac{1}{z}\int_0^z \Theta_w dz - \Theta_{\text{wet}}\right) \tag{38}$$

4 Numerical Results and Discussion

4.1 Plate Temperature at the Moving Front. The function $g_0(z)$ calculated by numerical solution of Eq. (26) is plotted in Fig. 2 for four values of Ls, ranging between 0.1 and 10. These data can be used to compute the plate temperature at the moving film front as a function of time. For the case of negligible heat of evaporation and sputtering, the predictions of Eq. (35) are given in Fig. 3. The form of the curve $\Theta_w(z)$ strongly depends on the Leidenfrost number, Ls. As Ls is increased, the plate cools faster, a smaller $(\Theta_w)_{\min}$ is obtained, and the time $z_{\min}$ required to reach $(\Theta_w)_{\min}$ decreases. As shown in Fig. 3, the relationship between $(\Theta_w)_{\min}$ and $z_{\min}$ is close to the linear function

$$(\Theta_w)_{\min} = 0.036 z_{\min} - 0.03 \tag{39}$$

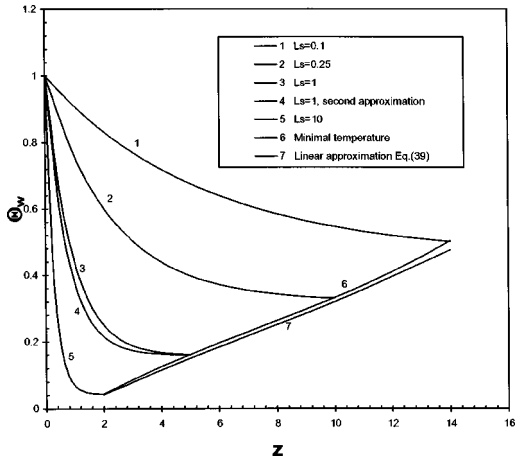

Fig. 3 Dimensionless plate temperature at the moving film front as a function of dimensionless time

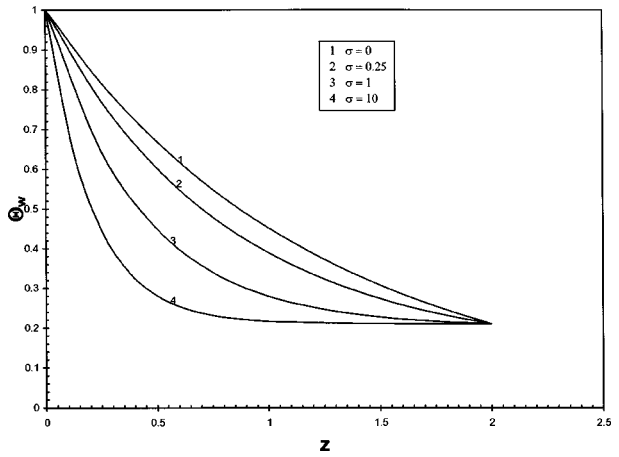

Fig. 4 Effect of evaporation and sputtering on dimensionless plate temperature at the moving film front, Ls=1, $\Theta_{\text{wet}}=0.21$, $z_{\text{wet}}=2$

At the same time, the analysis shows that $z_{\min}$ may be related to Ls number by an approximate quadratic function given by

$$z_{\min} = 5 - 6\log(\text{Ls}) + 3\log^2(\text{Ls}) \tag{40}$$

Since Eq. (36) is the same as Eq. (35) in the case of $h_w = 0$, the results shown in Fig. 3 can also be used to establish the relationship between Θ_{wet} and z_{wet}. However, since we consider the wetting temperature as a given value, this relationship is useful only if $\Theta_{\text{wet}} \geqslant (\Theta_w)_{\min}$. In this case, Eqs. (39) and (40) could be used.

It should be noted that we only consider the transient part of the wetting process when the plate temperature at the moving front is higher than the wetting temperature. Although the developed model does not describe the part of the process with practically constant wetting temperature, this model consists of a dry semi-infinite plate portion with initial high temperature T_i. Therefore, in this case, the plate temperature at the moving front starts to increase after it reaches the minimum value, and consistent with condition (3), ultimately in the limit as $t \to \infty$ becomes equal to the initial plate temperature.

4.2 Effect of Evaporation and Sputtering. The effect of the evaporation and sputtering is shown in Fig. 4 for Ls=1, $\Theta_{\text{wet}}=0.21$, and different value of $\sigma = (h_w/h)\text{Bi}^{1/2}$. According to Eq. (36), z_{wet} does not depend on σ, and all the curves thus have the same end point $\Theta_{\text{wet}}(z_{\text{wet}}=2)=0.21$. The results shown in Fig. 4 indicate that the evaporation and sputtering significantly affect the form of the cooling curve $\Theta_w = f(z,\sigma)$. At the same time, it follows from these results that the onset time, i.e., the time required to cool the hot surface to the wetting temperature, depends only on the Leidenfrost number Ls and the dimensionless wetting temperature Θ_{wet}. Thus, if the assumption of proportionality in Eq. (11) is correct, the onset time is independent of h_w, as in the case when the heat of evaporation and sputtering is negligible.

Experimental studies of wetting processes are usually based on a constant flow rate related to $1/U_w$ and the initial plate temperature T_i. Using such experimental data, in principal Eq. (38) could be used for estimating the heat transfer coefficient of evaporation and sputtering h_w. To show this, we rewrite Eq. (38) as

$$\left(1 - \frac{U_w}{U}\right)\frac{m h_L}{(T_i - T_f)(hk\delta)^{1/2}} = \frac{h_w}{h}\text{Bi}^{1/2}\left(\frac{1}{z}\int_0^z \Theta_w dz - \Theta_{\text{wet}}\right) \tag{41}$$

From Eq. (35), the dimensionless temperature Θ_w (and hence the integral in (41)) are a function of Ls, $\sigma = (h_w/h)\text{Bi}^{1/2}$, the wetting temperature, Θ_{wet}, and the dimensionless time, z. If the wetting

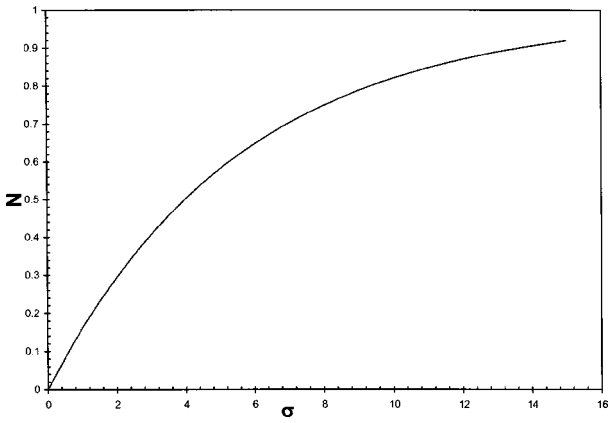

Fig. 5 An example of relationship between dimensionless parameters *N* (Eq. (41)) and $\sigma=(h_w/h)\mathrm{Bi}^{1/2}$ calculated on the basis of Fig. 4

temperature is reached, and $z=z_{\mathrm{wet}}$, then the integral in Eq. (41) depends only on Ls, σ, and Θ_{wet}, because the onset time, z_{wet}, depends only on Ls and Θ_{wet} (see Eq. (36)). Thus, in that case, the whole expression on the right hand side of Eq. (41), which we denote by *N*, is a function of the same three parameters, Ls, σ, and Θ_{wet}. If two of them, namely Ls and Θ_{wet}, are known from experimental data, then the relationship $N=f(\sigma)$ can be obtained using Eqs. (35) and (36). As an example, such a dependence calculated on the basis of Fig. 4 is presented in Fig. 5. With the relationship $N=f(\sigma)$ and using the experimental data for determining the left hand side of Eq. (41),

$$N=\left(1-\frac{U_w}{U}\right)\frac{mh_L}{(T_i-T_f)(hk\delta)^{1/2}}, \tag{42}$$

and with $\sigma=(h_w/h)\mathrm{Bi}^{1/2}$ the heat transfer coefficient, h_w could be obtained.

However, identification of Heat Transfer Coefficient is ill-posed Inverse Heat Transfer problem and, as such, it should be solved by special regularized or iterative with regularizing methods, for instance, [17–19].

4.3 Uncertainty and Improvement. The results presented demonstrate the feasibility of the suggested model with a semi-infinite plate. These results should be considered as a first approximation solution of the conjugate problem given by Eqs. (5)–(10). To estimate uncertainty in these results, the second approximation is obtained by solving Eq. (33). If we denote the coefficients of Eq. (33) as P_1, P_2, and P_3, its solution is

$$\Theta_w=\exp\left(-\int\frac{P_2}{P_1}dz\right)\left[\int\exp\left(\int\frac{P_2}{P_1}dz\right)\left(-\frac{P_3}{P_1}\right)dz+C\right]. \tag{43}$$

The coefficient P_1 contains the function $g_1(z)=[A_1(z)-B_1(z)]/z$ where $A_1(z)$ and $B_1(z)$ are found numerically solving a system of equations similar to Eqs. (26),

$$\frac{dA_1}{dz}=A_1(z)\left(-\frac{28\mathrm{Ls}}{z^2}+\frac{14}{3z}-1\right)+B_1(z)\frac{16}{3}\left(\frac{\mathrm{Ls}}{z^2}-\frac{1}{z}\right)+28z+28 \tag{44}$$

$$\frac{dB_1}{dz}=A_1(z)10\left(-\frac{2\mathrm{Ls}}{z^2}+\frac{1}{3z}\right)-B_1(z)\left(\frac{20\mathrm{Ls}}{3z^2}+\frac{11}{3z}+1\right)+20z+20$$

The numerical results have been obtained for Ls=1. The effect of evaporation and sputtering was not taking into account. Because of the singularity at $z=0$, Taylor series are employed for small *z* (see Eq. (27)). The function $g_1(z)$ is given in Fig. 2. The constant *C* in Eq. (44) is estimated by satisfying the boundary condition given by Eq. (34). According to coefficients given by Eq. (27), the terms of Eq. (44) are on the order of: $g_0\sim z^2$, $g_1\sim z$, $P_1\sim z$, $P_2\sim 1$, $P_3\sim -1$ when $z\sim 0$. Hence, $\Theta_w\sim 1$ and $C=0$.

The function $\Theta_w(z)$ (obtained numerically using "Mathcad 8 Professional") is presented in Fig. 3. For small and large values of the dimensionless time *z*, the differences between the first and second approximations are minor. This is due to the small values of the first term of Eq. (33). Although for small *z*, the derivatives $d\Theta_w/dz$ are relatively large (see Fig. 3), the values of the other factor in the first term, which is proportional to *z*, are small. For large values of *z*, the first term of Eq. (33) is small because of small derivatives $d\Theta_w/dz$.

Thus, the greatest deviation between the two approximations corresponds to mean values of *z*. For the considered case, Ls=1, this difference is on the order of 15–20% in the range of z~0.5–1.5 (Table 1). Due to the form of the curves in Fig. 3, one may expect that the deviations are greater for Ls<1 and smaller for Ls>1.

To get even more accurate results, one would numerically solve the conjugate problem given by Eqs. (5)–(10) for the whole plate from $\eta=-1$ to $\xi\to\infty$ using a special MathSoft's. In this case, the temperature fields in the two areas described by different differential equations are compute continuously (see for example, [20]).

5 Conclusion

The heat transfer between a semi-infinite hot plate and a cooling thin liquid film flowing over it has been investigated as a transient problem. Previous work on this topic has focused on infinite surfaces to avoid the time dependency. In this study, the finite portion of the plate covered by the film and the dry portion of the plate are studied separately, and the corresponding solutions are conjugated using an energy balance at the moving film front. To account for the effect of evaporation and sputtering in the energy balance, the heat absorbed by these processes is assumed to be proportional to the difference between the plate temperature at the moving front and the wetting temperature.

To convert the time varying length of the wet portion to a constant, and minimize the number of parameters in the governing equations, dimensionless variables have been used. By applying the superposition method in the form of a series, the conjugate problem with an unknown and variable plate temperature at the moving front is reduced to infinite system of equations with known boundary conditions. An approximate solution is derived based on the first two terms of the series containing the plate temperature at the moving film front, and the first derivative of this temperature with respect to time.

Table 1 Comparison between the first and second approximations

	z	0	0.4	0.8	1.2	1.6	2.0	2.8	4.8
1st approximation	Θ_w	1.0	0.691	0.519	0.388	0.289	0.237	0.195	0.172
2nd approximation	Θ_w	1.0	0.633	0.460	0.324	0.246	0.209	0.185	0.172

It is shown that:

1. When the heat of evaporation and sputtering is negligible, the basic characteristics of the transient cooling process are determined by a dimensionless parameter which, similar to Leidenfrost point, is named the Leidenfrost number, $\mathrm{Ls}=\mathrm{Bi}/\mathrm{Pe}^2$. The larger this number, Ls, the faster the plate cools, and the lower the smallest plate temperature at the moving front $(\Theta_w)_{\min}$, and the shorter the time $z_{\min}$ required to reach it.

2. In the case when the heat of evaporation and sputtering is taken into account, the function $\Theta_w=f(z)$ depends on the Leidenfrost number, Ls, and two additional dimensionless parameters, $\sigma=(h_w/h)\mathrm{Bi}^{1/2}$ and Θ_{wet}.

3. Applying an assumption of proportionality (see Eq. (11)) between the heat absorbed by evaporation and sputtering, and the temperature difference (T_w-T_{wet}), we show that this heat, $q_w(t)$, affects the form of the cooling curve, $\Theta_w=f(z)$, but that (see Fig. 4) the onset time depends only on the Leidenfrost number, Ls, and dimensionless wetting temperature Θ_{wet}. As such, the onset time is independent of h_w, as in the case when the heat of evaporation and sputtering is negligible.

4. The results presented demonstrate the feasibility of the developed model with a semi-infinite plate. However, these results should be considered as a first approximation to the solution of the conjugate problem formulated in Eqs. (5)–(10). As an example of how to improve the result, the second approximation has been calculated for the case when Ls=1. More accurate results may be obtained through numerical solution of the conjugate problem given by Eqs. (5)–(10) for the whole plate using a special MathSoft's.

Nomenclature

$A_n(z)$, $B_n(z)$ = functions of dimensionless time, Eqs. (23), (24)
Bi = $h\delta/k$=Biot number
c = specific heat, J/kg K
$G_n(\eta,z)$, $H_n(\eta,z)$ = coefficients of series, Eqs. (16), (17)
$g_0(z)$, $g_1(z)$ = functions of dimensionless time, Eqs. (32), (33)
h, h_w = convective and sputtering heat transfer coefficients, Eq. (1) and Eq. (11), W/m^2 K
h_L = liquid latent heat, J/kg
k = conductivity of the plate material, W/m K
Ls = $kh/\delta(c\rho U)^2=\mathrm{Bi}/\mathrm{Pe}^2$=Leidenfrost number, Eq. (6)
m = flow rate, kg/m
N = dimensionless parameter Eq. (42)
Pe = $U\delta/\alpha$=Peclet number
q = heat flux, W/m^2
q_w = heat flux absorbed by evaporation and sputtering, W/m^2, Eq. (10)
T, T_{f} = plate and liquid film temperatures, K
T_{wet} = wetting temperature, K
t = time, s
U = supplied film velocity, m/s
U_w = average film front velocity, m/s
x = longitudinal coordinate, m
z = $(h/c\rho\delta)t$=dimensionless time, Eq. (4)
z_{wet} = onset time required to cool plate to wetting temperature, Eq. (36)
α = thermal diffusivity, m^2/s
δ, δ_f = plate and film thicknesses, m
η = x/Ut=dimensionless coordinate for the wet portion of the plate, Eq. (4)
Θ = $(T-T_f)/(T_i-T_f)$=dimensionless temperature of the wet portion of the plate, Eq. (4)
θ = $(T-T_i)/(T_f-T_i)$=dimensionless temperature of the dry portion of the plate, Eq. (8)
ξ = $x(h/k\delta)^{1/2}$=dimensionless coordinate for the dry portion of the plate, Eq. (8)
ρ, ρ_f = plate and film densities, kg/m^3
σ = $(h_w/h)\mathrm{Bi}^{1/2}$=dimensionless parameter Eq. (41)

Subscripts

f, i, w, min = liquid film, initial, moving film front, minimum

Superscripts

$-$, $+$ = wet and dry portions at the moving film front, Eq. (10)

References

[1] Duffey, R. B., and Porthouse, D. T. C., 1973, "The Physics of Rewetting in Water Reactor Emergency Core Cooling," Nucl. Eng. Des., **25**, pp. 379–394.
[2] Thomas, R. M., 1988, "Methods for Calculating the Conduction-Controlled Rewetting of a Cladded Rod," Nucl. Eng. Des., **110**(1), pp. 1–16.
[3] Peng, X. F., Peterson, G. P., and Wang, B. X., 1992, "The Effect of Plate Temperature on the Onset of Wetting," Int. J. Heat Mass Transfer, **35**(6), pp. 1605–1613.
[4] Satapathy, A. K., and Sahoo, R. K., 2002, "Analysis of Rewetting of an Infinite Tube by Numerical Fourier Inversion," Int. Commun. Heat Mass Transfer, **29**(2), pp. 279–288.
[5] Yamanouchi, A., 1968, "Effect of Core Spray Cooling in Transient State After Loss-of-Coolant Accident," J. Nucl. Sci. Technol., **5**, pp. 547.
[6] Blair, J. M., 1975, "An analytical Solution to a Two-Dimensional Model of Hot Dry a Rod," Nucl. Eng. Des., **32**, pp. 159–170.
[7] Elias, E., and Yadigaroglu, G., 1977, "A General One-Dimensional Model for Conduction-Controlled Rewetting of a Surface," Nucl. Eng. Des., **42**, pp. 185–186.
[8] Olek, S., 1988, "On the Two-Region Rewetting Model With a Step Change in the Heat Transfer Coefficient," Nucl. Eng. Des., **108**, pp. 315–322.
[9] Peng, X. F., and Peterson, G. P., 1991, "Analytical Investigation of the Rewetting Characteristics of Heated Plates With Grooved Surfaces," AIAA Paper No. 91-4004.
[10] Chan, S. H., and Zhang, W., 1994, "Rewetting Theory and the Dryout Heat Flux of Smooth and Grooved Plates With a Uniform Heating," ASME J. Heat Transfer, **116**, pp. 173–179.
[11] Thompson, T. S., 1972, "An Analysis of the Wet-Side Heat Transfer Coefficient During Rewetting of a Hot Dry Patch," Nucl. Eng. Des., **22**, pp. 212–214.
[12] Raj, V. V., and Pate, A. W., 1986, "Analysis of Conduction Controlled Rewetting of Hot Surfaces Based on Two-Region Model," *Proceedings of 8th International Heat Transfer Conference*, IP-20, **4**, Chang L. Tien, V. P. Cary, J. K. Ferrell, eds., Hemisphere Pub. Corp., Washington, pp. 1987–1992.
[13] Carslaw, H. S., and Jaeger, J. C., 1986, *Conduction of Heat in Solids*, 2nd ed., Clarendon Press, Oxford.
[14] Schlichting, H., 1968, *Boundary Layer Theory*, 6th ed., McGraw-Hill, New York.
[15] Dorfman, A. S., 1985, "A New Type of Boundary Condition in Convective Heat Transfer Problems," Int. J. Heat Mass Transfer, **28**(6), pp. 1197–1203.
[16] Dolinskiy, A. A., Dorfman, A. S., and Davydenko, B. V., 1989, "Conjugate Heat and Mass Transfer in Continuous Processes of Convective Drying," Int. J. Heat Mass Transfer, **34**(11), pp. 2883–2889.
[17] Matsevity, Y. M., and Moultanovsky, A. V., 1984, "Statistical Identification of Local Heat Transfer Parameters," Consultants Bureau, New York, pp. 1298–1300.
[18] Morozov, V. A., 1984, *Methods for Solving Incorrectly Posed Problems*, Springler-Verlag, New York.
[19] Matsevity, Y. M., Moultanovsky, A. V., and Timchenko, V., 1992, "Modeling of Thermal Processes and Identification of Local Heat Transfer Parameters With Help of an Adaptive Iterative Filter," Consultants Bureau, New York, pp. 71–78.
[20] Patankar, S. V., 1980, *Numerical Heat Transfer and Fluid Flow*, Heisphere Publishing Corporation, McGraw-Hill, New York.

Francis C. Wessling
e-mail: wesslif@uah.edu

Marlow D. Moser

James M. Blackwood

Department of Mechanical and Aerospace Engineering,
The University of Alabama in Huntsville,
301 Sparkman Dr. TH N270,
Huntsville, AL 35899

Subtle Issues in the Measurement of the Thermal Conductivity of Vacuum Insulation Panels

Vacuum insulation panels have values of thermal conductivity that are extremely low (~4 mW/m·K) compared to the thermal conductivity of most common insulations. Typical ASTM test methods are not designed for testing these very low thermal conductivity materials. An apparatus has been built and tested that uses a thin foil heater and vacuum chamber to test vacuum insulation panels. Several different measurement configurations are studied to determine the effects of the parasitic heat losses. The differences between the ASTM standards and this technique are described and the rationale explained. A new ASTM technique for vacuum panels appears to be needed. [DOI: 10.1115/1.1683674]

Introduction

Vacuum insulation panels are used as insulation in many applications, such as a low temperature passive carrier called LoTEC© [1]. These insulation panels have a core made of fiber reinforced, carbon-opacified, silica aerogel of densities in the range of 150 kg/m^3 to 170 kg/m^3. A getter and desiccant material are also added to the core. This core is then vacuum wrapped in a thin metallized polyester bag that is 0.08mm thick. The core pressure is approximately 0.13 Pa (10^{-3} Torr). There are two heat transfer modes through vacuum insulation panels, conduction and radiation. Aerogel has a low thermal conductivity because of its structure and fine particle size. Chemical vapor infiltration of carbon decreases thermal radiation. Low gas pressure makes gas conduction negligible [2]. This produces a vacuum insulation panel with a very low thermal conductivity ($\sim 10^{-3}$ W/m·K) that is highly dependent on the composition.

The ASTM C 177 [3] test method for measuring thermal conductivity uses a guarded-hot-plate. This method does not take into account the conduction of vacuum insulation panels through the metallized wrapping. Measurements indicate that the heat conduction through the metallized wrap is approximately 6 percent of the total for vacuum panels of the size tested. Hunt et al. [4] show that it can be as much as 25 percent for a smaller size panel. The actual percentage depends on the dimensions and core material of the panel.

The ASTM C 518 [5] test method makes use of measuring the heat flow through an additional standard insulation with a known thermal conductivity. This introduces an uncertainty that could be significant in the case of vacuum insulation panels. Also, all insulations that can be used as standards have a thermal conductivity two orders larger than the thermal conductivity of vacuum insulation panels. This requires extremely accurate temperature measurements.

A method that may be accurate enough for vacuum insulation panels is ASTM C 745 [6]. This method uses a boil-off calorimeter to measure heat flow through the test specimen. Similar to the others, this does not take into account the heat conduction through the metallized wrapping.

An alternative to these methods is the thin-heater test method, ASTM C 1114 [7]. Although similar to our proposed method, this method has several weaknesses if used to test vacuum insulation panels. Namely, no vacuum is used leading to convective heat transfer that is significant and difficult to accurately characterize. Also, the difference in temperature suggested by this method (2 to 5 K) leads to extremely small heat flows with even large vacuum insulation panels.

Therefore, a modified version of the thin heater apparatus is proposed which takes into account the significant heat flows generally considered insignificant by ASTM test methods. The tests are conducted in a vacuum bell jar with pressure on the order of 1.3 mPa (10 μTorr). The distance between the insulation panels and the vacuum chamber wall is approximately 0.5 m. The mean free path of air at a temperature of 298K and a pressure of 1.3 mPa is 5.3 m. Consequently, the air in the chamber is in the free molecular flow regime. Conduction through the air is inconsequential under these conditions being approximately 0.3 percent of the energy supplied to the panel. The heater is actively controlled such that the temperature is typically the same as the temperature of the vacuum chamber walls hereafter referred to as the chamber wall temperature. This reduces the effects of radiation from the sides and conduction in any temperature sensor/heater wires. Also, the temperature difference between the heater and cold plates is typically 50 K. This raises the total power such that it is large compared to the parasitic losses. Without care, the parasitic losses, which are temperature dependent, can be as large as 0.5 W while the total power is 1.4 to 7.0 W. Larger total power also reduces the uncertainty of the power measurement.

This apparatus is to be used to compare measured thermal conductivities with the manufacturer's reported values; to determine the effects of aging, and to compare panels from different manufacturers. The test is set up to include the effect of membrane conduction on panel performance. The apparatus and data reduction methodology are presented along with an uncertainty analysis. The effect of several different configurations and operating conditions are presented to show their effect on parasitic losses.

Apparatus

The test apparatus consists of a heater sandwiched by two insulation samples, which in turn are sandwiched by thick aluminum cold plates. See Figs. 1, 2, and 3. The temperatures of the heater and cold plates are measured with several RTD sensors. All sensors are read by an IOtech TempScan/1100 which communicates with a computer via a GPIB serial interface. A Labview program collects and reduces the data, which is then displayed on the screen and stored to disk.

The thin heater consists of two Minco HK5532 30.48 cm $\times$ 22.86 cm Kapton thermal foil heaters taped together thus creating a heating surface of 30.48 cm $\times$ 45.72 cm. The heaters have resistances of 152.8 and 156.8 Ω. The resistance of the heaters is measured by a Fluke Voltmeter. The resistance of the heaters is constant over the temperature range of these tests. The heaters are

Contributed by the Heat Transfer Division for publication in the JOURNAL OF HEAT TRANSFER. Manuscript received by the Heat Transfer Division May 9, 2003; revision received January 12, 2004. Associate Technical Editor: A. F. Emery.

Fig. 1 Insulation panels are shown between the cold plates. The thin heater is sandwiched between the panels. The entire assembly is suspended in the vacuum chamber. Tubes covered by radiation shielding supply coolant to the cold plates.

connected in parallel so that the current required by the experiment is in the mid-range of the power supply. The power is controlled by an Omega CN76000 PID controller. The power is supplied by a Hewlett Packard E3617A DC power supply. The control voltage from the PID controller is measured by an IOtech TempScan/1100 and is converted to the voltage sent to the heaters. The total power supplied to the heaters is calculated by $P = V^2/R$ where P is the power to the heater, V is the voltage supplied to the heater and R is the resistance of the heater. The power is smoothed over time by a Labview program. A total of six Minco S3238PE platinum thermal ribbons (3 on each side) are

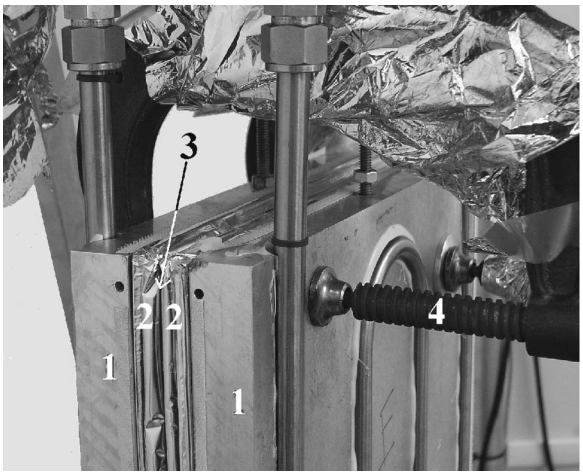

Fig. 2 Close-up of top of test assembly: (1) 25.4 mm aluminum cold plates; (2) 12.5 mm vacuum insulation panels; (3) 0.16 mm thin foil heater between the vacuum insulation panels; and (4) C-clamps on four corners to hold assembly together.

Fig. 3 Top corner of test assembly with thin threaded rod replacing C-clamp

placed on the heater to measure the temperature. The PID controller uses one RTD in the center of the heater foil to sense the heater temperature and thereby supply the correct power. The other five are read by the computer and averaged to give the temperature of the heater T_h.

One 30.48 cm×45.72 cm×1.27 cm piece of aerogel is placed on each side of the heater. Each piece of aerogel is held in place by two 30.48 cm×45.72 cm×2.54 cm aluminum cold plates. A Neslab ULT-80 chiller is used to cycle coolant through tubing embedded in the aluminum plates. Three Minco S308PD platinum RTDs are placed on the center line of each cold plate such that they measure the surface temperature next to the insulation. These are recorded and averaged to give the cold plate temperature, T_c. The assemblies are clamped to each other at their corners using either steel C-clamps (Fig. 2) or small diameter (2.0 mm) stainless steel threaded rods (Fig. 3). The clamping pressure is approximately 27.5 kPa. This compresses the vacuum insulation panels approximately 0.25 mm. A temperature change of 50 K changes the clamping pressure due to thermal expansion and contraction by less that 3 percent.

The dimensions of the aerogel panels are measured using calipers to give the area, A. The entire thickness of the aluminum plates, heater, and aerogel panels is measured at the four corners using a Mitutoyo micrometer. Then, the average thickness of the heater and plates are subtracted out, yielding an average thickness for the aerogel panels.

The entire apparatus is suspended inside a vacuum chamber. A Varian Turbo V-60 turbo pump and a Varian SD-90 oil pump maintain the vacuum. The chamber pressure is measured using a Varian UHV-24 ionization gauge.

Data Reduction

Thermal conductivity of the insulation, k, is calculated using

$$k = \frac{\dot{q}\Delta x}{A(T_h - T_c)} \tag{1}$$

where $\dot{q}$ is the energy through one insulation panel, which is half the measured power to the heater, Δx is the insulation thickness, A is the insulation area, T_h and T_c are the average temperatures of the heater and cold plates, respectively.

The actual heat energy that the insulation conducts can be greater than or less than that measured depending on the test conditions. For example, energy can be lost or picked up from the surroundings through radiation from the edge of the heater and insulation, or by conduction down the sensor wires and heater

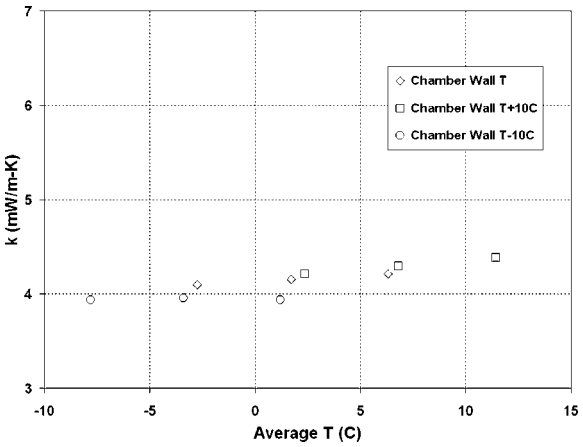

Fig. 4 Uncorrected measured thermal conductivity versus the average of heater and cold plate temperatures with the thin heater and no C-clamps. Data are for heater temperatures at the chamber wall temperature, 10 deg above the chamber wall temperature, and 10 deg below the chamber wall temperature.

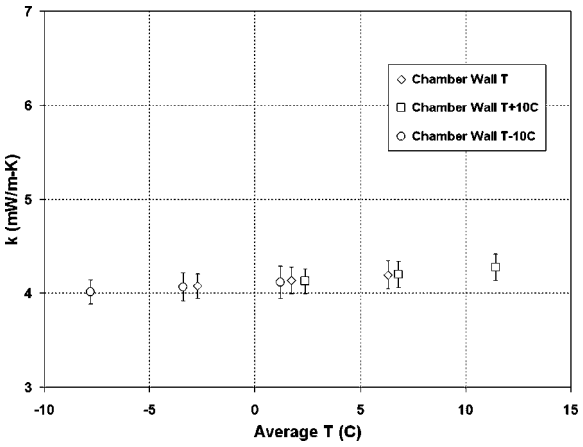

Fig. 6 Corrected measured thermal conductivity versus the average of heater and cold plate temperatures with the thin heater and no C-clamps. Data are for heater temperatures at the chamber wall temperature, 10 deg above the chamber wall temperature, and 10 deg below the chamber wall temperature.

wires. Also thermal conductivity is a function of temperature. A number of set points and test configurations are used to determine the effect of different parameters on the results.

Each test sequence starts with the temperature of the heater set to the chamber wall temperature. This minimizes heat transfer between the heater and the environment. The cold plate is set to $-30°C$. The system is allowed to come to equilibrium, which takes approximately 12 hours. This process is repeated for the cold plate set to $-20°C$ and $-10°C$. These three cold plate conditions are repeated with the heater set at 10°C above and below the chamber wall temperature.

Typical results are shown in Figs. 4 and 5 where the ordinate is the thermal conductivity, k, and the abscissa is the average of T_h and T_c. These figures show data from the final and initial configurations, respectively. The parasitic losses are larger in Fig. 5 than in Fig. 4. The net heat exchange to the environment can thus be quantified.

When the heater temperature is greater than the chamber wall temperature, energy is transferred from the heater to the surroundings without going through the insulation, increasing the apparent thermal conductivity. When the heater is below the chamber wall temperature the system gains an unmeasured amount of energy from the environment thus decreasing the apparent thermal conductivity. This heat transfer is a combination of conduction in the wires and radiation with the chamber wall. Significant heat transfer occurs from the edges of the insulation as well. Because the radiation is across a relatively small temperature difference, at most 50°C, the panel radiation heat transfer can be linearized such that the heat transfer rate is proportional to the temperature difference between the heater and the chamber wall. The different heat transfer modes can now be lumped together in one equation where the heat loss is equal to a constant multiplied by the temperature difference between the heater and the chamber wall. The power is then corrected by

$$\dot{q} = \dot{q}_h - C(T_w - T_h) \tag{2}$$

where $\dot{q}_h$ is the power supplied to the heater, T_w is the temperature of the chamber wall, and T_h is the temperature of the heater. The constant C is a measure of the effective heat transfer between the edges of the heater and insulation with the chamber wall. C is then adjusted until the correlation coefficient squared, R^2, of a least squares line through the data is maximized ($R^2 = 1$ for a perfect fit.) The result is Fig. 6. The value of C used to correct these data is 0.0088 W/K. Using Eq. 2 and the maximum temperature difference of 10 K gives an estimated side loss or gain of approximately 0.1 W.

A simple test is conducted to observe the correlation between the correction factor and the parasitic losses. To this end, the heater is turned off and the cold plates are set to various constant temperatures (-30 to $0°C$). This is done so that the parasitic losses are isolated and magnified. In this scenario, the heater is 3.7 K to 1.4 K hotter than the cold plates. This temperature difference is due to the energy gained from the surroundings by conduction through the wires and radiation with the surroundings. Similar results are seen in data presented by Zeng et al. [8] where a 0.6 K difference is seen with the cold plate at 10°C. Analysis shows that these temperature differences are consistent with the correction factor. However, quantitative results using these small temperature differences (3.7 K to 1.4 K) are not possible since they are of the same order as the uncertainties of the heater and cold plate temperatures (1.4 K and 0.3 K, respectively).

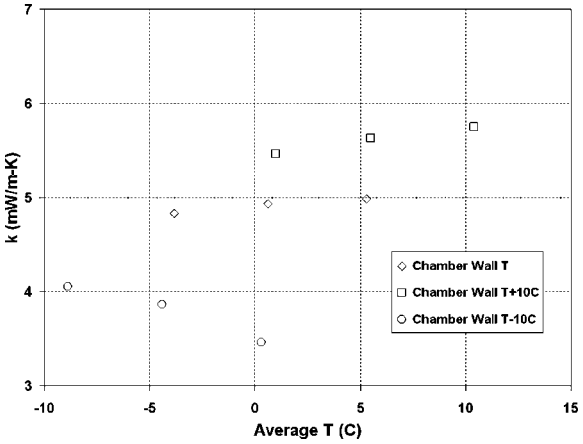

Fig. 5 Uncorrected measured thermal conductivity versus the average of heater and cold plate temperatures with the thick heater and C-clamps. Data are for heater temperatures at the chamber wall temperature, 10 deg above the chamber wall temperature, and 10 deg below the chamber wall temperature.

Uncertainty

A detailed uncertainty analysis [9] is done for a test sequence. At a 95 percent confidence level, the uncertainty in thermal conductivity for the nine data points ranges between 3 percent and 4.5

percent of the specified values. The two factors that have the largest uncertainty percentage coefficients, UPCs, (greatest contributors to overall uncertainty) are the thickness of the panel and the heater temperature measurement. Variations in the insulation thickness due to manufacturing tolerances with a resulting uncertainty of 3 percent cause the panel thickness UPC to be high.

The uncertainties due to manufacturer tolerance in the RTDs used to measure the heater and cold plates are 1.4 K and 0.3 K, respectively. Maximum spatial variations (standard deviation of the measurements) for the heater and cold plate temperature for any one test are 1.0 K and 0.5 K, respectively. This spatial variation includes a ground loop error. Upon averaging, the total uncertainties of the heater and cold plate average temperatures are 0.6 K and 0.2 K respectively. The dominant factor is the ground loop error, which had not been discovered until after these tests were conducted.

A useful method for evaluating experimental uncertainty is the uncertainty magnification factor, UMF, defined as

$$UMF_i = \frac{X_i}{k}\frac{\partial k}{\partial X_i} \tag{3}$$

where X_i is the i^{th} measured variable and k is defined by Eq. 1. UMF is a nondimensional sensitivity and indicates the influence of the uncertainty of a particular variable on the uncertainty of the result [10]. Even though each temperature measurement has UMFs much greater than one, only the heater temperature measurement dominates because of its large total uncertainty. Other factors that have UMFs larger than one are the thickness measurement and the voltage measurement. The systematic uncertainty in voltage is 0.16 percent, which is small enough to render its contribution to the overall uncertainty small.

Various modes of heat transfer that are not taken into account in the determination of the thermal conductivity are estimated. Conduction through the RTD and heater wires is considered. This is estimated to have an effect of less than 0.5 percent on the determined thermal conductivity. Although conditions were set such that radiation effects with the chamber wall were minimized, radiation side effects have not yet been fully characterized.

Changes Over ASTM

Several changes over ASTM C 1114 [7] are made because the ASTM method is not adequate for very low thermal conductivity insulation. The thermal conductivity of vacuum panels is an order of magnitude lower than typical insulation. For example, glass fiber, paper faced insulation has a thermal conductivity of 0.046 W/m·K [11]. These low values necessitate the several changes outlined below.

The initial heater (called ''thick heater'' in this paper) consists of a thin foil heater sandwiched between two aluminum plates 6 mm thick. Since the lateral heat flux would be very low, this ensures a uniform temperature across the heater.

The sample size specified in the standard is not specific other than the thickness should be no more than one third the maximum linear dimension of the metered region. This is to maintain edge losses to less than 0.5 percent. Vacuum insulation panels need to have a large area compared to the thickness for two reasons: (1) to reduce the edge losses, and (2) to make the power level to the heater sufficient to reduce the uncertainty in measuring the power. For these tests each panel was $30.48\ \text{cm}\times 45.7\ \text{cm}\times 1.27\ \text{cm}$. Power ranges from 1.4 to 7 W depending on the set point.

Even with thin panels the convection losses can still be significant. Therefore, the entire experiment is placed in a large bell jar and the pressure reduced to approximately 1.3 mPa (10 μTorr). This reduces convection losses from the edge of the heater and from the edge of the insulation to the environment. With standard insulations the losses due to convection are negligible for most cases. With vacuum panels, the heat transfer through convection at atmospheric pressure can be greater than energy going through the insulation.

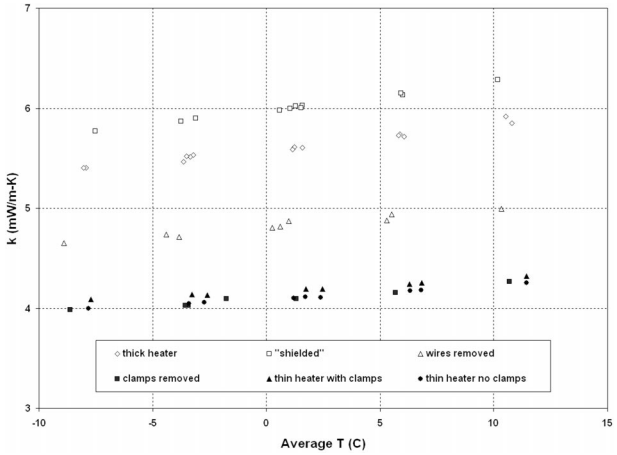

Fig. 7 Corrected measured thermal conductivity versus the average of heater and cold plate temperatures. These data show that the difference between heater temperatures at the chamber wall temperature, 10 deg above the chamber wall temperature, and 10 deg below the chamber wall temperature are within the uncertainty of the measurement and are therefore not differentiated.

The temperature differences between the heater and the cold plates are typically 2 to 5 K in the ASTM standard. For the vacuum panels the temperature difference is 30 to 60 K. This is necessary to increase the heat flux through the insulation to a point where the power is at a level where the uncertainty is reasonable.

The ASTM standard suggests using spacers along the edges to provide the spacing between the plates. In this case any material rigid enough to be used as a spacer would produce a significant heat path between the heater and the cold plates. Even though the contact area would be small compared to the insulation panel, it would be a significant amount of energy. Threaded rods or clamps attached to the cold plates are used to hold the assembly in compression. The clamping pressure is adjusted until the thickness is nearly uniform and the clamping pressure is sufficient to maintain contact between the insulation panels and the heater and cold plates. The thickness of the assembly is measured with a micrometer.

There are two methods for controlling the power to the heater. One is to use constant power and wait for the system to come to equilibrium. The second is to use a constant temperature controller that adjusts the power to the heaters in response to the difference between the set point and the temperature measured in the center of the heater. The latter method is used for two reasons. First, it reduces the time for the system to come to equilibrium. The time to reach equilibrium with the former method is several days. Through active control the power applied to the heater is greater initially, during warm up, reducing time to reach equilibrium to approximately 8 hours. The second reason is to maintain the heater temperature at a known predetermined temperature, usually the chamber wall temperature.

Temperature fluctuations in the room make it very difficult for the experiment to reach equilibrium. A room temperature change requires several hours for the test setup to reach a new equilibrium. A dedicated air conditioning unit is installed to hold the room temperature constant independent of the rest of the building. This caused the standard deviation of the chamber wall temperature to be 0.6 K for a typical measurement.

Initial Results and Modifications

A number of test sequences are conducted with different configurations to determine potential errors and to correct for these errors. The results are shown in Fig. 7. The different configura-

Table 1 Test sequence configurations for data shown in Fig. 7

Chart Symbol	Chart label	12.7 mm thick heater	Radiation shielding	Minimal RTD wires used	C-clamps used for clamping	Thin rod used for clamping
◇	thick heater	X			X	
□	shielded	X	X		X	
△	wires removed	X		X	X	
■	clamps removed	X		X		X
▲	thin heater with clamps			X	X	
●	thin heater no clamps			X		X

tions are in Table 1. The first sequence, which is labeled ''thick heater,'' is with the thick heater (a heater foil sandwiched between 6 mm aluminum plates), a large number of sensors and C-clamps. The next sequence labeled ''shielded'' has radiation shielding added as seen in Fig. 8. Data labeled ''wires removed'' has the number of sensors reduced and the radiation shielding removed. The data labeled ''clamps removed'' are data with the C-clamps replaced with small diameter threaded rod. The final two sequences labeled ''thin heater with clamps'' and ''thin heater no clamps'' have the thin heater, with C-clamps and with threaded rod respectively. Each of these is explained below.

The initial heater (thick heater) consists of a thin foil heater sandwiched between two 6 mm aluminum plates. The data labeled ''thick heater'' in Fig. 7 have 13 RTDs on each cold plate and 15 RTDs on each 6mm aluminum plate. These are installed to determine the temperature uniformity across the plates. The high conductivity of the aluminum ensures a more uniform temperature across the heater. The spatial variations in temperature as measured by the RTDs are less than 1.2 K for the cold plates and 0.6 K for the thick heater.

The first change is to shield the test from the environment. Several layers of aluminized Mylar are wrapped around the experiment. This results in an increase in thermal conductivity as shown with open squares in Fig. 7 (see ''shielded''). Several variations are tried and show that the shielding causes the edges of the heater and insulation panels to reflect energy to the cold plate as shown in Fig. 8. Thus, the shields are removed.

The next change is to remove the majority of the sensors leaving only three RTDs on each cold plate and three on each side of the heater. This results in a decrease in measured thermal conductivity of approximately 14 percent as compared to the ''thick heater'' results (see ''wire removed'' in Fig. 7).

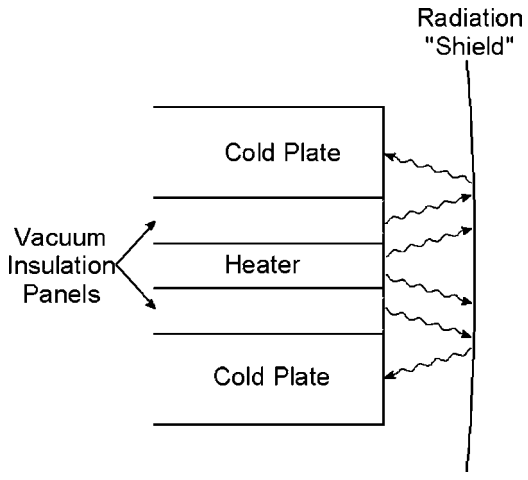

Fig. 8 Test assembly with thick heater and radiation ''shield.'' Radiation from heater and edges of vacuum insulation panel reflects from radiation ''shield'' to cold plates.

Even with these changes, there is still evidence that the heater is radiating directly to the cold surfaces. The coolant tubes are insulated with Mylar resulting a 3 percent decrease in measured thermal conductivity. The C-clamps are in contact with the cold plates. The sides of the clamps are therefore cold and in close proximity to the heater and therefore could radiate a significant amount of energy between them. When the clamps are replaced by thin threaded rods, which greatly reduce the area, the result as shown in Fig. 7 (see ''clamps removed'') is an additional 15 percent decrease in measured thermal conductivity.

Because reducing the area of the clamps reduced the heat loss from the heaters, a reduction in the exposed area of the heater should have a similar result. A thin foil heater, 0.16 mm thick, is installed between the two vacuum insulation panels. The result is a slight increase in thermal conductivity of approximately 2 percent (see ''thin heater with clamps'' in Fig. 7) which is within the uncertainty estimate for these tests. The thin heater has an added benefit of reducing the time required to reach equilibrium from 24+ hours to approximately 8 hours.

The final configuration has the thin film heater and threaded rod. The result is nearly identical to the test with the thick heater and threaded rod labeled as ''clamps removed'' and the test labeled ''thin heater with clamps'' in Fig. 7. The correction factor needed for the thin heater is nearly an order of magnitude smaller than the correction factor needed for the thick heater.

The thermal conductivity increases with temperature in all cases (see Fig. 7). The increase is most likely due to two effects: first, the temperature dependence of thermal conductivity of the core material, second, not all the radiation is blocked by the added carbon. This radiation appears linear over this small temperature range.

The ionization gage is located in one of the ports at the base of the bell jar (Fig. 1). The heat from the element, if left on, causes a noticeable change in apparent thermal conductivity. In some cases the effect can be approximately 1.2 percent. Therefore the ionization gage is turned on only long enough to get a pressure reading.

In addition, contact resistance was considered between the vacuum insulation panel and the heater and cold plates. A thermal contact resistance for rough aluminum plate is on the order of 1 m^2K/kW, [12] which is similar to plastics such as Teflon, at our estimated contact pressure. Assuming that 10 percent of the surface is in contact because of the irregularity of the vacuum insulation panel surface causes about 0.1 K temperature drop. This amount is insignificant.

Conclusions

Comparing the thermal conductivity for vacuum panels is difficult because pressure, composition, packing fraction, granule size, density, test method and packaging can have a significant effect on the overall thermal conductivity. Typical values measured (4 mW/m·K) are within 10 percent of the manufacturer's value of 3.6 mW/m·K measured using ASTM C 518. They are also comparable to those measured by Zeng et al. (6.5 mW/m·K) [8], and Smith et al. (4.25 mW/m·K) [13] which are measured

without an outer wrapper. Hunt et al. [4] report values of 9.6 mW/m·K with a plastic packaging and 7.2 mW/m·K without the plastic packaging.

Thermal conductivity coefficient for vacuum insulation panels can not be measured adequately with the standard ASTM techniques. Seemingly small amounts of energy which are inconsequential when applied to typical insulation materials using standard ASTM methods cause differences in the measured thermal conductivity of more than 50 percent. Even with the convective losses minimized by conducting the experiment in a vacuum, the temperature of the surroundings and heat sources such as the ionization gage can have a significant effect on the result.

The experiments show that adding thin radiation shields to isolate the system from the surroundings decreases accuracy. Radiation interchange between the edges of the thick heater, edges of the insulation panels and the cold plates increases. Using C-clamps to hold the assembly consisting of the thick heater, the insulation panels and the cold plates causes significant heat transfer between the thick heater and the cold plates. Using a thin heater negates this effect. Similar conductivity results are obtained with a thick heater and no clamps, a thin heater and no clamps, or a thin heater with clamps.

The differences between the ASTM techniques and the various techniques explained here are described and the rationale explained. A new ASTM technique for vacuum panels appears to be needed.

Acknowledgment

This work is supported by grant NCC8-137 from the National Aeronautics and Space Administration.

Nomenclature

A = insulation area, m^2
C = correction factor, W/K
P = power to heater, W
R = heater resistance, Ω
T_c = cold plate temperature, °C
T_h = heater temperature, °C
T_w = chamber wall temperature, °C
UMF_i = Uncertainty Magnification Factor
V = voltage to heater, V
X_i = ith measured variable
k = thermal conductivity, W/m·K
$\dot{q}$ = heat transfer rate through insulation, W
$\dot{q}_h$ = power supplied to heater, W
Δx = insulation thickness, m

References

[1] Wessling, F. C., Stodieck, L. S., Hoehn, A., Woodard, S., O'Brien, S., and Thomas, S., 2000, "Low Temperature, Low Energy Carrier (LoTec©) and Phase Change Materials (PCMs) for Biological Samples," 30th International Conference on Environmental Systems, OOICES-338, Toulouse, France, July 10–13, 2000.
[2] Zeng, S. Q., Hunt, A., and Greif, R., 1995, "Theoretical Modeling of Carbon Content to Minimize Heat Transfer in Silica Aerogel," J. Non-Cryst. Solids, **186**, pp. 271–277.
[3] ASTM C 117-97, "Standard Test Method for Steady-State Heat Flux Measurements and Thermal Transmission Properties by Means of the Guarded-Hot-Plate Apparatus," American Society for Testing and Materials, Philadelphia, PA.
[4] Hunt, A. J., Jantzen, K., and Cao, W., 1991, "Aerogel—A High Performance Insulation Material at 0.1 bar," *Insulation Materials: Testing and Applications*, ASTM STP 1116, R. S. Graves, and D. C. Wysocki, eds., **2**, American Society for Testing and Materials, Philadelphia, pp. 455–463.
[5] ASTM C 518-98, "Standard Test Method for Steady-State Thermal Transmission Properties by Means of the Heat Flow Meter Apparatus," American Society for Testing and Materials, Philadelphia, PA.
[6] ASTM C 745-92, "Standard Test Method for Heat Flux Through Evacuated Insulations Using a Guarded Flat Plate Boiloff Calorimeter," American Society for Testing and Materials, Philadelphia, PA.
[7] ASTM C 1114-00, "Standard Test Method for Steady-State Thermal Transmission Properties by Means of the Thin-Heater Apparatus," American society for Testing and Materials, Philadelphia, PA.
[8] Zeng, J. S. Q., Stevens, P. C., Hunt, A. J., Grief, R., and Lee, D., 1996, "Thin-Film-Heater Thermal Conductivity Apparatus and Measurement of Thermal Conductivity of Silica Aerogel," Int. J. Heat Mass Transf., **39**(11), pp. 2311–2317.
[9] Coleman, H. W., and Steele, W. G., 1999, *Experimentation and Uncertainty Analysis for Engineers*, 2nd ed., John Wiley & Sons, Inc., New York.
[10] Coleman, H. W., and Steele, W. G., 1999, *Experimentation and Uncertainty Analysis for Engineers*, 2nd ed., John Wiley & Sons, Inc., New York, p. 50.
[11] Incropera, F. P., and DeWitt, D. P., 1996, *Fundamentals of Heat and Mass Transfer*, 4th ed., John Wiley & Sons, Inc., New York.
[12] Hewitt, G. F., Shires, G. L., and Polezhaev, Y. V., eds., 1997, *International Encyclopedia of Heat and Mass Transfer*, CRC Press LLC., Boca Raton FL., p. 1949.
[13] Smith, D. M., Maskara, A., and Boes, U., 1998, "Aerogel-based Thermal Insulation," J. Non-Cryst. Solids, **225**, pp. 254–259.

A Method for Assessing the Importance of Body Force on Flow Boiling CHF

Hui Zhang

Issam Mudawar
e-mail: mudawar@ecn.purdue.edu

Boiling and Two-phase Flow Laboratory,
School of Mechanical Engineering,
Purdue University,
West Lafayette, IN 47907, USA

Mohammad M. Hasan
NASA Glenn Research Center,
21000 Brookpark Road,
Cleveland, OH 44135, USA

Experiments were performed to examine the effects of body force on flow boiling CHF. FC-72 was boiled along one wall of a transparent rectangular flow channel that permitted photographic study of the vapor-liquid interface just prior to CHF. High-speed video imaging techniques were used to identify dominant CHF mechanisms corresponding to different flow orientations and liquid velocities. Six different CHF regimes were identified: Wavy Vapor Layer, Pool Boiling, Stratification, Vapor Counterflow, Vapor Stagnation, and Separated Concurrent Vapor Flow. CHF showed significant sensitivity to orientation for flow velocities below 0.2 m/s, where extremely low CHF values where measured, especially with downward-facing heated wall and downflow orientations. High flow velocities dampened the effects of orientation considerably. The CHF data were used to assess the suitability of previous CHF models and correlations. It is shown the Interfacial Lift-off Model is very effective at predicting CHF for high velocities at all orientations. The flooding limit, on the other hand, is useful at estimating CHF at low velocities and for downflow orientations. A new method consisting of three dimensionless criteria is developed to determine the minimum flow velocity required to overcome body force effects on near-saturated flow boiling CHF. [DOI: 10.1115/1.1651532]

Keywords: Boiling, Channel Flow, Heat Transfer, Microgravity, Phase Change

1 Introduction

The vast majority of flow boiling critical heat flux (CHF) studies in the heat transfer literature concern vertical upflow. This is not surprising given this orientation provides the greatest flow stability, with the buoyancy force aiding in vapor removal in the same direction as the liquid flow. Numerous horizontal flow CHF studies have also been published, albeit to a much lesser degree than vertical upflow.

For all orientations other than vertical upflow, buoyancy can greatly complicate both the vapor coalescence at the heated wall, including the CHF mechanism itself, and the vapor removal along the flow channel. The role of buoyancy becomes even more complex where only one side of the flow channel is heated. Orientations associated with upward moving fluid and an upward-facing heated wall are generally advantageous because these orientations capitalize upon buoyancy forces to both remove vapor from the wall and expel it axially in the direction of fluid flow. The opposite is true for a downward moving fluid and a downward-facing heated wall. Here, buoyancy causes accumulation of the vapor along the wall, as well as pushes vapor in a direction opposite to that of the incoming liquid. Hence, vapor accumulation along the heated wall and vapor removal along the flow channel are both highly dependent upon the magnitude of buoyancy force relative to liquid inertia.

Low velocity flows are particularly prone to both low CHF and complex flow interactions for downward flow and a downward-facing heated wall. Here, weak liquid inertia greatly magnifies the role of buoyancy forces. Very small velocity flows approach pool boiling conditions for which studies have demonstrated appreciable sensitivity of CHF to heated wall orientation [1–5]. Drastically different CHF mechanisms were identified for different orientation ranges relative to gravity. These mechanisms could be divided into three main orientation regions [5]. The classical description of CHF from a horizontal surface encompasses upward-facing heated wall orientations. Near-vertical orientations, on the other hand, produce a wavy vapor layer that is driven by buoyancy forces along the wall, mimicking flow boiling CHF. Downward-facing orientations produce very low CHF values resulting from stratification of a fairly continuous vapor layer beneath the heated wall.

Most studies on the effects of orientation on flow boiling concern the drastic differences in CHF between vertical upflow and vertical downflow. Simoneau and Simon [6] showed vapor motion in vertical downflow switches from concurrent at high liquid velocities to countercurrent at low velocities. CHF values for vertical downflow were lower than for vertical upflow at the same velocity, but differences between the two opposite orientations decreased with increasing liquid velocity. Mishima et al. [7] also measured smaller CHF for downflow than for upflow at the same velocity. They examined the delicate equilibrium between liquid inertia and buoyancy force for downflow, illustrating how this balance can bring about stagnation of vapor masses in the channel and unusually low CHF values. Gersey and Mudawar [8] confirmed the findings of Simoneau and Simon and Mishima et al.in a study of the effects of flow orientation on CHF in microprocessor cooling.

The primary objective of the present study is to (a) identify and explore CHF mechanisms associated with different flow boiling orientations, and (b) develop a systematic method for assessing the importance of body force on flow boiling CHF. High-speed video imaging is employed to capture vapor behavior at conditions just preceding the occurrence of CHF. These photographic studies yielded clear images of the vapor-liquid interface and helped track both the spatial and temporal behavior of the vapor-liquid interface. CHF data are compared to predictions of previous models and correlations in an assessment of the suitability of these tools to thermal design of boiling systems at different orientations and different flow velocities. Finally, this information is used to develop a new systematic theoretically-based method for assessing the significance of body force on flow boiling CHF.

Contributed by the Heat Transfer Division for publication in the JOURNAL OF HEAT TRANSFER. Manuscript received by the Heat Transfer Division June 3, 2003; revision received November 19, 2003. Associate Editor: M. K. Jensen.

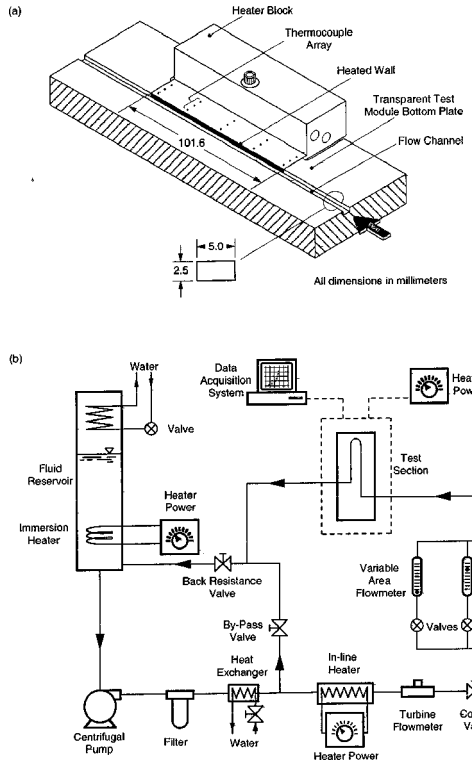

Fig. 1 (*a*) Heater inserted into bottom plate of test module; and (*b*) Two-phase flow loop

2 Experimental Method

2.1 Experimental Apparatus. The apparatus for this study featured a transparent test module which enabled side-viewing of vapor behavior along a heated wall. The module was formed by bolting together two plates of Lexan, a polycarbonate plastic which combines the attractive attributes of machinability, optical clarity and relatively high deflection temperature. A 5.0 $\times 2.5\ \mathrm{mm}^2$ rectangular flow channel was milled into the bottom plate of the test module. As shown in Fig. 1(*a*), the heated wall consisted of a thin edge of a copper heater which was inserted into the bottom plate, and carefully aligned with one side of the flow channel. Liquid FC-72 was introduced from a compression fitting leading to a small plenum that was fitted with a honeycomb flow straightener. An entry length 106 times the channel hydraulic diameter provided fully-developed flow upstream of the heated wall. Thermocouples were inserted into the flow channel both upstream and downstream of the heated wall. Similarly, pressure transducers were connected to pressure taps at about the same locations as the flow thermocouples. Output signals from these thermocouples and pressure transducers enabled continued monitoring of the changes in fluid state during the tests.

The heater was fabricated from a single block of pure copper. The heated wall measured 2.5 mm in width and 101.6 mm along the flow direction. Heat was supplied by four 150-W cartridge heaters that were embedded in the thick portion of the copper block. As shown in Fig. 1(*a*), five sets Type-K thermocouples, each consisting of three thermocouples, were inserted along the heater to determine axial variations of both wall flux and wall temperature. A linear fit to the three thermocouple readings was determined at each of the five thermocouple locations. This temperature profile was extrapolated to the wall to determine the wall temperature, T_w, while the heat flux, q'', was calculated from the temperature gradient. Table 1 summarizes the uncertainty estimates for the key measured and derived quantities of this study.

Fluid conditioning was accomplished with the aid of a compact two-phase loop illustrated schematically in Fig. 1(*b*). Fluid temperature was modulated by a water-cooled flat-plate heat exchanger followed by an in-line electrical immersion heater. The latter was controlled by a variable transformer to finely-tune liquid temperature at the inlet to the test module.

Table 1 Uncertainty estimates for key measured and derived quantities

Parameter	Symbol	Uncertainty
Thermocouples	-	$<0.3°C$
Pressure	P_o	$<0.01\%$
Velocity	U	$<2.3\%$
Heat Flux	q'', q''_m	$<7.9\%$
Temperature difference	$T_w - T_{in}$	$<0.9°C$

The working fluid used in this study, FC-72, is well suited for flow visualization of the CHF mechanism. Unlike water, whose CHF detection is sometimes accompanied by permanent damage to test module hardware, the low boiling point (56°C at atmospheric pressure) and low heat of vaporization of FC-72 produce relatively mild temperature excursions at CHF. This helps ensure reusability of the test module following repeated CHF tests, as well as provide ''ample'' time for photographic study of vapor behavior at CHF with less concern over the likelihood of test module physical burnout.

2.2 Photographic Techniques. A Redlake MotionScope PCI 8000s high-speed digital video system was used to capture vapor-liquid interfacial features just prior to CHF. The video camera in this system is capable of recording speeds from 60 to 8000 frames per second (fps) with 256 gray scale levels, and its electronic shutter can be modulated from $1/60^{\mathrm{th}}$ s down to 10 μs. Selecting an appropriate speed for the present study was based on several requirements, most important of which were lighting, resolution, and minimal interfacial shift. Optimum video imaging was realized with a recording rate of 1000 fps and a shutter speed of 50 μs. The system recorded over 2 s of video, which consisted of 2048 individual frames, each consisting of 240×210 pixels.

The video camera was positioned normal to the front of the flow channel. The high shutter speed adopted in this study demanded intense back lighting, which was made possible by a 0–2400 W light source that was separated from the channel by a diffuser plate. A high stability translation platform maneuvered the camera along the flow direction. Three different camera positions were used, which enabled video imaging of either the upstream, middle, or downstream sections of the heated wall. This paper provides sequential images of the downstream one-third of the heated wall where CHF is detected. The time interval between two successive images is 2 ms.

2.3 Operating Conditions and Test Procedure. Tests were conducted at eight different flow orientations as illustrated in Fig. 2. Each orientation is characterized by a specific flow direction relative to Earth's gravity, as well as orientation of the heated wall. The orientation $\theta = 0$ deg marks the horizontal flow orientation with the heated wall facing upwards. Other orientations, which were examined at 45 deg increments, produced horizontal flow, upflow or downflow, with the heated wall facing upwards or downwards.

Five inlet liquid velocities ($U = 0.1$, 0.2, 0.5, 1.0, and 1.5 m/s) were studied for each orientation. Since CHF occurred at the downstream thermocouple set, the CHF data were referenced to thermodynamic conditions at the heated wall exit. A constant outlet pressure of $P_o = 1.38$ bar (20 psia), corresponding to a saturation temperature of $T_{\mathrm{sat},o} = 66.3°C$, was maintained throughout the study. For each velocity, the inlet temperature was modulated to produce an outlet temperature of 63.3°C, corresponding to a 3°C outlet subcooling, when CHF occurred.

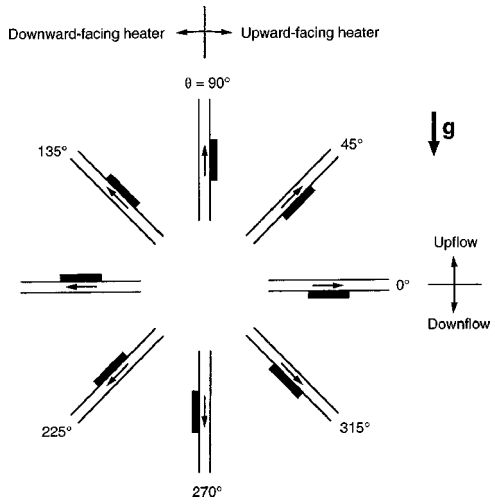

Fig. 2 Flow orientation guide indicating flow direction, channel orientation, and heater location (indicated by black rectangle)

A consistent operating procedure was adopted throughout the study. Each test commenced by controlling the various components of the flow loop to yield the desired inlet temperature, outlet pressure and flow rate. Heat was then supplied to the test module heater in increments of $1-3\ \mathrm{W/cm^2}$ (which were reduced as CHF was approached to refine CHF detection), and data were recorded once hydrodynamic and thermal conditions were deemed steady. Each test progressed through the single-phase and nucleate boiling regimes, generating a boiling curve, and was terminated immediately after CHF detection.

3 CHF Regimes

Figure 3(*a*) shows all CHF data collected from this study in a flow velocity-flow orientation plane. The CHF data are grouped into six different regimes for which representative photographs are depicted in Fig. 3(*b*). The most obvious feature of this CHF map is the existence of a dominant *Wavy Vapor Layer Regime* corresponding to all high velocities at all orientations. At and below 0.5 m/s, there exist a number of complex CHF regimes. Notice that the Wavy Vapor Layer Regime is prevalent even for low velocities for the vertical and near-vertical orientations, $\theta = 90$ and 135 deg, respectively. This regime is consistent with CHF depictions of flow boiling by Galloway and Mudawar [9,10].

A *Pool Boiling Regime* exists for low velocities, and $\theta = 0$, 45, and 315 deg. Bubble behavior within these horizontal and near-horizontal orientations with an upward-facing heated wall resembles pool boiling CHF from large horizontal surfaces. All four remaining CHF regimes are associated with downflow and downward-facing heated wall orientations at low velocities.

The six CHF regimes are described below in terms of both the shape and temporal behavior of liquid-vapor interface. All the photographs discussed below correspond to the downstream one-third of the heated wall.

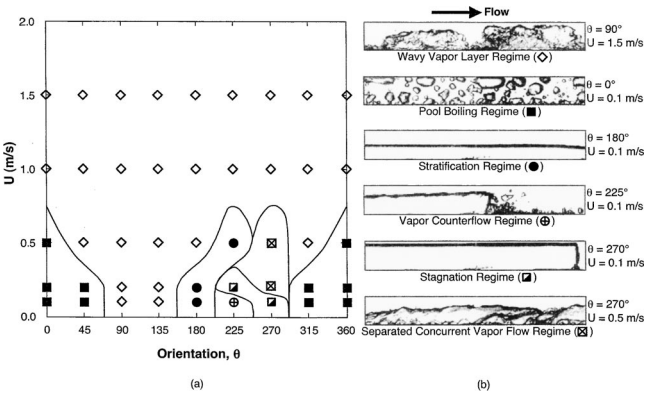

Fig. 3 (*a*) CHF regime map; and (*b*) Typical flow characteristics for each regime

3.1 Wavy Vapor Layer Regime. As depicted in Fig. 3(*b*), this regime is characterized by large vapor patches that form along the heated wall, resembling a fairly continuous wavy vapor layer. This layer prevents liquid contact with much of the heated wall, producing broad regions of dry wall, except in wetting fronts, located in troughs between vapor patches, where virtually all the heat is dissipated. This regime was encountered at velocities of $U = 1.0$ and 1.5 m/s regardless of orientation and encompasses upflow orientations at lower velocities as well.

Figure 4(*a*) shows a series of seventeen sequential video images of conditions corresponding to the Wavy Vapor Layer Regime. These images were captured at 1000 fps, which allowed prominent vapor features to be carefully tracked with time. Clearly, the vapor patches and wetting fronts are not stationary, but propagate along the heated wall. The waviness associated with this CHF regime lends credence to the adoption of hydrodynamic instability theory is describing the vapor layer shape, amplitude, and propagation speed [9,10].

Figure 4(*a*) shows the liquid-vapor wavy interface is marred by smaller interfacial disturbances, apparently the result of increased turbulence intensity at high liquid velocities. Galloway and Mudawar [9,10] encountered the same Wavy Vapor Layer Regime in vertical upflow along a short heated wall. They too noticed that the wavy vapor layer interface became increasingly marred by small disturbances with increasing velocity.

3.2 Pool Boiling Regime. Figures 3(*a*) shows this regime encompasses velocities below 0.5 m/s with the heated wall facing upwards ($\theta = 315$, 0, and 45 deg). Figure 3(*b*) shows small bubbles coalescing into larger ones, which are detached by buoyancy and driven across the flow channel to the opposite wall, where the vapor accumulates into yet larger vapor masses.

Figure 4(*b*) shows sequential images of this regime corresponding to $\theta = 0°$ and $U = 0.1$ m/s. While the vapor masses seem to propagate along the heated wall, the speed of propagation is much smaller than in Fig. 4(*a*), corresponding to $\theta = 90$ deg and $U = 1.5$ m/s. The low liquid velocity in Fig. 4(*b*) produces very mild drag forces on the vapor features, evidenced both by the aforementioned low speed of propagation of vapor masses, as well as the relatively mild deformation in the shape of coalescent bubbles departing normal to the heated wall. This is the primary reason behind the authors' naming of this regime, which is dominated by buoyancy forces. However, even in this Pool Boiling Regime, increasing liquid velocity should help remove vapor along the flow channel and preclude merging of vapor masses between the heated wall and opposite wall.

3.3 Stratification Regime. The same low velocities that caused buoyancy to dominate vapor formation in the previous Pool Boiling Regime are responsible for the formation of a well separated vapor layer which stratifies against the heated wall for horizontal and near-horizontal downward-facing wall orientations, $\theta = 180$ and 225 deg, respectively. As shown in Fig. 3(*b*), this thick continuous vapor layer greatly impedes liquid access to the heated wall, resulting in very low CHF values.

The sequential video images of the stratified vapor layer in Fig. 4(*c*) show the vapor layer interface is somewhat wavy, but the wavelength is fairly long, exceeding the entire heated length, and has a very small amplitude. This behavior points to hydrodynamic conditions which promote a stable liquid-vapor interface. Such a stable interface is very detrimental to the heat transfer process. An

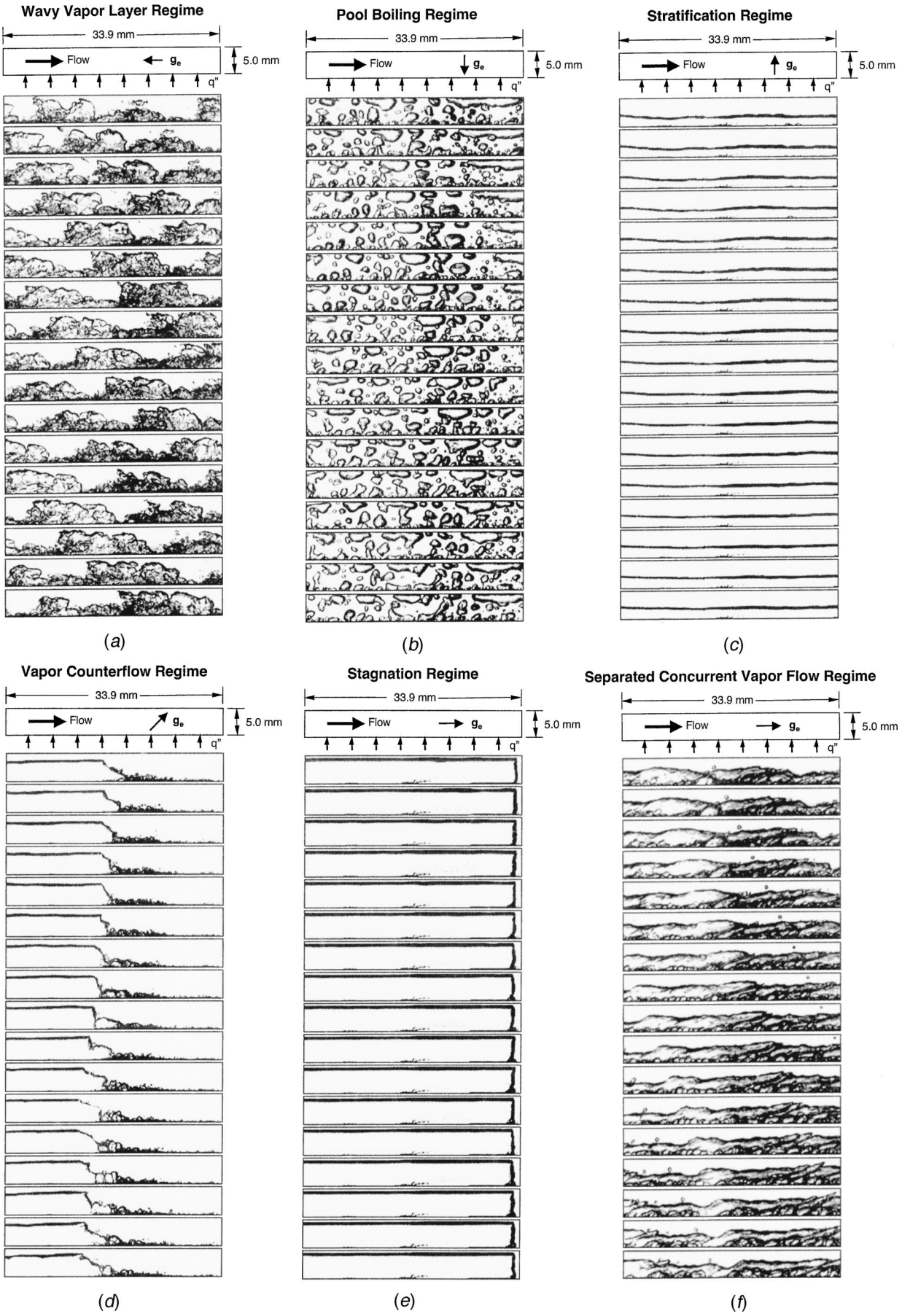

Fig. 4 Sequential images of vapor layer at (*a*) θ=90 deg and U=1.5 m/s, (*b*) θ=0° and U=0.1 m/s, (*c*) θ=180 deg and U=0.1 m/s, (*d*) θ=225 deg and U=0.1 m/s, (*e*) θ=270 deg and U=0.1 m/s, and (*f*) θ=270 deg and U=0.5 m/s

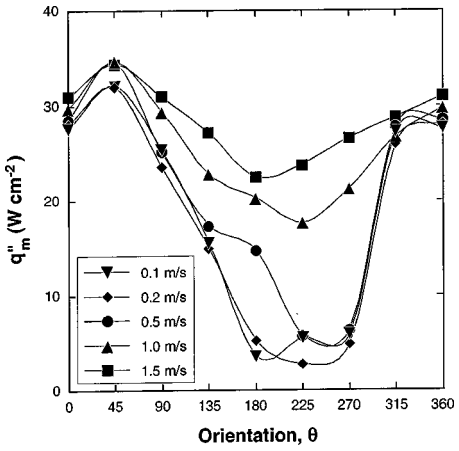

Fig. 5 CHF variation with orientation and flow velocity

unstable interface, on the other hand, causes both spatial and temporal growth of interfacial amplitude, permitting liquid access to the heated wall.

3.4 Vapor Counterflow Regime. This regime as well as the two remaining CHF regimes discussed below are closely related to the relative magnitude of liquid inertia and buoyancy force for downflow orientations at low velocities. As shown in Fig. 3(*a*), the Vapor Counterflow Regime was encountered at $\theta=225$ deg for $U=0.1$ m/s. At this low velocity, the liquid drag force exerted downwards upon the vapor is far too weak to overcome the opposing buoyancy force. The later pushes vapor backwards (upwards) against the incoming liquid. The sequential images in Fig. 4(*d*) show the thick coalescent vapor layer moving backwards, albeit very slowly, as liquid continues to make contact over the downstream portion of the heated wall.

3.5 Stagnation Regime. This regime was encountered when the liquid drag force and inertia came into balance, effectively freezing a thick coalescent vapor mass in place. As shown in Fig. 3(*a*), this condition occurs at $\theta=225$ deg for $U=0.2$ m/s and $\theta=270$ deg for $U=0.1$ m/s. Figure 3(*b*) and the sequential images in Fig. 4(*e*) show liquid contact with the downstream section of the heated wall is available over of a very small region. The sequential images show the thick, continuous vapor layer is virtually stationary. This behavior produced the lowest CHF values of the present study. In fact, at $\theta=225$ deg, CHF at 0.1 m/s (corresponding to the Vapor Counterflow Regime) was actually greater than CHF at the higher velocity of 0.2 m/s corresponding to the Stagnation Regime.

3.6 Separated Concurrent Vapor Flow. The stagnant vapor layer described in the previous section was purged from the channel with an increase in inlet liquid velocity that allowed the liquid drag force to overcome buoyancy. Figure 3(*a*) shows this regime is encountered at $\theta=270$ deg for $U=0.2$ and 0.5 m/s. This regime is complicated by significant disturbances along the vapor-liquid interface and bubble formation in a thin liquid layer at the heated wall which is, for the most, separated from the bulk liquid flow. The sequential images in Fig. 4(*f*) show the vapor layer interface propagating with a large wavelength and small amplitude along the channel. Figure 3(*a*) shows increasing liquid velocity at this orientation from 0.5 to 1.0 m/s causes the vapor layer interface to become unstable, marking a transition to the Wavy Vapor Layer Regime described before.

4 CHF Results

Figure 5 shows the variation of CHF with orientation for the five velocities tested. As indicated before, all these data are referenced to thermodynamic conditions based on the heated wall exit: $P_o=1.38$ bar, $T_{\mathrm{sat},o}=66.3$ deg C, and 3 deg C outlet subcooling. For all velocities, CHF increases from $\theta=0$ deg to a maximum around 45 deg, followed by a decrease to a minimum between 180 and 270 deg, before recovering again to the $\theta=0°$ value. The three lowest velocities of $U=0.1$, 0.2, and 0.5 m/s exhibit strong variations of CHF with orientation. These velocities produce very small CHF values in the range of $180<\theta<270$ deg. This further demonstrates the significance of buoyancy force compared to liquid inertia at low flow velocities. As illustrated in Figs. 3(*b*) and 4(*c–f*), the relatively weak liquid inertia enables buoyancy to dominate vapor behavior, causing vapor stratification against the heated wall for $\theta=180$ deg, and inducing Vapor Counterflow, Stagnation, or Separated Vapor Concurrent Flow for $\theta=225$ and 270 deg. Clearly, downflow and downward-facing heated wall orientations should be avoided at low velocities.

Figure 5 shows the two highest velocities, 1.0 and 1.5 m/s, cause appreciable diminution in the orientation effects on CHF. Nonetheless, buoyancy still influences CHF at these two velocities. A CHF maximum at $\theta=45$ deg can be explained by the buoyancy force both aiding vapor removal away from the heated wall as well as along the channel. At $\theta=0$ deg, buoyancy is perpendicular to the heated wall but does not aid the vapor removal along the channel, while the opposite is true for $\theta=90$ deg. CHF for $U=1.0$ and 1.5 m/s decreases for all downflow and downward-facing heated wall orientations, but to a much lesser degree than for the lower velocities.

Since the Wavy Vapor Layer Regime was observed for a large fraction of the present operating conditions, it is prudent to explore the dependence of interfacial instability on the forces which influence vapor behavior at different velocities and orientations. The speed of an idealized sinusoidal liquid-vapor interface between a vapor layer moving at velocity U_g and a liquid layer at U_f can be expressed as [10]

$$c=\frac{\rho_f U_f+\rho_g U_g}{\rho_f+\rho_g} \pm \sqrt{\frac{\sigma k}{\rho_f+\rho_g}-\frac{\rho_f\rho_g(U_g-U_f)^2}{(\rho_f+\rho_g)^2}-\frac{(\rho_f-\rho_g)}{(\rho_f+\rho_g)}\frac{g_e\cos\theta}{k}} \quad (1)$$

where k is the wave number. A negative argument in the radical of Eq. (1) results in a wave speed containing both real and imaginary components. The imaginary component

$$c_i=\sqrt{\frac{\rho_f\rho_g(U_g-U_f)^2}{(\rho_f+\rho_g)^2}+\frac{(\rho_f-\rho_g)}{(\rho_f+\rho_g)}\frac{g_e\cos\theta}{k}-\frac{\sigma k}{\rho_f+\rho_g}} \quad (2)$$

represents the combined effect of the different forces and dictates the stability (or instability) of the interface. The first term under the radical in Eq. (2) is a measure of the destabilizing effect of inertia, or velocity difference between the vapor and liquid phases. The second term is the body force effect, which, for a terrestrial environment, may be stabilizing or destabilizing depending on orientation of the wall relative to gravity. The third term accounts for surface tension which is always stabilizing to the interface.

The critical wavelength, defined as the wavelength of a neutrally stable wave, can be determined by setting the radical in Eq. (2) equal to zero.

$$\frac{2\pi}{\lambda_c}=\frac{\rho_f\rho_g(U_g-U_f)^2}{2\sigma(\rho_f+\rho_g)} + \sqrt{\left[\frac{\rho_f\rho_g(U_g-U_f)^2}{2\sigma(\rho_f+\rho_g)}\right]^2+\frac{(\rho_f-\rho_g)g_e\cos\theta}{\sigma}}. \quad (3)$$

Figure 6 shows CHF data for the limiting velocities of 0.1 and 1.5 m/s versus orientation angle. Also shown are predictions based on previous semi-empirical and theoretical CHF models. The Interfacial Lift-off Model, first proposed by Galloway and Mudawar [9,10] in the early 1990s, is intended for the dominant Wavy Vapor Layer Regime depicted in Figs. 3(*b*) and 4(*a*). This model is based on the assumption that the wavy layer makes contact with

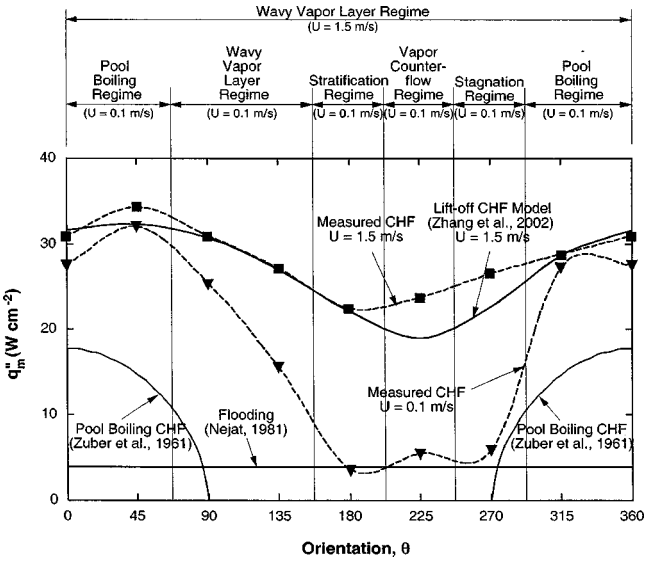

Fig. 6 Comparison of CHF data for lowest and highest velocities with predictions based on previous models and correlations for 5 mm×2.5 mm rectangular channel and operating conditions of present study

the heated wall over relatively short discrete regions corresponding to the wave troughs. It postulates that CHF will occur when the intense momentum of vapor generated normal to the wall exceeds the pressure force resulting from the interfacial curvature. Recently, the authors of the present study modified this model to explore the effects of orientation and interfacial wave growth [11]. Their model predictions show good agreement with the 1.5 m/s data as shown in Fig. 6. Convergence was never achieved with this model for $U=0.1$ m/s because of the large critical wavelength. Data for this lower velocity are compared to predictions of the classical CHF model of Zuber et al. [12] for pool boiling from a horizontal upward-facing heated wall. The gravitational acceleration, g_e, in the original model was replaced by $g_e \cos\theta$ since the Taylor instability employed in the model is based on only the component of gravity perpendicular to the heated wall.

$$q''_m = 0.131 \rho_g h_{fg} \left[\frac{\sigma(\rho_f - \rho_g) g_e \cos\theta}{\rho_g^2} \right]^{1/4}. \tag{4}$$

Figure 6 shows the pool boiling CHF model underpredicts CHF data corresponding to the present Pool Boiling Regime because it does not incorporate the benefits of liquid motion and its contribution to vapor removal along the channel.

Also shown in Fig. 6 are CHF predictions based on Negat's [13] flooding criterion

$$q''_m = 0.36 \left(\frac{L}{D_h} \right)^{0.1} \left(\frac{A}{A_w} \right) \rho_g h_{fg} \left[\frac{(\rho_f - \rho_g) g_e D_h}{\rho_g} \right]^{1/2} \left[1 + \left(\frac{\rho_g}{\rho_f} \right)^{1/4} \right]^{-2}, \tag{5}$$

which was derived for a closed-end vertical heated tube, where L, D_h, A, and A_w are the heated length, hydraulic diameter, heated area, and channel cross-sectional area, respectively. Figure 6 shows all 0.1 m/s CHF data belonging to the Stratification, Vapor Counterflow, and Stagnation Regimes approach the flooding limit. This limit occurs when vapor upflow in a pipe with a closed bottom prevents liquid from flowing downwards to replenish liquid that has been evaporated. This situation resembles the vapor behavior observed in this study in conjunction with the Vapor Counterflow and Stagnation Regimes, but not the Stratification Regime.

Figure 6 proves the Interfacial Lift-off Model is an effective tool for predicting high velocity flow boiling CHF for all orientations, while the flooding limit is useful for estimating CHF at low velocities and downflow orientations. However, a more systematic and comprehensive methodology is needed to design thermal management systems that can overcome the effects of body force on flow boiling CHF for different fluids and gravitational fields. Aside for terrestrial applications, such a tool is highly desired for design of thermal management hardware in space applications.

5 Methodology for Overcoming Body Force on Flow Boiling CHF

Flow orientation is sometimes dictated by system considerations other than heat dissipation. As indicated before, body force influences flow boiling CHF in the following three ways:

1. The body force component that is perpendicular to the heated wall influences hydrodynamic instability of the vapor-liquid interface.
2. The body force component in the direction of (or opposite to) the liquid flow influences vapor removal from the channel and may trigger flooding at low velocities.
3. A very long critical wavelength may preclude liquid contact with a large fraction of the heated wall.

Therefore, three separate criteria must be developed to overcome the effects of body force on flow boiling CHF.

5.1 Effects of Component of Body Force Perpendicular to Heated Wall. Equation (2) reveals interfacial instability of a vapor-liquid interface in a flow channel is governed by the combined effect of inertia, surface tension, and component of body force that is perpendicular to the heated wall. Equation (3) can be rearranged in the following form:

$$\frac{2\pi}{\lambda_c} \frac{\sigma(\rho_f + \rho_g)}{\rho_f \rho_g (U_g - U_f)^2} = \frac{1}{2} \left\{ 1 + \sqrt{1 + 4 \frac{(\rho_f - \rho_g)(\rho_f + \rho_g)^2 \sigma g_e \cos\theta}{\rho_f^2 \rho_g^2 (U_g - U_f)^4}} \right\} \tag{6}$$

The right-hand-side of Eq. (6) approaches unity when the component of body force perpendicular to the heated wall is too weak to influence interfacial instability. This constitutes a sufficient condition for negating the influence of this component of body force on CHF and which corresponds to flows that fall into the Wavy Vapor Layer Regime. This condition can be expressed as

$$\left| \frac{(\rho_f - \rho_g)(\rho_f + \rho_g)^2 \sigma g_e \cos\theta}{\rho_f^2 \rho_g^2 (U_g - U_f)^4} \right| \ll \frac{1}{4}. \tag{7}$$

This criterion was examined by substituting the phase velocity difference by the characteristic velocity of the flow channel, namely U. The left-hand-side of Eq. (7) can also be expressed as $\mathrm{Bo/We}^2$, where Bo and We are the Bond and Weber numbers, respectively, which are defined as

$$\mathrm{We} = \frac{\rho_f \rho_g U^2 L}{(\rho_f + \rho_g)\sigma} \tag{8}$$

and

$$\mathrm{Bo} = \frac{(\rho_f - \rho_g) g_e \cos\theta L^2}{\sigma}. \tag{9}$$

Figures 7(*a*) and 7(*b*) show the variation of $\mathrm{Bo/We}^2$ with orientation and flow velocity. The peak values of $\mathrm{Bo/We}^2$ for $U=0.1$, 0.2, 0.5, 1.0 and 1.5 m/s are 4503, 281, 7.2, 0.45, and 0.09, respectively. The large values corresponding to $U=0.1$ and 0.2 m/s are consistent with the strong influence of orientation on CHF for these velocities. Conversely, the small values of $\mathrm{Bo/We}^2$ for $U=1.0$ and 1.5 m/s are indicative of a very weak influence of body force on CHF for these velocities, as was clearly demonstrated in the flow boiling experiments. Since the CHF data

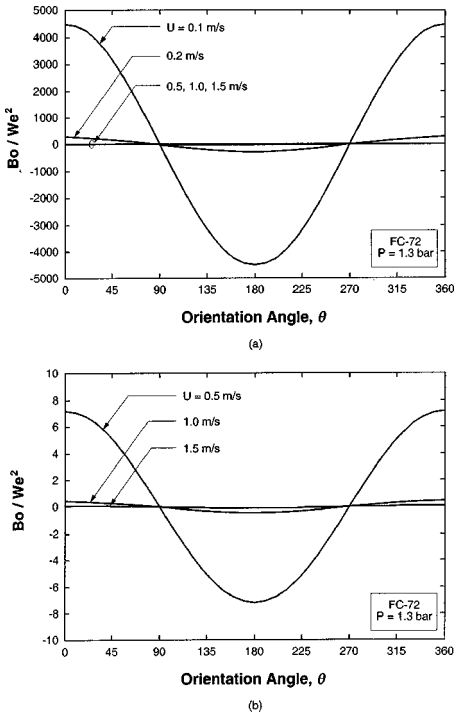

Fig. 7 Variation of Bo/We^2 with flow orientation and velocity for (*a*) all velocities tested and (*b*) $U \geqslant 0.5$ m/s

showed little dependence on orientation for $U \sim 1.5$ m/s, the magnitude of Bo/We^2 for $U=1.5$ m/s is used as a criterion for overcoming body force effects on CHF.

$$\frac{\mathrm{Bo}}{\mathrm{We}^2} = \frac{(\rho_f - \rho_g)(\rho_f + \rho_g)^2 \sigma g_e}{\rho_f^2 \rho_g^2 U^4} \leqslant 0.09. \tag{10}$$

5.2 Effects of Component of Body Force Parallel to Heated Wall. Several complex CHF regimes were identified in the present study for predominantly downflow orientations at low velocities. The Vapor Counterflow and Vapor Stagnation CHF regimes were both the result of the relative velocity between the vapor and liquid phases, while the Separated Concurrent Vapor Flow was a transitional regime between the Vapor Stagnation and Wavy Vapor Layer CHF regimes. In the Vapor Stagnation and Vapor Counterflow Regimes, the vapor took the form of a long slug bubble as shown in Fig. 4(*e*). The rise velocity of a slug bubble relative to liquid can be expressed as [14]

$$U_\infty = 0.35 \frac{[(\rho_f - \rho_g) g_e \sin\theta \ D_h]^{1/2}}{\rho_f^{1/2}} \tag{11}$$

When U_∞ exceeds the liquid velocity, U, the vapor tends to flow backwards relative to the liquid. Vapor Stagnation occurs when the two velocities are equal. A sufficient condition for negating vapor counterflow and vapor stagnation is $U_\infty \ll U$, which, for $\sin\theta = 1$, can be represented in terms of the Froude number,

$$\frac{1}{\mathrm{Fr}} = \left| \frac{(\rho_f - \rho_g) g_e \sin\theta \ D_h}{\rho_f U^2} \right| \ll 8.16. \tag{12}$$

Figures 8(*a*) and 8(*b*) show the variation of 1/Fr for different orientations and flow velocities. For $U=0.1$ and 0.2 m/s and $\theta = 225$ and 270 deg, where vapor counterflow and vapor stagnation were observed, Fig. 8(*a*) shows the magnitude of 1/Fr is larger than 0.82. Conversely, Fig. 8(*b*) shows the magnitude of 1/Fr for the other higher velocities is less than 0.13. Since vapor counterflow and vapor stagnation where not observed for $U=0.5$ m/s, a

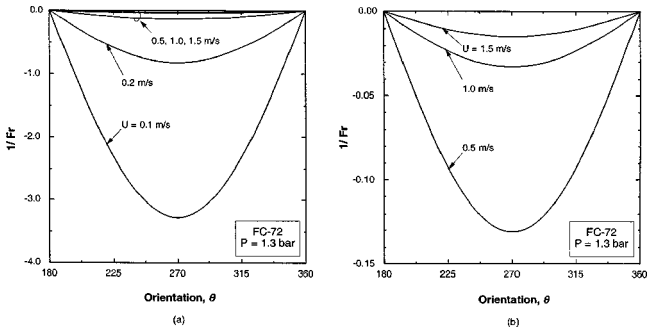

Fig. 8 Variation of 1/Fr with flow orientation and velocity for (*a*) all velocities tested and (*b*) $U \geqslant 0.5$ m/s

sufficient criterion for precluding the occurrence of these flow anomalies can be expressed for $\sin\theta = 1$ by the criterion

$$\frac{1}{\mathrm{Fr}} = \frac{(\rho_f - \rho_g) g_e D_h}{\rho_f U^2} \leqslant 0.13 \tag{13}$$

5.3 Critical Wavelength Versus Heated Length. As discussed before, low flow velocities can produce very large values of critical wavelength. Replacing the phase velocity difference by the characteristic velocity of the flow channel, Eq. (6) reveals the largest value of critical wavelength is given by

$$\lambda_c = \frac{2\pi\sigma(\rho_f + \rho_g)}{\rho_f \rho_g U^2}. \tag{14}$$

Thus, to maintain a critical wavelength shorter than the heated length, L, the following Weber number criterion must be satisfied:

$$\mathrm{We} = \frac{\rho_f \rho_g U^2 L}{(\rho_f + \rho_g)\sigma} \geqslant 2\pi. \tag{15}$$

5.4 Minimum Flow Velocity Required to Overcome Body Force Effects. It is now possible to combine the above three criteria in pursuit of a comprehensive methodology to overcome body force effects. Equations (10), (13), and (15) reveal that increasing flow velocity is perhaps the most effective means for satisfying these criteria. Velocity is an important parameter for the design of thermal management systems in both terrestrial and space applications. For the latter, coolant velocity has a strong bearing on pumping power and therefore overall power consumption. Using low velocities is therefore vital to reducing power consumption provided the aforementioned flow anomalies can be prevented.

Figure 9 shows the minimum velocity required to satisfy the above criteria as a function of a/g_e, the ratio of body force per unit mass to Earth's gravity. This was accomplished by substituting g_e in Eqs. (10) and (13) by a. Avoiding body force effects requires that flow velocity exceed values predicted by each of the three criteria. Only one of these criteria is dominant for a given value of a/g_e. Figure 9 shows fairly appreciable flow velocities will be required to overcome flooding effects, should a large body force of $a/g_e > 75$ be present in a direction opposite to the liquid flow. Instability effects are dominant when a body force of $a/g_e < 75$ is present in a direction perpendicular to the heated wall, as surface tension effects become increasingly important. These instability effects span Earth, Lunar and Martian environments. The heater length criterion is dominant for relatively low values of a/g_e. However, the transition a/g_e value between the instability-dominated and heater-length-dominated regimes is a function of the heated length; shorter heaters require higher velocities to decrease critical wavelength below the heated length. Overall, the heater-length-dominated regime appears quite significant for microgravity conditions.

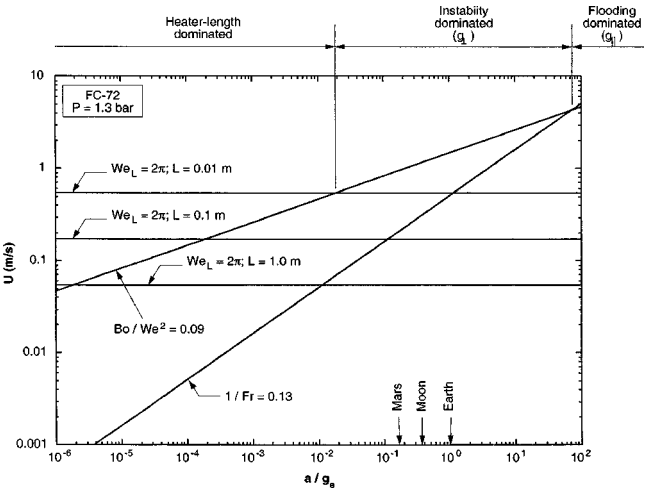

Fig. 9 Determination of minimum flow velocity required to overcome all body force effects on flow boiling CHF

Obviously, the validation of this methodology for determining the minimum velocity required to overcome body force effects on flow boiling CHF will require future tests with other coolants, especially in a reduced gravity environment. Such tests represent future goals for a follow-up study.

6 Conclusions

This study examined the complex interactions between liquid inertia and buoyancy force in flow boiling at different orientations. High-speed video imaging provided representative images of the vapor-liquid interface for different operating conditions and helped track both the spatial and temporal characteristics of the interface. Heat transfer measurements complemented the photographic study by providing a database for assessment of previous CHF models and correlations. Finally, a systematic methodology was developed to determine the minimum liquid velocity required to overcome the effects of body force on CHF. Key findings from this study are as follows:

1. Six different CHF regimes were identified: Wavy Vapor Layer, Pool Boiling, Stratification, Vapor Counterflow, Vapor Stagnation, and Separated Concurrent Vapor Flow. CHF is very sensitive to orientation for flow velocities below 0.2 m/s, where extremely low CHF values are measured, especially with downward-facing heated wall and downflow orientations. High flow velocities dampen the effects of orientation considerably. The Interfacial Lift-off Model is very effective at predicting CHF for high velocities at all orientations. The flooding limit, on the other hand, is useful at estimating CHF at low velocities and for downflow orientations.

2. Three dimensionless criteria were developed to determine the minimum flow velocity required to overcome body force effects on flow boiling CHF. Only one of the three criteria is dominant for a given gravitational field. This methodology may help reduce electric power consumption in space thermal management systems, provided it is ultimately validated for other coolants, especially in microgravity.

Acknowledgment

The authors are grateful for the support of the National Aeronautics and Space Administration under Grant No. NAG3-2336.

Nomenclature

a = body force per unit fluid mass
A = channel cross-sectional area
A_w = heated area of channel
Bo = bond number
c = wave speed
c_i = imaginary component of wave speed
D_h = channel hydraulic diameter
Fr = Froude number
g_e = earth's gravitational acceleration
$g_\perp$ = acceleration in flow direction
$g_\parallel$ = acceleration perpendicular to heated wall
h_{fg} = latent heat of vaporization
k = wave number
L = heater length in flow direction
P_o = outlet pressure
q'' = wall heat flux
q''_m = critical heat flux
$T_{\mathrm{sat},o}$ = saturation temperature based on measured outlet pressure
T_{in} = mean inlet liquid temperature
T_w = wall temperature
U = mean inlet liquid velocity
ΔU = velocity difference between vapor and liquid layers
U_f = velocity of liquid layer
U_g = velocity of vapor layer
U_∞ = rise velocity of slug bubble
We = Weber number

Greek Symbols

θ = flow orientation angle
λ_c = critical wavelength
ρ_f = density of saturated liquid
ρ_g = density of saturated vapor
σ = surface tension

References

[1] Class, C. R., DeHaan, J. R., Piccone, M., and Cost, R. B., 1960, "Boiling Heat Transfer to Liquid Hydrogen from Flat Surfaces," *Advances in Cryogenic Engineering*, K. D. Timmerhaus, ed., Plenum Press, New York, **5**, pp. 254–261.
[2] Marcus, W. R., and Dropkin, D., 1963, "The Effect of Surface Configuration on Nucleate Boiling Heat Transfer," Int. J. Heat Mass Transfer, **6**, pp. 863–867.
[3] Nishikawa, K., Fujita, Y., Uchida, S., and Ohta, H., 1983, "Effect of Heating Surface Orientation on Nucleate Boiling Heat Transfer," *Proc. ASME-JSME Thermal Engineering Joint Conference*, Y. Mori and W. J. Yang, eds., Honolulu, HI, **1**, pp. 129–136.
[4] Mudawar, I., Howard, A. H., and Gersey, C. O., 1997, "An Analytical Model for Near-Saturated Pool Boiling CHF on Vertical Surfaces," Int. J. Heat Mass Transfer, **40**, pp. 2327–2339.
[5] Howard, A. H., and Mudawar, I., 1999, "Orientation Effects on Pool Boiling CHF and Modeling of CHF for Near-Vertical Surfaces," Int. J. Heat Mass Transfer, **42**, pp. 1665–1688.
[6] Simoneau, R. J., and Simon, F. F., 1966, "A Visual Study of Velocity and Buoyancy Effects on Boiling Nitrogen," NASA Tech Note TN D-3354.
[7] Mishima, K., Nishihara, H., and Michiyoshi, I., 1985, "Boiling Burnout and Flow Instabilities for Water Flowing in a Round Tube under Atmospheric Pressure," Int. J. Heat Mass Transfer, **28**, pp. 1115–1129.
[8] Gersey, C. O., and Mudawar, I., 1993, "Orientation Effects on Critical Heat Flux from Discrete, In-Line Heat Sources in a Flow Channel," ASME J. Heat Transfer, **115**, pp. 973–985.
[9] Galloway, J. E., and Mudawar, I., 1993, "CHF Mechanism in Flow Boiling from a Short Heated Wall-Part 1. Examination of Near-Wall Conditions with the Aid of Photomicrography and High-Speed Video Imaging," Int. J. Heat Mass Transfer, **36**, pp. 2511–2526.
[10] Galloway, J. E., and Mudawar, I., 1993, "CHF Mechanism in Flow Boiling from a Short Heated Wall-Part 2. Theoretical CHF Model," Int. J. Heat Mass Transfer, **36**, pp. 2527–2540.
[11] Zhang, H., Mudawar, I., and Hassan, M. M., 2002, "Experimental and Theoretical Study of Orientation Effects on Flow Boiling CHF," Int. J. Heat Mass Transfer, **45**, pp. 4463–4478.
[12] Zuber, N., Tribus, M., and Westwater, J. W., "The Hydrodynamic Crisis in Pool Boiling of Saturated and Subcooled Liquids," *Int. Dev. Heat Transfer: Proc. Int. Heat Transfer Conf.*, Boulder, CO, 1961, pp. 230–236.
[13] Nejat, Z., 1981, "Effect of Density Ratio on Critical Heat Flux in Closed End Vertical Tubes," Int. J. Multiphase Flow, **7**, pp. 321–327.
[14] Wallis, G. B., 1969, *One-Dimensional Two-Phase Flow*, New York, McGraw-Hill Book Company.

Stability and Oscillations in an Evaporating Corner Meniscus

L. Zheng

J. L. Plawsky

P. C. Wayner, Jr.

The Isermann Department of Chemical Engineering,
Rensselaer Polytechnic Institute,
Troy, NY-12180

S. DasGupta

Department of Chemical Engineering,
Indian Institute of Technology, Kharagpur,
PIN-721302,
India

A Constrained Vapor Bubble Loop Thermosyphon, CVBLT, made of quartz was used to study the stability and oscillations of an evaporating curved wetting film of pentane in a corner. The film thickness profile was measured as a function of heat input, time, and axial position using image analyzing interferometry. The curvatures and apparent contact angles for the evaporating film under various operating conditions were obtained from the measured film thickness profiles. Instability (oscillation) of the liquid film was observed at relatively higher values of the heat input. The behavior of the curvature and the apparent contact angle of an oscillating film with changes in heat input was evaluated. Moving velocities of the oscillating film were calculated from the measured values of the liquid-wall wetted lengths and were found to be directly proportional to the difference between the instantaneous force acting on the curved film and the reference force. Using an augmented Young-Laplace pressure jump model, the effect of the excess free energy at the contact line on the oscillations was demonstrated. [DOI: 10.1115/1.1652046]

Keywords: Evaporation, Heat Transfer Instability, Surface Tension, Visualization, Contact line

Introduction

Intermolecular interactions in the three phase contact line region, where a liquid-vapor interface intersects a solid substrate, have been extensively studied because of their importance to many equilibrium and nonequilibrium phenomena such as contact angle, adsorption, spreading, evaporation, condensation, wetting and stability. The gradient in the liquid pressure due to interfacial and viscous forces along with the pressure and temperature differences at the liquid-vapor interface control fluid flow and phase change heat transfer processes in these microscale systems. Although there are numerous theoretical studies for these systems, we find that there is a lack of data on the oscillating contact line region with phase change. Such data are presented herein for an evaporating extended meniscus in a corner.

Deryaguin and his coworkers [e.g., [1–3]] demonstrated the use of the disjoining pressure gradient to evaluate the effect of interfacial forces on surface films and film transfer due to interfacial forces on enhanced evaporation of liquid from capillaries. This led to the use of a Kelvin-Clapeyron model to describe the effects of both interfacial shape (capillary and disjoining pressure jumps) and interfacial temperature jump on the heat transfer characteristics of a stationary evaporating meniscus [4–6]. A more detailed analysis of the same configuration was done by Homsy and coworkers [7,8]. Additional research on the stationary evaporating extended meniscus has been done [e.g., [9–15]]. These concepts have also been used to study the motion of volatile [16–18] and nonvolatile [19] drops subject to capillary, thermocapillary, and gravity forces. Burelbach et al. [20] and Sharma [21] have analyzed the effect of evaporation and condensation on the stability of thin film domains. A review is given in [22].

Capillary fluid flow in the corner of the Constrained Vapor Bubble Loop Thermosyphon, CVBLT, used herein is important. Related research includes extensive studies on the behavior of liquid films in the grooves of heat transfer devices [23–28]. Ayyaswamy et al. [23] obtained solutions to the two-dimensional equations of motion governing steady laminar flow in a triangular groove with the free surface governed by surface tension forces. Xu and Carey [24] used an analytical model to predict the heat transfer characteristics of film evaporation on a microgroove surface assuming that the evaporation takes place only from the thin film region of the meniscus. Stephan and Busse [13] have presented a model for the calculation of the radial heat transfer coefficient in heat pipes with open grooves and have shown why the assumption of an interface temperature equal to the saturation temperature of the vapor leads to a large over-prediction of the radial heat transfer coefficient. Swanson and Peterson [14] developed a mathematical model of the evaporating extended meniscus in a V-shaped channel to investigate the effect of wedge half-angle and vapor mass transfer on meniscus morphology, fluid flow, and heat transfer. Khrustalev and Faghri [27] developed a mathematical model to describe heat transfer through thin liquid films in the evaporator of heat pipes with capillary grooves. Babin et al. [25] tested a trapezoidal heat pipe with a square cross-section of 1 mm^2 and a length of 57 mm. Wu and Peterson [26] studied a wickless micro heat pipe of dimension $1\times1\times10-100$ mm^3. They successfully used the Young-Laplace equation to describe the internal fluid dynamics of this integrated device. From these works it was concluded that the longitudinal groove design was crucial to increase the heat transport capacity of these miniature devices and the small grooves provided the necessary capillary forces for the liquid to flow back into the evaporative zone. Analytical prediction of the axial dry out point for evaporating liquids in axial microgrooves and experimental verification of the predicted locations of the dry out points were also carried out [29].

While the above investigations provide valuable information on evaporating flow in microgrooves and thin films, the detailed experimental measurements and complementary analyses of the resulting data on curvature, apparent contact angle and particularly instabilities of thin evaporating films are not found in the literature. In the CVBLT system developed for this study, the thermal conditions were well controlled. The stable film could be driven to instability when the input heat flow rate due to conduction in the glass substrate was increased to a critical level. Using image analyzing interferometry, the apparent contact angle and interfacial curvature of the meniscus in the three-phase contact line region were obtained from the measured film thickness profiles. Effects of power input to the heater and axial location on the instabilities of thin films of pentane were also measured. Moving velocities of the oscillating film were calculated from the measured values of the liquid-wall wetted lengths. A force balance for the oscillating meniscus involving intermolecular, and shape governed forces

Contributed by the Heat Transfer Division for publication in the JOURNAL OF HEAT TRANSFER. Manuscript received by the Heat Transfer Division April 3, 2003; revision received December 2, 2003. Associate Editor: K. D. Kihm.

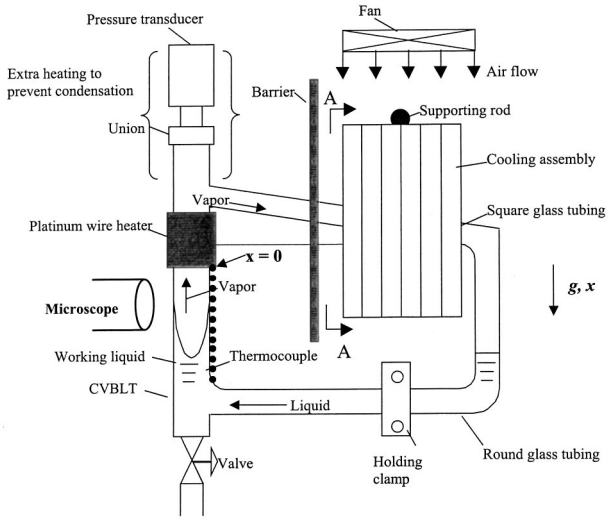

Fig. 1 Experimental setup of the CVBLT (not to scale). The region viewed by the microscope has a square cross-section.

was used to describe the oscillating velocity. Additional details concerning the experimental study beyond those presented in the next section can be found in [30].

The objectives of this paper are to describe a new experimental design, to present a set of experimental results, and to analyze the measured force balance for fluid flow and stability in the contact line region. Due to the complex, transient, large temperature gradients in the system, a theoretical analysis of the details of the three dimensional temperature and heat flux fields is beyond the scope of this paper.

Experimental Studies

Purification of the Liquids. Pentane, which is completely wetting in the fused quartz cell, (with purity of 99+ percent, as supplied by Aldrich Chemicals) was chosen as the working fluid. To remove the noncondensable gas (i.e., air) in the working fluid, a vacuum distillation setup was built based on the fact that when the vapor of the working fluid solidifies in a liquid nitrogen condenser, the noncondensable gas remains in the vapor phase [30]. Experimental results show that air can be completely removed by purifying twice.

General Experimental Setup of the CVBLT

Figure 1 shows the experimental setup of the vertical loop cell. The loop system consists of a quartz CVBLT cell (square cross section; inside dimension: 3 mm×3 mm; outside dimensions: 5.5 mm×5.5 mm; length: 60 mm), square glass tubing (inside dimension: 6 mm×6 mm; length: 100 mm) and round glass tubing (inside diameter: 3 mm). Although quartz has a low thermal conductivity, the advantages of transparency were more important than this limitation. The inclined tubing prevents the condensate from flowing back to the quartz cell. In addition, the square tubing conveniently allows the placement of eight thermoelectric coolers (Melcor®), which were used in conjunction with extruded fin heat sinks on each side. A highly thermal conductive paste was applied to all the contacting surfaces. A fan was placed above the fins to effectively carry away the heat. The cell was isolated from the resulting forced convection environment by a plastic barrier. The design of the cooling system was important since only efficient heat removal can generate sufficient vapor flow from the evaporator to the condenser.

A platinum wire with a nominal resistance of 12.84 ohm was wrapped onto grooves on the outer wall of the upper position of the CVBLT cell. The grooves were made with a spacing of 2 mm to permit a long wire, and therefore high heating power. An insulation paste was then applied to the wire. With the platinum wire wrapping around the cell, a symmetrical temperature distribution on the vertical cell wall is ensured. The heaters and the cooler were powered by two separate DC power supply. Due to the large three dimensional temperature gradients in the solid, the DC power input, Q_H, is used to discuss the data herein. In turn, this was correlated with a temperature gradient on the wall surface.

The outside wall temperature profile was measured using an automated PC-based LabView data acquisition system. Twenty-one Chromel-Alumel thermocouple beads (shown as bold black dots in Fig. 1.) with a diameter of 0.3 mm were pasted onto the quartz cell with a spacing of 2 mm. A 32-channel thermocouple amplifier (National Instrument *SCXI-1102*) was used that filtered and isolated noise from the signals, and amplified low signals. A cable assembly connected the module to the data acquisition board (National Instrument *PCI-MIO-16E-4*) in the PC. In these experiments, the gain was set at 100 so that the accuracy of the temperature measurement can reach 0.5°C. In fact, the effect of the uncertainty of the temperature was further reduced since the temperature difference with respect to the surroundings will be used in future theoretical analysis.

To measure the vapor pressure directly, a pressure transducer was placed on the top. A heating tape was wrapped onto the portion of the tubing close to the transducer. In this way, the vapor condenses significantly only in the condenser region. The pressure transducer data confirmed that the vapor was pure within the cell.

To facilitate cleaning, the setup was designed to have two ends of the quartz cell straight open during assembly. A syringe with a plastic tubing on top of the needle was used to flush the cell at high speed with the working liquid. The vertical loop cell was fixed onto the aluminum base plate and was mounted on a three-way translation stage for the microscope. The loop system was placed on an air-buffered optical bench to eliminate any vibration affecting the image from the CCD camera, specially at higher magnifications.

Measurement Techniques and Data Analysis

The interference phenomena associated with reflected monochromatic light were used to determine the thickness profile of the liquid film in the CVBLT experiments. When monochromatic light from the microscope was normally incident on the CVBLT cell through the objective, the reflected light from the solid-liquid and the liquid-vapor interface of the thin liquid film interfered constructively or destructively [e.g., [30–32]]. A picture of the observed interference fringe patterns for two different cases is presented in Figs. 2(*a*) and (*b*). Destructive interference occurred when the optical paths of the two reflected beams were such that they were out of phase by π due to a phase shift at each interface. In this case, $n_v < n_l < n_s$, where n was the refractive index, and subscripts v, l, and s denoted vapor, liquid and solid, respectively. Constructive interference occurred when the two reflected beams were in phase. The relationships for the film thickness (δ) associated with the intensity for these two cases are

$$\delta = (2m+1)\frac{\lambda}{4n_l} \quad \text{Minima} \tag{1}$$

$$\delta = m\frac{\lambda}{2n_l} \quad \text{Maxima} \tag{2}$$

where m was the order of the fringes, $m = 0,1,2 \ldots$, n_l was the refractive index of the liquid, and λ was the wavelength of the monochromatic light. Note that the smallest film thickness for a wavelength that could be determined directly (Eq. (1), with $m = 0$), were 0.0802 μm for blue, 0.1 μm for green.

Using a conventional microscope light source projected through the objective of the microscope (Leitz Model SM-LUX HL), monochromatic light from a *Hg* arc with a narrow band filter (543.5 nm or 435.8 nm) was used to illuminate the cell. The image

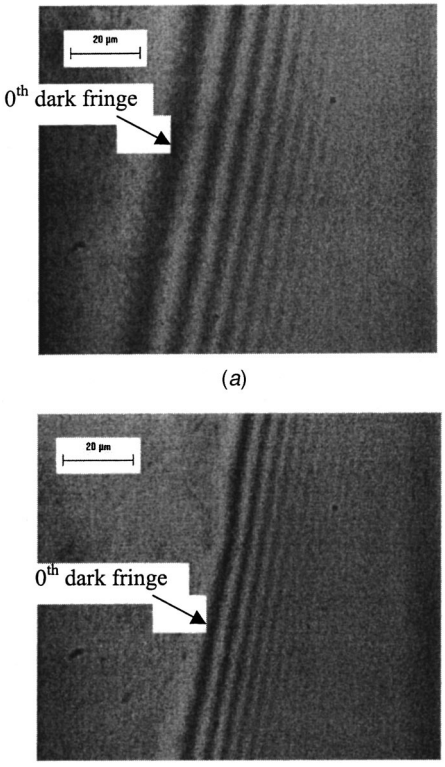

Fig. 2 (*a*) Interference pattern of the stationary film at $x=2.13$ mm $Q_H=0$, $\theta_c=0$, $K=961\pm8$ m^{-1}; and (*b*) Interference pattern of the stationary film at $x=2.13$ mm with $Q_H=1.92$ W, $\theta_c=1.23°$, $K=2015\pm24$ m^{-1}.

captured through a CCD camera (Javelin Ultrichip™) was digitized into 640 pixels (horizontal)×480 pixels (vertical) by the frame grabber (Data Translation, *DT 3155*), and the digitized image was assigned one of 256 possible gray values representing an intensity from 0 (black) to 255 (white). For the CCD camera–microscope, at 100× objective combination used in this study, each pixel represented a diameter of 0.088 μm; for a CCD camera–microscope at 50× objective combination, each pixel represented a diameter of 0.1777 μm. A plot of gray values versus the distances was then extracted from the interference fringes using the image processing software (Media Cybernetics, Image Pro-Plus). The curvature of the curved film was obtained using image analyzing techniques. Due to the fact that thicker liquid films absorb more light, the upper value of the film thickness that could be accurately measured was limited to about 5–6 μm.

In general, the optical technique used herein can be called Image Analyzing Interferometry, IAI. A similar approach used by Weigand et al. [33] has been called reflection interferometry. Das-Gupta et al. [31] and Karthikeyan et al. [32] used an image analyzing interferometry to measure curvatures of a completely wetting liquid film. Under the assumption that the square of the slope, $(d\delta/dy)^2$, was very small compared to one, the curvature was obtained from the slope of the plot of the square root of the film thickness $(d\delta^{1/2}/dy)$. For the isothermal CVBLT with a small inclination angle and the intermediate region of the non-isothermal CVBLT, the curvatures were relatively small and the experimental data agreed well with the theoretical results. However, with high evaporating rates and/or with partially wetting liquids, a new analyzing technique is needed since the value of $(d\delta/dy)^2$ becomes too large. Therefore, using the definition of the curvature, an improved analytical expression for the curvature as a function of the film thickness profile and the apparent contact

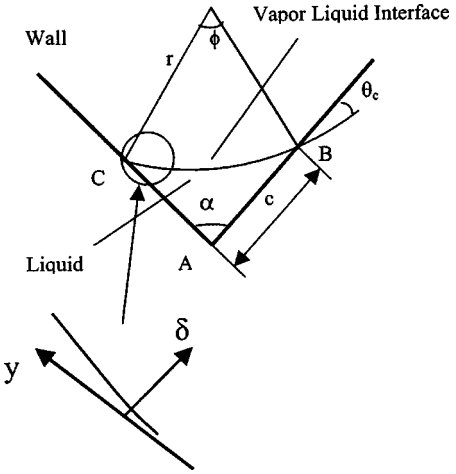

Fig. 3 One corner of the CVBLT with the geometrical parameters. Relative distance, *y*, is along AB and film thickness δ is measured perpendicular to AB.

angle was presented in Zheng et al. [30,34,35] and used for this study as well. The expression developed in that work can be used to obtain simultaneously the curvature and the apparent contact angle for a curved film of either a partially wetting fluid or a completely wetting fluid in the region where disjoining pressure can be neglected. Following their derivation, the location (y) of the film thickness (δ) for the corner meniscus drawn in Fig. 3 can be written as

$$y=c+\frac{\sin\theta_c}{K}-\sqrt{\frac{1}{K^2}-\left(\frac{\cos\theta_c}{K}-\delta\right)^2} \tag{3}$$

The two unknowns, $K=r^{-1}$ (curvature) and θ_c (apparent contact angle at $\delta=0$) can be obtained simultaneously by best fitting the experimental film thickness profile to obtain the minimum of the function, $(\Sigma_{i=1}^{N}(y_{\exp,i}-y_{\mathrm{cal},i})^2)$, where N is the total number of observable dark and bright fringes. The subscripts "exp" and "cal" denote the experimental data and best fitted values obtained from Eq. (3), respectively. Note that the liquid-wall contact line length, c, in Eq. (3) is canceled out during the data fitting since only the relative distances between the fringes to the first fringe are needed. Equation (3) is used here to obtain the curvature of a concave film in the corner of the cell.

The work by Zheng et al. [30,34] also included a detailed error analysis associated with the resolution of the image processing system. They have shown that the error associated with the system resolution increases as the curvature increases, the apparent contact angle increases, the wavelength decreases, and the number of dark fringes used for the data fitting decreases. Their experimental results with pentane as the working fluid showed that Eq. (3) described the film profile in the thicker portion of the meniscus within an accuracy of 1 percent when the curvature is constant. The accuracy of the data fitting based on the assumption of a constant curvature can also be used to determine the region where the disjoining pressure or viscous flow affects the profile because of an observable curvature gradient.

Results

It was observed in the pentane/fused-quartz system that when no heat was supplied to the CVBLT, the film was at equilibrium, very stable, and the apparent contact angle of the film was equal to zero. Isothermal hydrostatics was used to confirm the accuracy of the experimental procedures by measuring the variation of interfacial curvature with vertical distance [30]. As the input heat flow rate due to conduction in the glass was increased, the shape of the meniscus changed and, at a certain level, the film was

Table 1 Variations of the values of D_1 and D_{12} for the fringe patterns at different power inputs to the heater at $x=2.13$ mm

Q_H (W)	D_1 (μm)	D_{12} (μm)
0	38	11
1.65	48	9
1.92	52	6
2.34	56	4
3.15	63	3

driven to instability and started to oscillate. The onset of instability, apparent contact angle and curvature of the meniscus varied with power input and axial location. The effects of power input to the heater and axial location on the instability of the thin film of pentane will be discussed first. Subsequently, the oscillating phenomena will be analyzed using a macroscopic interfacial force balance that relates contact line velocity to interfacial forces and apparent contact angles.

Effect of Power Input to the Heater on Pentane Film Instabilities. To study the effect of power input to the heater (Q_H) on the film oscillation in the vertical loop cell, a particular axial location, x, was chosen. The position $x=0$ was located immediately below the platinum wire heater where the first thermocouple was pasted. The power input to the heater was increased gradually. At each level of the power, data were taken after the CVBLT reached steady state, which usually took about one or two hours. The interference patterns (Fig. 2(*a*) and (*b*)), which give the film profile, were found to be a function of local thermal conditions on the surface. We note that the profile change is easily observed. The film was very stable when no heat was applied. As the power input to the heater was increased gradually, the film started to recede towards the corner of the cell. The spacing between interference fringes decreased. The apparent contact angle, evaluated at zero thickness, as obtained from Eq. (3), the interfacial curvature and the temperature profiles were obtained. The uncertainty in the location reading was ± 0.01 mm and the uncertainty in the power reading was ± 0.05 W. The power input to the cooler was set at 4.35 W. In order to give a clear demonstration of the receding of the film, the distance between a leftmost position and the position of the first dark fringe, D_1 and the spacing between the first two dark fringes, D_{12}, were measured. Table 1 lists variations of the values of D_1 and D_{12} for the fringe patterns as a function of power input. As the power input to the heater increased from 0 to 1.92 W, the first dark fringe of the film receded from $D_1=38$ μm to $D_1=52$ μm towards the corner. The uncertainty in the fringe spacing reading was 2.5 percent. The spacing, D_{12}, decreased from 11 μm to 6 μm. At $Q_H=2.34$ W, the film started to oscillate, representative values of D_1 and D_{12} were 56 μm and 4 μm, respectively. The film length decreased, and then increased. The motion of the film for any power higher than 3.15 W was very fast, and the fringes became blurred indicating the oscillation of the film.

The film thickness profiles at an axial location of $x=2.13$ mm of the CVBLT under different power inputs to the heater are shown in Fig. 4. For two of the Profiles, the apparent contact angles, θ_c, and curvatures, K, are given at the bottom of Fig. 2 with an error estimate for the curvature. Since it involves only the slope, the error in apparent contact angle is considerably less. The circles in Fig. (4) represent the experimental data, and the solid line represents theoretical results from Eq. (3). The number of fringes observable decreased when Q_H increased. At the higher power inputs to the heater, the film oscillated faster and the film profile became steeper. A representative figure (Fig. 5) shows the film at different stages of oscillation with the values of curvature and apparent contact angle at each instant. The apparent contact angles and curvatures for the film thickness profiles presented in Fig. 4, were obtained and plots of their variations with the power input to the heater are shown in Fig. 6(*a*) and (*b*), respectively.

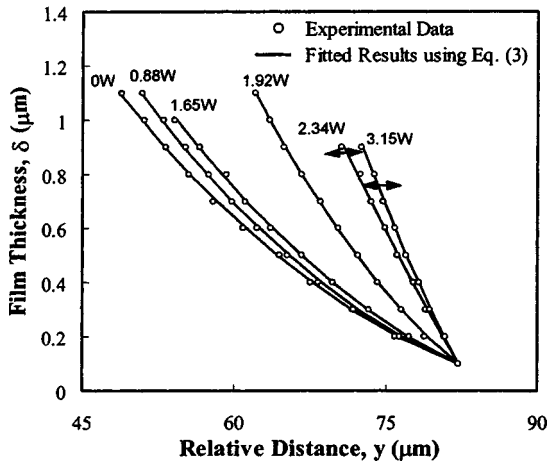

Fig. 4 Film thickness profiles at $x=2.13$ mm under different power inputs to the heater. The arrows represent oscillating film.

The apparent contact angle remained zero when the power input to the heater was increased from 0 to 0.88 W, and the film was stable throughout this range. The curvature varied little around 1000 m^{-1} when $\theta_c=0$. When the power input to the heater was increased from 0.88 W to 2.33 W, the film was still stable, but the apparent contact angle increased from 0 to 2.4 deg, and the curvature increased to 2000 ± 64 m^{-1}. The apparent contact angle was obtained from a constant curvature fit to the data and above a thickness of $\delta=0.1$ μm, the constant curvature fit was very good. However, there was a curvature gradient theoretically near the contact line (which could not be measured) that should theoretically result in a real contact angle at $\delta\rightarrow 0$ equal to zero [e.g., [12]]. When the power input to the heater reached 2.34 W, the film became unstable, and the apparent contact angle and curvature oscillated around an average value of 2.64 deg and 1819 ± 58 m^{-1}. As power input to the heater was further increased to 3.15 W, the contact angle oscillated around a larger average value of 4.1 deg, and the curvature oscillated around an average value of 2391 ± 131 m^{-1}. Similar results were obtained at different axial locations in the CVBLT and will be discussed next.

Effect of Axial Location on Film Instabilities. To systematically study the effect of axial location (x) on film instabilities, the variations of film profiles, apparent contact angles, and curvatures were measured at a number of axial locations under different power inputs to the heater. The power input to the cooler was set at $Q_C=4.35$ W. Two values of the power input to the heater were chosen, $Q_H=1.79$ W and $Q_H=2.26$ W.

The axial variations of the apparent contact angles at these two power inputs are plotted in Figs. 7 and 9 and the curvature variations are plotted in Fig. 8 and 10. As is evident from these two figures, the film was stable and spread out close to the cooler (higher values of x) for both the power inputs. At a location between $x=3$ mm and $x=3.6$ mm, i.e., near the cooler, the apparent contact angle was zero for $Q_H=1.79$ W, as shown in Fig. 7. For x less than 3 mm, the apparent contact angle started to increase but the film still remained stable till $x=2.74$ mm. The two vertical dashed lines represent two distinct regimes of operation. The region right to the rightmost dashed line represents a region where the film was stable, the apparent contact angle was equal to zero and the curvature was nearly constant. In the region between the two vertical dashed lines, the film was still stable (no oscillation), but a gradual increase in the apparent contact angle and curvature were observed. In the region left of the dashed lines, oscillations of the film were noticed as can be seen in the multiple values of curvature and apparent contact angles at a specific heat input.

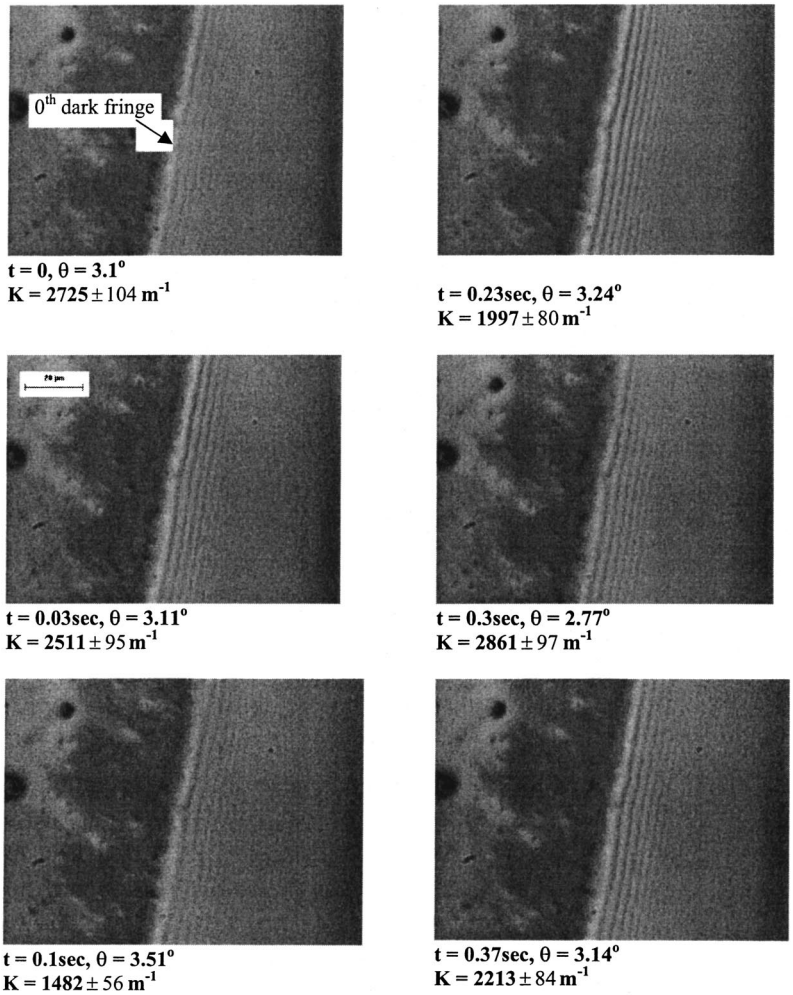

Fig. 5 Interference pattern of the oscillating film at $x=2.34$ mm with $Q_H=1.79$ W

Closer to the heater, the local heat flow rate increased and the film receded to the corner and started to oscillate for a specific heat input. At $x=2.74$ mm, the film started to oscillate around an average contact angle of 1.54 deg. As can be seen from Fig. 8, the curvature near the heater was about $814\pm8\ \mathrm{m}^{-1}$ and increased slowly to $1438\pm29\ \mathrm{m}^{-1}$ at $x=2.74$ mm. The resulting pressure gradient caused the liquid condensate to flow from the condenser to the evaporator against both gravitational force and viscous stress. For $Q_H=1.79$ W, in Figs. 7 and 8, the film started to oscillate at $x=2.74$ mm, shown by the multiple values of contact angles and curvatures at a specific axial location and highlighted by vertical lines showing the amplitude of the oscillation. At $x=2.74$ mm in Fig. 7, the contact angle started to oscillate around an average apparent contact angle of $\theta_c=1.54$ deg. Closer to the heater at $x=1.99$ mm, the film oscillated around a larger average apparent contact angle of $\theta_c=3.82$ deg indicating more intense evaporation. The average contact angle was found to increase linearly with axial location. The average value of the curvature remained relatively less affected by the axial location with values changing from $1438\pm29\ \mathrm{m}^{-1}$ to $2113\pm106\ \mathrm{m}^{-1}$.

Figures 9 and 10 represent a comparison with a higher power input to the heater equal to 2.26 W. Compared to a lower power input to the heater, the film receded further towards the corner, and the fringe spacing became sharply smaller. Figure 9 gives a comparison of the apparent contact angle variations at these different power inputs to the heater. In the unstable region, the slope of the average contact angle versus axial location at the higher power input to the heater ($Q_H=2.26$ W) was 4, which is 1.4 times larger than that at the lower power input to the heater ($Q_H=1.79$ W). The apparent contact angle started to increase towards the heater end at $x=3.6$ mm, where the length of the unstable region was 0.5 mm longer. These results clearly demonstrate that the contact angle varies more rapidly with a higher power input to the heater, indicating more intense evaporation. The increase of the power input to the heater also elongated the dry out region. Figure 10 shows the variation of the curvature in the axial direction. As can be seen, in the stable region, the curvature increased from $986\pm8\ \mathrm{m}^{-1}$ to $1689\pm30\ \mathrm{m}^{-1}$ to provide the driving force in the corner for the condensate return. In the unstable region, the film oscillated around its average curvature at each axial location with the average value changing from $1700\pm50\ \mathrm{m}^{-1}$ to $2000\pm110\ \mathrm{m}^{-1}$. At even higher power inputs, the fringe spacing became smaller and as the film experienced more intense oscillations at higher values of heat input, the fringes became blurred and generated a wave-like front due to rapid movements.

Figure 11 shows the corresponding temperature profiles for different power inputs to the heater with the power input to the cooler at $Q_C=4.35$ W. It is to be noted that Q_C and Q_H are not balanced due to heat loss to the surrounding and that the outside surface temperatures in the bulk liquid region at different heater power inputs were slightly different. The temperature profile became steeper as the power input to the heater was increased. The temperature data was fit with a smooth curve to obtain the temperature gradient. The local heat flow rate calculated using $Q_x=-k_sA_s dT/dx|_{x=1.21\ \mathrm{mm}}$ for different power inputs to the heater is shown in Fig. 12. As can be seen, the local heat flow rate in-

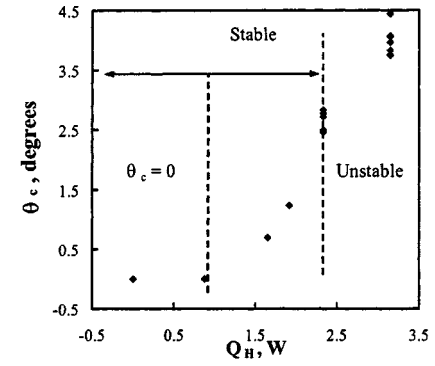

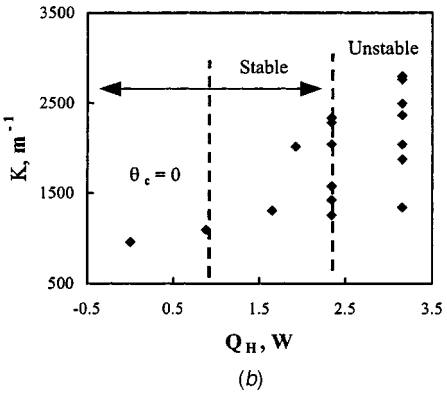

Fig. 6 (*a*) Variation of the apparent contact angle with the power input to the heater at $x=2.13$ mm; and (*b*) Variation of the curvature with the power input to the heater at $x=2.13$ mm.

creased as the power input to the heater increased. When the film became unstable at 1.76 W, the slope of the local heat flow rate increased significantly, from 0.00303 to 0.013. This indicates that the instabilities of the film promoted heat transfer. Although the outside surface temperature profile did not give more obvious information about the details of the phase change process on the inside, a close inspection of the data demonstrates that the temperature measurements above $x\approx 3$ mm fit a different profile than those below $x\approx 3$ mm. Unfortunately, insufficient information were available to resolve the meaning of this beyond saying that it indicated the location of an evaporation-condensation process. To use these temperature profiles further, a three dimensional numerical analysis beyond the scope of this paper is needed.

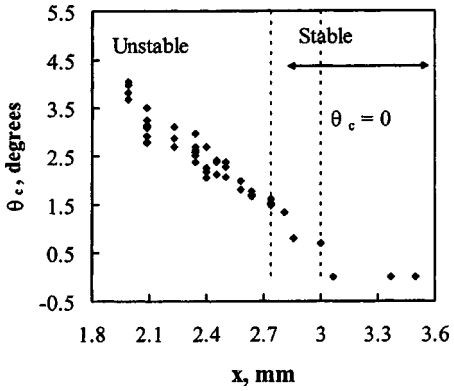

Fig. 7 Variation of the apparent contact angle with the axial location for $Q_H=1.79$ W

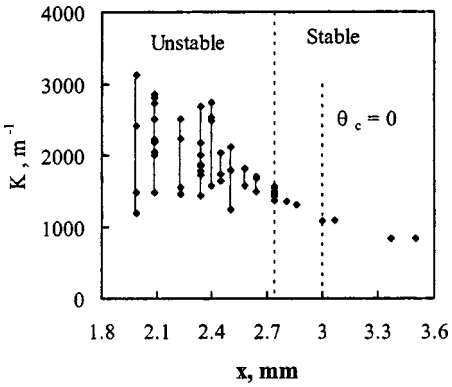

Fig. 8 Variation of the curvature with the axial location for $Q_H=1.79$ W. The solid lines are guides for the reader's eye.

Oscillating Films. Figure 13 illustrates the macroscopic interfacial force balance that relates viscous losses to interfacial forces and apparent contact angles in the oscillating film for the control volume from δ_o to δ at a particular axial location, x, of the CVBLT. Due to the extremely small momentum of the system, we assume that the sum of the forces acting on the interfaces of the control volume is balanced. Using the methodology presented in [36,30], and [35], an interfacial force balance between the menis-

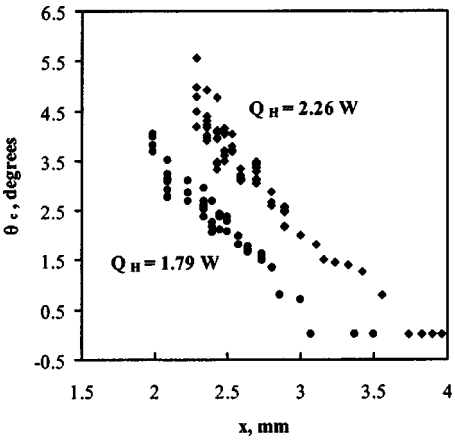

Fig. 9 Variations of the apparent contact angles with the axial location at different power inputs to the heater

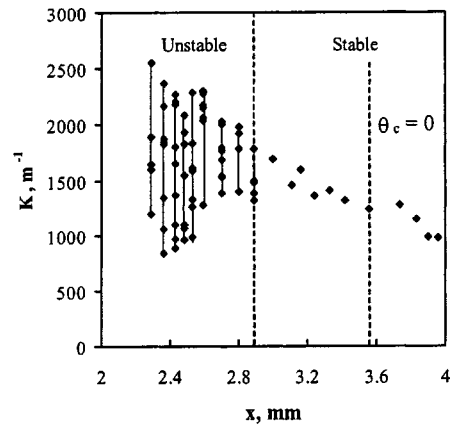

Fig. 10 Variation of the curvature with the axial location for $Q_H=2.26$ W. The solid line is a guide for the reader's eye.

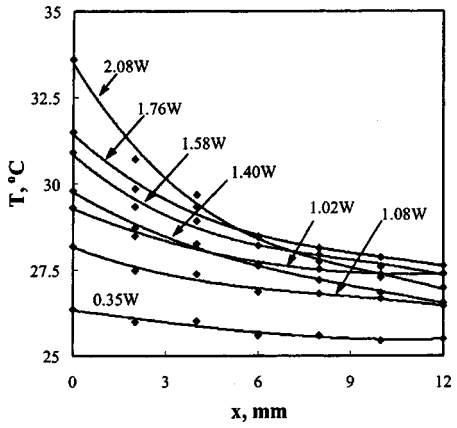

Fig. 11 Temperature profiles at different power inputs to the heater with Q_c=4.35 W

cus in the corner (measured at δ=0.1 μm) at a reference average (in terms of oscillation) state, *r*, and the flat liquid film on the quartz surface (at δ_o) is given as

$$\sigma_{lv}\cos\theta_{ir}+\sigma_{ls}+(\sigma_{lv}K_r+\Pi_r)\delta = \tau_0 L_0+\sigma_{lv,0}+\sigma_{ls,0}+(\sigma_{lv,0}K_0+\Pi_o)\delta_o \quad (4)$$

where τ_0 is the average shear stress that the solid exerts on the fluid over the length L_0, δ_o is the average film thickness at the contact line end of the control volume, Π_o is the disjoining pressure, The need to define a reference state in the relatively thicker portion of the film necessitates the selection of a specific thickness, to be used for the oscillating film study. The thickness of the zeroth dark fringe in the interferometric images corresponding to a thickness of 0.1 μm, was chosen for this study. At this thickness, the relevant quantities, e.g., the curvature, apparent contact angle,

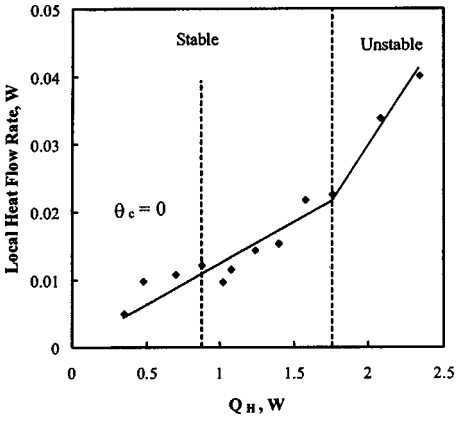

Fig. 12 Local heat flow rates at x=1.21 mm at different power inputs to the heater with Q_c=4.35 W

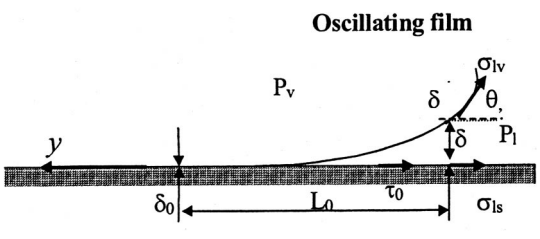

Fig. 13 A schematic of the macroscopic interfacial force balance for the oscillating film in the corner of the CVBLT when $U>0$, $\tau_0<0$

disjoining pressure were calculated and/or estimated and compared with the corresponding values at the flat, adsorbed end of the film using Eq. (4). Thus θ_{ir} is the value of the apparent contact angle at δ=0.1 μm at a reference state. It is to be noted that this apparent contact angle (evaluated at δ=0.1 μm), though different from that used in Eq. (3), represents a very small difference in actual values. ($\Pi_o\delta_o+\sigma_l K_o\delta_o$) represents the suction at δ_o due to interfacial forces. The product $\tau_0 L_0$ represents a retarded force, opposite to the direction of *U*. Π_o represents the force per unit area at the contact line (disjoining pressure representing free energy per unit volume) and is positive for a completely wetting fluid. The acceleration of the system under consideration was calculated from experimental results and was found to be negligibly small. The value of the apparent contact angle is a function of the location because of the curvature, *K*. We also note that the value of the contact angle at δ_0 cannot be measured directly but only inferred from the variation of the tangent angle using a model for the curvature.

Assuming that $\sigma_{lv}=\sigma_{lv,0}=\sigma_l$, $\sigma_{ls}=\sigma_{ls,0}$, Eq. (4) can be simplified as

$$\tau_0 L_0+\Pi_0\delta_0+\sigma_l K_o S_o=\sigma_l(\cos\theta_{ir}-1)+(\sigma_l K_r+\Pi_r)\delta \quad (5)$$

In the above equation, the sum of $\tau_0 L_0$ and $\Pi_o\delta_o$ can not be measured using interferometry because δ_0 is too small, but inferred from the measurements given on the right hand side of Eq. (5). To overcome the difficulty of measuring the disjoining pressure at the thicker end of the control volume, δ, the film thickness (δ) is taken to be the thickness at the first destructive interference fringe, 0.1 μm, where the apparent contact angles can be measured. This approach has been widely used in the literature on isothermal systems. At this thickness, the disjoining pressure can be neglected and for $\delta \geqslant 0.1$ μm, the curvature of the meniscus is found to be approximately constant within experimental measurements.

Equation 5 can be rewritten in dimensionless form by dividing by σ_l to give the dimensionless force, F_r, for the curved film at a reference state.

$$F_r=\cos\theta_{ir}+K_r\delta=\left[\frac{\tau_0 L_0+\Pi_0\delta_0+\sigma_l K_o\delta_o+\sigma_l}{\sigma_l}\right]_r \quad (6)$$

Since the right hand most term of the above equation is equal to the force at the reference state, the subscript "*r*" is added to this term. The difference in the measured force at the reference state and at any instant (*i*) can now be expressed as

$$\Delta F=F_r-F_i=\left[\frac{\tau_o L_0+\Pi_o\delta_o+\sigma_l K_o\delta_o+\sigma_l}{\sigma_l}\right]_r - \left[\frac{\tau_o L_0+\Pi_o\delta_o+\sigma_l K_o\delta_o+\sigma_l}{\sigma_l}\right]_i \quad (7)$$

For an oscillating film, the difference between the dimensionless retarded force of the oscillating film ($\cos\theta_i+K_i\delta$) at any instant of time (*i*) and that at the reference state ($\cos\theta_{ir}+K_r\delta$) will govern the magnitude of the resulting velocity measured during the next interval. This will be discussed in more detail later. θ_i and K_i represent apparent contact angle and curvature at a moment t_i. θ_i is measured at a film thickness of δ=0.1 μm.

As discussed earlier, the film oscillated by receding towards the corner and then spreading out towards the flat film. The variations of the contact angle and curvature with time at a fixed location are presented in Figs. 14 and 15 at x=2.65 mm and x=2.98 mm. The power inputs to the heater and cooler were 1.97 W and 15.3 W, respectively. Note that the apparent contact angles, θ_c, shown in these figures are extrapolated values at δ=0, as defined by Eq. (3), although the apparent contact angle (tangent angle, θ_i) at δ=0.1 μm as defined in Eq. (4), was used below in the force balance. There is a small difference in these values which is calculated using *K*. As can be seen in Figs. 14 and 15, variations of

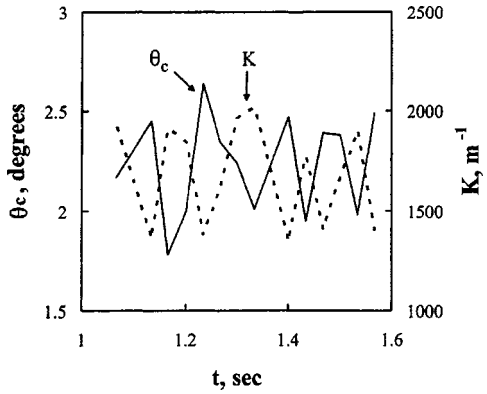

Fig. 14 Variations of the apparent contact angle and curvature with time at $x=2.65$ mm. The solid lines are guides for the reader's eye.

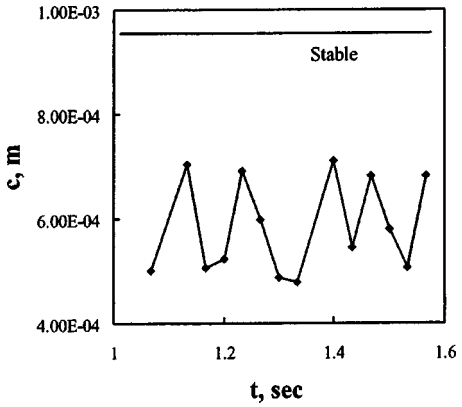

Fig. 16 Variation of the liquid-wall wetted length with time at $x=2.65$ mm. The solid line is a guide for the reader's eye.

contact angle and curvature followed a certain trend, oscillating around average values. In the unstable region, both the contact angle and the curvature oscillated around an average value, and the average values of each increased linearly with power input to the heater.

The liquid-wall wetted length and the film velocity were also used to characterize the oscillating film in the CVBLT. The liquid-wall wetted length, c_i, at a moment t_i is given as

$$c_i = \frac{1}{K_i}\frac{\sin\frac{\phi}{2}}{\sin\frac{\alpha}{2}} \tag{8}$$

where $\phi=\pi-(2\theta_c+\alpha)$, α was the vertex angle of the groove, $\alpha=\pi/2$ for the CVBLT that was studied, θ_c was the apparent contact angle between liquid and wall at $\delta=0$. The analysis (using Eq. (3)) of the captured images of the fringes was used to obtain the values of the curvature and contact angle at a specific instant. They, in turn, were used to estimate the wetted length (c_i) from the above equation. The moving velocity of the oscillating film could be calculated from the change of wetted length between times t_{i-1} to t_i by

$$U_i = \frac{c_i - c_{i-1}}{t_i - t_{i-1}} \tag{9}$$

If the contact line velocity was positive, it indicated that the contact line moved towards the flat film. If negative, the contact line moved towards the corner. An example of the variations of c with time is presented in Fig. 16.

The dimensionless forces of the oscillating film ($K_i\delta+\cos\theta_i$) and the moving velocity of the contact line, U_i, at a fixed location of $x=2.65$ mm were calculated from the data and are presented in the Table 2. The reference value of the dimensionless force, F_r, was calculated to be equal to 0.99925. The apparent contact angle, its contribution to the force, the difference of the reference force and the difference between the reference and instantaneous con-

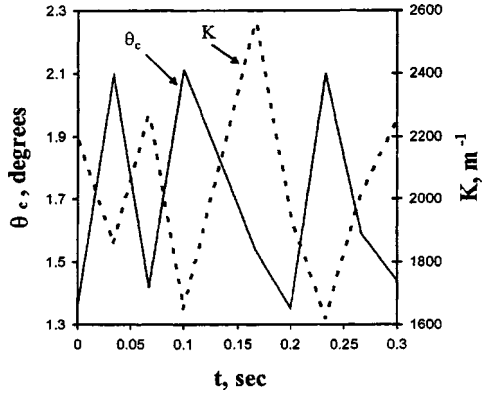

Fig. 15 Variations of the apparent contact angle and curvature with time at $x=2.98$ mm. The solid lines are guides for the reader's eye.

Table 2 Velocities, contact angles and dimensionless forces of an oscillating film at different times. The velocity in column 2 is for the time instant given in column 1 of the same row, whereas the entries for the cause in column 3 to 7 are evaluated at the previous time instant of measurement.

Time, (t) Sec	Velocity, U_i μm/sec calculated at time t	Apparent contact angle, θ_i at 0.1 μm (°)	Apparent contact angle difference $\theta_{ir}-\theta_i$	Dimensionless force, F $(K_i\delta+\cos\theta_i)$	Force due to apparent contact angle alone, $\cos\theta_i$	Force difference causing flow $\cos\theta_{ir}-\cos\theta_i$
1.13	3048.5	2.44	0.031	0.99928	0.99909	−2.40e−5
1.20	−5916.1	2.62	−0.151	0.99909	0.99895	1.174e−4
1.26	5057.4	2.28	0.191	0.99939	0.99920	−1.39e−4
1.30	−3280.5	2.56	−0.089	0.99916	0.99900	6.78e−5
1.33	−308.6	2.51	−0.037	0.99924	0.99904	2.72e−5
1.40	3482.1	2.31	0.158	0.99938	0.99918	−1.16e−4
1.43	−4953.6	2.64	−0.168	0.99907	0.99893	1.30e−4
1.46	4075.4	2.23	0.246	0.99942	0.99924	−1.77e−4
1.50	−3059.8	2.57	−0.101	0.99913	0.99899	7.69e−5
1.53	−2166.5	2.60	−0.123	0.99914	0.99897	9.45e−5
1.56	5260.3	2.27	0.201	0.99940	0.99921	−1.46e−4

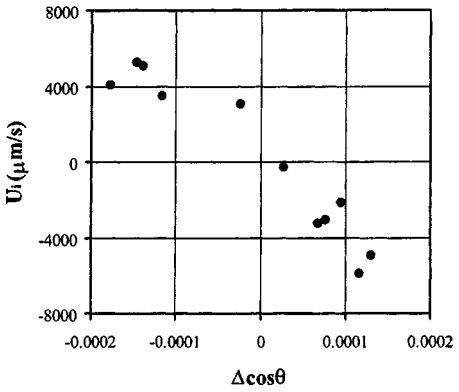

Fig. 17 Plot of contact line velocity in μm/s as a function of the change in the force due to contact angle [$\Delta \cos \theta (=\cos \theta_{ir} - \cos \theta_i)$]

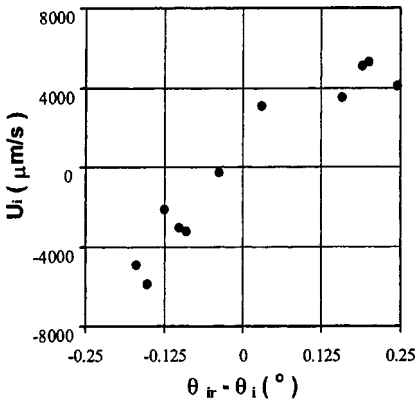

Fig. 18 Plot of contact line velocity in μm/s as a function of the change in contact angle [$\theta_{ir} - \theta_i$]

tact angle are also presented. The reference contact angle is 2.48° and its contribution to the force is cos θ_{ir} and is equal to 0.999067. The moment that the velocity is zero cannot be captured with the present camera, a high speed camera is needed. We postulate that the resulting contact line velocity, U_i, for the time period between "$i-1$" and "i" is a direct function of the measured state (K,θ) of the contact line at the initial instant, "$i-1$." Thus the values in columns 3 to 7 represent measurements taken at the previous time instant, e.g., the contact angle of 2.62 in the second row and third column of the table for $U_i = -5916.1$ μm/s for $t = 1.20$ s is the contact angle measured at time $t = 1.13$ s. The data tell us that when $\theta_i < \theta_{ir}$, i.e., $\theta_{ir} - \theta_i > 0$, the suction at the contact line is larger than the reference condition and $U > 0$, with flow towards the flat surface. When $\theta_i > \theta_{ir}$, the reverse is true.

Comparing columns 5 and 6 in Table 2, it is clear from the data that the major apparent contribution to the dimensionless force is from the term containing the cosine of the contact angle (in Eq. 6) with very little apparent contribution from the curvature (capillary force). However, we note that this observation does not affect the following conclusions. The data present in the table clearly indicates that if the force, F_i, was more than the reference force for an oscillating meniscus ($\Delta \cos \theta$ negative), it was associated with a positive value of the velocity (i.e., flow towards the flat film from the corner of the CVBLT) and the development of a larger contact angle. The data demonstrate that if the magnitude of the force measured at the thicker end of the film at any instant (F_i) was greater than the magnitude of the reference force (F_r) at the same location, the system would try to flow back to the reference state. This would happen not only at δ_i (where the measured forces acting are F_r and F_i) but also for $\delta < \delta_i$ (with the modeled forces being denoted by $F_{r,o}$ and $F_{i,o}$ plus the shear). Thus, because the magnitude of $F_{i,o}$ was larger than $F_{r,o}$, the oscillating film would try to reduce the magnitude of $F_{i,o}$. As the principal component of the force at δ_o was $\pi_o \delta_o$, a reduction in the force would be accomplished by a decrease in Π_o which varies as δ_o^{-3}. This increase in δ_o requires a flow towards the flat film, i.e., U_i was positive according to the sign convention used herein. Therefore, any negative value of $(F_r - F_i)$ should signify a flow towards the flat film or a positive value of U. Note that a negative value of $(F_r - F_i)$ signified that $(\theta_{ir} - \theta_i)$ was positive. The data presented in the Table 2 is consistent with the previous discussion. At the present time, further resolution of the details of the process in the region $\delta < 0.1$ μm is beyond the scope of this paper.

We postulated that the contact line velocity at any instant was a function of the degree of departure of the system from its reference condition in terms of the dimensionless forces. Therefore the contact line velocity would depend on the difference $(\Delta \cos \theta)$ between the cosine of the reference contact angle $(\cos \theta_{ir})$ and that at any instant $(\cos \theta_i)$. Figure 17 is a plot of the contact line velocity as a function of $\Delta \cos \theta$ showing an almost linear dependency between the apparent cause $(\Delta \cos \theta)$ and the effect (U). The next figure (Fig. 18) is a plot of the instantaneous velocity as a function of the contact angle difference $(\theta_{ir} - \theta_i)$ and it is consistent with the previous discussion. The significance of the consistency of these results with the physical understanding of the underlying phenomena cannot be overemphasized considering the difficulties associated with the acquisition of data at higher values of heat inputs (rapidly oscillating meniscus).

Conclusions

- A novel Constrained Vapor Bubble Loop Thermosyphon, CVBLT, was used to study the transport processes and instabilities associated with an evaporating, extended meniscus of pentane.
- Image analyzing interferometry was used to measure the film thickness profile, the apparent contact angle and curvature of the curved liquid film.
- At a particular axial location, as the heater power input increases, both the apparent contact angle and curvature increase. As the heater power input is increased to a certain level, the film starts to oscillate around an average value of the contact angle and curvature. As the heater power input is increased further, the film oscillates around a larger value of the contact angle, while the average value of the curvature undergoes relatively small change.
- At the same heater input powers, the apparent contact angle increases along with the axial location in the stable film region. As it gets close to the heater, the film starts to oscillate around an average apparent contact angle. The curvature increases with the axial location in the stable region. In the unstable region, the film oscillates around an average curvature.
- The oscillating phenomena were described using a macroscopic interfacial force balance that relates viscous losses to interfacial forces and the apparent contact angles. Contact line velocities of the oscillating film were obtained and were found to be directly proportional to the difference between the instantaneous force acting on the curved film and the reference force.
- Using an augmented Young-Laplace pressure jump model, the effect of the excess free energy at the contact line on the oscillations was demonstrated.

Acknowledgment

This material is based on work supported by the National Aeronautics and Space Administration under grant #NAG3-2383 and NAG3-2351.

Nomenclature

A = area (m^2) or Hamaker constant (Jm)
a = inner diameter of the CVBLT (m)

c = wetted length (m)
D_1 = distance between the position of the leftmost and first dark fringe (μm)
D_{12}, = spacing between first two dark fringes (μm)
K = curvature of liquid film (m^{-1})
m = order of interference fringes
n = refractive index
P = pressure (Pa)
Q = power input or heat flow rate (W)
r = radius of curvature (m)
T = temperature (°C)
U = velocity (m/s)
x = axial distance (m)
y = coordinate shown in Fig. 3

Greek Characters

α = angle at the corner of the CVBLT cell
β = inclination angle
δ = liquid film thickness (m)
θ_c = apparent contact angle at zero thickness
θ_i = apparent contact angle at a thickness of 0.1 μm
θ_{ir} = reference apparent contact angle at a thickness of 0.1 μm
λ = wavelength of the monochromatic light (m)
$-\Pi$ = disjoining pressure (Pa)
σ = surface tension (N/m)
τ = shear stress (Pa)
ϕ = angle covered by the arc of the meniscus at the corner of the CVBLT cell

Subscripts

C = cooler
cal = calculated results
exp = experimental results
H = heater
r = reference state
s = solid
v = vapor

References

[1] Derjaguin, B. V., Nerpin, S. V., and Churaev, N. V., 1965, ''Effect of Film Transfer Upon Evaporation of Liquids from Capillaries,'' Bulletin Rilem,, **29**, pp. 93–98.
[2] Derjagin, B. V., and Churaev, N. V., 1976, ''The Definition of Disjoining Pressure and its Importance in the Equilibrium and Flow of Thin Films,'' Colloid J. USSR, **38**, pp. 438–448.
[3] Derjaguin, B. V., 1989, *Theory of Stability of Thin Films and Colloids*, Consultant Bureau/Plenum, New York.
[4] Potash, Jr., M., and Wayner, Jr., P. C., 1972, ''Evaporation from a Two-Dimensional Extended Meniscus,'' Int. J. Heat Mass Transfer, **15**, pp. 1851–1863.
[5] Wayner, Jr., P. C., Kao, Y. K., and LaCroix, L. V., 1976, ''The Interline Heat-Transfer Coefficient of an Evaporating Wetting Film,'' Int. J. Heat Mass Transfer, **19**, pp. 487–492.
[6] Wayner, Jr., P. C., 1991, ''The Effect of Interfacial Mass Transport on Flow in Thin Liquid Films,'' Colloids Surf., **52**, pp. 71–84.
[7] Moosman, S., and Homsy, S. M., 1980, ''Evaporating Menisci of Wetting Fluids,'' J. Colloid Interface Sci., **73**, pp. 212–223.
[8] Ajaev, V. S., and Homsy, G. M., 2001, ''Steady Vapor Bubbles in Rectangular Microchannels,'' J. Colloid Interface Sci., **240**, pp. 259–271.
[9] Holm, F. W., and Goplen, S. P., 1979, ''Heat Transfer in the Meniscus Thin Film Region,'' ASME J. Heat Transfer, **101**, pp. 543–547.
[10] Renk, F. J., and Wayner, Jr., P. C., 1979, ''An Evaporating Ethanol Meniscus, Part I: Experimental Studies,'' ASME J. Heat Transfer, **101**, pp. 55–58.
[11] Renk, F. J., and Wayner, Jr., P. C., 1979, ''An Evaporating Ethanol Meniscus, Part II: Analytical Studies,'' ASME J. Heat Transfer, **101**, pp. 59–62.
[12] DasGupta, S., Kim, I. Y., and Wayner, Jr., P. C., 1994, ''Use of the Kelvin-Clapeyron Equation to Model an Evaporating Curved Microfilm,'' ASME J. Heat Transfer, **116**(4), pp. 1007–1015.
[13] Stephan, P., and Busse, C. A., 1992, ''Analysis of the Heat Transfer Coefficient of Grooved Heat Pipe Evaporator Walls,'' Int. J. Heat Mass Transfer, **35**, pp. 383–391.
[14] Swanson, L. W., and Peterson, G. P., 1995, ''The Interfacial Thermodynamics of Micro Heat Pipes,'' ASME J. Heat Transfer, **115**, pp. 195–201.
[15] Morris, S. J. S., 2001, ''Contact Angles for Evaporating Liquids Predicted and Compared with Existing Experiments,'' J. Fluid Mech., **432**, pp. 1–30.
[16] Anderson, D. M., and Davis, S. H., 1995, ''The Spreading of Volatile Liquid Droplets on Heated Surfaces,'' Phys. Fluids, **7**, pp. 248–265.
[17] Shanahan, M. E. R., 2001, ''Condensation Transport in Dynamic Wetting,'' Langmuir, **17**, pp. 3997–4002.
[18] Zheng, L., Wang, Y.-X., Plawsky, J. L., and Wayner, Jr., P. C., 2002, ''Effect of Curvature, Contact Angle, and Interfacial Subcooling on Contact Line Spreading in a Microdrop in Dropwise Condensation,'' Langmuir, **18**, pp. 5170–5177.
[19] Ehrhard, P., and Davis, S. H., 1991, ''Nonisothermal Spreading of Liquid Drops on Horizontal Plates,'' J. Fluid Mech., **229**, pp. 365–388.
[20] Burelbach, J. P., Bankoff, S. G., and Davis, S. H., 1990, ''Steady Thermocapillary Flows of Thin Liquid Layers. II. Experiments,'' Phys. Fluids A, **2**, pp. 322–333.
[21] Sharma, A., 1998, ''Equilibrium and Dynamics of Evaporating or Condensing Thin fluid Domains: Thin film Stability and Heterogeneous Nucleation,'' Langmuir, **14**, pp. 4915–4928.
[22] Bankoff, S. G., 1990, ''Dynamics and Stability of Thin Heated Liquid Films,'' ASME J. Heat Transfer, **112**, pp. 538–546.
[23] Ayyaswamy, P. S., Catton, I., and Edwards, D. K., 1974, ''Capillary Flow in Triangular Grooves,'' J. Appl. Mech., **41**, pp. 332–336.
[24] Xu, X., and Carey, V. P., 1990, ''Film Evaporation from a Micro-Grooved Surface-An Approximate Heat Transfer Model and Its Comparison with Experimental Data,'' J. Thermophysics, **4**(4), pp. 512–520.
[25] Babin, B. R., Peterson, G. P., and Wu, D., 1990, ''Steady-State Modeling and Testing of a Micro Heat Pipe,'' ASME J. Heat Transfer, **112**, pp. 595–601.
[26] Wu, D., and Peterson, G. P., 1991, ''Investigation of the Transient Characteristics of a Micro Heat Pipe,'' J. Thermophys., **5**, pp. 129–134.
[27] Khrustalev, D., and Faghri, A., 1995, ''Thermal Characteristics of Conventional and Flat Miniature Axially-Grooved Heat Pipes,'' ASME J. Heat Transfer, **117**(1), pp. 1048–1054.
[28] Peterson, G. P., and Ha, J. M., 1998, ''Capillary Performance of Evaporating Flow in Micro Grooves: An Approximate Analytical Approach and Experimental Investigation,'' ASME J. Heat Transfer, **120**, pp. 743–751.
[29] Anand, S., De, S., and DasGupta, S., 2002, ''Experimental and Theoretical Study of Axial Dry Out Point for Evaporation From V-Shaped Microgrooves,'' Int. J. Heat Mass Transfer, **45**, pp. 1535–1543.
[30] Zheng, L., 2002, ''Study of Microscale Transport Processes and the Stability of the Thin Film in a Loop Constrained Vapor Bubble,'' Ph.D. thesis, Rensselaer Polytechnic Institute, Troy, NY.
[31] DasGupta, S., Plawsky, J. L., and Wayner, Jr., P. C., 1995, ''Interfacial Force Field Characterization in a Constrained Vapor Bubble Thermosyphon,'' AIChE J., **41**, pp. 2140–2149.
[32] Karthikeyan, M., Huang, J., Plawsky, J. L., and Wayner, Jr., P. C., 1998, ''Experimental Study and Modeling of the Intermediate Section of the Nonisothermal Constrained Vapor Bubble,'' ASME J. Heat Transfer, **120**, pp. 166–173.
[33] Wiegand, G., Jaworek, T., Wegner, G., and Sackman, E., 1997, ''Studies of Structure and Local Wetting Properties on Heterogeneous, Micropatterned Solid Surfaces by Microinterferometry,'' J. Colloid Interface Sci., **196**, pp. 299–312.
[34] Zheng, L., Wang, Y.-X., Plawsky, J. L., and Wayner, Jr., P. C., 2002, ''Accuracy of Measurements of Curvature and Apparent Contact Angle in a Constrained Vapor Bubble Heat Exchanger,'' Int. J. Heat Mass Transfer, **45**, pp. 2021–2030.
[35] Zheng, L., Wang, Y.-X., Wayner, P. C., Jr., and Plawsky, J. L., 2002, ''Curvature and Contact Angle Measurements in an Unstable Evaporating Extended Meniscus,'' *Proceedings of the 12th International Heat Transfer Conference*, Grenoble, France, Aug. 18–23. Paper No. 0451, pp. 443–447.
[36] Kim, Y., and Wayner, Jr., P. C., 1996, ''Shape of an Evaporating Completely Wetting Extended Meniscus,'' J. Thermophys. Heat Transfer, **10**, pp. 320–325.

Critical Heat Flux of Steady Boiling for Subcooled Water Jet Impingement on the Flat Stagnation Zone

Zhen-Hua Liu
e-mail address: liuzhenh@sjtu.edu.cn

Tie-Feng Tong

Yu-Hao Qiu

School of Mechanical and Power Engineering,
Shanghai Jiaotong University,
Shanghai, 200030, P. R. China

An experimental investigation was carried out for predicting the critical heat flux (CHF) of steady boiling for a round subcooled water jet impingement on the flat stagnation zone. The experimental data were measured in a steady nucleate boiling state. Three main influencing parameters, i.e., subcooling, impact velocity and jet nozzle size were widely changed and their effects on the critical heat flux were systemically studied. An empirical correlation was obtained using the experimental data over a wide experimental range for predicting the critical heat flux of steady boiling for a round subcooled water jet impingement on the flat stagnation zone. [DOI: 10.1115/1.1668054]

Keywords: Boiling, Experimental, Heat Transfer, Impingement, Jets

1 Introduction

Water free jet impingement provides heat transfer coefficients that are among the highest available in any forced convection flow. Water jet cooling has been widely used in the iron and steel industry, nucleate power processes, and the microelectronic devices making and thermal management processes. According to the temperature ranges of the hot body, the heat transfer modes of jet impingement may be divided into forced convection, nucleate boiling, transition boiling, and film boiling. For water jet impingement boiling on a hot plate, the assessment of critical heat flux (CHF) is very important that corresponds to the boiling crisis phenomenon in nucleate boiling and represents the largest cooling capacity for the jet cooling. The geometries of a water jet impingement on a flat hot plate can be divided into two modes as shown in Fig. 1. One mode is the free film flow (Fig. 1(a)) named mode A in this paper. In mode A, a great heated disk or rectangular plate is cooled by a small liquid jet and the ratio of the heated disk diameter to the nozzle diameter is much larger than unity. In general, for this geometric condition, the jet cooling experiments can only be carried out for the forced convection and nucleate boiling heat transfer regimes. After the boiling crisis occurs, the heat-transfer surface would be divided into two zones; the jet stagnation zone and dry-out zone. Hence, the temperature and heat flux on the heat-transfer surface would be very different. The other mode is the stagnation jet flow (Fig. 1(b)) named mode B in this paper. In mode B, the heat-transfer surface has a diameter equal to or smaller than that of the jet nozzle, and the heat-transfer surface is in the jet stagnation zone. For this geometric condition, the jet cooling experiments can be extensively carried out in total boiling regimes including transition and film boiling with uniform wall temperatures and wall heat fluxes.

In the past two decades, Studies of steady boiling heat transfer for mode A associated with the CHF of saturated and subcooled water on a disk or rectangular plate have been performed extensively. A variety of the experimental results have been reported and various semi-theoretical correlations and empirical correlations have been proposed for predicting CHF for different parameter ranges such as impact velocities, ratios of liquid density to vapor density and multiple jet systems [1–11].

Contributed by the Heat Transfer Division for publication in the JOURNAL OF HEAT TRANSFER. Manuscript received by the Heat Transfer Division August 20, 2003; revision received December 15, 2003. Associate Editor: M. K. Jensen.

Although many experimental studies of mode B have been carried out for the boiling heat transfer of water jet impingement on the stagnation zone, these studies focused mainly on the boiling heat transfer characteristics in partial or whole boiling range and most previous experiments were non-steady [12–16]. Only a few of steady boiling experiments of mode B were carried out and the CHF data were included in these experimental results [17–18].

Recently, Liu and Zhu [19] performed a systemically steady experiment for the CHF of saturated water jet impingement on the flat stagnation zone under atmospheric pressure and proposed semi-theoretical correlations for the CHF of steady saturated water jet impingement boiling of mode B

$$\frac{q_{c,0}}{Gh_{fg}} = 0.132\left(1+\frac{\rho_v}{\rho_l}\right)^{1/3}\left(\frac{\sigma\rho_l}{G^2 d}\right)^{1/3}\left(\frac{\rho_v}{\rho_l}\right)^{1.4/3}. \tag{1}$$

Because the thermophysical properties are constant for saturated water at atmospheric pressure, Eq. (1) can be simply expressed as

$$q_{c,0} = 0.36\times 10^6\left(\frac{v}{d}\right)^{1/3} \quad [\mathrm{W/m^2K}]. \tag{2}$$

where, the units of v and d are [m/s] and [m].

For mode B, the fundamental understanding for the CHF of steady boiling of subcooled water jet impingement on the stagnation zone is still quite poor. The most recent experiments for subcooled water were carried out under the nonsteady state condition; i.e., under quenching-cooling conditions. In the nonsteady state experiments, the nucleate boiling characteristics and the CHF not only depend on the systemic influencing parameters (subcooling, impact velocity and jet nozzle size), but also depend on the rate of the wall temperature change, which is not a systemic parameter [20]. Therefore, the steady experimental data of the CHF for subcooled water are quite necessary to correlate an essential correlation for predicting the CHF.

In this study, the objective was focused on the CHF of the subcooled water jet boiling for mode B. An experimental investigation was carried out for the critical heat flux of nucleate boiling for a round subcooled water jet impingement on the flat stagnation zone. The experimental data were measured in a steady boiling state. Three influencing parameters, subcooling, impact velocity and jet nozzle diameter, were widely changed and their effects on the CHF were systemically studied. An empirical correlation was

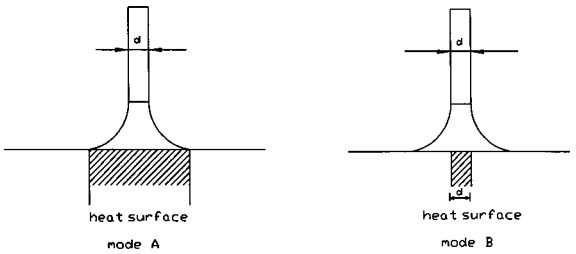

Fig. 1 Schematic diagrams of the physical model: (*a*) Mode A; (*b*) Mode B.

obtained using the experimental data over wide experimental range for predicting the CHF for a round subcooled water jet impingement on the flat stagnation zone.

2 Experimental Apparatus

In the present study, steady heat transfer experiments were conducted for the nucleate boiling regime to obtain boiling curves and determine critical heat fluxes in the steady state. Figure 2 shows the schematic diagram of the experimental apparatus. It consisted mainly of the test box, the circulation system of water, the measuring devices and electric power supply. Figure 3 shows the schematic diagram of the test box, in which a heated block was mounted. The heated block was a vertical copper bar having 50 mm diameter and 120 mm height, whose top surface was a smooth, horizontally circular heat-transfer surface, and it was heated with a ribbon electric heater (main heater) twisted outside of the copper bar. The isinglass sheet was used as the insulator between the copper bar and main heater. The copper bar was placed in a thick ceramic tube; another ribbon electric heater (auxiliary heater) was twisted outside of the ceramic tube for preventing the heat losses from the heated block. Four round heat-transfer surfaces with diameters of 12 mm, 8 mm, 6 mm, and 3 mm were used in this experiment and they corresponded to four round nozzles with the same diameters. In the upper column of the copper bar, three Φ 0.1 mm thermocouples were horizontally inserted at the center axial line of the copper bar. The distances between the thermocouples were 3.0 mm and the distance between the top thermocouples and the heat transfer surface was 2.0 mm. Signals from the thermocouples mounted in the copper bar were measured

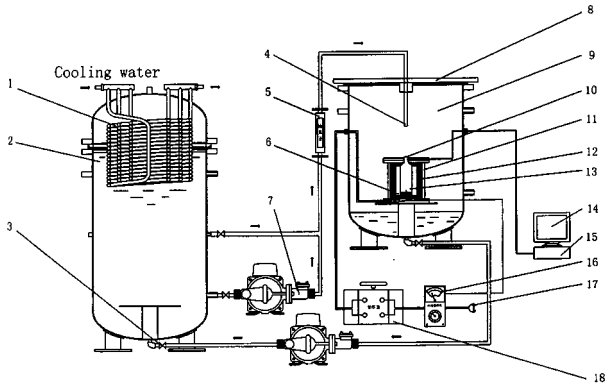

Fig. 2 Schematic diagram of the experimental apparatus

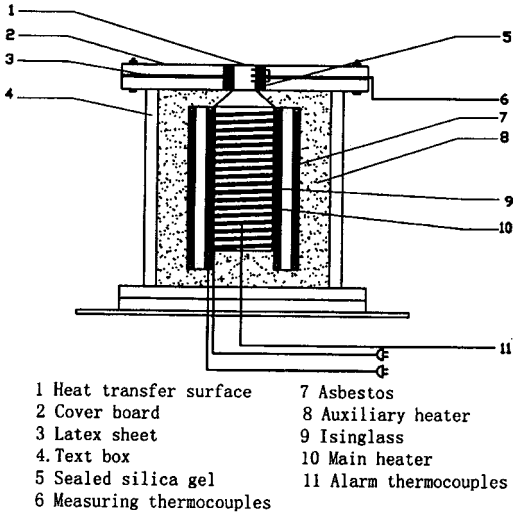

Fig. 3 Schematic diagram of test box

by a digital voltmeter (Agilent-34950A) and then fed into a computer, which converted them to wall temperature and wall flux using a steady one-dimensional thermal conduction equation along the vertical direction. One of them was fed into a PID temperature controller as a feed back signal, which adjusted the power supply. In the tests, the electric power of the auxiliary heater was carefully adjusted for preventing the heat losses from the main heater. The test box made of stainless steel and had a diameter of 250 mm and a height of 200 mm. The space inside the test box was filled by asbestos. All of the measurements were performed in the steady state, the temperature and heat flux of the heat-transfer surface were calculated from the temperature difference between two thermocouples mounted on the center axial line of the copper bar. An alarm thermocouple inserted at the bottom of the copper bar was connected to a temperature controller that prevents the maximum temperature of the copper bar from exceeding 750°C. In this experiment, it has been confirmed that the assumption of one-dimensional heat conduction is well satisfied in the upper column of the copper bar by a numerical simulation and test results.

Ion-exchanged water was used as the coolant (the maximum electric conductivity was less than $10\ \mu\Omega\cdot\mathrm{cm}^{-1}$ in the experiments). Water was heated in the water tank, which was fitted with two immersion heaters on its bottom section. A reflux condenser was mounted above the tank for condensing vapor. The subcooled water was drained from the water tank by a water pump, passed through a regulating valve and a flow meter, flowed into the jet nozzle made of a quartz glass tube, in which the temperature of water was measured by a thermocouple. The water jet impinged onto the heat-transfer surface, and then was drained into a drain tank to be recycled. The distance between the heat transfer surface and the nozzle was fixed at 5.0 mm in all tests. Prior to the formal tests, it has been affirmed that the distance between the heat transfer surface and the nozzle has no effect on the jet boiling characteristics.

During each run, electric power was increased gradually. The computer not only measured the wall temperature and wall heat flux instantaneously, but also gave an alarm when the wall temperature increased quickly and did not attain a steady state. Such an alarm means that the boiling crisis has occurred; therefore, the electric power was cut automatically off. After the boiling crisis occurred, the test was repeated from the steady state of the former time, the output electric power increased slowly in an increment of 2% of the electric power of the former time. When the boiling crisis occurred again, the test was stopped and the wall heat flux of the former time was determined as the critical heat flux.

Table 1 The experimental conditions

Test fluid	Ion-exchanged water
Heating condition	steady state
Test pressure	atmospheric pressure
Impact velocity (m/s)	0.5～6.0
Nozzle diameter (mm)	3, 6, 8, 12
Subcooling (K)	15～80

Table 1 shows the experimental conditions. In this experiment, the calibration errors of the thermocouples were less than 0.2 K. The maximum location deviation between thermocouples was about 0.1 mm. The maximum uncertainties of the wall superheat and wall heat flux were about 4% and 6%.

3 Results and Discussion

Figure 4 shows some samples of the temperature distributions in the upper column of the copper bar at different experimental conditions. The temperatures measured by the thermocouples are the ordinate and the distances from the wall along the vertical direction are the abscissa. The measured results show clearly linear temperature distributions along the vertical direction in the upper column of the copper bar.

Figure 5 shows the experimental results of the fully developed nucleate boiling regime for the subcooled water jet for the jet nozzles with 6 mm diameter and an impact velocity of 0.5 m/s. Heat transfer data are plotted in the form of wall heat flux against wall superheat for different subcoolings. It is found that prior to fully developed nucleate boiling, higher subcooling increases the heat transfer coefficient and delayed boiling incipience. The boiling curves lied in the fully developed nucleate boiling regime are quite shot. The experimental range belongs mainly to the partial boiling regime.

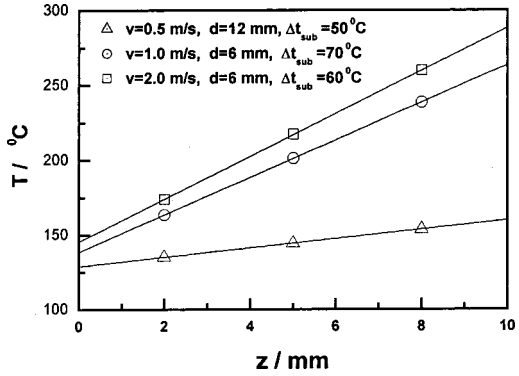

Fig. 4 Temperature distributions of thermocouples in the heated body

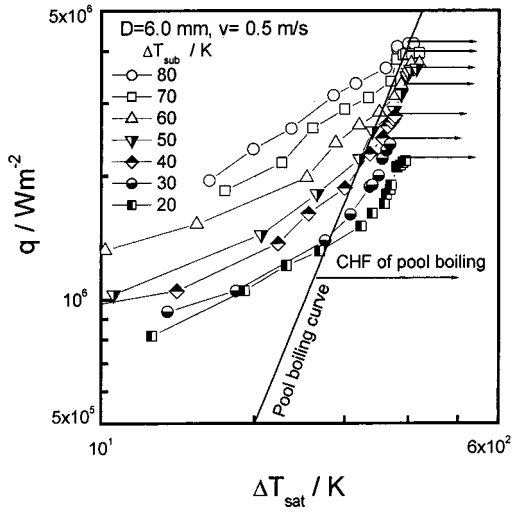

Fig. 5 Nucleate boiling curves of subcooled water jet for Φ6.0 mm nozzle

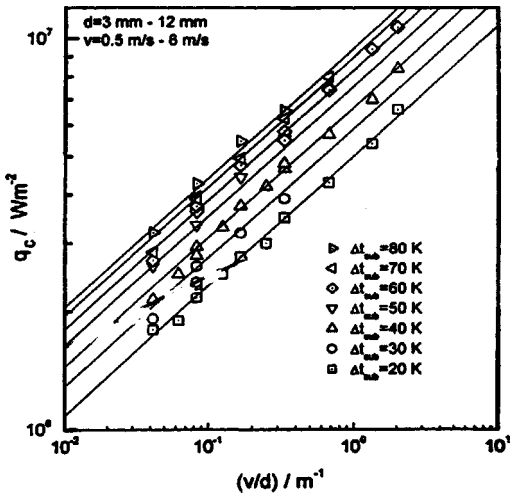

Fig. 6 Relation between CHF and (v/d) for different subcoolings

The Stephan-Abdelsalam's empirical correlation [21] for nucleate pool boiling of saturated water at atmospheric pressure is also shown in Fig. 5 in the form of a solid line.

$$q = 52.4\Delta T_{\text{sat}}^{3.058} \quad [\text{W/m}^2\text{K}] \tag{3}$$

In the fully developed nucleate boiling regime, the data resulted from different subcoolings converged essentially into the extending line of pool boiling curve. The insensitivity of the boiling curve to changes in the subcooling indicates that heat transfer in the fully developed nucleate boiling regime is dominated by bubble activity at the surface, regardless of the contribution of single-phase turbulent transport in the bulk flow. This phenomenon is similar to other forced convective boiling characteristics. However, the effects of the subcooling on the critical heat flux are quite significant. The CHF increases greatly with increasing subcooling of water. This trend is attributed to increased liquid-solid contact on the heat transfer surface and decreased void fraction in the liquid flow.

As shown in Eq. (2), the CHF of saturated water is of $q_{c,0} \propto (v/d)^{1/3}$. Hence, (v/d) could be considered as a parameter that affects the CHF for saturated water. If (v/d) could still be considered as a parameter that affects the CHF for subcooled water, the correlation for predicting the CHF would have a simple form. Figure 6 shows the relation between the CHF of subcooled water and (v/d) for different subcoolings. It is found that all of the solid lines have a gradient of one third, and thence there is the same relationship of $q_c \propto (v/d)^{1/3}$, for subcooled water as for saturated water.

For the CHF of subcooled liquids for pool boiling and forced convective boiling, the following form is frequently applied [22–24].

$$\frac{q_c}{q_{c,0}} = 1 + c\left(\frac{\rho_v}{\rho_l}\right)^n \left(\frac{c_{p,l}\Delta T_{\text{sub}}}{h_{fg}}\right)^m \tag{4}$$

where c, m, and n would be determined by the experimental data. The form of Eq. (4) is also applied in the present study.

Because the densities of subcooled water and saturated vapor could be considered as constants under atmospheric pressure, the relationship between q_c and ΔT_{sub} could be simply expressed as

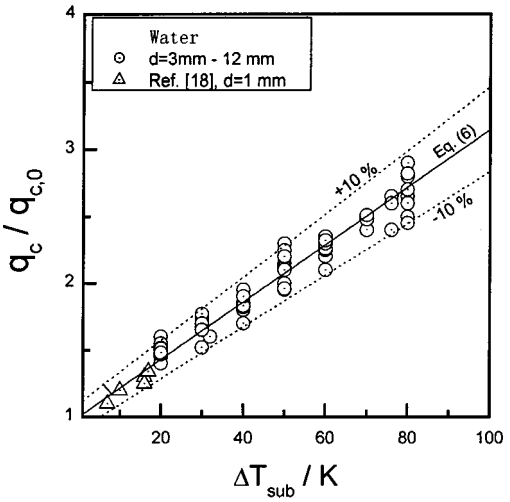

Fig. 7 Comparison of CHF data with Eq. (6)

$$\frac{q_c}{q_{c,0}} = 1 + c\left(\frac{c_{p,l}\Delta T_{\text{sub}}}{h_{fg}}\right)^m \tag{5}$$

By correlating the present experimental data of the CHF, the following empirical correlation is obtained

$$\frac{q_c}{q_{c,0}} = 1 + 11.82\left(\frac{c_{p,l}\Delta T_{\text{sub}}}{h_{fg}}\right) \tag{6}$$

Figure 7 shows the comparison of the CHF data with Eq. (6). Equation (6) correlates the CHF data with the maximum relative error less than 10%, and could be recommended for predicting the CHF of subcooled water jet boiling at the stagnation zone.

In Fig. 7, the CHF data of steady experiment proposed by Robidou and co-workers [18] were also plotted for comparison. The nozzle in this study has a slot shape with a width of 1.0 mm. These CHF data agree well with Eq. (6).

Since the present experiment was carried out at atmospheric pressure and only subcooled water was used as a coolant, the CHF data cannot present the effects of thermophysical properties in a wide range. Therefore, further work would still be needed to check and improve reliability of Eqs. (1) and (6) in a wide experimental range.

4 Conclusions

1. Both the impact velocity and the nozzle diameter provide a relatively strong effect on the CHF of subcooled water. A higher CHF was achieved with higher impact velocities and smaller nozzle diameters. The relationship of $q_c \propto (V/d)^{1/3}$ is available for the sublooed water as for saturated water.

2. The subcooling of water has a quite strong effect on the CHF. There is a linear relation between the CHF of the subcooled water and the subcooling.

3. Equation (6) correlates the CHF data from the subcooled water jet experiments, and could be recommended for predicting the CHF of subcooled water jet boiling at the stagnation zone.

4. Further work would be still needed to check and improve reliability of Eq. (6) in a wide range.

Acknowledgments

This work was supported by the Natural Science Foundation of China under Grant No. 50176029.

Nomenclature

c = correlation factor (−)
d = diameter of jet nozzle (m)
G = mass flux of liquid jet ($\text{kg m}^{-2}\,\text{s}^{-1}$)
h_{fg} = latent heat of evaporation (Jkg^{-1})
q = wall hat flux ($\text{Jm}^{-2}\,\text{s}^{-1}$)
q_c = critical heat flux ($\text{Jm}^{-2}\,\text{s}^{-1}$)
T = temperature (K or °C)
ΔT_{sat} = wall superheat; $\Delta T_{\text{sat}} = T_w - T_0$ (K)
ΔT_{sub} = subcooling of cooling water; $\Delta T_{\text{sub}} = T_0 - T_\infty$ (K)
v = impact velocity of jet flow at nozzle exit (ms^{-1})
z = axial distance from the heat transfer surface (m)

Greek Symbol

λ = thermal conductivity ($\text{Jm}^{-1}\,\text{K}^{-1}\,\text{s}^{-1}$)
ν = kinematics viscosity ($\text{m}^2\,\text{s}^{-1}$)
σ = surface tension (Nm^{-1})
ρ = density (kgm^{-3})

Subscripts

0 = saturation state
l = liquid
v = vapor
w = wall
∞ = initial water temperature at nozzle exit

References

[1] Monde, M., and Kotto, Y., 1978, "Bournout in a High Heat-Flux Boiling System With an Impingement Jet," Int. J. Heat Mass Transfer, **21**, pp. 295–305.
[2] Katto, Y., and Shinizu, M., 1979, "Upper Limit of CHF in the Saturated Forced Convection Boiling on a Heated Disk With a Small Impinging Jet," J. Heat Transfer, Trans. ASME , **101**, pp. 265–269.
[3] Monde, M., 1980, "Burnout Heat Flux in Saturated Forced Convection Boiling With an Impinging Jet," Heat Transfer - Japanese Research **9**, pp. 31–41.
[4] Haramura, Y., and Katto, Y., 1983, "A New Hydrodynamic Model of Critical Heat Flux, Applicable Widely to Both Pool and Forced Convection Boiling on Submerged Bodies in Saturated Liquids," Int. J. Heat Mass Transfer, **26**, pp. 389–399.
[5] Monde, M., and Okuma, Y., 1985, "Critical Heat Flux of Saturated Forced Convection Boiling on a Heated Disk With an Impinging Jet-CHF in L-Regime," Int. J. Heat Mass Transfer, **28**, pp. 547–552.
[6] Sharan, A., and Lienhard, J. H., 1985, "On Predicting Boiling Burnout in the Jet-Disk Configuration," J. Heat Transfer, Trans. ASME , **107**, pp. 398–401.
[7] Monde, M., 1987, "Critical Heat Flux of Saturated Forced Convection Boiling on a Heated Disk With an Impinging Jet," J. Heat Transfer, Trans. ASME , **109**, pp. 991–996.
[8] Katto, Y., and Yokoya, S., 1988, "Critical Heat Flux on a Disk Heater Cooling by a Circular Jet of Saturated Liquid Impinging at the Center," Int. J. Heat Mass Transfer, **31**, pp. 219–227.
[9] Monde, M., and Inoue, T., 1991, "Critical Heat Flux in Saturated Forced Convection Boiling on a Heated Disk With Multiple Impinging Jets," J. Heat Transfer, Trans. ASME , **113**, pp. 722–727.
[10] Monde, M., 1991, "Critical Heat Flux in Saturated Forced Convection Boiling on a Heated Disk With One or Multiple Impinging Jets," Trends in Heat, Mass and Momentum Transfer, **1**, pp. 33–44.
[11] Monde, M., and Mitsutake, Y., 1996, "Critical Heat Flux in a Convection Subcooled Boiling With Multiple Impinging Jets," J. Heat Transfer, Trans. ASME , **117**, pp. 241–243.
[12] Ishigani, S. K., Nakanishi, J. K., and Hikoshichi, T. A., 1978, "Boiling Heat Transfer for a Plane Water Jet Impinging on a Hot Surface," *Proceedings of the 6th International Heat Transfer Conference*, Paris, **1**, pp. 445–450.
[13] Nakanishi, J. K., Ishigani, S. K., Ochi, T., and Morita, I., 1980, "Two-Dimensional Water Jet Impinging for Cooling of High Temperature Plate," Transaction of JSME, (B), **46**, pp. 714–724.
[14] Kumagai, S., Sano, T., Kamata, T., Suzuki, S., and Kubo, R., 1994, "Boiling Heat Transfer to an Impinging Jet in Cooling a Hot Metal Slab," Transaction of JSME, (B), **60**, pp. 259–263.
[15] Kumagai, S., Sano, T., Kamata, T., Suzuki, S., and Kubo, R., 1995, "Transient Cooling of Hot Plate With Impinging Water Jet," Transaction of JSME, (B), **61**, pp. 351–356.
[16] Liu, Z. H., and Wang, J., 2001, "Study on Film Boiling Heat Transfer for Water Jet Impinging on a High Temperature Flat Plate," Int. J. Heat Mass Transfer, **44**, pp. 2475–2481.
[17] Ma, C. F., and Bergles, A. E., 1986, "Jet Impinging Nucleate Boiling," Int. J. Heat Mass Transfer, **29**, pp. 1095–1101.
[18] Robidou, H., Auracher, H., Gardin, P., and Lebouche, M., 2002, "Controlled Cooling of a Hot Plate With a Water Jet," Exp. Therm. Fluid Sci., **26**, pp. 123–129.
[19] Liu, Z. H., and Zhu, Q. Z., 2002, "Predication of Critical Heat Flux for Convective Boiling of Saturated Water Jet Impingement on the Stagnation Zone," J. Heat Transfer, Trans. ASME, **124**, pp. 1125–1130.

[20] Yao, S. C., and Salepour, A., 1983, ''An Investigation of Transient Boiling Transfer With Conjugate Nature,'' Int. J. Heat Mass Transfer, **26**, pp. 901–909.
[21] Stephan, K., and Abedelsalam, M., 1980, ''Heat Transfer Correlations for Natural Convective Boiling,'' Int. J. Heat Mass Transfer, **23**, pp. 73–81.
[22] Ueda, T., Inoue, M., and Nagatome, S., 1981, ''Critical Heat Flux and Droplet Entrainment Rate in Boiling of Falling Liquid Films,'' Int. J. Heat Mass Transfer, **24**, pp. 1257–1266.
[23] Baines, R. P., EI-Masri, M. A., and Rohsenow, W. M., 1984, ''Critical Heat Flux in Flowing Liquid Films,'' Int. J. Heat Mass Transfer, **27**, pp. 1623–1629.
[24] Mudawwar, I. A., Incroea, T. A., and Incropera, F. P., 1987, ''Boiling Heat Transfer and Critical Heat Flux in Liquid Films Falling on Vertically-Mounted Heat Sources,'' Int. J. Heat Mass Transfer, **30**, pp. 2083–2095.
[25] Liu, W., Nariai, H., and Inasaka, F., 2000, ''Prediction of Critical Heat Flux for Subcooling Boiling,'' Int. J. Heat Mass Transfer, **43**, pp. 3371–3390.

Experiments on Heat Transfer in a Thin Liquid Film Flowing Over a Rotating Disk

B. Ozar

B. M. Cetegen

A. Faghri

Department of Mechanical Engineering,
University of Connecticut,
Storrs, CT 06269-3139

An experimental study of heat transfer into a thin liquid film on a rotating heated disk is described. Deionized water was introduced at the center of a heated, horizontal disk with a constant film thickness and uniform radial velocity. Radial distribution of the disk surface temperatures was measured using a thermocouple/slip ring arrangement. Experiments were performed for a range of liquid flow rates between 3.0 lpm and 15.0 lpm. The angular speed of the disk was varied from 0 rpm to 500 rpm. The local heat transfer coefficient was determined based on the heat flux supplied to the disk and the temperature difference between the measured disk surface temperature and the liquid entrance temperature onto the disk. The local heat transfer coefficient was seen to increase with increasing flow rate as well as increasing angular velocity of the disk. Effect of rotation on heat transfer was largest for the lower liquid flow rates with the effect gradually decreasing with increasing liquid flow rates. Semi-empirical correlations are presented in this study for the local and average Nusselt numbers. [DOI: 10.1115/1.1652044]

Keywords: Film Cooling, Heat Transfer, Liquid, Rotating, Thin Films

1 Introduction

Heat transfer and fluid flow in thin liquid films with rotation is of particular interest in several mechanical engineering and chemical processing applications. Thin liquid films on rotating surfaces are encountered in gas-turbine engines, manufacturing of micro-electronics, vapor absorption heat pumps, and heat exchangers. In recent years, interest in thin liquid film heat transfer on rotating surfaces has increased due to potential applications in the microgravity thermal-fluid handling systems. These systems are attractive since rotational forces cause thinning and acceleration of liquid films, resulting in high heat transfer performance independent of gravitational forces.

Traditionally, thin liquid films on rotating surfaces have been studied using an impinging jet to deliver the liquid onto a rotating disk surface. The liquid spreads outward from the impingement zone in a high velocity thin film until a hydraulic jump occurs. An excellent review of these studies was compiled by Webb and Ma [1]. The first major contribution to the study of impinging jet flow phenomenon was made by Watson [2] in 1964, who considered the case of a free liquid jet, impinging on a stationary flat plate. Watson divided the flow into four distinct regions. The first region was the central stagnation zone immediately beneath the impinging jet. In this region, both momentum and thermal boundary layer thicknesses are independent of radial location. In the second region, a growing momentum boundary layer reached a point where the boundary layer is of sufficient thickness to influence the free surface. The third region consisted of the transition of the velocity profile from where the free surface was first influenced (Blasius type profile), to a fully developed velocity profile that includes the free surface. Finally, in the fourth region, a fully developed velocity profile existed for which Watson developed a similarity profile. This region extended through the remainder of the supercritical flow, and was bounded by the hydraulic jump diameter. This regional segregation methodology has been adopted by numerous subsequent investigators including Chadhury [3], who extended Watson's approach to include heat transfer phenomena. Wang et al. [4] developed a unique analytical approach in which, the heat transfer in the disk and liquid film were treated separately and then the solutions were matched at the disk surface. Thomas et al. [5] developed a one-dimensional analytical solution to the quasi-steady momentum equation. The model assumed solid body rotation in predicting film thickness, including the hydraulic jump. The resulting velocity distribution was coupled with conservation of energy to predict the heat transfer performance. Rahman et al. [6] studied the influence of turbulence on the free surface height and hydraulic jump for the case of controlled impinging jets in both plane and radial flows. A numerical model was developed that employed a body-fitted moving grid method and a k-ε turbulence model. Rahman and Faghri [7] studied heating and evaporation from a rotating disk by considering three distinct regimes. For developing flow and heat transfer, a three dimensional numerical model was utilized. Also, a two dimensional analytical solution was formulated for developing heat transfer and fully developed flow assuming solid body rotation. For the case of fully developed heat transfer and fluid flow, a closed form solution was developed. This solution predicted that the Nusselt number, based on film thickness, approached a constant value in the fully developed regime.

In an experimental study, Carper and Deffenbaugh [8] evaluated the convective heat transfer from a jet of cooling oil to an approximately isothermal rotating disk. Correlations were presented for the average Nusselt number as influenced by rotational Reynolds number, jet Reynolds number and radius of impingement. In a later study, Carper et al. [9] extended this study to consider Prandtl number effects. Average heat transfer coefficients were presented with no information on its local values. Vader et al. [10] studied the effects of jet velocity and temperature on the heat transfer between a planar water jet and a stationary heated plate. They concluded that the heat transfer performance was affected by the free stream turbulence intensity and the Prandtl number. A similar study was presented by Stevens and Webb [11] in which the influence of jet Reynolds number, nozzle to plate spacing and jet diameter were evaluated. Empirical correlations were developed for stagnation point, local and average Nusselt numbers.

Mudawwar et al. [12] investigated convective heat transfer for a rotating thin film flowing through an internal channel within a high speed rotating disk. The study was motivated by gas turbine

Contributed by the Heat Transfer Division for publication in the JOURNAL OF HEAT TRANSFER. Manuscript received by the Heat Transfer Division January 24, 2003; revision received December 9, 2003. Associate Editor: R. M. Manglik.

blade cooling applications. A semi-empirical turbulence model was developed to predict heat transfer performance. Faghri et al. [13] presented heat transfer results for a controlled liquid impinging jet on a stationary disk. They presented a numerical study of the system showing good agreement between heat transfer predictions and experimental data. Auone and Ramshaw [14] performed heat and mass transfer experiments of a rotating disk for controlled jet impingement. They predicted the heat transfer coefficients analytically by adapting the solution that Nusselt used for the film condensation under the influence of gravity.

From the above literature review, it is evident that comprehensive experimental data on heat transfer for controlled jet impingement on a rotating disk is not available. Additionally, the relation between the liquid film flow characteristics and heat transfer performance has not been studied simultaneously in the past investigations.

The present study considers measurement of local and average heat transfer coefficients for a thin liquid film flowing on a rotating heated disk. The thin water film is generated via a unique flow collar device that provides a circumferentially uniform, radial flow onto the disk. This flow collar device differs from the impinging jet system described by Watson [2]. Watson's stagnation region does not exist for the flow collar system. Instead the water exits the flow collar with a fully developed radial velocity distribution and is suddenly bounded by a free surface. In this study, the inlet liquid flow rate, the collar gap height through which the fluid enters the disk surface and the rotational speed of the disk are used as the experimental control parameters. A film Reynolds number is defined based on the inlet gap height and the entrance velocity of the film onto the disk. Film thickness measurements are made with and without rotation. Local Nusselt numbers are calculated from temperature measurements taken from the rotating disk. In this study, angular velocity and flow rate on the heat transfer performance are presented. Semi-empirical correlations are derived for the local and average Nusselt numbers.

2 Experimental

2.1 Rotating Disk Setup. The experimental setup described by Faghri et al. [13] was modified for the present study. A basic description of the apparatus is provided here with emphasis on the design modifications. A schematic of the experimental set-up is shown in Fig. 1. The 40.6 cm diameter, 0.58 cm thick aluminum disk is mounted onto a precision stainless steel spindle. Deionized water is pumped through a rotating coupling into the hollow spindle and emerges through 8 holes on the spindle and flow radially outward between the flow collar and the disk before it exits onto the disk surface. The spindle-disk and flow collar rotate all together in this experimental arrangement. The collar extends a radial distance of 5.1 cm from the center. It serves to make the flow circumferentially uniform, and ensure a fully developed velocity profile as the liquid exits onto the disk surface. The vertical distance between the disk and the collar can be adjusted. After the liquid flows over the disk, it is collected by an annular tank surrounding the disk. The liquid flow rate is varied by large and small metering valves while the volumetric flow rate is measured by an in-line turbine flow meter. A flat etched foil heater (Minco Inc., Minneapolis, MN) with a maximum heat input rate of 6.7 kW is installed in the disk which is insulated on the bottom side. The heater has an outside diameter of 35.6 cm and inside diameter of 10.2 cm, which is the same as the outside diameter of the collar. The heater is powered by a 440 Volt variable AC transformer. A power slip-ring (UEA Inc., Waverly, IA) is used to transmit the electrical power to the rotating disk-heater assembly.

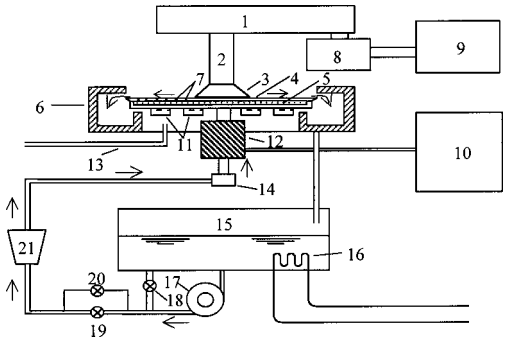

Fig. 1 Experimental setup for heat transfer experiments for a liquid film flowing over a rotating disk. (1) Pulley assembly, (2) High precision spindle, (3) Flow collar, (4) Disk, (5) Etched foil heater, (6) Annular tank, (7) Thermocouples, (8) Motor, (9) Variable speed motor control, (10) 0-500V heater control, (11) Thermocouple transmitters, (12) Precision slip ring, (13) Cooling air, (14) Rotating coupling, (15) External process tank, (16) Heat exchanger, (17) Pump, (18) Bypass valve, (19) Large metering valve, (20) Small metering valve, and (21) Flow meter.

Several temperature measurement techniques were considered for the rotating disk system. These included the thermographic liquid crystal technique of Metzger et al. [15], which proved impractical due to difficulties associated with water resistant binders and its limited range at higher temperatures. Also considered was a laser-induced fluorescence thermal imaging technique developed by Bizzak and Chyu [16]. This technique was not selected because of measurement discontinuities in the required temperature range. A thermocouple slip ring was considered. However, errors associated with slip-ring noise, ambient temperature, and induced voltages resulted in unacceptable measurement accuracy. These considerations ultimately led to an arrangement where the thermocouple voltage signals were first converted to electrical current using thermocouple transmitter modules installed under the rotating disk. The resulting electric current signals were then passed through a precision slip ring with acceptable noise characteristics. The temperature measurement system consisted of 11 T-type thermocouples accurate to $\pm 0.5°C$, installed in 1.6 mm diameter holes drilled on the underside of the disk, terminating at a depth of 1.52 mm away from the upper disk surface. The thermocouples were located between 7 cm and 16.5 cm away from the center of the disk with equal spacing. A maximum of seven temperatures can be monitored at a time because of the limitation of the number of transmitters. The thermocouples were installed in their location using a high thermal conductivity cement (Omega OB-4000). The transmitter assembly consisted of seven Watlow WG5900 transmitters ($\pm 0.02°C$ span, $\pm 0.3°C$ ambient temperature effects, and $\pm 0.02°C$ cold junction compensation) mounted on to a low thermal conductivity phenolic plate underneath the disk. These transmitters were extensively checked for their linearity of the input and output characteristics during the calibrations. An 18 conductor precision slip ring was mounted to the spindle in the annular space and transmitted the electrical signals from the thermocouple transmitters. The slip ring was tested for conductor crosstalk and impedance variation, both of which were found to be negligible as stated by the manufacturer. Shunt resistors (250Ω) were used to convert the 4–20 mA current output range of the thermocouple transmitters to 1–5 volts voltage output. The voltage signals were measured with a Fluke model 2625A data logger. An additional T-type thermocouple was used to measure the inlet temperature just before the fluid flows into the spindle. A heat exchanger was placed in the water tank to maintain the inlet water temperature at a constant value.

Heat transfer measurements (± 12 percent maximum uncertainty in heat transfer coefficient) were taken for heater powers between 3000 and 4500 watts (± 1.5 percent). Rotational speed of the disk was varied from 0 to 500 rpm (± 1 rpm). A range of flow rates between 3.0 lpm (liters per minute) and 15.0 lpm (± 2.5 percent) was considered. Disk surface temperatures were determined from the measurements using a one-dimensional heat con-

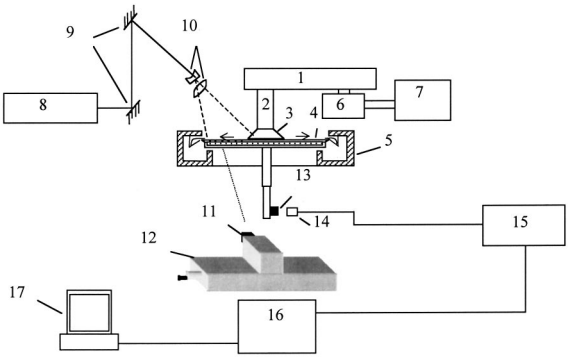

Fig. 2 Experimental setup for flow visualization experiments for a liquid film flowing over a rotating disk. (1) Pulley assembly, (2) High precision spindle, (3) Flow collar, (4) Disk, (5) Annular tank, (6) Motor, (7) Variable speed motor control, (8) Ar ion laser, (9) Mirrors, (10) Cylindrical lenses, (11) CCD Camera, (12) Precision linear slide, (13) Magnet, (14) Magnetic sensor, (15) Timing circuit, (16) Camera controller, and (17) Image acquisition/processing computer.

duction model to extrapolate the measured temperatures to the disk surface. These maximum corrections for the surface temperatures were typically less than 0.45°C in all of the experiments reported here. The properties of water were evaluated at the inlet temperature.

2.2 Laser Light Interface Reflection Experimental Setup for Liquid Film Thickness Measurements. Laser light reflection from the liquid/air interface was utilized to measure the liquid film thickness distribution on the disk in the radial direction. With this technique, the location and topography of the air/liquid free surface, and position and shape of the hydraulic jump can be determined as described by Ozar et al. [17].

The liquid film thickness measurements were made with the experimental setup shown in Fig. 2. The beam of an Argon ion laser (Coherent Innova 90-5) at a wavelength of 488 nm was directed to the measurement region after being formed into a thin sheet (vertical to the disk surface) of light by two cylindrical lenses. The first cylindrical lens (focal length, $f=-40$ mm) transformed the laser beam into a laser sheet. The second cylindrical lens ($f=200$ mm) was used to decrease the thickness of the laser sheet to approximately 0.1 mm in the measurement region. Thus, a thin laser sheet was obtained over the disk surface. The reflected light at the liquid/gas interface was imaged by a high-spatial resolution 1300×1030 CCD camera (Micromax, Roper Scientific Inc.). Before performing the experiments, the image of a millimetric measuring scale was recorded for calibrating the magnification parameters. In order to eliminate the error that could be introduced because of the slight wobbling (typically less than 1mm vertical distance at the outer edge) of the disk, the image acquisition was always triggered at the same angular position of the disk. The triggering mechanism consisted of a magnet, a magnetic sensor and an electronic trigger circuit. As the magnet passed in front of the sensor, the induced voltage signal was conditioned to trigger the CCD camera. In order to validate the effectiveness of this method, the dry disk surface reflection images were captured multiple times. It was found that the disk surface was consistently located within five pixels out of 1030 translating to a position accuracy of 0.06 mm. Since the CCD camera field of view is limited to 12 mm distance in the measurement plane at high magnification, 15 overlapping regions were imaged successively to cover the whole disk radius. At each location, film surface reflection images were recorded for up to 10 times and they were averaged to determine the average position of the interface. Variations up to 30 percent in the film thickness were observed near the hydraulic jump and for the wavy films under rotation. In order to position the CCD camera accurately, a precision linear slide was used. Quantitative comparison of these images with reference images of the dry disk surface allowed determination of the film thickness with an uncertainty of ±0.025 mm as discussed in Ref. [17].

3 Results and Discussion

3.1 Liquid Film Visualization and Measurements. Visualization of the liquid film was performed with the purpose of identifying the characteristics of the liquid film flow over stationary and rotating disk surfaces. Figure 3 shows photographs of the liquid film at different conditions. In Fig. 3(*a*), the liquid film on the stationary disk surface at a flow rate of 3.0 lpm ($\mathrm{Re}_i=238$) undergoes a sudden increase in its thickness right at the edge of the collar and the liquid film is in the subcritical region downstream of the hydraulic jump all over the disk surface. The hydraulic jump is the sudden increase in the film thickness and it is located where the momentum is balanced between the supercritical and subcritical flows. At a higher flow rate of 7.0 lpm ($\mathrm{Re}_i=555$), as shown in Fig. 3(*b*), the hydraulic jump location moves to a larger radius on the disk and the waviness of the liquid's free surface increases indicating a more turbulent nature of the film surface. Figures 3(*c*) through 3(*f*) present the liquid film topography for varying rotation speeds. With rotation, the hydraulic jump is pushed outwards and is not present on the disk surface at a rotation speed of 100 rpm. Spiral waves begin to emerge due to centrifugal forces acting on the liquid film. Additionally, as the rotation speed is increased from 100 rpm to 500 rpm, the wave amplitudes decrease because of the thinning of the liquid film due to increased centrifugal effects.

Figure 4 shows the film thickness for Reynolds numbers between $\mathrm{Re}_i=238$ and 1188 for the stationary case and for the rotation speeds of 100 rpm and 300 rpm. As the Reynolds number increases, the hydraulic jump moves towards the outer edge of the disk because the liquid leaves the collar with a higher radial momentum. For $\mathrm{Re}_i=238$, the hydraulic jump is attached to the collar. However at $\mathrm{Re}_i=555$, the hydraulic jump occurs between $r/r_i=1.6$ and 2.5. At $\mathrm{Re}_i=1188$, it moves near the outer edge of the disk. For $\mathrm{Re}_i=555$, the film thickness is nearly uniform in part of the subcritical region between $r/r_i=2.5$ and 3.5 but then drops off near the outer edge of the disk. This decrease in the film thickness is due to the acceleration of the flow as the liquid leaves the disk surface. Also the liquid film thickness in the subcritical region is an order of magnitude greater than that in the supercritical region.

At moderate rotation speeds such as 100 rpm shown in Fig. 4(*b*), the film thickness exhibits a maximum whose location propagates outward with increasing flow rate. For these cases, the liquid film behavior can be divided into three zones; the inner inertia-dominated region, the outer rotation-dominated region and the transition region in between. In the inertia-dominated region, the inertia, and friction forces are dominant. Because of the friction forces, the liquid tends to slow down and the film thickness increases as reported by Thomas et al. [18]. In the rotation-dominated region, centrifugal forces come into play causing a thinning of the liquid film. Meanwhile in the transition region, both of these forces are in play. Thus, the film thickness reaches a maximum in the transition region, where deceleration of the velocity due to friction is compensated and eventually balanced by the acceleration due to centrifugal effects.

As apparent in both Figs. 4(*b*) and 4(*c*), the location where the maximum film thickness occurs, changes as a function of Reynolds number and rotational speed. An increase in the Reynolds number causes an increase in the film inertia. Therefore, higher centrifugal forces are required to overcome higher inertial forces. If the rotation speed is kept constant and the Reynolds number is increased, then the maximum film thickness location travels towards the edge of the disk. Since radial location influences the magnitude of centrifugal effects, the region where the centrifugal

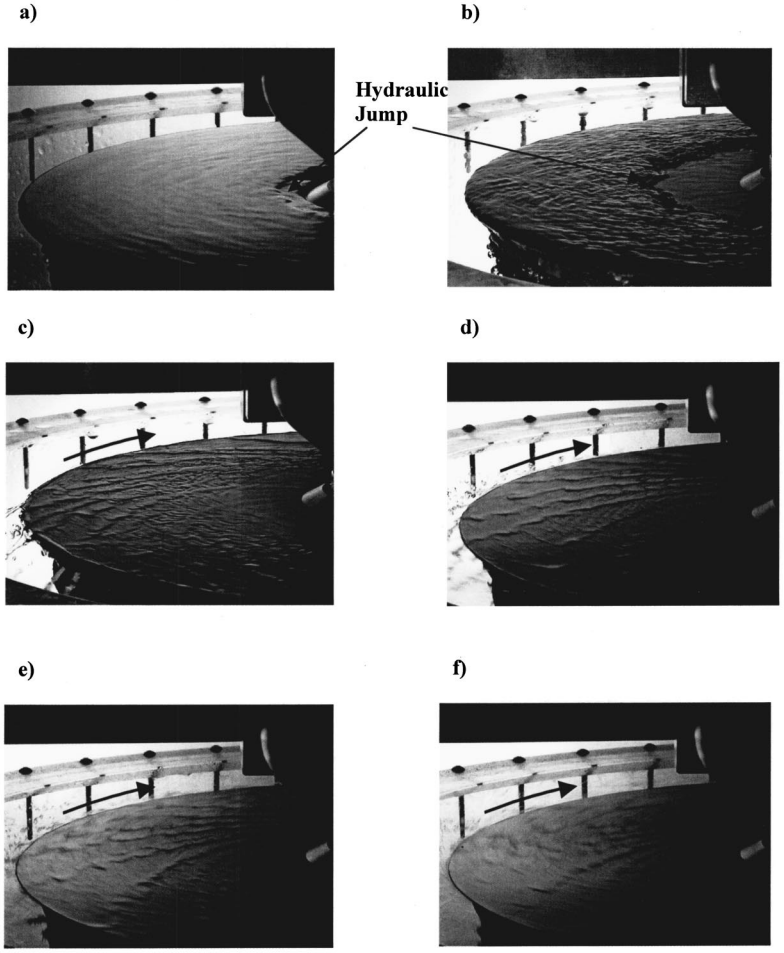

Fig. 3 Flow visualization of a liquid film flowing on a rotating/stationary disk for (*a*) Re_i=238, 0 rpm; (*b*) Re_i=555, 0 rpm; (*c*) Re_i=555, 100 rpm; (*d*) Re_i =555, 200 rpm; (*e*) Re_i=555, 300 rpm; (*f*) Re_i=555, 500 rpm. Direction of disk rotation is indicated by the arrow.

and inertia forces are comparable, moves towards the edge of the disk. Figure 5 shows the change in the film thickness, when the Reynolds number is kept constant and the rotation speed is increased. In this situation, the point where the centrifugal and the inertia forces are comparable moves towards the collar. Thus, the maximum film thickness location travels towards the center of the disk. The film thickness decreases as the rotation speed increases. For 300 rpm, the centrifugal forces are dominant over the whole disk surface such that the film thickness decreases with increasing radial distance.

3.2 Heat Transfer Measurements. Measurements of the disk surface temperature distribution were made for different flow rates and different rotation speeds. The heat transfer coefficient is defined in terms of the heat input per unit area supplied by the heater and the temperature difference between the liquid inlet temperature and the determined disk surface temperatures. The total heat input was chosen as 3000 W for the flow rates between 3.0 lpm and 9.0 lpm and 4500 W for the flowrates between 12.0 lpm and 15.0 lpm. These variables were chosen to obtain sufficiently high disk surface temperatures so that the maximum error in the heat transfer coefficient is limited to approximately 10 percent.

The Nusselt number distributions are shown in Fig. 6 for a range of liquid film flow rates (or Re_i) and rotation speeds. Here the Nusselt number is based on the heat transfer coefficient determined based on the difference between the wall and liquid inlet temperatures and the supplied heat flux. The distributions of Nusselt number are shown for different rotation speeds and Reynolds numbers between Re_i=238 (3.0 lpm) and Re_i=1188 (15.0 lpm). In all cases, the Nusselt numbers increase with increasing liquid film flow rate and the rotation speed. The Nusselt numbers are higher at the inner portions of the disk close to the collar and decrease towards the outer edge. For the supercritical region, close to the collar exit, inertial forces have a significant effect on the flow and the maximum temperature differences exist in this region. Thus, the highest heat transfer rates are also obtained in this area. Away from the collar, due to the radial spread, the flow begins to slow down which causes a decrease in the Nusselt number. Also, the developing thermal boundary layer causes a decrease in the Nusselt number. For the case where the disk is stationary and the subcritical flow of the liquid film is present over the disk, the behavior of the Nusselt number profiles changes. As shown in Fig. 3(*a*), the hydraulic jump is attached to the collar and the disk is cooled by the subcritical region of the liquid film for the stationary case at Re_i=238. The liquid velocities within the subcritical region are quite low and result in low Nusselt numbers over the disk. The Nusselt numbers for the stationary disk are significantly lower than the rotating disk cases. Increasing rotation progressively results in an increase of the heat transfer coefficient and the Nusselt number as expected due to thinning of the liquid film and more effective heat transfer.

For Re_i=555, the hydraulic jump exists only for the stationary case and it resides between r/r_i=1.5 and 2.5. The Nusselt number

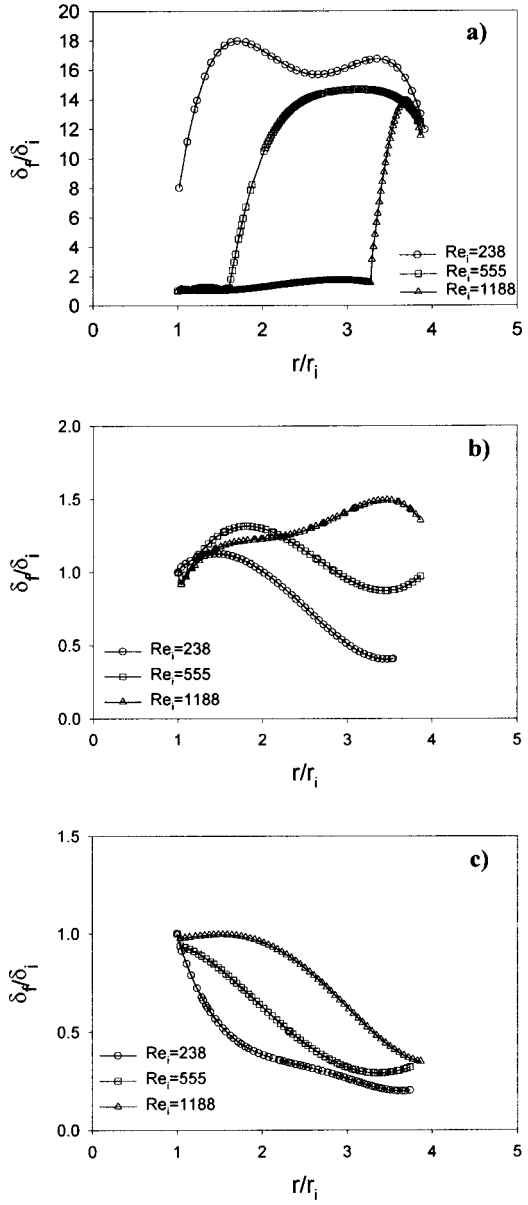

Fig. 4 Film thickness distribution along the radial direction for a liquid film flowing on a stationary/rotating disk at (*a*) 0 rpm; (*b*) 100 rpm; and (*c*) 300 rpm.

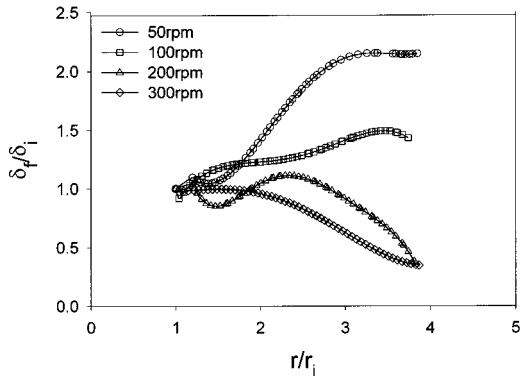

Fig. 5 Film thickness distribution along the radial direction for a liquid film flowing on a rotating disk at Re$_i$=1188

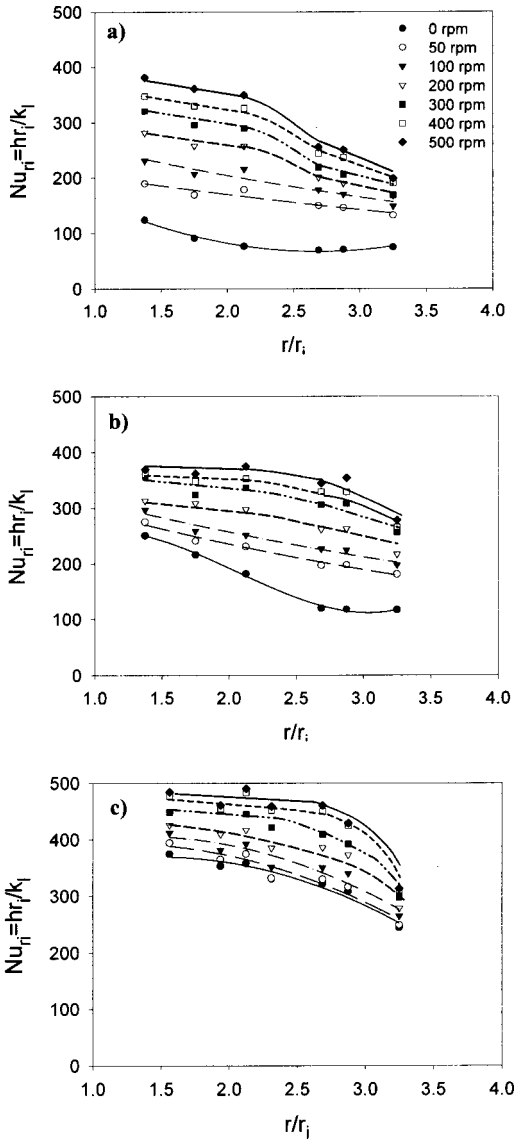

Fig. 6 Nusselt Number distributions along the radial direction for a thin liquid film flowing on a stationary and rotating disk for (*a*) Re$_i$=238 (3.0 lpm), $\dot{Q}$=3000 W, (*b*) Re$_i$=555 (7.0 lpm), $\dot{Q}$ =3000 W, and (*c*) Re$_i$=1188 (15.0 lpm), $\dot{Q}$=4500 W

variation shown in Fig. 6(*b*) exhibits this effect as the Nusselt number is significantly higher in the supercritical region (r/r_i <2.0) as compared to the subcritical region ($r/r_i>2.5$). For the rotating disk cases, the hydraulic jump is not present on the disk surface and consequently the heat transfer coefficients are consistently higher. The effect of higher liquid flow rate and higher liquid film velocity is to enhance the heat transfer in the inner regions as seen in Figs. 6(*a*) and 6(*b*). Additionally, the Nusselt number in the inner disk regions approaches a constant value at high flow rates. The magnitude of Nusselt number increases slightly at the high rotation speeds. The approach to a constant Nusselt number at high flow rates is expected as the inner regions of the disk are cooled by the thin liquid film which has a high velocity in these regions. It is interesting that the rotational effects are still present in this region. Figure 6(*c*) shows the heat transfer data for 15.0 lpm liquid flow rate corresponding to $\mathrm{Re_I}=1188$. The Nusselt numbers are higher than the previous two cases (3.0 lpm and 7.0 lpm) and the constancy of the Nusselt number in the inner regions is more apparent. In fact, it is evident from all these

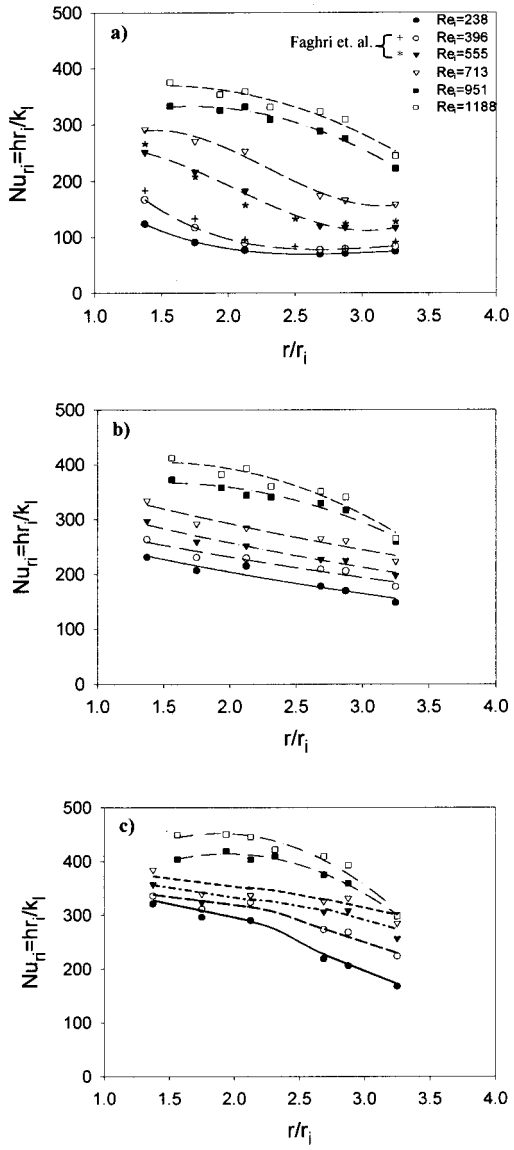

Fig. 7 Nusselt number distributions along the radial direction for a thin liquid film flowing on a stationary and rotating disk for (*a*) 0 rpm, (*b*) 100 rpm, and (*c*) 300 rpm

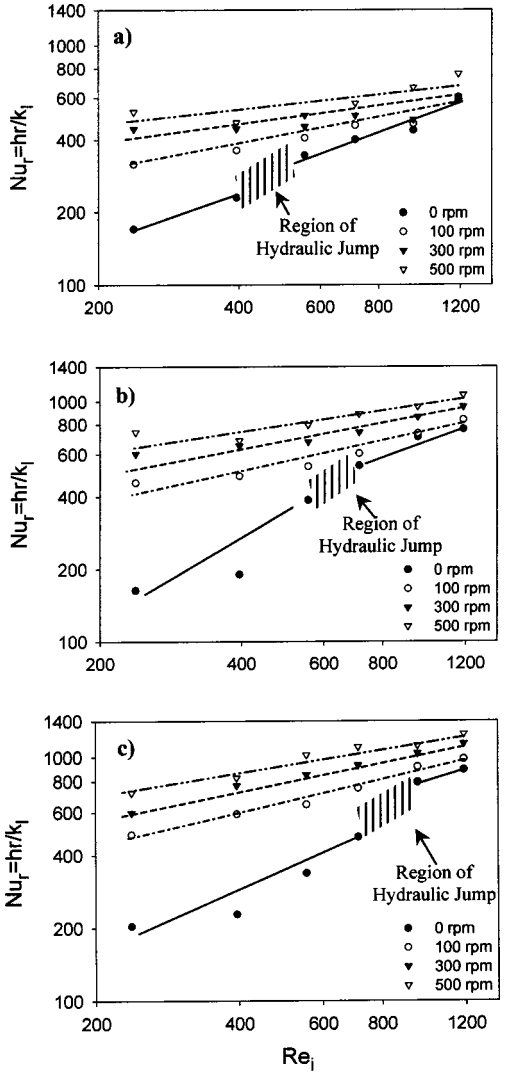

Fig. 8 Local Nusselt Number distribution for a thin liquid film flowing on a stationary and rotating disk as a function of Reynolds number for Pr=4.2 at (*a*) $r/r_i=1.4$, (*b*) $r/r_i=2.1$, and (*c*) $r/r_i=2.9$

data that the character of the Nusselt number distribution changes from that of a continuous decrease from the center to the outer edge of the disk to that of a constant inner part and a decrease towards the outer edge. As explained before, this trend is a result of the interplay between the effects of the high velocity liquid film in the inner regions and the pronounced effects of the rotation in the outer regions.

The Nusselt number distributions are shown in Fig. 7 at different flow rates for stationary disk and two rotational speeds of 100 and 300 rpm. In these experiments the flow rates are 3.0, 5.0, 7.0, 9.0 12.0, and 15.0 lpm with the corresponding Re_i of 238, 396, 555, 713, 951, and 1188. Also shown in Fig. 7(*a*) is the data obtained earlier by Faghri et al. [13] for the stationary disk case. The agreement between those and the current data is quite good with a maximum deviation of 9 percent which is within the uncertainty of each data set. As the liquid flow rate increases, the Nusselt numbers also increase in all cases. However, the increase is most pronounced for the stationary case, particularly in the inner regions of the disk. For $Re_i=238$ and 396, the hydraulic jump is very close to the collar exit and as such the Nusselt numbers are low and have similar magnitude for the subcritical liquid film flow. For $Re_i=555$, the hydraulic jump resides between $r/r_i=1.5$ and 2.5 and the data exhibit a significantly different variation as discussed earlier. At higher liquid flow rates, the inner part of the disk attains a uniformly higher cooling from the high velocity thin liquid film. As the rotational speed of the disk increases, the variation of the Nusselt number with respect to flow rate decreases.

In Fig. 8, the previously shown data are plotted at several locations on the disk to determine the effect of flow rate (or inlet Reynolds number) on the Nusselt number. At all rotation speeds, the Nusselt number increases as the Re_i increases. At the inner region of the disk ($r/r_i=1.4$) shown in Fig. 8(*a*), the Nusselt number increases with the inlet Reynolds number with a power law dependence for the rotating disk data. For the stationary disk case, the presence of the hydraulic jump influences the Reynolds number dependence. Hydraulic jump is present in the vicinity of $r/r_i=1.4$ between $Re_i=400$ and 600 for the stationary case. Below $Re_i=400$ the liquid film is in the subcritical region and the Nusselt number appears to exhibit a stronger Reynolds number dependence as compared to the thin film region. In the thin liquid film regime, The Nusselt number dependence on the inlet Reynolds number is similar for all cases including the supercritical

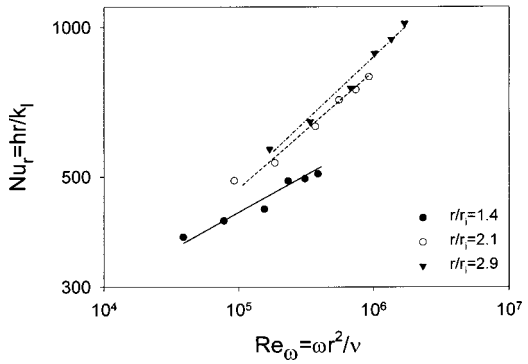

Fig. 9 Local Nusselt Number distribution for a thin liquid film flowing on a rotating disk as a function of rotational Reynolds number for $Re_i=555$ at $\dot{Q}=3000$ W

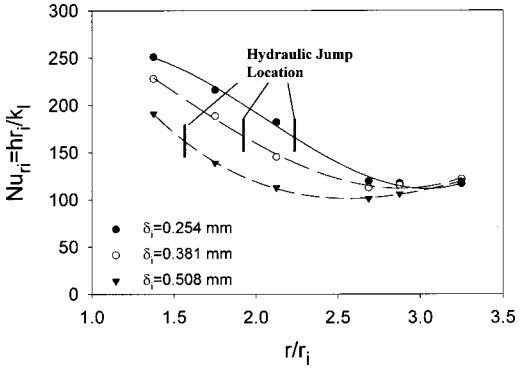

Fig. 11 Comparison of Nusselt number distributions along the radial direction for a liquid film flowing over a stationary disk for $Re_i=555$ at $\dot{Q}=3000$ W for $\delta_i=0.254$ mm, 0.381 mm and 0.508 mm

regions of the film on the stationary disk. However, Nusselt number shifts to higher values with increasing rotational speed for all cases.

Figure 9 shows the dependence of local Nusselt number on the rotational Reynolds number at three locations on the disk surface. This dependence becomes stronger and more pronounced at larger radii on the disk surface as expected since the influence of rotation becomes progressively more dominant at larger radii. The power law dependence on rotational Reynolds number is similar for the two outer locations shown in this figure. In a similar fashion, the Nusselt number dependence on the Rosby number is shown in Fig. 10. It is clearly seen that data also exhibit a power law dependence on the Rosby number, which is a measure of the relative importance of the radial and tangential components of the film flow. As the rotation speed increases for a given film flow rate or Rosby number decreases, the heat transfer coefficient is enhanced as expected.

In Fig. 11, the effect of the collar gap height through which the liquid film emerges, is shown for the stationary disk. There is a substantial dependence of the local heat transfer rate and Nusselt number on the initial gap height at small radii $r/r_i<2.5$. With increasing gap height, the Nusselt number decreases, particularly in the supercritical region. It is also interesting to note that this effect persists for sometime into the subcritical region.

The heat transfer results presented here could have been influenced to some degree by the conjugate heat transfer effects in the disk although the experimental setup was designed to minimize such effects. However, earlier work by Faghri et al. [13] suggests that conjugate heat transfer effects can be significant under certain conditions. In light of this, we are currently investigating the influence of the conjugate heat transfer effects by computational modeling to better assess these effects on the experimental findings.

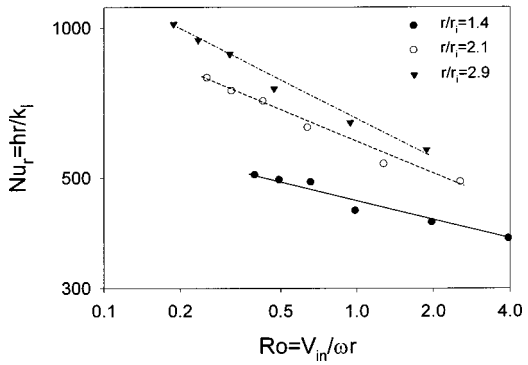

Fig. 10 Local Nusselt Number distribution for a thin liquid film over a rotating disk as a function of Rosby number for $Re_i=555$ at $\dot{Q}=3000$ W

3.3 Heat Transfer Correlation. A heat transfer correlation was developed by dividing the domain into two regions. Region I represents the thermal entry length over the disk, and thus extends from the flow collar to the radius where the free surface temperature is first influenced by the wall heat flux. Region II extends from this point downstream but does not include the hydraulic jump. A scale analysis is presented here to identify the controlling parameters. For Region I, heat transfer coefficient can be written as

$$h=\frac{q''}{\Delta T}=\frac{k_l\dfrac{\partial T}{\partial Z}}{\Delta T} \tag{1}$$

where $\partial T/\partial Z = T_w-T_i/\delta_T$, $\Delta T=T_w-T_i$ thus,

$$h=\frac{k_l}{\delta_T} \qquad \text{or} \qquad \mathrm{Nu}_{\delta_T}=1 \tag{2}$$

To predict the heat transfer coefficient, a knowledge of the thermal boundary layer is required. For Prandtl numbers of order one, thermal boundary layer development is highly dependent on the nature of the momentum boundary layer. The relationship between the thermal and hydrodynamic boundary layers can be written as

$$\frac{\delta_T}{\delta}=C\mathrm{Pr}^b \tag{3}$$

Since the velocity distribution is in a transitional mode, the prediction of δ requires some simplifying assumptions. Namely, the inlet velocity profile can be neglected and a uniform radial velocity distribution at the inlet can be assumed. This is similar to Watson's second region [2] with the addition of rotational effects. For this case, a developing radial boundary layer exists in a rotating flow field for which a scale analysis of the momentum equation yields

$$\frac{\delta}{r}=C_1\,\mathrm{Re}_r^{-1/2}+C_2\left(\frac{\mathrm{Ro}}{\mathrm{Re}_\omega}\right)^{1/2} \tag{4}$$

The first term in the above equation relates to the viscous growth of the hydrodynamic boundary layer, which is the significant term for radial flow regime. The second term results from rotational forces and has the effect of accelerating and thinning the boundary layer. This centrifugal thinning term governs the relation for rotationally dominant regimes. Thus, a correlation for Region I can be formulated as

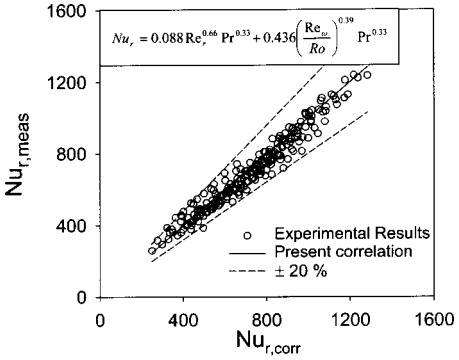

Fig. 12 Experimental results versus correlation for the local Nusselt number for a liquid film flowing on a stationary/rotating disk

$$\text{Local Nusselt number;}\quad \mathrm{Nu}_r = (hr/k_l) = C_1\,\mathrm{Re}_r^a \mathrm{Pr}^b + C_2\,\mathrm{Re}_\omega^c \mathrm{Ro}^d \mathrm{Pr}^b \tag{5}$$

Following the same procedure for Region II we can write

$$h = \frac{q''}{\Delta T} = \frac{k_l \dfrac{\partial T}{\partial Z}}{\Delta T} \tag{6}$$

where $\partial T/\partial Z = T_w - T_s/\delta_f, \Delta T = T_w - T_i$, thus,

$$h = \frac{k}{\delta_{\text{film}}} \frac{T_w - T_s}{T_w - T_i} \tag{7}$$

Additionally, if the assumption is made that $T_w - T_s/T_w - T_i \approx 1$ then the correlation for Region II reduces to the identical form as that for Region I with δ_{film} replacing δ_T. In order to evaluate the validity of the above assumption, a heat balance was used to calculate the maximum bulk temperature of the fluid. A conservative estimate of the free surface temperature was derived from the assumption $T_{\text{bulk}} = T_w + T_s/2$. Using this approach for specific data sets, it was found that $T_w - T_s/T_w - T_i = 0.8 \rightarrow 1.0$ which was considered to be acceptable. Since the correlation equations for both Regions I and II were of the same form, a single correlation equation was used to represent both regions. The best fit correlations to all of the data presented in this study are given as follows. For the local and average Nusselt number, respectively,

$$\text{Local Nusselt number:}\quad \mathrm{Nu}_r = 0.088\,\mathrm{Re}_r^{0.66}\mathrm{Pr}^{0.33} + 0.436(\mathrm{Re}_\omega/\mathrm{Ro})^{0.39}\mathrm{Pr}^{0.33} \tag{8}$$

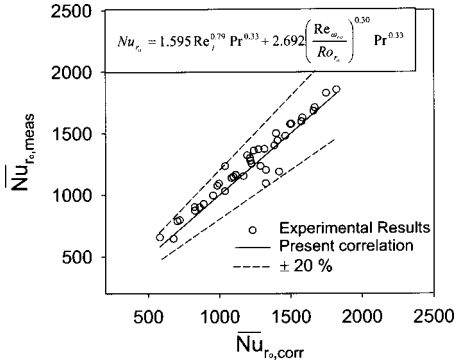

Fig. 13 Experimental results versus correlation for average Nusselt number for a liquid film flowing on a stationary/rotating disk

$$\text{Average Nusselt number:}\quad \overline{\mathrm{Nu}}_{ro} = 1.595\,\mathrm{Re}_j^{0.79}\mathrm{Pr}^{0.33} + 2.692(\mathrm{Re}_{\omega_{ro}}/\mathrm{Ro})^{0.30}\mathrm{Pr}^{0.33} \tag{9}$$

Note that in the correlation for local Nusselt number, Nu is defined using the local radius and local heat transfer coefficients while in the case of average Nusselt number, it is defined by the outer disk radius and average heat transfer coefficient based on the arithmetic mean of the disk surface temperature. The validity of these data fits are shown in Figs. 12 and 13 for the local and overall Nusselt numbers respectively. The correlations for the local and the overall Nusselt numbers were both found to be accurate to within ±20 percent. In developing these correlations only the data in the thin liquid film region (i.e. supercritical regions for those cases having a hydraulic jump) were taken into account. Also, due to possible cooling effects near the outer edge of the disk as the liquid exits the disk surface, the data at the outermost location closest to the disk outer edge were not included in the correlations.

4 Conclusions

The characteristics of a thin liquid film with a free surface on a stationary and rotating disk have been examined experimentally. The change in the position of the hydraulic jump was observed qualitatively by a photographic study. Also, the film thickness was measured for different Reynolds numbers and rotational speeds with the laser light reflection technique. On the stationary disk surface, the liquid film experienced a hydraulic jump in which the liquid velocity decreased and the film thickness increased. With increasing flow rates the hydraulic jump migrated towards the outer edge of the disk. It was also observed that the hydraulic jump washed off the disk surface under rotation. It was found that three regions existed in the rotating thin liquid film: the inertia dominated region, where the inertia and the frictional forces were prevalent; the rotation dominated region, where the centrifugal forces had a more significant effect; and a transition region which contained elements of both the inertia and the rotation dominated regions.

The experimental study of heat transfer of a thin water film on a rotating disk was also presented. It was found that the heat transfer was affected by different flow conditions over the disk surface. Nusselt number was higher at the inner portions of the disk, close to the collar, and decreased towards the outer edge due to radial spread, convective heating of the liquid and the developing thermal boundary layer. When hydraulic jump occurred on the disk, low Nusselt numbers were observed in the subcritical region due to the significant increase in the film thickness and reduced liquid velocities. However, the Nusselt numbers attained high values in the supercritical region. The increase in the rotation speed caused an increase in the Nusselt numbers because of the thinning effect. As the liquid flow rate increased, Nusselt numbers also increased. This increase was more pronounced for the stationary case, especially on the inner parts of the disk surface. With the increasing flow rate, the hydraulic jump migrated to outer radii and the larger portions of the disk were cooled by the supercritical region of the liquid film. In addition, the increase in the flow rate caused a more uniform temperature and Nusselt number distribution at the inner regions due to the high liquid velocities.

Finally, semi-empirical correlations were presented for the local and overall Nusselt numbers. Both of the correlations represented the experimental data within ±20 percent. It should be also noted here that the conjugate heat transfer effects may influence the experimental results. Currently, a computational study of such effects is being carried out in this configuration to assess their contribution.

Acknowledgment

This work was sponsored by the NASA Microgravity Fluids Physics Program, Glenn Research Center, Cleveland, Ohio, under the grant No. NCC3-789 with Dr. Subramanian Sankaran as the grant monitor.

Nomenclature

a,b,c,d,C_1,C_2 = correlation coefficient
A_h = area of the heater, m^2
d_h = hydraulic diameter, $(2\delta_i)$, m
h = local heat transfer coefficient, $(\dot{Q}/A_h)/(T_w - T_i)$, W/m^2K
$\overline{h}$ = average heat transfer coefficient, $(\dot{Q}/A_h)/(T_{av}-T_i)$, W/m^2K
k_l = thermal conductivity of the liquid, W/mK
Nu_r = local Nusselt number, (hr/k_l)
Nu_{ri} = Nusselt number based on inlet radius, (hr_i/k_l)
$\overline{Nu}_{r_o}$ = average Nusselt number, $(\overline{h}r_o/k_l)$
Pr = Prandtl number, (ν/α)
$\dot{Q}$ = total heat input power, W
r = local radius, m
r_i = liquid inlet collar radius, m
r_o = outer disk radius, m
Re_i = inlet Reynolds number, $(V_{in}\delta_{in}/\nu)$
Re_j = jet Reynolds number, $(V_{in}d_h/\nu)$
Re_r = local Reynolds number, $(V_{in}r/\nu)$
Re_ω = rotational Reynolds number, $(\omega r^2/\nu)$
$Re_{\omega^{ro}}$ = rotational Reynolds number based on the outer disk radius, $(\omega r_o^2/\nu)$
Ro = Rossby number, $(V_{in}/\omega r)$
Ro_{ro} = Rossby number based on the outer disk radius, $(V_{in}/\omega r_o)$
T_{av} = average disk surface temperature, °C
T_{bulk} = bulk liquid film temperature, °C
T_w = local disk surface temperature, °C
T_i = inlet fluid temperature, °C
T_s = free surface temperature of the liquid film, °C
V_{in} = radial velocity component at the exit of the collar, $(\dot{V}/2\pi r_i\delta_i)$, m/s
$\dot{V}$ = volumetric flow rate, m^3/s

Greek Symbols

α = thermal diffusivity, m^2/s
δ = momentum boundary layer thickness, m
δ_f = film thickness, m
δ_i = inlet gap height, m
δ_T = thermal boundary layer thickness, m
ν = kinematic viscosity of the liquid, m^2/s
ω = rotational speed, rad/s

References

[1] Webb, B. W., and Ma, C.-F., 1995, "Single-Phase Liquid Jet Impingement Heat Transfer," Adv. Heat Transfer, **26**, pp. 105–217.
[2] Watson, E. J., 1964, "The Radial Spread of a Liquid Jet over a Horizontal Plane," J. Fluid Mech., **20**, pp. 481–499.
[3] Chadhury, Z. H., 1964, "Heat Transfer in a Radial Liquid Jet," J. Fluid Mech., **20**, pp. 501–511.
[4] Wang, X. S., Dagan, Z., and Jiji, L. M., 1989, "Heat Transfer Between a Circular Free Impinging Jet and a Solid Surface with Non-Uniform Wall Temperature of Wall Heat Flux: 1: Solution for the Stagnation Region," Int. J. Heat Mass Transfer, **32**, pp. 1351–1360.
[5] Thomas, S., Hankey, W., and Faghri, A., 1990, "One-Dimensional Analysis of the Hydrodynamic and Thermal Characteristics of Thin Film Flows Including the Hydraulic Jump Rotation," ASME J. Heat Transfer, **112**, pp. 728–736.
[6] Rahman, M. M., Faghri, A., and Hankey, W., 1991, "Computation of Turbulent Flow in a Thin Liquid Layer of Fluid Involving a Hydraulic Jump," J. Fluids Eng., **113**, pp. 411–418.
[7] Rahman, M. M., and Faghri, A., 1992, "Analysis of Heating and Evaporation from a Liquid Film Adjacent to a Horizontal Rotating Disk," Int. J. Heat Mass Transfer, **35**, pp. 2655–2664.
[8] Carper, H. J., and Defenbaugh, D. M., 1978, "Heat Transfer from a Rotating Disk with Liquid Jet Impingement," Proceedings of 6th Int. Heat Transfer Conference in Toronto, pp. 113–118.
[9] Carper, Jr., H. J., Saavedra, J. J., and Suwanprateep, T., 1986, "Liquid Jet Impingement Cooling of a Rotating Disk," ASME J. Heat Transfer, **108**, pp. 540–546.
[10] Vader, D. T., Incropera, F. P., and Viskanta, R., 1991, "Local Convective Heat Transfer From a Heated Surface to an Impinging, Planar Jet of Water," Int. J. Heat Mass Transfer, **34**, pp. 611–623.
[11] Stevens, J., and Webb, B. W., 1991, "Local Heat Transfer Coefficients Under and Axisymmetric, Single-Phase Liquid Jet," ASME J. Heat Transfer, **113**, pp. 71–78.
[12] Mudawwar, I. A., El-Masri, M. A., Wu, C. S., and Ausman-Mudawwar, J. R., 1985, "Boiling Heat Transfer and Critical Heat Flux in High-Speed Rotating Liquid Films," Int. J. Heat Mass Transfer, **28**, pp. 795–806.
[13] Faghri, A., Thomas, S., and Rahman, M. M., 1993, "Conjugate Heat Transfer from a Heated Disk to a Thin Liquid Film Formed by a Controlled Impinging Jet," ASME J. Heat Transfer, **115**, pp. 116–123.
[14] Aoune, A., and Ramshaw, C., 1999, "Process Intensification: Heat and Mass Tyransfer Characteristics of Liquid Films on Rotating Discs," Int. J. Heat Mass Transfer, **42**, pp. 2543–2556.
[15] Metzger, D. E., Bunker, R. S., and Bosch, G., 1991, "Transient Liquid Crystal Measurement of Local Heat Transfer on a Rotating Disk with Jet Impingement," ASME J. Turbomach., **113**, pp. 52–59.
[16] Bizzak, D. J., and Chyu, M. K., 1995, "Use of a Laser—Induced Fluorescence Thermal Imaging System for Local Jet Impingement Heat Transfer Measurement," Int. J. Heat Mass Transfer, **38**, pp. 267–274.
[17] Ozar, B., Cetegen, B. M., and Faghri, A., 2003, "Experiments on the Flow of a Thin Liquid Film over a Horizontal Stationary and Rotating Disk Surface," Exp. Fluids, **34**, pp. 556–565.
[18] Thomas, S., Faghri, A., and Hankey, W., 1991, "Experimental Analysis and Flow Visualization of a Thin Liquid Film on a Stationary and Rotating Disk," J. Fluid Mech., **113**, pp. 73–80.

Spatially Resolved Surface Heat Transfer for Parallel Rib Turbulators With 45 Deg Orientations Including Test Surface Conduction Analysis

S. Y. Won

N. K. Burgess

S. Peddicord

P. M. Ligrani
Fellow ASME Professor

Convective Heat Transfer Laboratory,
Department of Mechanical Engineering,
MEB 2110, University of Utah,
Salt Lake City, UT 84112-9208, USA

Spatially resolved Nusselt numbers, spatially-averaged Nusselt numbers, and friction factors are presented for a stationary channel with an aspect ratio of 4 and angled rib turbulators inclined at 45 deg with parallel orientations on two opposite surfaces. Results are given at different Reynolds numbers based on channel height from 9000 to 76,000. The ratio of rib height to hydraulic diameter is 0.078, the rib pitch-to-height ratio is 10, and the blockage provided by the ribs is 25 percent of the channel cross-sectional area. Nusselt numbers are determined with three-dimensional conduction considered within the acrylic test surface. Test surface conduction results in important variations of surface heat flux, which give decreased local Nusselt number ratios near corners, where each rib joins the flat part of the test surface, and along the central part of each rib top surface. However, even with test surface conduction included in the analysis, spatially-resolved local Nusselt numbers are highest on tops of the rib turbulators, with lower magnitudes on flat surfaces between the ribs, where regions of flow separation and shear layer re-attachment have pronounced influences on local surface heat transfer behavior. The augmented local and spatially averaged Nusselt number ratios (rib turbulator Nusselt numbers normalized by values measured in a smooth channel) decrease on the rib tops, and on the flat regions away from the ribs, especially at locations just downstream of the ribs, as Reynolds number increases. With conduction along and within the test surface considered, globally averaged Nusselt number ratios vary from 3.53 to 1.79 as Reynolds number increases from 9000 to 76,000. Corresponding thermal performance parameters also decrease as Reynolds number increases over this range. [DOI: 10.1115/1.1668046]

Keywords: Augmentation, Conduction, Heat Transfer, Roughness, Turbines, Turbulent

Introduction

Rib turbulators are one of several techniques that are used for enhancing convective heat transfer rates by increasing advection driven by secondary flows, and turbulence transport over larger portions of the flow fields. Reviews of recent experimental and numerical research on the influences and effects of rib turbulators are presented by Lau [1] and Ligrani et al. [2]. Discussed are a variety of arrangements, including single-pass and multi-pass channels, square and rectangular channels, channels with and without rotation, and rotating channels with different orientations with respect to the axis of rotation [3–11].

The present experimental study is conducted using a large-scale test section, without rotation, so that detailed, spatially resolved surface Nusselt numbers, and friction factors can be measured. A single-pass channel with aspect ratio of 4 is employed. The ribs are placed so that they are parallel and aligned with repect to each other on the two widest, opposite walls of the channel with 45 deg angles with respect to the streamwise flow direction. Reynolds numbers, based on channel height, range from 9000 to 76,000. Related studies either do not present spatially resolved surface heat transfer data [4], or use channels with different aspect ratios [7,9]. Unlike the present investigation, none of these studies account for detailed conduction variations along and within the ribbed test surfaces employed.

Contributed by the Heat Transfer Division for publication in the JOURNAL OF HEAT TRANSFER. Manuscript received by the Heat Transfer Division June 6, 2003; revision received December 23, 2003. Associate Editor: C. Amon.

The present results are thus different from and unique compared to existing studies, and extend the rib turbulator data base by presenting detailed, spatially-resolved surface Nusselt number distributions along a test surface, especially on and very near angled-parallel ribs. Analysis of conduction variations within the ribbed test surface is included to account for spatially-varying surface heat flux. This approach gives more accurate surface Nusselt number distributions than have been measured in other investigations, especially in regard to the presence of hot spots along the test surface. Without the spatially resolved measurements, and conduction analysis applied to these measurements, the presence, extent and nature of these hot spots (and associated surface Nusselt number variations) would not be known. Included in the present study for different channel Reynolds numbers are (i) spatially resolved, spatially averaged, and globally averaged surface Nusselt number data for variable surface heat flux next to the air stream (determined from conduction analyses applied to the ribbed test surface), and (ii) friction factor data. Also discussed are the effects of thermal boundary layer development on Nusselt number ratios.

Experimental Apparatus and Procedures

The overall experimental apparatus (but not the test section) is similar to the one described by Mahmood and Ligrani [12] and Ligrani and Mahmood [13]. A brief description of this apparatus is also presented here.

Channel and Test Surface for Heat Transfer Measurements A schematic of the facility used for heat transfer measurements is

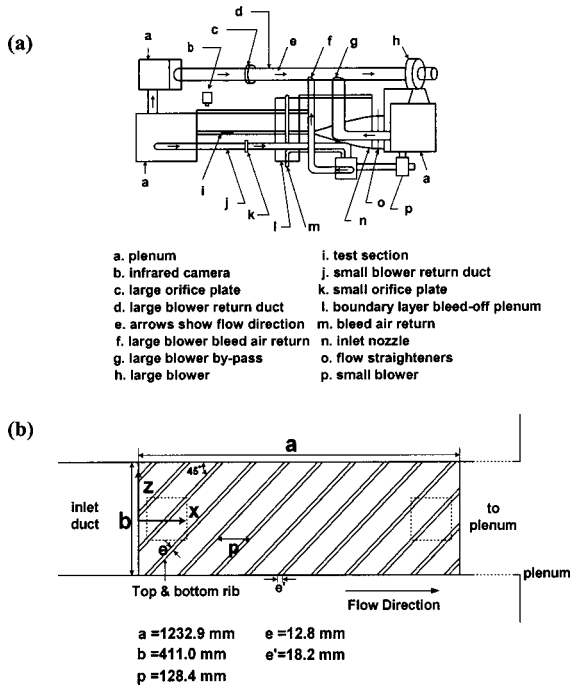

Fig. 1 Schematic diagrams of (*a*) the experimental apparatus used for heat transfer measurements, and (*b*) the rib turbulator test surfaces, including coordinate system

shown in Fig. 1(*a*). The air used within the facility is circulated in a closed-loop. The air mass flow rate from the test section is measured (upstream of the blower employed) using an ASME standard orifice plate and Validyne M10 digital pressure manometer. The blower then exits into a series of two plenums (0.9 m square and 0.75 m square). A Bonneville cross-flow heat exchanger is located between two of these plenums, and is cooled with liquid nitrogen at a flow rate appropriate to give the desired air temperature at the exit of the heat exchanger. As the air exits the heat exchanger, it enters the second plenum, from which the air passes into a rectangular bell mouth inlet, followed by a honeycomb, two screens, and a two-dimensional nozzle with a contraction ratio of 5.6. This nozzles leads to a rectangular cross-section, 411 mm by 103 mm inlet duct which is 1219 mm in length. This is equivalent to 7.4 hydraulic diameters (where hydraulic diameter is 164.7 mm). Two trips are employed on the top and bottom surfaces of the inlet duct, just upstream of the test section, which follows with the same cross-section dimensions. It exits to another duct, and then to a 0.60 m square plenum, which is followed by two pipes, each containing an orifice plate, mentioned earlier.

Figure 1(*b*) gives the geometric details of the acrylic test surface, including rib turbulator geometry. A total of 13 acrylic ribs or rib segments are used on the top wall and on the bottom wall of the test section. As mentioned, these are arranged with 45 deg angles with respect to the streamwise flow direction, such that the ribs on opposite walls of the channel are parallel and aligned with respect to each other. Each rib has 12.8 mm height and square cross-section. The ratio of rib height to hydraulic diameter is 0.078, the rib pitch-to-height ratio is 10, and the blockage provided by the ribs is 25 percent of the channel cross-sectional area. The top wall of the test section also has two cut-out regions (one at the upstream end and one at the downstream end) where a zinc-selenide window can be installed to allow the infrared camera to view a portion of the test surface on the bottom wall. The disturbances to the flow and thermal fields are believed to be minimal when this window is employed. When this window is not in use, inserts with ribs (which exactly match the adjacent rib turbulators on the top wall) are used in its place. Also identified in Fig. 1(*b*) is the test section coordinate system employed for the study. Note that the Y coordinate is directed normal to the bottom wall.

All exterior surfaces of the facility (between the heat exchanger and test section) are insulated with Styrofoam ($k=0.024$ W/mK), or 2 to 3 layers of 2.54 cm thick, Elastomer Products black neoprene foam insulation ($k=0.038$ W/mK) to minimize heat losses. Calibrated copper-constantant thermocouples are located between the three layers of insulation located all around the test section to determine conduction losses. Between the first layer and the 3.2 mm thick acrylic test surfaces are custom-made Electrofilm etched-foil heaters (each encapsulated between two thin layers of Kapton) to provide a constant heat flux boundary condition on the test surface. The acrylic surfaces, which are adjacent to the airstream, contain 35 copper-constantant thermocouples, which are placed within the ribs as well as within flat portions of the test surfaces between the ribs. Each of these thermocouples is located 0.051 cm just below the surface to provide measurements of local surface temperatures, after correction for thermal contact resistance and temperature drop through the 0.051 cm thickness of acrylic. Acrylic is chosen because of its low thermal conductivity ($k=0.16$ W/mK at 20°C) to minimize streamwise and spanwise conduction along the test surfaces, and thus, minimize ''smearing'' of spatially varying temperature gradients along the test surfaces. Energy balances, performed on the heated test surfaces, then allow determination of local magnitudes of the convective heat flux.

The mixed-mean stagnation temperature of the air entering the test section is measured using five calibrated copper-constantan thermocouples spread across its cross-section. To determine this temperature, thermocouple-measured temperatures are corrected for thermocouple wire conduction losses, channel velocity variations, as well as for the differences between stagnation and recovery temperature. All measurements are obtained when the test facility is at steady state.

Local Nusselt Number Measurement. To determine the surface heat flux (used to calculate heat transfer coefficients and local Nusselt numbers), the convective power levels provided by the etched foil heaters are divided by flat test surface areas. Spatially resolved temperature distributions along the bottom rib turbulator test surface are determined using infrared imaging in conjunction with thermocouples, energy balances, and *in situ* calibration procedures [12–15]. To accomplish this, the infrared radiation emitted by the heated interior surface of the channel is captured using a VideoTherm 340 Infrared Imaging Camera, which operates at infrared wave lengths from 8 μm to 14 μm. Temperatures, measured using the calibrated, copper-constantant thermocouples distributed along the test surface adjacent to the flow, are used to perform the *in situ* calibrations simultaneously as the radiation contours from surface temperature variations are recorded.

This is accomplished as the camera views the test surface through a custom-made, zinc-selenide window (which transmits infrared wave lengths between 6 and 17 μm, at transmission percentages ranging from 70 to 90 percent) located on the top wall of the test section. Note that the portion of the test surface viewed by the infrared camera is painted flat black to improve its emissivity. Eleven to thirteen thermocouple junction locations are usually present in the infrared field viewed by the camera. The exact spatial locations and pixel locations of these thermocouple junctions and the coordinates of a 12.7 cm by 12.7 cm field of view are known from calibration maps obtained prior to measurements.

Images from the infrared camera are recorded as 8-bit gray scale directly into the memory of a Dell Dimension XPS T800r PC computer using a Scion Image Corporation Frame grabber video card, and Scion image v.1.9.2 software. Three sets of 60 frames are recorded at a rate of one frame per second. This is done after the rib turbulator flows are established to obtain data when the test surface is at a steady state condition. All of 180 resulting

images are then ensemble-averaged to obtain the final gray scale data image. This final data set is then imported into Matlab version 6.0.0.88 (Release 12) software to convert each of 256 possible gray scale values to local Nusselt number values, at each pixel location using calibration data. Each resulting individual image then covers a 300 pixel by 300 pixel area. Thermal conductivity in the Nusselt number is based on the average of the local wall temperature and the mixed-mean temperature of the air at the upstream inlet. Sargent et al. [15], and Mahmood and Ligrani [12] provide additional details on portions of the infrared imaging and measurement procedures.

Friction Factors. Wall static pressures are measured along the test section simultaneously as the heat transfer measurements are conducted, using 12 side wall pressure taps, located 25.4 mm apart near the downstream portion of the test section. These measurements are made in the test section with rib turbulators, as well as in a baseline test section with smooth surfaces on all four walls. Friction factors are then determined from streamwise pressure gradient magnitudes. Friction factors are measured using the facility shown in Fig. 1(*a*). Pressures from the wall pressure taps are measured using Celesco LCVR pressure transducers. Signals from these transducers are processed using Celesco CD10D Carrier-Demodulators. Voltages from the Carrier-Demodulators are acquired using a Hewlett-Packard 44422A data acquisition card installed in a Hewlett-Packard 3497A data acquisition control unit, which is controlled by a Hewlett-Packard A4190A Series computer.

Uncertainty Estimates. Uncertainty estimates are based on 95 percent confidence levels, and determined using procedures described by Kline and McClintock [16] and Moffat [17]. Uncertainty of temperatures measured with thermocouples is 0.15°C. Spatial and temperature resolutions achieved with the infrared imaging are about 0.52 mm and 0.8°C, respectively. This magnitude of temperature resolution is due to uncertainty in determining the exact locations of thermocouples with respect to pixel values used for the *in situ* calibrations. Local Nusselt number ratio uncertainty is then about ± 0.13 (for a ratio of 2.00), or about ± 6.5 percent. Reynolds number uncertainty is approximately ± 1.7 percent for Re_H of 10,000. The estimated uncertainty of local channel friction factors is ± 4.5 percent.

Conduction Analysis Within the Test Surface

Three-dimensional conduction along and within the acrylic test surface is determined using version 6.0 of the ANSYS numerical code. To accomplish this, a portion of the test surface, with one acrylic rib segment, is modeled using approximately 17,480 numeric node elements. In addition, a constant heat flux boundary condition (determined from values used in the experiments) is imposed on the back side of the 3.2 mm thick acrylic test surface. Local surface temperatures, measured experimentally using infrared thermography, are used for the thermal boundary condition on portions of the test surface next to the air stream, including the top of the rib segment and the flat parts of the test surface around the rib. Temperatures are also imposed as the thermal boundary condition on the vertical parts of the rib segment, which are determined by interpolation of values measured at the edge of the rib top and at the corner (between each rib side and flat parts of the test surface).

Ordinarily, without the conduction analysis applied, the same heat flux produced by the etched-foil heater is assumed to leave the test surface next to the air stream at the rib top and along the flat parts of the test surface around the rib. This means that no heat is assumed to leave the vertical side walls of the rib, and that all of the thermal power into the test surface leaves entirely only from the horizontal surfaces next to the air stream. This is referred to as a ''constant heat flux boundary condition.'' The ANSYS version 6.0 conduction analysis is used to determine the non-uniform variations of surface heat flux into the air stream, which are actually present, including along the vertical sides of the rib segment. As mentioned, this is accomplished using experimentally measured values as thermal boundary conditions around the numerical domain solved by the numerical code.

Experimental Results and Discussion

Baseline Nusselt Numbers. Baseline Nusselt numbers Nu_o, used to normalize the ribbed channel values, are measured in a smooth rectangular test section with smooth walls replacing the two ribbed test surfaces. Except for the absence of the ribs, all geometric characteristics of the channel are the same as when the ribbed test surfaces are installed. These measurements are made in the downstream portions of the test section where the channel flow is hydraulically and thermally fully developed. All Nu_o baseline values are obtained using a T_{oi}/T_w temperature ratio of 0.93 to 0.95. In addition, baseline measurements are conducted with all four surfaces wrapped with etched foil heaters to provide a heat flux boundary condition around the entire test section. Note that the same constant flux heating arrangement is also employed with the ribbed test section. The variation of baseline Nusselt numbers with Reynolds number Re_{Dh} are in agreement with the Dittus-Boelter smooth circular tube correlation [18] for $Re_{Dh} < 180{,}000$ [12–14].

Spatially Resolved Distributions of Local Nusselt Numbers Figure 2(*a*) presents spatially resolved Nusselt number ratios,

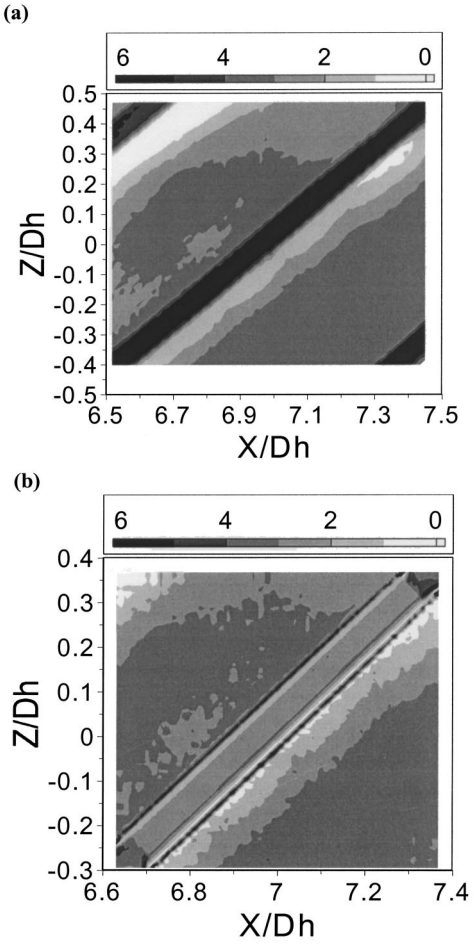

Fig. 2 Local Nusselt number ratio Nu/Nu_o distribution along the rib turbulator test surface for $Re_H = 17{,}000$ and $T_{oi}/T_w = 0.94$. (*a*) With constant surface heat flux and no surface conduction analysis applied. (*b*) With variable surface heat flux and surface conduction analysis applied.

measured over about two periods of ribbed pattern, on the bottom test surface. The results are shown for $Re_H=17{,}000$ and $T_{oi}/T_w=0.94$, and are obtained with constant surface heat flux and no surface conduction analysis applied. In the figure, flow is directed from left to right in the increasing X/D_h direction. The darker diagonal regions show Nu/Nu_o values measured on the tops of the ribs. The data presented are time-averaged, determined from 25 instantaneous data sets acquired over a period of 25 seconds.

As indicated in Fig. 2(*a*), Nu/Nu_o ratios are relatively very high along the tops of the ribs. When compared along the rib tops, values are fairly uniform at different locations. As one moves from the rib in the streamwise or $+X/D_h$ direction, local Nu/Nu_o values initially decrease, and then are low relative to other locations on the test surface. This is due to a re-circulating flow region just downstream of the rib, where the flow direction next to the surface is opposite to the bulk flow direction. Note that a shear layer forms between this re-circulating flow region and the bulk flow located just above the rib. A region with relatively higher values of Nu/Nu_o then follows at slightly higher X/D_h (where $Nu/Nu_o>2.5$), which is due to reattachment of the shear layer which is initially formed above the re-circulating flow region. With an additional increase in streamwise development, Nu/Nu_o values are approximately constant as a second 45 deg rib is approached. This pattern of flow and surface Nusselt number variations then repeats itself as additional ribs are encountered along the test surface. Other factors that affect the heat transfer augmenations are the strong secondary flows, and the skewing and three-dimensional nature of the boundary layer that develops due to the angled orientations of the ribs [2].

The results presented in Fig. 2(*a*) for $Re_H=17{,}000$ are again given in Fig. 2(*b*), but with variable surface heat flux and surface conduction analysis applied. Comparison of these two figures thus provides information on the effects of three-dimensional conduction along and within the test surface. The results at this experimental condition are chosen to illustrate these effects, because variations due to conduction are qualitatively similar to ones observed at other Reynolds numbers. Note that the results in the latter figure cover smaller ranges of X/D_h and Z/D_h values. A comparison of the data in Figs. 2(*a*) and 2(*b*) shows that Nu/Nu_o ratio changes due to three-dimensional conduction are most apparent on the top of the rib segment, and on flat base regions immediately adjacent to the rib segment. Such three-dimensional conduction effects are limited, in part, because of the high-quality construction and performance of the heated test surface, within which, conduction is one-dimensional over most of its volume.

The Nu/Nu_o data in Fig. 2(*a*) are obtained by assuming that all of the heat flux into the rib segment leaves entirely from the top of the rib (with none leaving from the sides). When three-dimensional conduction is present and a portion of the heat transfer leaves the vertical sides of the rib, the surface Nu/Nu_o distribution in Fig. 2(*b*) is produced. As before, the darker diagonal regions with relatively high Nu/Nu_o ratios are again present along the tops of the ribs in this figure. Relative to constant heat flux values in Fig. 2(*a*), Nusselt number ratios in Fig. 2(*b*) are then lower in the middle part of the rib top, with higher Nu/Nu_o values near the upstream and downstream edges of the rib top. Nusselt number ratios on the flat surfaces just adjacent the ribs are also lowered in corners and then increased (compared to constant heat flux values) along lines which are approximately parallel to the rib segment.

The effects of three-dimensional conduction within and along the test surface are further illustrated by the results presented in Figs. 3(*a*) and 3(*b*). In both cases, local Nusselt number ratios Nu/Nu_o for constant surface heat flux (no surface conduction analysis) and for variable surface heat flux (with surface conduction analysis) are presented for a Reynolds number Re_H of 17,000 and T_{oi}/T_w of 0.94 In the first of these figures, local Nu/Nu_o data are given as they vary with X/D_h for constant $Z/D_h=0$. In the second of these figures, Nu/Nu_o data are given as they vary with

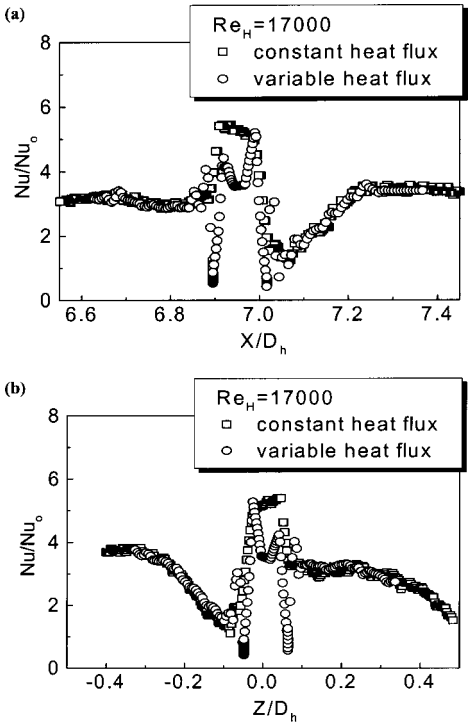

Fig. 3 Variable surface heat flux, local Nusselt number ratios Nu/Nu_o along the rib turbulator test surface for a Reynolds number $Re_H=17{,}000$ and T_{oi}/T_w of 0.94. Data are given for constant surface heat flux (no surface conduction analysis) and for variable surface heat flux (with surface conduction analysis). (*a*) At constant $Z/D_h=0.0$ as X/D_h varies. (*b*) At constant $X/D_h=7.0$ as Z/D_h varies.

Z/D_h for constant $X/D_h=7.0$. Both figures show variable heat flux Nu/Nu_o ratios which are significantly lower than constant heat flux values in the central part of the rib. As mentioned, this is partially due to heat transfer from the sides of the ribs, which also causes local Nu/Nu_o increases, determined with a variable heat flux thermal boundary condition, to be higher than values measured with constant heat flux, near the edges of the rib top. Other variations of importance in Figs. 3(*a*) and 3(*b*) are present on the flat surfaces near the edges of the ribs, where variable flux Nu/Nu_o values are locally lower than constant flux Nu/Nu_o values over very small areas.

The effects of Reynolds number on spatially-resolved Nusselt number ratios (obtained with variable surface heat flux determined from the surface conduction analyses) are illustrated by the data presented in Figs. 4(*a*) and 4(*b*). The data presented in both figures at all Re_H are measured on the same part of the test surface. All of the results are also time-averaged using 25 instantaneous data sets. In the first of these figures, local Nu/Nu_o data are given as they vary with X/D_h for constant $Z/D_h=0$. In the second of these figures, Nu/Nu_o data are given as they vary with Z/D_h for constant $X/D_h=7.0$. These data are obtained from survey results (such as the ones shown in Fig. 2(*b*)) at Re_H ranging from 9,000 to 76,000, and about constant temperature ratio T_{oi}/T_w of 0.93-0.95. In Fig. 4(*a*), local Nu/Nu_o values at $X/D_h=6.60$ to $X/D_h=6.90$ correspond to locations upstream of the central rib. $X/D_h=6.90$ to $X/D_h=7.01$ are then located on the rib, and $X/D_h=7.01$ to $X/D_h=7.40$ correspond to the flat surface downstream of the rib. In Fig. 4(*b*), $Z/D_h=-0.40$ to $Z/D_h=-0.04$ and $Z/D_h=0.08$ to $Z/D_h=0.40$ correspond to spanwise locations on the flat portions of the surface between ribs, and $Z/D_h=-0.04$ to $Z/D_h=0.08$ correspond to locations on the central rib.

Figures 4(*a*) and 4(*b*) both show that the highest Nusselt number ratio values are again present on the rib tops, especially near

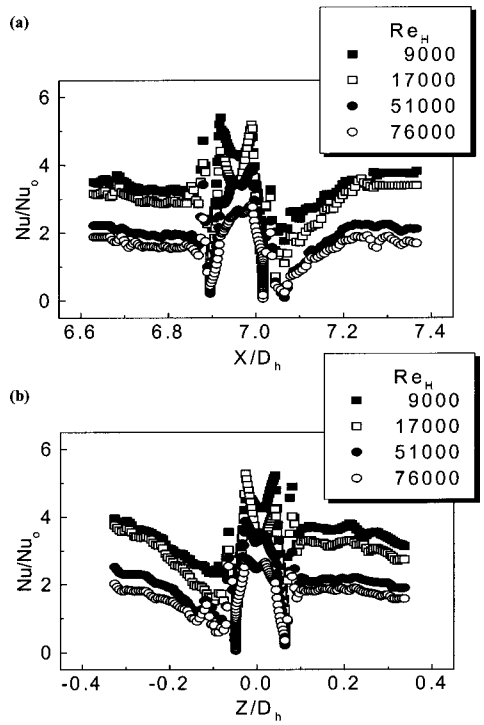

Fig. 4 Variable surface heat flux, local Nusselt number ratios Nu/Nu_o along the rib turbulator test surface for different Reynolds numbers Re_H and T_{oi}/T_w of 0.93–0.95. (*a*) At constant $Z/D_h=0.0$ as X/D_h varies. (*b*) At constant $X/D_h=7.0$ as Z/D_h varies.

the edges, at all Reynolds numbers. Nu/Nu_o ratios also decrease on the rib tops, and on the flat regions away from the ribs, especially at locations just downstream of the ribs, as Re_H increases. These two figures also show that Nu/Nu_o values generally increase continually downstream of the rib either as X/D_h increases or as Z/D_h decreases, for all Re_H investigated. This increase is partially due to shear layer re-attachment. Irrespective of the value of Reynolds number employed, the results in Figs. 4(*a*-*b*) also show that Nu/Nu_o values are generally higher than 1.0 on most of the test surface, including the flat regions between the ribs.

Spatially Averaged Nusselt Numbers. Spatially averaged Nusselt number ratios $\overline{Nu}/Nu_o$, determined from local data (such as that shown in Fig. 2(*b*),) are determined for the diagonal directions shown in Fig. 5(*a*). These diagonal directions are oriented parallel to and perpendicular to the direction of the ribs located along the bottom test surface. As shown in Fig. 5(*a*), W/D_h is then the diagonal directed normal to the ribs, and L/D_h is the diagonal directed parallel to the ribs. The origin of the L/D_h and W/D_h axes is positioned at $X/D_h=6.53$. $(W/D_h)_{max}$ then equals the spacing between adjacent ribs, or the rib pitch in the direction normal to the ribs. The resulting data are shown in Figs. 5(*b*-*c*), 6(*a*-*b*), and 7(*a*-*b*). Figures 5(*b*-*c*) are obtained with the surface conduction analysis applied, and are thus representative of a variable surface heat flux thermal boundary condition next to the air stream.

Figures 5(*b*) and 5(*c*) show data for Re_H from 9000 to 76,000 at constant T_{oi}/T_w of 0.93–0.95. The $\overline{Nu}/Nu_o$ data in the second of these figures are averaged in the W/D_h direction, and shown as they vary with $L/D_h/(L/D_h)_{max}$. The data are approximately constant with L/D_h at each Reynolds number, Re_H. This is important because it means that the flow at each Reynolds number consid-

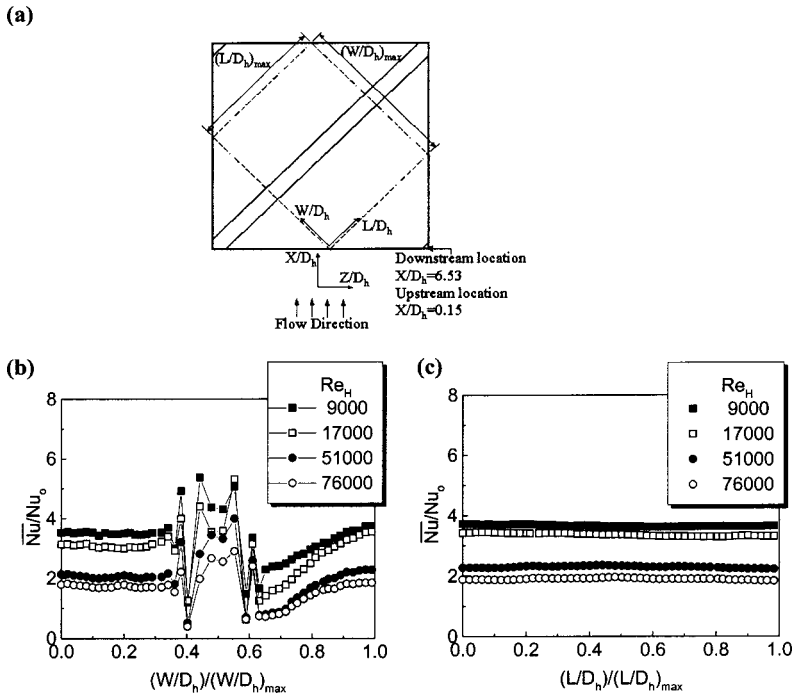

Fig. 5 (*a*) Schematic diagram of a portion of the bottom rib turbulator test surface showing the coordinates which are oriented perpendicular to and parallel to the rib turbulators. (*b*) (*c*) Nusselt number ratios $\overline{Nu}/Nu_o$, obtained with variable surface heat flux, for fully-developed conditions measured at the downstream end of the test section for different Reynolds numbers and $T_{oi}/T_w=0.93-0.95$. (*b*) Data averaged in the L/D_h direction, as dependent upon the $W/D_h/(W/D_h)_{max}$ coordinate. (*c*) Data averaged in the W/D_h direction, as dependent upon the $L/D_h/(L/D_h)_{max}$ coordinate.

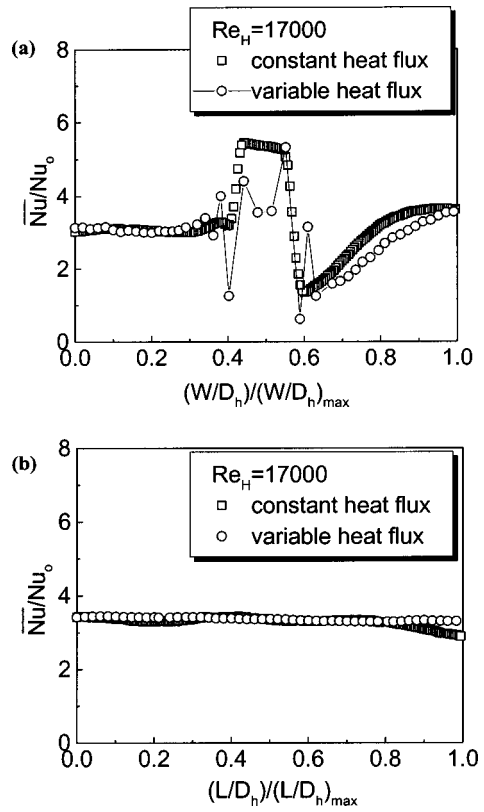

Fig. 6 Nusselt number ratios $\overline{Nu}/Nu_o$ for fully-developed conditions measured at the downstream end of the test section for a Reynolds number number Re_H=17,000 and T_{oi}/T_w of 0.94. Data are shown with and without conduction analysis applied (variable and constant surface heat flux, respectively). (*a*) Data averaged in the L/D_h direction, as dependent upon the $W/D_h/(W/D_h)_{max}$ coordinate. (*b*) Data averaged in the W/D_h direction, as dependent upon the $L/D_h(L/D_h)_{max}$ coordinate.

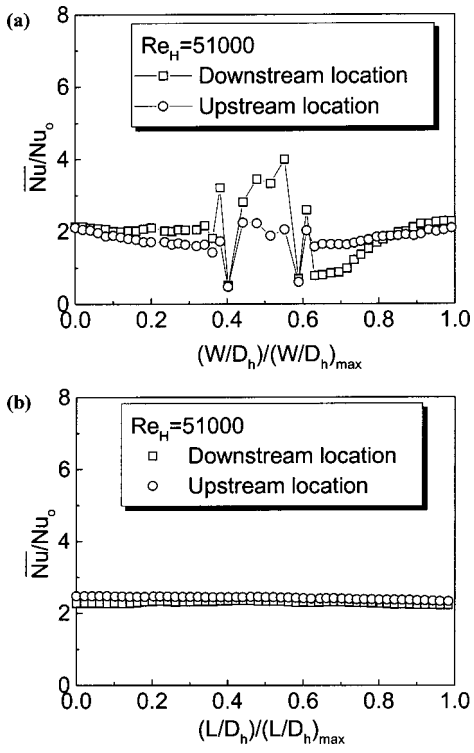

Fig. 7 Nusselt number ratios $\overline{Nu}/Nu_o$, obtained with variable surface heat flux, for a Reynolds number number Re_H=51,000 and T_{oi}/T_w of 0.94. Data are shown which are measured at the downstream end of the test section with thermally fully-developed flow, and measured at the upstream end of the test section with thermally developing flow. (*a*) Data averaged in the L/D_h direction, as dependent upon the $W/D_h/(W/D_h)_{max}$ coordinate. (*b*) Data averaged in the W/D_h direction, as dependent upon the $L/D_h/(L/D_h)_{max}$ coordinate.

ered is thermally fully developed. Note also that some of the side wall effects apparent in Figs. 2(*a*-*b*) are not apparent in Fig. 5(*c*).

The $\overline{Nu}/Nu_o$ distributions at each Re_H in Fig. 5(*b*) (averaged in the L/D_h direction and shown as they vary with $W/D_h/(W/D_h)_{max}$), then show important variations with $W/D_h/(W/D_h)_{max}$ because this coordinate is oriented perpendicular to the direction of the ribs. In some cases, these include $\overline{Nu}/Nu_o$ increases with Re_H at the top of the central rib. At larger $W/D_h/(W/D_h)_{max}>0.58$, which correspond to locations downstream of the central rib, $\overline{Nu}/Nu_o$ values then decrease substantially as Re_H increases. This is mostly due to changes to the strength and size of the flow re-circulation region downstream of the rib, which occurs as the Reynolds number Re_H becomes larger, as mentioned.

The results in Figs. 6(*a*) and 6(*b*) are presented to further illustrate the influences of three-dimensional test surface conduction on spatially-averaged $\overline{Nu}/Nu_o$ values. These Nusselt number ratios are given for fully developed conditions because they are measured at the downstream end of the test section. Here, data are present for the same layout as the data in the previous two figures. The data are given for a Reynolds number number Re_H of 17,000 and T_{oi}/T_w of 0.94. The data are shown with and without the test surface conduction analysis applied (i.e., for variable and constant surface heat flux, respectively). Apparent in Fig. 6(*a*) are a number of important variations due to surface conduction, which are present along most of the extent of the rib. For example, variable flux $\overline{Nu}/Nu_o$ values are significantly lower than constant flux values along the central part of the rib top. At $W/D_h/(W/D_h)_{max}>0.58$, which corresponds to locations downstream of the central rib, variable flux $\overline{Nu}/Nu_o$ values are again generally lower than constant flux values. Variable-flux Nusselt number ratios are also significantly lower than constant flux ratios at corners (where the ribs join the flat surrounding surface), which is important because it means that these are potential hot spots, especially when located just downstream of a rib near the largest flow re-circulation zone. The $\overline{Nu}/Nu_o$ values presented in Fig. 6(*b*), obtained with and without three-dimensional conduction taken into account, are about the same at different $L/D_h/(L/D_h)_{max}$ values.

The $\overline{Nu}/Nu_o$ data presented in Figs. 7(*a*) and 7(*b*) are obtained for Re_H of about 51,000, and the same surface layout given in Fig. 5(*a*), except that some of these data are obtained at a location farther upstream where the thermal boundary layers are still developing. In this case, the origin of the L/D_h and W/D_h coordinates is located at $X/D_h=0.15$. Note that the surface conduction analysis is applied to obtain the results in the Figs. 7(*a*) and 7(*b*). In Fig. 7(*b*), the $\overline{Nu}/Nu_o$ data measured upstream show almost no variation with $L/D_h/(L/D_h)_{max}$, which means that the thermal boundary layers at this measurement location are fully developed, or are nearly fully developed.

The upstream-measured $\overline{Nu}/Nu_o$ data in Fig. 7(*a*) are shown as they depend upon $W/D_h/(W/D_h)_{max}$, and show more evidence of incomplete thermal development. For regions upstream of the rib ($W/D_h/(W/D_h)_{max}<0.40$), on the rib ($0.40<W/D_h/(W/D_h)_{max}<0.58$), and downstream of the rib ($W/D_h/(W/D_h)_{max}>0.58$), the $\overline{Nu}/Nu_o$ values measured at the upstream channel locations are generally different than values measured at the downstream chan-

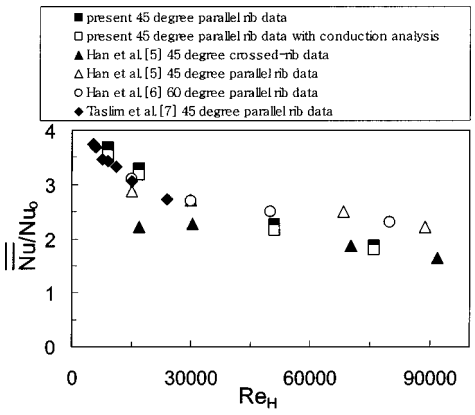

Fig. 8 Parallel-rib-turbulator channel globally averaged Nusselt number ratios for fully developed flow, averaged over the surface area corresponding to one period of rib turbulator geometry, as dependent upon Reynolds number for $T_{oi}/T_w = 0.93-0.95$. Comparisons with results from other investigations [5,6,7] are included.

nel locations, when compared at the same $W/D_h/(W/D_h)_{\max}$. This is partially because of thinner, less-than-fully developed thermal boundary layers at the upstream location.

Globally Averaged Nusselt Numbers and Friction Factors Figures 8, 9, and 10 present globally-averaged Nusselt number ratios for fully-developed flow conditions, which are determined by averaging all the local data in the rectangular area enclosed by the lengths $(L/D_h)_{\max}$ and $(W/D_h)_{\max}$ shown in Fig. 5(*a*). Globally-averaged Nusselt number ratios are thus determined from results like the ones in Figs. 5(*b*) and 5(*c*). The data in Figs. 8–10 are given for Reynolds numbers Re_H from 9000 to 76,000 and T_{oi}/T_w of 0.93–0.95. Results from Han et al. [5,6], and Taslim et al. [7] are included for comparison. Note that the present data with the conduction analysis included (and a variable heat flux boundary condition) are slightly lower than data obtained with no conduction analysis and a constant heat flux boundary condition.

Recall that the present 45 deg square ribs are arranged so that they are parallel and aligned on opposite channel walls. They are installed in a channel with aspect ratio of 4, ratio of rib height to hydraulic diameter e/D_h of .078, rib pitch-to-height ratio p/e of 10, and ratio of rib blockage area to channel cross-sectional area $2e/H$ of 0.25 or 25 percent. The Han et al. [5] data used for comparison are obtained in a square channel with $e/D_h = .0625$, $p/e = 10$, and $2e/H = .125$. These investigators consider nine different configurations of ribs placed on two opposite walls, including 90 deg ribs, 45 deg and 60 deg parallel ribs, 45 deg and 60 deg crossed-ribs, 45 deg and 60 deg V-shaped ribs, and 45 deg and 60 deg Λ-shaped ribs. The data used for comparison from Han et al. [6] are for square channels with 90 deg continuous ribs, 60 deg continuous ribs, and 60 deg broken ribs. In all cases, the ribs are parallel on opposite channel walls, e/D_h is .063, p/e is 10, and $2e/H$ is .126. The Taslim et al. [7] data used for comparison are also obtained in a square channel with $p/e = 10$. For these data, $e/D_h = .083$, and $2e/H$ is .166. In addition, the 45 deg oriented ribs are arranged in the same direction on opposite channel walls, and placed at streamwise locations so that they are staggered with respect to each other.

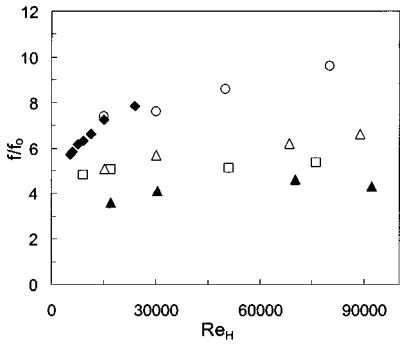

Fig. 9 Rib turbulator channel friction factor ratios f/f_o for fully developed flow conditions as dependent upon Reynolds number for $T_{oi}/T_w = 0.93-0.95$. Symbols are defined in Fig. 8. Comparisons with results from other investigations [5,6,7] are included.

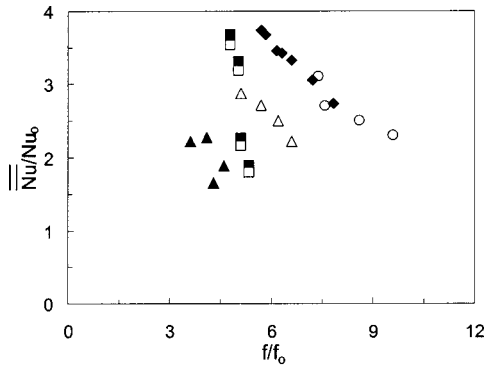

Fig. 10 Rib turbulator channel globally-averaged Nusselt numbers for fully developed flow and $T_{oi}/T_w = 0.93-0.95$ as dependent upon friction factor ratios, including comparisons with results from other investigations [5,6,7]. Symbols are defined in Fig. 8.

Figure 8 shows that globally-averaged Nusselt number ratios generally decrease as Re_H increases for all of the configurations. For the present rib-turbulator arrangement, globally averaged ratios (with test surface conduction analysis employed) vary from 3.53 to 1.79 as Re_H increases from 9000 to 76,000. The present parallel-rib data are then slightly higher than the 45 deg and 60 deg parallel rib data from Han et al. [5,6] and the 45 deg parallel rib data from Taslim et al. [7] for $\mathrm{Re}_H < 30{,}000$, and either slightly lower or in rough agreement with these data at higher Reynolds numbers. Differences between the present data and the Han et al. [5] parallel-rib data are due to different channel aspect ratios (1 and 4), different rib blockage percentages (12.5 percent and 25.0 percent), and because the Han et al. [5] results are based on measurements made at discrete locations, which can give differences when compared to data based on spatially resolved measurements, such as the ones from the present study.

Measured friction factor ratios in the rib-turbulator channel for Re_H of 9000 to 76,000 at T_{oi}/T_w of 0.93–0.95 are shown as they depend upon Re_H in Fig. 9. These f/f_o data are also compared with results from Han et al. [5,6], and Taslim et al. [7]. The present data cover approximately the same range of values as the 45 deg parallel-rib data from Han et al. [5]. The present f/f_o data are then lower than the continuous, 60 deg parallel rib data from Han et al. [6] and the 45 deg parallel rib data from Taslim et al. [7] for all Reynolds numbers considered.

Globally-averaged Nusselt number ratios and friction factor ratios from Figs. 8 and 9 are plotted together in Fig. 10. The present Nusselt number ratios cover the same range of values as the data from Taslim et al. [7] and Han et al. [6], however, friction factor ratios are lower. The present results then appear to bracket the 45 deg parallel-rib data from Han et al. [5] in Fig. 10.

Thermal Performance Parameters. These comparisons are further illustrated by the thermal performance parameters which are presented as they depend upon Re_H in Fig. 11. This performance parameter is employed because it gives the ratio of heat

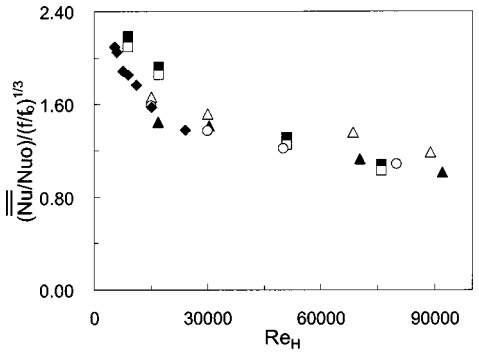

Fig. 11 Rib turbulator channel globally averaged performance parameters for fully developed flow and $T_{oi}/T_w = 0.93-0.95$ as dependent upon Reynolds number, including comparisons with results from other investigations [5,6,7]. Symbols defined in Fig. 8.

transfer augmentation to friction augmentation, where each is given for the same ratio of mass flux in an internal passage with augmentation devices to mass flux in the internal channel with smooth surfaces [19]. Performance parameter magnitudes for the present study are determined from the data in Figs. 8–10 (with test surface conduction included), and decrease from 2.09 to 1.03 as Re_H increases from 9000 to 76,000in Fig. 11. These values are slightly higher than data from Taslim et al. [7] and Han et al. [6] at lower Reynolds numbers, and in approximate agreement with the data from Han et al. [6] at higher Reynolds numbers Re_H greater than 30,000.

Summary and Conclusions

Spatially resolved Nusselt numbers, spatially-averaged Nusselt numbers, and friction factors are presented for a stationary channel with an aspect ratio of 4 and angled rib turbulators inclined at 45 deg with parallel and aligned orientations on two opposite surfaces. Results are given at different Reynolds numbers based on channel height from 9000 to 76,000, and ratios of air inlet stagnation temperature to surface temperature ranging from 0.93 to 0.95. The ratio of rib height to hydraulic diameter is 0.078, the rib pitch-to-height ratio is 10, and the blockage provided by the ribs is 25 percent of the channel cross-sectional area.

Nusselt numbers are given with three-dimensional conduction considered along and within the acrylic test surface employed in the study. When data are adjusted to account for three-dimensional conduction (and variable surface heat flux) along and within the test surface, Nusselt number ratios show different quantitative variations (with location along the test surface), compared to variations when no test surface conduction is included and the heat flux is assumed to be constant. Changes include (i) local and spatially-averaged Nusselt number ratios, obtained with variable surface heat flux, which are significantly lower than constant flux values along the central part of the rib tops, and (ii) variable flux Nusselt number ratio decreases (relative to constant flux values) on the flat regions between the ribs, near corners where the ribs join the flat surrounding surface. This last characteristic is important because it means such corners are potential hot spots, especially when located just downstream of a rib near the largest flow re-circulation zone.

Spatially resolved, local Nusselt numbers, determined using test surface conduction analyses and normalized by values measured in a smooth channel, are highest on tops of the rib turbulators, with lower magnitudes on flat surfaces between the ribs, where regions of flow separation and shear layer re-attachment have pronounced influences on local surface heat transfer behavior. The augmented local and spatially-averaged Nusselt number ratios (rib turbulator Nusselt numbers normalized by values measured in a smooth channel) decrease on the rib tops, and on the flat regions away from the ribs, especially at locations just downstream of the ribs, as Reynolds number increases. Such changes are partially due to alterations to the size and strength of the flow re-circulation region located downstream of the ribs, and the shear layer associated with it, as the Reynolds number increases. Other phenomena that affect the heat transfer augmentations are the strong secondary flows, and the skewing and three-dimensional nature of the boundary layer which develops due to the angled orientations of the ribs. Because of such effects, local and spatially-averaged Nusselt number ratios are generally much higher than 1.0 over most of the ribbed test surface, including the flat regions between the ribs, irrespective of the value of Reynolds number employed.

Globally averaged Nusselt number ratios (obtained with the conduction analysis applied to the test surface) vary from 3.53 to 1.79 as Reynolds number increases from 9000 to 76,000. The present parallel-rib data are then slightly higher than the 45 deg and 60 deg parallel rib data from Han et al. [5,6] and the 45 deg parallel rib data from Taslim et al. [7] for $\mathrm{Re}_H < 30{,}000$, and either slightly lower or in rough agreement with these data at higher Reynolds numbers. Thermal performance parameters also decrease somewhat as Reynolds number increases over the same range of values. These values are slightly higher than data from Taslim et al. [7] and Han et al. [6] at lower Reynolds numbers, and in approximate agreement with the data from Han et al. [6] at higher Reynolds numbers Re_H greater than 30,000.

Acknowledgment

The work presented in this paper was sponsored by a AGTSR Advanced Gas Turbine Research Program research subcontract sponsored by the U.S. Department of Energy-National Energy Technology Laboratory through a cooperative agreement with the South Carolina Institute for Energy Studies at Clemson University.

Nomenclature

a = streamwise extent of test surface
b = spanwise extent of test surface
b/H = channel aspect ratio
D_h = channel hydraulic diameter
e = rib turbulator width and height
e' = rib turbulator width in streamwise direction
f = friction factor
f_o = baseline friction factor in a smooth channel with no rib turbulators
H = channel height
h = heat transfer coefficient based on flat projected area, $\dot{q}''/(T_w - T_m)$
k = thermal conductivity
L = coordinate in direction parallel to ribs
Nu = local Nusselt number, hD_h/k
Nu_o = baseline Nusselt number in a smooth channel with no rib turbulators
p = streamwise pitch spacing of rib turbulators
Pr = Prandtl number
$\dot{q}''$ = surface heat flux
Re_H = Reynolds number based on channel height
Re_{Dh} = Reynolds number based on hydraulic diameter
T = local static temperature
$\overline{U}$ = streamwise bulk velocity averaged over the channel cross section
W = coordinate in direction normal to ribs
X = streamwise coordinate measured from the test section inlet
Y = normal coordinate measured from the test surface between the ribs
Z = spanwise coordinate measured from the test surface centerline

Subscripts

a = ambient value
i = test section inlet value
m = time-averaged, local mixed mean value
o = total or stagnation value
w = local wall value
max = maximum value

Superscripts

$-$ = spanwise or streamwise-averaged value
$(=)$ = globally averaged value

References

[1] Lau, S. C., 2001, ''Enhanced Internal Cooling of Gas Turbine Airfoils,'' *Heat Transfer in Gas Turbines*, S. Sunden, and M. Faghri, eds., WIT Press, Southampton, U.K., pp. 109–175.

[2] Ligrani, P. M., Oliveira, M. M., and Blaskovich, T., 2003, ''Comparison of Heat Transfer Augmentation Techniques,'' AIAA J., **41**(3), pp. 337–362.

[3] Han, J. C., Glicksman, L. R., and Rohsenow, W. M., 1978, ''An Investigation of Heat Transfer and Friction For Rib-Roughened Surfaces,'' Int. J. Heat Mass Transfer, **21**(7), pp. 1143–1156.

[4] Han, J. C., and Park, J. S., 1988, ''Developing Heat Transfer in Rectangular Channels With Rib Turbulators,'' Int. J. Heat Mass Transfer, **31**(1), pp. 183–195.

[5] Han, J. C., Zhang, Y. M., and Lee, C. P., 1991, ''Augmented Heat Transfer in Square Channels With Parallel, Crossed, and V-Shaped Angled Ribs,'' ASME J. Heat Transfer, **113**, pp. 590–596.

[6] Han, J. C., Huang, J. J., and Lee, C. P., 1993, ''Augmented Heat Transfer in Square Channels With Wedge-Shaped and Delta-Shaped Turbulence Promoters,'' J. Enhanced Heat Transfer, **1**(1), pp. 37–52.

[7] Taslim, M. E., Li, T., and Kercher, D. M., 1996, ''Experimental Heat Transfer and Friction in Channels Roughened With Angled, V-Shaped, and Discrete Ribs on Two Opposite Walls,'' ASME J. Turbomach., **118**, pp. 20–28.

[8] Taslim, M. E., Li, T., and Spring, S. D., 1998, ''Measurements of Heat Transfer Coefficients and Friction Factors in Passages Rib-Roughened On All Walls,'' ASME J. Turbomach., **120**, pp. 564–570.

[9] Wang, Z., Ireland, P. T., Kohler, S. T., and Chew, J. W., 1998, ''Heat Transfer Measurements to a Gas Turbine Cooling Passage With Inclined Ribs,'' ASME J. Turbomach., **120**, pp. 63–69.

[10] Thurman, D., and Poinsatte, P., 2000, ''Experimental Heat Transfer and Bulk Air Temperature Measurements for a Multipass Internal Cooling Model With Ribs and Bleed,'' ASME Paper No. 2000-GT-233.

[11] Cho, H. H., Lee S. Y., and Wu S. J., 2001, ''The Combined Effects of Rib Arrangements and Discrete Ribs on Local Heat/Mass Transfer in a Square Duct,'' ASME Paper No. 2001-GT-175.

[12] Mahmood, G. I., and Ligrani, P. M., 2002, ''Heat Transfer in a Dimpled Channel: Combined Influences of Aspect Ratio, Temperature Ratio, Reynolds Number, and Flow Structure,'' Int. J. Heat Mass Transfer, **45**(10), pp. 2011–2020.

[13] Ligrani, P. M., and Mahmood, G. I., 2003, ''Variable Property Nusselt Numbers in a Channel With Pin-Fins,'' AIAA Journal of Thermophysics and Heat Transfer, **17**(1), pp. 103–111.

[14] Burgess, N. K., Oliveira, M. M., and Ligrani, P. M., 2003, ''Nusselt Number Behavior on Deep Dimpled Surfaces Within a Channel,'' ASME J. Heat Transfer, **125**(1), pp. 11–18.

[15] Sargent, S. R., Hedlund, C. R., and Ligrani, P. M., 1998, ''An Infrared Thermography Imaging System For Convective Heat Transfer Measurements in Complex Flows,'' Meas. Sci. Technol., **9**(12), pp. 1974–1981.

[16] Kline, S. J., and McClintock, F. A., 1953, ''Describing Uncertainties in Single Sample Experiments,'' Mech. Eng. (Am. Soc. Mech. Eng.), **75**, pp. 3–8.

[17] Moffat, R. J., 1988, ''Describing the Uncertainties in Experimental Results,'' Exp. Therm. Fluid Sci., **1**(1), pp. 3–17.

[18] Lienhard, J. H., 1987, *A Heat Transfer Textbook*, Second Edition, Prentice-Hall Inc., Englewood Cliffs, NJ.

[19] Gee, D. L., and Webb, R. L., 1980, ''Forced Convection Heat Transfer in Helically Rib-Roughened Tubes,'' Int. J. Heat Mass Transfer, **23**, pp. 1127–1136.

Convective Heat Transfer Near One-Dimensional and Two-Dimensional Wall Temperature Steps

Debjit Mukerji
e-mail: debjit@stanfordalumni.org
Department of Mechanical Engineering,
Thermosciences Division,
Stanford University,
Stanford, CA 94305-3030

John K. Eaton
e-mail: eaton@vk.stanford.edu
Department of Mechanical Engineering,
Thermosciences Division,
Stanford University,
Stanford, CA 94305-3030

Robert J. Moffat
e-mail: rmoffat@stanford.edu
Department of Mechanical Engineering,
Thermosciences Division,
Stanford University,
Stanford, CA 94305-3030

Steady-state experiments with one-dimensional and two-dimensional calorimeters were used to study the convective heat transfer near sharp steps in wall temperature in a turbulent boundary layer. Data acquired under low and high freestream turbulence conditions indicated that spanwise turbulent diffusion is not a significant heat transport mechanism for a two-dimensional temperature step. The one-dimensional calorimeter heat transfer data were predicted within ±5 percent using the STAN7 boundary layer code for situations with an abrupt wall temperature step. The conventional correlation with an unheated starting length correction, in contrast, greatly under-predicts the heat transfer for the same experimental cases. A new correlation was developed that is in good agreement with near and far-field semi-analytical solutions and predicts the calorimeter heat transfer data to within ±2 percent for temperature step boundary condition cases.
[DOI: 10.1115/1.1650387]

Keywords: Boundary Layer, Convection, Experimental, Forced Convection, Heat Transfer, Turbulent

Introduction

The fact that a one-dimensional step in wall temperature significantly impacts the convective heat transfer coefficient (h) downstream of the step has been known for many years. Temperature step solutions have long been used as basis functions in superposition techniques, since the energy equation is linear under the constant fluid properties assumption and such solutions permit relatively simple reconstruction of arbitrarily complex thermal boundary conditions.

Reynolds et al. [1] reported an approximate solution for the heat transfer downstream of a wall temperature step in a smooth wall flat plate turbulent boundary layer, given by the expression

$$St(x) = 0.0287\,\mathrm{Re}_x^{-0.2}\,\mathrm{Pr}^{-0.4}\left[1-\left(\frac{\xi}{x}\right)^{9/10}\right]^{-1/9} \quad (1)$$

where ξ represents the unheated starting length and x is the distance from the virtual origin of the boundary layer. The same authors validated this solution in an associated series of smooth-wall, flat plate experiments. Reynolds et al. [2] also conducted experiments with non-uniform thermal boundary conditions, and used Eq. (1) as a superposition basis function to predict such cases with good success.

Taylor et al. [3,4] studied the convective heat transfer downstream of a wall temperature step for a broad range of Reynolds numbers (Re_ξ), for both smooth and rough wall situations. They found that the rough and smooth wall unheated starting length correction data scatter about a single curve.

The correlation in Eq. (1) is based upon a 1/7th power law for the boundary layer velocity and temperature profiles, and is applicable to regions relatively far downstream of the step where the profiles have been allowed to develop. However, the heat transfer behavior very near the step location—within about one boundary layer thickness—has not been quantified to the same accuracy as the far-field behavior. The few researchers who have studied the near-step region, including Saetran [5] and Browne and Antonia [6], have reported the significant inaccuracy of Eq. (1) in the immediately vicinity of the temperature step. Saetran [5] measured mean temperature profiles in the boundary layer and inferred the heat transfer just downstream of the temperature step by fitting his data to the thermal law of the wall. He also compared the results to the analytical solution presented by Kestin and Persen [7] with good agreement. He found that Eq. (1) under-predicted his experimental data by roughly 25 percent at one boundary layer thickness downstream of the step ($x/\delta_0 = 1.0$), and by more than 30 percent for $x/\delta_0 = 0.25$. Browne and Antonia [6] studied the boundary layer relaxation after a sharp change in the wall temperature distribution. Mean temperature and heat flux distributions within the developing thermal boundary layer downstream of the step were calculated using estimates of the effective turbulent Prandtl number, Pr_t. The predictions were compared against several sets of experimental data from three independent sources, with good agreement. The same benchmark data reveal a consistent under-prediction of the heat transfer near the step using Eq. (1), with the reported error as high as ≈20 percent at $x/\delta_0 \approx 1.0$. Antonia and co-workers (Antonia et al. [8]; Subramanian and Antonia [9]; Teitel and Antonia [10]) have also experimentally examined the detailed evolution of the temperature, velocity, turbulence, and turbulent heat flux profiles downstream of step changes in the wall heat flux, for both boundary layer and channel flows.

Many heat transfer studies to date have focused on nominally two-dimensional turbulent boundary layers with a one-dimensional wall temperature distribution. Much less attention has been directed toward three-dimensional boundary layers or even three-dimensional convective heat transfer in two-dimensional boundary layers. The latter case requires a two-dimensional thermal boundary condition that possibly generates lateral turbulent diffusion contributions to the heat transfer, in spite of the two-dimensionality of the mean flow. This is based on the conjecture that the spanwise turbulent diffusion term could be modeled in an analogous fashion as the wall-normal contribution, using an eddy diffusivity for heat transfer in the spanwise direction ($\varepsilon_{H,S}$),

Contributed by the Heat Transfer Division for publication in the JOURNAL OF HEAT TRANSFER. Manuscript received by the Heat Transfer Division February 20, 2003; revision received November 20, 2003. Associate Editor: S. Acharya.

$$\overline{w'T'} = \varepsilon_{H,S}\frac{\partial \overline{T}}{\partial z} \tag{2}$$

Although the body of supporting data is limited, there is experimental evidence that spanwise turbulent flux terms can be large. For example, Elkins and Eaton [11] found that the spanwise (radial) turbulent heat flux in a three-dimensional boundary layer on a rotating disk was of the same order as the wall-normal flux. This implied a large lateral eddy diffusivity for heat transfer, $\varepsilon_{H,S}$, because the mean temperature gradient was small in the lateral direction. By extension to the case of a small heated two-dimensional element with a relatively large lateral temperature gradient, these observations suggested that spanwise turbulent diffusion could be a significant effect.

The objective of the current study was to produce a set of reference-quality heat transfer data for an abrupt, spanwise uniform step in wall temperature that was approximately one boundary layer thickness in streamwise extent. In contrast to previous studies, which have focused only on heat transfer behavior downstream of a one-dimensional step in wall temperature, in the present work heat transfer over a short two-dimensional square pulse in wall temperature is also examined. In principle, the effects of sharp temperature steps in a two-dimensional geometry should be captured by modern CFD codes. However, the issue of modeling the spanwise turbulent diffusion has not been addressed in most codes, other than to assume an isotropic diffusivity. The present experiments were expected to indicate the deficiencies of such assumptions by quantifying the relative magnitude of the spanwise contributions. The experimental results were also to be used in conjunction with computations to develop a new correlation describing the complete variation of the convective heat transfer coefficient downstream of a sharp step in wall temperature. The development of a semi-empirical correlation may seem outmoded, particularly since many current CFD codes are capable of handling sharp one-dimensional wall temperature steps. However, a closed-form representation for the heat transfer (particularly very near the temperature step) can be useful in the evaluation of devices such as small heat transfer and skin-friction gages.

Steady-state experiments with one-dimensional (rectangular) and two-dimensional (square) calorimeters were conducted. The calorimeters were used to obtain the spatially-averaged heat transfer using global energy measurements, in contrast to the higher-uncertainty approach of measuring local mean temperature profiles in very thin developing thermal boundary layers. The purpose of having two different calorimeters was to investigate the physical relevance of spanwise heat diffusion. The streamwise boundary conditions for the rectangular and square calorimeters were nominally matched, but the rectangular calorimeter was seven times longer in the lateral direction. Under baseline conditions, with no temperature step, the two calorimeters were expected to agree within the measurement uncertainty band. If spanwise diffusion were an important effect, it was expected to be associated with temperature step boundary conditions, in the presence of a mean spanwise temperature gradient in accordance with Eq. (2), and generate a higher rate of heat transfer for the square calorimeter than the rectangular calorimeter.

Experimental Apparatus and Procedure

Wind Tunnel Facility. Steady-state heat transfer experiments were conducted in a closed-loop wind tunnel at ambient temperature and pressure. The test section was 0.24 m high by 0.50 m wide by 2.44 m long. An air-to-water heat exchanger maintained the freestream temperature to within 0.1°C of the desired value. The freestream velocity was measured with a Kiel total pressure probe at the test section centerline and was maintained to within 1 percent of the target value. The test section top wall was adjusted to maintain a zero streamwise static pressure gradient. The tunnel was equipped with a 2 mm high, rough boundary layer trip at the start of the test section. The tunnel could be operated with low and high levels of freestream turbulence. The low turbulence intensity was approximately 0.4 percent. For high freestream turbulence experiments, the tunnel was fitted with a custom turbulence generator consisting of a 69 percent open square bar grid followed by a jet grid. The turbulence generator raised the level to $Tu = 7-10$ percent over the majority of the test section.

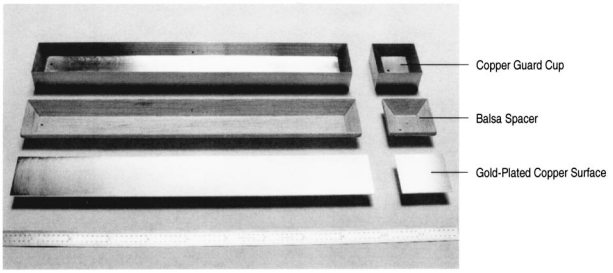

Fig. 1 Rectangular and square calorimeter components prior to assembly

Hot-wire velocity profile data indicated that under low turbulence conditions, the skin friction coefficient was spanwise-uniform to within ± 7 percent, and the momentum thickness was spanwise-uniform to within ± 10 percent. The mean velocity profiles were in excellent agreement with the law of the wall.

The working surface of the test section was comprised of four equal-sized removable sections. Twelve stainless steel foil strips covered the first two sections. The power distribution to these foil heaters was set to approximate a uniform wall temperature boundary condition. The third section of the heat transfer surface was an electrically-heated, 25 mm thick aluminum plate with a recess in its center to accommodate an insert section bearing one of two calorimeters. The calorimeters registered the convective heat transfer on a locally heated, thermally isolated region. The fourth section was an unheated dummy plate.

The mean temperature of the aluminum surface surrounding the calorimeter was matched to that of the upstream foils within 0.1°C by adjusting the power inputs to the plate heaters. The calorimeter temperature was controlled independently, as described in the following section. The upstream edge of the calorimeter was roughly 1.5 m downstream of the start of the heat transfer surface. The origins of the hydrodynamic and thermal boundary layers were assumed to be located at this leading edge.

Calorimeter Design. Two calorimeters were constructed: a square 35 mm calorimeter and a rectangular calorimeter with a 7:1 (245 mm×35 mm) aspect ratio. Each calorimeter had an independent heating system, enabling its temperature to be set to a different value from that of the surrounding wall. This generated a localized square pulse (one-dimensional for the rectangular and two-dimensional for the square calorimeter) in the wall temperature. In designing the calorimeters, the primary performance objective was to minimize heat loss due to conduction and radiation, thereby generating a ''true'' temperature step and limiting the uncertainty in the measured heat transfer coefficient.

Each calorimeter consisted of three components. The first was an oxygen-free high conductivity (OFHC) copper section with a flat top surface and beveled sides, with a shape resembling that of an inverted truncated pyramid. The top surface of this main component was directly exposed to the flow. It was plated with a thin, uniform gold coating to reduce radiation losses. The second component, a balsa wood insulating spacer, minimized conduction losses from the surface component. The final component was an OFHC copper guard cup into which the surface piece and balsa spacer snugly fit. The top surface, balsa spacer, and guard cup were epoxied together to form a single integrated unit. These three components are identified for the rectangular and square calorimeters in a pre-assembly photograph in Fig. 1. The copper sections

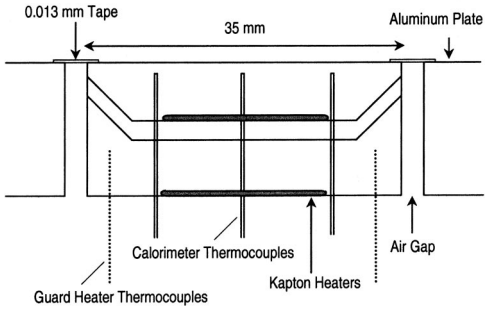

Fig. 2 Calorimeter layout and instrumentation

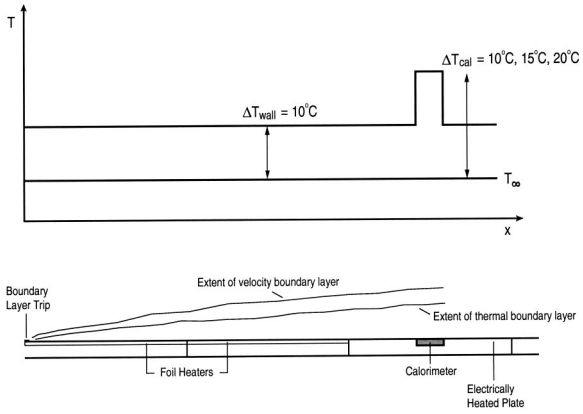

Fig. 3 Calorimeter experiment thermal boundary conditions

were heated with 0.30 mm-thick Kapton heaters (Minco Products, Inc.) that were affixed with pressure-sensitive adhesive. By maintaining the guard cup at a temperature within 0.2°C of the calorimeter surface, back conduction losses were reduced significantly. The OFHC copper rendered the calorimeter surface component and guard cup nearly isothermal.

Five AWG #36 Type K thermocouples were embedded in the rectangular calorimeter main copper component, and three in the square calorimeter. The guard cups of both calorimeters were each instrumented with two thermocouples. Thermocouple holes in the main element were drilled to within 1.0 mm of the top (flow-exposed) surface. Each hole was filled with thermally conductive epoxy to ensure good thermal contact and control over lead-wire conduction losses.

Each calorimeter was mounted in the center of its respective insert piece that fit into a stepped square opening in the surrounding surface. The insert pieces and surrounding plate, both constructed from aluminum, were independently heated with Kapton heaters. Each calorimeter was precisely leveled flush with the surrounding surface.

The calorimeter was isolated from its surroundings by a 2 mm-wide air gap. The use of an air gap insulator reduced the uncertainty of the correction for lateral heat loss significantly. The lateral dimension of the air gap was sufficiently small to prevent the formation of free convection cells. The gaps were bridged at the surface by 0.013 mm thick polyester film electrical tape that was thin relative to the dimension of the viscous sublayer and hence did not interfere with the flow. Even in the presence of large temperature gradients, heat conduction through the tape was negligible due to its very small thickness and low thermal conductivity. An illustration of the calorimeter layout and instrumentation is provided in Fig. 2.

The hydrodynamic boundary layer thickness δ in the wind tunnel at the calorimeter location was approximately 27 mm at a nominal freestream velocity of 10.5 m/s. The ratio of the streamwise calorimeter dimension (35 mm) to this boundary layer thickness is representative of the scaling of certain families of transient heat flux gages.

The overall uncertainty in the Stanton number calculation of each calorimeter was estimated at approximately ± 8 percent, taking into account the details of the data acquisition process and the uncertainties of material properties and dimensions.

Experimental Procedure and Data Comparison. For all of the experimental cases, all surfaces except for the calorimeter were maintained at 10°C above the freestream temperature. The calorimeter was maintained at 0, 5, and 10°C above the surrounding wall (10, 15, and 20°C above the freestream, respectively). The zero-temperature difference situations were used for baseline uniform wall temperature studies. The experiments were run with freestream velocities of $U_\infty = 12.0$, 15.0, and 18.0 m/s.

The calorimeter results were compared to heat transfer predictions using the unheated starting length correlation in Eq. (1). For temperature step boundary conditions, the correlation was used in the superposition of two wall temperature step solutions. The thermal boundary conditions (including temperature step locations) are shown with a cross-section of the physical layout in Fig. 3.

The calorimeter experimental data were also compared against predictions from a standard two-dimensional boundary layer code, STAN7. STAN7 is a finite-difference code that starts from an initial user-specified velocity profile at the origin and solves the boundary layer momentum and energy equations as it marches downstream. The mixing-length model incorporating the van Driest sublayer function was used. The step size used by STAN7 (Δx) is specified as a fixed fraction of the local hydrodynamic boundary layer thickness, δ. For all STAN7 runs, the step size was chosen to be $\Delta x = 0.2\delta$ from the leading edge to immediately upstream of the calorimeter. At that point, the step size was changed to 0.01δ for greater spatial resolution near the temperature step and over the calorimeter surface. The STAN7 cases were run under constant property mode, with the specified air properties corresponding to the experimental conditions.

Experimental Qualification. The surface temperature distribution of the calorimeter and immediate surroundings was imaged using thermochromic liquid crystal (TLC) paint, to determine the ''sharpness'' of the temperature steps at the streamwise calorimeter edges. The center of the rectangular calorimeter and part of the surrounding aluminum insert plate were coated with layers of black paint (Hallcrest BBG-1) and sprayable TLC paint (Hallcrest BM/R35C5W/C17-10) using an airbrush. The TLC activation temperature was 35°C with an active range of 10°C. The calorimeter was imaged with a Sony XC-003 RGB color video camera and a processing system consisting of a Matrox IM-1280 board installed in a personal computer. The light source was a Kodak slide projector. The test conditions included a freestream velocity of 15.0 m/s and a freestream temperature of 27°C. The surfaces upstream of and surrounding the calorimeter were maintained at 37°C, and the calorimeter temperature was set to 45°C. Figure 4 shows a spanwise-averaged profile of the surface temperature as indicated by the TLC measurements, with flow direction from left to right. The profile confirms that an approximate square-wave thermal boundary condition was being produced, with nearly ''true'' temperature steps at the upstream and downstream edges of the calorimeter.

The performance of the stainless steel foil heating surfaces upstream of the calorimeter was evaluated by acquiring heat transfer data under uniform wall temperature conditions. Each of the 12 upstream foils yielded a single averaged Stanton number (based on overall power input and average centerline temperature), and the centerline x location of each foil was used to scale the Reynolds number. The upstream edge of the first foil corresponds to $x = 0$. Experimental data were compared with the correlation in Eq. (1), with $\xi = 0$.

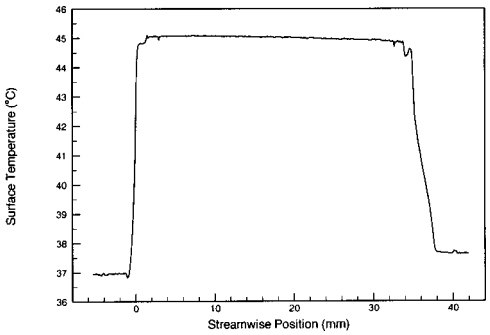

Fig. 4 TLC-indicated temperature step over calorimeter

Baseline Stanton number data for the rectangular calorimeter in the spanwise orientation (long axis normal to the flow direction) are plotted in Fig. 5. The corresponding data for the square calorimeter are provided in Fig. 6. The three calorimeter data points in each plot correspond to the three Reynolds number cases investigated. The qualification data presented are for a nominal freestream velocity of 15.0 m/s and low freestream turbulence conditions. The foil and calorimeter heat transfer data were fully corrected for losses due to conduction and radiation.

The experimental Stanton number data on the foils agree to within 4 percent of the correlation, except over the first two foils of the test section, where the deviation is between 7 percent and 16 percent. It was not possible to generate a uniform surface temperature boundary condition with the relatively large, uniform heat flux foils near the start of the test section. The power to the first two foils was set such that their average centerline temperature was within roughly 0.2°C of the target isothermal value.

The rectangular calorimeter data extrapolate smoothly from the foil experimental data curves, and lie almost exactly on the trend predicted by the correlation. These results indicate that the uniform surface temperature distribution was being reasonably approximated on the foils, with minor error near the leading edge. They also show that the calorimeter heat transfer measurements were consistent with the well-qualified foil heaters. Comparing Figs. 5 and 6 shows that the square calorimeter registered consistently higher Stanton number values than the rectangular calorimeter. The two calorimeter types agreed, however, to within 3 percent under low turbulence conditions for all three Reynolds number cases. This disparity is appreciably less than the estimated calorimeter measurement uncertainty of approximately 8 percent for the Stanton number.

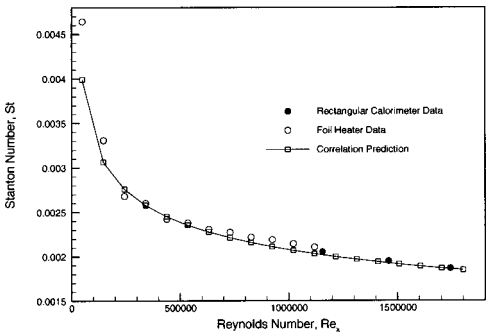

Fig. 5 Baseline heat transfer data under low turbulence conditions with rectangular calorimeter

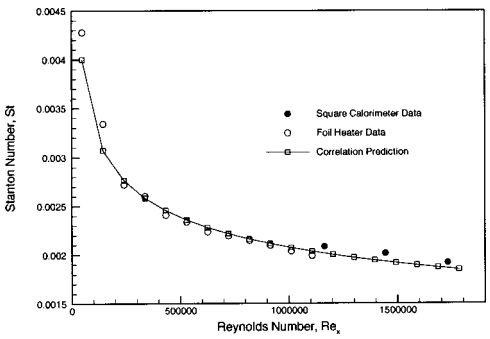

Fig. 6 Baseline heat transfer data under low turbulence conditions with square calorimeter

Table 1 Rectangular calorimeter experimental data (spanwise orientation) and comparison with STAN7

Re_ξ	ΔT_{cal} (°C)	St_{cal} $\times 10^{-3}$	St_{STAN7} $\times 10^{-3}$	St, Eq. (1) $\times 10^{-3}$	Error [%] STAN7/Eq. (1)
1.14×10^6	0	2.05	1.95	2.02	5.1/1.7
1.14×10^6	5	2.95	2.82	2.50	4.3/15.3
1.14×10^6	10	3.37	3.26	2.74	3.2/18.7
1.44×10^6	0	1.95	1.88	1.93	3.7/1.2
1.44×10^6	5	2.77	2.68	2.39	3.2/13.7
1.44×10^6	10	3.18	3.08	2.62	3.2/17.6
1.72×10^6	0	1.87	1.83	1.86	2.2/0.4
1.72×10^6	5	2.62	2.58	2.29	1.5/12.3
1.72×10^6	10	3.01	2.96	2.53	1.6/15.9

Results and Discussion

Heat Transfer From Isothermal Calorimeters

Rectangular (One-Dimensional) Calorimeter Results. The rectangular calorimeter was studied in spanwise (35 mm dimension aligned with flow direction) and streamwise (245 mm dimension aligned with flow direction) orientations. The spanwise orientation was a geometry that could be compared directly with the square calorimeter. In the streamwise orientation, the flow experienced a larger-length, two-dimensional temperature step, and the heat transfer coefficient was hence not influenced as significantly by near-step effects.

The heat transfer data under low turbulence conditions ($Tu \approx 0.4$ percent) for the rectangular calorimeter in the spanwise orientation are provided in Table 1. Spatially-averaged STAN7 and unheated starting length correlation predictions are shown for comparison. The magnitude of the calorimeter temperature step (the difference between calorimeter and average surrounding temperature) is represented by ΔT_{cal}. The data show that the baseline cases (temperature step=0°C) agree well with both the correlation and STAN7. The experimental results are higher than the correlation by 2 percent or less, and greater than STAN7 predictions by 5 percent or less.

The results for the temperature step cases reveal, however, that the correlation greatly under-predicts the calorimeter heat transfer coefficient. The larger the magnitude of the temperature step, the greater the inaccuracy of the correlation. The correlation underpredicts the experimental heat transfer by up to ≈20 percent for the cases studied here. Agreement between STAN7 and the experimental results, on the other hand, is roughly as good (or better) for the wall temperature step situations than for the baseline conditions. The numerical code thus functions well in calculating the heat transfer behavior just downstream of a sharp step in wall temperature. A further implication is that streamwise thermal conduction within the boundary layer, in the vicinity of the step, is not significant. Additionally, the program appears to properly model the turbulence physics near the step location. The conduction model for the turbulent Prandtl number, Pr_t, used in STAN7 (see Kays and Crawford [12]) seems effective for wall temperature step boundary conditions.

Table 2 Rectangular calorimeter experimental data (streamwise orientation) and comparison with STAN7

Re_ξ	ΔT_{cal} (°C)	St_{cal} $\times 10^{-3}$	St_{STAN7} $\times 10^{-3}$	St, Eq. (1) $\times 10^{-3}$	Error [%] STAN7/Eq. (1)
1.07×10^6	0	2.05	1.95	2.02	5.1/1.8
1.07×10^6	5	2.53	2.36	2.28	6.5/9.8
1.07×10^6	10	2.76	2.57	2.41	6.7/12.5
1.33×10^6	0	1.93	1.88	1.93	2.8/0.3
1.33×10^6	5	2.38	2.27	2.18	4.6/8.3
1.33×10^6	10	2.59	2.47	2.31	4.9/10.9
1.59×10^6	0	1.87	1.83	1.86	2.1/0.4
1.59×10^6	5	2.27	2.20	2.11	3.0/7.0
1.59×10^6	10	2.48	2.38	2.23	3.7/10.1

Data for the rectangular calorimeter in the streamwise orientation, presented in Table 2, show trends similar to those observed for the spanwise cases. The agreement between baseline experimental data and STAN7 is within 5 percent for all Reynolds number cases. STAN7 predicts the Stanton number for cases with temperature step within ≈7 percent for the lowest Reynolds number case, and with better agreement for the other two. With the spanwise geometry, the agreement between the calorimeter and STAN7 is better for the temperature step situations (relative to the baseline cases). In contrast, for the streamwise configuration the disparity between the code and experiment is larger by a few percent for the temperature step cases. Because the calorimeter in this orientation is narrow in the lateral dimension, this implies that spanwise turbulent diffusion may be increasing the heat transfer by only a few percent. The differences are not great, but perceptible and consistent. Note that spanwise diffusion is not represented in the two-dimensional boundary layer code.

Table 3 displays heat transfer data acquired under high freestream turbulence conditions for the rectangular calorimeter in the spanwise orientation. The ratio of the high to low freestream turbulence Stanton numbers illustrates that the effect of the turbulence is less important with greater temperature step size. The ratios are largest for the baseline cases and smallest for the largest temperature step situations (10°C). The sensitivity to freestream turbulence conditions is overshadowed by the augmentation in heat transfer due to the step change in wall thermal boundary condition.

The effect of high freestream turbulence may also be considered in the context of the Discrete Green's Function (DGF) concept. The principles of the superposition-based DGF technique are discussed in Batchelder and Eaton [13]. The main diagonal terms of the DGF matrix relate the temperature rise values on discretized heated elements to their respective power inputs. The off-diagonal terms reflect the thermal influence of these heated elements on downstream regions. The augmentation in calorimeter heat transfer due to high freestream turbulence is moderate for the temperature step cases and large for the baseline (uniform surface temperature) boundary conditions. The temperature step results are dominated by the main diagonal terms of the DGF, whereas the baseline data are determined by a sum of equally-weighted main and off-diagonal terms. The experimental results thus indicate that high freestream turbulence influences the off-diagonal terms to a much greater extent than the main diagonal terms. This may be explained by physical arguments. The main diagonal terms, quantifying self-heating effects, are governed largely by heat transfer phenomena very near the wall and by the skin friction. The effect of freestream turbulence on these terms is hence not very strong. The off-diagonal terms are, in contrast, reduced significantly by high freestream turbulence, due to increased turbulent mixing in the log layer and wake region of the boundary layer. This reduces the thermal "wake" effect of a heated element on the wall downstream.

Table 3 Rectangular calorimeter experimental data (spanwise orientation) with high freestream turbulence

Re_ξ	ΔT_{cal} (°C)	St_{cal}	$St_{high\ turb}/St_{low\ turb}$
1.14×10^6	0	2.81×10^{-3}	1.37
1.14×10^6	5	3.70	1.26
1.14×10^6	10	4.13	1.23
1.44×10^6	0	2.58	1.32
1.44×10^6	5	3.36	1.21
1.44×10^6	10	3.76	1.18
1.72×10^6	0	2.38	1.27
1.72×10^6	5	3.07	1.18
1.72×10^6	10	3.45	1.15

Table 4 Square calorimeter experimental data and comparison with STAN7

Re_ξ	ΔT_{cal} (°C)	St_{cal} $\times 10^{-3}$	St_{STAN7} $\times 10^{-3}$	St, Eq. (1) $\times 10^{-3}$	Error [%] STAN7/Eq. (1)
1.14×10^6	0	2.08	1.95	2.02	6.6/3.3
1.14×10^6	5	3.10	2.82	2.50	9.0/19.3
1.14×10^6	10	3.60	3.26	2.75	9.5/23.6
1.44×10^6	0	2.01	1.88	1.93	6.6/4.2
1.44×10^6	5	2.91	2.69	2.40	7.6/17.7
1.44×10^6	10	3.36	3.09	2.64	8.0/21.5
1.72×10^6	0	1.92	1.83	1.86	4.7/3.0
1.72×10^6	5	2.73	2.59	2.32	5.3/14.9
1.72×10^6	10	3.16	2.96	2.55	6.3/19.3

The augmentation in heat transfer due to high turbulence at the calorimeter location should, according to the uniform heat flux data of Batchelder and Moffat [14], be in the 30–38 percent range at $U_\infty = 10.5$ m/s. The data in Table 3 are consistent with this benchmark. The increases in St are between 27 percent and 37 percent for baseline thermal boundary conditions. The augmentation is reduced at higher freestream velocities because the turbulence intensity levels correspondingly decrease.

Square (Two-Dimensional) Calorimeter Results. Table 4 presents the low turbulence data for the square calorimeter along with the numerical and correlation predictions. The disagreement between predictions and experiment is slightly higher for the square calorimeter than for the rectangular calorimeter. Consistent with the rectangular calorimeter data, the correlation under-predicts the heat transfer for the 10°C temperature step boundary conditions by between 19 percent and 24 percent. One of the trends observed in the data from the rectangular calorimeter in the streamwise orientation emerges here as well: the disagreement between STAN7 and experiment is larger for the temperature step cases than for baseline conditions. For the square calorimeter, this disagreement is larger by only 1–3 percent for the three velocities investigated. This implies that spanwise heat transport was present, but was not a major effect.

High turbulence results for the square calorimeter are tabulated in Table 5. The ratios of the Stanton numbers in the final column are similar to those for the rectangular calorimeter in Table 3. The augmentation in heat transfer due to high freestream turbulence is several percent higher for the square calorimeter. As observed previously, the augmentation decreases as the magnitude of the calorimeter temperature step is increased.

The square calorimeter and rectangular calorimeter in the spanwise orientation are compared in Table 6, which displays results for low and high turbulence conditions. If spanwise turbulent diffusion were a significant effect, it was expected to produce higher Stanton number values for the square calorimeter under temperature step boundary conditions. The results show that under low freestream turbulence, the rectangular and square calorimeters agree to within 7 percent for all boundary condition cases. This is

Table 5 Square calorimeter experimental data with high freestream turbulence

Re_ξ	ΔT_{cal} (°C)	St_{cal}	$St_{high\ turb}/St_{low\ turb}$
1.14×10^6	0	2.95×10^{-3}	1.42
1.14×10^6	5	3.92	1.26
1.14×10^6	10	4.41	1.22
1.44×10^6	0	2.76	1.37
1.44×10^6	5	3.64	1.25
1.44×10^6	10	4.06	1.21
1.72×10^6	0	2.61	1.36
1.72×10^6	5	3.38	1.24
1.72×10^6	10	3.77	1.19

within the estimated uncertainty band of the measurement. For the baseline cases with no calorimeter temperature step, the agreement was on the order of 3 percent for all three Reynolds number cases.

The disagreement increases, however, for the high freestream turbulence cases. With high freestream turbulence, the disparity between the square and rectangular results is consistently higher than for low turbulence conditions, even for the baseline cases with nominally uniform wall temperature. The disagreement between the two calorimeter types increases at higher freestream velocities. The greatest discrepancy occurs at the highest Reynolds number, for which the difference is nearly 10 percent for both baseline and temperature step boundary conditions. Spanwise diffusion cannot be cited as responsible for this result.

For the baseline situation, the two calorimeter types should have registered roughly the same Stanton numbers, but the square calorimeter data are consistently high. One potential explanation is non-uniformity in the flowfield. The freestream turbulence intensity and velocity fields showed moderate spanwise non-uniformities under high turbulence conditions. The mean freestream velocity field, for example, indicated higher values over the center 50 mm of the test section than at the sides (by roughly 2–5 percent), with greater non-uniformity at higher freestream velocities. This was not evident under low turbulence conditions, which showed better than 0.5 percent uniformity across the center 300 mm of the test section. Furthermore, the heat transfer values measured with the square calorimeter reflect an average of a smaller spanwise sample than its rectangular counterpart. In this context, the characteristically ''streaky'' structure of a typical turbulent boundary layer, producing extensive longitudinal streaks of alternately high and low heat transfer, may have had a contributing influence. The small dimension of the square calorimeter implies that only 5–10 of these streaks may have intersected the calorimeter, representing a small statistical sample.

Under the low turbulence conditions, the disagreement between the square and rectangular data increases by a few percent for the temperature step cases relative to the baseline uniform temperature situations. This can be attributed to the difference in the lateral boundary condition, indicating that spanwise diffusion may increase the heat transfer coefficient for a spot-shaped heated element by a few percent. For the high turbulence conditions, the results are less dependent on the thermal boundary condition, with virtually the same agreement for the baseline cases and the temperature step cases.

In summary, if spanwise turbulent diffusion was present, it apparently augmented the two-dimensional heat transfer rate by less than 5 percent under low turbulence conditions. The augmentation is even less, if present at all, under conditions of high freestream turbulence. For engineering calculations it is acceptable to neglect spanwise diffusion for all but very small heated spots.

Table 6 Heat transfer comparison between rectangular and square calorimeters

Re_ξ	ΔT_{cal} (°C)	Low Turbulence Difference in St_{cal} [%]	High Turbulence Difference in St_{cal} [%]
1.14×10^6	0	1.5	4.9
1.14×10^6	5	5.3	6.1
1.14×10^6	10	6.9	6.7
1.44×10^6	0	3.3	7.3
1.44×10^6	5	5.1	8.4
1.44×10^6	10	5.6	8.0
1.72×10^6	0	2.8	9.9
1.72×10^6	5	4.4	9.8
1.72×10^6	10	5.3	9.4

Heat Transfer Correlations Near a Wall Temperature Step. The rectangular calorimeter results indicate that the conventional unheated starting length correlation in Eq. (1) underestimates the spatially-averaged experimental data by as much as 19 percent for temperature step boundary conditions, confirming the pattern noted by earlier researchers. A new correlation, applicable over a range of Reynolds numbers and valid within a fraction of a boundary layer thickness from the wall temperature step to far downstream, would allow closed-form analysis of the heat transfer for small heated elements.

Development of Modified Correlation. The STAN7 boundary layer code, having been qualified using calorimeter data, was employed as a reference for the development of an algebraic expression quantifying heat transfer just downstream of a step change in wall temperature. A series of STAN7 cases spanning an order of magnitude in Reynolds number ($5.0\times10^5\leqslant Re_\xi\leqslant5.0\times10^6$) was run, each case simulating a single 10°C step change in wall temperature at $x=\xi$. The STAN7 results were taken as reference values and compared with the predictions of the correlation in Eq. (1) to determine the error associated with the earlier form. A new term ϕ was added to the previous unheated starting length correction, preserving the Reynolds number dependence of the original expression. The new form was thus represented as

$$St(x)=0.0287\,Re_x^{-0.2}\,Pr^{-0.4}\left(\left[1-\left(\frac{\xi}{x}\right)^{9/10}\right]^{-1/9}+\phi(\xi,x,Re_\xi)\right) \tag{3}$$

where ϕ was found to be

$$\phi=(-0.0139\ln(Re_\xi)+0.246)\left(\frac{\xi}{x}\right)^2\frac{1}{\sqrt{1-\left(\frac{\xi}{x}\right)}} \tag{4}$$

The $(\xi/x)^2$ term ensures that the new additive term decays far downstream of the step and that the modified solution converges to Eq. (1), which is well-established for large x/δ_0. The square root term governs the shape of the curve near the step, and fits the St versus x/δ_0 data from STAN7 well for the Re_ξ range examined.

Table 7 provides local Stanton number values for six different x/δ_0 locations. The local agreement between STAN7 and the new correlation is excellent, generally within ±5 percent. Furthermore, the new correlation predicts $St_{avg,\delta}$, the Stanton number spatially-averaged over one boundary layer thickness downstream of the step, within less than 5 percent of STAN7. The Stanton number values predicted by Eq. (1) are included for comparison.

For all Reynolds number cases except for $Re_\xi=5.0\times10^6$, the error in Stanton number between the new correlation and STAN7 is less than 7 percent for $x/\delta_0\geqslant0.05$. For Re_ξ of 5.0×10^6 and larger, the error increases to roughly 10 percent far downstream of the step (x/δ_0 much greater than 20). The ϕ term (Eq. (3)) in the correlation approaches zero for large x/δ_0, so this error can probably be attributed to the fact that Eq. (1) begins to lose its validity for Reynolds numbers above a few million.

Table 7 Comparison of STAN7 with correlation data local St

Re_ξ	x/δ_0	STAN7	St Eqs. (3), (4)	Eq. (1)
5.0×10^5	0.05	10.79×10^{-3}	10.06×10^{-3}	5.21×10^{-3}
	0.2	7.06	6.95	4.49
	0.5	5.45	5.60	4.05
	1	4.60	4.83	3.75
	5	3.42	3.55	3.12
	10	3.09	3.13	2.86
8.0×10^5	0.05	9.25	8.85	4.78
	0.2	6.11	6.19	4.12
	0.5	4.78	5.03	3.72
	1	4.10	4.36	3.44
	5	3.14	3.23	2.86
	10	2.85	2.86	2.63
1.25×10^6	0.05	7.99	7.82	4.40
	0.2	5.35	5.54	3.79
	0.5	4.28	4.55	3.43
	1	3.70	3.95	3.17
	5	2.90	2.95	2.64
	10	2.65	2.62	2.43
2.0×10^6	0.05	7.33	6.99	4.07
	0.2	4.73	4.93	3.48
	0.5	3.81	4.05	3.14
	1	3.35	3.54	2.91
	5	2.68	2.68	2.42
	10	2.46	2.39	2.23
3.0×10^6	0.05	6.43	6.26	3.79
	0.2	4.24	4.44	3.24
	0.5	3.47	3.67	2.92
	1	3.09	3.22	2.70
	5	2.50	2.46	2.25
	10	2.31	2.20	2.07
5.0×10^6	0.05	5.17	5.20	3.41
	0.2	3.69	3.84	2.94
	0.5	3.11	3.23	2.65
	1	2.81	2.86	2.46
	5	2.31	2.21	2.04
	10	2.13	1.99	1.88

The new correlation was derived from a straightforward qualitative data fitting procedure. The form of the expression does not necessarily reflect anything fundamental about the physics of near-step heat transfer. Its primary virtue is that it performs significantly better than Eq. (1), and thus represents a usefully accurate correction for the error in the previous correlation.

Comparisons between the modified correlation and data from the rectangular calorimeter in the spanwise orientation are shown in Table 8. The differences between the predictions and experiment are statistically insignificant. The maximum deviation between the correlation and experimental data is only 1.6 percent, for the highest Re_ξ case. These results represent a substantial improvement over the previous correlation in Eq. (1), which underpredicted the heat transfer for the same experimental cases by up to nearly 20 percent.

Prediction of Temperature Step Heat Transfer Using an Analytical Approach. The modified correlation presented in the preceding section can also be considered a ''patching'' solution between semi-analytical solutions for heat transfer in the near-field

Table 8 Comparison of experimental data with modified correlation predictions, $St_{avg,\delta}$

Re_ξ	ΔT_{cal} [°C]	St_{cal}	$St_{correlation,mod}$ Eqs. (3), (4)	Error [%]
1.14×10^6	5	2.95×10^{-3}	2.95×10^{-3}	0.1
1.14×10^6	10	3.37	3.37	−0.1
1.44×10^6	5	2.77	2.78	−0.3
1.44×10^6	10	3.18	3.21	−0.8
1.72×10^6	5	2.62	2.65	−1.2
1.72×10^6	10	3.01	3.05	−1.6

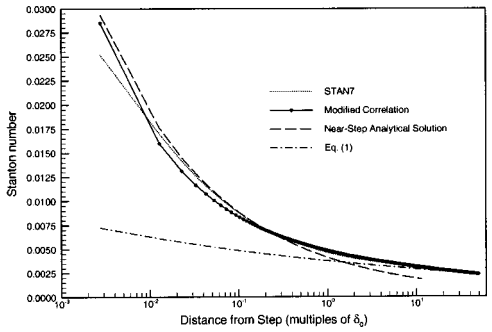

Fig. 7 Comparison of heat transfer with wall temperature step change, $Re_\xi=5.0\times10^5$

and far-field of the step change in wall temperature. The 1/7th power law solution, given in Eq. (1), is valid only far downstream of the step. Very near the step change in surface temperature, the heat remains so close to the wall that the thermal boundary layer is confined to the viscous sublayer. A more accurate solution for the heat transfer problem near the step assumes a linear velocity profile with slope given by

$$\frac{\partial \overline{u}}{\partial y}=\frac{\tau_w}{\mu} \tag{5}$$

Using standard boundary layer approximations with a zero pressure gradient and neglecting viscous dissipation and axial conduction, a similarity solution can be obtained due to the absence of characteristic length scales in the problem. The analysis proceeds in the same direction as the work of Kestin and Persen [7]. The governing constant-properties energy equation to be solved is

$$\overline{u}\frac{\partial \overline{T}}{\partial x}=\alpha\frac{\partial^2 \overline{T}}{\partial y^2} \tag{6}$$

Defining a nondimensional temperature ratio Θ as

$$\Theta=\frac{\overline{T}-T_\infty}{T_{\text{wall}}-T_\infty} \tag{7}$$

and permitting the skin friction coefficient C_f to vary with x for convenience (only for short distances from the temperature step) according to the standard turbulent correlation,

$$\frac{C_f}{2}=0.0287\,\mathrm{Re}_x^{-0.2} \tag{8}$$

yields the following simplified expression for the Stanton number:

$$St=0.1648\,\mathrm{Re}_x^{-2/5}\,\mathrm{Pr}^{-2/3}\left[1-\frac{\xi}{x}\right]^{-1/3} \tag{9}$$

Figures 7–9 illustrate the excellent agreement obtained between the new correlation from Eqs. (3) and (4) and STAN7 for a broad range of x/δ_0 values. Predictions using the semi-analytical solution from Eq. (9) as well as the earlier unheated starting length correlation in Eq. (1) are also included in the plots. Low, intermediate, and high Reynolds numbers are represented, with Re_ξ values of 5.0×10^5, 1.25×10^6, and 5.0×10^6. The near-step semi-analytical solution is shown to under-predict the heat transfer significantly beyond $\approx$0.5 boundary layer thicknesses downstream of the temperature step. It agrees very well, however, with both the STAN7 results and the new correlation in the region immediately downstream of the step.

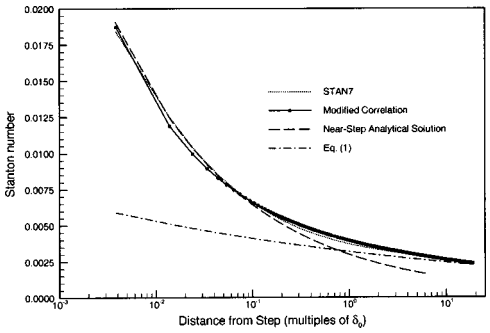

Fig. 8 Comparison of heat transfer with wall temperature step change, $Re_\xi = 1.25 \times 10^6$

Conclusions

Steady-state experiments with one-dimensional (rectangular) and two-dimensional (square) calorimeters were conducted to study the heat transfer in the vicinity of sharp steps in wall temperature. The critical calorimeter dimension was selected to be on the order of the local boundary layer thickness. Data acquired under low and high freestream turbulence conditions revealed that spanwise transport of heat through turbulent diffusion is not an important effect for a two-dimensional heated element, increasing the one-dimensional heat transfer rate by at most 5 percent. The augmentation appears more pronounced under low freestream turbulence conditions.

The rectangular calorimeter data were predicted within a band of ± 5 percent by the two-dimensional boundary layer code STAN7 for the low turbulence, temperature-step boundary condition runs. This indicated that streamwise thermal conduction in the boundary layer is not significant, and generated confidence in the ability of the code to predict heat transfer near abrupt changes in wall temperature. The calorimeter results also showed, in agreement with previous researchers, that the conventional equation for heat transfer with an unheated starting length greatly underpredicts the heat transfer rate near a wall temperature step. The magnitude of the error can exceed 30 percent within one-fifth of a boundary layer thickness of the step.

A new unheated starting length correlation, valid over a broad range of Reynolds numbers, was developed using STAN7 as a qualified reference. The modified correlation was shown to capture the behavior of both near and far-field semi-analytical solutions. The correlation predicts the calorimeter heat transfer data to within 1.6 percent for temperature step boundary condition cases, representing a great improvement over the earlier closed-form solution.

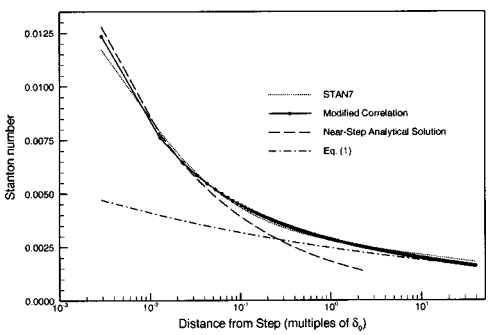

Fig. 9 Comparison of heat transfer with wall temperature step change, $Re_\xi = 5.0 \times 10^6$

Acknowledgment

The authors would like to thank General Electric Aircraft Engines (GEAE) for financial support of this research.

Nomenclature

C_p = specific heat at constant pressure
C_f = skin friction coefficient
h = heat transfer coefficient, based on local heat flux and difference between freestream temperature and local surface temperature
Pr = Prandtl number $= \nu/\alpha$
Pr_t = turbulent Prandtl number $= \varepsilon_M / \varepsilon_H$
Re_x = Reynolds number based on streamwise location x
Re_ξ = Reynolds number based on temperature step location ξ
St = Stanton number $= h/\rho U_\infty C_p$
$St_{avg,\delta}$ = Stanton number averaged over one boundary layer thickness downstream of temperature step
$\overline{T}$ = mean temperature in boundary layer
T' = fluctuating temperature in boundary layer
T_{cal} = calorimeter temperature
T_{wall} = wall temperature
T_∞ = freestream temperature
Tu = freestream turbulence intensity
$\overline{u}$ = mean velocity in boundary layer
U_∞ = freestream velocity
w' = fluctuating velocity in boundary layer, lateral direction
x = coordinate in streamwise direction or distance downstream from wall temperature step
y = coordinate in wall-normal direction
z = coordinate in lateral (spanwise) direction
α = thermal diffusivity
δ = 99 percent hydrodynamic boundary layer thickness
δ_0 = hydrodynamic boundary layer thickness at temperature step location
$\varepsilon_{H,S}$ = eddy diffusivity for heat in spanwise direction
ϕ = additive term in modified correlation
ΔT_{cal} = temperature step at the calorimeter
ΔT_{wall} = wall temperature above freestream $= T_{wall} - T_\infty$
Θ = nondimensional temperature
Δx = streamwise step size used in STAN7
ρ = density
ξ = streamwise location of wall temperature step
τ_w = wall shear stress
μ = absolute viscosity
ν = kinematic viscosity

References

[1] Reynolds, W. C., Kays, W. M., and Kline, S. J., 1958, "Heat Transfer in the Turbulent Incompressible Boundary Layer—Step Wall Temperature Boundary Conditions," NASA Memo 12-2-58W, Washington, D.C.

[2] Reynolds, W. C., Kays, W. M., and Kline, S. J., 1958, "Heat Transfer in the Turbulent Incompressible Boundary Layer—Arbitrary Wall Temperature and Heat Flux," NASA Memo 12-3-58W, Washington, D.C.

[3] Taylor, R. P., Love, P. H., Coleman, H. W., and Hosni, M. H., 1990, "Heat Transfer Measurements in Incompressible Turbulent Flat Plate Boundary Layers With Step Wall Temperature Boundary Conditions," ASME J. Heat Transfer, **112**, pp. 245–247.

[4] Taylor, R. P., Hosni, M. H., Garner, J. W., and Coleman, H. W., 1992, "Rough-Wall Turbulent Heat Transfer With Step-Wall Temperature Boundary Conditions," J. Thermophys. Heat Transfer, **6**, pp. 84–90.

[5] Saetran, L. R., 1989, "Turbulent Boundary Layer With a Step in the Wall Temperature," *Forum on Turbulent Flows-ASME Fluids Eng. Div. Publ. FED*, **76**, pp. 107–114.

[6] Browne, L. W. B., and Antonia, R. A., 1979, "Calculation of a Turbulent Boundary Layer Downstream of a Step Change in Surface Temperature," ASME J. Heat Transfer, **101**, pp. 144–150.

[7] Kestin, J., and Persen, L. N., 1962, "The Transfer of Heat Across a Turbulent Boundary Layer at Very High Prandtl Numbers," Int. J. Heat Mass Transfer, **5**, pp. 355–371.

[8] Antonia, R. A., Danh, H. Q., and Prabhu, A., 1977, "Response of a Turbulent

Boundary Layer to a Step Change in Heat Flux,'' J. Fluid Mech., **80**, part 1, pp. 153–177.
[9] Subramanian, C. S., and Antonia, R. A., 1981, ''Response of a Turbulent Boundary Layer to a Sudden Decrease in Wall Heat Flux,'' Int. J. Heat Mass Transfer, **24**, pp. 1641–1647.
[10] Teitel, M., and Antonia, R. A., 1993, ''A Step Change in Wall Heat Flux in a Turbulent Channel Flow,'' Int. J. Heat Mass Transfer, **36**, pp. 1707–1709.
[11] Elkins, C. J., and Eaton, J. K., 2000, ''Turbulent Heat and Momentum Transport on a Rotating Disk,'' J. Fluid Mech., **402**, pp. 225–253.
[12] Kays, W. M., and Crawford, M. E., 1993, *Convective Heat and Mass Transfer*, 3rd ed., McGraw Hill Book Co., Inc.
[13] Batchelder, K. A., and Eaton, J. K., 2001, ''Practical Experience With the Discrete Green's Function Approach to Convective Heat Transfer,'' ASME J. Heat Transfer, **123**, pp. 70–76.
[14] Batchelder, K. A., and Moffat, R. J., 1997, ''Towards a Method for Measuring Heat Transfer in Complex 3-D Flows,'' Ph.D. thesis, Department of Mechanical Engineering, Stanford University, Stanford, CA.

Heat Transfer Enhancement Using Shaped Polymer Tubes: Fin Analysis

Zhihua Li
e-mail: jhd@me.umn.edu

Jane H. Davidson

Susan C. Mantell

Department of Mechanical Engineering,
University of Minnesota,
111 Church St., S.E.,
Minneapolis, MN

The use of polymer tubes for heat exchanger tube bundles is of interest in many applications where corrosion, mineral build-up and/or weight are important. The challenge of overcoming the low thermal conductivity of polymers may be met by using many small-diameter, thin-walled polymer tubes and this route is being pursued by industry. We propose the use of unique shaped tubes that are easily extruded using polymeric materials. The shaped tubes are streamlined to reduce form drag yet the inside flow passage is kept circular to maintain the pressure capability of the tube. Special treatment is required to predict convective heat transfer rates because the temperature distribution along the outer surface of the shaped tubes is nonuniform. The average forced convection Nusselt number correlations developed for these noncircular tubes can not be used directly to determine heat transfer rate. In this paper, heat transfer rates of shaped tubes are characterized by treating the tubes as a base circular tube to which longitudinal fin(s) are added. Numerical solution of an energy balance on the fin provides the surface temperature distribution and a shaped tube efficiency, which can be used in the same manner as a fin efficiency to determine the outside convective resistance. The approach is illustrated for three streamlined shapes with fins of lenticular and oval profile. The presentation highlights the effects of the geometry and the Biot number on the tube efficiency and heat transfer enhancement. Convective heat transfer is enhanced for the oval shaped tube for $2000 \leqslant Re \leqslant 20{,}000$ when $Bi < 0.3$. For polymeric materials, the Biot number in most applications will be greater than 0.3, and adding material to the base tube reduces the heat transfer rate. The potential benefit of reduced form drag remains.
[DOI: 10.1115/1.1683663]

Introduction

Polymer heat exchangers are an attractive alternative to metal heat exchangers in numerous applications that involve corrosive or high purity chemicals, are prone to mineral build-up, or have significant weight restrictions. In addition, polymers may be manufactured in innovative shapes that are easily and attractively integrated with other components and that provide large heat transfer surface area in a compact volume. One potential disadvantage of using polymers is their low thermal conductivity, which lies in a narrow range from 0.1 to 0.3 W/m·K. Particles of aluminum and graphite have been added to various polymers to yield an increase in the bulk thermal conductivity [1–3]. However, the increase in thermal conductivity is not isotropic, and, in particular for extruded tubes, is primarily in the longitudinal rather than the radial direction. For example, the addition of 10% chopped glass fiber, 15% powdered graphite, and 5% carbon black increases the thermal conductivity of nylon 6,6 10-fold in the in-plane direction and 3-fold out-of-plane, i.e., the primary direction of heat transfer [2]. Consequently, the focus of efforts to develop polymer tube bundles is small-diameter, thin-walled tubes. To reduce the conductive resistance of the polymer wall, the ratio of wall thickness-to-outer diameter should be minimized. For a given tube diameter, the minimum wall thickness is limited by the long term strength and stiffness requirements of the application. One US polymer manufacturer is developing heat exchangers for gas applications that use nylon tubes ranging from 1.5 mm to 3.8 mm in outer diameter. For these tubes, flow across the tubes is expected to be in the subcritical range ($Re < 10^5$) assuming gas velocities less than 30 m/sec for a tube diameter equal to 3.6 mm.

Contributed by the Heat Transfer Division for publication in the JOURNAL OF HEAT TRANSFER. Manuscript received by the Heat Transfer Division May 8, 2003; revision received September 15, 2003. Associate Editor: P. M. Ligrani.

The objective of on-going research is to assess the possible fluid dynamic and thermal benefits of using ''shaped'' polymer tubes in bundles comprised of such small diameter tubes (Fig. 1). There are two unique features of the shaped tube. The outer surface is streamlined to reduce form drag and the inner flow passage is kept circular to maintain pressure capability. The use of noncircular tubes in heat exchangers has been considered [4–14], but none of the prior studies considered tubes with nonuniform wall thickness.

The focus here is on tubes of oval and lenticular shape which are known to reduce drag at subcritical Reynolds numbers. Reduction of pressure drop for flow across noncircular tubes has been demonstrated for oval tubes at $700 < Re < 10^4$ [9,10,15], and for lenticular tube bundles at $500 < Re < 10^4$ [11–13]. Badr et al. [15] predicted form drag and skin friction of an oval cylinder at various orientations. With the major axis parallel to the flow direction, the total drag coefficient is 0.8 at $Re = 3700$ and 0.9 at $Re = 700$ for an oval with a length ratio of minor-to-major axis (hence forth referred to as the tube shape factor, λ_b) equal to 0.6. The form drag is 80 to 90% of the total drag. Compared with a circular tube, the drag coefficient is reduced 10 to 20%. The drag force decreases as the oval tube is made more slender, i.e., the shape factor is decreased. At $3000 < Re < 4 \times 10^4$, the drag coefficient is reduced 20 to 40% for an oval cylinder with $\lambda_b = 0.5$ [9] and 30 to 50% for $\lambda_b = 0.3$ [10]. Drag may be reduced further in tube banks [6,16]. Jang and Li [16] simulated flow over oval tube banks with $\lambda_b = 0.35$ and found that the drag coefficient is 20% of that of the circular tubes for $1000 < Re < 3000$. Merker and Hanke [6] measured the pressure loss for oval tube banks with $\lambda_b = 0.25$ and a transverse tube pitch-to-minor axis ratio of 2. The total drag was reduced 95% compared with an array of circular tubes. Ruth [11] measured the pressure loss and heat transfer rate for a lenticular tube bundle with $\lambda_b = 0.25$ at $1000 < Re < 5 \times 10^4$. With a transverse tube pitch-to-diameter ratio of 2, the drag was

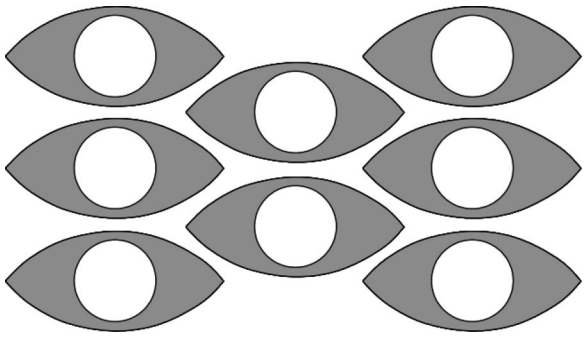

Fig. 1 Tube bundle of 'shaped' polymer tubes

reduced by 70% compared to an array of circular tubes. These results are confirmed by numerical study [12,13].

The wall thickness of the shaped tube is nonuniform to withstand the pressure of the internal fluid. This approach is justified by prior analysis of the stress in elliptical tubes [17]. The stress is reduced as material is preferentially added to make the inner flow passage more circular. A numerical analysis of stress and deformation of the shaped tubes considered here confirms this result (to be published), but is not the focus of the present work.

The objective of this paper is to present a method for characterizing the thermal performance of tubes with nonuniform cross section by using the thermal performance definitions normally defined for the performance of fins. The method is illustrated for the lenticular, teardrop and oval shaped tubes shown in Fig. 2, but is applicable to other shapes. Only streamlined shapes are considered here. The circular tube in Fig. 2(*a*) serves as the baseline to which the other tubes are compared. The lenticular tube, the teardrop tube, and the oval tube are shown in Figs. 2(*b*) through 2(*d*). The temperature distribution along the outer surface of the shaped tubes is nonuniform, and the nonuniformity is more pronounced for polymers because of the low thermal conductivity. Consequently, average Nusselt number correlations developed for noncircular tubes can not be used directly to determine heat transfer rates of shaped tubes. We propose treating the tubes as a base circular tube with the added material viewed as a fin. The outer surface of the lenticular tube is described by the intersection of two arcs, each given by $(r\cos\beta)^2+(r\sin\beta+R-r_b)^2=R^2$, thus forming two symmetric fins of length ℓ. The outer radius of the base tube (r_o) is thus the radius of the base of the fin (r_b). The teardrop tube in Fig. 2(*c*) has only one fin of the same shape as those on the lenticular tube. The oval shaped tube in Fig. 2(*d*) has two fins of elliptic profile.

Treating the tubes in this manner permits the use of a shaped tube efficiency χ, which accounts for the difference in the temperature of the base circular tube and the average temperature along the surface of the tube, in much the same manner as a fin efficiency, to determine the outside convective resistance.

$$R_{th,o}=\frac{1}{\chi\overline{h_o}A_oL} \tag{1}$$

where A_o is the outside surface area per unit length of the shaped tube, including the fin, and $\overline{h_o}$ is the average convective heat transfer coefficient. For each shape, the efficiency depends solely on Biot number, $\mathrm{Bi}=\overline{h_o}r_b/k$, and a dimensionless length, $\lambda_b=r_b/\ell$, referred to as the tube shape factor. To illustrate the usefulness of the shaped tube efficiency, the convective heat transfer rate of the oval shaped tube (Fig. 2(*d*)) is compared to that of a circular tube.

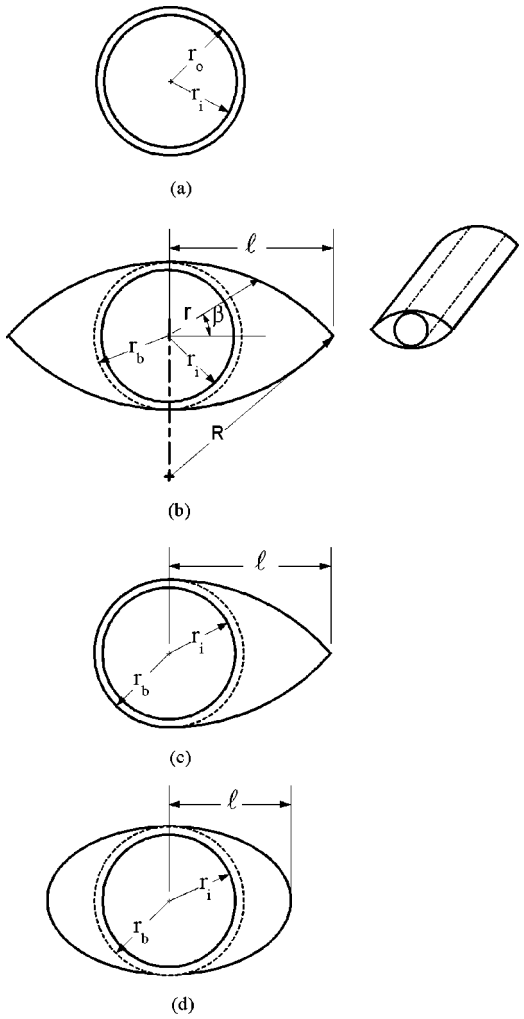

Fig. 2 Shaped tubes (*a*) baseline circular, (*b*) lenticular, (*c*) teardrop, and (*d*) oval. The area outside the dashed circle is considered the fin

Shaped Tube Efficiency

The shaped tube efficiency is defined as

$$\chi\equiv\frac{q}{q_{\max}}=\frac{\overline{T_o}-T_\infty}{T_b-T_\infty}, \tag{2}$$

where q is the actual heat transfer rate of the shaped tube and $q_{\max}$ is the heat transfer rate that would be achieved if the spatially averaged temperature of the surface of the shaped tube, $\overline{T_o}$, were equal to the temperature of the base of the fin, T_b at $r=r_b$. For a circular tube, $\chi=1$. For shaped tubes with symmetrical longitudinal fins that cover the entire surface of the base circular tube, for example, for the lenticular and oval shaped tubes, χ equals the fin efficiency η_f,

$$\eta_f\equiv\frac{q_f}{q_{f,\max}}=\frac{\overline{T_{o,f}}-T_\infty}{T_b-T_\infty}, \tag{3}$$

where $\overline{T_{o,f}}$ is the spatially averaged temperature of the surface of the fin. On the other hand, when the fins cover a fraction of the outer surface of the base circular tube, the temperature of the "unfinned" portion of the outer surface is the base temperature and thus $\chi\neq\eta_f$. For example, for the teardrop shaped tube, the shaped tube efficiency is determined by substituting the expression for fin efficiency (Eq. (3)) into the definition of shaped tube efficiency (Eq. (2)):

$$\chi_{\text{teardrop}} = \frac{q}{q_{\max}} = \frac{\pi r_b (T_b - T_\infty) + A_f (\overline{T_{o,f}} - T_\infty)}{A_o (T_b - T_\infty)}$$

$$= \frac{\pi r_b + A_f \left[\dfrac{\overline{T_{o,f}} - T_\infty}{T_b - T_\infty} \right]}{A_o} = \frac{1 + \eta_f \left[\dfrac{A_f}{\pi r_b} \right]}{1 + \left[\dfrac{A_f}{\pi r_b} \right]}$$

$$= \frac{1 + \eta_f \left[\dfrac{1+\lambda_b^2}{\pi \lambda_b^2} \arcsin\left(\dfrac{2\lambda_b}{1+\lambda_b^2} \right) \right]}{1 + \dfrac{1+\lambda_b^2}{\pi \lambda_b^2} \arcsin\left(\dfrac{2\lambda_b}{1+\lambda_b^2} \right)}, \tag{4}$$

where $A_f = 1 + \lambda_b^2/\lambda_b \cdot \ell \arcsin(2\lambda_b/1+\lambda_b^2)$ is the area of the fin surface per unit length.

The temperature distribution along the surface of the shaped tubes is estimated from a one-dimensional energy balance on the nonuniform cross-section fin (Fig. 3) using the standard assumptions of uniform base temperature and uniform convective heat transfer coefficient along the surface of the fin. This relatively simple one-dimensional approach yields accurate values of χ for the oval and lenticular tubes for Bi<5. A justification of the assumptions and a comparison of the one-dimensional solution with a two-dimensional solution are presented in the appendix.

The one-dimensional energy balance in the radial direction is given by

$$d\left[r\beta(r) k \frac{dT(r)}{dr} \right] = h_o(r)[T(r) - T_\infty] ds(r), \tag{5}$$

where the angular coordinate $\beta(r)$ and differential fin length $ds(r)$ are both specified by the geometry. The expressions of $\beta(r)$, $ds(r)$, the heat transfer surface area of the fin (A_f) and the entire shaped tube (A_o) are listed in Table 1. The analyses for the teardrop and lenticular tubes are identical with an adjustment made for the number of fins (one for the teardrop and two for the lenticular tube). The convective heat transfer coefficient h_o in Eq. (5) is assumed to be a constant equal to the average heat transfer coefficient $\overline{h_o}$ determined from experiment or from numerical study.

Substituting expressions for $\beta(r)$ and $ds(r)$ into Eq. (5) and expressing the result in terms of dimensionless variables yields a nonlinear, second-order, homogeneous differential equation for the excess temperature, $\theta(\lambda) = T(\lambda) - T_\infty$, where $\lambda = r/\ell$ is a dimensionless radial coordinate. Each fin extends from $\lambda = \lambda_b$ at the base circular tube to $\lambda = 1$ at the fin tip. For lenticular and teardrop fins, the differential equation for the excess temperature is

$$\frac{d\left\{ \lambda \arcsin\left[\left(\dfrac{\lambda_b}{\lambda} \right) \dfrac{1-\lambda^2}{1-\lambda_b^2} \right] \cdot \dfrac{d\theta(\lambda)}{d\lambda} \right\}}{d\lambda}$$

$$= \frac{\text{Bi}}{\lambda_b} \cdot \theta(\lambda) \frac{\lambda(1+\lambda_b^2)}{\sqrt{(\lambda^2 - \lambda_b^2)(1 - \lambda_b^2 \lambda^2)}}. \tag{6}$$

For oval fins,

$$\frac{d\left\{ \lambda \arctan\left[\lambda_b \sqrt{\dfrac{1-\lambda^2}{\lambda^2 - \lambda_b^2}} \right] \cdot \dfrac{d\theta(\lambda)}{d\lambda} \right\}}{d\lambda}$$

$$= \frac{\text{Bi}}{\lambda_b} \cdot \theta(\lambda) \frac{\lambda \sqrt{1 + \lambda_b^2 - \lambda^2}}{\sqrt{(\lambda^2 - \lambda_b^2)(1 - \lambda^2)}}. \tag{7}$$

Equations (6) and (7) are solved assuming a constant wall temperature boundary condition at the surface of the circular tube (i.e., the fin base)

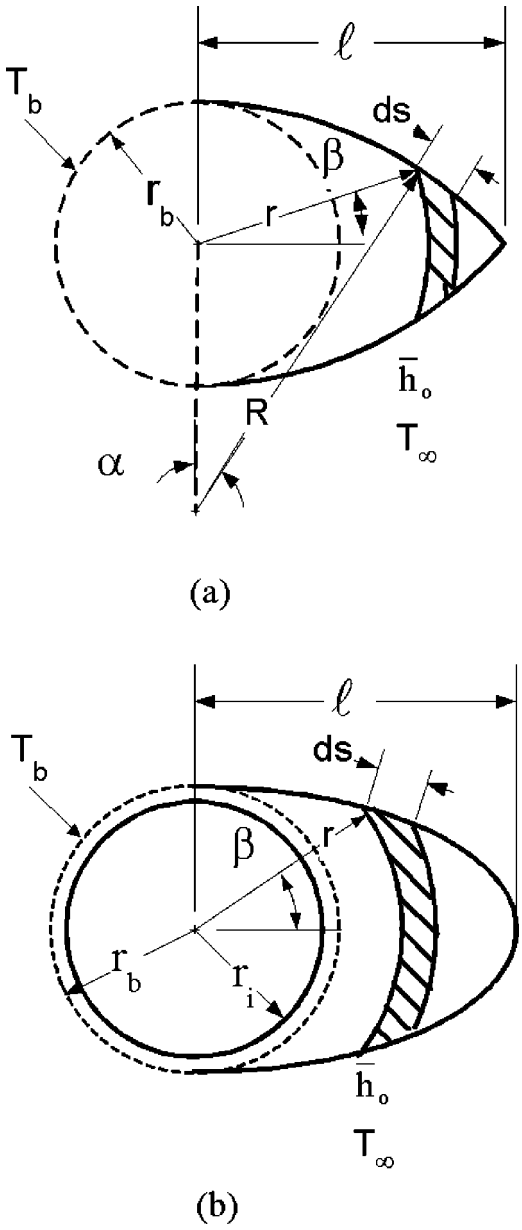

Fig. 3 Differential element for a one-dimensional energy balance for a single-sided fin on a shaped tube (*a*) lenticular and (*b*) oval

$$\theta(\lambda_b) = T_b - T_\infty \equiv \theta_b \quad \text{at} \quad \lambda = \lambda_b \tag{8a}$$

A convective boundary condition is specified at the fin tip

$$\frac{d\theta(\lambda)}{d\lambda} = \frac{\text{Bi}}{\lambda_b} \cdot \theta(\lambda) \quad \text{at} \quad \lambda = 1 \tag{8b}$$

Equation (6) or (7) with the boundary conditions in Eq. (8) is solved numerically using the upwind differential method. For each geometry, the differential element is refined until the fin efficiency varies less than 1%. The solution for the excess temperature distribution in the radial direction permits determination of the shaped tube efficiency χ defined in Eq. (2). For each tube, $\theta(\lambda)$ depends solely on the tube shape factor $\lambda_b = r_b/\ell$, and Bi.

Results and Discussion

The presentation which follows is structured to highlight the effects of tube shape factor (λ_b) and Biot number on temperature

Table 1 Geometric parameters for the lenticular, teardrop and oval shaped tubes

	Lenticular	Teardrop	Oval
A_f	$2R\arcsin\left(\frac{\ell}{R}\right)$ where $R=\frac{1+\lambda_b{}^2}{2\lambda_b}\ell$.	$\left(2R\arcsin\left(\frac{\ell}{R}\right)\right)$	$\frac{\pi(r_b+\ell)}{2}$
A_o	$2A_f$	πr_b+A_f	$2A_f$
$\beta(r)$	$\arcsin\left[\left(\frac{r_b}{r}\right)\frac{\ell^2-r^2}{\ell^2-r_b{}^2}\right]$	Same as lenticular	$\arctan\left(\frac{r_b}{\ell}\sqrt{\frac{\ell^2-r^2}{r^2-r_b{}^2}}\right)$
$ds(r)$	$\frac{r(r_b{}^2+\ell^2)}{\sqrt{(r^2-r_b{}^2)(\ell^4-r_b{}^2r^2)}}dr$	Same as lenticular	$\frac{r\sqrt{r_b{}^2+\ell^2-r^2}}{\sqrt{(r^2-r_b{}^2)(\ell^2-r^2)}}dr$

distribution ($\theta(\lambda)$) and shaped tube efficiency (χ) of the lenticular, teardrop and oval tubes. The temperature distribution and shaped tube efficiency are determined for Bi$\leqslant$5 and for shape factors from 0.1 to 1, which is the limiting case of a circular tube.

The results are interpreted to determine the conditions under which the shaped tube is feasible from the perspective of enhancing the heat transfer rate in cross flow. To help interpret the results, the variation of Bi with changes in material, tube shape factor, and Reynolds number is shown in Table 2. Biot numbers are listed for oval tubes made of polymeric and metallic materials with λ_b equal to 0.1 (a long fin), 0.5 and 0.9 (a short fin), and Reynolds numbers based on the flow length (2ℓ) equal to 2000, 4000, and 6000. The heat transfer coefficient is estimated from the correlation for circular and oval tubes given by Zukauskas and Ziugzda [18]

$$\mathrm{Nu}_{2\ell}=0.27\mathrm{Re}_{2\ell}^{0.6}\mathrm{Pr}^{0.37}\left(\frac{\mathrm{Pr}}{\mathrm{Pr}_w}\right)^{0.25}\quad 2000\leqslant\mathrm{Re}_{2\ell}\leqslant 2\times10^4 \qquad (9)$$

The length scale in Eq. (9) is the length of the tube axis in the streamwise direction, i.e., 2ℓ for symmetrically shaped tubes and $2r_b$ for a circular tube. For polymer tubes, Bi is of the order 0.1 for relatively long fins ($\lambda_b=0.1$) and of the order 1 for shorter fins ($\lambda_b=0.9$). Tubes made of polymers with enhanced thermal conductivity of 1 W/m·K would have Biot numbers that are correspondingly an order of magnitude lower than those made of unfilled polymers.

Temperature Distribution

The distributions of dimensionless excess temperature ratio $\theta(\lambda)/\theta_b$ of a lenticular fin (on both the lenticular and teardrop shaped tube) and oval fin are plotted in Figs. 4(*a*) and (*b*), respectively, with respect to the dimensionless coordinate λ. Results are shown for tubes with $\lambda_b=0.3$ and 0.5 and Bi=0.1, and 1. The dimensionless temperature distributions of the lenticular and oval tubes are shown on the same plot in Fig. 4(*c*) for λ_b equal to 0.5. To read the plots, note that for each tube, the fin extends from $\lambda=\lambda_b$ to $\lambda=1$. Vertical dashed lines indicate the location of the base of the fin for each λ_b. There are two curves shown for each value of λ_b, corresponding to Bi=0.1 and 1.

The most striking feature of these plots is the dramatic decrease in temperature along the fins for Bi=1, e.g., for polymer tubes in most applications. This result is expected as a higher Biot number implies a greater conductive resistance. Shaped tubes with relatively short fins (lower λ_b) tend to have more uniform temperature than do the tubes with longer fins. A lower λ_b implies a lower convective resistance due to a larger convective surface area. Figure 4(*c*) shows that there is no significant difference in the temperature distribution along the three shapes considered.

Shaped Tube Efficiency

Attention is now turned to the shaped tube efficiency, which for symmetrical tubes such as the lenticular and oval tubes equals the fin efficiency. The shaped tube efficiencies (χ) for the lenticular tube, the teardrop tube and the oval tube are plotted with respect to Biot number in Figs. 5(*a*), (*b*), and (*c*), respectively. Curves are shown for tubes with $\lambda_b=0.05$, 0.3, 0.5, and 0.8. The baseline circular tube is represented by $\lambda_b=1$, corresponding to $\chi=1$. For a fixed Bi, the effect of adding material to the base circular tube on the efficiency may be estimated by considering decreasing values of λ_b. (This interpretation is an estimate because the magnitude of the average convective heat transfer coefficient is sensitive to shape [11,18].) As expected from the temperature distributions presented in Fig. 4, χ decreases with increasing Bi and decreasing

Table 2 Expected range of Biot number for shaped oval tubes in gas flows with Reynolds numbers from 2000 to 6000[1]

			Bi (approximate)			
$\mathrm{Re}_{2\ell}$	$\mathrm{Nu}_{2\ell}{}^2$	λ_b	Polymer $k=0.2$ W/m·K	Enhanced Polymer $k=1$ W/m·K	Aluminum $k=271$ W/m·K	Copper $k=401$ W/m·K
2000	22	0.1	0.1	0.03	0.0001	0.00007
		0.5	0.7	0.2	0.0005	0.0004
		0.9	1.3	0.3	0.001	0.0007
4000	34	0.1	0.2	0.05	0.0002	0.0001
		0.5	1.1	0.2	0.0008	0.0006
		0.9	2	0.4	0.0015	0.001
6000	44	0.1	0.3	0.06	0.0002	0.0001
		0.5	1.4	0.3	0.001	0.0007
		0.9	2.6	0.5	0.002	0.001

[1]The gas is assumed to be air at 300 K and 1 atm
[2]$\mathrm{Nu}_{2\ell}$ is based on Eq. (9)

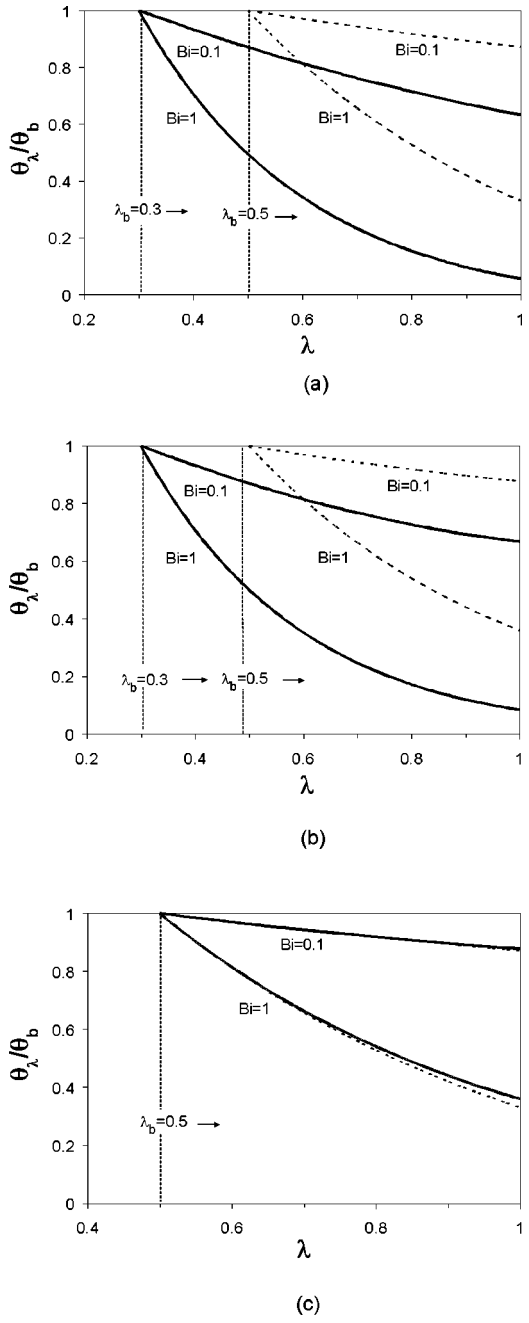

Fig. 4 Dimensionless excess temperature ratio as a function of Biot number and the dimensionless coordinate $\lambda = r/\ell$ (*a*) lenticular fin, (*b*) oval fin, and (*c*) lenticular fin (dashed line) and oval fin (solid line) with $\lambda_b = 0.5$

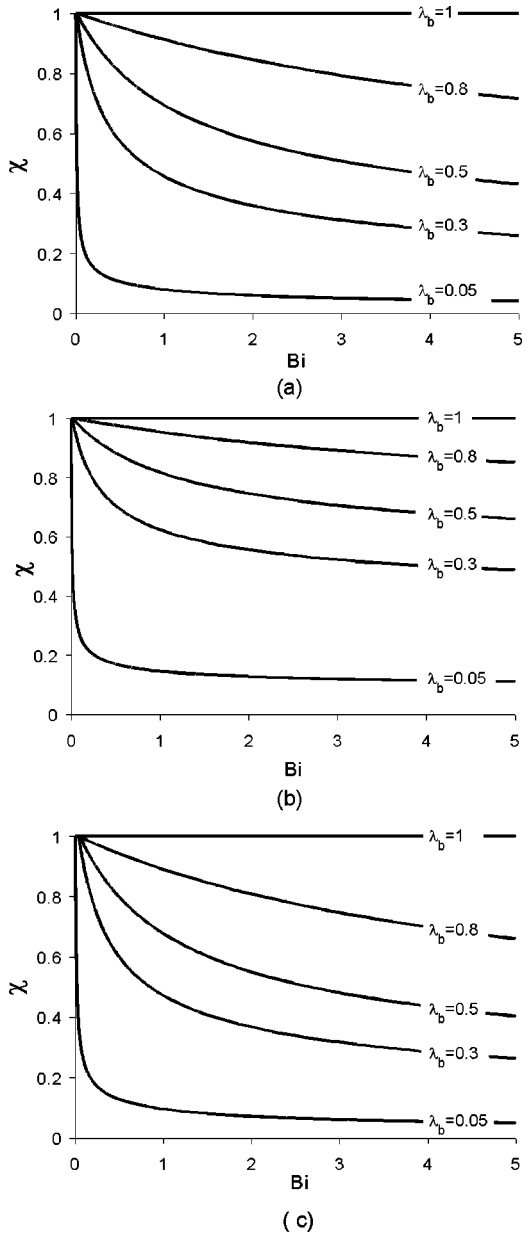

Fig. 5 Shaped tube efficiency plotted as a function of Biot number and λ_b (*a*) lenticular tube, (*b*) teardrop tube, and (*c*) oval

λ_b. The rate of decrease of χ with increasing Bi is greatest for Bi$<$0.3, i.e., the range for most metals. The shaped tube efficiency of polymer tubes can be enhanced by enhancing the thermal conductivity of polymers. For example, Table 2 shows that the Biot number is approximately 1 for polymer oval tubes with $\lambda_b = 0.5$ at Re$=$4000. The corresponding tube efficiency is 0.7. Using an enhanced polymer with thermal conductivity three times higher than that of an unfilled polymer, the Biot number is reduced to 0.3 and the tube efficiency is increased to 0.9.

The tube efficiencies of the three shaped tubes are compared in Fig. 6 for $\lambda_b = 0.3$, 0.5 and 0.8 at $0 < \mathrm{Bi} \leqslant 5$. The trends of the plots are similar. The teardrop tube has the highest efficiency because the fin extends over only half of the surface of the base circular tube. The decrease in efficiency with increasing Bi follows the same trend as that of the temperature distributions plotted in Figs. 4 and 5.

Comparison of Convective Heat Transfer of Circular and Shaped Tubes. Once the shaped tube efficiency is known, it can be used in conjunction with average heat transfer coefficients to compare the heat transfer rate of a shaped tube to the rate that would be achieved with the base circular tube. This comparison is presented in terms of the shaped tube effectiveness (ε) defined as the heat transfer rate of a shaped tube q divided by that of the base circular tube q_c at the same base temperature

$$\varepsilon_{\text{shaped tube}} \equiv \frac{q}{q_c} = \frac{\overline{\chi h_o} A_o (T_b - T_\infty)}{\overline{h_{o,c}} A_{o,c} (T_b - T_\infty)} = \frac{\overline{\chi h_o} A_o}{\overline{h_{o,c}} A_{o,c}}. \qquad (10)$$

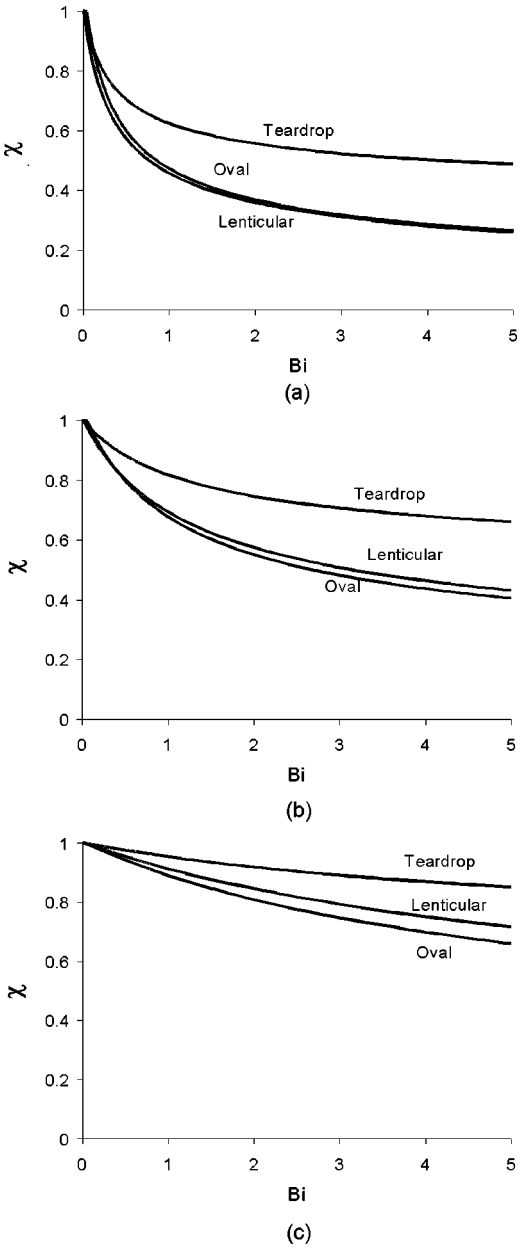

Fig. 6 Comparison of the shaped tube efficiencies for tubes with (*a*) $\lambda_b=0.3$, (*b*) $\lambda_b=0.5$, and (*c*) $\lambda_b=0.8$

Measured heat transfer coefficients for an oval tube (h_o) with $\lambda_b=0.5$ are 25% less than that of the circular tube ($h_{o,c}$) for $2000 \leqslant Re_{2\ell} \leqslant 2\times10^4$ [18]. The average heat transfer coefficient measured with lenticular tubes is 25% lower than that of a circular tube for $1000 \leqslant Re \leqslant 5\times10^4$ [11]. A Nusselt number correlation for the teardrop tube was not found by the authors.

To illustrate the use of Eq. (10), consider the oval tube. The Nusselt correlation for circular and oval tubes given in Eq. (9) is used to determine convective heat transfer coefficients for both shapes. Assuming the working fluid is gas, Pr/Pr_w is set equal to 1. Substituting the heat transfer coefficients determined with Eq. (9) for the base circular tube and for the shaped oval tube into Eq. (10) yields an expression for ε_{oval}.

$$\varepsilon_{oval}=\chi\cdot\lambda_b^{0.4}(1+1/\lambda_b)/2 \tag{11}$$

In this case, the tube effectiveness depends solely on the shaped tube efficiency and the tube shape factor. The behavior of ε_{oval} as a function of Bi and λ_b is displayed in Fig. 7 for oval tubes with $\lambda_b=0.3$, 0.5, and 0.8 and Bi from 0 to 5. For $Bi<0.3$, the oval tube enhances heat transfer for $\lambda_b<0.8$. Longer fins are desirable because the conductive resistance is lower than the convective resistance. Moreover, as discussed previously, longer fins would further reduce pressure drop [15]. At $Bi=0.3$, the heat transfer of the shaped tubes is the same as the base circular tube. For $Bi>0.3$, the penalty of added conductive resistance outweighs the benefit of increased surface area. The penalty increases as more material is added to make longer fins.

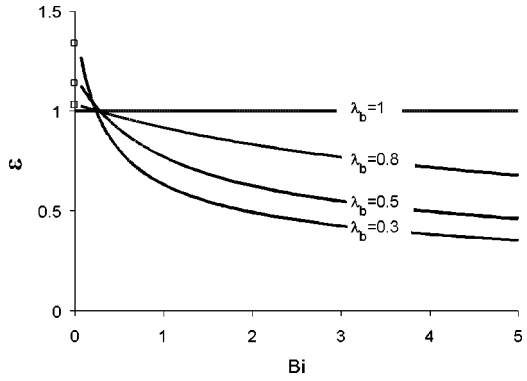

Fig. 7 Predicted heat transfer efficiency of an oval shaped tube for air flows with $2000 \leqslant Re \leqslant 20{,}000$

Concluding Remarks

Unique shaped tubes extruded with an inner circular flow passage and an outer streamlined profile are proposed to maintain the ability of the tubes to withstand the internal pressure of the inside fluid and to reduce the pressure drop across tube bundles comprising of hundreds of small-diameter, thin-walled polymer tubes. The effect of the material added to the base circular tube on heat transfer rates is characterized by treating the shaped tubes as a base circular tube to which longitudinal fins of oval and lenticular profile are attached. The shaped tube efficiency, χ, similar in function to the fin efficiency, is determined from numerical solution of a one-dimensional energy balance on the fin. The shaped tube efficiency is provided for lenticular, teardrop and oval shaped tubes as a function of Biot number and a dimensionless length ratio of the base tube radius and the length of the fin. The heat transfer effectiveness, defined as the heat transfer rate of a shaped tube divided by that of a circular tube at the same operating conditions, is used to compare the thermal behavior of the shaped tubes to that of a circular tube in cross flow.

For Biot numbers less than 0.3, the oval shaped tube enhances heat transfer. For polymeric materials, the Biot number in most applications will be greater than 0.3, and adding material to the base tube reduces the heat transfer rate. If the thermal conductivity of the polymer could be increased from 0.2 to 1 W/m·K, the shaped tubes would be more attractive from the standpoint of heat transfer. However, regardless of thermal conductivity, the benefit of reduced form drag remains. From the standpoint of overall performance, the shaped tubes should be designed to maximize an enhancement criteria objective suitable for the specific application. Future work will address the flow field and temperature distribution in heat exchanger tube bundles.

Acknowledgment

This work was supported by the U.S. National Science Foundation Grant DMII-0084765 and DuPont Canada.

Nomenclature

A_f = outer surface area of the fin, per unit length of tube, m
A_o = outer surface area of shaped tube, per unit length, m
Bi = Biot number, $\mathrm{Bi}=\overline{h_o} r_b/k$
$ds(r)$ = differential length of fin arc curve, m
h = convective heat transfer coefficient, $\mathrm{W/m^2 \cdot K}$
k = material thermal conductivity, $\mathrm{W/m \cdot K}$
ℓ = length of the fin, m
L = length of the tube, m
Nu = Nusselt number based on $2r_b$
$\mathrm{Nu}_{2\ell}$ = Nusselt number based on flow length, used in Eq. (9)
Pr = Prandtl number of the fluid, evaluated at the fluid bulk temperature.
Pr_w = Prandtl number of the fluid, evaluated at the tube wall surface temperature.
Q = heat transfer rate, W
R = circle radius corresponding to the fin arc, m
Re = Reynolds number based on $2r_b$
$\mathrm{Re}_{2\ell}$ = Reynolds number based on flow length, used in Eq. (9)
R_{th} = thermal resistance, K/W
r = radial coordinate, m
r_b = tube radius at fin base, m
r_i = tube inner radius, m
r_o = outer radius of circular tube, m
s = length of fin arc curve, m
t = tube wall thickness, $t=r_b-r_i$, m
T = temperature, K

Greek

α = arc angle corresponding to the fin arc, radian
β = angular coordinate, radian
χ = tube efficiency, Eq. (2)
ε = tube effectiveness, Eq. (9)
η_f = fin efficiency, Eq. (3)
λ = relative radial coordinate, $\lambda=r/\ell$
λ_b = shape factor, $\lambda_b=r_b/\ell$
θ = excess temperature $\theta=T-T_\infty$, K

Superscript

$\overline{\ }$ = overbar indicates average quantity

Subscript

b = refers to value at fin base
c = refers to baseline circular tube
f = fin
i = inside the tube
max = refers to maximum heat transfer rate
o = outside tube
oval = refers to oval shaped tube
teardrop = refers to teardrop shaped tube
∞ = Fluid free stream

Appendix

Justification of One-Dimensional Analysis. The results presented in the main body of the paper are based on solution of a one-dimensional energy balance on the fin. They point out the impact on heat transfer of adding material to a circular tube in order to obtain a streamlined outer shape. Assumptions made in the one-dimensional analysis are: (1) conduction is in the radial direction, (2) the fin base temperature is uniform, (3) the fin material is homogeneous, and (4) the convective heat transfer coefficient is a constant that may be represented by the average value along the outer surface of the fin.

A two-dimensional analysis in the radial and angular (β) directions was conducted to determine the range of Bi and t/r_b over which the first two assumptions required for the one-dimensional analysis provide accurate results. The two-dimensional energy equation was solved in Fluent for ratios of tube wall thickness to tube base radius (t/r_b) of 0.1 and 0.5, tube shape factors (λ_b) of 0.05. 0.3, 0.5 and 0.8, and $\mathrm{Bi}<5$. The shaped tube is not practical for higher Biot number or for thicker walled tubes. A constant heat transfer coefficient boundary condition is specified along the outer surface. An isothermal boundary condition is specified at the inner tube wall. The mesh within Fluent was refined until the heat transfer rate varied less than 1%.

A comparison of the one-dimensional and two-dimensional predictions of shaped tube efficiency is provided for the three shapes considered in this paper in Fig. 8. Over the range of conditions simulated, the prediction of shaped tube efficiency with a 1-D

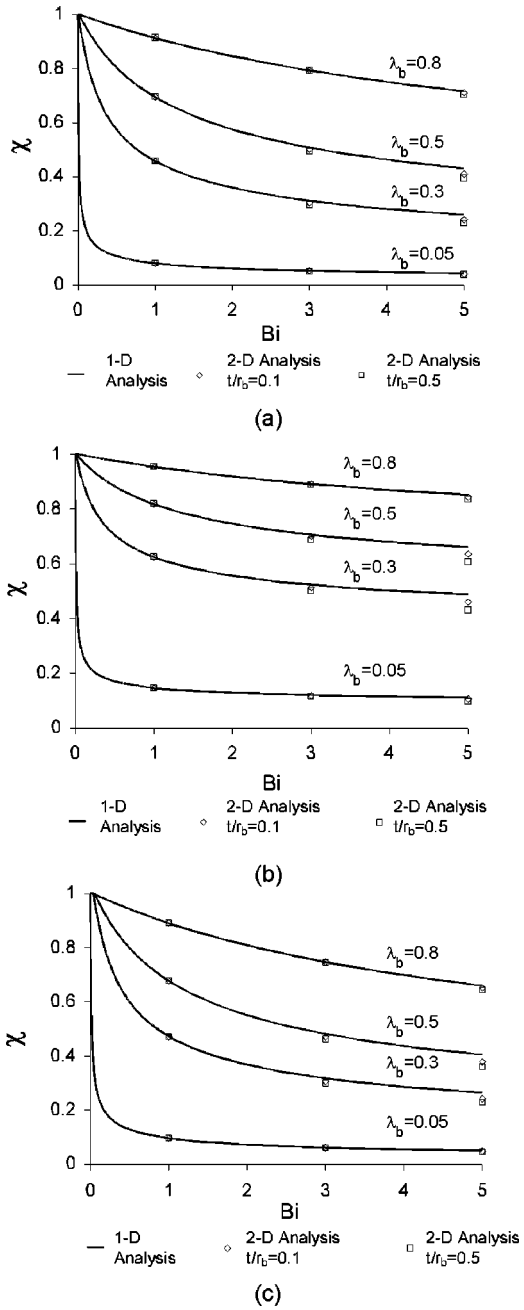

Fig. 8 Comparison of the shaped tube efficiency determined from one-dimensional and two-dimensional solutions (*a*) lenticular tube, (*b*) teardrop tube, and (*c*) oval tube

analysis is extremely accurate. The difference in the 1-D and 2-D results is negligible for $Bi < 1$, and even at $Bi = 5$, the error of the 1-D assumption is less than 10%.

The assumption that the material properties of the tube are homogenous (assumption 3) is justified for unfilled polymers. If enhanced polymers are to be used, it may be desirable to incorporate the directional dependence of thermal conductivity. The assumption that the convective heat transfer coefficient is uniform and equal to the average value (assumption 4) is commonly used and permits engineering estimates of heat transfer rates in heat exchangers. Based on computational fluid dynamic models of the flow and temperature fields in these shapes, the error introduced by this assumption is greatest for the teardrop shaped tube but the total error remains less than 10%.

References

[1] Danes, F., Garnier, B., and Dupuis, T., 2002, ''Predicting, Measuring and Tailoring the Transverse Thermal Conductivity of Composites from Polymer Matrix and Metal Fiber,'' Int. J. Thermophys., **24**(3), pp. 771–784.

[2] King, J. A., Tucker, K. W., Vogt, B. D., Weber, E. H., and Quan, C., 1999, ''Electrically and Thermally Conductive Nylon 6,6,'' Polym. Compos., **20**(5), pp. 643–654.

[3] Sherman, L. M., 2001, ''Plastics that Conduct Heat,'' Plast. Technol., **47**(6), pp. 52–57.

[4] Jin, J., Feng, M., Zhang, M., and Qiu, L., 1996, ''Experimental Investigation of a New Kind of Heat Exchanger Tube Bank,'' *Proceedings of the International Conference on Energy and Environment*, Begell House Inc, New York, NY, USA., pp. 417–421.

[5] Matos, R. S., Vargas, J. V. C., Laursen, T. A., and Saboya, F. E. M., 2001, ''Optimization Study and Heat Transfer Comparison of Staggered Circular and Elliptic Tubes in Forced Convection,'' Int. J. Heat Mass Transfer, **44**(20), pp. 53–61.

[6] Merker, G. P., and Hanke, H., 1986, ''Heat Transfer and Pressure Drop on the Shell-Side of Tube-Banks Having Oval-Shaped Tubes,'' ASME J. Heat Transfer, **29**(12), pp. 1903–1909.

[7] Merker, G. P., Hanke, H., and Baehr, M., 1987, ''Analogy Between Momentum and Heat-Transport in Cross-Flow Tube Banks with Oval-Shaped Tubes,'' Warme und Stoffubertragung (Thermo and Fluid Dynamics), **21**(2–3), pp. 95–102.

[8] Nishiyama, H., Ota, T., and Matsuno, T., 1988, ''Forced Convection Heat Transfer from Two Elliptic Cylinders in a Tandem Arrangement,'' Heat Transfer-Jpn. Res., **17**, pp. 19–31.

[9] Ota, T., Aiba, S., Tsuruta, T., and Kaga, M., 1983, ''Forced Convection Heat Transfer from an Elliptic Cylinder,'' Bull. JSME, **26**(212), pp. 262–267.

[10] Ota, T., and Nishiyama, H., 1984, ''Heat Transfer and Flow Around an Elliptic Cylinder,'' Int. J. Heat Mass Transfer, **27**(10), pp. 1771–1779.

[11] Ruth, E. K., 1983, ''Experiments on a Crossflow Heat Exchanger with Tubes of Lenticular Shape,'' ASME J. Heat Transfer, **105**, pp. 571–575.

[12] Rühlich, I., and Quack, H., 1998, ''New Regenerator Design for Cryocoolers,'' 17th International Cryogenic Engineering Conference, Bournemouth, England, pp. 291–294.

[13] Rühlich, I., and Quack, H., 1999, ''Investigations on Regenerative Heat Exchangers,'' 10th International Cryocooler Conference, Monterey, CA, pp. 265–274.

[14] Tauscher, R., 2000, ''Wärmeübergang Mit Turbulenzanregung Bei Niedrigen Reynoldszahlen,'' Vollständiger Abdruck der von der Fakultät für Maschinenwesen, Technischen Universität München.

[15] Badr, H. M., Dennis, S. C. R., and Kocabiyik, S., 2001, ''Numerical Simulation of the Unsteady Flow Over an Elliptic Cylinder at Different Orientations,'' Int. J. Numer. Methods Fluids, **37**(8), pp. 905–931.

[16] Jang, J., and Li, B., 1996, ''A Numerical Analysis of Two-Dimensional Laminar Flow Over an Elliptic Tube Bank,'' *Proceedings of the 4th International Symposium on Heat Transfer*, Beijing, China, pp. 547–552.

[17] Holland, M., 1976, ''Pressurized Member with Elliptic Median Line: Effect of Radial Thickness Function,'' J. Mech. Eng. Sci., **18**(5), pp. 245–253.

[18] Zukauskas, A., and Ziugzda, J., 1985, *Heat Transfer of a Cylinder in Crossflow*, Hemisphere Publishing Corporation, p. 150.

A Numerical Model Coupling the Heat and Gas Species' Transport Processes in a Tubular SOFC

Pei-Wen Li

Laura Schaefer

Minking K. Chyu
e-mail: mkchyu@engr.pitt.edu

Department of Mechanical Engineering,
University of Pittsburgh,
Pittsburgh, PA 15261, USA

A numerical model is presented in this work that computes the interdependent fields of flow, temperature, and mass fractions in a single tubular solid oxide fuel cell (SOFC). Fuel gas from a pre-reformer is considered to contain H_2, CO, CO_2, H_2O (vapor), and CH_4, so reforming and shift reactions in the cell are incorporated. The model uses mixture gas properties of the fuel and oxidant that are functions of the numerically obtained local temperature, pressure, and species concentrations, which are both interdependent and related to the chemical and electrochemical reactions. A discretized network circuit of a tubular SOFC was adopted to account for the Ohmic losses and Joule heating from the current passing around the circumference of the cell to the interconnect. In the iterative computation, local electrochemical parameters were simultaneously calculated based on the local parameters of pressure, temperature, and concentration of the species. Upon convergence of the computation, both local details and the overall performance of the fuel cell are obtained. These numerical results are important in order to better understand the operation of SOFCs. [DOI: 10.1115/1.1667528]

Keywords: Conjugate, Energy Conversion, Heat Transfer, Mass Transfer, Modeling

1 Introduction

Fuel cells have drawn an increasing amount of attention from the automotive and power industries. Compared to conventional combustion technologies, fuel cells have relatively small exergy losses [1]. While the efficiency of a conventional power system that employs a heat engine is fundamentally limited by the Carnot efficiency [2], fuel cells convert the chemical energy of fuel directly into electrical power, and thus can maintain a high energy conversion efficiency. However, there are numerous issues that still need to be addressed for the various types of fuel cells [3–5]. This paper will focus on the issues that impact the performance of a solid oxide fuel cell (SOFC).

To function efficiently, a SOFC needs to maintain a high operating temperature, which facilitates the ion conductance of the solid oxide electrolyte and the high electrochemical reaction kinetics. However, too high a temperature may lead to electrode sintering and a chemical reaction between the electrode and the electrolyte. Therefore, the temperature of a SOFC has to be controlled within a narrow range for safety and efficiency. Other issues that can improve a SOFC's performance include optimization of the fuel-oxidant ratio (or the stoichiometry of the oxidant) and the flow direction. Since optimizing these concerns and predicting the performance of a SOFC through experimental testing is expensive and labor-intensive, a numerical model must be developed.

There are several challenges in simulating both the overall and the detailed operation of a SOFC. The heat transfer, gas species' diffusion, chemical and electrochemical reactions, and conduction of electricity and ions are all interdependent. Additionally, fuel fed to a SOFC generally contains a mixture of H_2, CO, CO_2, H_2O, and CH_4, so the chemical reactions of fuel reforming and shift will occur with the electrochemical reaction within a SOFC. Therefore, the temperature field in a SOFC is a function of the heat generated from the chemical and electrochemical reaction as well as Joule heating (at high temperatures, radiation heat transfer can also occur). Furthermore, the ion and electricity conduction in the electrolyte and electrode is temperature dependent, and the concentrations of the reactants and products determine the partial pressures that affect the cell's electromotive force. The variation of the gas fractions and temperatures in the flow also affect the fluid properties and the flow field.

In 1992, Hirano et al. [6] evaluated the performance of a tubular SOFC. They assumed a laminar convection heat transfer coefficient and fully-developed flow, and obtained the mean temperature variation along the cell tube through a one-dimensional analysis. Also the temperature dependency of the electrolyte ion conductivity was ignored, as was the radiation heat transfer between the cold air-inducing tube and hot cell tube. Other investigations can be found in [7–12]; however, few studies have tried to employ a field solution to the flow, heat and mass transfer. They either assume a plug flow, ignoring the mass diffusion in the radial direction, or use a theoretical heat/mass transfer coefficient based on a fully developed laminar pipe flow to account for the heat and mass diffusion between the flow and the cell tube. In fact, the boundary conditions of the heat and mass transfer in a fuel cell are neither uniform over temperature/concentration nor uniform over the heat/mass flux. In order to better understand the detailed internal variations of temperature, concentration, and electricity conduction in a SOFC, this study has developed a model employing a field solution to the temperature and species' concentration based on the governing equations. The radiation heat transfer between the cold air-inducing tube and the hot cell tube has also been considered. Additionally, there is a relatively long current path around the circumference of the cell tube to the interconnect in a tubular SOFC [13,14]. This results in larger Ohmic losses and Joule heating, and increases the complexity of these calculations. In this work, a network circuit model [15,16] was used to solve the electrical potentials in the anode and cathode, and thereby to find the cell output voltage and to account for the Ohmic losses and Joule heating.

2 Problem Formulation: The Fundamentals of Reforming, Shift, and Electrochemical Reactions

Figure 1 is a schematic view of the cross section of a typical tubular SOFC, in which a laminated structure composed of the cathode, electrolyte and anode is fabricated around a support tube

Contributed by the Heat Transfer Division for publication in the JOURNAL OF HEAT TRANSFER. Manuscript received by the Heat Transfer Division January 31, 2003; revision received December 23, 2003. Associate Editor: B. Farouk.

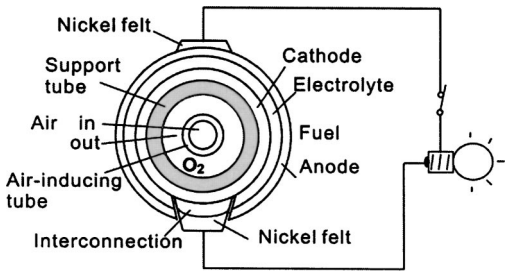

Fig. 1 Cross-sectional view of a tubular SOFC system

in the form of a thin cylindrical shell with one end closed. A typical configuration of the flow streams of fuel and oxidant in a tubular SOFC is shown in Fig. 2. Air is supplied through a concentric air-inducing tube inserted inside the tubular cell from its open end. Oxygen in the air diffuses across the porous support tube and is ionized at the cathode (air electrode). The produced oxide ion is conducted through the electrolyte toward the anode (fuel electrode) and is de-ionized at the anode-electrolyte interface through a chemical reaction with the fuel, which diffuses inward from the core of the fuel flow passage. Chemical products formed in the reaction diffuse across the porous anode, and then into the fuel flow and are exhausted to the outside. Electrons released at the anode move back to the cathode as an electric current if the cathode and anode are connected by an external circuit. An electric current is thus induced between the cathode and the anode, and electrical work is produced in the external circuit.

If methane-reformed fuel gas is supplied, it will contain a mixture of H_2, H_2O, CO_2, CO, and CH_4. The air that is supplied to the cathode side contains O_2 and N_2. In this model, it is assumed that the reforming and shift reaction on the anode side is in equilibrium, and that the reaction of H_2 and O_2 is responsible for the electromotive force, as in Onuma et al. [17]. The assumption of equilibrium of the reforming and shift reaction is quite commonly utilized in SOFC studies, as seen in Costamagna et al. [11], Aguiar et al. [12], and Massardo and Lubelli [18]. In fact, Achenbach and Riensche [19] have reported that the reforming reaction is endothermic and can almost attain equilibrium. The shift reaction can also be assumed to be in equilibrium for a SOFC; in the experimental study of Peters et al. [20], it was found that the CO concentration is only slightly higher than that given by the equilibrium composition at the anode. Therefore, the reactions inside the present fuel cell are [18,21]

$$\overset{\bar{x}}{\text{CH}_4 + \text{H}_2\text{O} \leftrightarrow \text{CO} + 3\text{H}_2} \quad \text{(reforming)} \tag{1}$$

$$\overset{\bar{y}}{\text{CO} + \text{H}_2\text{O} \leftrightarrow \text{CO}_2 + \text{H}_2} \quad \text{(shift)} \tag{2}$$

$$\overset{\bar{z}}{\text{H}_2 + 1/2\text{O}_2 \leftrightarrow \text{H}_2\text{O}} \quad \text{(electrochemical)} \tag{3}$$

The potential between the cathode and anode is expressed by Nernst equation [7]

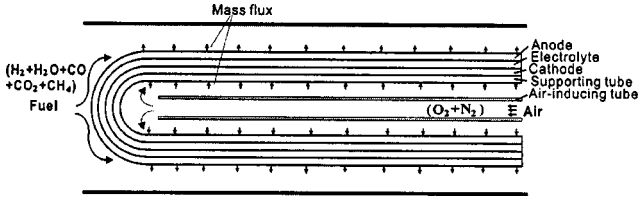

Fig. 2 Arrangement of fuel and oxidant streams in a single tubular SOFC

$$E = \frac{-\Delta G_0}{2F} + \frac{RT}{2F}\ln\left(\frac{P_{H_2}P_{O_2}^{0.5}}{P_{H_2O}}\right) \tag{4}$$

where ΔG_0 is the standard Gibbs' free energy change of Eq. (3) at temperature T, P is the ratio of the local partial pressure over the standard state pressure of 1.0 atm for reactants and products at the electrolyte/electrode interfaces, F is Faraday's constant, and R is the gas constant.

The equilibrium states as a function of temperature are

$$K_{PR} = \frac{P_{H_2}^3 P_{CO}}{P_{CH_4}P_{H_2O}} = \exp\left(-\frac{\Delta G_0^{\text{reforming}}}{RT}\right) \tag{5}$$

$$K_{PR} = \frac{P_{CO_2}P_{H_2}}{P_{CO}P_{H_2O}} = \exp\left(-\frac{\Delta G_0^{\text{shift}}}{RT}\right) \tag{6}$$

Equilibrium constants must be utilized to evaluate the molar variations of the gas species on the anode side. In the equations given below, the mole numbers are represented by the corresponding chemical symbols, and the reaction-consumed mole numbers of CH_4, CO, and H_2 are represented by $\bar{x}$, $\bar{y}$, and $\bar{z}$, respectively. The variations of the species in the fuel channel are

$$\text{CH}_4^{\text{out}} = \text{CH}_4^{\text{in}} - \bar{x} \tag{7}$$

$$\text{CO}^{\text{out}} = \text{CO}^{\text{in}} + \bar{x} - \bar{y} \tag{8}$$

$$\text{CO}_2^{\text{out}} = \text{CO}_2^{\text{in}} + \bar{y} \tag{9}$$

$$\text{H}_2^{\text{out}} = \text{H}_2^{\text{in}} + 3\bar{x} + \bar{y} - \bar{z} \tag{10}$$

$$\text{H}_2\text{O}^{\text{out}} = \text{H}_2\text{O}^{\text{in}} - \bar{x} - \bar{y} + \bar{z} \tag{11}$$

The fuel mole numbers in the bulk flow between the inlet and outlet of the section of interest can then be correlated as

$$MF^{\text{out}} = MF^{\text{in}} + 2\bar{x} \tag{12}$$

and the equilibrium conditions can be rewritten

$$K_{PR} = \frac{\left(\dfrac{\text{CO}^{\text{in}} + \bar{x} - \bar{y}}{\text{MF}^{\text{in}} + 2\bar{x}}\right)\left(\dfrac{\text{H}_2^{\text{in}} + 3\bar{x} + \bar{y} - \bar{z}}{MF^{\text{in}} + 2\bar{x}}\right)^3 P^2}{\left(\dfrac{\text{CH}_4^{\text{in}} - \bar{x}}{MF^{\text{in}} + 2\bar{x}}\right)\left(\dfrac{\text{H}_2\text{O}^{\text{in}} - \bar{x} - \bar{y} + \bar{z}}{MF^{\text{in}} + 2\bar{x}}\right)} \tag{13}$$

$$K_{PS} = \frac{\left(\dfrac{\text{H}_2^{\text{in}} + 3\bar{x} + \bar{y} - \bar{z}}{MF^{\text{in}} + 2\bar{x}}\right)\left(\dfrac{\text{CO}_2^{\text{in}} + \bar{y}}{MF^{\text{in}} + 2\bar{x}}\right)}{\left(\dfrac{\text{CO}^{\text{in}} + \bar{x} - \bar{y}}{MF^{\text{in}} + 2\bar{x}}\right)\left(\dfrac{\text{H}_2\text{O}^{\text{in}} - \bar{x} - \bar{y} + \bar{z}}{MF^{\text{in}} + 2\bar{x}}\right)} \tag{14}$$

For this modeling work, the known conditions are flow rates, temperatures, species' compositions for both the fuel and air at the fuel cell inlet, and the fuel utilization factor (which is related to the total output current from the cell). The local concentrations in both the fuel and air streams are based on the variations of the gas species (for example, $\bar{x}$, $\bar{y}$, $\bar{z}$, in the fuel flow), which can be used to obtain the local partial pressures, electromotive forces, and heat generation due to the reactions and Joule heating. Additionally, the consumption mole numbers for hydrogen (represented by $\bar{z}$) and oxygen can be correlated to the ion-carrying charge transfer rate across over the area of the electrolyte layer by

$$\bar{z} = I/(2F) \tag{15}$$

$$\overline{zo} = I/(4F) \tag{16}$$

3 Steady-State Flow and Heat/Mass Transfer

Several important features of the flow and heat/mass transfer problem in a SOFC must be considered. First, the fuel and oxidant

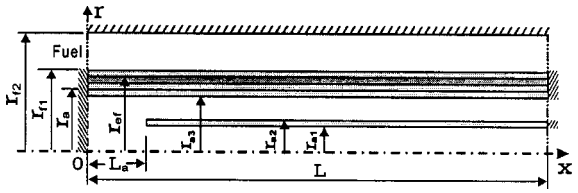

Fig. 3 Conjugate computational domain

in the SOFC are gas mixtures that vary due to the electrochemical reaction. This can be accounted for by using incompressible flow momentum equations with variable properties in solving the velocity fields. Second, there is both electrochemical reaction heating and Joule heating due to the conduction of ions and electrons in the cell components. These types of heating can affect the temperature fields of both the fuel and air flows, and thus the conjugation of the flow streams with the cell components is necessary. Third, the consumption and/or production of mass in the fuel channel and air channel needs to be considered. Fourth, the determination of the heat and mass consumption/generation due to the electrochemical reactions and Joule effect must rely on the parameters of temperature, pressure, and concentrations. Each of the above processes is interdependent. Finally, the temperature difference between the air-inducing tube and the support tube might be sufficiently high that radiation heat exchange occurs between them.

To couple the flow and heat/mass transfer fields, a two-dimensional axi-symmetric computational domain is created, as shown in Fig. 3. For convenience, the shape of the closed end of the cell tube is simplified as flat in this model.

3.1 Governing Equations. The flow velocity in both the fuel channel and air channel for the fuel cell is rather low. However, due to the variation of the species' concentrations, the fluid properties may have large fluctuations. Two assumptions are adopted for the equations and computational domain. First, the energy diffusion driven by the concentration gradient of the gas species is very small, and thus neglected [22,23]. Secondly, the ceramic porous support tube, anode, and cathode all have small thicknesses and can be treated as solid. Due to the electrochemical reaction, the gas reactants and products diffuse across the porous layers, which produces mass fluxes. However, the mass transfer is treated as a mass flux in or outward from the interface [6,24]. This treatment can avoid the complexities of the mass transfer in the thin porous layers of the support tube and electrodes [25]. It should be noted that the reduction of the electromotive force caused by the mass diffusion in the porous layers is considered properly in later sections [6]. Therefore, the governing equations are

$$\frac{\partial(\rho u)}{\partial x}+\frac{1}{r}\frac{\partial(r\rho v)}{\partial r}=0 \tag{17}$$

$$\frac{\partial(\rho uu)}{\partial x}+\frac{1}{r}\frac{\partial(r\rho vu)}{\partial r}=-\frac{\partial p}{\partial x}+\frac{\partial}{\partial x}\left(\mu\frac{\partial u}{\partial x}\right)+\frac{1}{r}\frac{\partial}{\partial r}\left(r\mu\frac{\partial u}{\partial r}\right)+\frac{\partial}{\partial x}\left(\mu\frac{\partial u}{\partial x}\right)+\frac{1}{r}\frac{\partial}{\partial r}\left(r\mu\frac{\partial v}{\partial x}\right) \tag{18}$$

$$\frac{\partial(\rho uv)}{\partial x}+\frac{1}{r}\frac{\partial(r\rho vv)}{\partial r}=-\frac{\partial p}{\partial r}+\frac{\partial}{\partial x}\left(\mu\frac{\partial v}{\partial x}\right)+\frac{1}{r}\frac{\partial}{\partial r}\left(r\mu\frac{\partial v}{\partial r}\right)+\frac{\partial}{\partial x}\left(\mu\frac{\partial u}{\partial r}\right)+\frac{1}{r}\frac{\partial}{\partial r}\left(r\mu\frac{\partial v}{\partial r}\right)-\frac{2\mu v}{r^2} \tag{19}$$

$$\frac{\partial(\rho CpuT)}{\partial x}+\frac{1}{r}\frac{\partial(r\rho CpvT)}{\partial r}=\frac{\partial}{\partial x}\left(\lambda\frac{\partial T}{\partial x}\right)+\frac{1}{r}\frac{\partial}{\partial r}\left(r\lambda\frac{\partial T}{\partial r}\right)+\dot{q} \tag{20}$$

$$\frac{\partial(\rho uY_j)}{\partial x}+\frac{1}{r}\frac{\partial(r\rho vY_j)}{\partial r}=\frac{\partial}{\partial x}\left(\rho D_{j,m}\frac{\partial Y_j}{\partial x}\right)+\frac{1}{r}\frac{\partial}{\partial r}\left(r\rho D_{j,m}\frac{\partial Y_j}{\partial r}\right) \tag{21}$$

The thermophysical properties of enthalpy, Gibbs free energy, and the transport properties for a single gas are taken from the standard definitions of [26,27]. Also, equations from [27] are adopted for calculating the properties of gas mixtures.

3.2 Boundary Conditions. There are two kinds of boundary conditions for this problem. One type is for the outermost outline of the overall computational domain, and the other is for the heat generation and mass fluxes of the interior solid region and solid/fluid interfacial boundaries (which are more influential for this problem). The general boundary conditions for the outline of the computational domain are

$$v=0,\quad \partial u/\partial r=0,\quad \partial T/\partial r=0,\quad \partial Y_j/\partial r=0\quad \text{at } r=0 \tag{22}$$

$$u=0,\quad v=0,\quad \partial T/\partial r=0,\quad \partial Y_j/\partial r=0\quad \text{at } r=r_{f2} \tag{23}$$

$$u=0,\quad v=0,\quad \partial T/\partial x=0,$$

$$\partial Y_j/\partial x=0\quad \text{at } x=0\quad \text{and } 0\leqslant r\leqslant r_{f1} \tag{24}$$

$$u=u_f=\left(\frac{RT_f^{\text{in}}}{P_f^{\text{in}}}\right)\left(\frac{I_0}{2FU_{H_2}C_{H_2}^{\text{in}}}\right)\Big/\left[\pi(r_{f2}^2-r_{f1}^2)\right],$$

$$v=0\quad \text{at } x=0\quad \text{and } r_{f1}<r<r_{f2} \tag{25}$$

$$u=u_{\text{air}}=\left(\frac{RT_{\text{air}}^{\text{in}}}{P_{\text{air}}^{\text{in}}}\right)\left(\frac{I_0}{4FU_{O_2}C_{O_2}^{\text{in}}}\right)\Big/(\pi r_{a1}^2),$$

$$v=0\quad \text{at } x=L\quad \text{and}\quad 0\leqslant r<r_{a1} \tag{26}$$

$$u=0,\quad v=0,\quad \partial T/\partial x=0,$$

$$\partial Y_j/\partial x=0\quad \text{at } x=L\quad \text{and}\quad r_{a1}\leqslant r\leqslant r_{a2} \tag{27}$$

$$\frac{\partial u}{\partial x}=0,\quad v=0,\quad \partial T/\partial x=0,$$

$$\partial Y_j/\partial x=0\quad \text{at } x=L\quad \text{and}\quad r_{a2}<r<r_{a3} \tag{28}$$

$$u=0,\quad v=0,\quad \partial T/\partial x=0,$$

$$\partial Y_j/\partial x=0\quad \text{at } x=L\quad \text{and}\quad r_{a3}\leqslant r\leqslant r_{f1} \tag{29}$$

$$\frac{\partial u}{\partial x}=0,\quad v=0,\quad \partial T/\partial x=0,$$

$$\partial Y_j/\partial x=0\quad \text{at } x=L\quad \text{and}\quad r_{f1}<r<r_{f2} \tag{30}$$

I_0 is the total output electric current of the fuel cell, which is correlated to the cell electric current density, $\dot{I}_0$, by

$$I_0=2L\cdot\pi r_{ef}\cdot\dot{I}_0 \tag{31}$$

3.3 Heat Generation and Mass Fluxes in the Interior Solid Region and Solid/Fluid Interfaces. Heat generation in the interior solid region of the computational domain, as denoted by $\dot{q}$ in Eq. (20), is due to the Joule effect and the entropy change of the reforming, shift, and electrochemical reactions. These heats are related to the local current conduction and charge transfer rate I (in amperes) across the electrolyte. Therefore, an analysis of the electrical conduction in the cell components is necessary.

3.3.1 Analyzing the Ion and Electricity Conduction. As has been mentioned in Eqs. (15) and (16), characterization of the ion

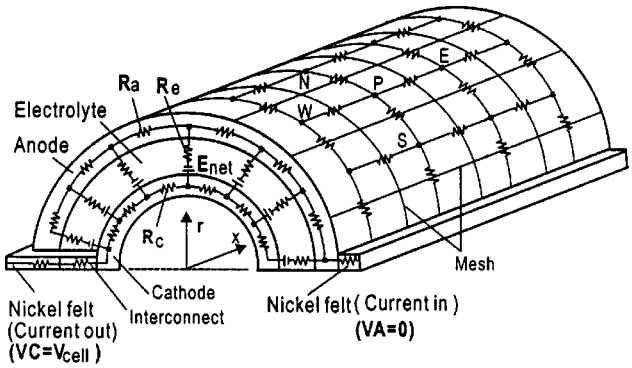

Fig. 4 Network circuit pertaining to half of a tubular SOFC tube (all layers of the electrode and electrolyte have been magnified)

and electricity conduction is required to determine the heat-production and mass transfer rates, so the current paths that comprise the network circuit must be analyzed [28]. For a tubular fuel cell, the current must flow peripherally in the electrode layers to reach the nickel felt collector. This can cause Ohmic losses and yield more Joule heating [15,16]. Since the current flow is symmetric from the inlet collector to the outlet collector, only half of the cell tube is analyzed. Discretization of half of the cell tube as a network circuit is shown in Fig. 4.

The local ion-carrying charge transfer rate across the electrolyte from the anode to cathode must be known to calculate the consumption rate of the hydrogen and oxygen in Eqs. (15) and (16). The ion transfer across the electrolyte, and the electricity conduction parallel in the cathode and anode, can produce Joule heating. Based on the available local electromotive forces (E_{net}), the model will predict the electrical potential difference, which is also the cell output voltage. The known conditions are: the total current across the electrolyte layers, which is given by the prescribed flow rate of fuel and the utilization factor; and the local E_{net} in Fig. 4, which is expressed by

$$E_{\text{net}}^{P}=E^{P}-\eta_{\text{act}}^{P} \tag{32}$$

where the electromotive force E is a function of the local temperatures and partial pressures. The η_{act} is a reduction of the electromotive force caused by the activation polarization and the mass transfer resistance across the porous layers of the support tube and electrodes. Chan et al. [29] have conducted an analysis of the Butler-Volmer equation for the activation polarization in SOFCs, and have concluded that when the activation polarization is less than $0.1\,V$ it is proportional to the current density. The relation and the proportionality constant suggested by Hirano et al. [6] are used

$$\eta_{\text{act}}^{P}=\frac{I_P}{\Delta A}\left(R_{\text{act}}^{\text{anode}}+R_{\text{act}}^{\text{cathode}}\right) \tag{33}$$

where $R_{\text{act}}^{\text{anode}}$ and $R_{\text{act}}^{\text{cathode}}$ are 90 and 200 $\text{m}\Omega\cdot\text{cm}^2$, respectively, and ΔA is the unit area of the electrolyte layer that I acts upon. If the tubular SOFC is cathode supported, in which the support tube is removed and a thicker cathode is used, the $R_{\text{act}}^{\text{anode}}$ and $R_{\text{act}}^{\text{cathode}}$ will be slightly smaller than the above values. Since the flow, temperature, and concentration fields are assumed to be axisymmetrical, E, η_{act} and E_{net} are circumferentially uniform.

Applying Kirchhoff's current law, the potentials at grid P and its four neighboring points can be correlated for the cathode (VC) and anode (VA) layers:

$$\frac{VA_E-VA_P}{R_{aE}}+\frac{VA_W-VA_P}{R_{aW}}+\frac{VA_N-VA_P}{R_{aN}}+\frac{VA_S-VA_P}{R_{aS}}+\frac{VC_P-VA_P-E_{\text{net}P}}{R_{eP}}=0 \tag{34}$$

$$\frac{VC_E-VC_P}{R_{cE}}+\frac{VC_W-VC_P}{R_{cW}}+\frac{VC_N-VC_P}{R_{cN}}+\frac{VC_S-VC_P}{R_{cS}}+\frac{VA_P-VC_P+E_{\text{net}P}}{R_{eP}}=0 \tag{35}$$

R_a, R_c, and R_e are discretized resistances in the layers and determined from the resistivity ρ_e, which is constant for the cathode and anode, but is temperature-dependent for the electrolyte, as is given later in tables for the material properties. R_a and R_c are located in the anode and cathode layers, and R_e is located in the electrolyte. It is easy to see from the network circuit that a larger cell tube diameter will result in a longer current pathway from the current inlet to the outlet, and thus will result in a higher Ohmic loss and Joule heating rate. To set an operating condition, the total charge transfer rate across the electrolyte is given as a prescribed external parameter. Once the values of E_{net} and the resistances in the electrolyte and electrode are determined for the network circuit, the local charge transfer rate I across the electrolyte can be obtained through iterative computation, and then the Joule heating can be found. Two additional important points are needed to solve the local current distribution. First, it is supposed that uniform electric potentials exist at the two nickel felt interfaces. Second, either the total charge transfer rate across the electrolyte or the potential difference at the two nickel felt interfaces is prescribed. The first point can be shown to be a reasonable assumption since the nickel felt has a very high conductivity, which can level the potentials. The second point is a requirement for the simulation, as discussed earlier in this paper. The sum of the charge transfer rate can be specified from the average current density of the cell, and the potential difference at the two nickel felt interfaces is the cell voltage. Either average current density or output voltage must be given in order to predict the other in the simulation.

3.3.2 Correlating the Electrical Parameters With the Heat Generation and Mass Flux. Local electrical potentials obtained from the above analysis can then be used to calculate the local ion-carrying charge transfer rate across the electrolyte, and the heat generation and mass transfer fluxes can also be obtained. Correlations for these parameters for one control volume are

$$I_P=\frac{(VA_P-VC_P+E_{\text{net}P})}{R_{eP}} \tag{36}$$

$$Q_{Oh}^{P}=I_P^2\cdot R_{eP} \tag{37}$$

$$Q_R^{P}=(\Delta G-\Delta H)\cdot I_P/(2F) \tag{38}$$

$$Q_{aP}=0.5\left[\frac{(VA_E-VA_P)^2}{R_{aE}}+\frac{(VA_W-VA_P)^2}{R_{aW}}+\frac{(VA_N-VA_P)^2}{R_{aN}}+\frac{(VA_S-VA_P)^2}{R_{aS}}\right] \tag{39}$$

$$Q_{cP}=0.5\left[\frac{(VC_E-VC_P)^2}{R_{cE}}+\frac{(VC_W-VC_P)^2}{R_{cW}}+\frac{(VC_N-VC_P)^2}{R_{cN}}+\frac{(VC_S-VC_P)^2}{R_{cS}}\right] \tag{40}$$

where ΔG and ΔH are the changes in the Gibbs free energy and enthalpy of the electrochemical reaction (Eq. (3)). The Joule heating is the heat generated in the P-control volume in the cathode, electrolyte, and anode layers. Dividing the Joule heating by the P-control volume results in a volumetric heat source. The electro-

chemical reaction heat is, however, located at the anode/electrolyte interface ($r=r_{ef}$) and should be treated as a surface heat source.

The mass variations of the hydrogen and oxygen in the electrochemical reaction at point P are correlated to I_P as expressed by Eqs. (15) and (16). For axi-symmetric flow, temperature, and concentration fields, the boundary conditions of the mass fluxes and heat sources are circumferentially uniform. The current and heat generation equations can therefore be integrated circumferentially at one axial position and averaged. For example, to find the current density at one axial position, circumferential integration for I_P at x is made for the Δx section and the local axial current density is obtained

$$I_{\Delta x}=2\cdot\sum_{\theta=0}^{\pi} I_P(x,\theta);\quad \dot{I}_x=I_{\Delta x}/(2\pi r_{ef}\Delta x) \tag{41}$$

For the current, an average molar consumption rate of hydrogen in the Δx section can be found

$$\overline{z}_{\Delta x}=\left(\frac{I_{\Delta x}}{2F}\right) \tag{42}$$

Other species' variations can be calculated by solving Eqs. (13) and (14) for a section in the streamwise direction from x to $x+\Delta x$. The reforming and shifting reactions take place at the anode surface, so the species' variations can be treated as mass fluxes going in to or out from the anode surface. The mass fluxes of CO, CO_2, CH_4, and H_2O on the anode surface at position x can be further correlated as

$$\dot{m}^x_{H_2}=M_{H_2}\frac{1}{2\pi r_{f1}\Delta x}(3\overline{x}_{\Delta x}+\overline{y}_{\Delta x}-\overline{z}_{\Delta x}) \tag{43}$$

$$\dot{m}^x_{CO}=M_{CO}\frac{1}{2\pi r_{f1}\Delta x}(\overline{x}_{\Delta x}-\overline{y}_{\Delta x}) \tag{44}$$

$$\dot{m}^x_{CO_2}=M_{CO_2}\frac{1}{2\pi r_{f1}\Delta x}(\overline{y}_{\Delta x}) \tag{45}$$

$$\dot{m}^x_{H_2O}=M_{H_2O}\frac{1}{2\pi r_{f1}\Delta x}(\overline{z}_{\Delta x}-\overline{x}_{\Delta x}-\overline{y}_{\Delta x}) \tag{46}$$

$$\dot{m}^x_{CH_4}=M_{CH_4}\frac{1}{2\pi r_{f1}\Delta x}(-\overline{x}_{\Delta x}) \tag{47}$$

The chemical enthalpy from the reforming and shift reactions is treated as a function of the heat fluxes located at the anode surface

$$q_x=\dot{m}^x_{CH_4}\Delta H^{\text{reforming}}+\dot{m}^x_{CO}\Delta H^{\text{shift}} \tag{48}$$

The mass fluxes of O_2 on the support tube at position x are

$$\dot{m}^x_{O_2}=M_{O_2}\frac{1}{2\pi r_{a3}\Delta x}\left(\frac{I_{\Delta x}}{4F}\right) \tag{49}$$

Once the boundary mass fluxes at the solid/fluid interfaces are found, the mass fractions at the interface are calculated [30,31]

$$\dot{m}_j=-D_{j,m}\rho\frac{\partial Y_j}{\partial r}+\rho Y_j\cdot v_x^{\text{surface}} \tag{50}$$

where the mass flux, $\dot{m}_j$, is determined according to the direction and the surface area upon which the mass transfer rate m_j acts. The velocity v_x^{surface} in Eq. (50) is the local convection velocity (towards the solid surface) induced by the local mass flux perpendicular to the fluid/solid interface, and is a function of the species mass transfer fluxes at the surface

$$v_x^{\text{surface}}=\left(\sum \dot{m}_j\right)/\rho \tag{51}$$

3.4 Numerical Procedure. The transport equations (Eqs. (17)–(21)) must be solved in conjunction with the above-listed boundary conditions and the electric conduction network in order to determine the local current across the electrolyte and the local Joule heating. Finite difference equations are obtained by volume integration of the transport equations over the discretized control volumes. Details concerning the method for deriving the finite difference equations and inclusion of the boundary conditions can be found in [32,33]. In a similar manner, the fuel cell layers in half of the tube are discretized as in Fig. 4 so that the finite difference equations for the current conduction can be obtained. Through solution of the difference equations, the current conduction and heat generation are circumferentially averaged to provide the boundary conditions for the axi-symmetrical transport equations.

The inner surface of the supporting tube and the outer surface of the air-inducing tube might have radiation heat exchange. The method of Beckermann et al. [34] is used to treat this problem. In this method, a heat source term is introduced in the discretized energy equations [32] in order to consider the radiation exchanged heat flux in the computational domain. To accomplish this, the length of the cell tube and the air-inducing tube that involve radiation heat exchange is divided into four axial sections. Since the length/interval ratio of each section of the two tubes is large, the radiation heat exchange is approximated to be a problem in two-surface enclosure. The average temperature of the surface is used to calculate the radiation heat exchange.

The numerical procedure used to solve the finite difference transport equations is based on the SIMPLE algorithm [32]. For this particular problem, the overall numerical procedure was designed as follows:

1. Determine the local EMFs and the resistances in the cathode, anode, and electrolyte using the latest available values of the pressure, temperature, and concentrations.
2. Assume an output voltage for the SOFC. Solve the discretized equations for electrical potential in the cathode and anode to obtain the electrical output and the local current distributions, and to determine the heat sources and mass transfer fluxes. An iterative assumption of output voltage is conducted to ensure matching of the total current integrated from the local charge transfer rate.
3. Solve the momentum, energy, and mass conservation equations to update the local distributions of pressure, temperature, and mass fractions.
4. Check the convergence of the electrical output, local temperature, mass fractions, and velocities. If convergence is not achieved, update the properties based on the newly obtained distributions of pressure, temperature, and concentrations, and then return to step (1).

4 Application

4.1 Geometric Dimensions and Operating Conditions for a Tubular SOFC. The dimensions of a single SOFC system are given in Table 1, the supplied fuel and air conditions are listed in Table 2, and the properties of the cell materials are listed in Table 3. The utilization percentages of hydrogen and oxygen are given as 85 percent and 20 percent, respectively. A mesh system of 600×64 was arranged in the axial and radial directions for the computation domain as given in Fig. 3, which ensured grid-independent results. A series of conditions for the cell current density can be investigated. Based on prescribed parameters such as current densities, utilization percentages of oxygen and fuel gases, and the gas thermal conditions, the inlet flow rates of the fuel and air can be determined from the ideal gas state equation

$$G_f=\left(\frac{RT_f^{\text{in}}}{P_f^{\text{in}}}\right)\left(\frac{\dot{I}_0\cdot 2\pi r_{ef}\cdot L}{2FU_{H_2}C_{H_2}^{\text{in}}}\right) \tag{52}$$

Table 1 Geometric dimensions

Thickness of cell layers	
Air-inducing tube	500 μm
Supporting tube	1500 μm
Cathode	1000 μm
Electrolyte	50 μm
Anode	150 μm
Diameters	
Inner side of air-inducing tube ($2\times r_{a1}$)	8.0 mm
Inner side of supporting tube ($2\times r_{a3}$)	13.8 mm
Outer side of anode ($2\times r_{f1}$)	19.2 mm
Outer boundary of fuel annulus ($2\times r_{f2}$)	29.2 mm
Tube lengths	
Cell unit (L)	500 mm
Air-inducing tube ($L-L_a$)	450 mm

$$G_{\text{air}}=\left(\frac{RT_{\text{air}}^{\text{in}}}{P_{\text{air}}^{\text{in}}}\right)\left(\frac{\dot{I}_0\cdot 2\pi r_{ef}\cdot L}{4FU_{O_2}C_{O_2}^{\text{in}}}\right) \tag{53}$$

4.2 Predicted Overall Performance of a Fuel Cell. The numerical prediction of the cell voltage versus the average current density is shown in Fig. 5. It is typical for cell voltage to decrease with increasing current density. It is known that the internal ohmic loss and activation polarization are both proportional to the current density. Thus, when the ohmic loss and activation polarization increase against current density, the cell output voltage will decrease accordingly. From Eqs. (15)–(16), it is known that the fuel consumption is proportional to the current density. Therefore, a high current density is an indication of large fuel consumption, which corresponds to a lower output voltage. This implies that a light power load results in a high efficiency for a fuel cell. Heat engines, however, prefer a heavy power load in order to operate at high efficiencies. This may support the idea of a hybrid power system [35,36] of a gas turbine and SOFC, where both components of the system can work at the most efficient condition.

Several experimental data from references [3] and [37] on cell output voltage versus current density are referenced in Fig. 5. They were obtained from SOFCs at cell dimensions and experimental conditions not exactly the same, but quite close to what was adopted in the present study. Therefore, the numerical predicted cell voltages fall close to the experimental data. This is an indication that the numerical model and computation indeed works well to predict the overall performance of a tubular SOFC.

Table 2 Inlet species and their mass fractions

Fuel	(900°C; 1.013×10^5 Pa)
H_2	0.5915
H_2O	0.0273
CO_2	0.0014
CO	0.3550
CH_4	0.0248
Air	(600°C; 1.013×10^5 Pa)
O_2	0.233
N_2	0.767

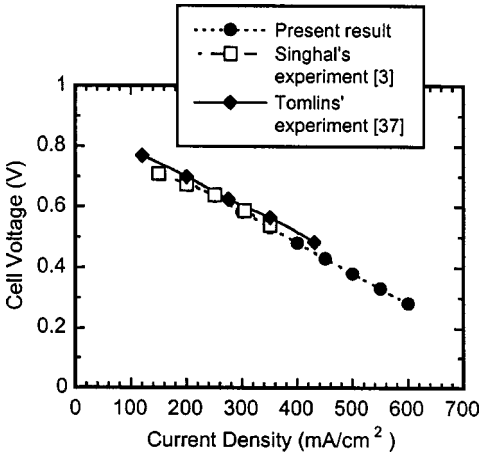

Fig. 5 Cell voltage versus current density

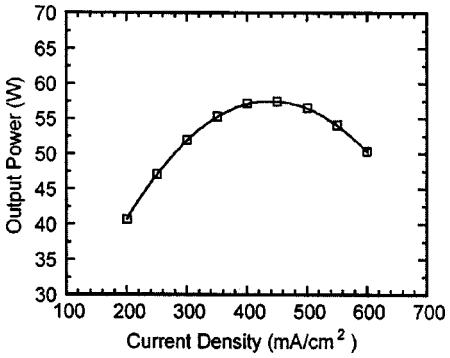

Fig. 6 Cell power versus current density

However, from the numerical computation one can obtain more detailed information on the flow velocities, temperature and mass fractions of the gas species for both the fuel and air streams, which will be given in the following sections.

From the voltage-current density curve, the relationship of power to current density can be obtained. As seen in Fig. 6, the cell output electrical power increases at first and then decreases with an increase in current density. Therefore, it is impossible to improve the electrical power further by increasing the current density beyond the point where it reaches a peak (for example, 450 mA/cm^2 in the present study). This feature may lead to identification of a certain current density as the maximum operational current density. Finding the maximum operational current density through numerical simulation should be of great significance.

4.3 Local Distributions of the Electrical Parameters and Temperature Fields. The local distribution of the electromotive force and current density are examined in this section. Figure 7 shows the local electromotive force with the activation polarization already subtracted. It can be seen that the electromotive force decreases from a higher value upstream to a lower value at the end

Table 3 Properties of solid materials in SOFC system

	λ [W/m° C)]	ρ_e (Ω cm)	Emissivity
Cathode	11.0	0.0186	···
Anode	6.0	0.0014	···
Electrolyte	2.7	$0.3685+0.002838\exp(10300/T)$	···
Supporting tube	1.1	···	0.9
Air-inducing tube	1.1	···	0.9

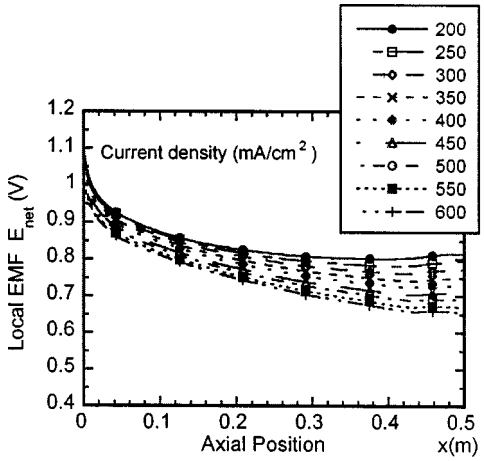

Fig. 7 Local distribution of electromotive force

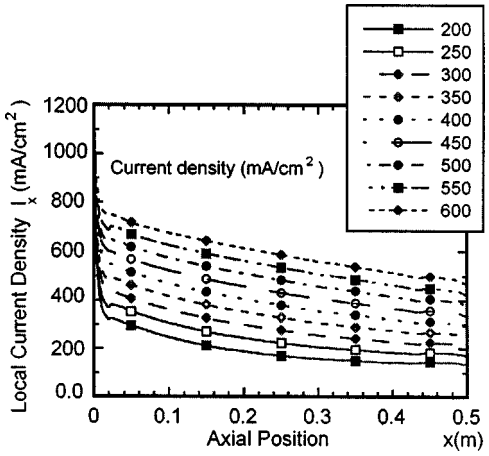

Fig. 8 Local distribution of current density

of the SOFC tube. This reflects the fact that depletion of fuel and oxidant along the stream has a significant effect on the local distribution of the electromotive force. In the downstream region, the electromotive force decreases dramatically because of the decreased reactant concentration and increased product concentration. The differences in voltage levels between the different curves reflect the significant reduction of the potentials due to an increase in activation polarization when current density increases.

In a similar manner, the peripheral averaged local current density versus axial distance can been seen in Fig. 8. It is clearly shown in this figure that a high local electromotive force can lead to a high local current density. Because heat generation is proportional to the current density, a high local current density will result in a high heating rate. It can therefore be deduced that heat generation in the upstream region of the fuel cell is higher than in the downstream region.

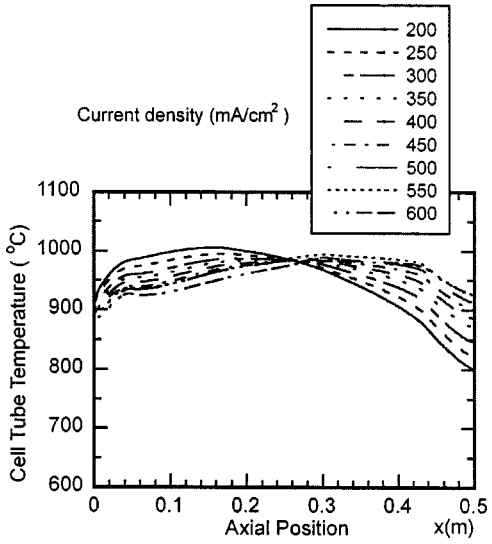

Fig. 9 Cell tube temperature distributions for a series of current densities

An important concern for SOFCs is the temperature field, or the hot spot in the cell components. However, it is rather difficult to measure the temperature in a SOFC. Hirano et al. [6] reported only three data tested for a SOFC that used fuel without methane and the reforming reaction. The present authors have simulated the same SOFC tested by Hirano et al. [6] in another investigation [38] and have obtained very good agreement with the experimental data. In the present study, simulated results for the cell tube temperatures are given in Fig. 9 for cases of differing current density. The position of the hot spots varies significantly with the current density. At a low current density, a hot spot occurs in the upstream area. With an increase in current density, the hot spot moves to the downstream area. To understand this feature of the temperature distribution in a cell tube, it is necessary to examine the heat transfer conditions in a tubular SOFC. The closed end of the cell tube receives an impingement of the fresh air from the air-inducing tube. For a high current density case, the air flow rate is accordingly high, and thus, the closed end could be cooled significantly, although the heat generation in this region is stronger than in the downstream region. However, for the low current density case, the fresh air impingement on the closed end of the cell tube is rather weak, and therefore high temperatures occur in the upstream region. The results of the temperature distributions also indicate that the cell temperature distribution along the tube is not simply affected by the heat generation, but also by the stream heating and cooling, which is why the hot spot position varies with the current density.

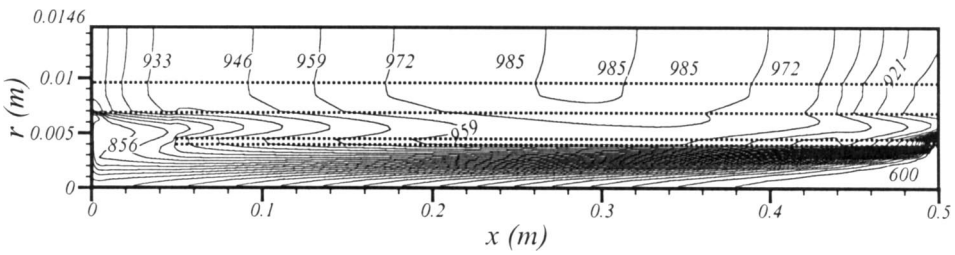

Fig. 10 Temperature (°C) contours in the whole computational domain (i_0=450 mA/cm^2; the boundaries of the cell tube and air-inducing tube are indicated by dotted lines)

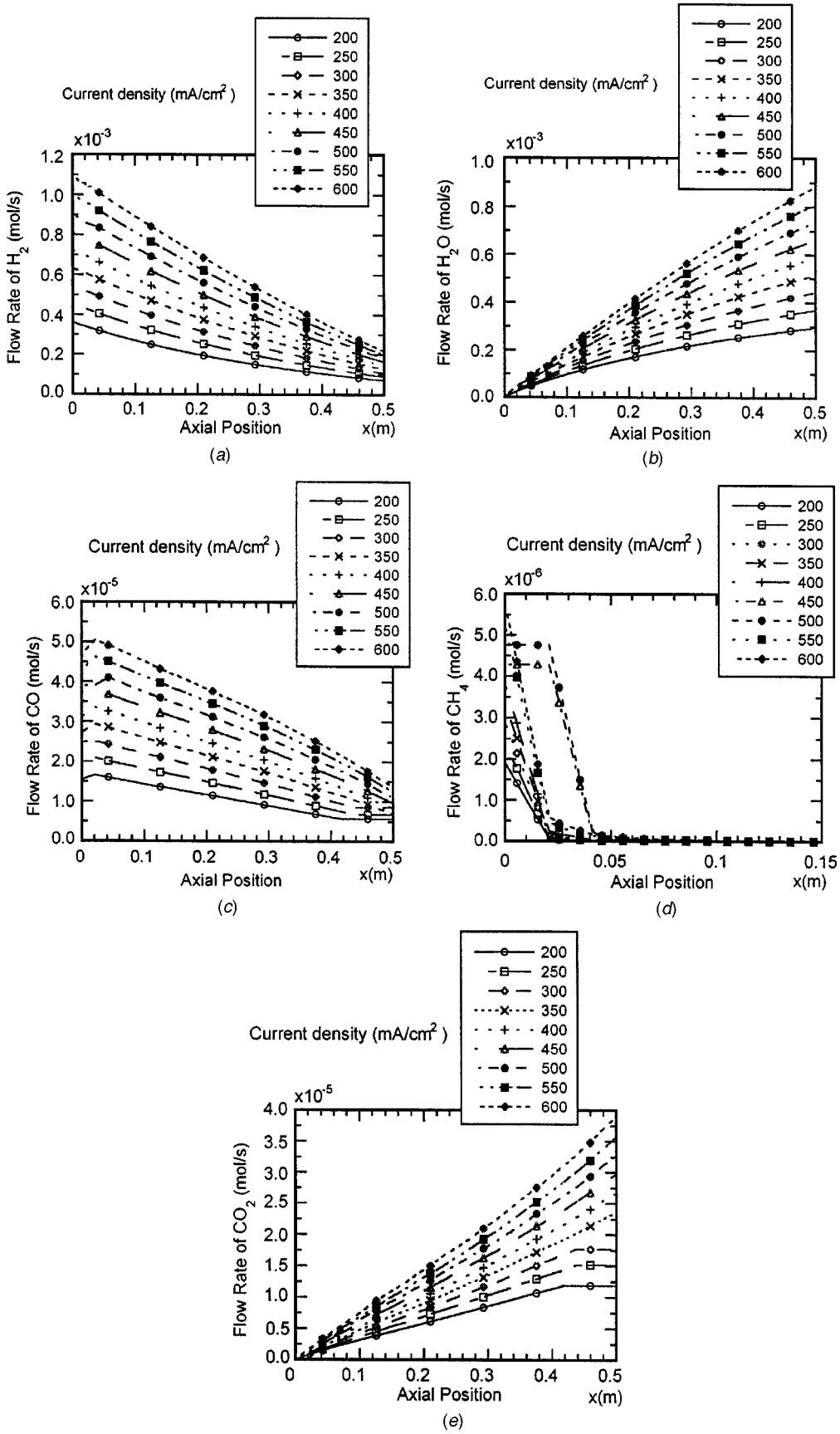

Fig. 11 Varying molar flow rates of gas species in the fuel stream for a series of current densities

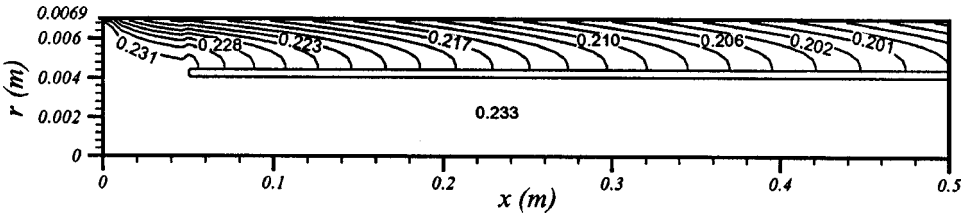

Fig. 12 Mass fraction distribution of oxygen (i_0=450 mA/cm^2)

An overall view of the temperature distribution in the fuel cell is given in Fig. 10 for a typical current density of 450 mA/cm^2 (this is where the maximum power can be obtained in the simulation). Temperature uniformity in the fuel channel is relatively good, but deteriorates at the two ends of the fuel cell. It is thus clear that the thermal stress problem will most probably occur at the two ends of the fuel cell tube. The temperature contour also shows that air is preheated in the air-inducing tube before it leaves the tube. This is because the hot air in the annular air space exchanges heat through convection with the air-inducing tube. Radiation heat exchange can also exist between the support tube and air-inducing tube. These heat transfer rates help to level the temperature differences on the cell tube.

4.4 Local Mass Fractions and Flow Rate Variations of the Gas Species. The variation of gas species' mass fractions can affect the electrochemical reaction in the cell. The exit gas species' mass fractions or flow rate has to be considered for the

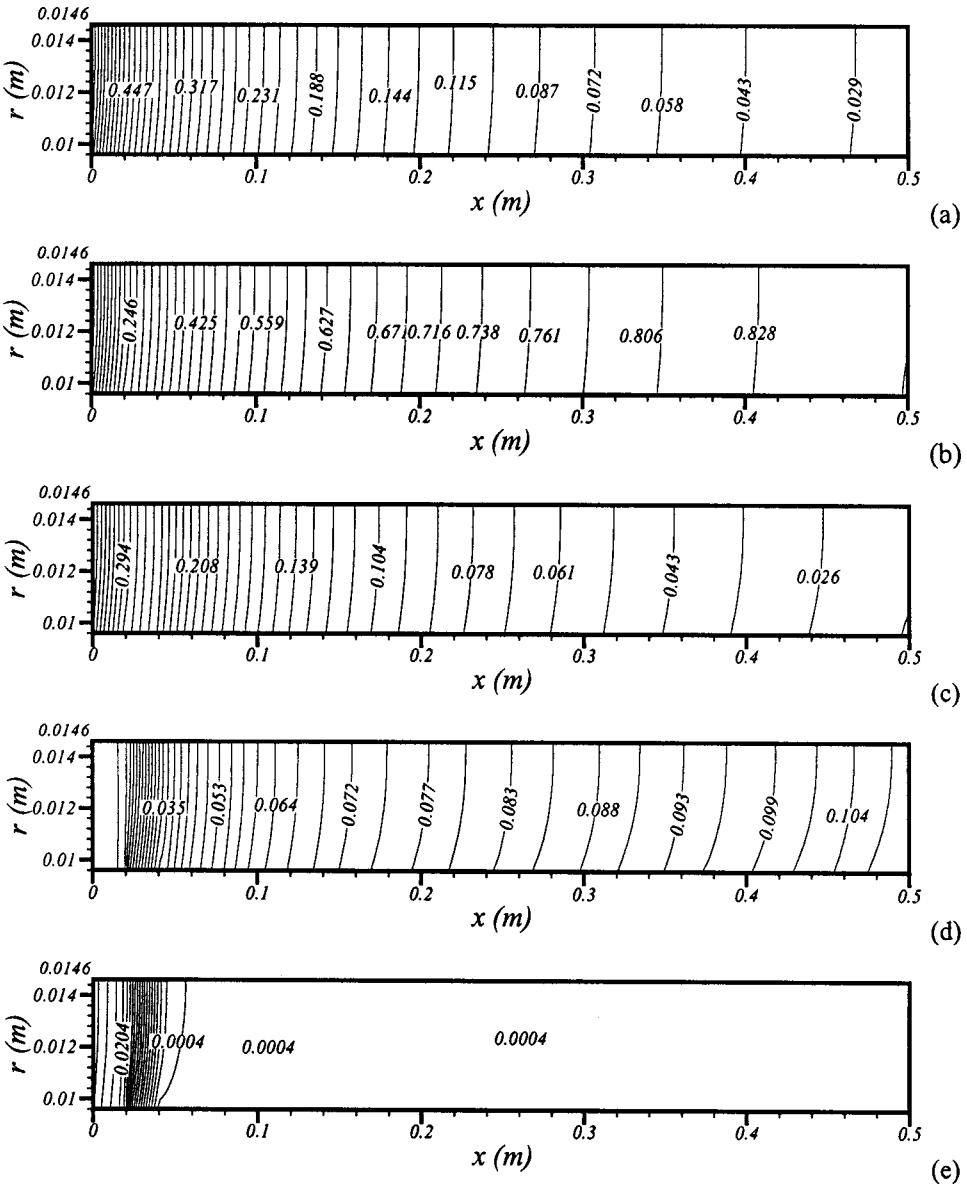

Fig. 13 Mass fraction distributions of gas species in fuel stream (i_0=450 mA/cm^2)

arrangement of downstream components in a SOFC-gas turbine hybrid power system [39]. Due to the reforming, shift, and electrochemical reactions, the flow rate of the reactants and products will vary in the streamwise direction, as shown in Fig. 11. The fuel for the electrochemical reaction is H_2, so its mole flow rate decreases gradually, with a slightly faster decrement seen at the fuel inlet region. This is a reflection of the strong electrochemical reaction in this region. As the major product, the water vapor increases as the electrochemical reaction proceeds. Furthermore, the variation of CO and CH_4 reflect the progress of the reforming and shift reactions. The reformation of CH_4 produces CO, while the overall decrease in CO reflects the shift reaction. The high temperature and high heat generation at the inlet region favor the endothermic reforming reaction. This is reflected by the fast reduction in the CH_4 concentration near the inlet region (where the CH_4 concentration in the fuel gas becomes almost zero within $x = 0.1$ m), and the increase in the mole flow rate of CO. The shift reaction of CO is exothermic, and has difficulty occurring in a high temperature environment, so the CO decreases gradually until the end of the fuel channel (correspondingly, CO_2, the shifting product, gradually increases).

The mass fraction contours for the major reactants and products are plotted in Figs. 12 and 13. In Fig. 12, variation in the oxygen mass fraction in the radial direction is seen in the annulus air channel. This reflects the fact that the diffusion of oxygen from the core region to the support tube surface can form a significant mass fraction gradient. This convection polarization of oxygen is detrimental to cell performance, which is why 4 to 6 stoichiometries of oxygen [37,40] are required for SOFC operation.

Compared with the contour map of oxygen in the air channel, the hydrogen (Fig. 13(*a*)) and water vapor (Fig. 13(*b*)) concentrations in the fuel channel do not show significant gradients in the radial direction. This is due to the strong diffusion of hydrogen in the fuel stream. In the axial direction, the inlet region shows a larger gradient, which is a reflection of the strong consumption rate of hydrogen and the production rate of water vapor. Nevertheless, the overall mass diffusion in the fuel side is strong, which is why the hydrogen utilization percentage can rise as high as 85 percent. The mass fractions of CO (Fig. 13(*c*)) and CO_2 (Fig. 13(*d*)) vary gradually in the axial direction, which reflects the fact that the shifting reaction is not very strong. A large mass fraction gradient for CH_4 (Fig. 13(*e*)) can be seen at fuel inlet region. As mentioned above, the CH_4 is reformed almost completely within a short distance from the fuel inlet, and thus shows almost no mass fraction variation downstream.

5 Conclusions

A flow and heat/mass transfer model considering multiple gases in the fuel stream for a single tubular solid oxide fuel cell (SOFC) system was presented in this work. Axi-symmetrical fields of flow, temperature, and mass fraction were solved numerically. Based on the temperature and mass fraction field data, the local and overall electrochemical performance of the cell can be predicted. A computational simulation was conducted for a sample SOFC with differing current densities. The maximum operational current density for the studied SOFC under the investigated operational conditions was found to be 450 mA/cm^2. A larger current density may result in a decrease in the electrical power output. Both the heat generation and cooling from the airflow can affect the hot spot position in the fuel cell tube. For the smaller current density case, the hot spot may occur upstream in the cell tube, while for a larger current density case, the hot spot occurs in the downstream region. At the two end regions of the fuel cell tube, poor uniformity in the temperature distribution was found, which may lead to larger thermal stresses. Weak diffusion of oxygen in nitrogen was also observed, which may be the major cause of convection polarization. Additionally, the reforming reaction of CH_4 is rather strong, so the CH_4 is almost completely reformed within a short distance from the fuel inlet. However, due to the high temperature environment, the exothermic shift reaction of CO is not as strong and continues to proceed until the end of the fuel channel.

Acknowledgment

The first author, Pei-Wen Li, is grateful to Professor Kenjiro Suzuki of Kyoto University for some valuable discussion.

Nomenclature

C = mole fraction
Cp = specific heat capacity at constant pressure [J/(kg K)]
$D_{j,m}$ = diffusion coefficient of jth species into the left gases of a mixture (m^2/s)
E = electromotive force or electric potential (V)
F = Faraday's constant [96486.7 (C/mol)]
G = volume flow rate (m^3/s)
I, I_0 = local electric current, total output current (A)
i, i_0 = electric current density, cell average current density (mA/cm^2)
L = tube length of the SOFC unit (m)
m = mass transfer rate (kg/s)
$\dot{m}$ = mass flux [kg/(m^{2}s)]
M = molecular weight (g/mol)
MF = total mole number of fuel flow (mol/s)
p, P = pressure (Pa; atm in Eqs. (4)–(6) and (13)), a position
q = heat flux (W/m^2)
$\dot{q}$ = heat source (W/m^3)
Q = heat energy (W)
r = radial coordinate (m)
R = universal gas constant [8.31434 J/(mol K)]
R_a, R_c, R_e = discretized electric resistance in anode, cathode and electrolyte (Ω)
R_{act} = resistance from activation polarization and mass diffusion across porous layers (m$\Omega\cdot$cm^2)
T = temperature (K)
u, v = velocities in axial and radial directions, respectively (m/s)
U = utilization percentage (0–1)
V = voltage
VA, VC = potentials in anode and cathode respectively (V)
x = axial coordinate (m)
$\overline{x}$, $\overline{y}$, $\overline{z}$, $\overline{zo}$ = reacted mole numbers of CH_4, CO, H_2 and O_2 respectively between inlet and outlet of a concerned section in corresponding flow channel (mol/s)
Y = mass fraction

Greek Symbols

ΔG = Gibbs free energy change of a reaction (J/mol)
ΔG_0 = standard state Gibbs' free energy change of a reaction (J/mol)
ΔH = enthalpy change of the electrochemical reaction (J/mol)
Δx = one axial section of fuel cell centered at x position (m)
ρ = density (kg/m^3)
ρ_e = resistivity in electrode and ionic resistivity of electrolyte ($\Omega\cdot$cm)
λ = thermal conductivity [W/(m°C)]
μ = dynamic viscosity (Pa s)
η_{act} = polarization from activation and mass transfer resistance in porous electrodes (V)
θ = circumferential position

Subscripts

a = anode
air = air
c = cathode
cell = overall parameter of cell
e = electrolyte
E,W,N,S = east, west, north, south neighbors of point P
f = fuel
j = gas species
net = electromotive force which already subtracted the activation polarization
Oh = ohmic
R = electrochemical reaction
x = axial position
Δx = variation in Δx section

Superscripts

in = fresh fuel or air at inlet
P = at point P
x = axial position

References

[1] Gardner, F. J., 1997, ''Thermodynamic Processes in Solid Oxide and Other Fuel Cells,'' Proc. Inst. Mech. Eng., **211**(Part A), pp. 367–380.
[2] Bevc, F., 1997, ''Advances in Solid Oxide Fuel Cells and Integrated Power Plant,'' Proc. Inst. Mech. Eng., **211**(Part A), pp. 359–366.
[3] Singhal, S. C., 1999, ''Process in Tubular Solid Oxide Fuel Cell Technology,'' S. C. Singhal, and M. Dokiya, eds., Electrochemical Society Proceedings, **99-19**, pp. 39–51.
[4] Srinivasan, S., Mosdale, R., Stevens, P., and Yang, C., 1999, ''Fuel Cells: Reaching the Era of Clean and Efficient Power Generation in the Twenty-First Century,'' Annual Review of Energy and the Environment, **24**, pp. 281–328.
[5] Joon, K., 1998, ''Fuel Cells—a 21st Century Power System,'' J. Power Sources, **71**, pp. 12–18.
[6] Hirano, A., Suzuki, M., and Ippommatsu, M., 1992, ''Evaluation of a New Solid Oxide Fuel Cell System by Non-Isothermal Modeling,'' J. Electrochem. Soc., **139**(10), pp. 2744–2751.
[7] Bessette, N. F., and Wepfer, W. J., 1995, ''A Mathematical Model of a Tubular Solid Oxide Fuel Cell,'' ASME J. Energy Resour. Technol., **117**, pp. 43–49.
[8] Haynes, C., and Wepfer, W. J., 2001, ''Characterizing Heat Transfer Within a Commercial-Grade Tubular Solid Oxide Fuel Cell for Enhanced Thermal Management,'' Int. J. Hydrogen Energy, **26**, pp. 369–379.
[9] Campanari, S., 2001, ''Thermodynamic Model and Parametric Analysis of a Tubular SOFC Module,'' J. Power Sources, **92**, pp. 26–34.
[10] Palsson, J., Selimovic, A., and Sjunnesson, L., 2000, ''Combined Solid Oxide Fuel Cell and Gas Turbine Systems for Efficient Power and Heat Generation,'' J. Power Sources, **86**, pp. 442–448.
[11] Costamagna, P., Arato, E., Antonucci, P. L., and Antonucci, V., 1996, ''Partial Oxidation of CH_4 in Solid Oxide Fuel Cells: Simulation Model of the Electrochemical Reactor and Experimental Validation,'' Chem. Eng. Sci., **51**(11), pp. 3013–3018.
[12] Aguiar, P., Chadwick, D., and Kershenbaum, L., 2002, ''Modeling of an Indirect Internal Reforming Solid Oxide Fuel Cell,'' Chem. Eng. Sci., **57**, pp. 1665–1677.
[13] Sverdrup, E. F., Warde, C. J., and Glasser, A. D., 1972, *From Electrocatalysis to Fuel Cells*, G. Sandstede, ed., University of Washington Press, Seattle, WA, p. 255.
[14] Archer, D. H., Elikan, L., and Zahradnik, R. L., 1965, *Hydrocarbon Fuel Cell Technology*, B. S. Baker, ed., Academic Press, New York, NY, p. 51.
[15] Li, P. W., and Suzuki, K., 2004, ''Numerical Modeling and Performance Study of a Tubular Solid Oxide Fuel Cell,'' J. Electrochem. Soc., **151**(4), pp. A548–A557.
[16] Nagata, S., Momma, A., Kato, T., and Kasuga, Y., 2001, ''Numerical Analysis of Output Characteristics of Tubular SOFC With Internal Reformer,'' J. Power Sources, **101**, pp. 60–71.
[17] Onuma, S., Kaimai, A., Kawamura, K., Nigara, Y., Kawada, T., Mizusaki, J., and Tagawa, H., 2000, ''Influence of Coexisting Gases on the Electrochemical Reaction Rates Between 873 and 1173 K in a CH4-H2O/Pt/YSZ System,'' Solid State Ionics, **132**, pp. 309–331.
[18] Massardo, A. F., and Lubelli, F., 1998, ''Internal Reforming Solid Oxide Fuel Cell-Gas Turbine Combined Cycles (IRSOFC-T) Part A: Cell Model and Cycle Thermodynamic Analysis,'' ASME Paper 98-GT-577, presented at the International Gas Turbine and Aeroengine Congress and Exhibition, Stockholm, Sweden.
[19] Achenbach, E., and Riensche, E., 1994, ''Methane/Steam Reforming Kinetics for Solid Oxide Fuel Cells,'' J. Power Sources, **52**, pp. 283–288.
[20] Peters, R., Dahl, R., Kluttgen, U., Palm, C., and Stolten, D., 2002, ''Internal Reforming of Methane in Solid Oxide Fuel Cell Systems,'' J. Power Sources **106**, pp. 238–244.
[21] Freni, S., and Maggio, G., 1997, ''Energy Balance of Different Internal Reforming MCFC Configurations,'' Int. J. Energy Res., **21**, pp. 253–264.
[22] Bird, R. B., Stewart, W. E., and Lightfoot, E. N., 1960, *Transport Phenomena*, John Wiley & Sons, Inc., New York.
[23] Williams, F. A., 1985, *Combustion Theory*, Benjamin/Cummings Publishing Co., Redwood City, CA.
[24] Shabbir, A., Charles, M. P., and Romesh, K., 1991, ''Thermal-Hydraulic Model of a Monolithic Solid Oxide Fuel Cell,'' J. Electrochem. Soc., **138**(9), pp. 2712–2718.
[25] Bessette, N. F., Wepfer, W. J., and Winnick, J., 1995, ''A Mathematical Model of a Solid Oxide Fuel Cell,'' J. Electrochem. Soc., **142**, pp. 792–800.
[26] Incropera, F. P., and DeWitt, D. P., 1996, *Introduction to Heat Transfer*, 3rd ed., Wiley, John & Sons, Inc., New York.
[27] Perry, R. H., Green, D. W., and Maloney, J. O., 1984, *Perry's Chemical Engineering Handbook*, 6th ed., McGraw Hill Book Co., New York.
[28] Sverdrup, E. F., Warde, C. J., and Eback, R. L., 1973, ''Design of High Temperature Solid-Electrolyte Fuel-Cell Batteries for Maximum Power Output per Unit Volume,'' Energy Convers., **13**, pp. 129–136.
[29] Chan, S. H., Khor, K. A., and Xia, Z. T., 2001, ''A Complete Polarization Model of a Solid Oxide Fuel Cell and Its Sensitivity to the Change of Cell Component Thickness,'' J. Opt. (Paris), **93**, pp. 130–140.
[30] Turns, S. R., 1999, *Introduction to Combustion: Concepts and Application*, 2nd Edition, McGraw-Hill Higher Education, New York.
[31] Eckert, E. R. G., and Drake, R. M., 1959, *Heat and Mass Transfer*, 2nd Edition, McGraw-Hill, New York.
[32] Patankar, S. V., 1980, *Numerical Heat Transfer and Fluid Flow*, McGraw-Hill, New York.
[33] Karki, K. C., and Patankar, S. H., 1989, ''Pressure Based Calculation Procedure for Viscous Flows at All Speeds in Arbitrary Configurations,'' AIAA J., **27**(9), pp. 1167–1174.
[34] Beckermann, C., and Smith, T. F., 1993, ''Incorporation of Internal Surface Radiant Exchange in the Finite-Volume Method,'' Numer. Heat Transfer, Part B, **23**, pp. 127–133.
[35] Veyo, S. E., and Lundberg, W. L., 1999, ''Solid Oxide Fuel Cell Power System Cycles,'' ASME Paper No. 99-GT-356.
[36] Campanari, S., and Macchi, E., 1999, ''The Combination of SOFC and Micro-Turbine for Civil and Industrial Cogeneration,'' ASME Paper No. 99-GT-84.
[37] Tomlins, G. W., and Jaszar, M. P., 1999, ''Elevated Pressure Testing of the Siemens Westinghouse Tubular Solid Oxide Fuel Cell,'' *Proceedings of The 3rd International Fuel Cell Conference*, pp. 369–372.
[38] Li, P. W., and Chyu, M. K., 2003, ''Simulation of the Chemical/Electrochemical Reactions and Heat/Mass Transfer for a Tubular SOFC in a Stack,'' J. Power Sources, **124**, pp. 487–498.
[39] Suzuki, K., Teshima, K., and Kim, J. H., 2000, ''Solid Oxide Fuel Cell and Micro Gas Turbine Hybrid Cycle for a Distributed Energy Generation System,'' *Proceedings of the 4th JSME-KSME Thermal Engineering Conference*, October 1–6, Kobe, Japan.
[40] Hagiwara, A., Michibata, H., Kimura, A., Jaszcar, M. P., Tomlins, G. W., and Veyo, S. E., 1999, ''Tubular Solid Oxide Fuel Cell Life Tests,'' *Proceedings of The 3rd International Fuel Cell Conference*, Nagoya, Japan, pp. 365–368.

Nancy Ma
e-mail: nancy_ma@ncsu.edu
Department of Mechanical and Aerospace Engineering,
Campus Box 7910,
North Carolina State University,
Raleigh, NC 27695

John S. Walker
e-mail: jswalker@uiuc.edu
Department of Mechanical and Industrial Engineering,
1206 West Green St.,
University of Illinois, Urbana, IL 61801

Laurent Martin Witkowski
e-mail: Laurent.Martin-Witkowski@limsi.fr
LIMSI,
BP133, F91403, Orsay Cedex,
France

Combined Effects of Rotating Magnetic Field and Rotating System on the Thermocapillary Instability in the Floating Zone Crystal Growth Process

This paper presents a linear stability analysis for the thermocapillary convection in a liquid bridge bounded by two planar liquid-solid interfaces at the same temperature and by a cylindrical free surface with an axisymmetric heat input. The two solid boundaries are rotated at the same angular velocity in one azimuthal direction, and a rotating magnetic field is applied in the opposite azimuthal direction. The critical values of the Reynolds number for the thermocapillary convection and the critical-mode frequencies are presented as functions of the magnetic Taylor number for the rotating magnetic field and of the Reynolds number for the angular velocity of the solid boundaries.
[DOI: 10.1115/1.1666883]

Keywords: Crystal Growth, Heat Transfer, Magnetohydrodynamics, Stability, Thermocapillary

1 Introduction

In the floating-zone (FZ) growth of semiconductor crystals, a body of molten semiconductor is held by surface tension between the melting end of a cylindrical, polycrystalline feed rod and the solidifying end of a coaxial, cylindrical single crystal. For the terrestrial, commercial FZ process, the melt zone is created and maintained by induction heating and the free surface is far from cylindrical. On the other hand, for future FZ crystal-growth experiments on the International Space Station (ISS), the free surface will be essentially cylindrical, while there will be axisymmetric radiant heating to create and maintain the melt zone. For these ISS experiments, the free-surface temperature will vary from a maximum at a middle circumference to the solidification temperature at both the feed rod and crystal interfaces. Since the surface tension of most molten semiconductors in an inert atmosphere decreases as the temperature is increased, the variations of surface tension will drive two toroidal melt circulations with flows along the free surface from the hottest circumference toward both the feed rod and crystal, and with axial return flows near the centerline. This surface-tension driven or thermocapillary convection has a very large radial derivative of the axial velocity near the free surface, and this large velocity gradient leads to a hydrodynamic instability even when the temperature difference along the free surface is quite small, e.g., 1–2°C. A much larger free-surface temperature difference is required in order to avoid the morphological instability of the crystal-melt interface which would lead to polycrystalline solidification. The thermocapillary instability involves a transition from steady axisymmetric melt motion to nonaxisymmetric steady or periodic melt motion. The quality of any semiconductor crystal depends on the uniformity of additives or dopants which give the crystal the desired electrical or optical properties. With a nonaxisymmetric melt motion, the mass transport of dopants in the melt leads to undesirable spatial oscillations of the dopant concentration in the crystal, which are called striations.

As part of the preparations for the future ISS experiments, Dold et al. [1] recently conducted terrestrial FZ experiments with radiant heating and with a small diameter for the feed rod and crystal. With this small diameter, the effects of buoyant convection and of the free-surface sag due to hydrostatic pressure were relatively small, thus roughly approximating the future experiments in microgravity. Dold et al. [1] found that the application of a rotating magnetic field (RMF) during FZ crystal growth dramatically reduced the average difference between adjacent maximum and minimum dopant concentrations in the striations. They attributed this improvement to an increase of the frequency of the periodic nonaxisymmetric thermocapillary convection. Thus in their experiments, the RMF did not eliminate the thermocapillary instability, but it reduced its deleterious effects. An RMF is produced by connecting the successive phases of a multiphase AC power source to inductors at equally spaced azimuthal positions around the melt. The inductors are generally designed to produce a spatially uniform transverse magnetic field which rotates at a constant angular velocity ω around the centerline of the melt. For the typical frequencies and field strengths used in crystal-growth experiments, an RMF produces a steady, axisymmetric, azimuthal body force on the melt. This body force drives an azimuthal velocity in the melt in the direction that the RMF rotates. If the solid boundaries are not rotating, then the axial variation of the centrifugal force due to the azimuthal velocity drives steady, axisymmetric, meridional circulations with radially inward flows near the planar liquid-solid interfaces and with radially outward flow near the plane midway between these interfaces. For the FZ process, the meridional circulations due to the RMF reinforce the thermocapillary circulations.

Walker et al. [2] recently presented a linear stability analysis for the present problem with an RMF, but without rotation of the crystal or feed rod about their common centerline. They showed that, as the strength of the RMF is increased from zero, its effects are destabilizing, i.e., the critical value of the Reynolds number for the thermocapillary convection, Re_{cr}, decreases. However, as the RMF strength is further increased, Re_{cr} reaches a minimum and then increases to values which are considerably higher than the Re_{cr} without an RMF. This stabilization emerges once the

Contributed by the Heat Transfer Division for publication in the JOURNAL OF HEAT TRANSFER. Manuscript received by the Heat Transfer Division May 23, 2003; revision received December 2, 2003. Associate Editor: V. Prasad.

azimuthal velocity produced by the RMF becomes large enough that the coupling of the radial convection of angular momentum and the centrifugal force due to the azimuthal velocity can significantly alter the base-flow thermocapillary convection.

For the FZ process, the azimuthal velocity is limited by the fact that the associated centrifugal force can overwhelm the surface tension, breaking the liquid bridge. In the FZ process, the angular velocities of the crystal and feed rod seldom exceed 30 rpm because of the free-surface stability. An RMF is also limited by the same constraint. For terrestrial FZ processes, the feed rod and crystal are often rotated with different angular velocities and in opposite azimuthal directions. However, for the future ISS experiments, the crystal and feed rod will both be clamped inside a sealed ampoule, so that only rotation with the same angular velocity and in the same azimuthal direction will be possible.

The purpose of this paper is to investigate whether combining rotation of the crystal and feed rod with an RMF can provide more stabilization of the thermocapillary convection than an RMF alone, given the constraint that the azimuthal velocity cannot exceed a certain value. If we initially apply an RMF which leads to the maximum allowable azimuthal velocity, the rotation of the crystal and feed rod in the same direction would mean that the strength of the RMF must be reduced to prevent increasing the azimuthal velocity. Thus rotation in the same direction as the RMF means reducing the stabilizing effects of the RMF, so it is not promising. On the other hand, applying an RMF in the azimuthal direction opposite to that of the crystal and feed-rod rotation might have significant effects on the thermocapillary instability without exceeding the azimuthal velocity limit. Before beginning this research, we identified a reason why this combination might be destabilizing and another reason why it might be stabilizing. Rotating the crystal and feed rod in the opposite direction from the RMF will decrease the average angular momentum. If the stabilizing effect of the RMF arises primarily from the radial convection of a strong angular momentum, then opposite rotation might be destabilizing. On the other hand, with rotation of the crystal and feed rod to produce the maximum allowable azimuthal velocity at the liquid-solid interfaces and with the RMF braking this angular velocity and possibly producing an azimuthal velocity in the opposite direction near the plane midway between these interfaces, the axial variation of the centrifugal force due to the azimuthal velocity drives two steady, axisymmetric meridional circulations with radially outward flow near the liquid-solid interfaces and with radially inward flow near the plane midway between these interfaces. These circulations tend to cancel the thermocapillary convection. Since the thermocapillary instability arises from the large radial gradient of the axial velocity near the free surface [3], the cancelation of part of the thermocapillary convection might be stabilizing. The objective of this paper is to determine whether the destabilizing effects of reduced average angular momentum or the stabilizing effects of canceling part of the thermocapillary convection dominate in this competition.

An alternative to a linear stability analysis is the time integration of the full three-dimensional governing equations. Time integrations of the full equations were presented by Rupp et al. [4] and by Fischer et al. [5] for the thermocapillary instability in the FZ process without and with an RMF, respectively. Linear stability analyses cannot be used to study nonlinear instabilities arising from finite-amplitude perturbations in the steady axisymmetric base flow. Recently Levenstam et al. [6] presented the predictions of both a linear stability analysis and of a time integration of the full three-dimensional equations for the thermocapillary instability in the FZ process, and they showed that there was good agreement between the results. This indicates that the present linear stability analysis gives accurate results for the primary transition from a steady axisymmetric flow to a periodic nonaxisymmetric flow. Many of the papers on the FZ process with an RMF were reviewed by Dold and Benz [7].

2 Problem Formulation

We assume that all the thermophysical properties of the melt are uniform and constant, except the surface tension, which decreases linearly with increasing temperature. We use cylindrical coordinates (r,θ,z) with the z axis along the centerline of the cylindrical melt zone, with the origin at the center of the melt, and with the unit vectors $(\hat{\mathbf{r}},\hat{\theta},\hat{\mathbf{z}})$. We normalize r and z with R, the radius of the melt zone, and we assume that the axial distance between the two liquid-solid interfaces is $2R$, because the height to diameter ratio of the melt zone in the actual FZ process is generally close to one.

The dimensionless governing equations are

$$\frac{\partial \mathbf{v}}{\partial t}+(\mathbf{v}\cdot\nabla)\mathbf{v}=-\nabla p+Tm f_\theta\hat{\theta}+\nabla^2\mathbf{v}, \tag{1a}$$

$$\nabla\cdot\mathbf{v}=0, \tag{1b}$$

$$\frac{\partial T}{\partial t}+\mathbf{v}\cdot\nabla T=\mathrm{Pr}^{-1}\nabla^2 T. \tag{1c}$$

The dimensionless variables t, $\mathbf{v}$, p, and T are time, the melt velocity, the melt pressure and the deviation of the melt temperature from the solidification temperature, each normalized by R^2/ν, ν/R, $\rho\nu^2/R^2$, and $(\Delta T)_c$, respectively. The dimensionless parameters here are the magnetic Taylor number $\mathrm{Tm}=\sigma\omega B^2R^4/2\rho\nu^2$, and the Prandtl number, $\mathrm{Pr}=\nu/\kappa$, where ν, ρ, σ, and κ are the kinematic viscosity, density, electrical conductivity, and thermal diffusivity of the melt, while $(\Delta T)_c$ is a characteristic temperature difference, and B is the magnetic flux density of the RMF. Assuming that the electric currents flowing through the crystal and feed rod are negligible, the dimensionless azimuthal body force due to the RMF [8] is

$$f_\theta=r-2\sum_{N=1}^{\infty}\frac{J_1(\lambda_N r)\cosh(\lambda_N z)}{(\lambda_N^2-1)J_1(\lambda_N)\cosh(\lambda_N)}, \tag{2}$$

where J_k is the Bessel function of the first kind and kth order, while λ_N are the roots of $\lambda_N J_0(\lambda_N)-J_1(\lambda_N)=0$. Equation (2) comes from a separation-of-variables solution for the electric potential function with the assumption that the melt velocity is much less than ωR. The characteristic equation for λ_N comes from the condition that the radial electric current is zero at the free surface at $r=1$ [8].

We assume that the radiant heat flux into the free surface varies parabolically from a maximum $q_{\max}$ at $z=0$ to zero at the liquid-solid interfaces at $z=\pm1$ [4], and we use $(\Delta T)_c=Rq_{\max}/k$ for the characteristic temperature difference, where k is the thermal conductivity of the melt. Therefore the boundary conditions at $r=1$ are

$$v_r=0,\quad \frac{\partial v_\theta}{\partial r}-v_\theta+\mathrm{Re}\frac{\partial T}{\partial\theta}=0, \tag{3a,b}$$

$$\frac{\partial v_z}{\partial r}+\mathrm{Re}\frac{\partial T}{\partial z}=0,\quad \frac{\partial T}{\partial r}=1-z^2, \tag{3c,d}$$

where $\mathrm{Re}=(-d\gamma/dT)(\Delta T)_c R/\rho\nu^2$ is the Reynolds number for the thermocapillary convection, and $d\gamma/dT$ is the constant, negative derivative of the surface tension with respect to temperature. The Marangoni number used in many other studies of thermocapillary convection is equal to $\mathrm{Pr\,Re}$. The temperature term in Eq. (3b) drops out for the axisymmetric base flow, but it is important for the nonaxisymmetric perturbation. The boundary conditions at $z=\pm1$ are $v_r=v_z=T=0$ and $v_\theta=\mathrm{Re}_\Omega r$, where $\mathrm{Re}_\Omega=\Omega R^2/\nu$ is the Reynolds number for the crystal and feed-rod rotation with the angular velocity Ω.

For each variable v_r, v_θ, v_z, p, and T, we introduce the form

$$v_r=v_{r0}(r,z)+\varepsilon\,\mathrm{Real}[v_{r1}(r,z)\exp(\lambda t-im\theta)]. \tag{4}$$

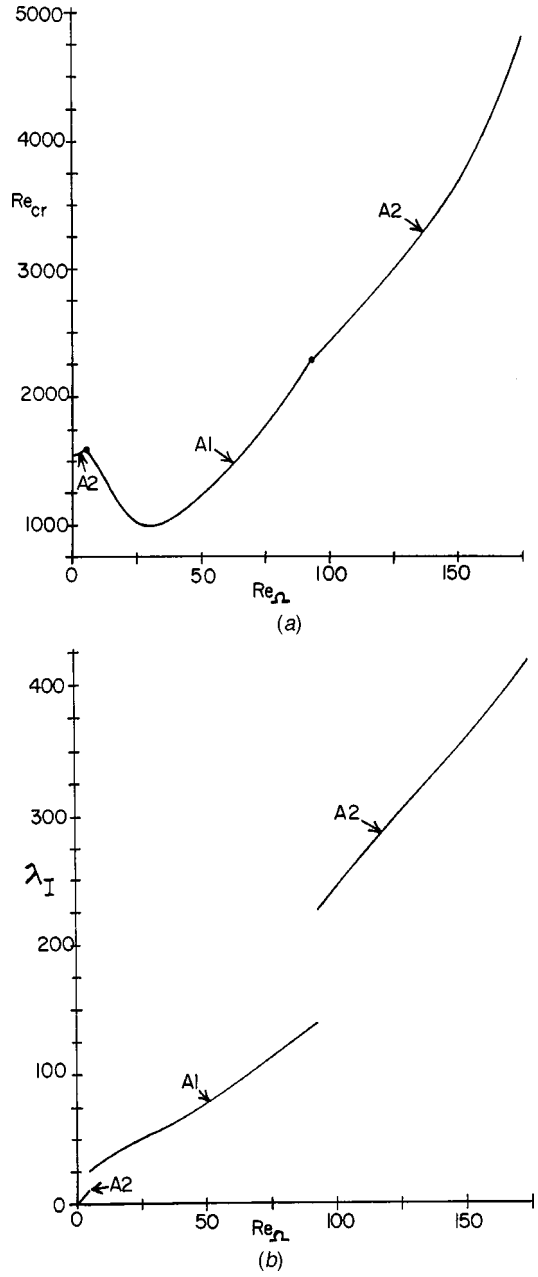

Fig. 1 Critical mode results for rotation of the crystal and feed rod without a rotating magnetic field: (a) Re_{cr} versus Re_Ω; and (b) λ_I versus Re_Ω

The subscript 0 denotes the variables for the steady, axisymmetric base flow, the subscript 1 denotes the complex modal functions, such as $v_{r1R}+iv_{r1I}$, for the small, $O(\varepsilon)$ perturbation in the linear stability analysis, $\lambda=\lambda_R+i\lambda_I$ is the complex eigenvalue, and m is the real, integer azimuthal wave number.

For the base flow, we introduce the stream function $\psi_0(r,z)$, where

$$v_{r0}=\frac{1}{r}\frac{\partial\psi_0}{\partial z}, \quad v_{z0}=-\frac{1}{r}\frac{\partial\psi_0}{\partial r}. \tag{5a,b}$$

We eliminate p_0 by cross-differentiating the r and z components of the momentum equation (1*a*) for the steady, axisymmetric base flow. Since $v_{\theta 0}$ and T_0 are even functions of z, while ψ_0 is an odd function of z, we need only treat $0<z<1$ for the base flow with symmetry conditions at $z=0$. We represent each base-flow variable by a sum of Chebyshev polynomials in r and z, and we insure

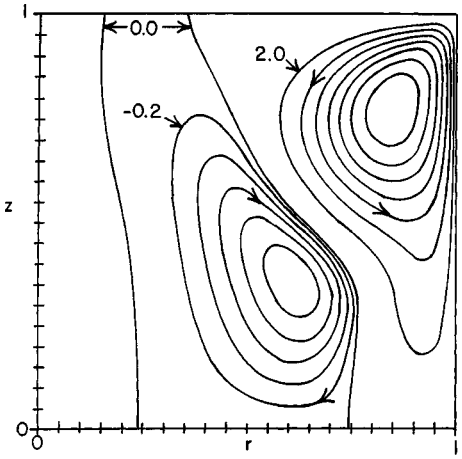

Fig. 2 Base-flow streamlines for $Tm=0$, $Re_\Omega=150$ and $Re_{cr}=3651.9$: $\psi_0=2.0k$ for $k=0$ to 7 and $\psi_0=-0.2k$, for $k=1$ to 5

that the representation for each variable has the correct Taylor series in r, e.g., the Taylor series of ψ_0 has only even powers of r, beginning with r^2. We apply the governing equations and boundary conditions at the Gauss-Lobatto collocation points. We solve the nonlinear, algebraic equations for the coefficients in the Chebyshev-polynomial representations using the Newton-Raphson method [9].

Since the base flow is symmetric in z, we need only treat $0<z<1$ for the small perturbations as long as we consider both symmetric and antisymmetric modes. For a symmetric mode, v_{r1}, $v_{\theta 1}$, p_1, and T_1 are even functions of z, while v_{z1} is an odd function of z, thus matching the symmetry of the base flow. For an antisymmetric mode, v_{r1}, $v_{\theta 1}$, p_1, and T_1 are odd functions of z, while v_{z1} is an even function of z. The small-perturbation boundary value problem for $m=0$ is different and simpler compared to that for $m\geqslant 1$, so that we treat four perturbation cases: namely symmetric and antisymmetric modes with $m=0$ and $m\geqslant 1$. We represent each perturbation variable as a sum of Chebyshev polynomials in r and z, and again we insure that each representation has the correct Taylor series expansion, e.g., the Taylor series for v_{r1} for $m\geqslant 1$ has the powers $r^{(m-1)}$, $r^{(m+1)}$, $r^{(m+3)}$, ... The linear perturbation equations and boundary conditions are applied at the Gauss-Lobatto collocation points to obtain a linear, matrix eigenvalue problem. The eigenvalues are obtained with subroutines from the EISPACK library of FORTRAN codes [10].

For each set of values for Pr, Tm, Re_Ω, and Re, we first used the Newton-Raphson iteration to find the steady, axisymmetric base flow, and then we used the EISPACK subroutines to find the eigenvalues for the symmetric and antisymmetric perturbation modes for $m=0$ to 4. For each set of values for Pr, Re_Ω, and Tm, we increased Re until one eigenvalue for one mode had $\lambda_R=0$, while all the other eigenvalues for this mode and for all the other modes had $\lambda_R<0$. This defines the critical value of the Reynolds number for the thermocapillary convection Re_{cr} and the dimensionless frequency λ_I of the critical mode for a given material represented by Pr, for a given angular velocity for the crystal and feed rod represented by Re_Ω, and for a given RMF strength represented by Tm.

3 Results

We only present results for Pr=0.02, corresponding to silicon. In order to validate our code, we first treated the "half-zone" problem, which has been treated in a number of previous papers. For the half-zone problem, the geometry is the same, but there is no heat transfer across the cylindrical free surface and the two liquid-solid interfaces are at different temperatures, so that the free surface temperature varies from a maximum at the hotter interface to a minimum at the colder interface. We consider the

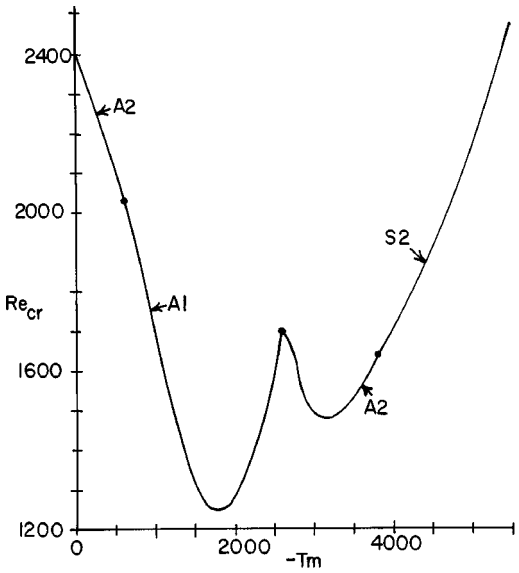

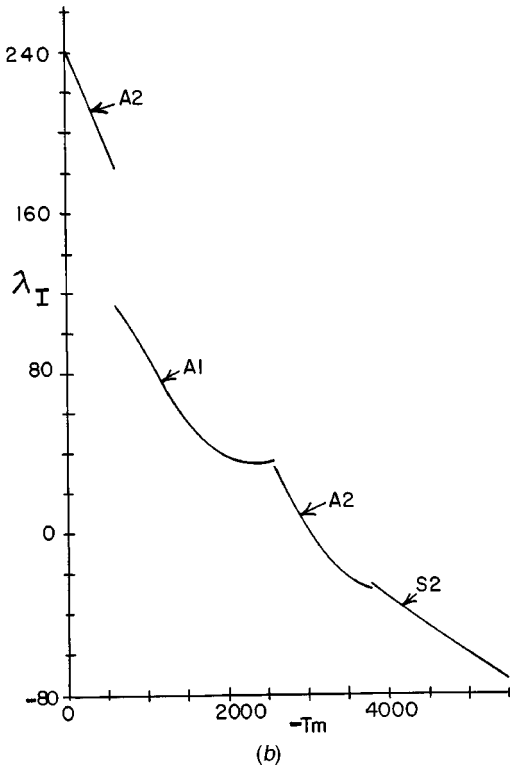

Fig. 3 Critical mode results versus $-Tm$ for $Re_\Omega=100$; (a) Re_{cr} versus $-Tm$; and (b) λ_I versus $-Tm$

half-zone problem with an axial distance between the liquid-solid interfaces equal to R, with no RMF ($Tm=0$), with no crystal or feed-rod rotation ($Re_\Omega=0$), and with $Pr=0.02$. For this case, our code gives $Re_{cr}=2059$, with $m=2$ and $\lambda_I=0$. Chen et al. [11] found that $Re_{cr}=2054$ and Wanschura et al. [3] found that $Re_{cr}=2062$, both with $m=2$ and $\lambda_I=0$.

For our FZ problem, we first consider the effects of crystal and feed-rod rotation without an RMF ($Tm=0$). The values of Re_{cr} and λ_I for $Tm=0$ and $0\leqslant Re_\Omega\leqslant 175$ are presented in Fig. 1. Here the critical mode is always an antisymmetric mode with either $m=1$ or $m=2$, denoted by A1 and A2, respectively. The meridional base flow consists of two opposite toroidal vortices with circular centerlines at some radius and at symmetric values of z.

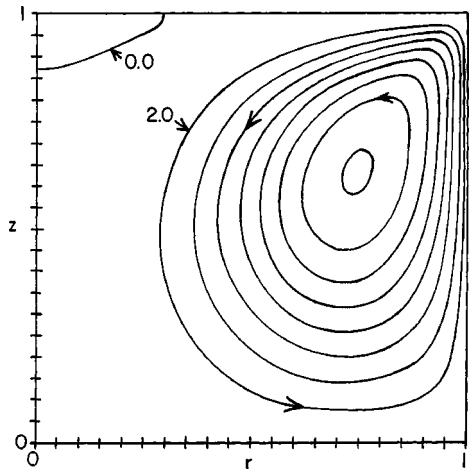

Fig. 4 Base-flow streamlines for $Re_\Omega=100$, $Tm=-5500$ and $Re_{cr}=2472.7$: $\psi_0=2.0k$, for $k=0$ to 8

An antisymmetric $m=1$ mode represents a transition to a flow with a primary transverse vortex about a straight centerline along some diameter in the $z=0$ plane. Rupp et al. [4] found this $m=1$ antisymmetric transition to a transverse vortex with a much weaker secondary opposite vortex near one side of each liquid-solid interface. Without an RMF, they found that this pattern is stationary ($\lambda_I=0$). With an RMF, Fischer et al. [5] found that this pattern rotates in the azimuthal direction of the RMF, and they suggested that this pattern is simply convected with the azimuthal velocity produced by the RMF. An antisymmetric $m=2$ mode leads to a flow with two opposite vortices about parabolic centerlines in the $z=0$ plane and extending from the free surface at $\theta=\pm\pi/4$ through the melt and back to the free surface at $\theta=\pm 3\pi/4$. Again the pattern rotates in the azimuthal direction if there is any azimuthal base-flow velocity. The value $Re_\Omega=175$ corresponds to the kinematic viscosity of molten silicon, a diameter of 10 mm and rotation at 23.4 rpm. Dold et al. [1] grew silicon crystals with 8–14 mm diameters. The effects on Re_{cr} of rotation alone are very similar to those of an RMF alone [2]. As Re_Ω is increased from zero, the antisymmetric $m=2$ mode is stabilized until the transition to an antisymmetric $m=1$ mode at $Re_\Omega=4.724$ and $Re_{cr}=1603.4$, while λ_I abruptly increases from 11.67 to 25.07 at this switch of modes. As Re_Ω increases from 4.724, Re_{cr} decreases to a minimum of 995.0 at $Re_\Omega=30.0$ and then begins to increase. At $Re_\Omega=93.3$ and $Re_{cr}=2282$, there is a switch from the antisymmetric $m=1$ mode back to the antisymmetric $m=2$ mode, while λ_I abruptly increases from 138.8 to 226.2 at this switch of modes. At $Re_\Omega=175$, $Re_{cr}=4819.3$ and $\lambda_I=417.59$. The Re_{cr} exceeds 1547.6 when $Re_\Omega>65$, so that rotation is stabilizing for $Re_\Omega>65$. From Eq. (4), the dimensionless angular velocity of the critical disturbance is λ_I/m. For both the $m=1$ and $m=2$ antisymmetric modes, $(\lambda_I/m)>Re_\Omega$, so that the critical disturbance propagates in the direction of the crystal and feed-rod rotation with an angular velocity which is greater than Ω. The difference is larger for the $m=1$ mode than for the $m=2$ mode. For the $m=1$ mode, the ratio $(\lambda_I/m\,Re_\Omega)$ decreases from 5.3 at $Re_\Omega=4.724$ to 1.49 at $Re_\Omega=93.3$. For the $m=2$ mode, this ratio is roughly 1.2 for both $Re_\Omega<4.724$ and $93.3<Re_\Omega<175$. The fact that $\lambda_I/m>Re_\Omega$ for both modes means that the perturbation is not simply convected with the azimuthal velocity created by system rotation. Instead the perturbation propagates in the azimuthal direction because of a coupling between the centrifugal force and the radial convection of angular momentum [2].

An azimuthal base-flow velocity opposes radial velocities through the Taylor-column effect, i.e., an inward radial convection of angular momentum causes the local $v_{\theta 0}$ to increase, leading to an increase of the radially outward centrifugal force opposing the inward velocity. For $Tm=Re_\Omega=0$, the meridional thermocapillary

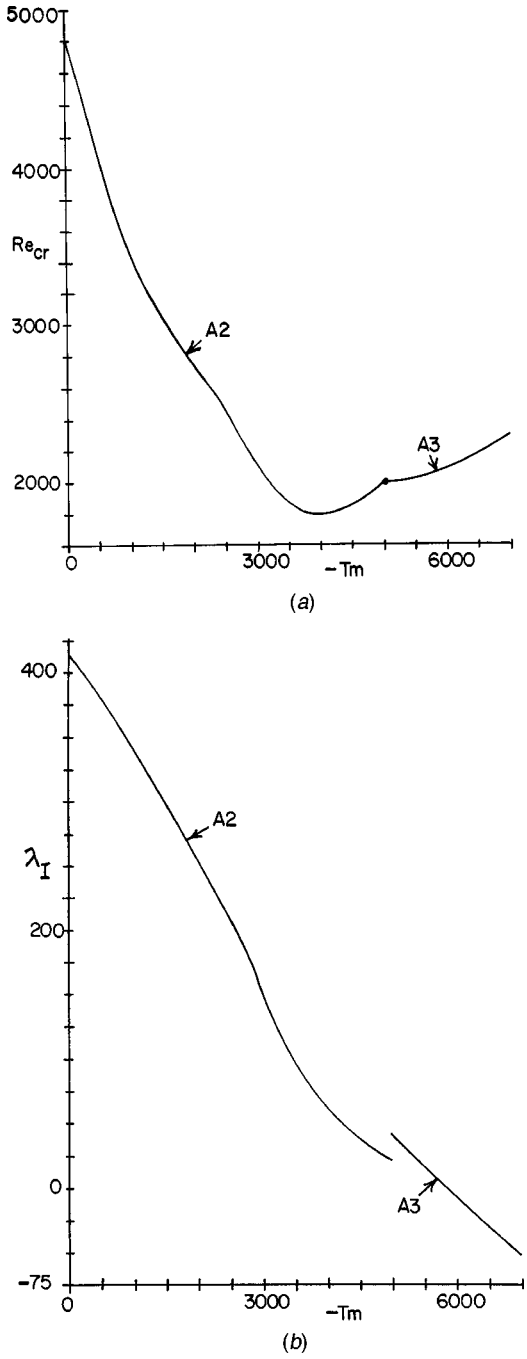

Fig. 5 Critical mode results for $Re_\Omega=175$: (a) Re_{cr} versus $-Tm$; and (b) λ_I versus $-Tm$

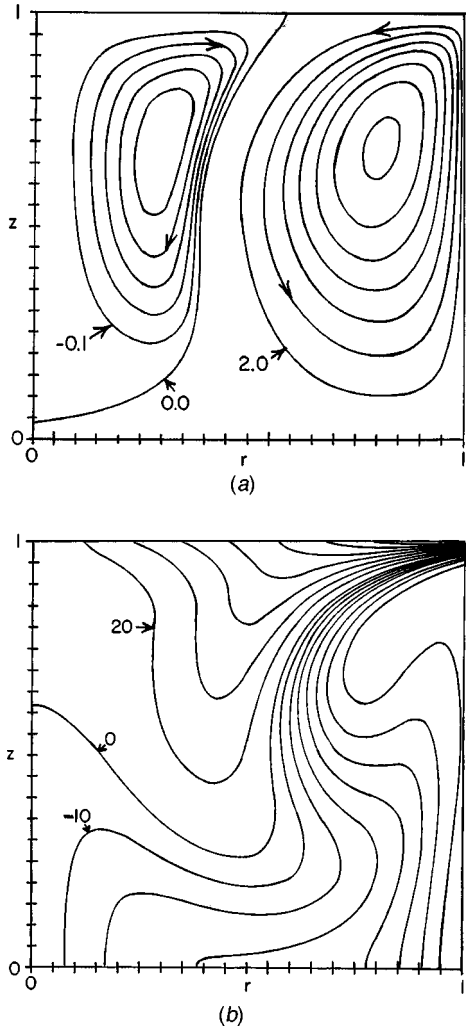

Fig. 6 Base-flow results for $Re_\Omega=175$, $Tm=-7000$ and $Re_{cr}=2297$: (a) Streamlines for meridional flow: $\psi_0=2.0k$, for $k=0$ to 7 and $\psi_0=-0.1k$, for $k=1$ to 5; and (b) Lines of constant azimuthal velocity: $v_{\theta 0}=20k$, k=0 to 8 and $v_{\theta 0}=-10k$, k=1 to 7

convection for $0\leqslant z\leqslant 1$ is a single counterclockwise circulation occupying most of $0\leqslant r\leqslant 1$. As Re_Ω is increased from zero, the Taylor-column effect opposes any radially inward flow, so that the meridional circulation is pushed toward the free surface, while the center of this circulation moves axially toward $z=1$ where the free-surface temperature gradient is largest. At roughly $Re_\Omega=40$, a second clockwise meridional circulation for $0\leqslant z\leqslant 1$ appears near $r=z=0$. This secondary circulation is driven by viscous shear from the primary circulation and by the axial variation of the centrifugal force created by the radial convection of angular momentum by the primary counterclockwise circulation. As Re_Ω is increased further, the primary counterclockwise circulation is pushed more toward the free surface, and the secondary clockwise circulation grows in magnitude and extent. At roughly $Re_\Omega=120$, a third counterclockwise circulation appears near $r=z=0$, although this third circulation is very small. The base-flow streamlines for $Tm=0$, $Re_\Omega=150$ and $Re_{cr}=3651.9$ are presented in Fig. 2. Here $-1.14\leqslant\psi_0\leqslant 15.72$, so that the secondary clockwise circulation is more than an order of magnitude smaller than the primary counterclockwise circulation driven by the surface tension variation at $r=1$. The counterclockwise circulation for $r<0.2$ is more than an order of magnitude smaller than the secondary circulation.

The mechanism which might make the combination of an RMF and system rotation more stabilizing than an RMF or rotation alone is the partial cancelation of the thermocapillary convection when the rotation of the feed rod and crystal produce the largest angular velocity at the liquid-solid interfaces, while the RMF in the opposite direction brakes the angular momentum, leading to a small or negative azimuthal velocity near $z=0$. Therefore, we consider two relatively large values of Re_Ω with Tm decreasing from zero to negative values corresponding to an RMF in the opposite azimuthal direction.

The values of Re_{cr} and λ_I for $Re_\Omega=100$ and $-5500<Tm<0$ are presented in Fig. 3. As Tm is decreased from zero, the addition of the RMF is clearly destabilizing. For the antisymmetric $m=2$ mode, Re_{cr} decreases from 2417.5 at $Tm=0$ to 2030.6 at $Tm=-625$, where the mode switches to an antisymmetric $m=1$ mode. As Tm decreases further, Re_{cr} decreases to a minimum of 1245.1 at $Tm=-1800$. At $r=1$ and $z=0$, $v_{\theta 0}$ first becomes negative at $Tm=-1200$, so that Re_{cr} does not reach its minimum until

the RMF has become strong enough to produce reverse azimuthal flow near $z=0$. There is a switch back to the antisymmetric $m=2$ mode at Tm$=-2604$ and $\mathrm{Re}_{cr}=1696.3$. After this mode switch, Re_{cr} decreases again, reaching a minimum of 1483.6 at $Tm=-3250$. As Tm decreases from -3250, Re_{cr} increases monotonically as the magnitude and extent of the negative azimuthal velocity both increase. There is switch from the antisymmetric $m=2$ mode to the symmetric $m=2$ mode at Tm$=-3797$ and $\mathrm{Re}_{cr}=1634$. At Tm$=-5500$, $\mathrm{Re}_{cr}=2472.7$ for the symmetric $m=2$ mode, so that we have roughly returned to the $\mathrm{Re}_{cr}=2417.5$ for Tm$=0$. The value of λ_I decreases as Tm is decreased from zero, except for a small increase just before the switch from the antisymmetric $m=1$ mode to the antisymmetric $m=2$ mode. At roughly Tm$=-3030$, λ_I becomes negative, so that the critical disturbance is propagating in the direction of the RMF rather than in the direction of the system rotation. For $\mathrm{Re}_\Omega=100$, the extent and magnitude of the secondary clockwise meridional base-flow circulation for $z>0$ decreases as Tm is decreased from zero. The base-flow streamlines for $\mathrm{Re}_\Omega=100$, $Tm=-5500$ and $\mathrm{Re}_{cr}=2472.7$ are plotted in Fig. 4. The secondary circulation is very weak and is confined to a very small region near $r=0$, $z=1$, while the primary counterclockwise circulation closely resembles that for $Tm=\mathrm{Re}_\Omega=0$. For $\mathrm{Re}_\Omega=100$ and Tm$=-5500$, $-98.3\leqslant v_{\theta 0}\leqslant 100.0$, so that the RMF has produced a reverse azimuthal velocity with nearly the same maximum magnitude as that driven by the system rotation. The RMF produces an azimuthal body force which is distributed over the entire domain, while the effects of the system rotation arise from the viscous shear stresses at the liquid-solid interfaces. At the relatively large values of Re_{cr}, the effects of the viscous shear stresses at the liquid-solid interfaces do not extend far into the liquid, so that the RMF has a larger effect than the system rotation. For $\mathrm{Re}_\Omega=100$, $Tm=-5500$ and $\mathrm{Re}_{cr}=2472.7$, the $v_{\theta 0}=0$ line extends from $z=0.97$ at $r=1.0$ to $z=0.86$ at $r=0.5$, and then drops to $z=0.28$ at $r=0.0$. This drop near $r=0$ arises from the local downward convection of the positive angular momentum produced by the rotating solid at $z=1$. For this case, more than 80% of the liquid has a negative base-flow azimuthal velocity.

The values of Re_{cr} and λ_I for $\mathrm{Re}_\Omega=175$ and $-7000\leqslant \mathrm{Tm}\leqslant 0$ are presented in Fig. 5. As Tm is decreased from zero, Re_{cr} for the antisymmetric $m=2$ mode decreases from 4819.3 to a minimum of 1790.8 at Tm$=-4000$. The $v_{\theta 0}$ first becomes negative at $r=1$ and $z=0$ for Tm$=-2750$, so that there is again reverse flow before Re_{cr} reaches its minimum. There is a switch from the antisymmetric $m=2$ mode to the antisymmetric $m=3$ mode at Tm$=-5000$ and $\mathrm{Re}_{cr}=1995.8$, when the minimum $v_{\theta 0}$ is -66.3. For Tm$=-7000$, Re_{cr} is 2297. As Tm is decreased for $\mathrm{Re}_\Omega=175$, λ_I for the antisymmetric $m=2$ mode decreases monotonically from 417.59 for Tm$=0$ to 22.0 for Tm$=-5000$, and λ_I for the antisymmetric $m=3$ mode decreases monotonically from 42.39 for Tm$=-5000$ through zero at Tm$=-5850$ to -51.23 for Tm$=-7000$. Again $\lambda_I<0$ means that the critical disturbance propagates in the direction of the RMF.

For $\mathrm{Re}_\Omega=175$, Tm$=-7000$ and $\mathrm{Re}_{cr}=2297$, the base-flow streamlines and the lines of constant $v_{\theta 0}$ are plotted in Fig. 6. As Tm is decreased from zero, the primary counterclockwise circulation expands from that in Fig. 2 to occupy roughly $0.4<r<1.0$ in Fig. 6, while the secondary clockwise circulation is pushed into $0<r<0.4$. However, unlike Fig. 4 for $\mathrm{Re}_\Omega=100$, the secondary flow is still significant for $\mathrm{Re}_\Omega=175$ and Tm$=-7000$. Both circulations involve axially downward flow for $0.3<r<0.8$, and the associated convection of the positive azimuthal velocity produced by the system rotation alters the balance between the effects of system rotation and the RMF from that for $\mathrm{Re}_\Omega=100$ and Tm$=-5500$. The $v_{\theta 0}=0$ line curves down from $z=0.96$ at $r=1.0$ to $z=0.25$ at $r=0.5$ and then curves up to $z=0.62$ at $r=0.0$. For this case, slightly more than half of the liquid has a negative azimuthal velocity.

4 Conclusions

The results presented here show that combining an RMF in one azimuthal direction with rotation of the crystal and feed rod in the opposite azimuthal direction leads to a thermocapillary instability for a smaller free-surface temperature difference than would be the case for either the rotation or the RMF alone. This indicates that the stabilizing effects of canceling part of the thermocapillary convection are overwhelmed by the destabilizing effects of reducing the average angular momentum. The partial cancelation of the thermocapillary convection does occur. For $\mathrm{Re}_\Omega=100$, the maximum value of ψ_0 decreases from 13.14 for Tm$=0$ to a minimum of 8.32 at Tm$=-1600$ when $v_{\theta 0}=-18.8$ at $r=1$ and $z=0$, and then increases to 16.18 for Tm$=-5500$. For $\mathrm{Re}_\Omega=175$, the maximum value of ψ_0 decreases from 18.9 for Tm$=0$ to a minimum of 9.43 for Tm$=-3500$ when $v_{\theta 0}=-47.8$ at $r=1$ and $z=0$, and then increases to 14.4 for Tm$=-7000$. However the destabilizing effects of the reduction of the average angular momentum are far greater than the stabilizing effects of the partial cancelation of the thermocapillary convection, so that this combination is not benefical.

Dold et al. [1] attributed the beneficial effects of the RMF to the increase of the frequency of the critical disturbance as the magnitude of Tm was increased. For both $\mathrm{Re}_\Omega=100$ and $\mathrm{Re}_\Omega=175$, the addition of the RMF in the opposite azimuthal direction decreases the value of λ_I. Therefore combining an RMF and system rotation in opposite azimuthal directions is also a bad idea because the frequency of the critical disturbance is less than that for either the RMF or system rotation alone.

Here we have only presented results for Pr$=0.02$, corresponding to molten silicon. There are important variations of the thermocapillary instability as Pr is varied over the small values for various semiconductors [6]. However the basic conclusion that combining rotating magnetic field and rotating system is not beneficial is certainly true for all molten semiconductors.

Acknowledgment

This research was supported by the National Science Foundation under Grant CTS-0129028 and by the National Aeronautics and Space Administration under Grants NAG 8-1705 and NAG 8-1817.

References

[1] Dold, P., Croll, A., Lichtensteiger, M., Kaiser, Th., and Benz, K. W., 2001, "Floating Zone Growth of Silicon in Magnetic Fields. IV. Rotating Magnetic Fields," J. Cryst. Growth, **231**, pp. 95–106.
[2] Walker, J. S., Martin Witkowski, L., and Houchens, B. C., 2003, "Effects of a Rotating Magnetic Field on the Thermocapillary Instability in the Floating Zone Process," J. Cryst. Growth, **252**, pp. 413–423.
[3] Wanschura, M., Shevtsova, V. M., Kuhlmann, H. C., and Rath, H. J., 1995, "Convective Instability Mechanisms in Thermocapillary Liquid Bridges," Phys. Fluids, **7**, pp. 912–925.
[4] Rupp, R., Muller, G., and Neumann, G., 1989, "Three-Dimensional Time Dependent Modelling of the Marangoni Convection in Zone Melting Configurations for GaAs," J. Cryst. Growth, **97**, pp. 34–41.
[5] Fischer, B., Friedrich, J., Weimann, H., and Muller, G., 1999, "The Use of Time-Dependent Magnetic Fields for Control of Convective Flows in Melt Growth Configurations," J. Cryst. Growth, **198/199**, pp. 170–175.
[6] Levenstam, M., Amberg, G., and Winkler, C., 2001, "Instabilities of Thermocapillary Convection in a Half-Zone at Intermediate Prandtl Number," Phys. Fluids, **13**, pp. 807–816.
[7] Dold, P., and Benz, K. W., 1999, "Rotating Magnetic Field: Fluid Flow and Crystal Growth Applications," Prog. Cryst. Growth Charact. Mater., **38**, pp. 7–38.
[8] Martin Witkowski, L., Walker, J. S., and Marty, Ph., 1999, "Nonaxisymmetric Flow in a Finite-Length Cylinder With a Rotating Magnetic Field," Phys. Fluids, **11**, pp. 1821–1826.
[9] Boyd, J. P., 2001, *Chebyshev and Fourier Spectral Methods*, 2nd ed., Dover Publications, New York.
[10] Smith, B. T. et al., 1976, *Matrix Eigensystem Routines—EISPACK Guide, Lecture Notes in Computer Science*, Vol. 6, New York, Springer-Verlag.
[11] Chen, G., Lizee, A., and Roux, B., 1997, "Bifurcation Analysis of the Thermocapillary Convection in Cylindrical Liquid Bridges," J. Cryst. Growth, **180**, pp. 638–647.

Investigation of Steady-State Drawing Force and Heat Transfer in Polymer Optical Fiber Manufacturing

Hayden M. Reeve

Ann M. Mescher
e-mail: mescher@u.washington.edu

Ashley F. Emery

University of Washington,
Department of Mechanical Engineering,
Box 352600, Seattle,
Washington 98195-2600

The force required to draw a polymer preform into optical fiber is predicted and measured, along with the resultant free surface shape of the polymer, as it is heated in an enclosed cylindrical furnace. The draw force is a function of the highly temperature dependent polymer viscosity. Therefore accurate prediction of the draw force relies critically on the predicted heat transfer within the furnace. In this investigation, FIDAP was used to solve the full axi-symmetric conjugate problem, including natural convection, thermal radiation, and prediction of the polymer free surface. Measured and predicted shapes of the polymer free surface compared well for a range of preform diameters, draw speeds, and furnace temperatures. The predicted draw forces were typically within 20% of the experimentally measured values, with the draw force being very sensitive to both the furnace wall temperature and to the feed rate of the polymer. [DOI: 10.1115/1.1677420]

Introduction

In this paper we examine the force required to draw polymer optical fiber (POF). POF is manufactured by heating a preform via radiative and convective heat transfer within a cylindrical furnace enclosure (Fig. 1). A preform, of diameter D, is fed at a constant velocity (V_p) into the furnace where its viscosity drops by several orders of magnitude when heated. The preform necks-down to the final fiber diameter (d_f) due to an applied draw force (F). The fiber then exits the furnace at a constant draw velocity (V_f). Under steady-state conditions, the fiber diameter is $d_f = D(V_p/V_f)^{0.5}$.

The exerted draw force affects both the viability of fiber drawing and the quality of the final fiber. If the draw force exceeds the ultimate yield strength of the polymer the fiber will break. Alternatively, if the draw force is too low (i.e., the polymer viscosity is too low) the fiber may ''glob'' causing detrimental variations in the fiber diameter [1]. Jiang et al. [2] have shown that the draw force can also affect both the fiber's mechanical properties (such as tensile strength and ductility) and the degree of polymer chain alignment, which can cause orientational birefringence.

Most investigations to date have focused on glass fiber drawing. One of the earliest investigations was by Glicksman [3] who studied the dynamics of a glass melt. Using a number of simplifying assumptions, including the small-slope approximation ($dr/dz < 0.1$), he developed the following one-dimensional momentum equation:

$$\frac{d}{dz}\left(\frac{\dot{m}^2}{\pi\rho r^2}\right) = \frac{d}{dz}\left[-\frac{6\dot{m}\mu}{\rho r}\frac{dr}{dz} + \pi\gamma r\cos\theta\right] + \pi\rho g r^2 - 2\pi\tau_a r\cos\theta \tag{1}$$

The term on the left hand side represents the change in axial momentum of an infinitesimally small element as it travels downward. This change in momentum is the result of the net viscous, surface tension, weight, and air resistance forces. The draw force is given by the expression within the square brackets. The effect of surface tension is often neglected and the following equivalent term is more commonly used [4,5]:

$$F = 3\mu A\frac{d\overline{u}}{dz} \quad \left(= -\frac{6\dot{m}\mu}{\rho r}\frac{dr}{dz}\right) \tag{2}$$

Evaluating the draw force in Eq. (2) requires accurate prediction of the highly temperature dependent polymer or glass viscosity. Therefore, a thorough understanding of the heat transfer within the furnace environment is needed. Furthermore, the heat transfer and draw force depend on the shape of the necking preform (dr/dz). The shape of the necking preform is in turn dependent on the polymer viscosity, thus creating a highly coupled problem.

Early predictions of the free surface shape involved many simplifying assumptions. Paek and Runk [4] predicted the neck-down shape of glass optical preforms using a radially lumped temperature and velocity approximation. The free-surface shape was calculated via a segregated method and the predicted free-surface profiles compared well to experimental values obtained from quenched preforms. Roy Choudhury, Jaluria, and Lee [5] carried out a more sophisticated treatment of the problem and solved the fully conjugate problem calculating the full flow and temperature fields in both the necking preform and surrounding gas. When solving the free surface they radially lumped the velocity and calculated the free surface shape using a segregated solution method.

Radiation is the principle mode of heating in both glass optical fiber drawing [6] and polymer fiber drawing [7]. In particular, the high processing temperatures common in glass fiber manufacture ($\sim 2200°C$) have prompted considerable investigation into the radiative heat transfer phenomena within the furnace environment. Lee and Jaluria [6] found that the net enclosure method was necessary for modeling the thermal radiation in order to correctly account for the self-viewing experienced by the furnace wall, which effectively increases the furnace wall's irradiance. Yin and Jaluria [8] examined the assumptions commonly used in radiative modeling (such as the Rosseland and optically thick approximations) by employing the zonal method. The optically thick approximation was found to be valid for small radial temperature variations within glass preforms. Finally, more recent work by Liu et al. [9] showed that assuming the interface behaved as a Fresnel surface did not result in substantially different preform temperatures from those predicted using the diffuse surface assumption.

Considerably less investigation has focused on modeling the

Contributed by the Heat Transfer Division for publication in the JOURNAL OF HEAT TRANSFER. Manuscript received by the Heat Transfer Division June 26, 2003; revision received November 24, 2003. Associate Editor: P. M. Ligrani.

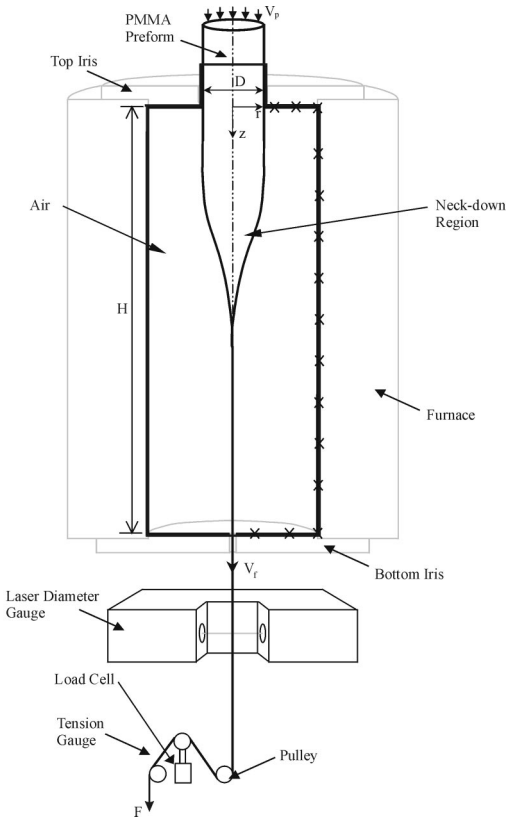

Fig. 1 The fiber drawing system. (The numerical domain is outlined in bold and all thermocouple locations are denoted with a '×'.)

radiative heat transfer of Poly(methyl methacrylate) (PMMA), the polymer studied in this paper. Sala [10] does report values of emissivity in the range of 0.6–0.8 for wavelengths between 2.5 and 13 μm. However, the fact that the radiative properties of PMMA (chemically $(C_5H_8O_2)_n$) are highly wavelength dependent [11] due to the many vibrational modes of PMMA's bonds further complicates matters. For example, there are many high absorptivity peaks around the 10 μm region due to the excitation of the C—H, C—O—C, and C═O bending frequencies, and this region also corresponds to the twisting frequencies of the methyl and ethyl groups [12]. In addition to regions of high absorptivity, PMMA also exhibits the low reflectivity common among nonmetallic substances [13]. Due to insufficient radiative properties for PMMA, we conducted experiments in which PMMA preforms with various surface treatments were heated within our furnace [14]. Thermocouple readings within the preforms indicated that unaltered PMMA preforms heat at a rate identical to those painted black, even when experiencing large internal temperature gradients. Furthermore, complementary numerical calculations demonstrated that the thermal radiation heat transfer can be accurately predicted by assuming that all of the radiation exchange occurs at the surface of the preform.

Because most glass optical fiber drawing systems utilize the forced convection of gas, there has been little investigation of the role that natural convection plays. One exception was the investigation of Papamichael, Pellon, and Miaoulis [15] who experimentally visualized the natural convection flow patterns within an open-ended cylindrical glass optical fiber tube heater, using water as the working fluid. We have shown in previous work that natural convection accounts for up to 50% of the initial heating of stationary polymer preforms [7,14]. More importantly we have shown that during fiber drawing the natural convection circulation within the furnace can become unstable [16]. In particular, as the buoyant potential within the furnace is increased the airflow can transition from a laminar (time-invariant) regime to an oscillatory or chaotic regime. The unsteady heating characteristic of these latter two regimes causes detrimental fiber diameter variations.

This study describes the first reported numerical investigation of the steady-state heat and mass transfer phenomena associated with polymer preform drawing. Our goals are to understand the nature of the buoyancy driven circulation within the furnace, to quantify the amount of heating due to natural convection and thermal radiation, and to predict the steady-state neck-down profile and the required draw force. This study also compares experimental measurements of the draw force and neck down profile with numerical predictions. To date there has been a conspicuous absence of experimental data and very little sensitivity analysis of numerical predictions. We therefore briefly comment on the challenges associated with accurately predicting the draw force.

Experimental System and Procedure

Our experimental system is shown in Fig. 1. The furnace has a height (H) of 0.39 m (15.5″) and an inner diameter of 0.064 m (2.5″). It was capped at both ends by irises that allowed the polymer to enter and exit but effectively prohibited bulk airflow into or out of the furnace. An extruded PMMA preform was fed through the top iris by a stepper motor at a specified feed velocity (V_p). Fiber exited the furnace through a 1.6 mm diameter hole in the bottom iris. The fiber diameter was not actively controlled and the draw speed (V_f) was held constant. The temperatures of the furnace wall and irises were recorded by 15 type K thermocouples accurate to ± 0.5°C (see Fig. 1 for locations). These measurements were used to specify the thermal boundary conditions in the numerical model. The furnace wall temperature profile was held constant during drawing by a proportional controller. The operating conditions for four experiments (E1 through E4) are shown in Table 1.

The fiber diameter was monitored 10 cm below the bottom iris by a laser diameter gauge. Steady-state was assumed to have been reached when the furnace wall temperatures remained constant for more than 30 minutes and the measured fiber diameter satisfied the conservation of mass requirements ($d_f = D(V_p/V_f)^{0.5}$). Further downstream the fiber passed over a load cell and the resultant force was measured. To reduce bias errors in the draw force measurement, the load cell was calibrated with a known weight (to within 1×10^{-5} N) before each fiber draw. The estimated 95% uncertainty limit for the draw force measurements is approximately ± 0.02 N.

After drawing was completed, the preform was removed from the furnace and rapidly quenched. The axial radius profile was then measured at 5 mm intervals. The radius profiles from three identical experimental runs (for case E1) exhibited an average standard deviation of 0.04 mm (1.5%). The 95% uncertainty limit in the radius profile is estimated at ± 0.1 mm.

Table 1 Experimental parameters

Operating Conditions	E1	E2	E3	E4	Uncertainty (±)
Draw speed (V_f) cm/s	10	20	5	10	0.2%
Feed speed (V_p) μm/s	25	50	12.5	11	1.0%
Preform dia. (D) mm	25.4	25.4	25.4	38.1	0.4
Max wall temp (T_w) °C	168.8	189.7	168.8	169.0	0.5

Mathematical Model

In this study, the steady-state axi-symmetric conjugate problem is solved. This investigation is therefore limited to conditions for which natural convection heat transfer is in the laminar regime [16]. The numerical domain includes both the air and the polymer and it extends one preform diameter above the top iris (see Fig. 1).

Governing Equations. The conservation of mass in cylindrical coordinates is represented by

$$\frac{1}{r}\frac{\partial(\rho r v)}{\partial r}+\frac{\partial(\rho u)}{\partial z}=0 \tag{3}$$

The momentum equations in the radial and axial directions are, respectively,

$$\rho\left(v\frac{\partial v}{\partial r}+u\frac{\partial v}{\partial z}\right)=-\frac{\partial P}{\partial r}+\frac{\partial}{\partial z}\left(\mu\left[\frac{\partial u}{\partial r}+\frac{\partial v}{\partial z}\right]\right)+\frac{1}{r}\frac{\partial}{\partial r}\left(2\mu r\frac{\partial v}{\partial r}\right)-\frac{2\mu v}{r^2} \tag{4}$$

and

$$\rho\left(v\frac{\partial u}{\partial r}+u\frac{\partial u}{\partial z}\right)=\frac{\partial}{\partial z}\left(-P+2\mu\frac{\partial u}{\partial z}\right)+\frac{1}{r}\frac{\partial}{\partial r}\left(r\mu\left[\frac{\partial u}{\partial r}+\frac{\partial v}{\partial z}\right]\right)+\rho g \tag{5}$$

The energy equation is

$$\rho c_p\left(v\frac{\partial T}{\partial r}+u\frac{\partial T}{\partial z}\right)=\frac{\partial}{\partial z}\left(k\frac{\partial T}{\partial z}\right)+\frac{1}{r}\frac{\partial}{\partial r}\left(kr\frac{\partial T}{\partial r}\right)+\Phi \tag{6}$$

where Φ represents the viscous dissipation function

$$\Phi=\mu\left\{2\left[\left(\frac{\partial v}{\partial r}\right)^2+\left(\frac{v}{r}\right)^2+\left(\frac{\partial u}{\partial z}\right)^2\right]+\left[\frac{\partial v}{\partial r}+\frac{\partial u}{\partial z}\right]^2\right\}$$

All air properties are considered temperature dependent [17]. The air density is assumed to vary as

$$\rho=\rho_o[1-\beta(T-T_o)] \tag{7}$$

where $\rho_o=0.995$ kg/m^3, $\beta=0.0023$ K^{-1}, and $T_o=350$ K. The values c_p, k, and μ were interpolated from the tabulated values in [18].

The thermophysical properties of PMMA are as follows; $\rho=1195$ kg/m^3; $c_p=1465$ J/kg.K; $k=0.193$ W/m^{2}K. The polymer's zero-shear viscosity was measured experimentally and a best-fit equation was obtained

$$\mu=1.506\times10^5\exp\left[2935\left(\frac{1}{T}-\frac{1}{170°\text{C}}\right)\right]\ \text{N.s/m}^2 \tag{8}$$

To prevent possible computational instabilities caused by the presence of very large values of the polymer viscosity (for example at room temperature Eq. (8) gives $\mu\approx10^{53}$ kg/m.s) [19], the polymer viscosity is held constant for temperatures below 109°C

$$\mu=2.3\times10^9\ \text{N.s/m}^2 \quad \text{for } T<109°\text{C} \tag{9}$$

For all cases studied the polymer's shear rate did not exceed 2 s^{-1}. For this reason the polymer's viscosity model has no shear dependence. In addition, all elastic effects are assumed to occur below the neck-down region and are therefore neglected.

Boundary Conditions. The boundary conditions are as follows:

At the bottom iris ($z=H$, $R_g\leq r\leq R_w$)

$$u=v=0, \quad T=T_b$$

At the top iris ($z=0$, $0.5D<r\leq R_w$)

$$u=v=0, \quad T=T_t$$

Along the furnace wall ($r=R_w$, $0\leq z\leq H$)

$$u=v=0, \quad T=T_w(z)$$

where $T_w(z)$ is given by a cubic piecewise spline fitted to the experimentally measured wall temperatures.

Along the axis of symmetry ($r=0$, $-D\leq z\leq H$)

$$|u|<\infty, \quad v=0, \quad |T|<\infty$$

At the radial surface of the preform located above the furnace cavity and adjacent to the top iris ($r=R_p$, $-0.32D<z\leq0$)

$$u=V_p, \quad v=0, \quad \frac{\partial T}{\partial r}=-\frac{U_t}{k}(T-T_t)$$

where the overall heat transfer coefficient is $U_t=30$ W/m^{2}K. This value accounts for heat transferred from the top iris to the adjacent preform via two parallel paths: one through the thin separating air gap, the other through a rubber "O"-ring used to seal the top iris [20].

At the radial surface of the preform located above the furnace cavity and adjacent to the ambient air ($r=R_p$, $-D<z\leq-0.32D$)

$$u=V_p, \quad v=0, \quad \frac{\partial T}{\partial r}=-\frac{h_\infty}{k}(T-T_\infty)$$

where the convective heat transfer coefficient is $h_\infty=10$ W/m^{2}K, an appropriate value for natural convection from a vertical surface [20], and $T_\infty=23$°C.

At the top of the preform ($z=-D$, $0\leq r\leq R_p$)

$$u=V_p, \quad v=0, \quad \frac{\partial T}{\partial z}=\frac{U_{\text{fin}}}{k}(T-T_\infty)$$

where U_{fin} is an overall heat transfer coefficient equivalent to the heat lost through the base of an infinitely long fin

$$U_{\text{fin}}=\sqrt{\frac{4h_\infty k}{D}}$$

At the fiber exit ($z=H$, $0\leq r\leq R_f$) the draw speed is specified and the thermal field is assumed to be dominated by convection

$$u=V_f, \quad v=0, \quad \frac{\partial T}{\partial z}=0$$

In the gap between the fiber and the bottom iris ($z=H$, $R_f\leq r\leq R_g$)

$$\frac{\partial u}{\partial z}=0, \quad v=0, \quad \frac{\partial T}{\partial z}=0$$

At the interface between the air and the polymer, flow normal to the interface is prohibited and the no-slip condition is applied. Furthermore, the contribution of surface tension (γ) is assumed to be negligible and the continuity of the normal and shear stresses is maintained. Temperature continuity is also satisfied at the interface and the energy balance gives

$$k\frac{\partial T}{\partial n}\bigg|_a+q=k\frac{\partial T}{\partial n}\bigg|_p$$

The net radiative method for enclosures [21] was used to calculate the thermal radiative heat flux (q) experienced by the polymer surface. The furnace enclosure and polymer were assumed to be optically thick with gray surfaces. The air did not participate in the radiation exchange. For each elemental surface the following equation applies:

$$\sum_{j=1}^{N}\left[\frac{\delta_{kj}}{\varepsilon_j}-F_{k-j}\frac{1-\varepsilon_j}{\varepsilon_j}\right]q_j=\sum_{j=1}^{N}\left(\delta_{kj}-F_{k-j}\right)\sigma T_j^4 \qquad (10)$$

The furnace wall was assigned a total hemispherical emissivity of 0.75 [22]. The irises (which were painted black) and the polymer were assigned values of 0.96 [14]. The lower gap in the air domain was assigned an emissivity of unity and a reference temperature that was equal to the ambient temperature. Therefore, all outgoing radiation through this surface is absorbed by the external environment, while all incoming radiation through this surface is emitted at the ambient temperature.

Numerical Solution Procedure

This is a highly coupled nonlinear problem due to the effects of thermal radiation, temperature dependent viscosity, buoyancy, and a free surface. The commercial finite element code FIDAP v8.7 was used to solve the velocity and temperature fields, which were represented as continuous, bi-quadratic polynomials within elements. The pressure was represented as a linear polynomial that was discontinuous across element boundaries [23]. The free-surface location was represented as a continuous quadratic polynomial, with nodes adjacent to the interface being displaced using the method of spines [24]. The view factors ($F_{k\text{-}j}$) used in Eq. (10) were evaluated using the HEMICUBE method [25]. The summation of view factors for each surface was within 5×10^{-6} of unity.

The mesh had a total of 1274 9-noded quadrilateral elements and 5295 nodes (169 nodes along the free surface and 31 in the radial direction). The mesh was graded to provide higher resolution near the irises, free-surface, and furnace wall. The polymer surface and furnace wall were divided into 60 radiating macro-elements each (approximately one per free surface element). The top and bottom irises and the air gap were each represented by one macro-element.

FIDAP's upwinding option was not utilized and our results indicate that any numerical diffusion inherent in the numerical scheme does not damp out secondary convective flows [26]. In particular, we used FIDAP to successfully predict the secondary multi-cellular flows observed by Vest and Arpaci [27]. Also, select results of Le Quéré and Pécheux's work [28], concerning natural convection oscillations within a tall annulus, were reproduced with excellent agreement.

Due to the complex nature of this problem it was solved incrementally, with the fully coupled Newton-Raphson method used at each step. First, the flow field within the polymer was solved using a fixed free surface shape (a linear piece-wise initial guess). Second, the full heat transfer problem was solved with the free surface still held fixed. Third, the free surface shape was calculated simultaneously with all other degrees of freedom using the solution to the previous step as the initial guess. Obtaining convergence in this final step required considerable under-relaxation (0.003) of all of the degrees of freedom due to the considerable coupling and mesh deformation. For this study the solution was considered converged when the tension and free surface predicted at one iteration were within 1% and 50 μm, respectively, of the values reported after an additional 900 iterations were performed.

Numerical Uncertainty

The model performed well under a number of self-consistency tests. The predicted free-surface was independent of the initial guess. Results were also compared to those obtained with a finer mesh (13,901 nodes) for the conditions of case E1. The results of the refinement studies will be expressed in terms of the grid convergence index (GCI) that is based on Richardson's extrapolation [29]. For a coarse grid:

$$GCI_{\text{coarse}}=\frac{3r^p(f_c-f_f)}{f_c(1-r^p)}$$

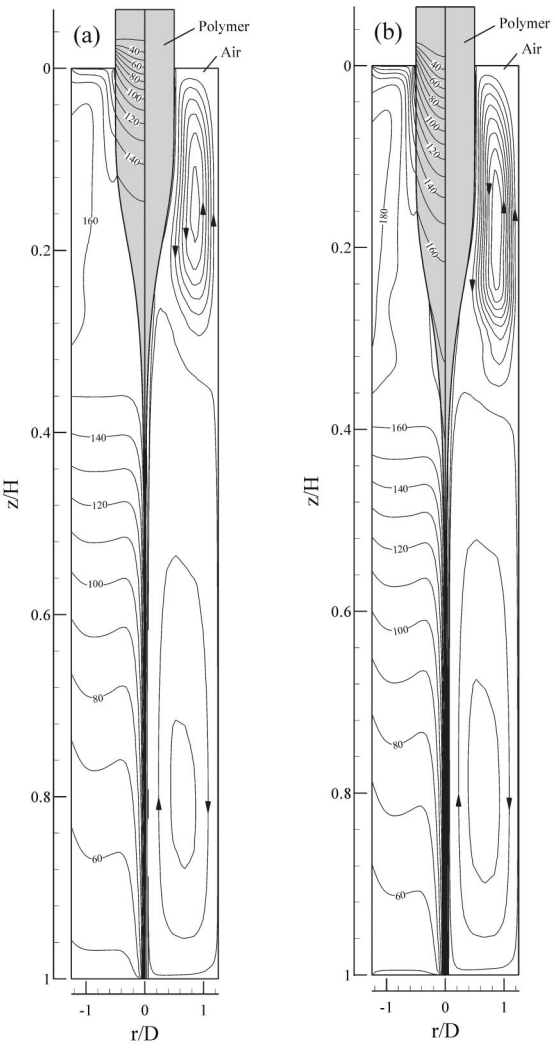

Fig. 2 Axial variation of the radiative and convective heat flux experienced at the polymer's surface for case E1

where f_f and f_c are some solution norm for the fine and coarse grids, respectively, r represents the ratio of grid densities, and p represents the order-of-accuracy of the method. The maximum absolute difference in the predicted free surface radius profile between the two grids was 0.15 mm (1.8%; $r=1.62$; $p=2$; GCI $=8.8\%$). The maximum difference in the polymer temperature predicted on the axis for the two grids was 0.2°C (0.1%). The draw force is the most important variable of interest and varied by only 0.02 N between the two grids (2.2%; GCI$=10.8\%$). When the number of radiating elements along the polymer surface and furnace wall was reduced from 60 to 30 the predicted polymer axis temperature varied by an average of 0.48°C (0.2%). The draw force changed by 0.056 N (5%). This sensitivity of the draw force to the number of radiating elements is due to the significant contribution of thermal radiation and the polymer viscosity's sensitive dependence on temperature. Both issues will be discussed in the next section.

Results and Discussion

Heat Transfer. Contour plots of the temperature and stream function for the drawing conditions of case E1 and E2 are shown in Fig. 2. For case E1 the peak wall temperature was located at $z/H=0.15$. As can be seen in Figs. 2(a) and 3 the furnace wall temperature rapidly decreases in the lower three quarters of the

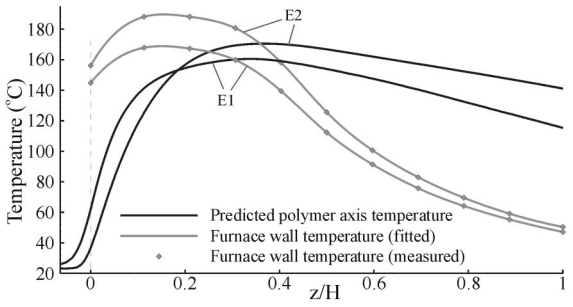

Fig. 3 Numerically predicted contour plots of temperature (at left in °C) and stream function (right) for (*a*) case E1 and (*b*) case E

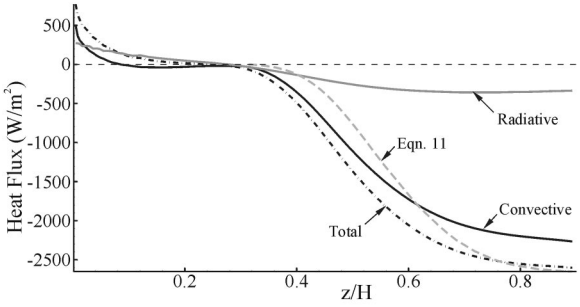

Fig. 4 Axial variation of the predicted polymer temperature (at $r=0$) and the furnace wall temperature for cases E1 ($V_f=10$ cm/s) and E2 ($V_f=20$ cm/s)

furnace. The preform enters the numerical domain ($z=-D$) at near ambient conditions. It experiences considerable heating in the zone above the top iris and in the upper region of the furnace. However, below approximately $z/H=0.3$ the polymer axis temperature exceeds the adjacent wall temperature and the polymer starts to cool.

Figure 2 shows that the free convection flow is divided into two cells. Particle image velocimetry (PIV) flow visualization conducted in a transparent model furnace confirms this bi-cellular flow pattern [16]. In the lower region of the furnace the fiber speed is high and the fiber is hot. This is because the heat gained by the polymer in the upper region of the furnace has been advected downstream. The temperature difference between the hot polymer and the cooler furnace region creates a weak convective cell. The accelerating fiber does entrain some air due to the no slip condition, but buoyancy forces dominate shear forces and this entrainment is limited to a thin boundary layer. The extent of the lower cell is limited by the presence of an upper cell. This upper cell is driven by the temperature difference between the hot furnace wall and the cooler preform surface.

For case E2 the feed speed is doubled and the peak wall temperature is increased 20°C to prevent the fiber from breaking due to an excessive draw force. The increased preform feed speed reduces the polymer's residence time resulting in less effective heating upstream of the furnace and a greater radial temperature gradient within the polymer. This increased feed speed also causes the polymer to progress further downstream before exceeding the local furnace wall temperature (see Fig. 3). The larger temperature difference between the furnace wall and the preform in the upper region of the furnace promotes more vigorous circulation than predicted in case E1. Despite these differences the convective flow patterns are qualitatively the same.

Comparison of cases E1 and E2 illustrates that the relative sizes of the two convective cells is determined in part by the location at which the polymer temperature exceeds the adjacent wall temperature. For case E1 the polymer temperature exceeds the adjacent wall temperature at approximately $z/H=0.3$. This corresponds to the lower extremity of the upper cell. Likewise, for case E2 the polymer temperature exceeds the adjacent wall temperature at $z/H=0.36$, again corresponding to the lower extremity of the upper cell.

Figure 4 shows the axial variation of the radiative and convective heat fluxes experienced at the polymer's free surface for case E1. Consistent with the above discussion the polymer begins to cool at approximately $z/H=0.3$. Thermal radiation accounts for approximately 70% of the polymer's heating but only 15% of the polymer's cooling. The increase in the convective heat flux in the lower section of the furnace ($z/H>0.4$) is due to the enhanced cooling caused by the higher fiber speed. The predicted heat flux is in good qualitative agreement with the empirical Nu-Re relationship found by Kase and Matsuo [30] for co-axial flow along a heated wire

$$\mathrm{Nu}=0.42\,\mathrm{Re}^{0.334} \tag{11}$$

Given the significance of thermal radiation heat transfer in the upper region of the furnace it is important to understand the dependence of the numerical solution on the radiative properties of the polymer material and furnace wall. The effect of emissivity can be illustrated by examining the equation for thermal radiation heat transfer between two infinitely long, co-axial, and isothermal cylinders

$$q''_{p-w}=\varepsilon_e\sigma(T_p^4-T_w^4) \tag{12}$$

where the effective emissivity, ε_e, is given by [20]

$$\varepsilon_e=\frac{\varepsilon_p}{1+\left(\dfrac{\varepsilon_p r_p}{\varepsilon_w r_w}\right)(1-\varepsilon_w)} \tag{13}$$

Equation (13) shows that as the ratio of the preform radius to the wall radius approaches zero, the denominator approaches unity and the radiative heat transfer has no dependence on the wall's emissivity value (provided it is nonzero). This is because the wall experiences considerable self-viewing as the preform radius approaches zero and therefore behaves as a blackbody regardless of its emissivity, while any error in the assigned polymer emissivity has a direct effect on the calculated radiative heat transfer. This shows that the numerical solution has a greater sensitivity to the preform's emissivity than to that of the wall. For example, with a polymer emissivity of $\varepsilon_p=0.96$, a wall emissivity of $\varepsilon_w=0.75$, a preform radius of $r_p=25.4\times10^{-3}$ m, and an inner wall radius of $r_w=64.0\times10^{-3}$ m, the preform's effective emissivity is 0.85. If the perform's emissivity is decreased by 10% the effective emissivity decreases by 9%. While, in contrast, if the wall's emissivity is decreased by 10% the effective emissivity is only decreased by 4.5%.

Comparison With Experimental Results. The numerically predicted and experimentally measured free surface shapes for case E1 are shown in Fig. 5. Neglecting the polymer's weight, the draw force (Eq. (2)) remains constant along the length of the necking polymer. Therefore, when the polymer is heated and its viscosity drops by several orders of magnitude there is a commensurate increase in the polymer's elongation (i.e., acceleration) and it necks down due to the conservation of mass constraint. In short, the greatest necking occurs in the vicinity of the polymer's maximum temperature. The maximum difference between the numerically predicted and experimentally measured local free surface radius profile was 0.7 mm (18%) for case E1 (the average difference was 0.23 mm (11%)).

As the feed rate is increased the polymer does not reach its maximum temperature until further downstream, delaying the on-

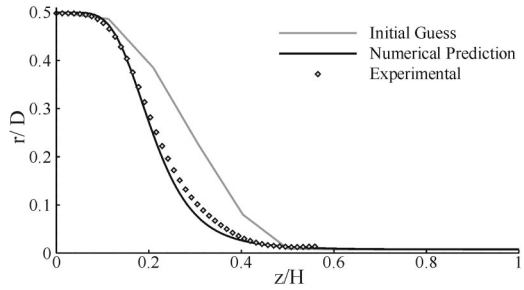

Fig. 5 Effect of preform feed speed on the predicted (solid line) and measured (symbols) free surface shapes

set of necking. Figure 6 shows that both the experimental and numerical results confirm this trend. The average discrepancies between the measured and predicted free surfaces for cases E2 and E3 were 0.44 mm (30%) and 0.19 mm (17%) respectively. Figure 7 shows the effect of a larger preform diameter (E4) while maintaining the same mass flow rate as case E1. The average difference for this case was 0.7 mm (23%), considerably larger than for cases E1-3.

In comparing the predicted and measured free surface profiles it is important to consider the effect of the polymer's thermal expansion. In this case the effect of thermal expansion is negligible. The coefficient of thermal expansion for PMMA is approximately 4.8×10^{-4} K^{-1} for temperatures above the glass transition temperature ($T_g=105°C$) and approximately 2.1×10^{-4} K^{-1} for temperatures below the glass transition [31]. For case E1 the maximum radial expansion is only 0.22 mm (1.8%) with an average radial expansion of 0.05 mm. These values are significantly less than the difference between the experimental and numerical findings and are comparable to the estimated uncertainty in the experimentally measured free surface profile.

Results of the predicted and measured draw forces are presented in Table 2. Cases E1 and E4 have identical mass throughputs and similar maximum predicted polymer axis temperatures

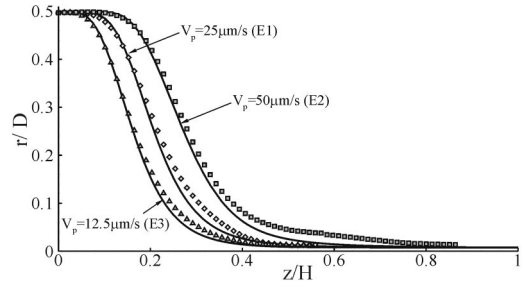

Fig. 6 Numerically predicted and experimentally measured free surface shapes for case E1. (The initial guess is shown for comparison.)

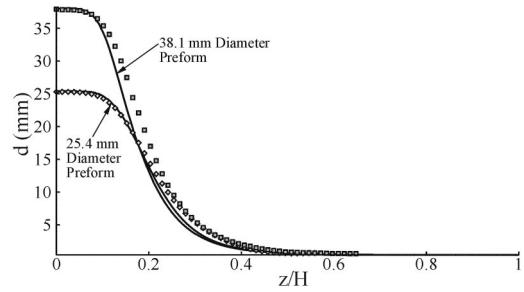

Fig. 7 Effect of preform diameter on the predicted (solid line) and measured (symbols) free surface shapes

Table 2 Summary of draw force (*N*) comparisons

Case	Experimental (±0.02 N)	Numerical	% difference
E1	0.92	1.11	21
E2	0.62	0.63	2
E3	0.41	0.45	10
E4	0.89	1.06	19

(which were within 0.5°C of each other). It is therefore unsurprising that these cases exhibit similar draw forces. By comparison, case E3 shows that when the polymer feed speed is halved there is a substantial drop in the required draw force. This is due to two reasons. First, at lower mass throughputs the polymer typically reaches a higher maximum temperature (3°C higher for case E3 than for case E1) resulting in a lower polymer viscosity. Second, a lower mass throughput results in a lower rate of elongation ($d\bar{u}/dz$) provided the free surface slope remains similar (see Eq. (2)). Finally, although case E2 has twice the throughput of case E1 it requires a lower draw force. This is explained by considering the competing influences of the highly temperature dependent polymer viscosity and the rate of elongation. The polymer in case E2 experiences a greater amount of heating and reaches a maximum temperature 10°C higher than that for case E1. This leads to a considerably lower polymer viscosity that more than compensates for the higher feed rate and, hence, leads to a lower reported draw force.

In order to investigate the effect that the furnace wall temperature has on the draw force, experiment E1 was rerun with several different peak wall temperatures. The preform diameter, feed speed, and draw speeds all remained the same. Figure 8 shows that when the furnace wall temperature was increased by approximately 15°C the draw force decreased by over 80%. This large decrease in draw force is a direct result of the polymer viscosity's sensitive temperature dependence. Manipulating Eq. (8) it can be shown that the percentage change in the polymer's viscosity per degree Celsius change in the polymer's temperature is given by

$$\frac{\Delta\mu}{\mu.\Delta T}=-100\frac{2935}{T^2}\quad \%/°C \tag{14}$$

For example if the polymer's temperature increases from 160°C to 161°C the predicted polymer viscosity decreases by 11.5%. The polymer viscosity has a first order effect on the draw force. Therefore, the high sensitivity of the polymer viscosity directly affects any attempts to accurately predict the draw force.

Given this high sensitivity it is clear that in order to accurately predict the draw force it is necessary to accurately predict the polymer's geometry and heat transfer phenomena. Small errors in the predicted polymer temperature, as a result of modeling assumption errors, discretization errors, inaccurate material property values, and errors in the prescribed boundary conditions, will be amplified by the polymer viscosity model leading to non-

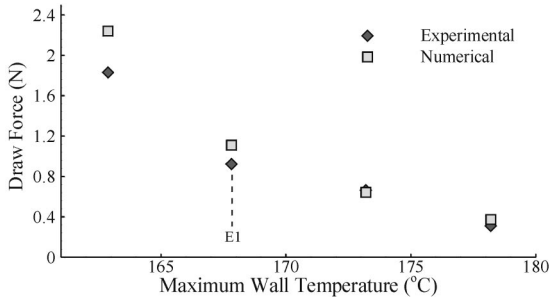

Fig. 8 Effect of upstream heating (U_t) on the predicted free surface shape. A comparison between the results for $U_t=0$ W/m²K (solid line) and $U_t=30$ W/m²K (dashed line) is shown.

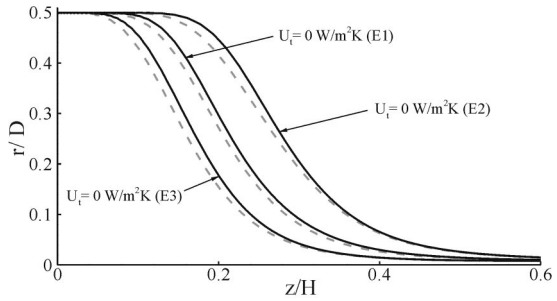

Fig. 9 Effect of the furnace wall temperature on the predicted and measured draw force (D=25.4 mm, V_f=10 cm/s, V_p =25 μm/s)

negligible errors in the predicted draw force. Equation (14) indicates that a 1°C error in the predicted temperature will lead to approximately a 10% error in the predicted draw tension. Therefore, any future efforts to accurately predict the fiber draw force will require further scrutiny of the polymer's heat transfer phenomena and rheology.

Effect of Upstream Heating. Most prior investigations have justifiably ignored any upstream preheating of the preform because of the high feed rates (i.e., Peclet numbers) associated with those studies. However, given the lower feed rates common in the development of POF [32], matched with lower processing temperatures, upstream heating can affect both the predicted free surface shape and draw force. Simulations were run in which the preform was assumed to receive no heating from the top iris prior to its entry into the furnace (i.e., $U_t = 0$ W/m^{2}K). This delays the onset of necking as shown in Fig. 9. Contrary to expectations, at the lowest feed rate (case E3) the change in draw tension was small. Despite a maximum 0.9 mm (12%) increase in the free surface shape the tension only increased by 0.014 N (3%). This is most likely because the polymer's low feed rate allows it to reach a psuedo-thermal-equilibrium with the furnace wall resulting in an almost identical maximum axis polymer temperature (to within 0.1°C) regardless of the presence of upstream heating.

For case E1 the maximum free-surface change is 0.68 mm (7.5%). However, in the absence of upstream heating the maximum polymer temperature is 2.8°C lower, leading to a draw tension 35% higher than that predicted with $U_t = 30$ W/m^{2}K. For case E2 the maximum free surface change is 0.86 mm (11%). Because the residence time in the vicinity of the top iris is less for case E2, the maximum polymer temperature is only 1.7°C lower than with $U_t = 30$ W/m^{2}K leading to a 20% increase in the predicted draw force. It is expected that as feed rates increase to those more common in industrial glass fiber drawing ($\sim$1–20 m/s) the importance of upstream heating will diminish.

Conclusions

Modeling the polymer optical fiber drawing system requires solving a highly coupled nonlinear problem. Accurately predicting the draw force is further complicated by the sensitive temperature dependence of the polymer viscosity. Our results show that the draw force can be accurately predicted provided that sufficient attention is paid to modeling the heat and mass transfer phenomena within the fiber drawing environment.

The natural convection flow is governed by the temperature difference between the polymer and adjacent furnace wall. In all cases the circulation was divided into two cells, one driven by the cool preform and hot wall in the upper region of the furnace, while the other counter-circulating cell is driven by the temperature difference between the hot fiber and the cooler lower wall. Thermal radiation contributes approximately 70% of the preform's heating. Results indicate that the net enclosure method adequately models the thermal radiation exchange within the furnace environment. However, care is required, to ensure that any developed model has a sufficient number of radiating elements and accurate view factors and emissivity values.

The draw force is highly dependent on both the polymer feed rate and the furnace wall temperature. Changes in polymer temperature as small as 1°C typically result in changes in the draw force on the order of 10%. Given this inherent sensitivity, improving accuracy will require improved knowledge of the polymer's thermal and rheological properties. As the development of POF manufacture progresses and draw speeds increase, investigation of shear-thinning and visco-elastic effects may also be warranted.

Acknowledgment

We are pleased to acknowledge support for this work from the National Science Foundation, Grant # ECS 9734438.

Nomenclature

A = area
c_p = specific heat
d = diameter
D = preform Diameter
F = draw Force
$F_{k\text{-}j}$ = view factor
g = acceleration due to gravity
h = convective heat transfer coefficient
H = furnace height
k = thermal conductivity
m = mass flow rate
n = surface normal
P = pressure
q = thermal radiation heat flux
r = radius
T = temperature
t = time
u = axial velocity
U = overall heat transfer coefficient
v = radial velocity
V = speed
z = axial coordinate

Greek Symbols

β = thermal expansion coefficient
ε = emissivity
γ = surface tension
τ = shear stress
θ = angle between vertical and free surface tangent
μ = dynamic viscosity
ρ = density
σ = Stefan-Boltzmann constant
Φ = viscous dissipation function

Superscripts & Subscripts

a = air
b = bottom iris
e = effective
f = fiber
g = gap
o = reference
p = preform
t = top iris
w = furnace wall
∞ = ambient

References

[1] Senior, J. M, 1992, *Optical Fiber Communication: Principles and Practice*, Prentice Hall.
[2] Jiang, C., Kuzyk, M. G., Ding, J.-L., Johns, W. E., and Welker, D. J., 2002,

''Fabrication and Mechanical Behavior of Dye-Doped Polymer Optical Fiber,'' J. Appl. Phys., **92**(1), pp. 4–12.
[3] Glicksman, L. R., 1968, ''The Dynamics of a Heated Free Jet of Variable Viscosity Liquid at Low Reynolds Number,'' ASME J. Basic Eng., **90**, pp. 343–354.
[4] Paek, U. C., and Runk, R. B., 1978, ''Physical Behavior of the Neck-Down Region During Furnace Drawing of Silica Fibers,'' J. Appl. Phys., **49**(8), pp. 4417–4422.
[5] Roy Choudhury, S., Jaluria, Y., and Lee, S. H.-K., 1999, ''A Computational Method for Generating the Free Surface Neck-Down Profile for Glass Flow in Optical Fiber Drawing,'' Numer. Heat Transfer, Part A, **35**, pp. 1–24.
[6] Lee, S. H.-K., and Jaluria, Y., 1995, ''The Effects of Geometry and Temperature Variations on the Radiative Transport During Optical Fiber Drawing,'' J. Mater. Process. Manuf. Sci., **3**, pp. 317–331.
[7] Reeve, H. M., and Mescher, A. M., 1999, ''A Study on Transient Heating of Polymer Fiber Preforms,'' J. Mater. Process. Manuf. Sci., **8**(2), pp. 94–105.
[8] Yin, Z., and Jaluria, Y., 1997, ''Zonal Method to Model Radiative Transport in an Optical Fiber Drawing Furnace,'' ASME J. Heat Transfer, **119**, pp. 597–603.
[9] Liu, J., Zhang, S. J., and Chen, Y. S., 2001, ''Advanced Simulation of Optical Fiber Drawing Process,'' Numer. Heat Transfer, Part A, **40**, pp. 473–496.
[10] Sala, A., 1986, *Radiation Properties of Materials*, Elsevier.
[11] Schrader, B., 1989, *Raman/Infrared Atlas of Organic Compounds*, Wiley-VCH.
[12] Manohar, S. S., and Thynell, S. T., 1995, ''In-Depth Absorption of Externally Incident Radiation in Nongray Media,'' ASME J. Heat Transfer, **117**, pp. 146–151.
[13] Touloukian, Y. S., and DeWitt, D. P., 1970, *Thermophysical Properties of Matter: Thermal Radiative Properties*, TPDR Data Series, **8**, IFI Plenum.
[14] Reeve, H. M., Mescher, A. M., and Emery, A. F., 2001, ''Experimental and Numerical Investigation of Polymer Preform Heating,'' J. Mater. Process. Manuf. Sci., **9**(4), pp. 285–301.
[15] Papamichael, H., Pellon, C., and Miaoulis, I. N., 1997, ''Air Flow Patterns in the Optical Fibre Drawing Furnace,'' Glass Technol., **38**(1), pp. 22–29.
[16] Reeve, H. M., and Mescher, A. M., 2003, ''Effect of Unsteady Natural Convection on the Diameter of Drawn Polymer Optical Fiber,'' Opt. Express, **11**, pp. 1770–1779.
[17] Gray, D. D., and Giorgini, A., 1975, ''The Validity of the Boussinesq Approximation for Liquids and Gases,'' Int. J. Heat Mass Transfer, **19**, pp. 545–551.
[18] Van Wylen, G., Sonntag, R., and Borgnakke, C., 1994, *Fundamentals of Classical Thermodynamics*, John Wiley and Sons.
[19] Lee, S. H.-K., and Jaluria, J., 1996, ''Effects of Variable Properties and Viscous Dissipation During Optical Fiber Drawing,'' ASME J. Heat Transfer, **118**, pp. 350–358.
[20] Incropera, F. P., and DeWitt, D. P., 1990, *Fundamentals of Heat and Mass Transfer*, Wiley.
[21] Siegel, R. and Howell, J. R., 1992, *Thermal Radiation Heat Transfer*, Taylor & Francis.
[22] Gubareff, G. G., and Janssen, J. E., 1960, *Thermal Radiation Properties Survey*, Honeywell.
[23] Fluent Inc, 1999, *FIDAP Users Manual*, Fluent Inc., Lebanon, NH.
[24] Saito, H., and Scriven, L. E., 1981, ''Study of Coating by the Finite Element Method,'' J. Comput. Phys., **42**, pp. 53–76.
[25] Cohen, M. F., and Greenberg, D. P., 1985, ''The Hemi-Cube: A Radiosity Solution for Complex Environments,'' Comput. Graphics, **19**(3), pp. 31–40.
[26] Drummond, J. E., Yovichen, A. J., and J. P. McKee, 1991, ''The Effect of Upwind Formulations on Secondary Flows in a Thermally Driven Cavity,'' *Proc. ASME-JSME Thermal Engineering. Joint Conf.*, **1**, pp. 147–154.
[27] Vest, C. M., and Arpaci, V., 1969, ''Stability of Natural Convection in a Vertical Slot,'' J. Fluid Mech., **36**, pp. 1–15.
[28] Le Quéré, P., and Pécheux, J., 1989, ''Numerical Simulations of Multiple Flow Transitions in Axisymmetric Annulus Convection,'' J. Fluid Mech., **206**, pp. 517–544.
[29] Roache, P. J., 1997, ''Quantification of Uncertainty in Computational Fluid Dynamics,'' Annu. Rev. Fluid Mech., **29**, pp. 123–160.
[30] Kase, S., and Matsuo, T., 1965, ''Studies on Melt Spinning. I. Equations on the Dynamics of Melt Spinning,'' J. Polym. Sci. A, **3**, pp. 2555–2565.
[31] Sperling, L. H., 1992, *Introduction to Physical Polymer Science*, Wiley, pp. 337.
[32] Marcou, J., 1997, *Plastic Optical Fibres: Practical Applications*, Wiley.

On the Group Front and Group Velocity in a Dispersive Medium Upon Refraction From a Nondispersive Medium

Z. M. Zhang

Keunhan Park

George W. Woodruff School of Mechanical Engineering,
Georgia Institute of Technology,
Atlanta, GA 30332

Conventional definitions of velocities associated with the propagation of modulated waves cannot clearly describe the behavior of the wave packet in a multidimensional dispersive medium. The conventional definition of the phase velocity, which is perpendicular to the wave front, is a special case of the generalized phase velocity defined in this work, since there exist an infinite number of solutions to the equation describing the wave-front movement. Similarly, the generalized group-front velocity is defined for the movement of a wave packet in an arbitrary direction. The group-front velocity is the smallest speed at which the group-front travels in the direction normal to the group front. The group velocity, which is the velocity of energy flow in a nondissipative medium, also satisfies the group-front equation. Because the group-front velocity and the group velocity are not always the same, the direction in which the wave packet travels is not necessarily normal to the group front. In this work, two examples are used to demonstrate this behavior by considering the refraction of a wave packet from vacuum to either a positive-index material (PIM) or a negative-index material (NIM). [DOI: 10.1115/1.1668035]

Keywords: Electromagnetic, Heat Transfer, Microscale, Nanoscale, Radiation

1 Introduction

In reality, all radiation propagates in a group of electromagnetic waves of different frequencies. In a nondispersive medium, the velocity at which the wave group travels is the same as the phase speed of each individual monochromatic wave. In a dispersive medium, however, individual waves travel with different phase speeds, resulting in interference effects that continuously change the amplitude of the wave group. The group amplitude is modulated as a wave with its own front, called group front, which travels at its own frequency and speed. The modulation of the group amplitude forms an envelope or wave packet. The speed at which the wave packet travels is called the group velocity, which is generally considered as the velocity of energy transport or signal propagation, with exceptions in anomalous dispersion media [1]. Therefore, the propagation of the wave group is important for radiant energy transfer in such applications as laser-materials interactions and optical diagnostics.

There has been a long history of distinguishing the group velocity from the phase velocity for waves propagating in one dimension. Hamilton formulated the concept of group velocity as early as 1839 [2], which was further developed by Stokes [3], Rayleigh [4], and Havelock [5]. Brillouin [6] published a monograph on the wave propagation and group velocity. Born and Wolf [1] suggested the three-dimensional definition of the group velocity that is consistent with that in the work of Brillouin. Lighthill [7] and Pedlosky [8] provided the three-dimensional definition of the group velocity, which is different from the definition used by Born and Wolf [1] and Brillouin [6]. Since the wave-group propagation was mostly studied in one-dimensional cases, the confusion had not caused serious problem until the direction of the refraction in a negative-index material was considered.

The publication of the experimental results for a structured metamaterial [9], with a negative refractive index in a narrow microwave region, excited tremendous interests to the so-called negative-index material (NIM). Veselago [10] was the first to theoretically predict the behavior of an NIM, also called left-handed material. He postulated that light would be refracted negatively from a positive-index material (PIM) to an NIM; and furthermore, a plane slab of NIM could focus light. Pendry [11] went further to claim that the NIM could be used to make a perfect lens that would focus an image with a resolution not restricted by the diffraction limit, which is about half of the wavelength. It has also been shown that a layer of NIM could enhance the energy transmittance through evanescent waves [12,13], suggesting that materials with negative refractive indexes may be used to construct microscale energy conversion devices.

Valanju et al. [14] cast doubt on the negative refraction of light. They pointed out that a real beam that has a finite spread of frequencies would be refracted ''positively'' in an NIM, even though the phase would be refracted ''negatively.'' Smith et al. [15] argued that Valanju et al. wrongly identified the group velocity as the direction of the interference pattern movement. A thorough understanding of wave-group propagation and refraction is required in order to resolve this dispute. It turns out that much of the confusion arose from inconsistent definitions of the group velocity in multidimensions. It becomes necessary to re-examine the conventional definitions of velocities, associated with a single wave and a wave packet, and introduce new concepts for clarity.

The present work deals with the propagation of a wave group, especially when it is incident on a dispersive medium (either PIM or NIM) from a nondispersive medium. Each medium is homogeneous and isotropic, with negligible loss or dissipation. The phase velocity will be discussed first with the introduction of the ''generalized phase velocity.'' In order to clearly describe the movement of the group front, the ''generalized group-front velocity'' needs to be used. It will be shown that both the group-front velocity and the group velocity are special cases of the generalized group-front velocity; however, in general they are not the same. With these concepts, the refraction of a modulated wave (or wave group) from vacuum to a dispersive medium, for cases with a PIM and an NIM, is investigated.

Contributed by the Heat Transfer Division for publication in the JOURNAL OF HEAT TRANSFER. Manuscript received by the Heat Transfer Division May 8, 2003; revision received December 23, 2003. Associate Editor: S. T. Thynell.

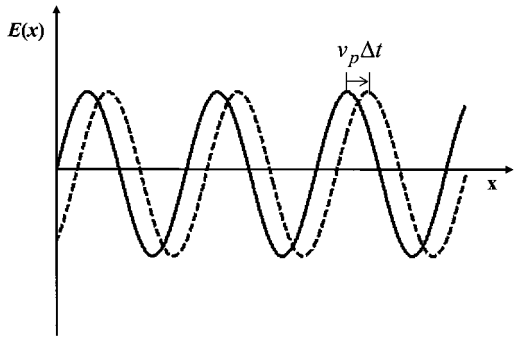

Fig. 1 A monochromatic wave propagating in one dimension

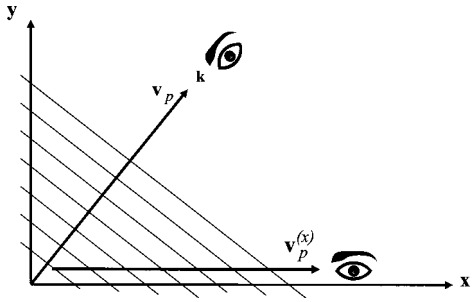

Fig. 2 A monochromatic wave propagating in two dimensions

2 Theory

2.1 The Generalized Phase Velocity. The phase velocity is a basic concept in wave propagation. It has been conventionally accepted as the speed at which the plane of a constant phase, called *wave front* or *phase front*, propagates in the direction of the wavevector $\mathbf{k}$ [8]. This definition is undoubtedly justified in the one-dimensional case. The one-dimensional time-harmonic wave can be expressed kinematically as

$$E(t,x)=E_0\cos(kx-\omega t) \tag{1}$$

where E_0 is the amplitude and ω the angular frequency of the wave. The phase speed can be obtained by differentiating the wave-front equation, $kx-\omega t=\text{const.}$, with respect to time. Hence,

$$v_p=\frac{dx}{dt}=\frac{\omega}{k} \tag{2}$$

The direction of the phase velocity in the one-dimensional case is apparently the same as that of wave propagation, as illustrated in Fig. 1. When wave propagation is extended to two-dimensional or three-dimensional space, however, the conventional definition does not clearly describe the movement of the wave front. Equation (1) is a simplified form of the plane scalar wave equation in the vector space,

$$E(t,\mathbf{r})=E_0\exp[-i(\omega t-\mathbf{k}\cdot\mathbf{r})] \tag{3}$$

The differentiation of the wave-front equation with respect to time yields

$$\mathbf{k}\cdot\frac{d\mathbf{r}}{dt}-\omega=0 \tag{4}$$

Unless $d\mathbf{r}/dt$ is perpendicular to $\mathbf{k}$, the above equation has an infinite number of solutions. As pointed out by Tailleux [16], the movement of the wave front can be interpreted with innumerable velocities, not with just one velocity as in the one-dimensional case. Therefore, the generalized phase velocity is defined in the present paper as follows:

$$\mathbf{v}_p^{(s)}=\frac{\omega}{\mathbf{k}\cdot\hat{\mathbf{s}}}\hat{\mathbf{s}} \tag{5}$$

where the superscript "s" indicates an arbitrary direction specified by the unit vector $\hat{\mathbf{s}}$.

The phase velocity in one-dimensional space can be extended to multidimensional space as the *smallest* speed at which the wave front travels. Since the shortest distance between two wave crests is the one perpendicular to the wave front, the phase velocity is in the same direction as the wavevector $\mathbf{k}$. Figure 2 shows a plane wave propagating in two-dimensional space, i.e., the x-y plane, where wave fronts are illustrated with parallel lines. Substituting $\hat{\mathbf{s}}$ in Eq. (5) by the unit wavevector $(\mathbf{k}/k)$ yields

$$\mathbf{v}_p=\frac{\omega}{k}\frac{\mathbf{k}}{k} \tag{6}$$

which is the universal definition of the phase velocity [1]. The magnitude of the phase velocity is $v_p=\omega/k$, which is consistent with the phase speed in the one-dimensional case. From Eq. (6), the x-component of the phase velocity is

$$v_{p,x}=\frac{\omega}{k}\frac{k_x}{k} \tag{7}$$

It should be noted that $v_{p,x}$ is not the same as the magnitude of the generalized phase velocity in the x-direction $v_p^{(x)}$, which can be found from Eq. (5) as

$$v_p^{(x)}=\frac{\omega}{k_x} \tag{8}$$

Clearly, $v_p^{(x)}\geqslant v_p\geqslant v_{p,x}$. As illustrated in Fig. 2, the wave front moves faster to the observer looking towards the x-direction than to the one looking towards the k-direction. The generalized phase velocity in the x-direction has often been misinterpreted as the x-component of the phase velocity in the literature. As remarked by Pedlosky [8], "the phase speed does not satisfy the rule of vector composition." The dilemma of vector composition is resolved by distinguishing the generalized phase velocity in the x-direction from the x-component of the phase velocity.

2.2 The Generalized Group-Front Velocity. The concept of the group front (or interference front) comes from the interference between waves of different frequencies in a wave group (or wave packet). For the sake of simplicity without loss of generality, two plane waves of the same amplitude with slightly different frequencies are used to demonstrate the movement of the group front. The interference of the two waves forms a wave packet (or a modulated wave), which can be represented by the superposition of the two monochromatic waves,

$$E(t,\mathbf{r})=E_0\exp[-i(\omega^- t-\mathbf{k}^-\cdot\mathbf{r})]+E_0\exp[-i(\omega^+ t-\mathbf{k}^+\cdot\mathbf{r})] \tag{9}$$

where $\omega^-=\omega-\delta\omega/2$, $\omega^+=\omega+\delta\omega/2$, $\mathbf{k}^-=\mathbf{k}-\delta\mathbf{k}/2$, and $\mathbf{k}^+=\mathbf{k}+\delta\mathbf{k}/2$ with a small and positive $\delta\omega$. Equation (9) can be re-written as follows:

$$E(t,\mathbf{r})=2E_0\cos\left[\frac{1}{2}(\delta\mathbf{k}\cdot\mathbf{r}-t\,\delta\omega)\right]\exp[-i(\omega t-\mathbf{k}\cdot\mathbf{r})] \tag{10}$$

The cosine term in Eq. (10) describes the change in the amplitude of the wave group. The constant-amplitude surface, or group front, is defined by

$$\delta\mathbf{k}\cdot\mathbf{r}-t\,\delta\omega=\text{const.} \tag{11}$$

Differentiating Eq. (11) with respect to time gives

$$\delta\mathbf{k}\cdot\frac{d\mathbf{r}}{dt}-\delta\omega=0 \tag{12}$$

The above equation is of the same form as Eq. (4) and has an infinite number of solutions. Hence, it is natural to introduce the generalized group-front velocity,

$$\mathbf{v}_{gf}^{(s)}=\frac{\delta\omega}{\delta\mathbf{k}\cdot\hat{\mathbf{s}}}\hat{\mathbf{s}} \tag{13}$$

which is defined in an arbitrary direction specified by the unit vector $\hat{\mathbf{s}}$.

Similarly, the group-front velocity represents the orthogonal propagation of the group front and is the smallest speed at which the group front travels. It can be shown from Eq. (13) that the group-front velocity is

$$\mathbf{v}_{gf}=\frac{\delta\omega}{\delta k}\frac{\delta\mathbf{k}}{\delta k} \tag{14}$$

where $\delta k=[(\delta k_x)^2+(\delta k_y)^2+(\delta k_z)^2]^{1/2}$. The group-front velocity is in the same direction as $\delta\mathbf{k}$. If all the waves in the wave group travel in the same direction, then $\delta\mathbf{k}$ and $\mathbf{k}$ are either parallel or antiparallel in an isotropic medium. If the waves travel in different directions or in an anisotropic medium, $\delta\mathbf{k}$ may not be parallel to $\mathbf{k}$. Therefore, the group-front velocity is generally not parallel to the phase velocity.

The group-front velocity can also be expressed as

$$\mathbf{v}_{gf}=\frac{\delta\mathbf{k}}{\delta k}\left[\left(\frac{\delta k_x}{\delta\omega}\right)^2+\left(\frac{\delta k_y}{\delta\omega}\right)^2+\left(\frac{\delta k_z}{\delta\omega}\right)^2\right]^{-1/2} \tag{15}$$

In the limit of $\delta\omega\to 0$, it can be approximated by

$$\mathbf{v}_{gf}=\frac{\delta\mathbf{k}}{\delta k}\left[\left(\frac{\partial k_x}{\partial\omega}\right)^2+\left(\frac{\partial k_y}{\partial\omega}\right)^2+\left(\frac{\partial k_z}{\partial\omega}\right)^2\right]^{-1/2} \tag{16}$$

Equation (15) or (16) was incorrectly identified by some classical texts as the group velocity. Examples are Born and Wolf [1], Eq. (56) in Chap. 1, and Brillouin [6], Eqs. (26) and (27) in Chap. 4.

The failure to identify the group-front velocity as a special case of the generalized group-front velocity and to distinguish it from the group velocity has frequently caused misinterpretation of the direction of energy propagation. The group velocity $\mathbf{v}_g$ and its relation with $\mathbf{v}_{gf}$ are discussed in the subsequent section.

2.3 The Group Velocity. The appropriate definition of the group velocity in a multidimensional space is [7,8,17]

$$\mathbf{v}_g=\nabla_{\mathbf{k}}\omega=\hat{\mathbf{x}}\frac{\partial\omega}{\partial k_x}+\hat{\mathbf{y}}\frac{\partial\omega}{\partial k_y}+\hat{\mathbf{z}}\frac{\partial\omega}{\partial k_z} \tag{17}$$

where $\nabla_{\mathbf{k}}$ denotes the gradient of ω in the wavevector space. Using the dispersion relation, $\omega=\omega(\mathbf{k})=\omega(k_x,k_y,k_z)$, the frequency perturbation $\delta\omega$ can be written as

$$\delta\omega=\frac{\partial\omega}{\partial k_x}\delta k_x+\frac{\partial\omega}{\partial k_y}\delta k_y+\frac{\partial\omega}{\partial k_z}\delta k_z=\delta\mathbf{k}\cdot\mathbf{v}_g \tag{18}$$

The comparison of Eq. (18) with Eq. (12) suggests that the group velocity is also a solution of the group-front equation and, therefore, is one special case of the generalized group-front velocity, Eq. (13). Nevertheless, the group velocity defined by Eq. (17) is a very important physical quantity because it identifies the direction and speed of energy propagation. Bers [18] proved the equality of the group velocity and energy velocity for propagating waves in a linear, nondissipative, and nonmagnetic medium with normal dispersion. The discussion of the group velocity in an anisotropic medium can also be found in Kong's work [17]. More recently, Ruppin [19] showed that the group velocity coincides with the energy velocity in the frequency region with a negative refractive index when an NIM is concerned. Notice that, under the condition of anomalous dispersion, the group velocity does not represent the velocity of energy flow and may be greater than the speed of light or negative [20]. Loudon [21] derived the energy velocity by dividing the Poynting vector by the total energy density in a dielectric medium and showed that the group velocity is not equal to the energy velocity in the presence of absorption.

The present work is confined in the region with normal dispersion, nondissipative, and isotropic medium. Under these conditions, the group velocity can be expressed as [15]

$$\mathbf{v}_g=\frac{\partial\omega}{\partial k}\frac{\mathbf{k}}{k} \tag{19}$$

By inserting $\mathbf{v}_{gf}$ into Eq. (12) and then combining it with Eq. (18) to eliminate $\delta\omega$, an explicit relation between the group-front velocity $\mathbf{v}_{gf}$ and the group velocity $\mathbf{v}_g$ can be written as

$$\delta\mathbf{k}\cdot(\mathbf{v}_{gf}-\mathbf{v}_g)=0 \tag{20}$$

There are two cases that satisfy the above equation. The first case is when $\mathbf{v}_{gf}$ is the same as the group velocity $\mathbf{v}_g$. This can only happen when $\delta\mathbf{k}$ is either parallel or antiparallel to $\mathbf{k}$; for instance, when the wave group travels in a nondispersive medium or when the beam is incident normally to a dispersive medium from a nondispersive medium. The second case is when the difference vector between $\mathbf{v}_{gf}$ and $\mathbf{v}_g$ is perpendicular to $\delta\mathbf{k}$ (or $\mathbf{v}_{gf}$). The group-front velocity $\mathbf{v}_{gf}$ was called the velocity of the interference front by Smith et al. [15], who pointed out that the group velocity can be decomposed into $\mathbf{v}_{gf}$ and another component normal to the group-front velocity.

3 Application to Refraction Phenomenon

This section deals with the refraction of a wave packet by considering two plane waves of same amplitude with slightly different frequencies incident from a nondispersive medium to a dispersive medium. As mentioned before, each medium is homogeneous and isotropic with negligible loss or dissipation. The real value of $E(t,\mathbf{r})$ in Eq. (10) can be used as the amplitude of the electric field or magnetic field. The wavevector for each medium is

$$\mathbf{k}_j=k_{j,x}\hat{\mathbf{x}}+k_{j,z}\hat{\mathbf{z}},\quad j=1,2 \tag{21a}$$

The magnitude of the wavevector is expressed as

$$k_j=\|\mathbf{k}_j\|=\sigma\frac{\omega}{c_0}n_j,\quad j=1,2 \tag{21b}$$

where $c_0=2.998\times10^8$ m/s is the speed of light in vacuum, n_j is the refractive index of the 1st ($j=1$) and 2nd ($j=2$) medium, and σ is chosen to be $+1$ for PIMs and -1 for NIMs because k_j should be positive regardless of the medium [14]. From the phase-matching condition, the x-component of the wavevector is given by

$$k_{1,x}=k_{2,x}=\frac{\omega}{c_0}n_1\sin\theta_1 \tag{21c}$$

The z-component of the wavevector in the second medium is

$$k_{2,z}=\sigma\sqrt{k_2^2-k_{2,x}^2}=\sigma\frac{\omega}{c_0}\sqrt{n_2(\omega)^2-n_1^2\sin^2\theta_1} \tag{21d}$$

Since the second medium is dispersive, n_2 is a function of frequency, whereas n_1 is taken as a constant to represent the nondispersive medium. Note that the present work deals with propagating waves only, that is, $\sqrt{k_2^2-k_{2,x}^2}$ in Eq. (21*d*) is always real and positive.

The phase velocity in a dispersive medium can be calculated from Eqs. (6) and (21*b*), yielding

$$v_{p,2}=\sigma\frac{c_0}{n_2} \tag{22}$$

and

$$\tan\theta_p=\frac{k_{2,x}}{k_{2,z}}=\frac{n_1\sin\theta_1}{\sigma\sqrt{n_2^2-n_1^2\sin^2\theta_1}} \tag{23}$$

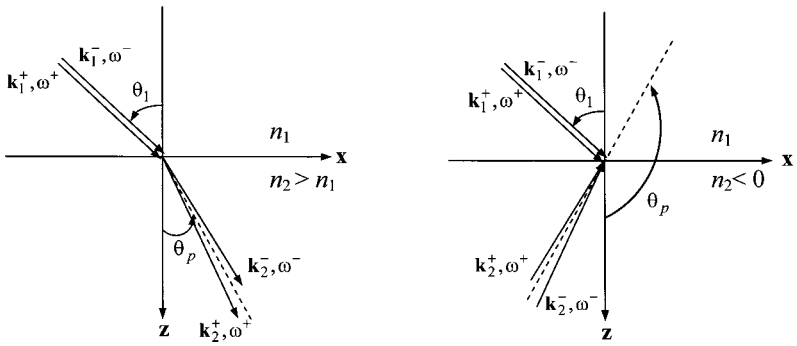

Fig. 3 Propagation of a modulated wave in (*a*) a positive-index material (PIM), and (*b*) a negative-index material (NIM)

where θ_p is the angle between $\mathbf{k}$ and the z-axis. Equation (23) is sometimes called the generalized Snell's law [22]. Figure 3(a) represents the geometry when the second medium is a PIM. Since the increase of ω in the normal dispersion region ($dn/d\omega > 0$) causes a decrease of $v_{p,2}$ and θ_p, the wave with a slightly higher frequency (ω^+) propagates closer to the z-axis than the other in the PIM. In contrast, as shown in Fig. 3(b), an NIM case gives a different tendency. According to Eq. (23), θ_p is between $\pi/2$ and π for a negative refractive index. That is, wave fronts in the NIM travel toward the interface and merge with those propagating in the first medium. When ω increases in the normal dispersion region, $v_{p,2}$ increases and θ_p and k_2 decrease. Hence, the ω^- wave is closer to the z-axis than the ω^+ wave.

From Eqs. (19) and (21b), the group velocity in the second medium becomes:

$$\mathbf{v}_{g,2} = \sigma \; v_{g,2} \frac{\mathbf{k}_2}{k_2} \tag{24}$$

where

$$v_{g,2} = \frac{c_0}{n_2 + \omega \dfrac{dn_2}{d\omega}} \tag{25}$$

The direction of the group velocity upon refraction is determined by

$$\tan \theta_g = \frac{k_{2,x}}{k_{2,z}} = \tan \theta_p \tag{26}$$

Therefore, θ_g must be equal to θ_p or $\theta_p - \pi$. The direction of the group velocity depends on the type of material in the second medium. For a PIM, θ_g is identical with θ_p because the Poynting vector is parallel to the wavevector $\mathbf{k}$ of a plane wave. For an NIM, however, the direction of the group velocity is anti-parallel to the wavevector according to σ in Eq. (24), which indicates that θ_g should be negative (or $\theta_g = \theta_p - \pi$). Hence, it is apparent that the velocity of energy flow, as determined by the group velocity, is refracted negatively into the NIM and propagates in the opposite direction of the wavevector. It is consistent with Veselago's claim that the Poynting vector propagates in the opposite direction of the wavevector in NIMs [10]. In addition, one can define the group index according to Eq. (25) as

$$n_g \equiv n_2 + \omega \frac{dn_2}{d\omega} = \frac{d(\omega n_2)}{d\omega} \tag{27}$$

which should be greater than unity regardless of the sign of the refractive index of the medium, as required by the principle of causality (i.e., an effect cannot occur before the cause). Note again that, in the anomalous dispersion region, the group index may be less than unity or even negative, and the group velocity no longer represents the propagation of energy.

In order to obtain the group-front velocity, it is necessary to derive the equation for $\delta\mathbf{k}_2$ first. Since each component of the wavevector $\mathbf{k}_2$ is a function of ω, it can be approximated to the following sets of equations for small $\delta\omega$:

$$\delta\mathbf{k}_2 = \hat{\mathbf{x}}\delta k_{2,x} + \hat{\mathbf{z}}\delta k_{2,z} \tag{28}$$

where

$$\delta k_{2,x} = \frac{\delta\omega}{c_0} n_1 \sin\theta_1 \tag{29}$$

and

$$\delta k_{2,z} = \sigma \frac{\delta\omega}{c_0}\left[\sqrt{n_2^2 - n_1^2 \sin^2\theta_1} + \left(\omega \frac{dn_2}{d\omega}\right)\frac{n_2}{\sqrt{n_2^2 - n_1^2 \sin^2\theta_1}}\right] \tag{30a}$$

Rearranging the z-component of $\delta\mathbf{k}_2$ yields

$$\delta k_{2,z} = \sigma \frac{\delta\omega}{c_0} \frac{n_2 n_g - n_1^2 \sin^2\theta_1}{\sqrt{n_2^2 - n_1^2 \sin^2\theta_1}} \tag{30b}$$

which is always positive in the normal dispersion region regardless of the type of the medium. The direction of the group-front velocity in the dispersive medium is derived from Eqs. (29) and (30b) as

$$\tan\theta_{gf} = \frac{\delta k_{2,x}}{\delta k_{2,z}} = \sigma \frac{n_1 \sin\theta_1}{\left[\dfrac{n_2 n_g - n_1^2 \sin^2\theta_1}{\sqrt{n_2^2 - n_1^2 \sin^2\theta_1}}\right]} \tag{31}$$

This equation was named the group Snell's law by Valanju et al. [14]. Equation (31) indicates that the group front is always oriented to the positive direction, even in a negative-index medium.

When the second medium is nondispersive, the phase velocity $\mathbf{v}_p$, group-front velocity $\mathbf{v}_{gf}$, and group velocity $\mathbf{v}_g$ are the same. This can happen only in a PIM because causality requires that all NIMs be dispersive [10]. The group front is parallel to the individual wave front. When the second medium is dispersive and radiation is incident normally ($\theta_1 = 0$) to the interface, $\mathbf{v}_g$ is the same as $\mathbf{v}_{gf}$ and both are in the positive z-direction (forward propagating). Their magnitude is $v_g = v_{gf} = c_0/n_g$. Both the group front and the phase front are parallel in the x-y plane. The phase velocity may be in the positive z-direction (PIM) or in the negative z-direction (NIM) with a magnitude $v_p = \sigma c_0/n_2$ that is different from v_g. In general, the phase velocity, the group-front velocity, and the group velocity possess different directions and magnitudes upon refraction into a dispersive medium at oblique incidence. It is important to distinguish these velocities in order to fully understand wave-group propagation.

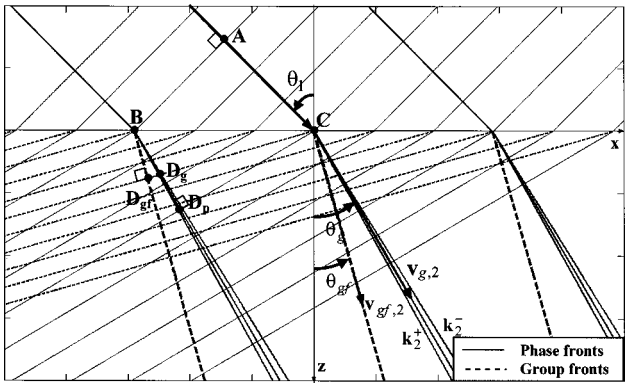

Fig. 4 The movement of the wave group that is incident on MgO ($n_2=1.395$) at $\lambda_0=9.091$ μm ($\omega=2.072\times10^{14}$ rad/s) from vacuum ($n_1=1.0$), for $\theta_1=45$ deg and $\Delta\omega/\omega=0.1$. The calculated values are $n_g=2.488$; $\theta_g=30.44$ deg; $\theta_{gf}=15.97$ deg; $\Delta\theta_p=2.65$ deg.

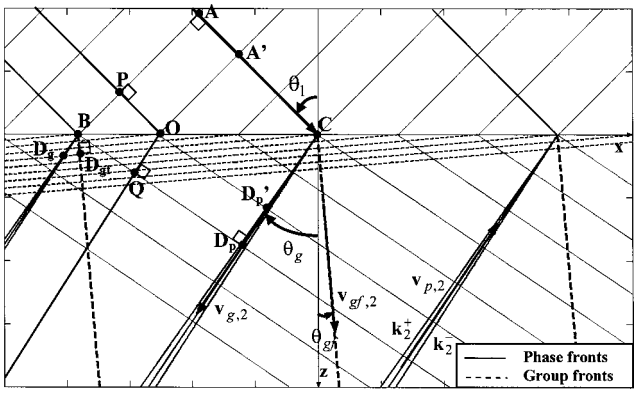

Fig. 5 The movement of the wave group that is incident on the NIM from vacuum ($n_1=1.0$) at $\lambda_0=5.996$ cm ($\omega=3.14\times10^{10}$ rad/s), for $\theta_1=45$ deg and $\Delta\omega/\omega=0.01$. The calculated values are $n_2=-1.262$; $n_g=6.467$; $\theta_g=-34.70$ deg; $\theta_{gf}=4.88$ deg; $\Delta\theta_p=2.37$ deg.

4 Results and Discussion

The behavior of wave-packet refraction into a dispersive medium is illustrated in this section for two cases, one with a PIM and the other with an NIM as the second medium. Even though only one specific incidence angle from vacuum onto the second medium is considered, these two cases represent the general features of wave-packet refraction because variations in the incidence angle and/or materials merely affect the quantities, such as the refracted direction of each velocity and spacing between adjacent fronts, without changing the general trend.

The locus of a wave packet, consisting of two monochromatic waves described by Eq. (9), is shown in Fig. 4 when the wave is incident onto a dispersive PIM from vacuum ($n_1=1$) at an incidence angle $\theta_1=45$ deg. The PIM is chosen as magnesium oxide (MgO) because of the relatively large frequency-dependence of its refractive index $dn/d\omega$ and low loss (i.e., little absorption) in the mid-infrared region. The refractive index $n_2=1.395$ at the wavelength $\lambda_0=9.091$ μm ($\omega=2.072\times10^{14}$ rad/s) is taken from Ref. [23]. At this wavelength, the extinction coefficient is less than 0.005, which is negligible when dealing with wave propagation near the surface. In the calculation, the interval between the frequencies of the two monochromatic waves is chosen to satisfy $\delta\omega/\omega=0.1$. The group index calculated from Eq. (27) is $n_g=2.488$. A uniform time step Δt is used for drawing wave fronts and group fronts.

In the first medium wave fronts and group fronts are the same and the two waves propagate in the same direction. When the waves are refracted into the second medium, they propagate into different directions. The angle between two refracted waves is $\Delta\theta_p=2.65$ deg; therefore, the distinction of the two wavevectors $\mathbf{k}_2^-=\mathbf{k}_2-\delta\mathbf{k}/2$ and $\mathbf{k}_2^+=\mathbf{k}_2+\delta\mathbf{k}/2$ is not very sharp. However, the group front and the wave front are apparently not parallel to each other. The group velocity $\mathbf{v}_g$ is parallel to $\mathbf{k}_2$, while the group-front velocity $\mathbf{v}_{gf}$ is parallel to $\delta\mathbf{k}_2$. The angle between $\mathbf{v}_g$ and the z-axis is $\theta_g=\theta_p=30.44$ deg, and that between $\mathbf{v}_{gf}$ and the z-axis is $\theta_{gf}=15.97$ deg.

Because group fronts are not parallel to phase fronts, an inhomogeneous wave exists in the second medium [1]. It is very interesting to see how the individual waves and the wave group propagate into the dispersive medium. Since wave fronts for the two individual waves are hardly distinguishable, in order to avoid confusion, Fig. 4 only shows averaged phase fronts that propagate in the direction of the mean wavevector $\mathbf{k}_2$. Group fronts, on the other hand, are perpendicular to the direction of the differential wavevector $\delta\mathbf{k}_2$. The spacing between adjacent wave fronts is greater than that between adjacent group fronts, indicating that the group front moves forward with a slower speed.

Consider wave front AB that is refracted into the second medium. When point A reaches point C, point B will reach point D_p, as shown in Fig. 4. The small squares at points A and D_p indicate the orthogonal relationship between the wavevector and the wave front. The square at a point D_{gf} indicates the orthogonal relationship between $\delta\mathbf{k}_2$ and the group front. If AB is considered as the group front, the group front will propagate from AB to CD_g rather than CD_{gf}. That is, the group front moves in a skewed direction according to the group velocity (from AB to CD_g), not according to the group-front velocity (from AB to CD_{gf}) which is normal to the group front. Notice that although the group index in Eq. (27) directly affects the speed of wave-group propagation (i.e., the magnitude of the group velocity), the group index has no relations with the direction of wave-group propagation (i.e., the direction of the group velocity). Instead, one must use the phase-matching condition to determine the angle of refraction or the direction of the group velocity. Notice that Eq. (31) should be used to determine the orientation of the group front. Although Smith et al. [15] was the first to point out that the group front moves in the direction of the group velocity that is not perpendicular to the group front in an NIM, it is difficult to experimentally confirm their theory because of the current limitations in fabricating NIMs with desired properties (e.g., isotropic and lossless). The analysis here using a dispersive PIM demonstrates the same phenomenon that can be experimentally validated with existing materials and instrumentation.

The behavior of wave-packet refraction into an NIM is shown in Fig. 5. For the refractive index of an NIM and its frequency dependence in the microwave region, the permittivity and permeability formulas and parameters are adopted from [24]. The calculated refractive index is $n_2=-1.262$ at $\lambda_0=5.996$ cm ($\omega=3.14\times10^{10}$ rad/s). The absorption in the second medium is neglected. The angle of incidence is fixed at $\theta_1=45$ deg. For $\delta\omega/\omega=0.01$, the angle between two refracted waves is about $\Delta\theta_p=2.37$ deg. The time step Δt for this figure is slightly larger than that used in Fig. 4. Again, only mean wave fronts are shown. Figure 5 clearly shows that group fronts are not parallel to the phase fronts in the NIM. The calculated group index is $n_g=6.467$; this means that the wave group will travel with a speed about 15.5 percent of the speed of light in free space. The spacing between adjacent group fronts is much closer in the NIM.

The wave front moves upwards in the NIM. For example, during the same time when the wave front in vacuum travels from AP to A′O, the average wave front in the NIM moves from D_pQ to $D_p'O$. Notice that the group velocity $\mathbf{v}_{g,2}$ is antiparallel to $\mathbf{k}_2$. The x-component of $\mathbf{v}_{g,2}$ is negative and $\theta_g=-34.70$ deg, suggesting that the wave packet is indeed refracted negatively into the NIM.

Group front AB in the first medium will travel to CD_g rather than CD_{gf} in the second medium. However, the speed for energy propagation is always positive. Thus, negative refraction does not violate the causality principle. Our result agrees with that of Smith et al. [15], who claimed that the wave packet will propagate not only in the direction parallel to $\mathbf{v}_{gf}$ but also in the direction normal to $\mathbf{v}_{gf}$. They also argued in the same paper that Valanju et al. [14] had misinterpreted the group-front velocity $\mathbf{v}_{gf,2}$ as the velocity of energy flow. Although Valanju et al. later admitted this oversight in their reply to Pendry and Smith's comments, they insisted that $\mathbf{v}_{gf,2}$ should be the group velocity [25]. Note that the claim of Valanju et al. [14] that the wave in NIM is inhomogeneous still holds. The existence of inhomogeneous waves in the NIM could have an impact on its ability to focus light. Loss or absorption is another practical issue to be addressed and it is expected that higher-quality NIMs will be fabricated as the technology advances and NIM can be realized in the infrared and shorter wavelength regions.

5 Conclusions

For a wave propagating in multidimensional space, there exist an infinite number of solutions to the wave-front equation. The present work introduces the concept of the generalized phase velocity, with which the phase velocity is extended to multidimensional space without losing consistency with existing publications. The phase velocity is the smallest speed at which the wave front travels and is always parallel to the wavevector. Furthermore, it obeys the rule of vector composition; however, its component is in general different from the generalized phase velocity in that direction.

The solution of the group-front equation in multidimensions is also not unique. The generalized group-front velocity is defined here and can be in any arbitrary direction; whereas the group-front velocity and the group velocity are two special cases, which are not identical in general. Nevertheless, these two velocities are often confused or used incorrectly in the literature. It is the group velocity that describes the direction and speed of energy flow in a lossless medium. This clarification may help understand the energy transport mechanisms in microsystems.

The difference between the group-front velocity and the group velocity in a dispersive PIM, upon refraction from a nondispersive medium, is demonstrated for the first time. This allows experimental validation to be performed in the near future, because many dielectric materials exhibit normal dispersion in a large spectral region. The wave packet propagates with the group velocity, which can be decomposed into a component normal to the group front (identified as the group-front velocity) and another component parallel to the group front; this is true not only in an NIM but also in a normally dispersive PIM.

It may be useful to extend the present work, which is valid for isotropic and lossless media, to anisotropic and/or dissipative media. Another issue to be addressed in the future is wave propagation in the anomalous dispersion region, where absorption is strong. Experimental studies are also needed to better understand the behavior of inhomogeneous waves, especially in NIMs, which are significantly dispersive.

Acknowledgment

This work was sponsored by the National Science Foundation (CTS-0236831) and the Georgia Tech Focused Research Program. The authors thank Ceji Fu, Bong Jae Lee, and Hyunjin Lee for valuable discussions and comments.

Nomenclature

c_0 = speed of light in vacuum
E = wave field
$\mathbf{k}$ = wavevector
n = refractive index
$\mathbf{r}$ = space vector
$\hat{\mathbf{s}}$ = unit vector in arbitrary direction
t = time
Δt = time step
$\mathbf{v}$ = velocity
$\mathbf{v}_p^{(s)}$ = generalized phase velocity
$\mathbf{v}_{gf}^{(s)}$ = generalized group-front velocity

Greek Symbols

γ = scattering rate
δ = small difference in value
ε = relative electric permittivity
θ = angle
λ_0 = wavelength in vacuum
μ = relative magnetic permeability
σ = sign which represents the type of the medium
ω = angular frequency

Subscripts

1, 2 = first medium and second medium
g = group
gf = group front
p = phase
x,y,z = components

References

[1] Born, M., and Wolf, E., 1999, *Principles of Optics*, 7th ed., Cambridge University Press, Cambridge, UK, Chap. 1.
[2] Hamilton, W. R., 1839, "Researches Respecting Vibration, Connected with the Theory of Light," Proc. R. Ir. Acad., Sect. A, **1**, p. 267, and p. 341.
[3] Stokes, G. G., 1966, Mathematical and Physical Papers **5**, Johnson Reprint Co., New York, p. 362 (Problem 11 of the Smith's Prize Examination Papers, Feb. 2, 1876).
[4] Lord Rayleigh, 1896, *The Theory of Sound*, 2nd ed., Macmillan and Co., London, UK (First ed. Published, 1878).
[5] Havelock, T. H., 1914, *The Propagation of Disturbances in Dispersive Media*, Cambridge University Press, Cambridge, UK.
[6] Brillouin, L., 1960, *Wave Propagation and Group Velocity*, Academic Press, New York.
[7] Lighthill, J., 1978, *Waves in Fluids*, Cambridge University Press, Cambridge, UK.
[8] Pedlosky, J., 1982, *Geophysical Fluid Dynamics*, Springer-Verlag, New York.
[9] Shelby, R. A., Smith, D. R., and Schultz, S., 2001, "Experimental Verification of a Negative Index of Refraction," Science, **292**, pp. 77–79.
[10] Veselago, V. G., 1968, "The Electrodynamics of Substances with Simultaneously Negative Values of ε and μ," Sov. Phys. Usp., **10**(4), pp. 509–514.
[11] Pendry, J. B., 2000, "Negative Refraction Makes a Perfect Lens," Phys. Rev. Lett., **85**(18), pp. 3966–3969.
[12] Zhang, Z. M., and Fu, C. J., 2002, "Unusual Photon Tunneling in the Presence of a Layer with a Negative Refractive Index," Appl. Phys. Lett., **80**(6), pp. 1097–1099.
[13] Fu, C. J., and Zhang, Z. M., 2003, "Transmission Enhancement Using a Negative Refractive-Index Layer," Microscale Thermophys. Eng., **7**(3), pp. 221–234.
[14] Valanju, P. M., Walser, R. M., and Valanju, A. P., 2002, "Wave Refraction in Negative-Index Media: Always Positive and Very Inhomogeneous," Paper No. 187401, Phys. Rev. Lett., **88**(18).
[15] Smith, D. R., Schurig, D., and Pendry, J. B., 2002, "Negative Refraction of Modulated Electromagnetic Waves," Appl. Phys. Lett., **81**(15), pp. 2713–2715.
[16] Tailleux, R., 2003, private communication, unpublished.
[17] Kong, J. A., 1990, *Electromagnetic Wave Theory*, 2nd ed., John Wiley & Sons, Inc., New York.
[18] Bers, A., 2000, "Note on Group Velocity and Energy Propagation," Am. J. Phys., **68**(5), pp. 482–484.
[19] Ruppin, R., 2002, "Electromagnetic Energy Density in a Dispersive and Absorptive Material," Phys. Lett. A, **299**, pp. 309–312.
[20] Dogariu, A., Kuzmich, A., and Wang, L. J., 2001, "Transparent Anomalous Dispersion and Superluminal Light-Pulse Propagation at a Negative Group Velocity," Paper No. 053806, Phys. Rev. A, **63**(5), p. 05386.
[21] Loudon, R., 1970, "The Propagation of Electromagnetic Energy through an Absorbing Dielectric," J. Phys. A, **3**, pp. 233–245.
[22] Modest, M. F., 1993, *Radiative Heat Transfer*, McGraw-Hill, New York.
[23] Palik, E. D., ed., 1991, *Handbook of Optical Constants of Solids II*, Academic Press, San Diego, CA, pp. 919–955.
[24] Smith, D. R., Padilla, W. J., Vier, S. C., Nemat-Nasser, S. C., and Schultz, S., 2000, "Composite Medium with Simultaneously Negative Permeability and Permittivity," Phys. Rev. Lett., **84**(18), pp. 4184–4187.
[25] Pendry, J. B., and Smith, D. R., "Comments," Paper No. 029703 Phys. Rev. Lett., **90**(2); Reply of Valanju, Walser, and Valanju, *ibid.*, Paper No. 029704.

Scale Analysis of Combined Thermal Radiation and Convection Heat Transfer

Peter A. Kottke
e-mail: gte638w@mail.gatech.edu

Timothy P. Ferguson

Andrei G. Fedorov

Georgia Institute of Technology,
G.W.W. School of Mechanical Engineering,
Atlanta, GA 30332

Simple order-of-magnitude relationships predicting heat transfer in limiting cases of combined convection and radiation problems in boundary layer flows are found using the method of scale analysis. Key nondimensional groups are developed that help identify the fundamental interactions between thermal radiation and convection modes of heat transfer for two cases of laminar, two-dimensional convection heat transfer from a semi-infinite vertical wall. The first case is that of heat transfer from a gray wall with a specified heat flux to a surrounding non-participating medium and considers both forced and natural convection effects. The second case is that of heat transfer from a black wall with a specified temperature to an optically thick, gray, nonscattering medium and considers forced, natural, and mixed convection effects. The scale analysis results are presented in terms of the local Nusselt number. They include closed form expressions for order-of-magnitude estimates of the heat transfer rate, and dimensionless parameters that indicate the dominant mode of heat transfer and correlate experimental data well. The scale analysis results are validated against both experimental data and theoretical results.
[DOI: 10.1115/1.1677409]

1 Introduction

Combined mode convection and radiation heat transfer occurs in many engineering applications. Examples of such systems include nuclear reactors, hypersonic jets, solid oxide fuel cells, combustion chambers, and solar energy collectors, where the interactions of thermal radiation with convection become important. Central to developing more robust and energy efficient systems is the need for improved understanding of the heat transfer interactions when radiation effects become significant and coupled to convection heat transfer. However, the inclusion of radiation effects in heat transfer analysis makes problems more complex, with the conservation of energy becoming governed by a nonlinear integro-differential equation. The increase in difficulty also arises from an increase in the number of independent variables, dependence of the radiative flux on the geometrical configuration of the system, interreflections between objects, and the potential lack in optical property data [1]. In addition, relevant radiative properties (such as absorptivity, reflectivity, emissivity, etc.) are often a strong function of wavelength, chemical composition, and temperature, and are difficult to measure. Thermal radiation alone is a strongly nonlinear phenomenon and is in general not only a function of time and space, but also depends on spectral and directional considerations. Since problems involving radiation interaction generally contain a large number of parameters, emphasis is often placed on evaluating only the first order radiation effects, which serves the useful purpose of simplifying the problem while indicating under what conditions the effect of radiation needs even be considered [2]. Examples of second order radiation effects would include reemission and reabsorption of radiant energy [3]. A solution depicting the interaction of radiation with absorbing and emitting media within the convective thermal boundary layer is both a mathematically and computationally intensive problem to solve.

Successful solution techniques have used simplifying assumptions in order to reduce the complexity of the radiative and convection boundary layer heat transfer problem. Examples of simplifying assumptions include but are not restricted to gray and diffuse radiative behavior, black surfaces, consideration of only first order radiation effects, negligible radiation scattering and radiation pressure, radiatively nonparticipating surrounding media, and optically thick or thin media [2,4,5]. Although these solutions do not account for all of the physical mechanisms of energy transfer, they do provide fundamental insight into the heat transfer interactions when both radiation and convection contributions are significant. Results from these studies have demonstrated that thermal radiation influences heat transfer both directly and indirectly. Directly, thermal radiation can affect heat transfer by being absorbed and emitted by surfaces within the system. Indirectly, thermal radiation can be partially absorbed in the thermal boundary layer and alter the temperature distribution, therefore changing the conduction and convection heat transfer characteristics of the system [6]. Typically, the complexity of the problem is inversely proportional to the number of simplifying assumptions used to arrive at a solution; however, even the most simplified analyses can yield positive contributions to gaining a better understanding of the effects of radiation on boundary layer flow.

For boundary layer flow of nonparticipating media, the presence of thermal radiation does not alter the standard conservation equations of both momentum and energy. Generally speaking, if the medium is radiatively nonparticipating, then radiation is introduced to the boundary layer flow problem as a nonlinear boundary condition. Consequently, the coupling between convection and radiation occurs only through the thermal radiation boundary condition at the surface of the walls; however, this coupling depends on whether the temperature or net heat flux is specified at the wall [7]. If temperature is specified, convection and radiation can be treated separately since the boundary surface temperature is fixed and the radiation will not alter it. However, if the net heat flux is specified, the presence of radiation at the boundary surface will alter the temperature and subsequently couple both the convection and radiation effects. As a result, one of the initial modifications to the classical similarity solution for the laminar forced convection over a flat plat was to introduce a surface boundary condition of radiative heat flux for a nonparticipating medium [2]. In addition to the standard convection assumptions such as constant properties, incompressible substance, and negligible viscous dissipation,

Contributed by the Heat Transfer Division for publication in the JOURNAL OF HEAT TRANSFER. Manuscript received by the Heat Transfer Division August 11, 2003; revision received October 21, 2003. Associate Editor: S. Thynell.

assumptions specific to the introduction of radiation effects include assuming the surface of the plate is opaque and gray with uniform emissivity.

The difficulty of the problem is increased when the medium is radiatively participating, as the conservation of energy equation that must be solved becomes a nonlinear integro-differential equation [7]. It should be noted that most investigations involving participating media limited their theoretical developments to simple geometries with gray media in order to investigate the general trends of the interaction between radiation and convection heat transfer. To further simplify the problem, the extreme cases of optically thin and thick media can also be implemented. For the limiting case of very large optical thickness, the integral terms that occur in the energy equation due to radiation are removed; consequently, conventional boundary layer solutions such as similarity solutions can be applied [7]. The removal of the integral terms is achieved by using the Rosseland (or diffusion) approximation, which can be used to represent the radiation flux and simplify the energy equation. Although the diffusion approximation works well within the interior of the media, it breaks down near the physical boundaries since it is unable to account for short-range radiation effects and does not account for radiative fluxes from boundary surfaces. Although this is a serious restriction, the optically thick approximation may be useful in the investigation of general effects of radiation on the temperature profile in the boundary layer [7].

Viskanta and Grosh performed a similarity analysis of laminar flow over a wedge (i.e., Falkner-Skan flow) for an absorbing and emitting, optically thick, gray medium [1]. They found that the net effect of radiation was to always increase the heat transfer rate when the medium absorbs and emits radiation. The thermal boundary layer was always found to thicken when radiation was present, which was attributed to the fact that radiation provides an additional mechanism to distribute energy. In addition, as the thermal radiation became the predominate mode of heat transfer, the temperature gradient at the wall departed more from linearity. The results from the analysis serve as a limiting solution for the case in which the optical thickness of the boundary layer is large.

The effect of radiation on heat transfer is more significant in free convection boundary layer flows than it is for forced convection [8]. Özisik considered a heated, opaque and gray vertical plate at uniform temperature submerged in an absorbing, emitting, incompressible, gray fluid of infinite extent [7]. Applying the diffusion approximation, he found a complete similarity solution. The results demonstrate that the net effect of radiation is to increase the thickness of the thermal boundary layer in free convection. This is supported by numerical results, which have also shown that radiation enhances the effect of buoyancy forces, as well as increases the temperature, velocity, and conductive heat transfer at the wall [9]. In addition, radiation coupling renders the heated surface temperature more nearly uniform than without radiation effects [10]. Other solutions presented by Cess [11], Arpaci [5], and Cheng and Özisik [12] address the issue of radiation in free convection. These investigations implemented the singular perturbation technique, approximate integral technique, and normal-mode expansion technique, respectively.

Scale analysis offers many complimentary benefits to other more sophisticated and complex solution techniques used in heat transfer and fluid mechanics. The overall objective of scale analysis is to produce physically accurate order-of-magnitude estimates for the quantities of interest. It is a highly efficient means of analysis, yielding considerable insight into a problem for a small investment of intellectual effort. When properly performed, scale analysis not only anticipates within a factor of order of one (or within percentage points) the same results produced by exhaustive exact analyses, but it is also a necessary precondition for good analysis in dimensionless form. Using the tools of scale analysis, governing equations are rewritten as balances; we use the same notation for scale analysis ''equations'' as Bejan [13]; the symbol ''$\sim$'' means ''is of the same order of magnitude as,'' and implies a proportionality constant of $O(1)$.

In this paper, the method of scale analysis was used to identify fundamental nondimensional groups to improve understanding of the relationship between convection and radiation in forced, natural, and mixed convection boundary layer flows. Scale analysis also yields expressions for ''back-of-the-envelope'' estimations of heat transfer in limiting situations. Similarity models were developed and used as semi-analytical solutions of the problems against which the results of scale analysis were verified. The ability of the dimensionless groups produced by scale analysis to correlate experimental data has also been demonstrated. The results of the scale analysis are summarized in Table 1 and should be of interest to academic researchers as well as practitioners because of the closed-form analytical representations.

2 Model

We consider combined radiation and convection heat transfer for two cases of laminar, steady, two-dimensional, forced, natural, and mixed convection heat transfer from a semi-infinite vertical wall. The first case is that of heat transfer from a gray wall with a specified heat flux to a non-participating medium. The second case is that of heat transfer from a black wall with a specified temperature to an optically thick, gray, non-scattering medium. These cases were chosen because they are amenable to scale analysis; however, they are also of interest in several state-of-the-art applications. For example, the first case can be a low order model for heat transfer in solar collectors and in gas phase CVD, including Gas-Jet CVD [14]. Likewise, the second case can be used for initial modeling of high temperature, liquid reagent CVD, as well as high temperature metallurgy and materials processing.

We always neglect the contribution of radiation to internal energy and the pressure tensor. Therefore, if radiation effects are to be included, they will appear only in the heat flux term in the energy equation, and in the boundary conditions. In addition, the following routine simplifications are made: (a) the viscous dissipation, flow work, and volumetric heat generation terms in the energy equations are negligible; (b) the boundary layer approximation may be applied (including the assumption that the variation of the radiative heat flux in the x direction is negligible compared to its variation in the y direction); and (c) all fluid properties (with the exception of density when applicable for the Boussinesq approximation) may be treated as constant.

Note that the constant property assumption, (c), includes radiative properties, and the effect of refractive index on emitted powers is not considered (i.e., refractive index is set equal to unity). It is also important to keep in mind that the presence of radiative heat transfer may make the boundary layer assumption incorrect due to thickening of the thermal boundary layer for participating media [1,15]; the scale analysis results provide a simple method of checking the validity of this assumption.

3 Nonparticipating Medium

For the case of a nonparticipating medium, we investigate forced convection and natural convection with the thermal boundary condition at $y=0$

$$q_w = -k\frac{\partial T}{\partial y} + \sigma\varepsilon(T_w^4 - T_\infty^4) \tag{1}$$

Equation (1) assumes that the wall exchanges radiant energy with a large enclosure at the same temperature as the free stream fluid, T_∞.

3.1 Scale Analysis of Nonparticipating Medium. To the best of our knowledge scale analysis has not previously been applied with radiation included. The problem of interest for a nonparticipating medium is one for which the wall heat flux, q_w, is specified, and the radiation effects are at the boundary condition.

Table 1 Summary of results and definitions

Θ	$(T_w^2+T_\infty^2)(T_w+T_\infty)$	The ratio of the difference of the temperatures to the fourth power, which drives radiative heat transfer, to the difference of the temperatures, which drives convective heat transfer.
	Nonparticipating Medium (δ_t defined in Eqs. (2) and (3))	
H_{RC}	$\frac{\sigma\varepsilon\Theta\delta_t}{k}$	Radiation to convection parameter; when H_{RC} is $O(1)$ or greater, convection effects quickly become negligible. If H_{RC} is less than $O(1)$, convection effects dominate
Wall Temperature Estimate	$\sigma\varepsilon(T_w^4-T_\infty^4)+k\frac{(T_w-T_\infty)}{\delta_t}\sim q_w$	T_w is estimated by finding the positive real root.
	Optically Thick Boundary Layer, $N\ll 1$	
N	$\frac{k\kappa}{\sigma\Theta}$.	The conduction to radiation parameter; N determines whether radiation or conduction dominates the heat transfer from the wall.
Pr_R	$N\nu/\alpha$	Radiative Prandtl number, the ratio of molecular diffusivity of momentum to radiative diffusivity of thermal energy
$\delta_{t,\mathrm{FC}}, \mathrm{Pr}_R\ll 1$	$x(\mathrm{Re}_x\mathrm{Pr}_R)^{-1/2}$.	Scale of thermal boundary layer thickness in combined forced convection and radiation heat transfer for an optically thick medium and small N, small Pr_R
$\delta_{t,\mathrm{FC}}, \mathrm{Pr}_R\gg 1$	$x\,\mathrm{Re}_x^{-1/2}\mathrm{Pr}_R^{-1/3}$,	Scale of thermal boundary layer thickness in combined forced convection and radiation heat transfer for an optically thick medium and small N, large Pr_R
$\delta_{t,\mathrm{NC}}, \mathrm{Pr}_R\ll 1$	$x(\mathrm{Pr}_R NRa_x)^{-1/4}$.	Scale of thermal boundary layer thickness in combined natural convection and radiation heat transfer for an optically thick medium and small N, small Pr_R
$\delta_{t,\mathrm{NC}}, \mathrm{Pr}_R\gg 1$	$x(NRa_x)^{-1/4}$,	Scale of thermal boundary layer thickness in combined natural convection and radiation heat transfer for an optically thick medium and small N, large Pr_R
$\delta_{\mathrm{NC}}, \mathrm{Pr}_R\gg 1$	$x\mathrm{Pr}_R^{1/2}(NRa_x)^{-1/4}$,	Scale of velocity boundary layer thickness in combined natural convection and radiation heat transfer for an optically thick medium and small N, large Pr_R
M_T	$\frac{\delta_{t,\mathrm{FC}}}{\delta_{t,\mathrm{NC}}}$	The thermal mixing parameter, M_T, goes to zero as forced convection dominates, to infinity as heat transfer becomes predominately due to natural convection effects, and is $O(1)$ when the transition between the two modes occurs
Heat Transfer Estimate	$Nu_x^* N\frac{\delta_t}{x}\sim 1$	

The analysis we performed is general to natural or forced convection, provided the appropriate boundary layer thickness scale from Eqs. (2) and (3) is chosen.

The scale analysis of the continuity, momentum and energy equations for forced and natural convection and a nonparticipating medium are identical to those presented by Bejan [13]. The scale of thermal boundary layer thickness, δ_t, depends upon the mode of convection and Pr, and for forced convection is given by

$$\mathrm{Pr}\ll 1: \frac{\delta_t}{x}\sim(\mathrm{RePr})_x^{-1/2}$$
$$\mathrm{Pr}\gg 1: \frac{\delta_t}{x}\sim \mathrm{Re}_x^{-1/2}\mathrm{Pr}^{-1/3} \tag{2}$$

while for natural convection it is given by

$$\mathrm{Pr}\ll 1: \frac{\delta_t}{x}\sim(\mathrm{Ra}_x\mathrm{Pr})^{-1/4}$$
$$\mathrm{Pr}\gg 1: \frac{\delta_t}{x}\sim \mathrm{Ra}_x^{-1/4} \tag{3}$$

Note that Eq. (3) is valid in the limits of the Boussinesq approximation used in the momentum equation for natural convection [13].

The scaling for the heat flux boundary condition at the wall as given by Eq. (1) requires that

$$q_w\sim k\frac{(T_w-T_\infty)}{\delta_t}+\sigma\varepsilon(T_w^4-T_\infty^4) \tag{4}$$

Note that here we depart momentarily from customary scale analysis [13] to include a summation of two terms, possibly of unequal magnitudes. This is acceptable only because the radiation term simply adds a constant with no approximation.

The local Nusselt number,

$$\mathrm{Nu}_x^* = \frac{q_w x}{(T_w - T_\infty)k} \tag{5}$$

is marked with an asterisk to emphasize that it no longer has the normal meaning of dimensionless temperature gradient.

Substitution of Eq. (4) into Eq. (5) yields

$$\mathrm{Nu}_x^* \sim \frac{x}{\delta_t} + \frac{\sigma\varepsilon\Theta}{k}x \tag{6}$$

$$\Theta \equiv (T_w^2 + T_\infty^2)(T_w + T_\infty) \tag{7}$$

Therefore, the relative importance of radiation and convection to the heat transfer problem can be determined by the magnitude of a radiation to convection parameter, H_{RC},

$$H_{RC} = \frac{\sigma\varepsilon\Theta\,\delta_t}{k} \tag{8}$$

The portion of H_{RC} that derives from radiation effects, $\sigma\varepsilon\Theta$, is sometimes used as a heat transfer coefficient for radiation in a linearized radiation rate equation [16]. The role performed by the radiation to convection parameter, H_{RC}, would more typically be assigned to Bo^{-1}, where Bo is the Boltzmann number, usually defined as [17]

$$\mathrm{Bo} \equiv \frac{\rho c_p u_\infty}{\sigma T_\infty^3}. \tag{9}$$

Because T_w is not known for the specified heat flux problem of interest, the value used in Eqs. (7) and (8) is the scale of the wall temperature, which is the real root of Eq. (4) that is greater than T_∞. It should be noted that Eq. (4) is not a simple polynomial in T_w for the case of natural convection, because the expressions for δ_t contain T_w in the Rayleigh number.

3.2 Similarity Model for Nonparticipating Medium. To verify the scale analysis results for the above case of a nonparticipating medium considering both forced and natural convection, similarity solutions are developed for each case by applying a single parameter group transformation method [18]. Successful similarity solutions are obtained by requiring the reservoir temperature to be zero (see Appendix). Based on our solutions, the similarity transformation for the forced convection is found by requiring the specified nondimensional wall heat flux to vary with the nondimensional distance according to

$$q^* = x^{*\,2n-2/3} \tag{10}$$

whereas the similarity transformation for natural convection is found by requiring the wall heat flux to vary as $x^{-4/11}$. Though the required boundary conditions made the similarity models of limited applicability in the solution of physical problems, the entire motivation was to produce semi-analytical results with which we could validate our scale analysis results.

When comparing the radiation to convection parameter, H_{RC}, obtained from scale analysis and defined in Eq. (8) to the similarity solution results, it becomes clear that the parameter correctly predicts the transition from the dominance of convection to radiation heat transfer. When convection effects dominate, the Nusselt number based upon the thermal boundary layer thickness scale, $\mathrm{Nu}_x^*\ (\delta_t/x)$, will be of order one. When radiation effects dominate, $\mathrm{Nu}_x^*\ (\delta_t/x)$ will vary linearly with H_{RC}. And indeed, as shown in Fig. 1, results confirm that when H_{RC} is $O(1)$ or greater, convection effects quickly become negligible. If H_{RC} is less than $O(1)$, convection effects dominate. As a result, the similarity solutions support the validity of the results obtained from scale analysis.

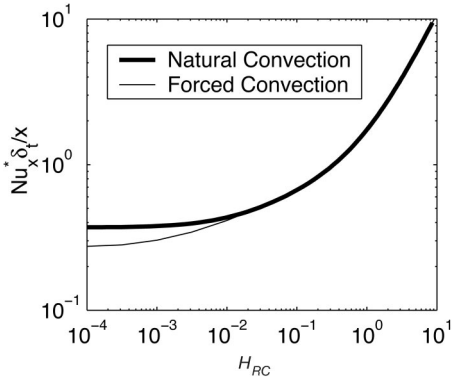

Fig. 1 Nonparticipating medium heat transfer results from similarity solution, Pr=1, $T_\infty=0$. For the forced convection case, the free stream velocity is uniform while the wall heat flux varies as $x^{-2/3}$.

3.3 Scaling Experimental Data. In addition to providing estimates in limiting cases and revealing the parameters that can be used to determine the dominant physics, scale analysis also yields combinations of dimensionless groups that can be used to best correlate experimental data.

Cess performed an asymptotic analysis of the case of free convection from a vertical wall with uniform imposed heat flux for which radiation effects were included [2]. He considered large and small values of the following parameter used for asymptotic expansion:

$$\xi = \frac{\sigma\varepsilon T_\infty^3}{k}\left(\frac{5k\nu^2 x}{g\beta q_w}\right)^{1/5}. \tag{11}$$

According to Cess, ξ determines the influence of radiation. In addition to developing the nondimensional parameter, ξ, Cess [2] also performed an experiment to validate his results (see insert, Fig. 2). The data is presented as $\mathrm{Nu/Gr}^{1/4}$ versus ξ, where Nu is the convective Nusselt number calculated with the radiative heat flux removed.

Although Cess' work [2] significantly advanced the understanding of convective and radiative effects in boundary layer flow, his nondimensionalization has several shortcomings. First, when considering Cess' experimental data plotted using his nondimensionalization of the problem, the value of ξ when the convective and radiative heat fluxes are equal is about 0.12; when ξ is 0.3, which is still well below unity, the radiative heat flux has become 2.9 times greater than the convective heat flux. Second, from Eq. (11), it is clear that for cold surroundings (i.e., low T_∞), ξ will be low despite the fact that if T_w is high radiation effects could be important. Consequently, although it is true that as ξ becomes very large or small limiting behavior is indeed approached, the magnitude of ξ when the transition occurs between the dominance of radiation and convection varies enormously.

If on the other hand we replot Cess' experimental data in Fig. 2 using the new scales that we identified using scale analysis, $\mathrm{Nu}_x^*(\delta_t/x)$ and H_{RC}, it becomes immediately apparent that the implementation of these scales reveals transitions much more readily. The data clearly follows the same trends as the similarity solution results in Fig. 1. When the two components of the heat flux are equal, H_{RC} is 0.49, and by the time the radiative heat flux is 2.5 times the convective heat flux, H_{RC} has exceeded unity. Unlike ξ, H_{RC} is always $O(1)$ when radiation and convection effects are both important.

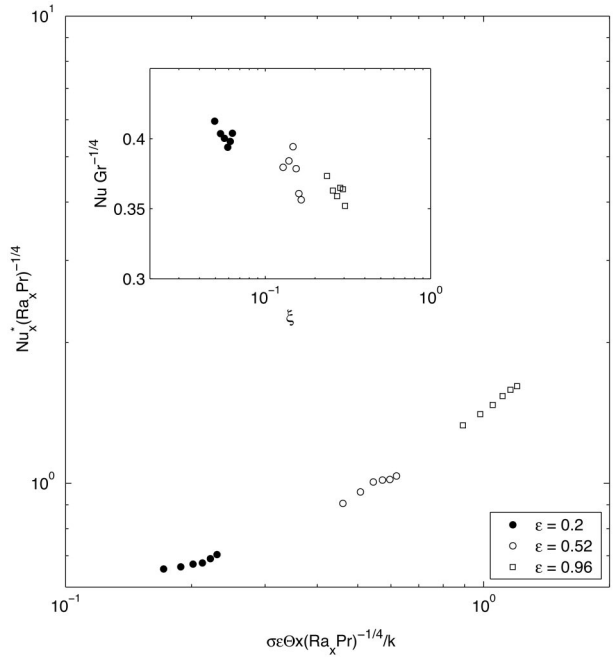

Fig. 2 Data from Cess [2]; heat transfer from isoflux surfaces of different emissivities to air. The insert, a semi-log plot, shows the data as Cess presented it. The outer log-log plot is the presentation suggested by scale analysis.

4 Optically Thick Medium

In an optically thick medium, the radiation penetration length is so small compared to the characteristic length of the fluid that the radiation transport process becomes diffusion-like, and the integral nature of the problem is removed [2]. Even in the extreme optically thick case, however, the diffusion approximation is not suitable for predicting temperature distribution in the immediate vicinity of the wall.

Assuming negligible axial radiative heat transport, the boundary layer energy equation retains its parabolic character, and includes the divergence of the radiative heat flux, which for a gray non-scattering medium, can be written

$$q_R = -\frac{4\sigma}{3\kappa}\frac{dT^4}{dy} \tag{12}$$

A medium can be considered optically thick if $\kappa y \gg 1$. Although the optically thick approximation fails for some region very close to the wall, so long as $\kappa\delta_t$ is sufficiently large, the results obtained from scale analysis of the optically thick case are valid.

The boundary layer assumption is valid when the boundary layer region is slender, i.e., $\delta \ll x$ and $\delta_t \ll x$. The scale analysis provides expressions to estimate the boundary layer thicknesses with radiation effects included, and therefore allows the validity of the boundary layer assumption to be quickly checked.

4.1 Scale Analysis of Optically Thick Medium. For an optically thick boundary layer, a surface energy balance on the wall, incorporating Deissler's approximation to reduce the error introduced by applying the optically thick approximation at the wall [7], yields

$$q_w = -k\frac{\partial T}{\partial y} - \frac{2\sigma}{3\kappa}\frac{\partial T^4}{\partial y} \tag{13}$$

Applying scale analysis, we rearrange Eq. (13) as the following balance

$$\mathrm{Nu}_x^* \sim \underbrace{\frac{x}{\delta_t}}_{\text{conduction}} \quad \text{or} \quad \underbrace{N^{-1}\frac{x}{\delta_t}}_{\text{radiation}} \tag{14}$$

N is the conduction to radiation parameter; it determines whether radiation or conduction dominates the heat transfer from the wall. It is commonly defined as [17], $N = k\kappa/(4\sigma T_w^3)$ yet in our scale analysis we find that the best definition of N is

$$N \equiv \frac{k\kappa}{\sigma\Theta} \tag{15}$$

The factor of 2/3 that would appear in Eqs. (14) and (15) is dropped because the analysis is order of magnitude.

4.1.1 Forced Convection. For forced convection, scale analysis of the continuity and momentum equations is unchanged from that for the nonparticipating medium case because we neglect radiation pressure.

The scale analysis of the energy equation, for an optically thick, nonscattering boundary layer flow with the previously mentioned simplifications starts with the following balance

$$\underbrace{\frac{4\sigma(T_w^4 - T_\infty^4)}{3\kappa\delta_t^2}}_{\text{radiation}} \sim \underbrace{k\frac{(T_w - T_\infty)}{\delta_t^2}}_{\text{conduction}} \quad \text{or} \quad \underbrace{\rho c_p \frac{u_s(T_w - T_\infty)}{x}}_{\text{advection}} \tag{16}$$

We are interested only in cases for which radiation is important. Therefore, we set the radiation term to $O(1)$ and find after rearrangement

$$\left(\frac{\delta_t}{x}\right)^2 \mathrm{Pe}_x^* N \quad \text{or} \quad N \sim \mathrm{O}(1). \tag{17}$$

We define Pe_x^* as the Peclet number, $(= u_s x/\alpha)$ based upon the velocity scale in the thermal boundary layer, u_s. The velocity scale in the thermal boundary layer will only be the free stream velocity, u_∞, if the thermal boundary layer is thicker than the velocity boundary layer [13].

From Eq. (17) we see that the limiting case for which there is a thermal boundary layer is that for which advection balances radiation. For this to be the case, Eq. (17) requires that conduction be negligibly small and

$$N \ll 1 \tag{18}$$

along with the restriction

$$\left(\frac{\delta_t}{x}\right)^2 \mathrm{Pe}_x^* \gg 1 \tag{19}$$

The requirement imposed by Eq. (18) on the validity of the scale analysis clarifies the balance in Eq. (14)

$$\mathrm{Nu}_x^* \sim \frac{1}{N}\frac{\delta_t}{x}. \tag{20}$$

For the limiting case described by Eq. (18), there are two possibilities that determine the appropriate velocity scale. If the thermal boundary layer is thicker than the velocity boundary layer ($\delta_t \gg \delta$) then the scale for velocity is the free stream velocity, i.e., $u_s = U_\infty$, and

$$\frac{\delta_t}{x} \sim \mathrm{Re}_x^{-1/2}(\mathrm{Pr}N)^{-1/2}. \tag{21}$$

Equation (21) provides the scale of thermal boundary layer thickness for the case of

$$(\mathrm{Pr}N)^{-1/2} \gg 1. \tag{22}$$

Because the thermal boundary layer is thicker than the velocity boundary layer for this case, Eq. (21) must be used when checking the validity of the boundary layer assumption for large PrN.

A similar analysis for the reversed relationship between the thermal and momentum boundary layers, $\delta_t \ll \delta$, leads to

$$\frac{\delta_t}{x} \sim \mathrm{Re}_x^{-1/2} (\mathrm{Pr}N)^{-1/3} \tag{23}$$

for

$$(\mathrm{Pr}N)^{-1/3} \ll 1 \tag{24}$$

The combination of Eq. (21) or (23) with Eq. (20) allows a quick estimation of the heat transfer. Additionally, Eq. (21) or (23) provides a means to easily determine when the diffusion approximation is valid by yielding a simple expression for $\kappa\delta_t$. Note that the result expressed by Eq. (23), although valid, holds only in the extreme case that both Eq. (18) and Eq. (24) are satisfied. The validity of Eqs. (20) and (21) in the limit of small N will be demonstrated using a similarity solution.

Following Cess' [2] definition of the "radiative Peclet number," the grouping PrN is termed the radiative Prandtl number and it is given the symbol, Pr_R. It can be thought of as a ratio of molecular diffusivity of momentum to radiative diffusivity of thermal energy.

4.1.2 Natural Convection. For natural convection the balance expressed by Eq. (16) is still true, and Eq. (17) is rearranged to obtain an expression for the scale of velocity in the thermal boundary layer when advection balances radiation (i.e., Eqs. (18) and (19) hold true):

$$u_s \sim \frac{\alpha x}{\delta_t^2 N}. \tag{25}$$

where α is the thermal diffusivity. The scaling of the momentum equation is identical to the nonparticipating medium case, [13], except the expression for the velocity scale provided by Eq. (25) has to be used, resulting in the following balance in which buoyancy terms are set to $O(1)$ and balanced by either inertial or frictional terms:

$$\underbrace{\frac{1}{\mathrm{Pr}_R}\left(\frac{x}{\delta_t}\right)^4 \frac{1}{N\mathrm{Ra}_x}}_{\text{inertia}} \text{ or } \underbrace{\left(\frac{x}{\delta_t}\right)^4 \frac{1}{N\mathrm{Ra}_x}}_{\text{friction}} \sim \underbrace{O(1)}_{\text{buoyancy}} \tag{26}$$

Comparison of the terms reveals that inertia balances buoyancy when

$$\mathrm{Pr}_R \ll 1. \tag{27}$$

And in this case, the resulting scale for thermal boundary layer thickness is

$$\frac{\delta_t}{x} \sim (N\mathrm{Pr}_R\mathrm{Ra}_x)^{-1/4}. \tag{28}$$

In turn, we find that the scale for velocity is

$$u_s \sim \frac{\alpha}{x}(\mathrm{Ra}_x\mathrm{Pr})^{1/2}, \tag{29}$$

For the case of inertia balancing buoyancy the velocity boundary layer thickness will be the same order of magnitude as the thermal boundary layer thickness [13] and the validity of the boundary layer approximation can be checked using Eq. (28).

That Eqs. (20) and (28) hold for natural convection in the limiting case of inertia balancing buoyancy and small N will be demonstrated using a similarity solution.

Alternatively, friction will balance buoyancy when

$$\mathrm{Pr}_R \gg 1. \tag{30}$$

For this case the scale for the thermal boundary layer thickness is given by

$$\frac{\delta_t}{x} \sim (N\mathrm{Ra}_x)^{-1/4} \tag{31}$$

and the scale for velocity is found to be

$$u_s \sim \frac{\alpha}{x}\left(\frac{\mathrm{Ra}_x}{N}\right)^{1/2}. \tag{32}$$

For the case of a thermal boundary layer in which friction balances buoyancy, the velocity boundary layer will be thicker than the thermal boundary layer, $\delta > \delta_t$, due to the presence of a region outside the thermal boundary layer in which buoyancy effects are absent, but fluid is moved through the action of viscous forces, which are balanced by inertial forces [13]

$$\underbrace{\nu\frac{u_s}{\delta^2}}_{\text{friction}} \sim \underbrace{\frac{u_s^2}{x}}_{\text{inertia}} \tag{33}$$

Combining Eqs. (32) and (33) we obtain an estimate for the boundary layer thickness, which allows the validity of the boundary layer assumption to be checked

$$\frac{\delta}{x} \sim \mathrm{Pr}_R^{1/2} (N\mathrm{Ra}_x)^{-1/4}. \tag{34}$$

It must be borne in mind that for radiation to be balanced by advection, Eq. (18) must again be satisfied. Thus, Eqs. (31), (32), and (34) are valid only when both Eq. (18) and Eq. (30) hold, and the condition of Pr_R very large when N is very small makes these results valid only when Pr is extremely large.

Finally, all of the natural convection results presented required the assumption that radiation is balanced by advection, and, therefore, that Eq. (18) be satisfied; consequently, Eq. (20) holds for natural convection when radiation effects balance advection effects.

4.1.3 Mixed Convection. Equation (20) holds for the natural and forced convection results provided advection rather than conduction balances radiation. It suggests that the importance of forced or natural convection to the convection-radiation heat transfer problem can be investigated in a manner identical to the case of advection-conduction boundary layer heat transfer [13]. A thermal mixing parameter, M_T, that goes to zero as forced convection dominates, to infinity as heat transfer becomes predominately due to natural convection effects, and is of order one when the transition between the two modes occurs, can be defined using the ratio of the respective effective thermal resistances of the boundary layer based upon pure forced convection and pure natural convection. Thus,

$$M_T = \frac{\delta_{t,\mathrm{FC}}}{\delta_{t,\mathrm{NC}}}, \quad N \ll 1 \tag{35}$$

where FC and NC indicate that the scales are for the pure convection cases. The resulting definition of M_T depends upon Pr_R and can be constructed using Eqs. (21) and (23), or (28) and (31)

$$\begin{aligned} \mathrm{Pr}_R \ll 1 &: M_T = \frac{(\mathrm{Ra}_x\mathrm{Pr})^{1/4}}{(\mathrm{Re}_x\mathrm{Pr})^{1/2}} \\ \mathrm{Pr}_R \gg 1 &: M_T = \frac{(N\mathrm{Ra}_x)^{1/4}}{\mathrm{Re}_x^{1/2}\mathrm{Pr}_R^{1/3}}. \end{aligned} \tag{36}$$

4.2 Similarity Solutions for Optically Thick Medium. To verify the scale analysis prediction of the heat transfer in an optically thick medium, Eq. (20), similarity solutions were obtained for both forced and natural convection optically thick boundary layer flows. The optically thick approximation yields similarity solutions for forced and natural convection with a constant wall temperature [7]. For the case of forced convection similarity so-

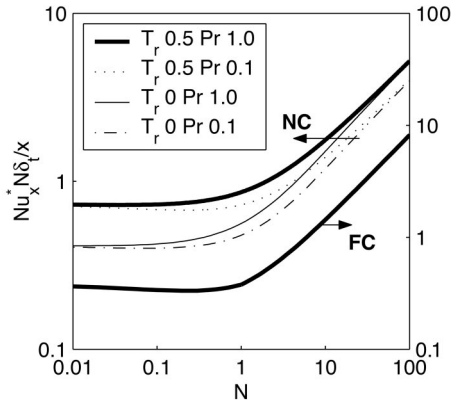

Fig. 3 Optically thick medium heat transfer results from similarity solution. Forced convection (FC) results are for Pr=1, u_∞ and T_w constant, and $T_\infty=0$, and are read using the right axis. Natural Convection (*NC*) results are for $T_w=1000°K$, $T_\infty=500°K$ or 0K ($T_r=0.5$ or 0 respectively), and Pr=1 or 0.1. They are read using the left axis.

lutions exists for Falkner-Skan wedge flows [7]. The wall heat flux is found using Deissler's approximation, Eq. (13), to reduce the error introduced by applying the optically thick approximation at the wall [7]. Results are plotted in Fig. 3 so that the validity of the scale analysis results given by Eq. (20) in the limit of small N becomes evident. For small N, $\mathrm{Nu}_x^* N\delta_t/x$ is $O(1)$ as Eq. (20) implies, while, for large N, $\mathrm{Nu}_x^* N\delta_t/x$ varies linearly with N, which indicates that convection dominates. The transition clearly occurs when N is $O(1)$.

A similarity model exists for the case of combined mixed convection and optically thick radiation heat transfer for a constant wall temperature and free stream velocity varying as $x^{1/2}$ (see Appendix). Using the similarity model, the wall heat transfer was calculated for a variety of M_T for the case of Pr=1 and $N=0.01$. Once again, Eq. (13) was used to compute the wall heat transfer, and results are presented in Fig. 4 so that the validity of the definition of M_T, Eq. (36), is evident. As predicted, for M_T less than order one, the resulting heat transfer scales with the results of the forced convection analysis, while for M_T greater than order one the natural convection scales apply.

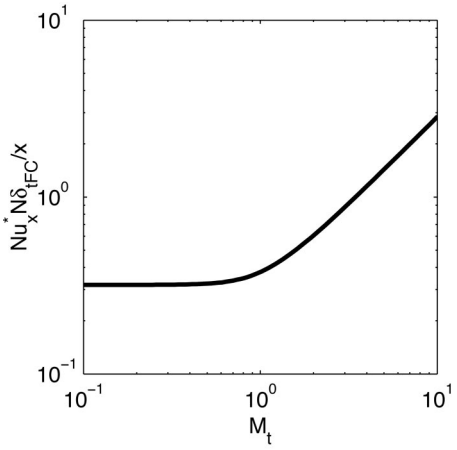

Fig. 4 Optically thick medium heat transfer results from similarity solution for mixed convection. u_∞ varies as $x^{1/2}$, T_w is constant, $T_\infty=0$, Pr=1, and $N=0.01$. Note that results are plotted in terms of the forced convection thermal boundary layer thickness scale, $\delta_{t,\mathrm{FC}}$, so that the transition from forced convection to natural convection dominance is clear; however, the resulting higher values for natural convection should not be misinterpreted as improved heat transfer.

5 Conclusions

Through scale analysis we have developed closed form analytical expressions that allow simple classification of several cases of combined convection-thermal radiation heat transfer problems. The first case considered included both forced and natural convection heat transfer components in conjunction with radiative heat transfer from a gray wall with a specified heat flux to a surrounding nonparticipating medium. The second case included forced, natural, and mixed convection heat transfer components in conjunction with radiative heat transfer from a black wall with a specified temperature to an optically thick, gray, nonscattering medium. Similarity models were developed and used to verify the scale analysis results and showed very good agreement for all cases considered. Additionally, the ability of the resulting nondimensional groups to correlate experimental data has been demonstrated. The following significant conclusions were obtained from the scale analysis results and are summarized in Table 1:

- For the case of a specified heat flux to a surrounding nonparticipating medium, scale analysis yields the dimensionless group in Eq. (8), $H_{RC}=\sigma\varepsilon\delta_t/k$, which determines whether radiation or convection effects dominate,
- Also for a specified heat flux to a surrounding nonparticipating medium, scale analysis provides an estimate of the wall temperature through the solution of an algebraic equation, Eq. (4).
- For the case of an optically thick, gray, nonscattering medium, scale analysis suggests that the best form of the conduction to radiation parameter, N, in optically thick boundary layer problems is that given by, Eq. (15), $N=k\kappa/(\sigma\Theta)$.
- Also for an optically thick, gray, nonscattering medium and for small N, we find that the determination of the importance of buoyancy effects in a forced convection flow with thermal radiation, or, conversely, the importance of assisting flow in a free convection-thermal radiation problem, can be found by determining the magnitude of a thermal mixing parameter, M_T, defined in Eq. (34).
- Finally, for an optically thick, gray, nonscattering medium, scale analysis yields a closed form expression, Eq. (20), for estimation of the nondimensional heat transfer when $N\ll 1$.

Nomenclature

H_{RC} = radiation to convection parameter
Gr = Grashoff number, $g\beta(T_w-T_\infty)x^3/\nu^2$
M_T = thermal mixing parameter
N = conduction to radiation parameter
Nu_x = convective Nusselt number, based on local convective heat flux
Nu_x^* = Nusselt number based on local total heat flux
Pe_x^* = Peclet number based on u_s, $u_s x/\alpha$
Pr = Prandtl number
Pr_R = radiative Prandtl number, PrN
Ra_x = Rayleigh number, $g\beta(T_w-T_\infty)x^3/(\alpha\nu)$
Re_x = Reynolds number, $u_\infty x/\nu$
k = thermal conductivity
q = heat flux
u = x-component of velocity
u_s = scale for velocity in the thermal boundary layer
x = coordinate aligned with wall
y = coordinate orthogonal to wall

Greek Symbols

α = thermal diffusivity, $k/(\rho c_p)$
δ = velocity boundary layer thickness scale
δ_t = thermal boundary layer thickness scale
ε = total hemispherical emissivity
κ = absorption coefficient

ν = kinematic viscosity
σ = Stefan-Boltzmann constant
ξ = Cess' convection to radiation parameter for natural convection

Subscripts

w = value at the wall
FC = forced convection
NC = natural convection
R = radiative
∞ = value in the free stream/reservoir

Appendix

Similarity Solution. The governing equations are considered in non-dimensional stream function form and are written using the simplifying assumptions described in section (2).

The stream function is Ψ, and U_r is the reference value for nondimensionalization of the free stream velocity u_∞. The meaning of all other variables and reference symbols should be clear. The following nondimensional parameters appear in the resulting equations (r denotes an appropriate reference value)

$$A=\frac{U_r^2 y_r^2}{\Psi_r^2},\quad B=\frac{\nu x_r}{\Psi_r y_r},\quad C=\frac{g\beta T_r x_r y_r^2}{\Psi_r^2}$$
$$D=\frac{\sigma\varepsilon y_r T_r^3}{k},\quad E=\frac{q_r y_r}{kT_r},\quad \text{and}\quad F=\frac{\sigma T_r^3 x_r}{\rho c_p \kappa y_r \Psi_r} \tag{37}$$

The thermal boundary conditions at the wall and the free stream velocity boundary condition for forced and natural convection are kept general, i.e.,

$$q(x,y=0)=q_w(x)\quad \text{or}\quad T(x,y=0)=T_w(x) \tag{38}$$

and

$$u(x,y\to\infty)=u_\infty(x). \tag{39}$$

A single group parameter transformation is found as described by Özisik [18], and the governing equations and boundary conditions are transformed. In order to find a transformation, it is necessary to specify the form of the variation of the boundary conditions in Eqs. (38) and (39), and it may be necessary to set T_∞ equal to zero. The similarity transformations, restrictions, and resulting equations are detailed below. The resulting boundary value problems were solved using a shooting technique.

Nonparticipating Medium, Forced Convection. A successful transformation of the governing equations and boundary conditions requires $T_\infty=0$, $u_\infty=x^n$ and $q_w=x^{(2n-2)/3}$

The similarity variables are

$$\eta=\frac{y}{x^{(1-n)/2}}$$
$$f=\frac{\Psi}{x^{(n+1)/2}} \tag{40}$$
$$h=\frac{T}{x^{(n-1)/6}}$$

The transformed governing equations are

$$f'''+\frac{n+1}{2B}ff''-\frac{n}{B}f'^2+\frac{An}{B}=0,\ \text{and}$$
$$h''+\Pr\frac{(n+1)}{2B}fh'-\Pr\frac{(n-1)}{6B}f'h=0 \tag{41}$$

The transformed boundary conditions are

$$f'(0)=0$$
$$f(0)=0$$
$$f'(\infty)=\sqrt{A} \tag{42}$$
$$h'(0)=Dh^4(0)-E$$
$$h(\infty)=0$$

Nonparticipating Medium, Natural Convection. A successful transformation of the governing equations and boundary conditions requires $T_\infty=0$, and $q_w=x^{-4/11}$. The similarity variables are

$$\eta=\frac{y}{x^{3/11}}$$
$$f=\frac{\Psi}{x^{8/11}} \tag{43}$$
$$h=Tx^{1/11}$$

The transformed governing equations are

$$f'''+\frac{8}{11B}ff''-\frac{5}{11B}f'^2+\frac{Ch}{B}=0,\ \text{and}$$
$$h''+\Pr\frac{8}{11B}fh'+\Pr\frac{f'h}{11B}=0 \tag{44}$$

The transformed boundary conditions are

$$f'(0)=0$$
$$f(0)=0$$
$$f'(\infty)=0 \tag{45}$$
$$h'(0)=Dh^4(0)-E$$
$$h(\infty)=0$$

Optically Thick Medium, Mixed Convection. A successful transformation of the governing equations and boundary conditions requires T_w constant and $u_\infty=x^{1/2}$. The similarity variables are

$$\eta=\frac{y}{x^{1/4}}$$
$$f=\frac{\Psi}{x^{3/4}} \tag{46}$$
$$h=T$$

The transformed governing equations are

$$f'''+\frac{3}{4B}ff''+\frac{f'^2}{2B}+\frac{A}{2B}+\frac{C}{B}\left(h-\frac{T_\infty}{T_r}\right)=0$$
$$h''+\Pr\frac{16}{3B}h''h^3+\Pr\frac{3}{4B}fh'+\Pr\frac{16F}{B}h^2h'^2=0 \tag{47}$$

The transformed boundary conditions are

$$f'(0)=0$$
$$f(0)=0$$
$$f'(\infty)=\sqrt{A} \tag{48}$$
$$h(0)=\frac{T_w}{T_r}$$
$$h(\infty)=\frac{T_\infty}{T_r}$$

References

[1] Viskanta, R., 1966, ''Radiation Transfer and Interaction of Convection with Radiation Heat Transfer,'' T. Irvine and J. Hartnett, eds., *Advances in Heat Transfer*, Academic Press, New York **3**, pp. 176–248.

[2] Cess, R., 1964, ''The Interaction of Thermal Radiation with Conduction and Convection Heat Transfer,'' T. Irvine and J. Hartnett, eds., *Advances in Heat Transfer*, Academic Press, New York **1**, pp. 1–50.

[3] Oliver, C., and McFadden, P., 1966, ''The Interaction of Radiation and Convection in the Laminar Boundary Layer,'' ASME J. Heat Transfer, **88**, pp. 205–213.

[4] Houf, W., Incropera, F., and Viskanta, R., 1985, ''Thermal Conditions in Irradiated Slowly Moving Liquid Layers,'' ASME J. Heat Transfer, **107**, pp. 92–98.

[5] Arpaci, V., 1968, ''Effect of Thermal Radiation on the Laminar Free Convection from a Heated Vertical Plate,'' Int. J. Heat Mass Transfer, **11**, pp. 871–881.

[6] Viskanta, R., and Grosh, J., 1962, ''Boundary Layer in Thermal Radiation Absorbing and Emitting Media,'' Int. J. Heat Mass Transfer, **5**, pp. 795–806.

[7] Özisik, M., 1973, *Radiative Transfer and Interactions with Conduction and Convection*, Wiley, New York.

[8] Krishnaprakas, C., and Narayana, K., 1999, ''Interaction of Radiation with Natural Convection,'' J. Thermophys. Heat Transfer, **13**, pp. 387–390.

[9] Zhang, L., Soufiani, A., Petit, J., and Taine, J., 1990, ''Coupled Radiation and Laminar Mixed Convection in an Absorbing and Emitting Real Gas Mixture Along a Vertical Plate,'' Int. J. Heat Mass Transfer, **33**, pp. 319–329.

[10] Webb, B., 1990, ''Interaction of Radiation and Free Convection on a Heated Vertical Plate: Experiment and Analysis,'' J. Thermophys. Heat Transfer, **4**, pp. 117–121.

[11] Cess, R., 1966, ''The Interaction of Thermal Radiation with Free Convection Heat Transfer,'' Int. J. Heat Mass Transfer, **9**, pp. 1269–1277.

[12] Cheng, E., and Özisik, M., 1972, ''Radiation with Free Convection in an Absorbing, Emitting, and Scattering Medium,'' Int. J. Heat Mass Transfer, **15**, pp. 1243–1252.

[13] Bejan, A., 1995, *Convection Heat Transfer*, Second ed., Wiley, New York.

[14] Duty, C., Johnson, R., Gillespie, J., Fedorov, A. G., and Lackey, J., 2002, ''Heat and Mass Transfer Modeling of an Angled Gas-Jet LCVD System,'' Applied Physics A, **76**, pp. 1–9.

[15] Cheung, F. B., Chan, S. H., Chawla, T. C., and Cho, D. H., 1980, ''Radiative Heat Transfer in a Heat Generating and Turbulently Convecting Fluid Layer,'' Int. J. Heat Mass Transfer, **23**, pp. 1313–1323.

[16] Incropera, F. P. and DeWitt, D. P., 1996, *Fundamentals of Heat and Mass Transfer*, Wiley, New York, p. 10.

[17] Modest, M. F., 1993, *Radiative Heat Transfer*, McGgraw-Hill, USA, p. 199.

[18] Özisik, M., 1980, *Heat Conduction*, first ed., Wiley, New York, pp. 452–454.

Y. Hong
Department of Mechanical and Aerospace Engineering,
State University of New York at Buffalo,
Buffalo, New York, 14260

N. Ashgriz
Department of Mechanical and Industrial Engineering,
University of Toronto,
5 King's College Road,
Toronto, Ontario, Canada M5S 3G8

J. Andrews
Wilson Center for Research and Technology,
Xerox Corporation,
Webster, New York, 14580

Experimental Study of Bubble Dynamics on a Micro Heater Induced by Pulse Heating

An experimental investigation of the rapid formation and collapse of bubbles formed on a micro heater ($25\times80\ \mu m^2$) is presented. Short electric pulses in the range of 1 μs to 4 μs are applied to the resistive heater, which is immersed in deionized water and generates a heat flux of more than 750 MW/m^2. A stroboscopic technique with a time resolution of 30 ns and spatial resolution of 2 μm was used to capture the dynamics of the bubble growth and collapse. From the nucleation theory, the nucleation temperatures are close to the kinetic limit of superheat and weakly depends on the heating rate. The velocity, acceleration, and the pressure profiles after the vapor sheet formation are presented.
[DOI: 10.1115/1.1650388]

Keywords: Boiling, Bubble Growth, Channel Flow, Heat Transfer, Two-Phase

1 Introduction

Desktop printing using a thermal inkjet printhead is a reliable and economical method of printing. In such systems, a short electric pulse (1 to 5 μs) generates a high heat flux on a micro size heater, which is exposed on one side to the ink. The ink becomes highly superheated and reaches metastable state, forming a vapor bubble. This type of rapid heating and bubble formation is referred to as explosive boiling [1–3]. Sudden formation of the vapor bubble generates a pressure impulse, which, in turn, results in the growth of the bubble. The rapid growth of the bubble ejects a small drop of ink out of a nozzle located close to the heater. Once the bubble collapses, the nozzle refills due to capillary forces, becoming ready for the next pulse.

The liquid must be superheated to form a vapor bubble. The degree of superheat depends on the properties of the liquid, such as surface tension, viscosity, and the conditions of the heating process. For conventional boiling process at low heating rate, the superheat is only a few degrees above the boiling point of the liquid. However, the superheat can approach 90 percent of the critical temperature of the liquid with high heat flux [4,5]. Bubble nucleation occurs when the liquid is sufficiently superheated. There are two classes of bubble formation mechanisms [4,6,7]. One is based on the heterogeneous nucleation, which occurs when small gas bubbles trapped in minute cracks or crevices on the heated surface become the initiation sites for bubble growth when the liquid is superheated at the liquid/solid interface. Heterogeneous nucleation depends strongly on the properties and the geometry of the heater surface. The other is based on the homogeneous nucleation, which is the result of thermally driven density fluctuations within the liquid. When the density fluctuation is sufficiently large, the low density volume can seed bubble growth. Therefore, homogeneous nucleation depends primarily on the liquid properties. The liquid properties, heated surface properties, and the heating kinetics can determine which of these mechanisms is dominant.

High heat flux condition creates a large temperature gradient adjacent to the heater surface. Under the experimental parameters of this study, the initial bubble growth is limited to a small volume of liquid very near the heater surface. Bubble growth outside the thin thermal layer is affected by cool liquid and is therefore controlled by the initial momentum generated from the pressure impulse. In these experiments the initial nucleation events appear to be localized to specific spots on the heater surface. Other bubbles, apparently not associated with specific locations on the heater surface, form later in the heating phase. This collection of early cooler bubbles and later hotter bubbles coalesce into a single vapor film that covers the entire heater surface. This vapor film expands to its maximum size and then collapses. The bubble size, the rate of expansion, and the time for bubble growth and collapse depend the the bubble nucleation and heating condition and they influence the magnitude of the impulse that can act to move fluid.

1.1 Literature Review.

A theoretical model for the heterogeneous nucleation was proposed by Hsu [8] for the growth of pre-existing nuclei in a cavity on a heated surface. The model included the effect of nonuniform superheated liquid. The equation for the activation curve of bubble nucleation was derived by combining the Clausius-Clapeyron and the Young-Laplace equations. Then, by substituting the linear temperature profile into the equation, the range of active cavity sizes on the heated surface was obtained.

The theory of bubble nucleation in a superheated liquid was first applied to the concept of thermal inkjet by Allen et al. [5]. They were able to determine the minimum conditions for the first bubble nucleation by applying Hsu's theory [8]. Time dependent temperature profiles above a heater surface were obtained. By superimposing the activation curve with the thermal boundary layer, the initial bubble size and the minimum temperature for nucleation were determined. Based on a one-dimensional model and by assuming the nucleation temperature to be the superheat limit of the liquid at 330°C, transient temperature profiles for the heater structure and the bubble surface after nucleation were obtained. It was noticed that the decay time to ambient temperature from its initial state was only several micro-seconds after 6 μs heating pulse. The thermal effects of the passivation (protective coating) layer on the heater surface were also analyzed. The results showed that the effective pulse energy required for bubble nucleation increases with the thickness of the passivation layer.

Asai [6,9,10] conducted a series of numerical and theoretical studies on the bubble nucleation and growth in thermal inkjets. A one-dimensional numerical model of bubble growth and collapse and the resulting flow motion was presented [9]. The model is divided into two phases. The first phase is for the state before bubble nucleation. The heat transfer process in this phase is approximated by a one-dimensional heat conduction equation from which nucleation temperature is estimated to be 270°C. The second phase describes the bubble generation, growth, and collapse.

Contributed by the Heat Transfer Division for publication in the JOURNAL OF HEAT TRANSFER. Manuscript received by the Heat Transfer Division November 8, 2002; revision received November 25, 2003. Associate Editor: V. P. Carey.

The temperature and pressure in the bubble are assumed to be uniform and to be related by Clausius-Clapeyron equation and the equation of state. Their results show that the initial pressure is around 4.5 MPa, but it decreases to less than 10 kPa in 10 μs. In addition, effects of viscosity of the ink, the nozzle outlet length, and three different operating voltages on the bubble formation were investigated. A theoretical model was also developed to predict the nucleation process. Nucleation probability was derived from the classical nucleation theory and was used to simulate the initial bubble growth process. It is concluded that the incipient boiling time is not a point value but a stochastic variable and as the heat input increases the initial bubble growth process becomes more reproducible and less random [6]. Another theoretical model of bubble dynamics was proposed by Asai [10]. The nucleation temperature as a function of heat flux was obtained from the classical nucleation theory. The result showed that the nucleation temperature increased linearly with the heat flux. An analytical expression for the time dependent bubble pressure was developed. The bubble growth process was described as an impulsive motion of a thin vapor film caused by initial bubble pressure.

An empirical equation for the nucleation criterion was derived from the experimental results by Runge [11]. By observing the nucleation time and calculating the unsteady heat conduction equation numerically, the temperature at the nucleation point was plotted against the temperature gradient. A linear dependency between nucleation temperature and temperature gradient was observed.

Avedisian et al. [12] measured the bubble nucleation temperature by measuring the electrical resistance. The measured resistance was converted into temperature using a calibration heater. An aluminum-tantalum heater with thickness of 0.2 μm, and width of 64.5 μm was used. The bubble nucleation temperature was found by identifying the inflection point from time dependent temperature profiles. Their results were in good agreement with the homogeneous nucleation theory. Therefore, they concluded that homogeneous nucleation governs the boiling process in micro-heaters at high heating rates. They also noted that the nucleation temperature increased with heating rate.

Chen et al. [13] presented a numerical study of the bubble growth and ink ejection process of a thermal inkjet printhead. Based on a one-dimensional unsteady heat conduction model and theories presented by Asai [10], the bubble volume, temperature, and pressure at various operating voltages were obtained [10,13]. It was found that the bubble volume decreases with increasing voltage. The relationship between threshold voltage and the pulse width was also presented. The threshold voltage was taken to be the minimum value that could generate enough heat for bubble nucleation at the end of the heating pulse.

Another experimental and numerical study for the dynamics of bubble and liquid flow in thermal inkjet were presented by Rembe et al. [3]. From the sequence of images captured by the stroboscopic technique, they measured the positions of the ejected liquid column and the velocity of the ejected ink from the nozzle. By employing mass balance and force balance, the dynamic equation of the liquid column exiting from the nozzle in terms of vapor bubble pressure was obtained. By considering thermal diffusion in the heater and the liquid, the thermodynamics of the bubble, and the conservation of the energy along with the dynamic equation, a state space representation of nonlinear differential equations was derived using the integral methods. The temperature in the bubble and the movement of the liquid column was simulated by solving the state representation numerically. The pressure propagation was also obtained. Furthermore, the effect of higher ambient pressure on the movement of the ejected liquid was presented.

Lin et al. [14] conducted an experimental study on the bubble formation on a line shaped polysilicon micro resistor, which was immersed in the sub-cooled liquids such as Fluorinert fluids (inert and dielectric fluids from 3M Company), water, and methanol. Three different types of input currents were applied after initial nucleation. First, a bubble grew and departed when the input current was constant or increased. Second, a bubble collapsed when the current was turned off abruptly. Third, the size of the bubble decreased and stayed on the top of the heater when the current was reduced gradually. Some important bubble formation phenomena such as Marangoni effects on a micro scale, controllability of the size of the micro bubbles, and bubble nucleation hysteresis were reported.

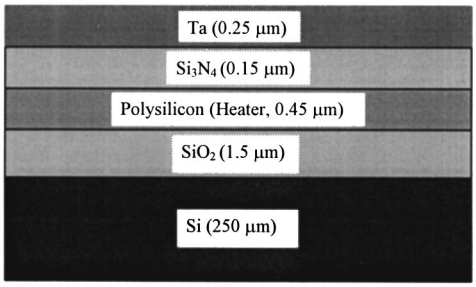

Fig. 1 Cross-section of the heater structure (not to scale)

Zhao et al. [15] conducted an experimental study of explosive vaporization of the bubble on a micro-heater. By detecting acoustic emissions during explosive vaporization process of the bubble, the bubble volume and the bubble expansion velocity and acceleration was reconstructed. The vapor pressure inside the bubble was also calculated using the Rayleigh-Plesset equation.

The mechanism of the nucleation process and subsequent physical phenomenon on a micro heater with high heating rates is still not well understood due to the small physical and time scales of the heater. In order to better understand the physical processes that occur in such systems, we have conducted a detailed experimental study of bubble nucleation on micro heaters having an area of 2000 μm^2, a heat flux of $\sim$1 GW/m^2 and on time scales of a few microseconds. Direct observations of the bubble nucleation, growth and collapse have been achieved using a laser stroboscopic technique. By comparing a one-dimensional thermal model [16] for a multi-layered heater structure with the experimental observations, we have determined the nucleation temperature for various heat fluxes and initial temperatures. Since bubble nucleation and growth is strongly dependent on the initial heating condition, effects of pulse width, input voltage, and ambient temperature on bubble growth have also been determined. In § 2 we describe the experimental setup, and the methods for measuring the current and resistances. In § 3, we discuss the method for estimating the nucleation temperature. In § 4, we provide the results of this study followed by the conclusion in § 5.

2 Experimental Setup and Measurement Techniques

The heaters under this study were made using a conventional microelectronic processing on a silicon substrate. The heater consisted of several hundred individually addressable heaters. Custom electronics controlled by a computer permitted firing an individual heater with a selected repetition frequency, applied voltage and pulse width. The size of an individual heater is 25×80 μm^2. The cross-section of the heater structure plus a liquid layer is depicted in Fig. 1. Each heater is 0.45 μm of doped polysilicon (Si) that is electrically and thermally isolated from the silicon substrate by 1.5 μm of thermally grown SiO_2. On top of the polysilicon heater is a 0.15 μm layer of silicon nitride (Si_2N_3) for electrical isolation. The heater interface with water is 0.25 μm of sputter-deposited tantalum (Ta). The thermal properties for the materials used in the structure are in Table 1. The heaters are located on a water-filled chamber that is 15 mm long by 1.5 mm wide by 0.5 mm high (perpendicular to the heater), as shown in Fig. 2. Small photo-patterned polymer walls 3 μm high and 17 μm wide separate the heaters. Microscope cover glasses form the top and front

Table 1 Thermal properties of the materials

Material	Conductivity k (W/m K)	Heat capacity ρc (J/m^3 K)	Thickness (μm)
Ink (Water)	0.67	4.09×10^6	∞
Ta	57.7	2.32×10^6	0.25
Si_3N_4	1.67	2.53×10^6	0.15
Si heater	141.2	1.63×10^6	0.45
SiO_2	13.9	1.66×10^6	1.5
Si substrate	141.2	1.63×10^6	250

wall through which it is possible to observe the heater surface and the bubble height (perpendicular to the heater surface). The chamber is not sealed by the cover glass, providing an atmospheric-pressure boundary condition for the fluid chamber. The back wall of the chamber is a small mirror that permits observation of the bubble height with epi-illumination.

The experimental setup shown in Fig. 3 is an improved version of a previously developed stroboscopic system [17]. Observations of an individual heater are made through two microscopes, one having the observation axis perpendicular to the heater surface and the second having the observation axis parallel to the heater surface and the heater long axis. The mirror is ~300 μm behind the heater. Both microscopes are set up for epi-illumination. For stroboscopic observation, the conventional light sources are replaced with pulsed diode lasers operating at a wavelength of 905 nm. The pulse duration of the lasers is 30 ns. Progressive area scan cameras are attached to each of the microscopes. The vertical and horizontal microscopes had 40X 0.5NA and 20X 0.45NA objectives, respectively. The theoretical optical resolution is ~2.2 μm but because of the cameras and imaging through a thickness of material, the actual resolution is somewhat reduced.

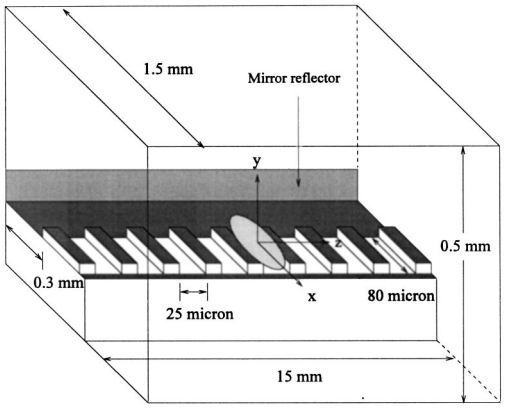

Fig. 2 Print head structure (not to scale)

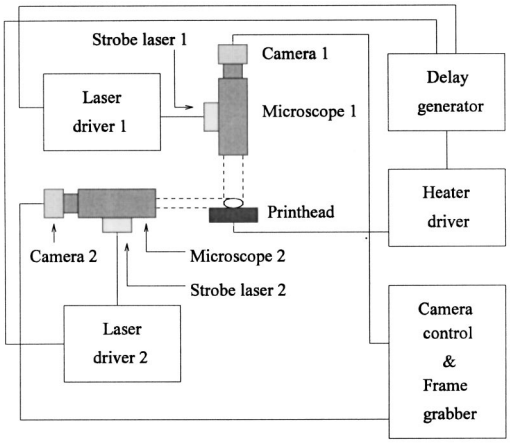

Fig. 3 Experimental setup

The stroboscopic measurements are controlled by the system clock. From the system clock, the heater driver and a delay generator are triggered at a set frequency between 1 Hz and 18 kHz. The delay generator allows selectable time delays from several microseconds preceding the firing of the heater to positive delay times limited by the firing frequency. The trigger from the delay generator is an input to an AND GATE. The other input to the AND GATE is from the vertical camera ''ready to acquire'' output. The output of the AND GATE then triggers both the laser strobe and the frame grabber. In this way each camera frame is the image of a single heater event at the selected time delay. By varying the delay, the time evolution of the nucleation and bubble growth are observed from the sequence of individual heater firings. The transient heater current is monitored by a high bandwidth current probe using an oscilloscope. A constant temperature recirculating water bath is used to keep the heatsink at a constant temperature. The heater firing frequency is typically 1 kHz to avoid local heating.

Top and front views of the bubble movement at specified time delay were captured for various heating conditions. The dimensions of the bubble at each time frame were obtained from direct measurement of bubble images.

The input current through the heater is measured from the digital oscilloscope. Figure 4 shows current pulses for various input voltages. The duration of the pulses are varied according to the input voltages applied. For all cases, the pulse is applied long enough to form a vapor sheet, which is considered to be the state of the homogeneous nucleation. (This will be further discussed in the next section.) It is noted that the magnitude of the current pulse during pulse heating decreases slightly due to the increase in resistance resulted from the temperature increase of the heater. The current drop, as indicated in Fig. 4, is larger for the higher input voltages because of the higher heating rate.

The total electrical resistance of the system, R_{total}, which is determined from the measured currents and applied voltages, is composed of following resistances:

$$R_{\text{total}} = R_{\text{heater}} + R_{\text{parasitic}} + R_{\text{driver}}$$

where $R_{\text{parasitic}} = R_{\text{contact}} + R_{n+\text{leads}}$. It varies from 734 $\Omega \pm 10$ Ω to 748 $\Omega \pm 10$ Ω and has tendency to decrease as the input power increases (Fig. 5). For the thermal calculation in the later section, however, R_{total} is assumed to be constant as the average value of 740 Ω in the range of operation since it varies only within 2 percent range. The measured values for R_{contact}, $R_{n+\text{leads}}$, and R_{driver} are 10 $\Omega \pm 1$ Ω, 20 $\Omega \pm 2$ Ω, and 34 $\Omega \pm 0.3$ Ω, respectively. However, the heater resistance, R_{heater}, is estimated from the other resistances ($R_{\text{parasitic}}$, R_{driver}, and R_{total}), because direct measurement of the heater resistance is not possible. Therefore, the estimated R_{heater} ranges from 670 $\Omega \pm 11$ Ω to 684 $\Omega \pm 11$ Ω. The dependency of the nucleation temperature within this range is discussed in the later section.

For input voltages between 36 V and 48 V, total heat fluxes of 791 MW/m$^2 \pm 16$ MW/m^2 to 1435 MW/m$^2 \pm 74$ MW/m^2 were generated at the silicon heater. The heat flux from the heater surface (Ta-water interface) ranged from 265 MW/m$^2 \pm 5.5$ MW/m^2 to 417 MW/m$^2 \pm 21.6$ MW/m^2 for the Ta-water interface.

3 Estimation of the Nucleation Temperature

Measuring the nucleation temperature directly is not a simple task because of the limited physical size of the heater and extremely small time scale. Avedesian et al. [12] have measured bubble nucleation temperatures on the surface of inkjet heater by identifying an inflection point on the temperature profile of the heater surface. In our experiment, the nucleation temperature is approximated by a method similar to that used by Runge [11]. A

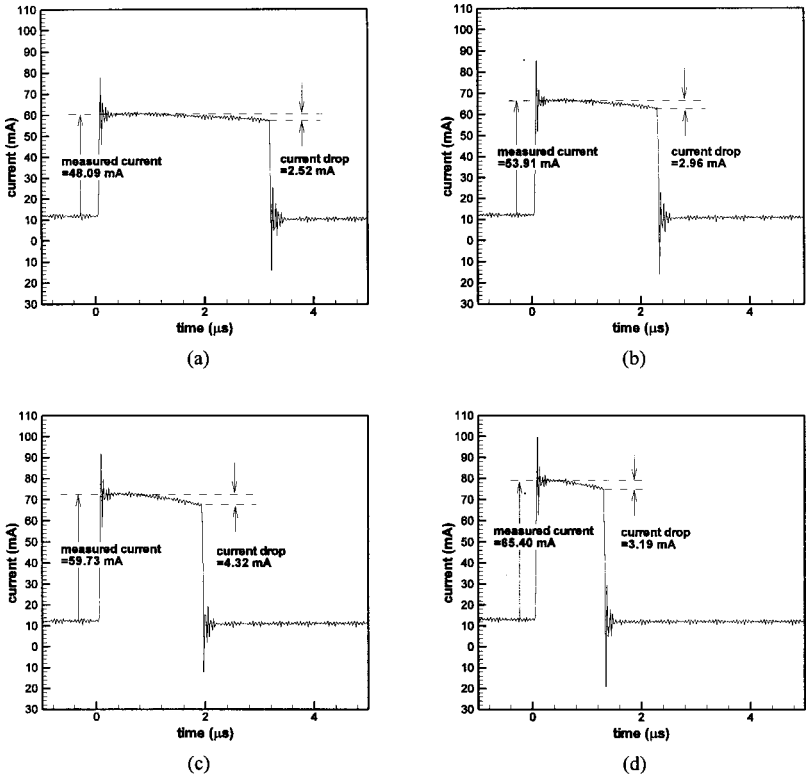

Fig. 4 Measured currents at (*a*) 36 V, (*b*) 40 V, (*c*) 44 V, and (*d*) 48 V

one dimensional heat conduction equation for a multi-layered heater structure bounded by a liquid on one side is solved numerically to determine the temperature of the Ta-Water interface (heater surface), T_{surf}. The actual nucleation temperature is estimated by the surface temperature at which the first vapor bubble appears from the observation. Here, the structure and the liquid are considered as one piece, thus

$$\rho c_v \frac{\partial T}{\partial t} = -\frac{\partial q''}{\partial z} + \dot{Q} \tag{1}$$

where $T(t,z)$ is the temperature, t is time, q'' is heat flux, and $\dot{Q}$ is the heat input to the heater per unit volume per unit time. The heat input, $\dot{Q}$, can be expressed as

$$\dot{Q} = \frac{\text{Power}}{\text{Vol}_{\text{heater}}} = \frac{I[V_0 - I(R_{\text{parasitic}} + R_{\text{driver}})]}{\text{Vol}_{\text{heater}}} \tag{2}$$

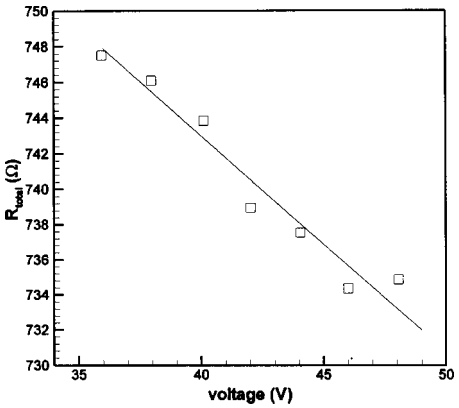

Fig. 5 Total resistance, R_{total}, as a function of voltage

$$I = \frac{V_0}{R_{\text{total}}} \tag{3}$$

where $\text{Vol}_{\text{heater}}$ is the heater volume, and I is the current. The governing heat equation is subject to the initial and boundary conditions. It is assumed that the structure and the water are initially at ambient temperature and are kept constant at that temperature to avoid general heating effect: $T(0,z) = T(t,0) = T(t,h) = T_{\text{amb}}$. Equations (1–3) subject to the given initial and boundary conditions are solved numerically by employing an implicit finite difference scheme. As mentioned in the earlier section, there is a current drop during the pulse heating due to the temperature increase in the heater. Therefore, a temperature coefficient of the resistance, TCR, is defined to account for the current drop in the time-dependent heat flux. The variable heater resistance, $R(t)$, due to the variable heater temperature, $T_{\text{heater}}(t)$, can be written as

$$R(t) = R_{\text{heater}}[1 + TCR(T_{\text{heater}}(t) - T_{\text{amb}})]. \tag{4}$$

By first guessing a value of TCR, $R(t)$is found and it is used for heater resistance in thermal calculation to obtain the variable current, $I(t)$, from the relationship, $I(t) = V_0/R(t)$. Then, the calculated values of $I(t)$ are compared with the measured values of the current. The process is repeated until the guessed TCR provides a correct current. The variation of TCR is plotted against the input voltages in Fig. 6. It ranges from $0.00015°\text{C}^{-1}$ to $0.00021°\text{C}^{-1}$. The nucleation temperature for the variable TCR and R_{total} is compared with the case when averaged TCR and R_{total} over input voltages is used in the thermal calculation (Fig. 7). Furthermore, the effect on the nucleation temperatures for the case of two different values of the remaining resistances ($R_{\text{driver}} + R_{\text{parasitic}}$) of 55 Ω and 64 Ω is tested and the results are shown in the figure. For all different cases, the change in the nucleation temperature is not significant. The possible error range is from 3°C to 5°C, which is less than 2 percent.

Figure 8 shows the temperature distributions at different time levels in water for the input powers corresponding to heater volt-

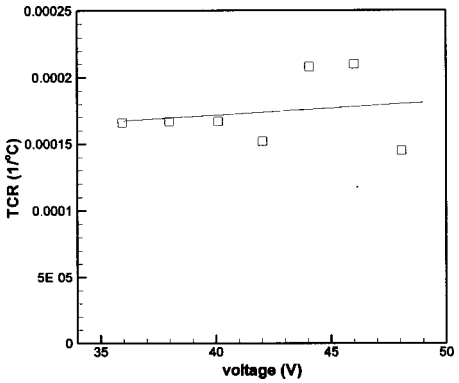

Fig. 6 Temperature coefficient of resistance, TCR, as a function of voltage

ages of 36 V and 48 V. These figures show very steep temperature gradients. The temperature drops to the ambient temperature within ~1.5 μm. The diameters of initially observed nucleate bubbles are usually bigger than 1.5 μm. This implies that the thermal effect on the bubble growth is negligible and the growth is controlled mainly by the inertial force generated by the pressure impulse. There is greater heat penetration depth into the water for lower heat flux, therefore, more energy is transferred to the water. The nucleation times are about 1 μs for 48 V and 2.1 μs for 36 V. By considering the uncertainty of the time measurement of 0.05 μs, the estimated nucleation temperatures are around 292°C±4°C for 36 V and 310°C±13°C for 48 V.

4 Results and Discussions

4.1 General Observation. Figure 9 shows the top and the front views of the explosive boiling for a heater voltage of 35 V with the pulse width of 4.4 μs at $T_{amb}=19°C$. The process consists of isolated bubble nucleation (Fig. 9(*a*)), formation of the vapor sheet (Fig. 9(*c*)), growth and collapse of the bubble (Figs. 9(*c–e*)), and bubble rebound (Fig. 9(*f*)). The first nucleation of the bubble starts at $t=2.8$ μs into the heater pulse, Fig. 9(*a*). Only few nucleate bubbles appear at this stage. While the initial bubbles are still growing, more nucleation sites are observed at $t=3.2$ μs into the heater pulse, Fig. 9(*b*). The location of nucleation sites and the size of bubbles for each event are almost identical over long period of time until the surface geometry and/or the material property of the heater change due to the hours of thermal stresses and cavitation processes. Figure 10 shows another nucleation site event at 45 V. Identical nucleation events

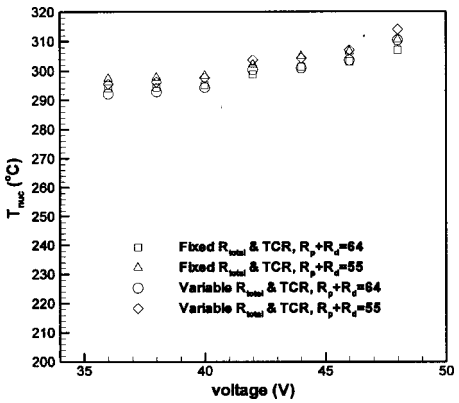

Fig. 7 Comparison of nucleation temperatures for the cases of constant and variable *R* and TCR as a function of voltage ($R_{average}=740.46\ \Omega$ and $TCR_{average}=0.000174°C^{-1}$)

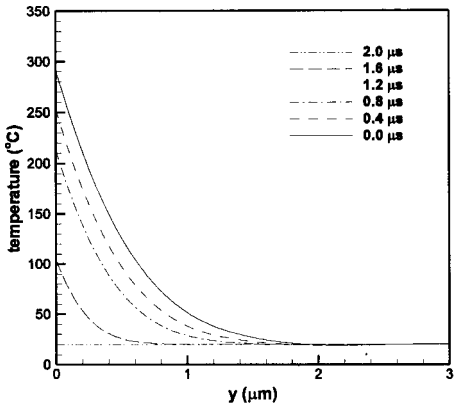

(a)

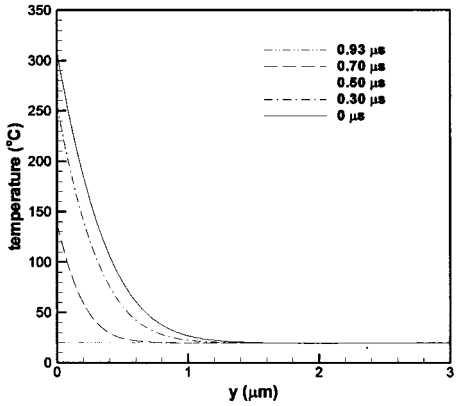

(b)

Fig. 8 Water temperature near the heater surface at (*a*) 36 V and (*b*) 48 V

occurred for all voltages tested here. Coalescence of the small bubbles leads to the formation of a vapor sheet, which covers the entire heater surface, as seen at $t=3.6$ μs into the heating pulse in Fig. 9(*c*). The bubble grows to a maximum size around $t=6.5$ μs (Fig. 9(*d*)). It then starts shrinking until it reaches to a minimum size around $t=10.2$ μs (Fig. 9(*e*)). A small rebounding bubble follows around $t=10.9$ μs (Fig. 9(*f*)) before it collapses completely around $t=12.0$ μs. Unlike the nucleation stage, in the rebound stage the process is not very repeatable. Although the location of the rebound is almost consistent, the formation of the rebounding bubble is different. Sometimes only a small spherical bubble is observed, whereas, other times several attached bubbles are seen. The shape of the bubble does not stay the same at the same time delay during the rebound phase. The radius of the regrowing bubble is around 10 μm and its life time is about 1.5 μs. The main cause of this rebound can be attributed to the compression of non-condensable gas within the bubble during bubble collapse [18,19].

4.2 Effects of Pulse Duration. Figure 11(*a*) shows the maximum bubble sizes at various pulse widths for the input voltages of 35 V and 45 V. Nucleate bubbles are not observed until the pulse width reaches the value of 3.2 μs for 35 V and 1.3 μs for 45 V. However, the pulse width is increased for each voltage until a threshold value is obtained above which the maximum bubble size does not change. The threshold value of 3.8 μs for 35 V and 1.9 μs for 45 V are shown in Fig. 11(*a*). It is noted that the vapor sheet forms at the end of these threshold pulse widths, e.g., $t=3.8$ μs for 35 V. Therefore, the pulse widths should be longer than these values for homogeneous nucleation and for a consistent

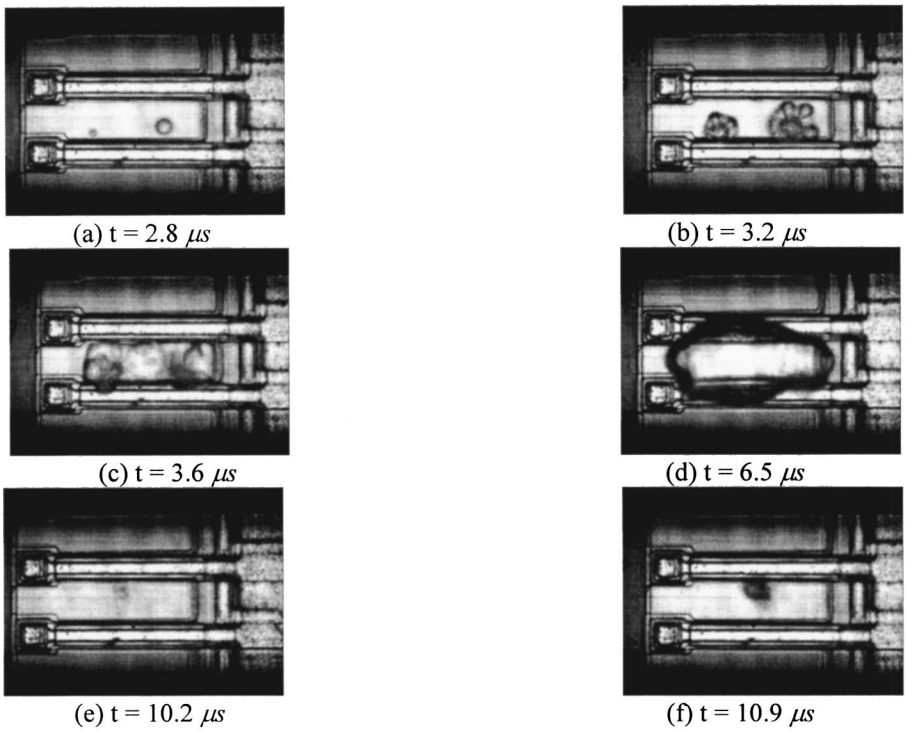

Fig. 9 Bubble growth and collapse: (*a*) and (*b*) nucleation and growth, (*c*) vapor sheet formation, (*d*) maximum size, (*e*) collapse, and (*f*) rebound.

bubble growth and collapse. However, a care should be taken for the heater surface not to exceed maximum allowable temperature for the surface material to prevent the surface damage when the pulse width is too long. It is also noted that the maximum size and the threshold value at 45 V are smaller than those at 35 V. This is discussed in the following section.

The effect of pulse width on the overall behavior of the bubble growth and collapse is also shown in Fig. 11(*b*). Three different pulse widths of 4.4 μs, 5.0 μs, and 6.3 μs, all of which are well above the threshold value, are applied at 35 V. The bubble behavior for each case is almost identical. The nucleation begins around 2.9 μs into the pulse. The vapor sheet is formed around 4 μs into the pulse. The bubble expands to a maximum size around 6 μs and collapses completely around 12.2 μs.

4.3 Effect of Initial Liquid Temperature. The effect of initial liquid temperature on the bubble growth is investigated. For this study an applied voltage of 35 V with a 4.4 μs heating pulse width is used. The liquid temperature is controlled by feeding the constant temperature water to the heat sink in contact with the silicon die. The error range of the temperature is within 1°C. The images of the bubble growth at different phases are shown in Fig. 12 for three temperatures of 20°C, 30°C, and 40°C. It shows that at the nucleation phase only a couple of vapor bubbles appear on

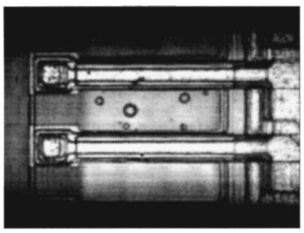

Fig. 10 Bubble nucleation at 45 V (t_p=4.4 μs)

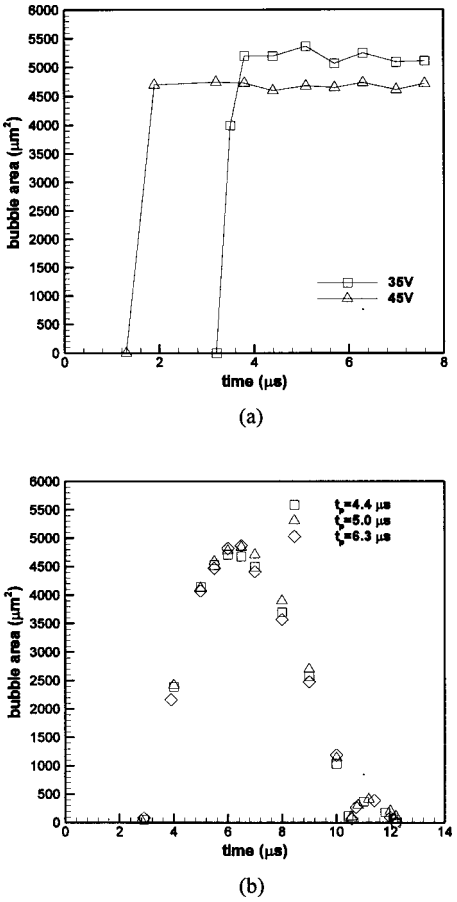

Fig. 11 (*a*) Effect of pulse widths on the bubble size, and (*b*) Bubble size versus time at different heating pulses

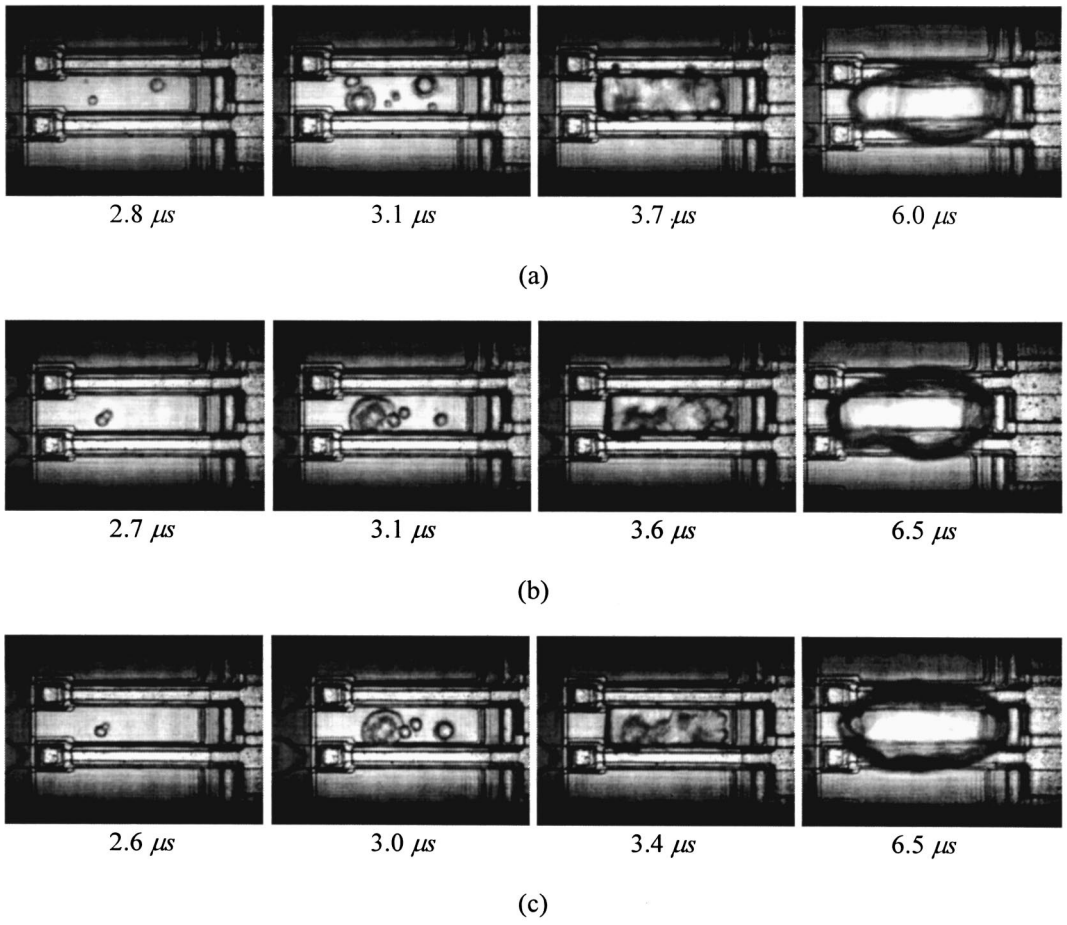

Fig. 12 Initial liquid temperature effect on bubble growth at (*a*) T_{ini}=20°C, (*b*) T_{ini}=30°C, and (*c*) T_{ini}=40°C

the heater surface for all cases. However, the nucleation occurs earlier for the higher liquid temperature. The bubble growth rates until the formation of the vapor sheet are almost identical. This implies that the initial liquid temperature has an effect on the nucleation time. However, its effect on the nucleation rate within the temperature range is not substantial. This is because the nucleation occurs at much higher temperature range (~300°C) than the liquid temperature (20°C–40°C) and the applied heat fluxes are the same for all cases. For a given heat flux, the liquid reaches the nucleation temperature more rapidly for higher initial liquid temperatures. The time history of the bubble growth and collapse for these cases are shown in Fig. 13. It is noticeable that the maximum bubble size increases with the initial liquid temperature. The overall life time of the bubble is increased as well. The higher the initial liquid temperature, the smaller the temperature gradient in the liquid close to the growing bubble surface is and the cooling effect on the growing bubble becomes less. Therefore, the bubble can grow further and longer.

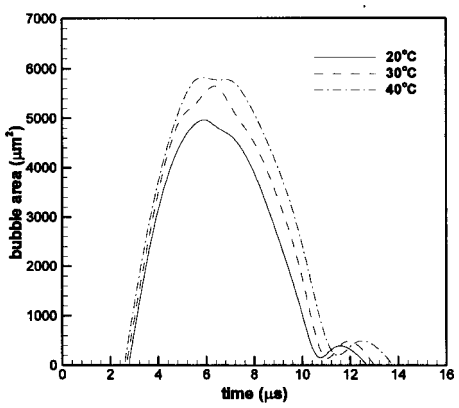

Fig. 13 Bubble size as a function of time at (*a*) T_{amb}=20°C, (*b*) T_{amb}=30°C, and (*c*) T_{amb}=40°C

4.4 Effect of Input Voltage. The heat flux, which is directly related to the input voltage, is an important parameter. Effect of various input voltages on the bubble growth at ambient temperature is considered. Since the voltage does not represent the actual thermal energy input, the heat flux from the heater surface needs to be calculated. Thermal energy generated from the heater depends on the material of the heater surface. To obtain the surface heat flux, q'', a one dimensional unsteady heat conduction equation with the following boundary and initial conditions is solved:

$$\frac{\partial T}{\partial t} = \alpha_l \frac{\partial^2 T}{\partial y^2} \tag{5}$$

$$T(t,y) = T_{\text{amb}}, \quad \text{at } t = 0 \tag{6}$$

$$k_l \frac{\partial T}{\partial y} = q'', \quad \text{at } y = 0 \quad \text{and} \quad \text{for } 0 < t < t_p \tag{7}$$

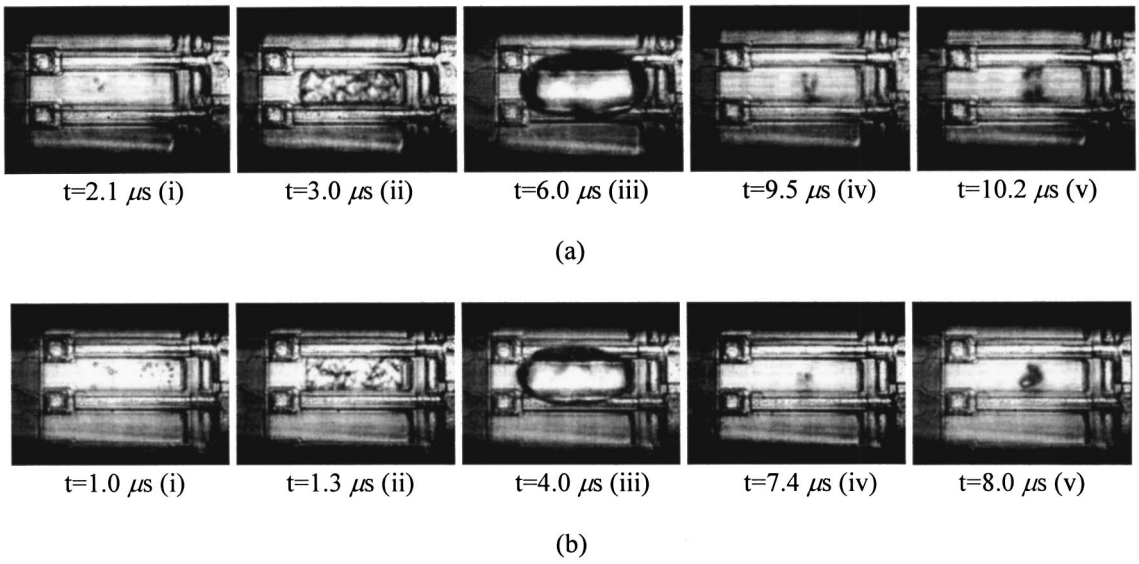

Fig. 14 Bubble growth and collapse at (*a*) 36 V and (*b*) 48 V: (i) Nucleation, (ii) vapor sheet formation, (iii) maximum size, (iv) collapse, and (v) rebound.

$$k_l \frac{\partial T}{\partial y} = 0, \quad \text{at } y = 0 \quad \text{and} \quad \text{for } t > t_p \tag{8}$$

where $\alpha_l = (k/\rho c)_l$ is the thermal diffusivity of the liquid, k_l, ρ_l, and c_l are the thermal conductivity, density, and the specific heat for the liquid, respectively, and t_p is the time for the heating pulse. By solving Eqs. (5–8) for q'' at the surface with a T_{surf} and t_{nuc} as calculated in section 3, we obtain

$$q'' = \frac{(T_{\text{surf}} - T_{\text{amb}})}{2} \left(\frac{\pi k \rho_l c_l}{t_{\text{nuc}}} \right)^{1/2} \tag{9}$$

Using Eq. 9 and the input voltages from 36 V to 48 V, the corresponding heat fluxes at the heater surface are calculated to range from 265 MW/m^2 to 417 MW/m^2 at the time of nucleation. Depending on the input voltage, the pulse width is also varied from 3.1 μs to 1.3 μs. Here, the pulse width is carefully chosen so that the power is turned off as soon as the vapor sheet is formed. This supplies enough thermal energy for repeatable bubble formation and reduces the chance of heater surface damage caused by overheating.

The top view of bubble growth and collapse are shown in Fig. 14 for two cases. One is at a heater voltage of 36 V with a pulse width of 3.1 μs and the other is at a heater voltage of 48 V with a pulse width of 1.3 μs. The time shown below each frame indicates the time elapsed since the beginning of the heating pulse. It is noted that at 36 V, only a couple of nucleate bubbles are initially observed at $t = 2.1$ μs. The isolated bubbles accumulate to form a vapor sheet at $t = 3.0$ μs. At 48 V, isolated nucleate bubbles are observed at $t = 1.0$ μs and fractions of a microsecond later, fine nucleate bubbles appear evenly on the heater surface. Therefore, a vapor sheet is formed rather instantly around $t = 1.3$ μs. The size of the nucleate bubbles are smaller for higher input power. This can be explained by the fact that the thin thermal boundary layer limits further growth of the bubbles. In addition, the time is not long enough for bubbles to grow before the formation of vapor sheet. It is noted that as the voltage increases, the times for nucleation, for vapor sheet formation, and for growth to the maximum size decrease almost linearly (Fig. 15). The time to reach the vapor sheet formation also represents the threshold pulse width as mentioned in an earlier section.

4.4.1 Effect on the Nucleation Temperature. From the one-dimensional heat transfer calculations and the direct observations of initial nucleate bubble formations, the nucleation temperatures at each voltage are determined. The results show the weak linear dependency of the nucleation temperature for a given range of an input voltage (Fig. 16). The temperature increase is only about 6 percent, while the q'' about 60 percent. The temperature at the time of a vapor sheet formation is also plotted and shows the same trend as the nucleation temperature. It is necessary to determine the kinetic limit of superheat of water, T_{sl}, to understand whether the mechanism of the nucleation at T_{nuc} is due to the thermal fluctuation of the liquid molecules or due to the activations from pre-existing nucleation sites. From the classical nucleation theory, the kinetic limit of superheat of water, T_{sl}, can be calculated. Since the water is in contact with solid surface, heterogeneous nucleation rate can be expressed as [10,20],

$$J_{he}(T, \theta) = N_l^{2/3} \varsigma \left(\frac{3\sigma_l(T)}{\pi m_l \phi} \right)^{1/2} \exp\left(\phi \frac{\Delta\Omega}{k_B T} \right), \tag{10}$$

$$\Delta\Omega(T) \equiv -\frac{16\pi\sigma_l(T)^3}{3(p_v(T) - p_{\text{amb}})^2}, \tag{11}$$

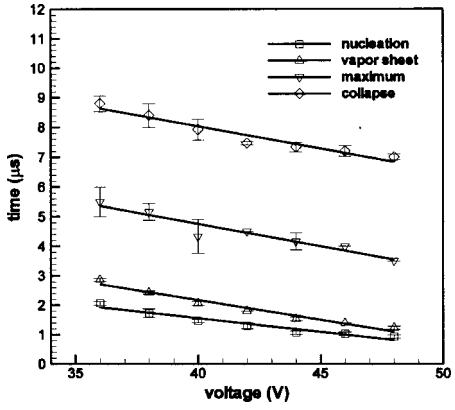

Fig. 15 Time to reach the phase of nucleation, vapor sheet formation, maximum size, and collapse as a function of input voltages

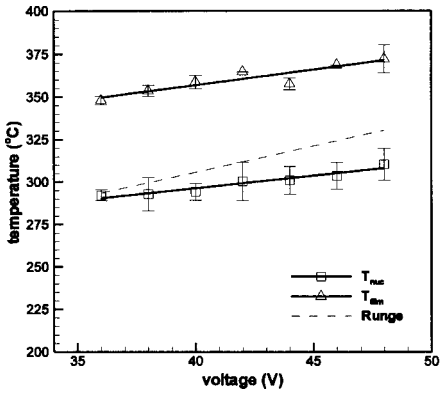

Fig. 16 Temperatures at the phase of nucleation and vapor sheet formation as a function of input voltage

$$p_v(T) = p_{\text{sat}}(T)\exp\left[\frac{p_{\text{amb}} - p_{\text{sat}}(T)}{\rho_l RT}\right], \tag{12}$$

$$\text{s} \equiv \frac{(1+\cos\theta)}{2}, \tag{13}$$

$$\phi \equiv \frac{(2+3\cos\theta - \cos^3\theta)}{4}, \tag{14}$$

where N_l is the number density of the liquid molecules per unit volume, k_B is the Boltzmann's constant, σ_l is the surface tension of the liquid, m_l is the mass of one liquid molecule, and θ is the contact angle of the liquid at the heating surface. The heterogeneous nucleation rate, J_{he}, represents the rate at which embryos of critical size are generated. If a threshold value of J_{he} is specified and J_{he} for a given temperature exceeds the threshold value, the corresponding liquid temperature becomes the limit of superheat. The contact angle of water on the metal surface is usually $\theta = 20$ deg [20]. By assuming $J_{he} \approx 10^{10}\,\text{m}^{-2}\,\text{s}^{-1}$ [4], the value of $T_{sl} \approx 309°\text{C}$ is determined for $\theta = 20$ deg. However, the value of J_{he} was measured under the condition of relatively low heating rate compared with that used in the current study. Avedisian [21] shows that

$$J_{he} \approx \frac{1}{A_h}\left|\frac{d}{dT}\left(\phi\frac{\Delta\Omega}{k_B T}\right)\right|\dot{T}, \tag{15}$$

where A_h is the heater surface area and $\dot{T}$ is the heating rate. From Eq. (15) using the temperature dependent property, the nucleation rate at T_{nuc} for a given heating rate can be estimated. The average value of J_{he} is about $10^{18}\,\text{m}^{-2}\,\text{s}^{-1}$ and the corresponding limit of superheat, $T_{sl} \approx 314°\text{C}$ with $\theta = 20$ deg. It is noted that even though experimentally determined nucleation temperatures are close to T_{sl}, they are still below the limit of superheat. This causes the weak linear dependency of T_{nuc} on an input voltage. Therefore, it can be concluded that the effect from the pre-existing nucleation sites is more dominant for lower heating rate. On the contrary, as the heating rate increases and T_{nuc} approaches to T_{sl}, the effect from the pre-existing nucleation sites is suppressed by the thermal fluctuation of water molecules.

The simple empirical relationship between T_{nuc} and q'' can be obtained from Fig. 16. First, to express T_{nuc} in terms of q'' an empirically determined relationship between q'' and V_0 is obtained as

$$q'' = 1.286\times 10^7 V_0 - 1.971\times 10^8 \tag{16}$$

Then, using Eq. (16) and the plot for T_{nuc} in Fig. 16, the equation for T_{nuc} as a function of q'' can be written as

$$T_{\text{nuc}} = 260 + 1.144\times 10^{-7} q'' \tag{17}$$

In our experiments, no nucleate bubbles were observed below 34 V, which corresponds to $q'' = 240\,\text{MW/m}^2$. Zhao et al. [15] have obtained the criteria for a minimum heat flux, q''_{min}, for explosive nucleation to happen as

$$q''_{\text{min}} \geqslant \rho_v h_{lv}\left(\frac{\bar{R}T_v}{2\pi\bar{M}}\right)^{1/2} \tag{18}$$

where ρ_v is the vapor density, h_{lv} the latent heat of vaporization, T_v vapor temperature, $\bar{R}$ the universal gas constant, and $\bar{M}$ the molecular weight. The right hand side of Eq. (18) is the theoretical maximum heat flux that can be attained in a phase change process [20]. Therefore, if Eq. (18) is satisfied, the pre-existing nucleation sites are not capable of transferring an excessive heat from the heater surface. This results in an explosive vaporization. From the right hand side of Eq. (18), $q''_{\text{max}} = 224\,\text{MW/m}^2$ for water at atmospheric pressure, which is about 7 percent less than the value expected from the experiment. Therefore, Eq. (18) may give a reasonable threshold heat flux that can be used with Eq. (17). A similar empirical expression for T_{nuc} with temperature gradient is proposed by Runge [11] and is also plotted in Fig. 16. Compared with the current experimental results, slightly higher T_{nuc} is estimated as the input voltage increases.

4.4.2 Estimation of Vapor Volume, Pressure Impulse, and Work. The effect of input voltage on the bubble volume is shown in Fig. 17. The rebounding phase is not plotted here. Our experimental results are compared with the theoretical model proposed by Asai [10]. In the model, a time dependent pressure profile for the later stage of bubble growth is proposed as

$$p_v(t) = [p_{\text{nuc}} - p_{\text{sat}}(T_{\text{amb}})]\exp[-(t/t_e)^{\lambda}] + p_{\text{sat}}(T_{\text{amb}}) \tag{19}$$

where p_{nuc} is the pressure at nucleation, p_{sat} is the saturation pressure, T_{amb} is the ambient temperature, t_e is a time constant, which depends on the heating condition and thermal property of the working fluid, and λ is a free parameter. Both t_e and λ must be chosen so that the pressure estimated from Eq. (19) gives the bubble volume which is in agreeament with the experimental value. In the present study, the value of λ is selected as 0.765. The theoretical bubble volume is calculated by following equations [10]:

$$V_v(t) = W(2\xi - \xi^2)/(p_{\text{amb}} - p_{\text{sat}}(T_{\text{amb}}))/A_l \tag{20}$$

where

$$\xi \equiv (p_{\text{amb}} - p_{\text{sat}}(T_{\text{amb}}))t/P \tag{21}$$

The pressure impulse, P, and the work done by the bubble to the liquid, W, are given by

$$P \approx \frac{p_{\text{nuc}} t_e}{\lambda}, \tag{22}$$

$$W \approx \frac{P^2}{2A_l}, \tag{23}$$

where the inertance of the liquid region, A_l, is given by

$$A_l \approx 0.43\rho_l / d_h \tag{24}$$

where d_h is the heater dimension and assumed as 52.5 μm. The nucleation pressure, p_{nuc} in Eq. (22) is estimated from the classical Clausius-Clapeyron equation:

$$p_{\text{nuc}} = p_a \exp\left\{\frac{h_{lv}}{k_B}\left(\frac{1}{T_{\text{boil}}} - \frac{1}{T_{\text{nuc}}}\right)\right\} \tag{25}$$

where p_a is the atmospheric pressure.

Since there is no direct way to measure the bubble volume from the experiment, it was estimated from calculations based on the actual measurements of area, length, and width. Three different cases are considered for the bubble volume calculations. The first

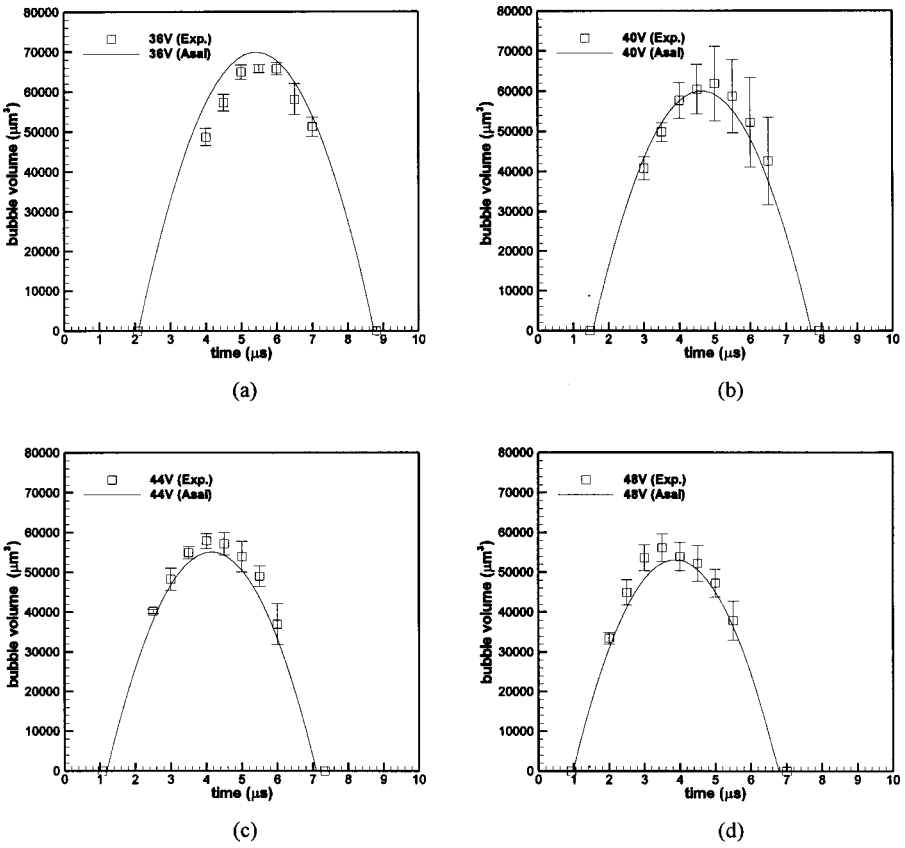

Fig. 17 Bubble volume in time at (*a*) 36 V, (*b*) 40 V, (*c*) 44 V, and (*d*) 48 V. Experimental results are compared with the theoretical model.

case is the volume of several small bubbles at the beginning of nucleation. In this case, the shape of each small bubble was assumed to be spherical, thus, the volume is simply $4\pi R_b^3/3$, where R_b is the bubble radius. At the stage of vapor sheet formation, the volume is estimated by multiplying the frontal area by the length of the vapor sheet since the vapor sheet resembles a rectangular block. The frontal area can be easily obtained from the image grabbing software. As the bubble grows, the shape from the top view becomes ellipsoidal. Therefore, the frontal area changes along the x (length) direction. It is assumed that the area is

$$A(x)=A^*\left(\frac{z(x)}{z^*}\right)^2 \tag{26}$$

where A^* and z^* are the maximum frontal area and the corresponding width of the bubble, respectively. The volume is obtained by integrating the area along the x direction and is expressed as

$$V=\int_{x_1}^{x_2} A(x)dx=\frac{2}{3}A^*l, \tag{27}$$

where x_1 and x_2 are the positions of two ends of the bubble and l is the length of the bubble.

Both experimental and theoretical results show that the bubble volume decreases as an input voltage increases (Fig. 17). This is because more thermal energy is generated from the heater during the pulse heating at lower input voltages even though the peak power is less (Fig. 18). Using Eqs. (22) and (23) with known constants, t_e and λ, the pressure impulse and work done by the bubble to the liquid are calculated (Fig. 19). Both the pressure impulse and the work done by the liquid decrease exponentially with increasing voltage.

4.4.2 Bubble Wall Velocity, Acceleration, and Pressure After Vapor Sheet Formation. By taking time derivatives of the bubble dimensions, bubble wall velocities and accelerations are estimated. The results are shown in Fig. 20 for the case of 40 V. Since the bubble is not spherical in the current experiment, velocities and accelerations for x, y, and z directions are considered. They are plotted up to the collapsing point just before the beginning of the rebounding phase. It is interesting to observe that the bubble keeps growing in the y (height) direction while it contracts in both the x (length) and z (width) direction. The bubble velocities for the x and z directions at the time of vapor sheet formation are around 20 m/s. The velocity in the z direction, however, is only around 4 m/s. This is because of the liquid body force or inertia is acting on the bubble surface against y direction. The velocity decreases almost linearly and the acceleration oscillates with the nearly constant amplitude until it reaches its maximum size. During the collapse, the velocity in x direction increases up to 50 m/s just before the collapse point. The velocities in the y and z direction are 20 m/s and 15 m/s, respectively. The acceleration shows the same pattern as the velocity. The acceleration in the x direction is considerably larger than those in the other directions. This tells that the momentum exchange is the largest in the x direction. This is mainly due to the existence of the channel wall. At the collapse point, all the velocities are assumed to be zero. This assumption results in the sudden increase in the acceleration near the collapse point. The effect of the input voltage on the acceleration at the collapse point is shown in Fig. 21. The velocity in the the x direction at 48 V contributes the overall decrease in velocity in the x direction. However, the velocities and accelerations in all other directions increase with increasing voltage. This is due to more sharp decrease of the vapor pressure (i.e., higher nucleation pressure and lower pressure impulse) for higher volt-

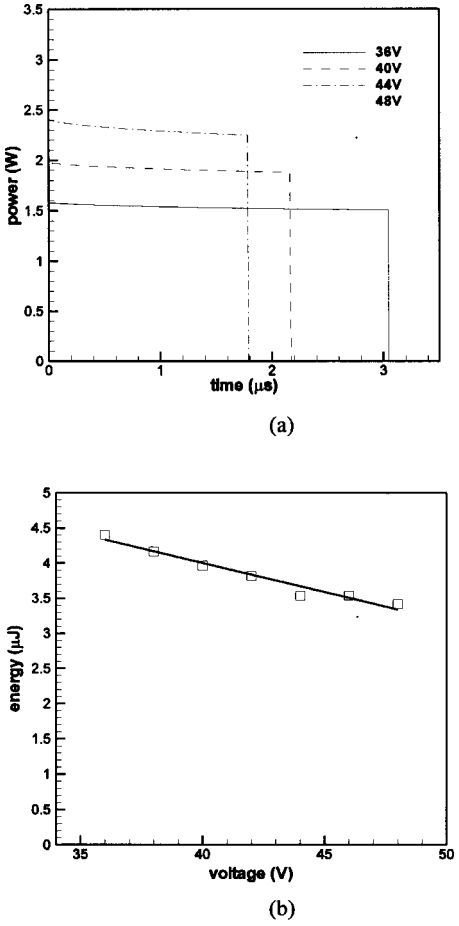

Fig. 18 (*a*) Power generated at different voltages as a function of time; and (*b*) Energy generated from the heater as a function of input voltage.

ages. By using Eq. (22) and Eq. (25), the pressure impulse and the nucleation pressure for 48 V are 111 atm and 2.9 atm μs and 85 atm and 3.4 atm μs for 36 V.

5 Error Analysis

Both hardware systems and human factors are possible sources of error during the experiment. It is, therefore, necessary to consider these errors for the analysis to see if the data obtained are valid and representative. The uncertainty caused by human factors are estimated from five different data sets of the same condition.

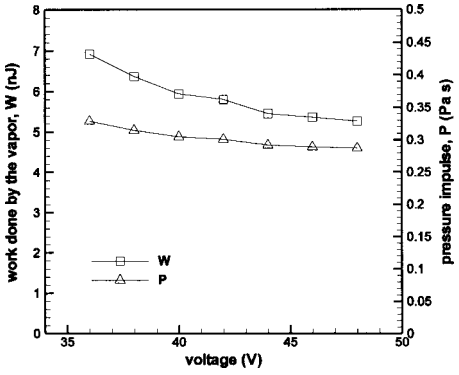

Fig. 19 Pressure impulse, *P*, and work, *W*, done by the bubble as a function of input voltages

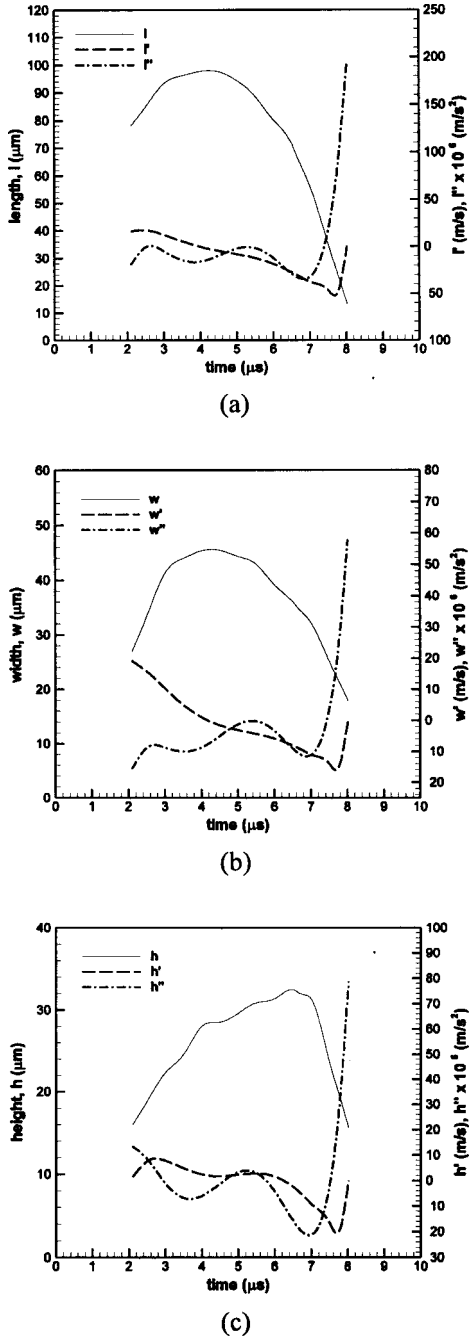

Fig. 20 Bubble dimensions, velocities and accelerations for (*a*) length (*x* direction), (*b*) width (*z* direction), and (*c*) height (*y* direction) as a function of time at 40 V

Since the experiment was involved with stroboscopic measurements, the error associated with the time delay from the logic gate that fire the laser strobe was considered. The uncertainty of time measurement caused by the time delay was assumed as ± 10 ns at most since we cannot observe jitter between the heater firing and the laser firing with the scope at 100 MHz. The other source of uncertainty associated with time measurements was the error due to inaccurate determination of the nucleation time. With the high heating rate condition, a small deviation of the nucleation time might results in substantially large nucleation temperature difference. The maximum error for the nucleation time was less than 0.05 μs because the minimum increment of the time delay was 0.05 μs. By considering the uncertainty of time measurements, the

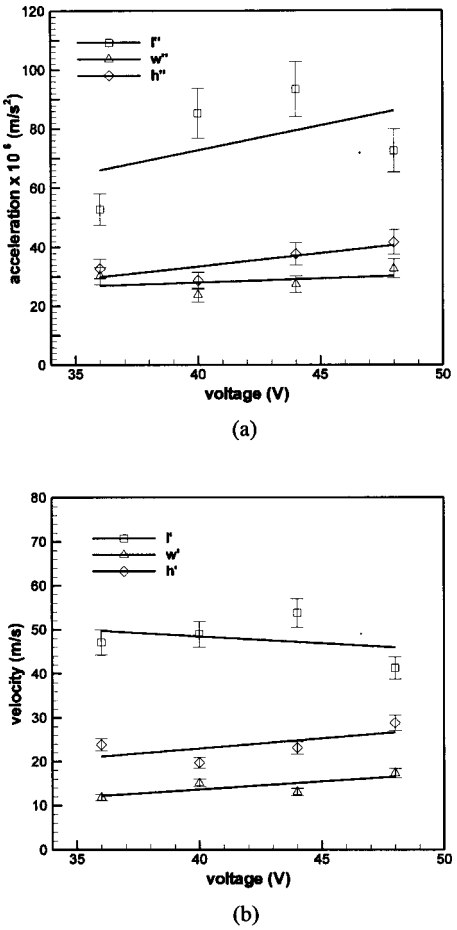

Fig. 21 The effect of input voltage on the (a) velocity and (b) acceleration near the collapsing point

nucleation temperatures and uncertainties were obtained. The maximum deviation of ± 15°C, which is about 5 percent, occurs at 38 V.

Voltages and current were monitored by a digital oscilloscope. The error range for the current was taken as the noise level which oscillate within ± 0.68 mAmp (1.4 percent). The uncertainty for voltage was ± 0.02 V (0.1 percent).

The uncertainty of the spatial measurement comes from the inaccurate determination of the bubble surface edge. The maximum error associated with measurements was about 4 percent with the standard deviation of ± 0.15 μm for the smallest dimension and 0.2 percent with ± 0.22 μm for the maximum dimension. The ambient temperature was controlled by the thermostat in the water bath and fluctuated within ± 1°C at most.

The uncertainty for the calculated values were estimated from the uncertainty of the measured values. The uncertainties of the R_{total} and R_{heater} were estimated from the uncertainties of $R_{\text{parasatic}}$ and R_{driver}. They are both less than 2 percent (± 11 Ω). The accuracy of the nucleation temperature depends on the accurate measurement of the nucleation time. Therefore, the uncertainty of the nucleation temperature was estimated from the nucleation temperature within the error range of the nucleation time. The relatively large errors occurred at 38 V with the uncertainty of ± 15°C and 42 V with ± 14°C, which are about 5 percent range since the error range of the nucleation time at those voltages were large. The uncertainty for the nucleation pressure was estimated from the Clausius-Clapeyron relation. Within the error margin of nucleation temperature, the pressure uncertainties were somewhat large for certain voltages. In some cases (38 V, 42 V, and 48 V), the margin of uncertainty was nearly 20 percent. The uncertainties for the rest (36 V, 40 V, and 44 V), however, were less than 9 percent. The uncertainties for the pressure impulse were around 8 percent at 38 V, 46 V, and 48 V and less than 4 percent for the rest. The uncertainties for the work done by the vapor to the liquid are somewhat large. They varied from 4 percent to 20 percent depending on the input voltage.

The uncertainties for the heat flux from the heater and from the Ta-water interface were less than 5 percent. The calculated heat flux varied from 265 MW/m^2 ± 5.5 MW/m^2 to 417 MW/m^2 ± 21.6 MW/m^2 for the Ta-water interface and 791 MW/m^2 ± 16 MW/m^2 to 1435 MW/m^2 ± 74 MW/m^2 for the heater element.

The estimated uncertainties for the bubble volume at different voltages are shown in Fig. 17. The maximum error is about 12 percent at 40 V. The error for the other voltages is less than 6 percent.

The uncertainties for the velocity and acceleration are estimated from the uncertainties of time and length. They are within 6% for the velocity and 10% for the acceleration.

6 Conclusions

The bubble dynamics on a micro heater induced by pulse heating is experimentally investigated. A laser stroboscopic system allows direct observations of bubble nucleation, growth, and collapse processes. Various heating conditions such as the duration of the heating pulse, the ambient temperature, and the input voltage are applied to see their influence on the bubble behavior. The following conclusions are made from this investigation:

1. There exists a threshold pulse duration above which the maximum size of the bubble no longer changes. This threshold value corresponds to the time of vapor sheet formation.
2. The initial liquid temperature does affect the time of nucleation and the maximum size of the bubble increases with increases in the initial liquid temperature.
3. Times to reach the phase of nucleation, vapor sheet formation, maximum bubble size, and bubble collapse decrease linearly with an increasing input voltage.
4. Experimentally determined nucleation temperatures for a given heating rate are slightly below the limit of superheat of water and show a weak linear dependency on the heating rate as provided by

$$T_{\text{nuc}} = 260 + 1.144 \times 10^{-7} q''$$

5. Since the nucleation temperature is close to the super heat limit of the liquid and the dependency to the heating rate is weak, the mechanism of the bubble formation is a combined homogeneous-heterogeneous nucleation.
6. The maximum size of the bubble decreases with an increasing input voltage since the energy transferred and the pressure impulse during pulse heating decreases.
7. The time evolution of the bubble wall velocity and acceleration are determined throughout the process. Both the velocity and acceleration show abrupt changes near the point of the collapse.
8. The pressure inside the bubble remains below the atmospheric pressure until it bounces back near the collapse point.

Acknowledgments

This work was supported by Xerox Foundation. The authors would like to thank Xerox staff Michael O'Horo and Narayan Deshpande for many fruitful discussions, Chen-li Sun for some initial experimental investigations, Roger Markham and Brad Gerner for electronics support, and Peter John for special packaging.

Nomenclature

A = frontal area of the bubble
A^* = maximum frontal area of the bubble
A_h = heater surface area, m^2
A_l = liquid inertance, $kg\,m^{-4}$
c = specific heat, J/kgK
I = current, Amp
J = nucleation rate per unit area, $m^{-2}\,s^{-1}$
k_l = thermal conductivity, W/mK
k_B = Boltzmann's constant, 1.38×10^{-23} J/K
L = latent heat of vaporization, J
P = pressure impulse, Pa s
p = pressure, atm
q'' = heat flux, W/m^2
R = resistance, Ohm (Ω)
R_b = bubble radius
t = time, s
t_e = time constant, s
T = temperature, K or °C
V = bubble volume, m^3
V_0 = operating voltage, V
W = work done by the bubble to the liquid, Joule (J)
x, y, z = coordinates, m
z^* = maximum bubble width
α = thermal diffusivity, m^2/s
λ = dimensionless parameter
ρ = density

Subscripts

amb = ambient condition
boil = boiling point
l = liquid
he = heterogeneous
nuc = nucleation
p = pulse
sat = saturation
sl = limit of superheat
surf = surface
v = vapor

References

[1] Shusser, M., and Weihs, D., 1999, "Explosive Boiling of a Liquid Droplet," Int. J. Multiphase Flow, **25**, pp. 1561–1573.
[2] Avedisian, C. T., 1986, "Bubble Growth in Superheated Liquid Droplets," in *Encyclopedia of Fluid Mechanics*, **3**, Gulf Publishing Co., Houston, TX, pp. 130–190; chpt. 8.
[3] Rembe, C., Wiesche, S., and Hofer, E. P., 2000, "Thermal Ink Jet Dynamics: Modeling, Simulation, and Testing," Microelectron. Reliab., **40**, pp. 525–532.
[4] Blander, M., and Katz, J. L., 1975, "Bubble Nucleation in Liquids," AIChE J., **21**(5), pp. 833–848.
[5] Allen, R. R., Meyer, J. D., and Knight, W. R., 1985, "Thermodynamics and Hydrodynamics of Thermal Ink Jets," Hewlett-Packard J., **36**, pp. 21–27.
[6] Asai, A., 1989, "Application of the Nucleation Theory to the Design of Bubble Jet Printers," Jpn. J. Appl. Phys., Part 1 **28**(5), pp. 909–915.
[7] Andrews, J. R., and O'Horo, M. P., 1995, "Initial Stages of Vapor Bubble Nucleation in Thermal Inkjet Processes," *Proceedings of SPIE—The International Society for Optical Engineering*, **2413**, pp. 182–188.
[8] Hsu, Y. Y., 1962, "On the Size Range of Active Nucleation Cavities on the Heating Surface," ASME J. Heat Transfer, **84**, pp. 207–216.
[9] Asai, A., Hara, T., and Endo, I., 1987, "One-Dimensional Model of Bubble Growth and Liquid Flow in Bubble Jet Printers," Jpn. J. Appl. Phys., Part 1, **26**(10), pp. 1794–1801.
[10] Asai, A., 1991, "Bubble Dynamics in Boiling Under High Heat Flux Pulse Heating," ASME J. Heat Transfer, **113**, pp. 973–979.
[11] Runge, W., 1992, "Nucleation in Thermal Ink-Jet Printers," *IS&T's Eighth International Congress on Advances in Non-Impacting Technologies*, pp. 299–302.
[12] Avedisian, C. T., Osbourne, W. S., McLeod, F. D., and Curley, C. M., 1999, "Measuring Bubble Nucleation Temperature on the Surface of a Rapidly Heated Thermal Inkjet Heater Immersed in a Pool of Water," Proc. R. Soc. London, Ser. A, **455**, pp. 3875–3899.
[13] Chen, P., Chen, W., and Chang, S. H., 1997, "Bubble Growth and Ink Ejection Process of a Thermal Ink Jet Print Head," Int. J. Mech. Sci., **39**(6), pp. 683–695.
[14] Lin, L., Pisano, A. P., and Carey, V. P., 1998, "Thermal Bubble Formation on Polysilicon Micro Resistor," ASME J. Heat Transfer, **120**, pp. 735–742.
[15] Zhao, Z., Gold, S., and Poulikakos, D., 2000, "Pressure and Power Generation During Explosive Vaporization on a Thin Film Microheater," Int. J. Heat Mass Transfer, **43**, pp. 281–296.
[16] Torpey, P. A., 1988, "Prevention of Air Ingestion in a Thermal Ink-Jet Device," *Proceedings of the 4th International Congress on Advances in Non-Impact Print Technologies*, March, pp. 70–78.
[17] Andrews, J. R., and O'Horo, M. P., 1995, "High Speed Stroboscopic System for Visualization of Thermal Inkjet Processes," Proceedings of SPIE—The Internation Society for Optical Engineering, **2413**, pp. 176–181.
[18] Hammitt, F. G., 1980, *Cavitation and Multiphase Flow Phenomena*, McGraw-Hill, New York.
[19] Brennen, C., 1995, *Cavitation and Bubble Dynamics*, Oxford University Press, New York.
[20] Carey, V. P., 1992, *Liquid-Vapor Phase-Change Phenomena*, Hemisphere, Washington, DC.
[21] Avedisian, C. T., 1985, "The Homogeneous Nucleation Limits of Liquids," J. Phys. Chem. Ref. Data, **14**, pp. 695–720.

A Leidenfrost Point Model for Impinging Droplets and Sprays

John D. Bernardin
International, Space, and Response Division,
Los Alamos National Laboratory,
P.O. Box 1663, MS D466,
Los Alamos, NM 87545

Issam Mudawar
Boiling and Two-phase Flow Laboratory,
School of Mechanical Engineering,
Purdue University,
West Lafayette, IN 47907

This study presents, for impinging droplets and sprays, a model of the Leidenfrost point (LFP); the minimum liquid/solid interface temperature required to support film boiling on a smooth surface. The present model is an extension of a previously developed sessile drop model, based on bubble nucleation, growth, and merging criteria, as well as surface cavity size characterization [3]. The basic concept of the model is that for liquid/solid interface temperatures at and above the LFP, a sufficient number of cavities are activated and the bubble growth rates are sufficiently fast that a continuous vapor layer is established nearly instantaneously between the liquid and the solid. For impinging droplets, the influence of the rise in interfacial pressure created by the impact of the droplet with the surface, must be accounted for in determining fluid properties at the liquid-solid interface. The effect of droplet impact velocity on the LFP predicted by the model is verified for single impinging droplets, streams of droplets, as well as sprays. While the model was developed for smooth surfaces on which the roughness asperities are of the same magnitude as the cavity radii (0.1–1.0 μm), it is capable of predicting the boundary or limiting Leidenfrost temperature for rougher surfaces with good accuracy.
[DOI: 10.1115/1.1652045]

Keywords: Boiling, Droplet, Heat Transfer, Impingement, Phase Change, Sprays

Introduction

Material processing leaders are under constant pressure to improve the material and performance characteristics of products, while at the same time, increase the efficiency of the processing techniques by reducing energy consumption, scrap material, and manufacturing time. For example, the needs for stronger, lighter, and cheaper materials in the automobile, railroad, and aerospace industries, have driven improvements in the processing of aluminum alloys. In particular, advances in heat treatment and forming operations have led to alloys with improved strength-to-weight ratios and enhanced corrosion resistance properties. However, lack of understanding scientific principles in several areas still leads to inefficient manufacturing cycles with large numbers of scrap parts and long production periods. One of the least understood areas of materials processing involves quenching, or the rapid cooling of a part, such as that which occurs following an extrusion, casting, forging, or heat treating operation. When done correctly, quenching can result in high performance parts. However, when performed incorrectly, quenching can result in parts with poor or nonuniform material properties, high residual stresses, and severe distortion.

One common method of quenching involves immersing the heated part in a deluge of water sprays. The spray quenching method is often preferred over bath immersion quenching, as the former can produce much higher heat transfer rates and more uniform or controlled temperature fields within the part. Figure 1 shows a typical temperature-time history of a part during a spray quench. The quench curve is divided into four distinct regimes, each possessing particular heat transfer characteristics. In the high temperature, or film boiling regime, the quench proceeds rather slowly as liquid-solid contact is minimized by the rapid formation of an insulating vapor blanket at the droplet-solid interface. In this regime, the droplets appear to shatter and bounce off of the solid surface upon contact. The lower temperature boundary of this regime is referred to as the Leidenfrost point (LFP). As surface temperatures drop below the LFP, a transition boiling regime is encountered, where partial and prolonged liquid-solid contact occurs and the cooling rates increase. Further cooling brings about the nucleate boiling regime, where complete wetting of the surface occurs and the heat transfer rates are the highest as vigorous vapor generation occurs as the droplets spread out on the solid surface. At the bottom end of the nucleate boiling regime, boiling ceases and the single-phase heat transfer regime is encountered, where heat transfer is dominated by single-phase convection.

As discussed in [1], during the quench phase of a heat treatment operation involving aluminum alloys, most of the material transformations occur at temperatures above the LFP, while warping and distortion, caused by thermal stresses generated by large cooling rates, take place at temperatures below the LFP. Consequently, accurate knowledge of the Leidenfrost temperature and the parameters that govern its behavior is paramount to controlling the quenching process and subsequent material properties.

In a previous investigation by the authors [2], an extensive experimental sessile droplet LFP database was developed and used to assess several existing LFP models. These assessments indicated that the previously developed LFP models were lacking in their ability to accurately and consistently predict the LFP for a variety of fluid and surface conditions. From that experimental study [2], Bernardin and Mudawar [3] developed a new LFP model for sessile droplets, based on surface cavity characterization as well as bubble nucleation, growth, and interaction criteria. The premise for that model was that as the Leidenfrost temperature is approached from the boiling incipience temperature, smaller and more numerous surface cavities become activated, and the growth rate of these bubbles increases appreciably. For liquid-solid interface temperatures at and above the LFP, a sufficient number of cavities are activated and the bubble growth rates are large enough that liquid in immediate vicinity of the surface is nearly instantaneously converted to vapor upon contact. These two features enable a continuous insulating vapor layer to form between the liquid and the solid.

The focus of the study reported here was to take the existing sessile drop LFP model [3] and extend its application to impinging drops and sprays. The main features of the previous sessile drop LFP model, as well as the additional concepts needed to extend the model to impinging drops, will be presented below.

Contributed by the Heat Transfer Division for publication in the JOURNAL OF HEAT TRANSFER. Manuscript received by the Heat Transfer Division April 9, 2003; revision received December 4, 2003. Associate Editor: R. M. Manglik.

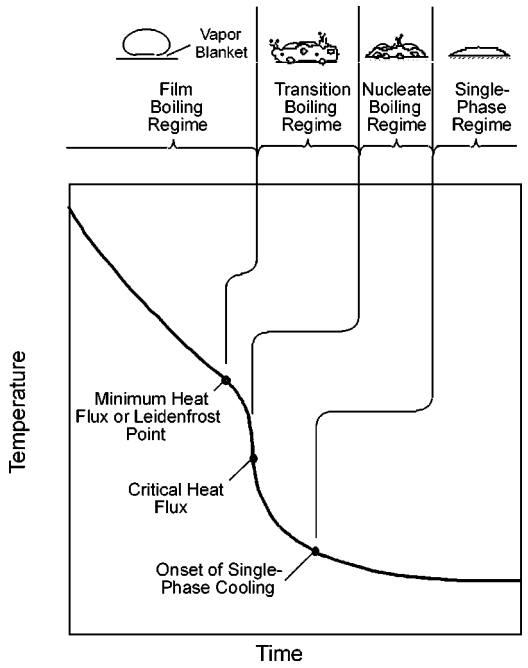

Fig. 1 Typical temperature-time history of a surface during spray quenching

The successful application of the extended LFP model will be demonstrated by a comparison between predicted and measured Leidenfrost temperatures for drops and sprays.

Leidenfrost Point Model Development

The methodology used to construct the LFP model is based on two aspects concerning bubble nucleation and its relationship to surface temperature and cavity shape and distribution. First, raising surface superheat beyond the boiling incipience temperature results in the activation of both larger and smaller surface cavities and an increase in the bubble growth rates. Secondly, for a typical polished surface, there is an exponential increase in the number of surface cavities with decreasing cavity mouth radius [4,5].

In the previous study by Bernardin and Mudawar [3], the authors postulated that at some large liquid-solid interface temperature corresponding to the LFP, a sufficient number of cavities would activate to produce enough vapor to completely separate the liquid from the solid, and hence, induce film boiling. Discussed below are the various sub-models used to support the overall LFP model for impinging droplets. In the next section, a solution procedure based upon these sub-models is outlined.

Bubble Nucleation. The first part of the LFP model involves the criteria for bubble nucleation from surface cavities as a liquid comes into contact with a solid surface. The minimum condition necessary for bubble nucleation is met when the available superheat, T_{ash}, in the liquid at a distance y from the solid surface, is equal to the required nucleation superheat, T_{rsh}, for a hemispherical bubble whose radius, r, is equal to y. This condition, as it applies to the transient condition when a liquid contacts a surface, is represented by

$$T_{sat}\exp\left(\frac{2\sigma v_{fg}}{rh_{fg}}\right)=T_i+(T_f-T_i)\mathrm{erf}\left(\frac{r}{2\sqrt{\alpha_f t}}\right) \tag{1}$$

where t is the time following liquid-solid contact and T_i is the liquid-solid interface temperature defined by

$$T_i=\frac{(k\rho c_p)_s^{0.5}T_s+(k\rho c_p)_f^{0.5}T_f}{(k\rho c_p)_s^{0.5}+(k\rho c_p)_f^{0.5}} \tag{2}$$

where T_s and T_f are, respectively, the surface and liquid temperatures prior to the contact. More details concerning this sub-model development can be found in [3].

Cavity Size Distribution. The second sub-model involves the surface cavity size distribution. Surface cavities and other defects, typically on the order of 1 to 10 μm, have long been known to be highly influential in controlling nucleate boiling by serving as nucleation sites.

In a previous study by the authors [3], scanning electron microscopy (SEM) was utilized to characterize the surface cavity distributions of macroscopically polished surfaces from which empirical Leidenfrost temperature measurements were made. From inspection of various SEM images at different magnifications, it was apparent that the number of cavities per unit area, n, having an equivalent mouth radius between r and $r+\Delta r$, could be fit by the exponential function

$$n=a_1\exp(-a_2 r) \tag{3}$$

Using the scanning electron microscopy images of the various surfaces from that study, the following curve fits were obtained over a cavity size range of 0.07 to 1.0 μm

$$n=3.379\exp(-10.12r)\quad(\text{aluminum}) \tag{4a}$$

$$n=4.597\exp(-12.20r)\quad(\text{nickel}) \tag{4b}$$

$$n=13.16\exp(-16.07r)\quad(\text{silver}), \tag{4c}$$

where the units for n and r are sites-μm^{-2}-μm^{-1} and μm, respectively. The curve fits had acceptable least square residuals greater than 0.9.

The cumulative number of surface cavities in the radius interval $r_{\min}\leqslant r\leqslant r_{\max}$, is then obtained through integration,

$$nc=\int_{r_{\min}}^{r_{\max}}n(r)dr=\frac{a_1}{a_2}[\exp(-a_2 r_{\min})-\exp(-a_2 r_{\max})] \tag{5}$$

Bubble Growth. The third sub-model is related to the bubble growth that occurs from activated cavities. Due to the relatively high superheat and short duration over which vapor is created in the film boiling regime, it is believed the rapid bubble growth is initially dominated by inertia rather than heat diffusion. For this condition, bubble growth is described by the Rayleigh equation (neglecting viscous effects) which can be derived from the momentum equation for incompressible and irrotational flow [6], or from energy conservation principles [7], incorporating the pressure drop across a spherical interface, $2\sigma/R$.

$$R\ddot{R}+\frac{3}{2}\dot{R}^2=\frac{1}{\rho_f}\left[(P_g-P_\infty)-\frac{2\sigma}{R}\right], \tag{6}$$

where $\dot{R}$ and $\ddot{R}$ are, respectively, the first and second derivatives of bubble radius with respect to time, and P_∞ is the liquid pressure far from the bubble interface.

In solving the Rayleigh equation, the following intermediate substitutions were performed:

$$\left[R\ddot{R}+\frac{3}{2}\dot{R}^2\right]R^{1/2}=\frac{d(R^{3/2}\dot{R})}{dt} \tag{7}$$

and

$$\frac{R^{1/2}}{\rho_f}\left[\Delta P-\frac{2\sigma}{R}\right]=\frac{1}{R^{3/2}\dot{R}}\frac{d}{dt}\left[\frac{\Delta P R^3}{3\rho_f}-\frac{\sigma R^2}{\rho_f}\right] \tag{8}$$

where $\Delta P=(P_g-P_\infty)$.

Substituting Eqs. (7) and (8) into Eq. (6) and performing the integration leads to the following integral:

$$t = \int_0^R \frac{dR}{\left[\frac{2\Delta P}{3\rho_f} - \frac{2\sigma}{\rho_f R}\right]^{0.5}}, \quad (9)$$

which can be solved by numerical techniques [3,8].

This model development assumed that the bubbles have a hemispherical shape and that the effect of viscosity could be neglected. Previous empirical studies [9–11] revealed that nucleating bubbles were generally hemispherical or near-spherical in shape. Furthermore, Johnson et al. [11] and Carey [12] both indicated that for rapid bubble growth, like that experienced near the Leidenfrost point, the inertial forces dominate and the bubbles have a hemispherical shape. Finally, previous analytical bubble growth models [7,10,13,14] that employed spherical bubble shapes and neglected the effect of viscosity, proved to be very accurate when compared to empirical bubble growth rate measurements.

Interaction of the Thermal Boundary Layer and the Growing Bubbles. The growth rate of a bubble, as predicted by the numerical solution to the Rayleigh equation, is several orders of magnitude faster than that of the thermal boundary layer (right-hand side of Eq. (1)). Therefore, it is assumed the early stage of bubble growth is described by the solution to Eq. (9) until the bubble dome reaches the maximum bubble stability point in the growing thermal boundary layer predicted by Eq. (1), after which the bubble growth is controlled by this slower diffusion rate of the thermal boundary layer.

As individual bubbles grow, they begin to merge and form a vapor layer. The formation of this vapor layer is influenced by a number of factors including entrainment of vapor within cavities, merging of bubbles, and cancellation of nucleation sites by growing bubbles. All of these factors serve to decrease the number of bubble nucleation sites participating in the growth of the vapor layer at the liquid-solid interface. More details and experimental observations of these factors, including the influence of these parameters in the prediction of the LFP, can be found in [3].

Influence of Droplet Impact Velocity. The approach for determining the Leidenfrost temperature for impinging droplets is identical to that for sessile droplets with the exception that the impact pressure must be correctly modeled when determining fluid properties at the liquid-solid interface. When a droplet impinges perpendicularly upon a rigid surface, the pressure rise at the liquid-solid interface at the moment of impact is significantly higher than the increase in stagnation pressure, $0.5\,\rho_f\,u_o^2$, because of compressibility effects. The most frequently used approximations to the pressure increase which develops during droplet impact are based upon one-dimensional elastic impact theory [15]. This theory states that the interfacial pressure increase that results when two elastic media collide, assuming Hooke's law is valid, is given by the solution to the one-dimensional longitudinal wave equation [16]:

$$\Delta P = \rho_f u_o u_{snd} \quad (10)$$

where u_o is the droplet impact velocity and u_{snd} is the speed of sound in the liquid.

Labeish [17] claimed that Eq. (10) could be applied to impinging droplets to predict the impact pressure. Engel [18], however, performed an analysis which accounted for droplet curvature and the transient impact behavior, concluding Eq. (10) overpredicts the impact pressure and must be multiplied by a correction factor, given as 0.20 for water on various solids including aluminum and copper [19].

Based upon Engel's findings [18,19], the following 20 percent elastic impact pressure relation was used in the present study to predict the pressure at the liquid-solid interface during the impact:

$$\Delta P = 0.20 \rho_f u_o u_{snd} \quad (11)$$

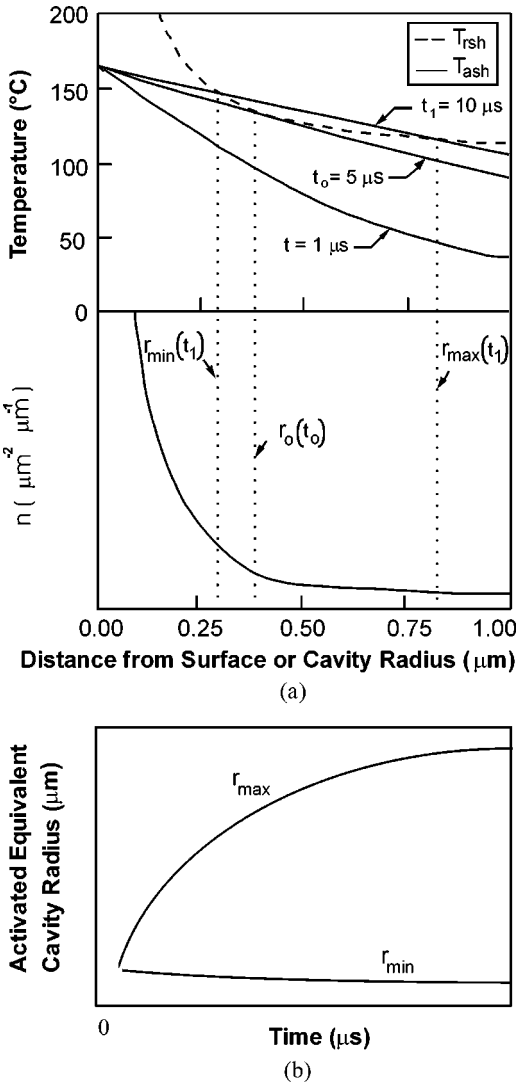

Fig. 2 Transient cavity nucleation model including (*a*) cavity nucleation superheat criteria and corresponding cavity size distribution with transient activation window, and (*b*) transient maximum and minimum active cavity radii for water in contact with a hot surface with an interface temperature of 165°C [3]

Leidenfrost Model Solution Procedure

To perform the LFP model solution procedure for impinging droplets, the pressure increase must first be determined with Eq. (11) so that fluid properties in the vicinity of the liquid-solid interface can be accurately determined.

Next, the surface cavity activation and bubble growth process must be modeled. To achieve this step, one must understand the thermal processes taking place during the initial impact of the droplet. Upon contact between an impinging droplet and a heated surface, a thermal boundary layer begins to develop in the liquid, as displayed in Fig. 2(*a*) for a water droplet in contact with a hot surface at 165°C. At some time t_o, the thermal boundary layer has grown sufficiently large such that the available superheat, T_{ash}, is equal to the required superheat, T_{rsh}, needed to satisfy the bubble nucleation criterion for conical-shaped cavities with a mouth radius r_o, (Eq. (1)), as shown in Fig. 2(*a*). For a polished surface, this radius is typically well within the range of cavity radii available on the surface. As time progresses and thermal boundary layer thickens, all cavities within a specific cavity radius interval are activated. This interval is given by the two roots of Eq. (1), namely, $r_{\min}(t)$ and $r_{\max}(t)$, as displayed in Fig. 2(*b*), where $r_{\max}$ is

the radius of the largest activated cavity at a given instant, not the largest cavity on the surface. Similarly, $r_{\min}$ is the smallest activated cavity.

Assuming only a fraction, ψ, of the cavities actively participate in the growth of the vapor layer due to the cancellation effects described in the previous section, and that bubbles grow from cavities as hemispheres, the time dependence of the cumulative number of activated cavities per unit area, nc_a, can be found by integrating the cavity size distribution, Eq. (3), over the active cavity radius limits $r_{\min}(t)$ and $r_{\max}(t)$:

$$nc_a(t)=\psi\int_{r_{\min}(t)}^{r_{\max}(t)} a_1\exp(-a_2 r)dr=\psi\frac{a_1}{a_2}\{\exp(-a_2 r_{\min}(t))-\exp(-a_2 r_{\max}(t))\}. \quad (12)$$

Since the inertia-controlled bubble growth rate predicted by Eq. (9) is orders of magnitude greater than the thermal boundary layer growth rate, it is assumed all bubbles initiated with $r_o<r_{\max}(t)$ will rapidly grow to $r_{\max}(t)$, the maximum stable hemispherical bubble radius supported by the growing thermal boundary layer. A hemispherical bubble will not be stable for sizes beyond $r_{\max}(t)$ as condensation on the leading front of the growing bubble would significantly reduce its growth rate [20]. This is consistent with bubble incipience model of Hsu [21] and the experimental results of Clark et al. [22]. Consequently, the limiting condition considered here is that once the bubbles reach the thermal boundary layer limit of $r_{\max}(t)$ they will continue to grow at the same rate as the thermal boundary layer, i.e., $\dot{r}_{\max}(t)$. This two-stage growth is consistent with the bubble growth findings of Lee and Merte [13].

Given this bubble growth model, the time-dependent percent area coverage of the liquid-solid interface by vapor, $AB\%(t)$, is then given by

$$AB\%(t)=nc_a(t)\pi r_{\max}^2(t)\times 100\% \quad (\%) \quad (13)$$

which, upon substitution of Eq. (12), gives

$$AB\%(t)=\psi\frac{a_1}{a_2}\times\{\exp(-a_2 r_{\min}(t))-\exp(-a_2 r_{\max}(t))\}\pi r_{\max}^2(t)\times 100\% \quad (\%) \quad (14)$$

where a_1 and a_2 are experimentally determined constants, such as those given in Eqs. (4*a*) through (4*c*).

Bernardin and Mudawar [3] used experimental evidence to arrive at a value of 0.05 for the cavity cancellation parameter, ψ. As Bernardin and Mudawar discuss, the present models for surface characterization and bubble nucleation are limited in their degree of accuracy and a more accurate means of determining the percent of actively participating surface cavities, ψ, is currently unavailable and warrants further investigation. Nevertheless, it should be emphasized that while the choice of ψ will influence the vapor layer growth rate, the strong temperature-dependence of the latter, $\Delta AB\%/\Delta t$, which is used to identify the LFP in the present model, is still very well preserved.

Shown in Fig. 3(*a*) is the temperature dependence of the transient vapor layer growth for a sessile water droplet on a polished aluminum surface with a cavity distribution given by Eq. (4*a*), as determined in the previous study by Bernardin and Mudawar [3]. The time for complete vapor layer development ($AB\%=100$) is shown to rapidly decrease as the interface temperature is increased from 145 to 185°C. While the model predicts an eventual 100% vapor layer growth for the interface temperature of 145°C, other effects such as bubble departure and liquid motion which are not accounted for in the model, would interrupt this development within a few milliseconds of liquid-solid contact, and hence prevent film boiling from occurring. Figure 3(*b*) displays the vapor layer growth rate, $\Delta AB\%/\Delta t$ or average slope of the curves in Fig. 3(*a*), as a function of the liquid-solid interface temperature. Figure 3(*b*) shows that as the interface temperature increases beyond the liquid saturation temperature, the average vapor layer

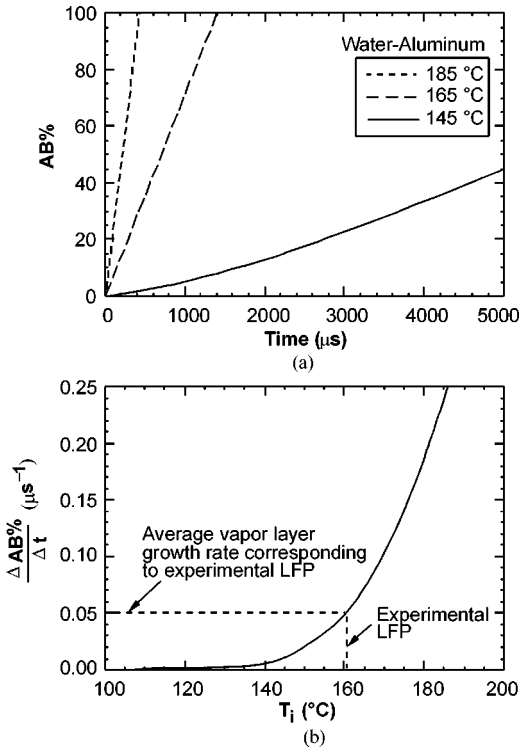

Fig. 3 Temperature dependence of the (*a*) transient vapor layer coverage and (*b*) average vapor layer growth rate for a sessile water droplet on a polished aluminum surface [3]

growth rate increases exponentially. Intuition suggests that at some minimum interface temperature, the LFP, the average vapor layer growth rate will become sufficiently high to support film boiling.

To determine the minimum average vapor layer growth rate required to support film boiling, experimental LFP data for sessile water droplets on aluminum were employed [2]. Shown in Fig. 3(*b*) is the experimentally determined Leidenfrost temperature of 162°C ($T_s=170$°C) for sessile water droplets on aluminum, which corresponds to an average vapor layer growth rate of 0.05 μs^{-1}. Note that the experimentally measured Leidenfrost temperature had an uncertainty of ±5°C [2]. Bernardin and Mudawar [3] employed this value of the average vapor layer growth rate to accurately identify the LFP for a sessile drop in a variety of liquid-solid systems. This same technique, as described by Carey [12], has been used to determine the critical vapor bubble formation rate needed to sustain homogeneous nucleation within a superheated liquid. In the homogeneous nucleation superheat limit model, the vapor bubble formation rate increases exponentially with increasing liquid temperature, much like the vapor blanket growth rate in the present study. Carey explains how empirical data were used to determine a critical vapor bubble formation rate, and how this single bubble formation rate was used to determine the homogeneous nucleation superheat limit of several different liquids including water.

Consequently, this average vapor growth rate of 0.05 μs^{-1} is used in the present study to identify the LFP for impinging droplets.

While this modeling process was presented for a single impinging droplet, it can also be used to predict the LFP for a spray. To predict the local LFP for a spray, the mean droplet velocity of the spray in the area of interest should be used in Eq. (11) to determine the average droplet impact pressure. The remaining modeling procedure is identical to that outlined above for a single droplet.

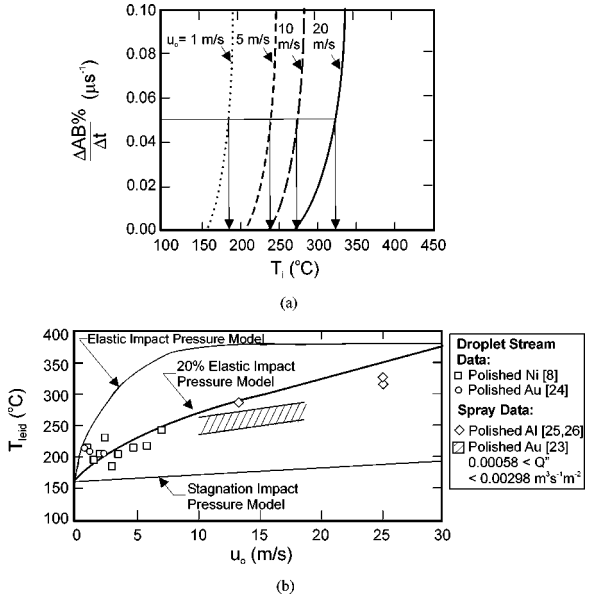

Fig. 4 (*a*) Velocity and temperature dependence of the average vapor layer growth rate for water droplets impinging upon a polished aluminum surface, and (*b*) comparison of the velocity dependent LFP model for water droplets impinging upon a polished surface, using different impact pressure sub-models, with experimental data. The uncertainties of experimental Leidenfrost temperatures and droplet impact velocities measured in studies [8,23–26] were reported not to exceed ±10°C and ±0.5 m/s, respectively.

Leidenfrost Model Assessment

Figure 4(*a*) displays the average vapor layer growth rate versus interface temperature for water droplets impinging at different velocities upon a polished aluminum surface. For the four different droplet velocities, the fluid properties were evaluated with the 20% elastic impact pressure relation given by Eq. (11). Using an average vapor layer growth rate of 0.05 μs^{-1}, the Leidenfrost temperatures corresponding to the various droplet velocities were determined. The following expression relating the Leidenfrost temperature to the water droplet velocity was determined from the data in Fig. 4(*a*):

$$T_{\text{leid}} = 162.0 + 24.3 u_o^{0.64} \quad (^\circ\text{C}) \tag{15}$$

where the units on u_o are m s^{-1}. Equation (15) is displayed in Fig. 4(*b*), and is labeled with "20 percent Elastic Impact Pressure Model," indicating that Eq. (11) was used in its development. Also displayed in Fig. 4(*b*) are the LFP predictions that would be obtained if the full elastic or stagnation impact pressure sub-models were used in place of Eq. (11) to determine the fluid properties. While Eq. (15), and the LFP model for that matter, does not explicitly give an upper temperature bound for the LFP, a maximum temperature limit does exist. The maximum temperature that a liquid can be heated to, above which it is nearly instantaneously converted to vapor, is referred to as the kinetic or thermodynamic superheat limit. Techniques for predicting this superheat limit can be found in [12]. Further details on the superheat limit for water and its relationship to the present LFP model can be found in [3].

To assess the accuracy of the LFP model for impinging droplets, experimental LFP data for single water droplet streams and sprays are included in Fig. 4(*b*). The shaded band representing the empirical LFP spray correlation of Klinzing et al. [23] covers the range of volumetric spray fluxes ($0.00058 < Q'' < 0.00298$ m^3 s^{-1} m^{-2}) used in that study. Although the experimental data used in the comparison correspond to different surface material types, the surface preparation for each was similar. Thus, the cavity size distributions and Leidenfrost temperatures for the various surface materials are expected to be fairly similar, as was found previously by Bernardin and Mudawar [3] for polished aluminum, nickel, and silver surfaces. The comparison in Fig. 4(*b*) indicates that the LFP models generated with either the full elastic impact or the stagnation impact pressure sub-models, yield significant deviations between the predictions and the empirical data. In contrast, the LFP model that used the 20 percent elastic impact pressure sub-model, agrees quite well with the experimental data. In most cases, the model lies within the experimental data's error bands of ±10°C in temperature and ±0.5 m/s in droplet velocity. In addition, the impinging water drop LFP model given by Eq. (15), predicts a Leidenfrost temperature of 162.0°C for a sessile water drop ($u_o = 0.0$ m s^{-1}), which is in agreement with the sessile drop LFP model prediction [3] and the experimentally measured value [2] for water on polished aluminum.

Differences between the LFP model predictions and experimental Leidenfrost temperature data may be attributed to a number of factors. First, the surface cavity size distribution, *nc*, and cavity cancellation parameter, ψ, used to arrive at Eq. (15), were taken from a study of water droplets on a polished aluminum surface [3], whereas the experimental LFP data of Fig. 4 came from studies using a variety of polished metal surfaces. A more accurate determination of Eq. (15) using a cavity size distribution for each particular surface may yield better agreement between the Leidenfrost temperature predictions and measurements. Further investigation of the cavity cancellation parameter is also warranted, as its value is dependent on the droplet fluid properties and solid surface finish [3].

The 20 percent elastic impact model may be a source of some uncertainty as well. This model, represented by Eq. (11), does not account for break-up of the impacting droplet and its subsequent influence on the impact pressure. The stability of the spreading droplet film has been observed in numerous empirical studies to be a function of, in part, droplet velocity and surface roughness, as summarized in [24]. Hence, by more accurately accounting for the effects of droplet velocity and surface roughness on the impact pressure, a better prediction of the Leidenfrost temperature of impinging drops may be obtained.

While some uncertainties do exist in the development of the present LFP model, Eq. (15) and Fig. 4(*b*) reveal the dependence of the LFP on droplet velocity, something that previous LFP models have failed to accomplish [2]. As Fig. 4(*b*) indicates, the Leidenfrost temperature for an impinging droplet or spray can be significantly higher than that predicted for a sessile droplet. Consequently, the present LFP model should prove beneficial in predicting and controlling the spray heat transfer process encountered in materials processing and other applications.

Application to Rough Surfaces. While the present model was developed for polished surfaces, it also provides a limiting condition for surfaces possessing roughness features orders of magnitude larger than the cavity radii responsible for bubble nucleation (0.1 to 1 μm). As discussed earlier, surface contamination and roughness promotes and enhances the shattering of droplets upon impact [24]. Consequently, rough surfaces would expect to have a lower interfacial impact pressure and a corresponding lower Leidenfrost temperature when compared to a polished surface. Figure 5 shows experimentally measured Leidenfrost temperatures for water droplets of different velocities, impinging upon polished and particle blasted surfaces. For each droplet velocity studied, the Leidenfrost temperature for the polished surface was consistently higher than that for the particle blasted surface. In addition, the measured Leidenfrost temperature for the particle blasted surface, for the most part, was lower than the LFP model prediction. Consequently, the LFP model outlined in this study appears to predict an upper limit to the Leidenfrost temperature for droplets impinging upon rough surfaces. The complex relationship between surface roughness, droplet impact stability,

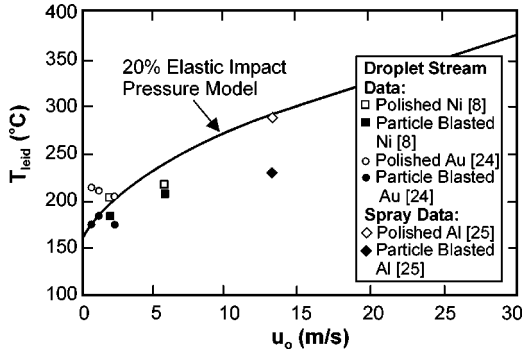

Fig. 5 Effect of surface roughness on the LFP for water droplets impinging upon metallic surfaces as determined experimentally and compared with the LFP model for a polished aluminum surface. The uncertainties of experimental Leidenfrost temperatures and droplet impact velocities measured in studies [8,24,25] were reported not to exceed ±10°C and ±0.5 m/s, respectively.

interfacial impact pressure, and the Leidenfrost temperature is the focus of ongoing studies in an effort to broaden and enhance the prediction capabilities of the current LFP model.

Conclusions

The present study employed an existing LFP model for sessile drops [3], and extended its capability to include impinging drops and sprays. The previous model, which was constructed around vapor bubble kinetics and surface cavity size characterization, was expanded to account for the sharp pressure rise that occurs at the liquid-solid interface during droplet impact. Upon evaluation of the current LFP model with an experimental database for droplets and sprays, the following key conclusions were drawn:

1. The Leidenfrost temperature for a droplet impinging upon a heated surface is highly dependent on the impact velocity. The model developed in this study successfully captured this velocity dependence.
2. The physical processes that govern the LFP of sessile drops are similar to those for impinging drops. The primary difference in the LFP predictions for sessile drops and impinging drops, is the evaluation of the liquid properties at the liquid-solid interface. For impinging drops, the sharp pressure rise that occurs at the liquid-solid interface during impact, must be accounted for so that the fluid properties can be accurately predicted.
3. This study revealed that the 20 percent elastic impact pressure model [18,19] is adequate for predicting the liquid properties of impinging drops at the liquid-solid interface.
4. The present LFP model was substantiated with experimental data for water drops impinging on a surface where the roughness feature sizes were of the same order of magnitude as the bubble nucleation cavities. Additional empirical data revealed that for rougher surfaces, the model predicts an upper bound of the Leidenfrost temperature.

Nomenclature

Symbol

$AB\%$ = percent liquid-solid interface area coverage by vapor
a_1, a_2 = coefficients in cavity size distribution
c_p = specific heat at constant pressure
h_{fg} = latent heat of vaporization
k = thermal conductivity
n = number of surface cavities per unit area per unit interval (sites $\mu m^{-2}\,\mu m^{-1}$)
nc = cumulative number of surface cavities per unit area (sites μm^{-2})
nc_a = cumulative number of active surface cavities per unit area (sites μm^{-2})
P = pressure
Q'' = volumetric spray flux ($m^3\,s^{-1}\,m^{-2}$)
R = bubble radius
$\dot{R}$ = first derivative of bubble radius with respect to time
$\ddot{R}$ = second derivative of bubble radius with respect to time
r = surface cavity radius
r_a = radius of active surface cavity (μm)
T = temperature
t = time
v_{fg} = specific volume difference between vapor and liquid
y = normal distance from solid surface

Greek Symbols

α = thermal diffusivity
$\Delta AB\%/\Delta t$ = average vapor layer growth rate
ΔT_{sat} = surface superheat, $T_s - T_{sat}$
ρ = density
σ = surface tension
ψ = fraction of cavities that participate in the vapor layer growth

Subscripts

a = active
f = liquid
g = vapor
i = liquid-solid interface
leid = Leidenfrost condition
max = maximum
min = minimum
o = initial, nucleation
s = surface, solid
sat = saturation
∞ = liquid condition far from bubble interface

References

[1] Bernardin, J. D., and Mudawar, I., 1995, "Use of the Quench Factor Technique to Predict Material Hardness in Heat Treatable Aluminum Alloys," Int. J. Heat Mass Transfer, **38**, pp. 863–873.
[2] Bernardin, J. D., and Mudawar, I., 1999, "The Leidenfrost Point: Experimental Study and Assessment of Existing Models," ASME J. Heat Transfer, **121**, pp. 894–903.
[3] Bernardin, J. D., and Mudawar, I., 2002, "A Cavity Activation and Bubble Growth Model of the Leidenfrost Point," ASME J. Heat Transfer, **124**, pp. 864–874.
[4] Yang, S. R., and Kim, R. H., 1988, "A Mathematical Model of the Pool Boiling Nucleation Site Density in Terms of the Surface Characteristics," Int. J. Heat Mass Transfer, **31**, pp. 1127–1135.
[5] Wang, C. H., and Dhir, V. K., 1993, "Effect of Surface Wettability on Active Nucleation Site Density During Pool Boiling of Water on a Vertical Surface," ASME J. Heat Transfer, **115**, pp. 659–669.
[6] Panton, R. L., 1984, *Incompressible Flow*, John Wiley & Sons, New York.
[7] Mikic, B. B., Rohsenow, W. M., and Griffith, P., 1970, "On Bubble Growth Rates," Int. J. Heat Mass Transfer, **13**, pp. 657–666.
[8] Bernardin, J. D., 1996, "Leidenfrost Point and Film Boiling Heat Transfer of Single Droplets and Sprays," Ph.D. thesis, Purdue University, West Lafayette, IN.
[9] Cole, R., and Shulman, H. L., 1965, "Bubble Growth Rates at High Jakob Numbers," Int. J. Heat Mass Transfer, **9**, pp. 1377–1390.
[10] Han, C. Y., and Griffith, P., 1965, "The Mechanism of Heat Transfer in Nucleate Pool Boiling-Part I," Int. J. Heat Mass Transfer, **8**, pp. 887–904.
[11] Johnson, Jr., M. A., De La Pena, J., and Mesler, R. B., 1966, "Bubble Shapes in Nucleate Boiling," American Institute of Chemical Engineers Journal, **12**, pp. 344–348.
[12] Carey, V. P., 1992, *Liquid-Vapor Phase-Change Phenomena: An Introduction to the Thermophysics of Vaporization and Condensation Processes in Heat Transfer Equipment*, Hemisphere, New York.
[13] Lee, H. S., and Merte, H., 1996, "Spherical Vapor Bubble Growth in Uniformly Superheated Liquids," Int. J. Heat Mass Transfer, **39**, pp. 2427–2447.

[14] Forster, H. K., and Zuber, N., 1954, ''Growth of a Vapor Bubble in a Superheated Liquid,'' J. Appl. Phys., **25**, pp. 474–478.
[15] Heymann, F. J., 1969, ''High-Speed Impact Between a Liquid Drop and a Solid Surface,'' J. Appl. Phys., **40**, pp. 5113–5122.
[16] Churchill, R. V., 1944, *Modern Operational Mathematics in Engineering*, McGraw-Hill, NY.
[17] Labeish, V. G., 1994, ''Thermodynamic Study of a Drop Impact against a Heated Surface,'' Exp. Thermal Fluid Sci., **8**, pp. 181–194.
[18] Engel, O. G., 1955, ''Waterdrop Collisions with Solid Surfaces,'' J. Research National Bureau Standards, **54**, pp. 281–298.
[19] Engel, O. G., 1960, ''Note on Particle Velocity in Collisions between Liquid Drops and Solids,'' J. Research National Bureau Standards-A. Phys. Chem., **64A**, pp. 497–498.
[20] Bankoff, S. G., and Mikesell, R. D., 1959, ''Bubble Growth Rates in Highly Subcooled Nucleate Boiling,'' Chem. Eng. Prog. Symp. Series, **55**, pp. 95–102.
[21] Hsu, Y. Y., 1962, ''On the Size Range of Active Nucleation Cavities on a Heating Surface,'' ASME J. Heat Transfer, **84**, pp. 207–213.
[22] Clark, H. B., Strenge, P. S., and Westwater, J. W., 1959, ''Active Sites for Nucleate Boiling,'' Chem. Eng. Prog. Symp., **55**, pp. 103–110.
[23] Klinzing, W. P., Rozzi, J. C., and Mudawar, I., 1992, ''Film and Transition Boiling Correlations for Quenching of Hot Surfaces with Water Sprays,'' J. Heat Treating, **9**, pp. 91–103.
[24] Bernardin, J. D., Stebbins, C. J., and Mudawar, I., 1997, ''Effects of Surface Roughness on Water Droplet Impact History and Heat Transfer Regimes,'' Int. J. Heat Mass Transfer, **40**, pp. 73–88.
[25] Bernardin, J. D., and Mudawar, I., 1996, ''An Experimental Investigation into the Relationship between Temperature-time and Surface Roughness in the Spray Quenching of Aluminum Parts,'' ASME J. Eng. Mater. Technol., **118**, pp. 127–134.
[26] Bernardin, J. D., 1993, ''Intelligent Heat Treatment of Aluminum Alloys: Material, Surface Roughness, and Droplet-Surface Interaction Characteristics,'' Masters thesis, Purdue University, West Lafayette, IN.

Measurement of Temperatures on In-Flight Water Droplets by Laser Induced Fluorescence Thermometry

V. M. Salazar
Department of Mechanical Engineering
University of Puerto Rico
Mayaguez 2, PR 00681-9045

J. E. González
e-mail: jgonzalezcruz@scu.edu

Department of Mechanical Engineering,
Santa Clara University
Santa Clara, CA 95053

L. A. Rivera
Department of Chemistry,
University of Puerto Rico-Mayagüez,
Mayaguez, PR 00681-9019

This work presents the use of laser induced fluorescence for instantaneous temperature measurements of 200 μm water droplets in a monodisperse stream while traveling downward in a standard stagnant atmosphere. The droplets are doped with small concentrations of a natural fluorescence dye (Pyrene), and with a surfactant substance, cetyldimetylbenzylammoniumchloride (CDBAC) to improve the fluorescence emission and the rate of its two band emission (excimer to monomer) is used to determine the temperature. The temperature distribution along the stream of droplets was determined for three different initial temperatures: 30°C, 40°C, and 50°C at the exit of the nozzle and it is compared very favorably with numerical results. [DOI: 10.1115/1.1667527]

Keywords: Droplet, Evaporation, Heat Transfer, Laser, Measurement Techniques, Temperature

1 Introduction

The full characterization of liquid droplets in sprays while in-flight is a very important engineering topic due to the wide range of technological applications in which atomization of liquid sprays is applied to, including spray cooling, combustion, spray drying among others. The heat and mass transfer from or to the droplets are important control variables in many of these applications. Spray cooling, for example, is a very efficient technique to remove heat from a hot surface. Examples of applications in which spray cooling can be applied includes the metallurgical industry to achieve fast and control quenching rates [1], and for the cooling of electronics components [2]. The spray cooling process consists of the generation of small subcooled droplets that are deposited over a heated surface whose temperature is higher than the liquid saturation point, and the heat transfer is achieved by the combined effect of sensible heating of the liquid and the phase change of the droplets. The size and initial temperature of the droplets influence the amount of sensible heating that can be removed from the liquid. Small in-flight droplets in the order of 500 μm or less may be affected by the rising hot gas or vapor resulting from the evaporation at the surface, inhibiting any subcooling effect as reported by González and Black [3]. Thus knowledge of droplets temperature while in-flight will assist in the characterization and further optimization of the heat transfer from the hot surfaces in spray cooling applications.

The major difficulty in determining the transient heat transfer from or to in-flight small droplets is the lack of a suitable noninvasive means to determine the droplet temperature during the heat transfer process. Thus the aim of this work is to present an advanced experimental technique based on the laser induced fluorescence (LIF) principle that can be used to characterize the temperature field of water droplets while traveling in a quiescent air environment in a nonintrusive manner. The droplets' properties that could be studied more exhaustively with the proposed tools are the heat and mass transfer rates, the determination of convection heat transfer coefficient, and the diffusion coefficients for mass transfer. Besides, this nonintrusive sensor should be able to quickly respond to temperature changes as the time response is in the order of nanoseconds, which is much faster than the expected thermal transients.

One of the first reported works in experimentally determining the droplet temperature was carried out by Ranz and Marshall [4], where the temperature was measured using thermocouples. A few optical methods have been reported for droplet temperatures and the most relevants will be described herein. One of these methods is the rainbow thermometry method reported by van Beeck et al. [5]. The principle of this technique is based on the change of the liquid drop refractive index with the variation in its temperature, and the technique is suitable only for cases where there is not a large temperature gradient inside the droplet. Another optical method reported to measure droplets' temperature made use of thermocromic liquid crystals (TLC) [6]. The principle is based on the color of white light scattered from a TLC droplet, which is a function of the inside temperature of the droplet. However the accuracy of this technique is not very good according to Sakakibara and Adrian [7]. Other technique used to determine the droplet temperature is to measure and analyze its infrared emission level [8]. However, the liquid emmisivity determination is a major constraint in this technique and the vapor influence in the surface evaporation plays a main role in the surface radiation.

Laser induced fluorescence (LIF) has been suggested as a promising technique to determine liquid droplets' temperature. This technique consists of adding a fluorescent dye in the liquid phase, exciting the solution with a laser source and recording its emission, which is a function of the temperature. An especial case of LIF is the exciplex thermometry, which is based in the exciplex photophysics principle and it has been already studied and applied by Murray and Melton [9] and Gossage and Melton [10].

2 Exciplex Photophysics Principle

Exciplex is short for ''excited state complex'' and is a form of laser-induced fluorescence. The exciplex equilibrium formation is given by Eq. (1)

$$M^* + G \leftrightarrow (MG)^* \tag{1}$$

Here M^* is the first single excited state of a ground state molecule M called the monomer. M^* is obtained by exciting M with a light source. M^* can react with other ground state molecule different to

Contributed by the Heat Transfer Division for publication in the JOURNAL OF HEAT TRANSFER. Manuscript received by the Heat Transfer Division August 22, 2002; revision received December 15, 2003. Associate Editor: K. D. Kihm.

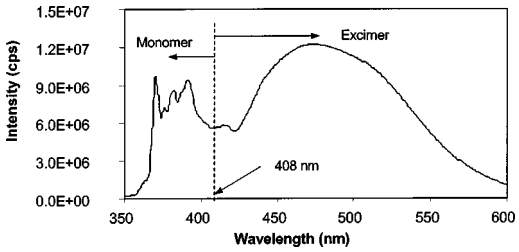

Fig. 1 Typical fluorescence emission spectra for an excimeric solution. In this case the solution is 5 mM pyrene in ethanol at ambient temperature.

M, to form an exciplex $(MG)^*$ or also can react with another molecule M to form the excimer $(MM)^*$. The reaction occurs and exists while the source of light is applied. When the energy source is released, the exciplex dissociate in the ground electronic state emitting a fluorescent emission. This emission is typically red shifted in the spectrum. The emission spectrum change according to the molecular configuration of the dye. This emission has temperature dependence and is reversible allowing this feature for use in thermometry. Figure 1 shows the excimer and monomer regions for an ethanol-pyrene solution at 5 mM concentration. The region to the left of the vertical line at 408 nm correspond to the monomer emission and the area under the curve to the right to this line corresponds to the excimer emission.

Reversibility of the reaction is a necessary condition for thermometers besides sensitivity to temperature changes. In this case, increasing the temperature, displaces the equilibrium to the left, favoring an increase in the relative concentration of the monomer versus the exciplex. Since the pyrene reaction shows reversibility, the technique to measure temperature has potential for success.

The exciplex fluorescence thermometry was used in the present work and has already been studied in a wide variety of experiments demonstrating to be a promising method with a high accuracy to measure temperature of liquid droplets of decane [11], hexadecane [12–14], ethanol [15], and water [16].

In recent years an especial case of LIF called ratiometric LIF has also been applied to measure temperature in macro and micro systems [7,17,18]. The technique is based in the normalization of the fluorescence emission of a temperature dependent dye (rhodamine B) with the correspondent emission of a nondependent temperature dye (rhodamine 110). In this case, the emission is not excimeric; however, the system rhodamine B/rhodamine 110 does show a good sensitivity to temperature.

A recent use of rhodamine B as a dye to measure the temperature of 200 μm diameter ethanol droplets was carried out by Lavieilli et al. [19]. Results obtained from the measurements were theoretically corrected by thermal expansion, and the phenomenon of droplet evaporation was not considered. An inconvenience with this technique is that fluorescence emissions for given positions in the stream are collected at different times and consequently there is a variation in time and space that the technique should overcome to provide representative results.

Despite recent advances in applying the LIF as a noninstrusive thermometer, the exciplex photochemical reaction seems to have the larger sensitivity for small scale systems such as droplets in liquid sprays. The objective of this work is to apply the LIF with an excimer reaction to measure the temperature of water droplets while in-flight in a standard quiescent atmosphere. The experimental setup and procedure used here is similar to that one reported by Escobar et al. [15] who reported measurements of ethanol single droplets. However, improvements have been implemented to collect the temperature of the entire spray field instead of a single droplet. The water based solution used is similar to that one reported by Parrado [16] in which the pyrene dye was combined with a surfactant to increase its solubility in water. The new experimental setup and solution are presented in detail, and the first set of measurements is reported. The measurements are calibrated against a simplified mathematical model for evaporating, and cooling droplets.

3 Fluorescent Solution

Initially pyrene, an aromatic hydrocarbon and arene molecule was chosen as a potentially useful sensor for measuring temperature. This arene is an effective fluorescence probe due to its long lifetime for formation of pyrene monomers ($t=450$ nanoseconds and quantum yield of 0.60 in cyclohexane) and efficient formation of excited dimers, ''excimers'' for short. A complete review on the photophysics of pyrene can be found in [20].

Pyrene has a poor solubility in water so the addition of a surfactant for the formation of micelles to solubilize the pyrene is necessary. The surfactant concentration would be greater than the critical micelle concentration, which is the point where the surfactant molecules group together to form micelles. In the present work the surfactant used was cetyldimethylbenzylammonium chloride ''CDBAC'' which is a cationic surfactant. Recently in [21] a proton Nuclear Magnetic Resonance (NMR) study on aggregation of cationic surfactants in water, including CDBAC was reported. Deionized water was chosen as solvent for this research. However, it is a poor solvent for pyrene. Nevertheless, the pyrene shows enhanced solubility in the surfactant molecule due to affinity to the nonpolar alkyl groups present in the surfactant molecules. In addition, the proximity introduced by micelles is well illustrated by efficient protection from the oxygen molecule and formation of excimer of arenes in micellar solution. Micelles provided by the CDBAC could improve fluorescence emission avoiding natural fluorescence quenching due to oxygen in the solutions. The distribution of pyrene molecules among the micelles is a controlling factor in forming excimers, while in homogeneous systems diffusion and medium viscosity are all important.

The pyrene/CDBAC/water solution used had a concentration of 5 mM for both the pyrene and the CDBAC. The weighed CDBAC was first diluted in half the volume of the required deionized water for the specific concentration. This mixture of CDBAC/water was mixed by means of an ultrasonic mixer during five minutes to enhance dissolution. Next the weighed amount of pyrene was added to this CDBAC/water mixture, and the rest of the deionized water needed to reach the final concentration on the solution was added. The pyrene/CDBAC/water mixture was mixed for 30 minutes with the ultrasonic mixer and allowed to rest until the undissolved pyrene precipitated. The sample for the fluorescence measurements was taken from the clear solution above the precipitate from the freshly prepared solution.

4 Experimental Setup

4.1 Chemicals and Solutions. The natural fluorescent pyrene was purchased from Aldrich Chemical Co. and it was used as received. The surfactant cetyldimethilbenzylammonium-chloride (CDBAC) rated as >97 percent was also purchased from Aldrich it was used as was received as well. The water for the solution used for the calibration curves as well as for the droplets generation was distilled and de-ionized.

4.2 Droplet Generator. Figure 2 shows a schematic of the atomization system used. A monodisperse droplet generator acquired from Fluid Jet Associates was used for the experiments. The principle of this droplet generator is the Rayleigh breakup hydrodynamic instability in a liquid jet [22], where the jet is perturbed with a piezoelectric crystal at a critical frequency breaking into drops of uniform size and velocity at the injection point. The pyrene/CDBAC/water solution is supplied to the droplet generator from a reservoir solution, which is pressurized with dry air in order to control the liquid head on the droplet generator. Two filters, one of 5μm and other of 0.8 μm, were used to filter the solution before it reached the droplet generator. In order to measure the solution temperature at the exit point of the nozzle, a

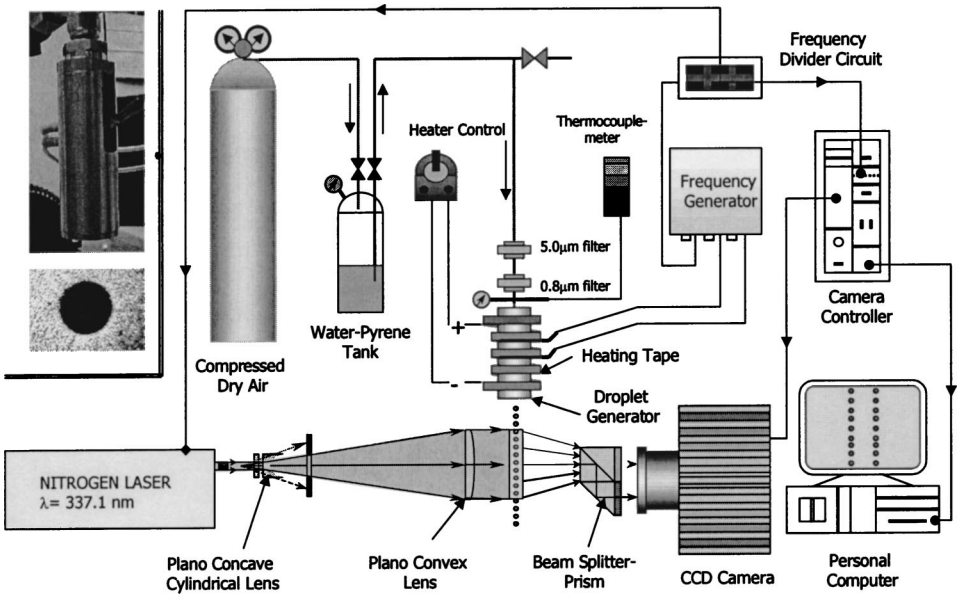

Fig. 2 (Left superior corner) Atomizer and orifice plate, (Right) Schematic diagram of the experimental setup for droplet temperature measurements

thermocouple was introduced conveniently inside the droplet generator just near the orifice plate. The temperature of the solution prior to atomization was controlled using a heater tape attached to the droplet generator body. A unique set of values of the orifices diameters in the plate, the excitation frequency of the piezoelectric and the fluid pressure provided a monodisperse stream of droplets [22]. For this particular work a single orifice plate was used with an orifice diameter of 100 μm, the fluid was pressurized to 34.473 kPa (5 psi) and the piezoloelectric crystal was excited at a frequency of 7.0 kHz. This set of values resulted in stable monodisperse droplet stream with droplet diameter of 200 μm at the exit of the nozzle.

4.3 Optical Device and Imaging. As a source of excitation light a nitrogen pulsed laser from Laser Science, model VSL-337ND-S, with energy per pulse greater than 300 μj was used. The laser has a working wavelength of 337.1 nm, a spectral bandwidth of 0.1 nm and a pulse duration (FWHM)$<$4 ns. To excite the complete stream of droplets in a distance of 50 mm, the shape of the laser beam was changed to approximately a square section of 6 mm of side to a rectangle of 50×3 mm^2. Figure 2 shows the optical arrangement that allowed modifying the cross section and the resulting optical cross section for the experiments. For this arrangement a plano-concave cylindrical lens, with a focal length of 25.4 mm, was used along with plano-convex lens, with a focal length of 245 mm.

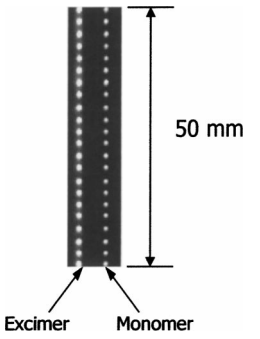

Fig. 3 Simultaneous observation of the stream of droplets at two different wavelengths range, the monomer and the red shifted excimer in a gray false color

A neutral UV beamsplitter-prism arrangement was used to separate the fluorescence signal into two parts. The first image was passed through two filters, one cut-on of 408 nm wavelength, and one 330–600 nm band pass filter. This image isolated the emission of fluorescence corresponding to the Excimer. The second image was filtered with a cut-on filter for wavelengths above 350 nm and by a 240–408 nm band pass filter. The second image quantified the monomer emission. All the filters were purchased from Oriel Corporation except the 240–408 nm band pass that was acquired from Edmund Industrial Optics. It is important to mention that both fluorescence emissions from the excimer and monomer are recorded simultaneously for each droplet in the stream by using this arrangement of a beam splitter-prism. A sample of the resulting images is given in Fig. 3. This optical arrangement represents a major step forward in simplifying the use of LIF as a thermometry technique for liquid sprays.

After the fluorescence signal was separated in the excimer and monomer emissions, a CCD camera recorded the two images. The CCD camera is the RTE/CCD-782-Y model from Princeton Instruments, which has a CCD format of 782×582 pixels, with a pixel size of 8.3×8.3 μm, and a dynamic range of 12 bits. The camera has a controller and software through which the images can be processed and recorded in a personal computer. The software used was WinView/32 version 2.5.8. The camera lens is a F1.4–16C acquired from Edmund Industrial Optics and was selected considering its 100 mm field of view, which allowed for the entire image to capture a cross section of a 50 mm in one frame. A schematic diagram of the complete optical setup is presented in Fig. 2.

The diameter of the droplets was measured with an Infinivar Video Inspection microscope from infinity Photo-Optical Company and a stroboscope light fired at the same frequency as the droplet generator. The XC-75 Sony black and white CCD video camera module attached to the microscope conveys the images to a video monitor. This video monitor had the option of freezing the images on the screen and it is useful to measure directly of the screen the droplet diameter using a convenient scale.

Synchronization of the electronics is essential for the success of the data acquisition process. In this sense a function generator

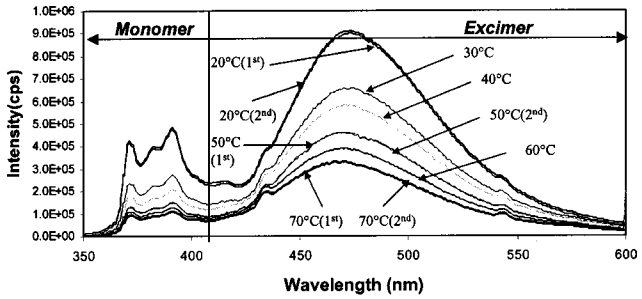

Fig. 4 Emission spectra taken in a fluorescence spectrophotometer for the water pyrene/CDBAC/water solution at 5 mM concentration of both pyrene and CBBAC, with excitation wavelength at λ=337 nm

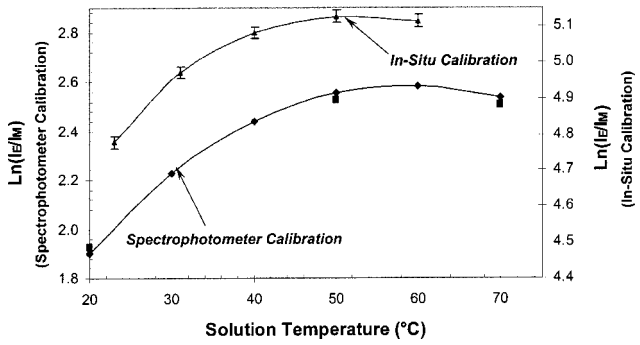

Fig. 5 LIF thermometry calibration curves for a pyrene/CDBAC/water solution at 5 mM concentration from data collected at a fluorescence spectrophotometer (continuous line refers to the heating process and the dots to the cooling process), and *in-situ* calibration curve developed with the spray experimental setup

with a frequency driver circuit were used to drive the droplet generator the laser and the CCD camera in phase.

4.4 Data Processing. The excimer and monomer emissions are recorded into the PC, as a single image (see Fig. 3) where each pixel of this image represents the intensity of fluorescence emission at this point. The size of the droplets in the images for the excimer emission was of approximately of 6 pixels in diameter and for the monomer of approximately 4 pixels in diameter, and the distance between adjacent droplets was about two diameters for both cases. Differences in sizes of the droplets for the excimer and monomer emissions could be observed due to the fact that similar color white-black scales were used to measure the intensity of both emissions. However, as it can be seen from Fig. 4 that the emission of monomer is lower than that one for the excimer. To quantify the ratio of excimer to monomer for each droplet it was necessary to compute the excimer and monomer for each droplet in both images and this process was repeated for all the droplets along the stream and for all the frames. The limits between the emissions of two droplets along the axis were considered to occur at the lowest value in intensity between both. Thus as the distance between droplets is of about 11 pixels the total emission of a droplet was counted as the total intensity of the pixels of a square of 11×11 pixels, with its center in the center of the fluorescent droplet image. The representative value for the droplet's excimer emission was then considered as the average of the excimer emissions of all the frames. The number of frames was varied between 30 and 120. The same procedure was carried out for the monomer emission. Thus with this method each emission was identified for each droplet separately eliminating the problem of positioning of the droplets in both images. The natural logarithm of the ratio of the excimer/monomer for each droplet was calculated and the calibration curve was used to determine the temperature indirectly.

5 Experimental Results

One of the first steps in applying LIF thermometry is to demonstrate temperature sensitivity and the development of a calibration curve. To determine the sensibility and dependence of the fluorescence intensity of solution pyrene/CDBAC/water to temperature, a spectrophotometer calibration curve was developed using the concentration of 5 mM in both pyrene and CDBAC. This concentration was chosen following the recommendations given by Parrado [16]. The spectrophotometer used is a FluoroMax2 from ISA Jobin Yvon-Spex Instruments S.A., Inc. with a water recirculator. The water recirculator allowed changing the temperature of the optical cell equipped with a water jacket. The resulting fluorescence intensity variations with wavelength from the spectrophotometer are shown in Fig. 4. The ratios of the excimer to monomer fluorescence intensities were taken to generate a base calibration curve and it is shown in Fig. 5. The reversibility of the solution was verified for three temperatures as indicated in Figs. 4 and 5. The first run refers to the heating direction while the second run to the solution when was heated until 75°C and then was cooled back. The maximum difference found was of 1.5 percent in the $\mathrm{Ln}(I_E/I_M)$, which confirms that the effect of the hysteresis can be discarded. The logarithmic transformation applied to the intensity ratio does not have any effect in the behavior of the curve, and the apparent curvature of the calibration curve for relatively high temperatures is circumstantial [11]. It is important to note from Figs. 4 and 5 that although the ratios of the emission intensities increase as the temperature increases, the excimer and monomer emissions both decrease. The calibration curve from the spectrophotometer shows a good dependence between temperature and fluorescence emission ratios for low temperatures. Parrado [16] found that the calibration curve developed in a spectrophotometer is not affected by the presence of an oxygen enriched environment confirming that minimum quenching effects are obtained for the proposed pyrene/CDBAC/water solution. This was verified in the present experiments.

A second step in using LIF thermometry is the development of an *in-situ* relation between fluorescence emissions and temperature. In this case, the monomer and excimer emissions were taken at known temperatures using a volume probe that was purchased from NSG Precision Cells Inc. The dimensions of this cell were 1 cm square of base by 5 cm height and it was filled with the pyrene/CDBAC/water solution. The quantity of liquid was of five mL, at a concentration of 5 mM of pyrene and 5 mM of surfactant. The same nitrogen laser used for the experiments with the stream of droplets was used to excite the fluorescence from the solution in the cell. The collection of fluorescence was taken at 90 deg with respect to the laser sheet, and, in this case, an arrangement of neutral filters was used to reduce the intensity of laser beam to eliminate the saturation of the CCD camera. For each measurement, about 30 minutes were necessary to stabilize the cell and the CCD camera temperature before the data could be collected. The cell was heated uniformly and the cell temperature was measured by a thermocouple inserted inside in contact with the liquid. The temperature was varied from 23 until 60°C.

The ratio of the Excimer to Monomer intensities were plotted as a function of solution temperature and the resulting curve was used as the *in-situ* calibration curve. This curve is shown in Fig. 5. The estimated uncertainty in using the output from the temperature measurement system was of ±1.66, ±1.14, ±3.17, and ±6.31°C for 23, 30, 40, and 50°C, respectively. These values were evaluated considering as error sources: the standard used in the calibration (thermocouple-meter), and the scattering error of the measurements of excimer and monomer due to temporal variation during the calibration process. As it can be observed the error is increased near the zone of 50°C that is near to the inflexion

point and it is due to the low sensibility of the calibration curve in this region. The uncertainty is increased considerably when the measurements are near to the inflexion point.

This *in-situ* calibration curve shows a similar shape as the curve obtained with spectrophotometer (Fig. 5). However, the range of emission ratios is different. This behavior can be inferred due to the presence of filters, camera lens and the CCD in the LIF setup. Therefore the combined effect of these components makes the ratio of excimer to monomer to be increased due to the reduced value of the monomer that is absorbed by the CCD. However, this effect is eliminated with this technique because it is based in intensity ratios.

The calibration curve was made under the same exact ambient conditions as the one the droplets were to be exposed, and it is the final calibration curve that was used to determine the temperature of falling droplets. It can be observed that the *in-situ* calibration curve shows two well defined regions, one region from 23°C until approximately 50°C where the $\mathrm{Ln}(I_E/I_M)$ ratio increases when the temperature increases, and the other region from 50 until 60°C where the $\mathrm{Ln}(I_E/I_M)$ changes the slope and the emission ratio decreases. This parabolic feature could create confusion and it is necessary to have a good orientation regarding in which branch of the curve the temperature measurements are made.

A very important final aspect in the determination of the calibration curve is to insure repeatability of the measurements and uniformity in the data collection process. Thus the solution was replaced for each temperature measurement following recommendations of Kim and Kihm [17], and Kim et al. [18] to reduce errors introduced by the photochemical and chemical decomposition when the laser beam exits the solution.

With the *in-situ* calibration curve at hand, reliable temperature measurements for in-flight droplets could be conducted. In this case the solution was preheated in the atomizer to set the initial thermal state of the droplets. Three different exit temperatures were used 30, 40, and 50°C. For all three temperatures the remaining exit conditions were the same including pressure equal to 34.473 kPa, frequency of droplet generation of 7.0 KHz, and the initial velocity of the droplets which was about 6.67 m/s. The ambient conditions for each run were: $T_{db}=24$°C, $T_{wb}=19$°C, and the atmospheric pressure was 101.325 kPa.

The droplets were falling in the downward vertical direction, and as reference for the distance was taken the nozzle tip. The temperature at the exit in the nozzle was controlled by a heat tape and it was stabilized for approximately 20 minutes for each temperature assuring in this manner the steady state and that there were no fluctuations in the exit temperature. The temperature measurements were taken along the jet and allowed to track the thermal history of a droplet along the traveling path.

Following the procedure to post-process the images discussed above in which the ratio of the monomer to excimer emissions is compared to the *in-situ* calibration curve, the final temperature of the in-flight droplets can be inferred and results are shown in Fig. 6.

The resulting curves in general show a decreasing temperature pattern as the droplets fly away from the nozzle. The total decrease in temperature along the 50 mm of traveling distance for an initial temperature of 30, 40, and 50°C are of 2.1, 4.24, and 5.01°C, respectively. It is important to mention that the diameter of the droplets is changing as the droplets travel along its path and the emission is a function of volume. However, with the present method, in which the images for the excimer and the monomer are gathered simultaneously, this problem of variable volume is overcome. The signal variation with time for a given position is also improved with this two images method. The droplet diameter was measured using the equipment described in Section 4.3 at 10 mm and at 50 mm of the trajectory, for the case of an initial temperature 50°C and were found to be of about 200 μm and 198 μm, respectively. The uncertainty in both measurements was of about ± 6 μm that represents about ± 3 percent of error, and, therefore,

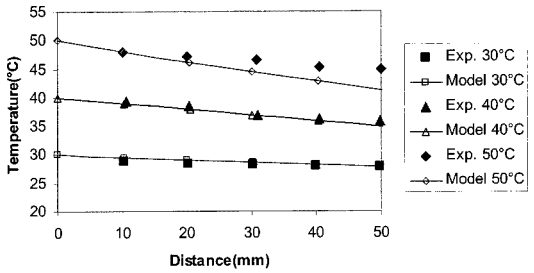

Fig. 6 Experimental temperature measurements [dots] for a single stream of in-flight water droplets (200 μm in diameter) doped with pyrene/CDBAC dye at 5 mM concentration, and a comparison with results of a theoretical model (solid lines), for initial temperatures of 30, 40, and 50°C

not appreciable difference in size was found, and it can be inferred that the evaporation process has little significance.

The first data point was taken at 10 mm after the jet was completely separated into uniform droplets to insure that droplets were spherical during the temperature readings. Near to the nozzle the jet is unstable and there is a deformed jet instead of discrete particles. In order to process the data for single droplets with the methodology presented in this work it is necessary to have a discrete and stable image of the object in order to determine both the excimer and monomer.

The droplet temperature measurements can be considered as surface based or volume average based. The droplet optical density (DOD) determines which region of the droplet will fluoresce and consequently from which region the temperature will be read [12]. The absorption across of the droplet determines whether the determined temperature is surface or volume averaged. For this case the molar extinction coefficient of the solution pyrene/CDBAC/water at 337 nm was measured with a UV/Vis spectrophotometer Cintra 40 given the value of 0.72×10^3 liter/mole-cm, and for a 200 μm droplet the optical droplet density ($\mathrm{DOD}=\varepsilon \cdot X \cdot D$, where ε is the molar extinction coefficient, X concentration, and D is the droplet diameter) was of $0.072(<1)$. These values indicate that the fluorescence was originated from all regions of the droplet and therefore this thermometer can be interpreted as volume-averaged of the droplets. For cases of low optical density ($\mathrm{DOD}<1$) the distribution of fluorescence is affected by the refraction phenomena at the droplet/air interface. In the present work there is no information of this spatial distribution of the fluorescence. A more detailed description of the transient temperature field within the droplet can be obtain using different techniques such as the combination of droplet sliced imaging and fluorescence shift thermometry which was reported by Lu and Melton [23].

The uncertainty analysis was based in the variation of the number of frames and was developed using the classical analysis method given in [24]. The general rule of assigning the uncertainties at the same 95 percent probability level for all analysis was followed. Thus, it is demonstrated that temperature measurements of water droplets can be obtained with LIF with a precision of 1.14, 3.17, and 6.31°C for the initial temperatures of 30, 40, and 50°C, respectively. It is important to note that the uncertainty increases, as the temperature increases, this could be a consequence from instability in the droplets at a given point of their path when the temperature increases and due to the fact that in the region of 50°C the sensibility of the calibration curve is low. For this reason the number of 30 frames taken for 30°C, was increased for the temperatures of 40 and 50°C in order to reduce the uncertainty in the measurements.

The validity of the present noninvasive LIF thermometry technique was verified by comparing the experimental results with a numerical simulation for in-flight stream of droplets. The mathematical model for in-flight droplets was based on a one-

dimensional Lagrangian viewpoint as presented by Gonzalez and Black [3] which considers the droplets to be spherical in shape, and neglects collision or coalescence between droplets. The resulting set of conservation of momentum, energy and mass equations are given as follows:

$$\frac{d(D^3 u_d)}{dt} = (D^3 g) - \left(\frac{3}{4}\right)\left(\frac{\rho_m}{\rho_l}\right) D^2 C_d (u_d - u_\infty)|u_d - u_\infty| \quad (2)$$

$$\frac{dT_d}{dt} = \frac{3h_{fg}}{c_{pl}} \frac{d\ln(D)}{dt} - \frac{6h}{D\rho_l c_{pl}} (T_d - T_\infty) \quad (3)$$

$$\frac{dD}{dt} = -2\left(\frac{M_v}{M_m}\right)\left(\frac{\rho_m}{\rho_l}\right)\left(\frac{\Delta p}{p_b}\right)\left(\frac{\mathrm{Dif}}{D}\right)(2.0 + 0.6 Sc^{1/3} \mathrm{Re}^{1/2}) \quad (4)$$

These equations were solved using the Runge Kutta fourth order method. The properties for air were evaluated from [25], for water from [26] and the diffusivity was obtained from [27]. The results of the simulation are shown in Fig. 6 and compared with the experimental data in the same figure.

It can be observed from the figure that the numerical simulation shows a good agreement with the experimental data for all three cases with a minor exception for the injection at a temperature of 50°C. Since the model considers that the droplets are completely spherically when it leaves the nozzle, the validation exercise was limited to a starting point 10 mm of distance from the nozzle tip when the droplets were observed to be completely spherical.

Finally it is important mention that the technique presented here has advantages over other fluorescence techniques where band emissions are taken separately. Normally the measurements of fluorescence droplets emissions corresponding to the monomer and the excimer are measured sequentially, first the excimer and then the monomer. Other important aspect of the present technique is that the complete field of droplets was taken in only one frame and its temperature was extracted directly from it.

5 Conclusions

The present work presents an innovative fluorescence sensor and an optical technique to apply the two bands Laser Induced Fluorescence Thermometry to perform simultaneous measurements of both fluorescence emissions, the excimer and the monomer, for an entire stream of droplets when flying into a quiescent environment. The sensor used was a solution of pyrene/CDBAC/water that allowed the solubilization of pyrene in water. This fluorescence water sensor is insensitive to the presence of oxygen making it robust for field measurements. The optical technique determines the temperature by averaging the emissions for a given number of frames.

The technique was applied to a single stream of droplets with diameter equal to 200 μm traveling a distance of 50 mm for three different initial conditions, 30, 40, and 50°C. The experimental results showed that the temperature decreases along the jet and the final temperature for a 50 mm path depends on the initial temperature which will affect the heat and mass transfer between the droplets and the ambient. The accuracy in determining the instantaneous temperature of the droplet depends on temporal variations of the images of the droplets between frames, and of the sensitivity of the calibration curve. The uncertainty analysis considering these variables showed that temperature measurements for falling droplets could have maximum errors of 1.14, 3.17, and 6.31°C for the initial temperatures of 30, 40, and 50°C, respectively.

The technique showed a good agreement when compared to numerical results from a mathematical model for single in-flight and evaporating droplets. Experimental results compared very favorably to the numerical results data sets.

The present technique improved the variability in the data acquisition process over previous attempts to apply LIF thermometry for in-flight droplets mainly because only one frame is used to characterize the entire thermal field of the droplet stream reducing typical errors for situations where the measurements are the averaged from two separate fluorescence emission events.

Nomenclature

C_d = drag coefficient
D = diameter of a droplet
Dif = diffusivity of water vapor in air
M = molecular weight
Re = Reynolds number of the droplet $= Du_d/\nu$
Sc = Schmidt number $= \nu/\mathrm{Dif}$
T = temperature
c_p = specific heat of liquid
g = acceleration of gravity
h = heat transfer coefficient for liquid droplets
h_{fg} = latent heat of vaporization of water
p = pressure
t = time
u = velocity component in the axial direction

Greek Symbols

Δp = water vapor pressure difference at the drop surface $= p_s - p_v$
ν = cinematic viscosity
ρ = density

Subscripts

b = dry air
d = droplet value
m = value of the mixture in the buoyant jet
l = liquid water
s = saturation
v = water vapor
∞ = surroundings

References

[1] Hall, H. H., and Mudawar, I., 1995, "Experimental and Numerical Study of Quenching Complex-Shaped Metallic Alloys With Multiple Overlapping Sprays," Int. J. Heat Mass Transfer, **38**, pp. 1202–1216.
[2] Sehmbey, M. S., Pais, M. R., and Mahefkey, T., 1995, "Effect of Spray Cooling With Liquid Nitrogen," J. Thermophys. Heat Transfer, **9**(4), pp. 757–765.
[3] Gonzalez, J. E., and Black, W. Z., 1997, "Study of Droplet Sprays Prior to Impact on a Heated Horizontal Surface," ASME J. Heat Transfer, **119**, pp. 279–287.
[4] Ranz, W. E., and Marshall, Jr., W., 1952, "Evaporation From Drops Part II," Chem. Eng. Prog., **48**, pp. 173–180.
[5] Van Beeck, J. P. A. J., Giannoulis, D., Zimmer, L., and Riethmuller, M. L., 2001, "Global Rainbow Thermometry For Average Temperature Measurement of Spray Droplets," *Proc. 10th International Symposium on Applications of Laser Techniques to Fluid Mechanics*, Lisbon, 10–13 July.
[6] Richards, C. D., and Richards, R. F., 1998, "Transient Temperature Measurements in a Convectively Cooled Droplet," Exp. Fluids, **25**, pp. 392–400.
[7] Sakakibara, J., and Adrian, R. J., 1999, "Whole Field Measurement of Temperature in Water Using Two-Color Laser Induced Fluorescence," Exp. Fluids, **26**, pp. 7–15.
[8] Ravel, O., 1999, "Aplication a la Mesure de la Temperature de Gouttes Dans un Ecoulement Diphasique, en Combustion et en Impact Parietal," Ph.D. thesis, L'ecole Nationale Seperieure de L'aeronautique et de L'space, France.
[9] Murray, A. M., and Melton, L. A., 1985, "Fluorescence Methods for Determination of Temperature in Fuel Sprays," Appl. Opt., **24**, pp. 2783–2787.
[10] Gossage, H. E., and Melton, L. A., 1987, "Fluorescence Thermometers Using Intermolecular Exciplexes," Appl. Opt., **26**, pp. 2256–2259.
[11] Wells, M., and Melton, L., 1990, "Temperature Measurements of Falling Droplets," ASME J. Heat Transfer, **112**, pp. 1008–1013.
[12] Hanlon, T. R., and Melton, L. A., 1992, "Exciplex Fluorescence Thermometry of Falling Hexadecane Droplets," ASME J. Heat Transfer, **114**, pp. 450–457.
[13] Kadota, T., Miyoshi, K., and Tsue, M., 1993, "Exciplex Method for Remote Probing of Fuel Droplet Temperature (Effects of Ambient Conditions of Fluorescence)," Japan Society of Mechanical Engineering Journal, **36**, pp. 371–377.
[14] Yoshizaki, T., Takemura, Y., Hisaeda, T., Nishida, K., and Hiroyasu, H., 1996, "Planar Measurements of the Liquid Phase Temperature in Diesel Sprays Injected into High-Pressure and High Temperature Environments," International Spring Fuels & Lubricants Meeting, Dearborn, Michigan, No. 961202, pp. 1–16.
[15] Escobar, S., González, J. E., and Rivera, L., 2001, "Laser Induced Fluorescence Temperature Sensor for In-Flight Droplets," Journal of Experimental Heat Transfer, **14**, pp. 119–134.

[16] Parrado, M., 2000, ''Characterization of In-Flight Droplets Generated by Thermal Ink-Jet Print Heads,'' M.S. thesis, University of Puerto Rico, Mayagüez.
[17] Kim, H. J., and Kihm, K. D., 2001, ''Application of a Two-Color Laser Induced Fluorescence (LIF) Technique for Temperature Mapping,'' *Proc. of 2001 ASME Int. Mechanical Engineering Congress and Exposition*, New York, 11–16 November, IMECE2001/HTD-24411.
[18] Kim, H. J., Kihm, K. D., and Allen, J. S., 2003, ''Examination of Ratiometric Laser Induced Fluorescence Thermometry for Microscale Spatial Measurement Resolution,'' Int. J. Heat Mass Transfer, **46**, pp. 3967–3974.
[19] Lavieilli, P., Lemoine, F., Lavergne, G., Virepinte, J. F., and Lebouche, M., 2000, ''Temperature Measurements on Droplets in Monodisperse Stream Using Laser-Induced Fluorescence,'' Exp. Fluids, **29**, pp. 429–437.
[20] Birks, J. B., 1970, *Photophysics of Aromatic Molecules*, Wiley-Interscience, New York.
[21] Okano, L. T., El Seoud, O. A., and Halstead, T. K., 1997, ''A Proton NMR Study on Aggregation of Cationic Surfactants in Water: Effects of the Structure of the Headgroup,'' Colloid and Interface Science, **275**(2), pp. 138–145.
[22] Takahashi, F., Schmoll, W., and Dressler, J., 1994, ''Characterization of a Velocity-Modulation Atomizer,'' Rev. Sci. Instrum., **65**(11), pp. 3563–3569.
[23] Lu, Q. Z., and Melton, L. A., 2000, ''Measurement of Transient Temperature Field Within a Falling Droplet,'' AIAA J., **38**(1), pp. 95–101.
[24] Figliola, R. S., and Beasley, D. E., 2000, *Theory and Design for Mechanical Measurements*, John Wiley & Sons, Inc., pp. 159–161.
[25] Johnson, R. W., 1998, *The Handbook of Fluid Dynamics*, CRC Press, Washington, D.C., USA, pp. C-2–C-3.
[26] Moran, M. J., and Shapiro, H. N., 2000, *Fundamentals of Engineering Thermodynamics*, John Wiley & Sons, Inc., New York, USA, p. 804.
[27] Mills, A. F., 2001, *Mass Transfer*, Prentice Hall, Inc., New Jersey, USA, p. 391.

Journal of Heat Transfer

Technical Notes

This section contains shorter technical papers. These shorter papers will be subjected to the same review process as that for full papers.

Spectral Emittance of Particulate Ash-Like Deposits: Theoretical Predictions Compared to Experimental Measurement

S. P. Bhattacharya
e-mail: spb@cleanpower.com.au
Cooperative Research Centre for Clean Power from Lignite, 8/677 Springvale Road, Mulgrave, Victoria 3170, Australia

This note presents results of a theoretical and experimental investigation on the emittance of particulate deposits. A simple model based on independent and multiple scattering and using discrete ordinate method has been developed to predict the spectral hemispherical and normal emittance of particulate deposits. The model predictions are compared with measurements carried out under this study-controlled spectral emission measurements between wavelengths of 2 and 12 μm on deposits of ground synthetic ash particles having known composition and particle size. The trends from the predictions matched well with the measured values, except for some differences in the wavelength region below 4 μm, and between 8 μm and 12 μm wavelength. Possible reasons for these differences are discussed. [DOI: 10.1115/1.1666885]

Keywords: Absorption, Experimental, Heat Transfer, Radiation

Introduction

Determination of emittance of particulate deposits is important in several applications such as radiative heat transfer and on-line monitoring of deposits in pulverised fuel (*pf*) fired furnaces [1], state of refractory in industrial furnaces [2], remote sensing, high-temperature energy saving materials, and stealth technology. Emittance (ε) of a surface, particulate or otherwise, is commonly defined as the ratio of its emission rate (E) to that from a blackbody (E_B) at the same temperature ($\varepsilon = E/E_B$). Emittance can be defined as hemispherical (ε_h) or normal (ε_n) depending on the direction of measurement, and as spectral (ε_λ) or total (ε_t) in which case it is referred to part or the entire wavelength spectrum with reference to the direction and spectral range. It can be defined as a combination of any two of the above. Spectral emittance can be used to calculate the total emittance [3]. Studies on emittance of particulate deposits are not common, particularly both modeling and spectral measurements with particle size relevant to deposits in *pf* fired furnaces. Studies by Boow and Goard [4] and Brajuskovic et al. [5] are on total emittance measurements of deposits at surface temperatures ranging from 200 to 1000°C showing the effect of temperature on total emittance. The study by Wall and Becker [3] is on spectral band measurements at temperatures ranging from 700 to 1000°C and shows the effect of iron content and temperature. The study by Markham et al. [6] is the only study, which shows comparison of theoretical and measured values of spectral emittance of ash deposits. Their model was based on 2-flux theory, and the model used an adjustable value for the asymmetry parameter (g) to get good match with measured values. Studies by Wall et al. [7] and Bhattacharya et al. [8,9] present theoretical predictions and separate measurements on the effects of particle size and concentration, physical state, heating, and iron content on spectral emittance of ash deposits. However, the predictions were not directly compared with measurements of the same particle size.

This paper presents results from a theoretical and experimental study on emittance of ash-like particulate deposits. A simple model has been developed for prediction of spectral hemispherical and spectral normal emittance of particulate deposits. The predictions can be made as a function of particle size, particle concentration, and optical constants (real and absorption indices, which in turn are function of chemical composition). Predictions from the model are then compared with spectral measurements on ash-like particulate deposits using emission spectrometry.

Model and Input Parameters

The ash deposit is modeled to be one dimensional axisymmetric layer. The equation for radiative transfer [10] is approximated using the discrete ordinate method with 16 ordinate directions, and weighting fractions corresponding to the solid angle represented [11]. Using appropriate boundary conditions, spectral reflectance (ρ) and spectral transmittance (τ) of the layer is calculated, from which absorbance (α) can be calculated as follows:

$$\alpha = 1 - \tau - \rho \tag{1}$$

According to Kirchoff's law, spectral emittance is equal to the spectral absorbance which may be evaluated from Eq. (1). For an opaque deposit, the thickness of the layer can be adjusted so that spectral transmittance is 2 percent or less, which is arbitrarily assumed to be the limit of opacity in the calculations. Spectral single particle properties (scatter matrix, extinction efficiency) were calculated using Mie theory using a code in Bohren and Huffman [12]. The following assumptions are made in the model: the particles in the deposit are spherical in shape, and all particles have same chemical composition, i.e., they have same complex refractive index. Also, only independent and multiple scattering is considered in the model. Further details of the model are available in Bhattacharya [13].

The model requires complex refractive index—real (n) and absorption index (k), density of deposit materials, and particle size (or distribution) as input parameters. Values of these input parameters were taken from Goodwin [14]. The samples used for model

Contributed by the Heat Transfer Division for publication in the JOURNAL OF HEAT TRANSFER. Manuscript received by the Heat Transfer Division September 11, 2002; revision received July 1, 2003. Associate Editor: S. T. Thynell.

Table 1 Composition (wt%) and Density (kg/m^3) of the samples

Sample	SiO_2	Al_2O_3	CaO	Fe_2O_3	Density
S2	54.95	27.25	15.80	2.00	2550
S10	50.46	24.87	14.67	10.00	2630

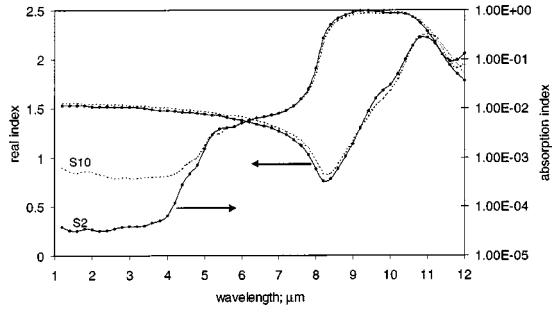

Fig. 1 Spectral complex refractive index of the samples used in model predictions [14]

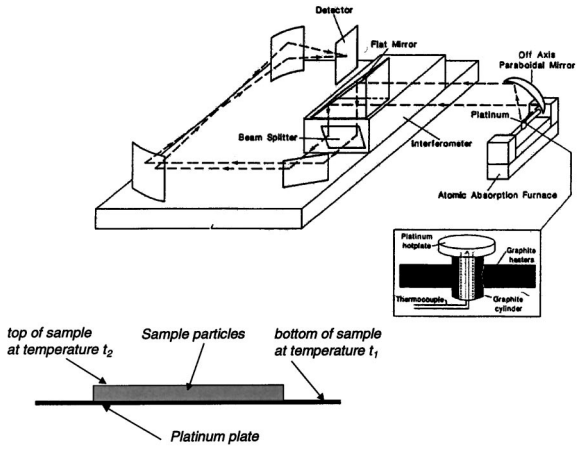

Fig. 2 Experimental setup (published with permission from Applied Spectroscopy)

predictions and in experiments vary in iron content from 2 percent to 10 percent. Goodwin obtained the real and absorption indices, *n* and *k*, from normal reflectance and transmission measurements on polished wafers of synthetic ash slags. Table 1 shows the composition and density, and Fig. 1 shows the spectral complex refractive index of the samples. As is evident from Fig. 1, the spectral absorption index increases with increasing iron content between wavelengths from 1.2 to 4 μm; thereafter the values are similar. The real index shows little increase with iron content between 1.2 and 8 μm wavelength. It varies from about 1.6 at 1.2 μm wavelength to below 1 at 8 μm, thereafter rising above 2. Among the samples, sample S2 is weakly absorbing and sample S10 is strongly absorbing. The predictions made in this paper are for isothermal and opaque deposits consisting of monosized particles, and for spectral normal measurements. A modified form of the model can also be used for prediction of spectral hemispherical emittance, apparent emittance of nonisothermal particulate deposits opaque and semi-transparent deposits [9], and radiative heat transfer calculations in one-dimensional geometry.

Experimental Work

Experimental work involving emission spectrometry was undertaken on particulate deposits to measure their spectral normal emittance, which are then compared with model predictions. The experimental equipment is located at the Division of Coal and Energy Technology, CSIRO at North Ryde in Sydney. It has primarily been used to study the structural changes occurring in coal and other minerals on heating [15,16]. The infrared emission cell consists of a modified atomic absorption graphite rod furnace and is illustrated in Fig. 2. The furnace was driven by a thyristor controlled ac power supply capable of delivering up to 150 amps at 12 volts. A platinum disk (6 mm diameter), which acts as a hotplate to heat the sample, is placed on the graphite rod. An insulated 125 μm type *R* thermocouple was embedded inside the platinum in such a way that the thermocouple junction was <0.3 mm below the surface of the platinum (Fig. 2 inset). Temperature control of ± 3°C at the maximum operating temperature of 1500°C was achieved by using an Eurotherm Model 808 proportional temperature controller, coupled to the thermocouple. An off-axis paraboloidal mirror with a focal length of 25 mm mounted above the heater captured the infrared radiation and directed it into a Digilab FTS-60A Fourier transform infrared spectrometer. The heater assembly was located so that the surface of the platinum was slightly above the focal point of the off-axis paraboloidal mirror. With this geometry, a spot of approximately 3 mm diameter is sampled by the spectrometer. The modifications to the spectrometer involved the removal of the aperture assembly and replacing it with a mirror. Reflection of modulated radiation back from the interferometer to the sample with subsequent additional modulation has been identified as a problem with this type of measurement. Very little distortion of the spectra due to this effect is observed. A room temperature Deuterated Triglycine Sulfate (DTGS) detector was used and as a result is not responsive to emission from surrounding objects. The entire spectrometer and sample furnace was covered with a perspex box which was purged with nitrogen to remove IR absorption by water vapor and carbon dioxide in the path of the sample emission.

Samples Used. Two different particulate samples were used in the measurement. These are slag samples ground after melting oxide mixtures at 1550°C in proportion similar to those found in power station ash. Particles of such samples are expected to be of uniform composition, which is presented in Table 1. To illustrate the effect of size on emittance, sample S2 (2 percent Fe_2O_3) was separated into two size groups, one having a size range of 5–35 μm (Sauter mean diameter of 12.9 μm), the other being sieve sized 45–53 μm. One size group of the sample S10 was used in the experiment, with a size range of 5–33 μm (Sauter mean diameter of 14.9 μm). A comparison of emittance between the samples S2 and S10 is intended to illustrate the effect of composition.

Experiment Procedure. The sample to be analyzed is carefully spread over the platinum surface. The sample heated to the desired temperature, was held at this temperature while accumulation of single beam spectrum took place. The spectra were recorded with the use of 64 scans at a nominal resolution of 4 cm^{-1}. The emittance measured at 600°C is used in this paper. A graphite plate with the same geometry as that of the platinum plate was used to approximate a blackbody source. Spectra from the graphite plate and the platinum plate were acquired at the same temperatures as those of the samples and stored for later use.

To ascertain the opaqueness, the samples were first subjected to transmission measurements before undertaking emission experiments. Thus for the same sample, two sets of spectral measurements, transmission and emission, were carried out. An infrared microscope was used for the purpose and the sample particles were spread horizontally over a 6 mm diameter area of a KBr window. For all the samples, concentration was such that the spectral transmittance across the layers was between 1 and 10 percent, but mostly under 2 percent. This amounted to using approximately

10 mg of sample. This compared favourably with the findings from another study [8] by the author, where it was observed that a sample density of about 400 gm/m^2 resulted in an opaque layer ($<$2 percent transmittance) for such samples.

Calculation Procedure. For a sample particulate layer distributed on the platinum plate during measurement (as shown in Fig. 2) emittance was determined as follows:

$$\varepsilon_{S,\lambda} = \left(\frac{I_{S,t2} - \tau \times I_{bg,t1}}{I_{bb,t2}} \right) \times \varepsilon_{g,\lambda} \tag{2}$$

where,

I_S = the intensity from the sample, as measured
I_{bg} = the intensity from the platinum plate, as measured
I_{bb} = the intensity from the graphite plate, as measured
τ = transmission across the sample, average of three measurements from the IR microscope
ε_g = spectral emittance of graphite, from Toloukian and Ho [17]

The temperature t_1 is measured during the experiment, whereas t_2 depends on the thermal conductivity (k) and thickness (t) of the sample layer, and radiative (and/or convective) loss from the surface. The transmittance (τ) depends primarily on the layer thickness. A procedure to estimate the top temperature t_2 and its effect on sample emittance is outlined in Bhattacharya [13]. It was observed that for the sample mass used in the experiment, the temperature t_2 was not significantly below the temperature t_1, and therefore, $I_{bb,t1}$ (which was measured) instead of $I_{bb,t2}$ was used in Eq. (2) to estimate the sample emittance. The contribution from the intensity emitted from the platinum plate was taken into account using Eq. (2). Data manipulation was performed on the interferograms.

Estimation of Error. The error estimation procedure has been formulated following Coleman and Steele [18]. The sources of error involve uncertainties in transmission measurement, uncertainties in the spectral emittance of the graphite plate, uncertainties in measurement of the intensity from the graphite plate, platinum plate and the samples. The details are presented in Bhattacharya [13]. The overall error in the measured emittance is estimated to be ± 0.06.

Comparison of Predicted and Measured Emittance

Effect of Size. Results of model predictions and measurements are presented in Figs. 3 and 4. In Fig. 3, predictions are made for the upper, lower and the mean size of the particles used. In Fig. 4, predictions are shown only for the mean size of the sample. In both figures, particulate character, as predicted earlier,

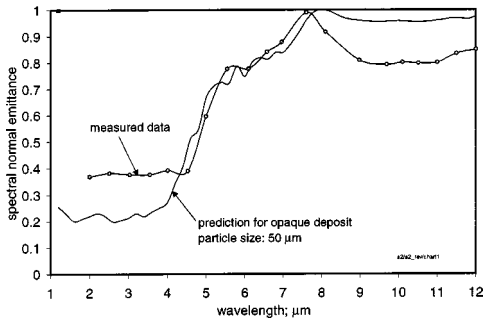

Fig. 4 Comparison of measured and predicted emittance of ash-like particulate deposits: sample S2, size range; 45–53 μm, mean diameter 50 μm.

of the emissive layer is evident. Measured emittance, as well as the predicted values are close to 1 between 7 and 8 μm wavelength. This is the region of Christiansen Effect, where real index (n) of the sample is 1, the real index of the surrounding medium. In fact, Goodwin's samples have real index of 1 between 7 and 8 μm wavelength. Apart from the reason of having similar composition, the similarity in real index values justifies the use of the complex refractive index of Goodwin's samples in the predictive calculations.

The model appears to underpredict emittance at wavelength below 4 μm, and overpredict above 8 μm wavelength. The model considers independent theory, multiple scattering, homogeneous composition and spherical particles. The slag particles are expected to be of homogeneous composition because of melting during preparation. Also, the radiative properties of an aggregate of irregular shaped particles are not affected significantly by the deviation of their shape from spherical [19,20]. Therefore, a comparison of the figures shows largely the effect of size on emittance, rather than the effects of irregular shape or inhomogeneous composition. Also, the larger particles recorded higher emittance, a trend consistent with predictions. The measurements indicate that spectral emittance of particulate deposits could be as low as 0.3 at low wavelengths, supporting the trend in model predictions and industrial measurements reported by Carter et al. [21]. The effect of particle size is primarily limited to the wavelength region below 6 μm, again supporting the predictions.

Apart from composition and particle size, emittance of a deposit depends on strongly coupled ways with its thermal conductivity, porosity and physical structure [22]. The effects of Dependent interactions, physical structure, or possible variation in thermal conductivity of the particles have not been considered in the simple model. Even then, good qualitative agreement is evident between the predicted and measured values.

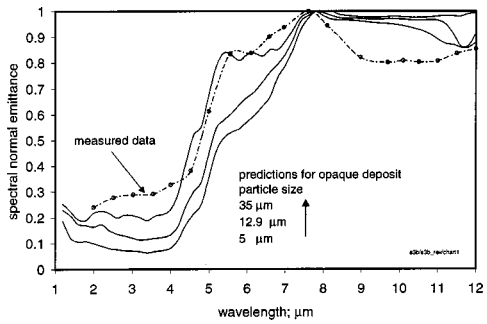

Fig. 3 Comparison of measured and predicted emittance of ash-like particulate deposits: sample S2, size range; 5–35 μm and sauter mean diameter 12.9 μm.

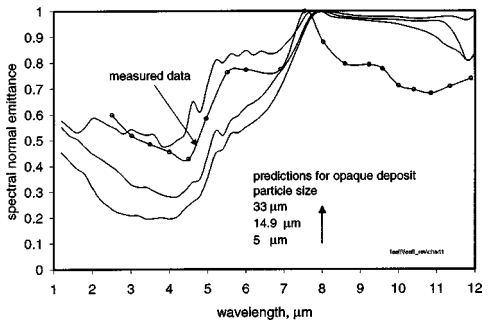

Fig. 5 Comparison of measured and predicted emittance of ash-like particulate deposits: sample S10, size range; 5–33 μm and sauter mean diameter 14.9 μm.

In a *pf* fired furnace, low wall emittance such as 0.3 may result in a decrease in heat absorption, and, therefore, in an increase in furnace exit temperature. The approximate changes in furnace exit temperature may be estimated by a well-mixed furnace model [23]. The model assumes a uniform build-up of ash deposits over the complete furnace walls, and requires, among others, total absorbance of the wall deposits as input. Spectral absorbance of a deposit is equal to the spectral emittance and the total absorbance of a deposit may be estimated once the spectral emittance and the flame temperatures are known [7]. It is estimated that for a 660 MWe *pf* fired furnace, a change in wall emittance from 0.7 (clean tube) to a low value of 0.3 affects the furnace heat absorption in a way that the exit gas temperature increases by 150°C.

Effect of Composition. Figure 5 shows the measured emittance of particulate deposits of sample S10. The ground particles of samples S2 and S10 had Sauter mean diameters of 12.9 μm and 14.9 μm, respectively. Both these samples had comparable amounts of silica, alumina and calcium oxide, and also similar particle sizes, so that a comparison of Figs. 3 and 5 reveals the difference predominantly due to the variation in iron content. As is evident, sample S10 with the higher iron content gave a higher emittance and the effect of iron is limited to wavelengths below 5 μm, a trend matched with the predictions [9]. The increase in emittance with iron content is due to the higher absorption index associated with high iron bearing sample (Fig. 1) at low wavelengths. As may be seen from Fig. 5, sample S10 showed a sharp drop in emittance at all temperatures going from 2 to 4 μm wavelength. In a separate experimental study involving reflectance and transmission spectroscopy (as opposed to emission and transmission spectroscopy used in this study), Bhattacharya et al. [8] observed that the difference between independent theory based predictions and the measured emittance of an opaque deposit is greater for weakly absorbing samples than strongly absorbing samples. Similar observations can be noted from Figs. 3–5.

Conclusions

This note presents results of a theoretical and experimental investigation of the emittance of particulate deposits. A simple model based on independent and multiple scattering has been developed to predict the spectral emittance of particulate deposits. The model predictions are compared with spectral emission measurements between 2 and 12 μm wavelength on deposits of ground synthetic ash particles having known composition and particle size. Emittance of particulate deposits is highly spectral. The measurements and the predictions show that fine particulate layers could be reflective, with emittances less than 0.3 especially at wavelengths below 4 μm. Such layers are formed during the initiation of deposits in *pf* furnaces. Layers of coarse particles are predicted to have higher emittance, a trend matched by measurements under this study. The effect of composition, in particular iron content, on emittance of deposits is found to be significant, with samples having higher iron content recording higher emittance. The effects are limited primarily to the wavelength region below 6 μm. This region is of primary interest to radiative heat transfer in *pf* fired furnaces. Even though there is good qualitative agreement between the model predictions and measured values, there are differences in the 1–4 μm wavelength, and again between 8–12 μm wavelength region. Further modeling efforts should be expended in improving the predictions, particularly incorporating the dependent effects [8]. Very few studies have been reported in the literature dependent effects have on emittance of ash deposits. All these studies [24–26] are limited to either very small particles (Rayleigh size) or very large particles (geometric range), but none of intermediate size range relevant to ash deposits in *pf* fired furnaces.

Acknowledgment

The author acknowledges Dr. Tony Vassallo of the CSIRO, Division of Energy Technology for allowing the use of his equipment, and assistance during measurements.

References

[1] Elliston, D. G., Gray, W. A., Hibberd, D. F., Ho, T. Y., and Williams, A., 1987, "The Effect of Surface Emissivity on Furnace Performance," J. Inst. Energy, pp. 155–167.
[2] Debellis, C. L., 1991, "Effect of Refractory Emittance in Industrial Furnaces," *Fundamentals of Radiative Heat Transfer*, HTD Vol. 160., pp. 104–115.
[3] Wall, T. F., and Becker, H., 1984, "Total Absorptivities and Emissivities of Particulate Coal Ash from Spectral Band Emissivity Measurements," ASME J. Eng. Gas Turbines Power, **106**, pp. 771–776.
[4] Boow, J., and Goard, P. R. C., 1969, "Fireside Deposits and Their Effect on Heat Transfer in a Pulverised Fuel Fired Boiler," Fuel, pp. 412–418.
[5] Brajuskovic, B., Uchiyama, M., and Makino, T., 1991, "Experimental Investigation of Total Emittance of Power Plant Boiler Ash Deposits," Experimental Heat Transfer, Fluid Mechanics, and Thermodynamics, J. F. Keffer et al., eds., Elsevier.
[6] Markham, J. R., Solomon, P. R., Best, P. E., and Yu, Z. Z., 1992, "Measurement of Radiative Properties of Ash and Slag by FT-IR Emission and Reflection Spectroscopy," ASME J. of Heat Transfer , **114**, pp. 458–464.
[7] Wall, T. F., Bhattacharya, S. P., Zhang, D. K., Gupta, R. P., and He, X., 1993, "The Properties and Thermal Effects of Ash Deposits in Coal Fired Furnaces," Prog. Energy Combust. Sci., **19**, pp. 487–504.
[8] Bhattacharya, S. P., Wall, T. F., and Schuster, M. A., 1997, "A Study on the Importance of Dependent Radiative Effects in Determining the Spectral and Total Emittance of Particulate Ash Deposits in Pulverised Fuel Fired Furnaces," J. of Chemical Engineering and Processing, **36**(6), pp. 423–432.
[9] Bhattacharya, S. P., 2000, "A Theoretical Investigation of the Influence of Optical Constants and Particle Size on the Radiative Properties and Heat Transfer Involving Ash Clouds and Deposits," J. of Chemical Engineering and Processing, **39**(5), pp. 471–483.
[10] Siegel, R., and Howell, J. R., 1992, *Thermal Radiation Heat Transfer*, Hemisphere Publishing, Washington.
[11] Chandrasekhar, S., 1960, *Radiative Transfer*, Dover Publications, NY.
[12] Bohren, C. F., and Huffman, D. R., 1983, *Absorption and Scattering of Light by Small Particles*, John Wiley and Sons.
[13] Bhattacharya, S. P., 1995, "The Radiative Properties and Thermal Effects of Ash Clouds and Deposits in Pulverised Fuel Fired Furnaces," Ph.D. Thesis, The University of Newcastle, Australia.
[14] Goodwin, D. G., 1986, "Infrared Optical Constants of Coal Slags," Ph.D. thesis, Stanford University.
[15] Vassallo, A. M., Cole-Clarke, P. A., Pang, L. S. K., and Palmisano, A. J., 1992, "Infrared Emission Spectroscopy of Coal Minerals and Their Thermal Transformations," Appl. Spectrosc., **46**(1), pp. 73–78.
[16] Vassallo, A. M., and Finnie, K. S., 1992, "Infrared Emission Spectroscopy of Some Sulfate Minerals," Appl. Spectrosc., **46**(10), pp. 1477–1482.
[17] Touloukian, Y. S., and Ho, C. J., 1989, Thermal Radiative Properties of Nonmetallic Solids, **8**, Plenum Press, New York.
[18] Coleman, W., and Steele, G., 1989, *Experimentation and Uncertainty Analysis for Engineers*, John Wiley, NY
[19] Viskanta, R., and Menguc, M., 1987, "Radiation Heat Transfer in Combustion Systems," Prog. Energy Combust. Sci., pp. 97–160.
[20] Wenlan, X., and Shen, S. C., 1997, "Infrared Emittance of Medium Containing Nonsphere-Shaped Particles," Applied Optics, **36**(7), pp. 1644–1649.
[21] Carter, H. R., Kokdsal, C. G., and Garabrant, M. A., 1992, "Furnace Cleaning in Utility Boilers Burning Powder River Basin Coals," *Proc. International Power Generation Conference*, Atlanta.
[22] Baxter, L. L., 1993, "In Situ Real Time Emission FTIR Spectroscopy as a Diagnostic for Ash Deposition During Coal Combustion," *Proc. Engineering Foundation Conference*, Solihull, UK.
[23] Hottel, H. C., and Sarofim, A. F., 1967, *Radiative Transfer*, McGraw Hill.
[24] Yamada, Y., Cartigny, J. D., and Tien, C. L., 1986, "Radiative Transfer With Dependent Scattering by Particles: Part 2—Experimental Investigation," J. Heat Transfer, **108**, pp. 608–613.
[25] Kumar, S., and Tien, C. L., 1990, "Dependent Absorption and Extinction of Radiation by Small Particles," J. Heat Transfer., **112**, pp. 178–185.
[26] Mazza, G. D., Berto, C. A., and Barreto, G. F., 1991, "Evaluation of Radiative Heat Transfer Properties in Dense Particulate Media," Powder Technol., **67**, pp. 137–144.

A Model of Heat and Mass Transfer Beneath an Ablating Concrete Surface

Michael Epstein
Fauske & Associates, Inc., 16W070 West 83rd Street, Burr Ridge, IL 60527

This paper presents a one-dimensional steady-state model of heat and water vapor transport just beneath an ablating concrete surface. In the model an evaporation front separates a dry porous region through which water vapor flows to the ablation front from a semi-infinite region that is partially wet with evaporable water. The predicted water vapor pressures at the evaporation front are quite high and could conceivably cause the concrete to spall. The model is quantitatively compatible with spallation events observed during tests involving the pouring of molten steel onto concrete and is capable of explaining the disparate results obtained in two rather extensive test series on the penetration of induction heated metallic pools into concrete. [DOI: 10.1115/1.1666884]

Keywords: Ablation, Decomposition, Heat Transfer, Porous Media, Vaporization

Introduction

Studies of postulated severe accidents in nuclear reactors have included consideration of the consequences of molten core debris draining from the reactor vessel onto the horizontal surface of the concrete foundation below the reactor vessel. Extensive experimental studies of the erosion rate of concrete by overlying molten steel were carried out at Sandia National Laboratory [1–3] and at Kernforshungszentrum Karlsruhe (KfK), Germany [see, e.g. [4],[5]]. In the KfK (so-called BETA) experiments and in the Sandia experiments the melt/concrete interaction was sustained by an induction heating coil placed around the interaction vessel. The metallic pool penetration rates measured in the BETA experiments were up to an order-of-magnitude higher than those reported by Sandia for similar pool temperatures and identical concrete substrates. In considering this discrepancy, for which no defensible explanation has yet been offered, it is proposed here that intense impingement heat transfer during the initial pouring of the steel melt from a relatively high elevation into the BETA test-section concrete cavity resulted in early, rapid concrete erosion. The erosion rate was so rapid that the free water in the concrete exerted a high vapor pressure just beneath the concrete surface which caused concrete surface spallation that wiped away the slag resistance to heat transfer. Once started, the rapid erosion rate was self-sustaining. Surface spallation did not occur in the inductively heated melt pools in the Sandia tests because the steel melt was either gradually generated in the test section or the pour stream was too short to initiate surface spallation.

A one-dimensional model is presented below that supports a spallation mechanism in the BETA tests, based on the presence of readily vaporized water and available measurements of the permeability of concrete as a function of temperature. Before the model is introduced it will prove useful to review early experiments involving steel melts poured onto concrete in the absence of an applied heat source [6], since concrete spallation was observed in these experiments.

Contributed by the Heat Transfer Division for publication in the JOURNAL OF HEAT TRANSFER. Manuscript received by the Heat Transfer Division November 22, 2002; revision received June 17, 2003. Associate Editor: J. N. Chung.

Experiments of Powers and Arellano

Early in the Sandia molten core debris-concrete interaction test program, exploratory experiments were performed in which steel melts were poured from an induction furnace into concrete crucibles [6]. These tests involved 200 kg steel melts initially heated to about 2000 K. The experiments were not well instrumented and no further heating was applied to the melt once it was poured on the concrete. The melts cooled to the steel solidification temperature in about 4 minutes. Each concrete crucible was used several times. The frozen mass of metal from a previous experiment was removed and another test was initiated in the eroded crucible. Motion picture records of the tests in which melts were poured into ''fresh'' concrete crucibles revealed concrete spallation events. The concrete spall fragments that escaped the crucible were collected and their thicknesses were found to vary from 2 to 7 mm. From the motion picture records the mean ejection velocity of limestone-type concrete fragments was determined to be about 5 $\mathrm{m\,s^{-1}}$ while that of basaltic concrete was about 3.75 $\mathrm{m\,s^{-1}}$.

Physical Model

A schematic diagram of the problem we wish to solve is presented in Fig. 1. It is assumed that the evaporable water held by the concrete is converted into vapor some distance below the ablating concrete surface. The vapor flows upward (in the negative x-direction) with superficial velocity j_g through hot porous concrete to the ablating surface where it is released to the overlying molten debris pool. Heat is conducted from the ablation front through the porous region to the plane of evaporation at $x=\delta_d$. The evaporation plane separates the dry porous region of thickness δ_d from the semi-infinite concrete region $x>\delta_d$ that is partially wet with evaporable water. At the evaporation front the water exerts an equilibrium pressure $P_{eq}(T_{\mathrm{sat}})$ at the local temperature T_{sat}. The water vapor released at the plane of evaporation is transported across the porous region to the ablation front by the imposed pressure difference $P_{eq}(T_{\mathrm{sat}})-P_\ell$ where P_ℓ is the pressure in the overlying pool. The objective of the analysis is to compute the vapor pressure P_{eq} at the evaporation front.

The prediction of P_{eq} is based on the following set of simplifying assumptions which are examined more quantitatively in a subsequent section: (1) the ablation front propagates at a constant velocity v_m so that constant-pattern (steady-state) temperature

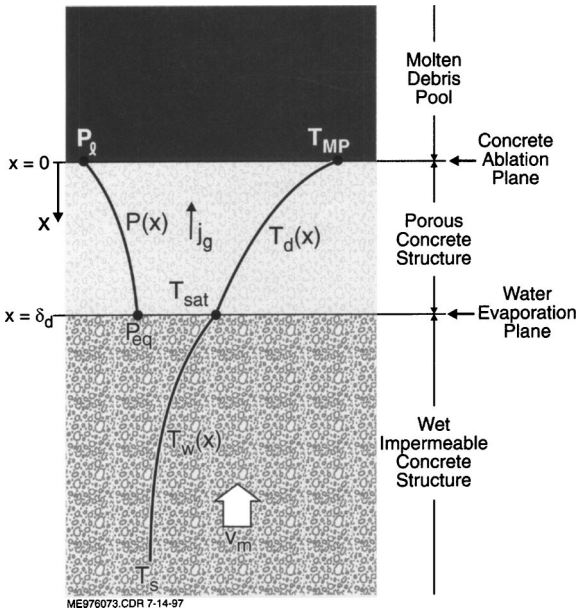

Fig. 1 Schematic diagram of concrete ablation model; indicating nomenclature and temperature and pressure profiles

profiles $T_d(x)$ and $T_w(x)$ are established in the dry and wet zones, respectively; (2) the evaporation plane is regarded as a sharp front that is very thin on the scale of the thickness of the porous region and the rate limiting process for concrete ''dehydration'' is taken to be water vapor convection (Darcy flow) through the porous layer between the water evaporation and concrete ablation fronts; (3) all the water vapor produced at the evaporation plane flows upward to the ablation front at the opposite end of the porous region; (4) forced and natural convection heat transfer in the porous region due to water vapor transport is negligible compared with conduction; (5) the pressure difference due to surface tension effects across the evaporation front is small compared to $P_{eq}-P_\ell$; and (6) the physical properties of the concrete and the viscosity μ_g of the water vapor may be replaced by constant average values appropriate to the temperature intervals of interest.

It is obvious from Assumption (1) that attention is focused on a one-dimensional system of coordinates in which the ablation front is at rest and the concrete medium moves with velocity v_m in the negative x-direction. The position of the ablation front is taken to be $x=0$.

Governing Equations

The conduction equation for the temperature profile $T_d(x)$ in the dry porous region of the translating concrete is

$$v_m\frac{dT_d}{dx}+a_d\frac{d^2T_d}{dx^2}=0;\quad 0<x<\delta_d \tag{1}$$

while the conduction equation for the temperature profile $T_w(x)$ in the region ''upstream'' of the evaporation plane, which is wet with evaporable water, is

$$v_m\frac{dT_w}{dx}+a_w\frac{d^2T_w}{dx^2}=0;\quad \delta_d<x<\infty \tag{2}$$

The momentum equation for the local mass-average velocity (superficial) j_g of the water vapor within the dry porous region is given by the differential form of Darcy's Law:

$$\frac{dP}{dx}=\frac{\mu_g j_g}{\kappa};\quad 0<x<\delta_d \tag{3}$$

In writing Eq. (3) the relative motion between the gas and the moving solid concrete was ignored since in all cases of interest $j_g\gg v_m$. The constant upward rate of water vapor mass flow through the porous region equals the rate at which vapor is generated at the evaporation plane:

$$\rho_w Y_g v_m=j_g\rho_g \tag{4}$$

The boundary conditions at the water evaporation plane ($x=\delta_d$) are

$$\rho_w Y_g v_m h_{fg}=-k_d\frac{dT_d}{dx}+k_w\frac{dT_w}{dx};\quad x=\delta_d \tag{5}$$

$$T_d(\delta_d)=T_w(\delta_d)=T_{\rm sat},\quad P(\delta_d)=P_{eq}(T_{\rm sat}) \tag{6}$$

Equation (5) states that the energy required to evaporate the water is equal to the difference between the heat conducted in and out of the evaporation plane. At the ablation front ($x=0$) and at $x=\infty$ the temperature and vapor pressure profiles must satisfy the conditions

$$T_d(0)=T_{mp},\quad P(0)=P_\ell,\quad T_w(\infty)=T_s \tag{7}$$

The model for evaporable water release from ablating concrete is complete with the addition of two equations. One equation is the ideal gas law for the vapor in the porous region, namely,

$$P=\rho_g R_g T_d \tag{8}$$

The other equation is for the permeability of the porous concrete region. The experimental measurements of McCormack et al. [7] show that the concrete permeability increases rapidly with temperature. Their data on the permeabilities of basaltic and limestone concretes were fit by the exponential function

$$\kappa=\kappa_0\exp(BT) \tag{9}$$

where the numerical values of the parameters κ_0 and B are given in Table 1. In the present problem the local concrete temperature may be as high as about 1600 K so that extrapolation of Eq. (9) would appear to be necessary. This issue will be discussed later on.

Table 1 Values of parameters in permeability equation (Eq. 9)

Concrete	Temp. Range (K)	κ_0 (m^2)	B (K^{-1})
Basaltic	373–900	2.18×10^{-17}	0.0110
Limestone	373–692	5.29×10^{-20}	0.0192
Limestone	692–1023	3.147×10^{-17}	0.01013

The solutions of Eqs. (1) and (2) that satisfy the relevant boundary conditions in Eqs. (5) to (7) give, after introducing the approximation $\rho_d c_d\cong\rho_w c_w$,

$$\frac{v_m\delta_d}{a_d}=\ln\left[1+\frac{T_{mp}-T_{\rm sat}}{Y_g h_{fg}/c_w+T_{\rm sat}-T_s}\right] \tag{10}$$

$$\frac{dT_d}{dx}=-\frac{v_m}{a_d}\left[T_d-T_s+\frac{Y_g h_{fg}}{c_w}\right] \tag{11}$$

Using Eq. (11) to eliminate independent distance variable x in Darcy's equation (Eq. 3) in favor of temperature T_d and by invoking Eqs. (4), (8), and (9), a separable first-order differential equation between pressure P and temperature T_d in the porous region of the concrete is obtained:

$$\frac{PdP}{dT_d}=-\frac{\mu_g a_d\rho_w Y_g R_g}{\kappa_0}\left(\frac{T_d}{T_d-T_s+Y_g h_{fg}/c_w}\right)\exp(-BT_d) \tag{12}$$

Equation (12) can be integrated between the ablation plane where $P=P_\ell$ and $T=T_{mp}$ and the evaporation plane where $P=P_{eq}$ and $T=T_{\rm sat}$ to obtain the closed form result:

$$P_{eq}^2=P_\ell^2+\frac{2\mu_g a_d\rho_w Y_g R_g}{\kappa(T_s)B}\cdot f(T_{\rm sat}) \tag{13}$$

where $\kappa(T_s)$ is Eq. (9) evaluated at T_s and the dimensionless function $f(T_{\rm sat})$ is defined as

$$\begin{aligned}f(T_{\rm sat})=&\exp[-B(T_{\rm sat}-T_s+Y_g h_{fg}/c_w)]-\exp[-B(T_{mp}-T_s\\&+Y_g h_{fg}/c_w)]+B(T_\infty-Y_g h_{fg}/c_w)\{{\rm Ei}[B(T_{\rm sat}-T_s\\&+Y_g h_{fg}/c_w)]-{\rm Ei}[B(T_{mp}-T_s+Y_g h_{fg}/c_w)]\}\end{aligned} \tag{14}$$

The function Ei[λ] in the above equation is the exponential integral

$${\rm Ei}[\lambda)]=\int_\lambda^\infty\frac{e^{-\xi}}{\xi}d\xi \tag{15}$$

Strictly speaking, Eqs. (13) and (14) are not valid for limestone concrete. The permeability versus temperature function for this material is composed of two exponentials connected in a piecewise continuous manner (see Eq. (9) and Table 1). Thus one would expect more terms to appear in Eqs. (13) and (14) involving two different κ_0, B pairs, one pair for the low temperature range 373–692 K and the other pair for the high temperature range 692 K to T_{mp}. It will be seen later on, however, that for the limestone concrete ablation problems considered here it is permissible to consider only one temperature range and, therefore, only one pair of κ_0, B values.

Equation (13) is a relationship between the two unknowns P_{eq} and T_{sat} at the evaporation front. Since thermodynamic equilibrium is assumed to prevail at the evaporation front the steam tables provide another relationship between P_{eq} and T_{sat} and the simultaneous numerical solution of these coupled relationships yields the pressure P_{eq} exerted by the vapor at the evaporation front. The actual numerical solution was performed using the following water vapor pressure fit of steam table data (to within 4.0 percent for $370 < T_{sat} < 584$ K):

$$P_{eq} = 10^6 \exp\left(-\frac{4795}{T_{sat}} + 10.55 \right) \tag{16}$$

where T_{sat} is in *K* and P_{eq} is in Pa.

The theory presented in the foregoing can also be used to calculate the pressure exerted by CO_2 gas within the concrete due to carbonate decomposition, providing that it is reasonable to regard the carbonate decomposition zone as a sharp front. Specifically, for the CO_2 case the water evaporation plane in Fig. 1 is replaced by a carbonate decomposition plane. In terms of obtaining numerical results with Eqs. (13) and (14) Y_g is now the mass fraction of CO_2 in the concrete, h_{fg} is identified with the heat of carbonate decomposition (decarboxylation), and R_g is the ideal gas constant for CO_2. Also, Eq. (16) is replaced by an equilibrium law for carbonate decomposition. Assuming CO_2 is produced in the concrete by the decarboxylation of calcium carbonate, we have

$$P_{eq} = 10^5 \exp\left(-\frac{2.085 \times 10^4}{T_{sat}} + 17.854 \right) \tag{17}$$

where P_{eq} is in Pa and T_{sat} is in *K*. Equation (17) is a fit to the saturation vapor pressure calculations for the reaction equilibrium $CaCO_3 = CaO + CO_2$. Assuming, instead, that CO_2 is produced from dolomite, $MgCa(CO_3)_2$, does not change the numerical results in a substantial way.

Discussion of Results

The physical property values used in the numerical solutions of Eqs. (13) and (16) for H_2O release and Eqs. (13) and (17) for CO_2 release are summarized in Table 2 (see also, Table 1). The thermophysical properties values of concrete were taken from [8]. Concrete does not melt at a single, sharp temperature. Rather it melts over a range. In the Sandia tests (see, e.g., [1]) the concrete ablation front was identified with the 1600 K isotherm as determined by thermocouples cast into the concrete substrate and this value is used here for T_{mp}.

The P_{eq} predictions are shown in Table 3 and they are compatible with the observations of Powers and Arellano [6]. We note that the driving pressure $P_{eq} - P_\ell$ for water flow in the limestone concrete is more than twice that in basaltic concrete, even though these concretes contain similar amounts of readily vaporized water (see Table 2). The reason for this difference is that the permeability of limestone concrete is about one order-of-magnitude less than the permeability of basaltic concrete [7]. The $P_{eq} - P_\ell$ results for H_2O are consistent with Powers and Arellano's observations of roughly 40 percent lower ejection velocities for basaltic concrete spall fragments relative to fragments ejected from limestone concretes. The ejection velocity can be shown to be proportional to $(P_{eq} - P_\ell)^{1/2}$, assuming that P_{eq} remains constant behind an ejecting spall fragment. The model results also confirm their conjecture that decarboxylation is not likely to be responsible for concrete spallation. The predicted low internal gas pressures associated with CO_2 release is a consequence of the fact that decarboxylation occurs in zones of high concrete temperatures having relatively high concrete permeabilities. A high-temperature porous concrete region offers little ''frictional'' resistance to the upward flow of CO_2 gas.

Table 2 Physical constants used in the numerical determinations of P_{eq}

Concrete Thermal Diffusivity	$a_d = 6.4 \times 10^{-7}$ m^2 s^{-1}
Gas Viscosity	$\mu_g = 2 \times 10^{-5}$ Pa s
Concrete Density	$\rho_w = 2340$ kg m^{-3}
Concrete Specific Heat	$c_w = 950$ J kg^{-1} K^{-1}
Ambient (Pool) Pressure	$P_\ell = 10^5$ Pa
H_2O Mass Fraction in Basaltic Concrete	$Y_g = 0.042$
H_2O Mass Fraction in Limestone Concrete	$Y_g = 0.039$
CO_2 Mass Fraction in Basaltic Concrete	$Y_g = 0.0292$
CO_2 Mass Fraction in Limestone Concrete	$Y_g = 0.357$
H_2O Heat of Evaporation	$h_{fg} = 2.2 \times 10^6$ J kg^{-1}
CO_2 Heat of Release	$h_{fg} = 3.8 \times 10^6$ J kg^{-1}
Ablation Temperature	$T_{mp} = 1600$ K
Cold Concrete Temperature	$T_s = 293$ K

Table 3 Predictions of equilibrium pressures exerted by the release of evaporable water and CO_2 in basaltic and limestone concretes

Concrete	Gas Released	Gas Mass Fraction	Predicted T_{sat} (K)	Predicted $P_{eq} - P_\ell$ (atm)
Basaltic	H_2O	0.042	409.6	2.13
Limestone	H_2O	0.039	436.5	5.46
Basaltic	CO_2	0.0292	1168.7	2.1×10^{-4}
Limestone	CO_2	0.357	1168.8	2.4×10^{-3}

The prediction $T_{sat} = 437$ K for limestone concrete is based only on the κ_0, *B* values in Table 1 for the low temperature range 373 to 692 K. For a change in temperature from 437 K to 692 K the permeability of limestone concrete increases by a factor of about 140. Thus practically all the resistance to upward water vapor flow in the porous region occurs close to the evaporation front and the precise values of the permeability at locations where the temperature is above 692 K are not important. Extrapolation of Eq. (9) to $T_{mp} = 1600$ K is indeed not required. Another way of stating this is that in Eq. (14) the terms containing T_{mp} are negligible compared with the terms containing T_{sat}. The predicted T_{sat} values for CO_2 gas release are outside and above the temperature range investigated by McCormack et al. [7] in their laboratory study of concrete permeability so that some extrapolation of Eq. (9) was required. However, any inaccuracies associated with this extrapolation does not alter the conclusion that the gas pressure generated by CO_2 release is negligible.

The fact that high-internal-water-vapor pressures are predicted by the model does not provide a complete explanation for the onset of spallation. If the plane of free water evaporation is far removed from the ablating surface, that is ''deep'' within the concrete, then it is reasonable to suppose that the concrete can withstand the few atmospheres of internal pressure produced by water release. However, spallation may occur if the zone of high pressure is just beneath the ablating surface. According to the observations of Powers and Arellano [6], the thicknesses of the spall fragments ranged in size from 2.0 to 7.0 mm. Thus a possible criterion for the onset of spallation is obtained by demanding that the thickness δ_d of the porous region of the concrete (see Fig. 1) be less than the largest measured spall fragment, denoted here as the critical size fragment $\delta_{d,crit} \cong 7.0$ mm. The criterion $\delta_d \cong \delta_{d,crit}$ can be combined with Eq. (10) for v_m to arrive at a critical ablation velocity $v_{m,crit}$, which if exceeded, results in spallation. Using the parameter estimates from Table 2 and the prediction $T_{sat} = 410$ K for basaltic concrete (see Table 3) in Eq. (10) leads to a threshold ablation velocity for spallation: $v_{m,crit} = 0.17$ mm s^{-1}. This value is consistent with the notion that spallation did not occur in the Sandia inductively heated pool tests but was important in most of the BETA tests in that the measured ablation rates in the Sandia tests fall well below this value while the ablation rates measured in the BETA tests are close to or exceed this value.

In all likelihood the mechanism of ablation is dictated early on during the melt pool formation stage. The BETA tests were initiated by pouring about 300 kg of steel melt into the interaction crucible from a height of several meters. Presumably the combination of intense impingement heat transfer, fresh concrete containing free water, and induction-heating power, led to the sustained, rapid concrete erosion rates measured in these tests. The rapid erosion process is achieved by concrete spallation which eliminates the slag resistance to heat transfer. In contrast, the inductively heated melt pools in the Sandia tests [2,3] developed gradually by melting at low power a solid steel cylinder initially placed in the interaction cavity. In these experiments the combination of low initial concrete heating rates and the possible loss of some free water by preheating of the concrete before the start of ablation prevented the possibility of spallation and concomitant rapid ablation. In the early transient cooldown tests performed at Sandia [6] spallation did not occur in concrete crucibles that were previously dried by exposure to steel melts. Note that this observation rules out a thermal stress mechanism of spallation. In the Sandia tests reported in [1] about 45 kg of steel melt was poured into the concrete crucible from a height of 1.0 m. Apparently the duration and intensity of the early stage melt-to-concrete heat transfer in these tests were limited by the relatively small melt mass poured and small pour height, compared with the melt mass and pour height in the BETA tests.

Discussion of Assumptions

In this section the validity of the assumptions underlying the model presented in the foregoing is examined. We begin with the assumption of steady-state ablation (Assumption 1).

In the BETA tests [4,5] the ablation front location was observed to vary linearly with time, starting from the first ablation depth measurement at about 10 s out to the end of the tests at about 400 s. It is apparent that steady-state catastrophic concrete erosion was established very quickly ($<$ 10 s). This observation is consistent with available solutions to the transient heat-conduction equation written for moving solids (see, e.g., [9]), from which the relaxation time t_{ss} to steady state is easily seen to be of the order

$$t_{ss} \sim \left(\frac{v_m^2}{4a_d} + \frac{\pi^2 a_d}{\delta_d} \right)^{-1} \tag{18}$$

Using the previous estimate $\delta_d \cong 7.0$ mm and the average ablation velocity measured in the BETA tests $v_m \cong 0.3\ \text{mm s}^{-1}$, gives $t_{ss} \sim 6$ s.

Assumption (2) concerning the sharp boundary between the wet and dry zones is based on experimental measurements. Measured temperature histories at various depths below an ablating concrete surface exhibit discontinuities in slope when the concrete temperature rises to the boiling point of water [1]. The wet/dry line interface assumption has been used in previous theoretical studies of water evaporation or condensation in porous media (see, e.g., [10,11]).

Assumption (3) (negligible downward vapor transport) will be valid if

$$\frac{\delta_d \kappa(T_s)}{\delta_w \kappa(T_{\text{sat}})} \ll 1.0 \tag{19}$$

In all the experiments cited here $\delta_d \ll \delta_w$. Also $\kappa(T_{\text{sat}}) \cong 4.0\ \kappa(T_s)$, thereby assuring a negligible amount of downward vapor escape. Measurements of the concrete off-gas flow rates indicate that practically all of the gas stored in the concrete ($H_2O + CO_2$) is released to the overlying steel melt [3].

Forced-convection vapor heat transport in the dry region is negligible (Assumption 4) providing that (see Eq. (4))

$$\frac{\rho_g j_g c_g}{\rho_w v_m c_w} = \frac{Y_g c_g}{c_w} \ll 1.0 \tag{20}$$

Since $Y_g \ll 1.0$ for water (see Table 2) this inequality is indeed satisfied. Natural convection in the dry region can be neglected (Assumption 4) if the appropriately defined Rayleigh number,

$$\text{Ra} = \frac{\kappa g \beta \delta_d (T_{mp} - T_{\text{sat}})}{\alpha \nu_g}, \tag{21}$$

is small. The approximate values of the parameters in Eq. (21) are: $\kappa = 1.3 \times 10^{-12}\ \text{m}^2$ [at $(T_{\text{sat}} + T_{mp})/2 = 10^3$ K], $\beta = 2.4 \times 10^{-3}\ \text{K}^{-1}$, $\delta_d = 7.0 \times 10^{-3}$ m, $T_{mp} - T_{\text{sat}} = 1190$ K, $\alpha = 4.7 \times 10^{-4}\ \text{m}^2\ \text{s}^{-1}$, and $\nu_g = 1.3 \times 10^{-5}\ \text{m}^2\ \text{s}^{-1}$. These estimates yield $\text{Ra} = 4.2 \times 10^{-5}$. It is well known that natural convection is negligible for Ra $<$ 40.0.

With respect to the influence of interfacial curvature on P_{eq} (Assumption 5), Satik and Yortsos [12] have shown that this effect is small unless the permeability of the porous medium is less than about $10^{-18}\ \text{m}^2$. For the concrete materials and temperature ranges presented in this study $\kappa > 2 \times 10^{-16}\ \text{m}^2$.

Concluding Remarks

Steel melts poured onto concrete may initiate a rapid concrete erosion process via the mechanism of concrete surface spallation by readily vaporized water. Concrete spallation was observed during the pouring of molten steel into concrete crucibles and prior to the cooldown of the metal. The present model of heat and water vapor transfer in the high temperature environment just beneath an ablating concrete surface rationalizes spallation observations during the transient cooldown tests and suggests that sustained spallation-driven concrete erosion occurred during experiments (BETA tests) in which the metal melt was continually heated after it was poured onto concrete. The present model can not predict whether or not a given metallic (or oxidic) pour will result in rapid concrete erosion by surface spallation. Such a prediction will require a new model which is capable of dealing with the transient period during which melt-pool heat transfer evolves from impingement heat transfer.

Nomenclature

- a = thermal diffusivity of concrete
- B = constant in permeability function, Eq. (9)
- c = specific heat of concrete
- c_g = specific heat of water vapor
- g = gravitational constant
- h_{fg} = latent heat of evaporation of water or heat of carbonate decomposition
- k = thermal conductivity of concrete
- j_g = superficial velocity of water vapor in dry porous region
- P = local water vapor pressure in dry porous region
- P_{eq} = equilibrium water vapor pressure at evaporation front
- P_ℓ = pressure in the overlying melt pool
- R_g = ideal gas constant for water
- t_{ss} = relaxation time to steady state
- T = local temperature
- T_{mp} = concrete melting (ablation) temperature
- T_s = temperature of wet concrete far from the evaporation plane
- T_{sat} = equilibrium (saturation) temperature at evaporation front
- v_m = concrete ablation velocity
- x = distance measured from ablation plane into concrete
- Y_g = mass fraction of evaporable water in wet concrete or mass fraction of CO_2 ''stored'' in concrete

Greek Letters

α = thermal diffusivity (concrete thermal conductivity divided by volumetric heat capacity of steam)
δ_d = thickness of dry porous region
δ_w = thickness of wet region
κ = local permeability of the dry porous region
κ_0 = permeability coefficient in Eq. (9)
μ_g = viscosity of water vapor
ν_g = kinematic viscosity of water vapor
ρ_g = local water vapor density in dry porous region
ρ_w = density of wet concrete

Subscripts

d = pertains to dry porous region
g = pertains to water vapor
w = pertains to wet region or liquid water

References

[1] Blose, R. E., Gronager, J. E., Suo-Anttila, A. J., and Brockmann, J. E., 1987, "SWISS: Sustained Heated Metallic Melt/Concrete Interactions with Overlying Pools," Sandia National Lab. Report SAND85-1546 (NUREG/CR-4727).
[2] Copus, E. R., Blose, R. E., Brockmann, J. E., Gomez, R. D., and Lucero, D. A., 1990, "Experimental Results of Core-Concrete Interactions Using Molten Steel with Zirconium," Sandia National Laboratory Report SAND86-2638 (NUREG/CR-4794).
[3] Copus, E. R., Blose, R. E., Brockmann, J. E., Gomez, R. D., and Lucero, D. A., 1989, "Core-Concrete Interactions Using Molten Steel with Zirconium on a Basaltic Basemat: The SURC-4 Experiment," Sandia National Laboratory Report SAND87-2008 (NUREG/CR-4994).
[4] Corradini, M., and Reineke, H. H., 1989, "A Review of the BETA Experimental Results and Code Comparison Calculations," Nucl. Sci. Eng., **102**, pp. 260–282.
[5] Alsmeyer, H., 1995, "Review of Experiments on Dry Corium Concrete Interaction," in *Molten Corium/Concrete Interaction and Corium Coolability—A State of the Art Report*, European Commission, Brussels, Report EVR 16649 EN, pp. 29–82.
[6] Powers, D. A., and Arrellano, F. E., 1982, "Large-Scale, Transient Tests of the Interaction of Molten Steel with Concrete," Sandia National Laboratory Report SAND81-1753 (NUREG/CR-2282).
[7] McCormack, J. D., Postma, A. K., and Schur, J. A., 1979, "Water Evolution from Concrete," Hanford Engng. Dev. Lab., Report HEDL-TME 78–87.
[8] Kao, L. S., and Kazimi, M. S., 1987, "Thermal Hydraulics of Core/Concrete Interactions in Severe LWR Accidents," MIT Report MITNE-276.
[9] Carslaw, H. S., and Jaeger, J. C., 1959, *Conduction of Heat in Solids*, 2nd ed., Oxford Univ. Press, p. 391.
[10] Rubin, A., and Schweitzer, S., 1972, "Heat Transfer in Porous Media with Phase Change," Int. J. Heat Mass Transfer, **15**, pp. 43–59.
[11] Chung, M., and Catton, I., 1993, "Steam Injection into a Slow Water Flow Through Porous Media," ASME J. Heat Transfer, **115**, pp. 734–743.
[12] Satik, C., and Yortsos, Y. C., 1991, "Percolation Models for Boiling and Bubble Growth in Porous Media at Low Superheats," in *Multiphase Transport in Porous Media*, FED-Vol. 122/HTD-Vol. 186, ASME, New York, pp. 61–72.

Investigation of the Initial Inverse Problem in the Heat Equation

Khalid Masood
e-mail: masood@kfupm.edu.sa
Hafr Al-Batin Community College, King Fahd University of Petroleum and Minerals, P.O. Box 5087, Dhahran 31261, Saudi Arabia

F. D. Zaman
e-mail: fzaman@kfupm.edu.sa
Department of Mathematical Sciences, King Fahd University of Petroleum and Minerals, Dhahran 31261, Saudi Arabia

We investigate the inverse problem in the heat equation involving the recovery of the initial temperature from measurements of the final temperature. This problem is extremely ill-posed and it is believed that only information in the first few modes can be recovered by classical methods. We will consider this problem with a regularizing parameter which approximates and regularizes the heat conduction model. [DOI: 10.1115/1.1666886]

Keywords: Analytical, Heat Transfer, Inverse, Stability, Temperature

1 Introduction

The classical direct problem in heat conduction is to determine the temperature distribution of a body as the time progresses. The task of determining the initial temperature distribution from the final distribution is distinct from the direct problem and is identified as the initial inverse heat conduction problem. This type of inverse problem is extremely ill-posed, e.g., Engle [1]. There is an alternative approach which consists of a reformulation of the classical heat equation by a hyperbolic heat equation (see Weber [2], Elden [3], and Masood et al. [4]).

We will present an alternative approach which approximates and regularizes the initial inverse heat conduction solution. The need to consider the alternative formulation has some physical advantages. In many applications, one encounters a situation where the usual parabolic heat equation does not serve as a realistic model. Since the speed of propagation of the thermal signal is finite, e.g., for short-pulse laser applications, the hyperbolic differential equation correctly models the problem; see Vedavarz et al. [5] and Gratzke et al. [6] among others. The initial inverse problem in the hyperbolic heat equation is stable and well posed. Moreover, numerical methods for hyperbolic problems are efficient and accurate. We will utilize the small value of the parameter and apply the WKBJ (Wentzel, Kramers, Brillouin, and Jeffreys) method to solve the initial inverse problem, see Bender and Orszag [7].

2 Initial Inverse Problem in the Heat Equation

Supposing we have a metal bar, which for the sake of convenience we take to extend over the interval $0 \leqslant x \leqslant \pi$, whose temperature at the point x and at time t is given by the function $u(x,t)$. Then, for an appropriate choice of units, $u(x,t)$ satisfies the equation

$$\frac{\partial u}{\partial t} = \frac{\partial^2 u}{\partial x^2}, \quad 0 < x < \pi, \quad t > 0 \tag{1}$$

with homogeneous Dirichlet boundary conditions

$$u(0,t) = u(\pi,t) = 0 \tag{2}$$

We assume the final temperature distribution of the bar at time $t = T$

$$f(x) = u(x,T) \tag{3}$$

and we want to recover the initial temperature profile of the bar

$$g(x) = u(x,0) \tag{4}$$

The condition (2) can be replaced by an insulated boundary, i.e., $u_x(0,t) = u_x(\pi,t) = 0$, since it is important in some applications, see for example Beck et al. [8] and Al-Khalidy [9].

We assume by the separation of the variables, the solution of the direct problem of the form

Contributed by the Heat Transfer Division for publication in the JOURNAL OF HEAT TRANSFER. Manuscript received by the Heat Transfer Division May 15, 2002; revision received August 14, 2003. Associate Editor: A. F. Emery.

$$u(x,t)=\sum_{n=1}^{\infty} v_n(t)\phi_n(x) \tag{5}$$

The eigenfunctions of d^2/dx^2 given by $\phi_n(x)\doteq\sqrt{2/\pi}\sin(nx)$ form a complete orthonormal system in $L^2[0,\pi]$. Thus, $g(x)\in L^2[0,\pi]$ can be expanded as

$$g(x)=\sum_{n=1}^{\infty} c_n\phi_n(x), \quad x\in[0,\pi] \tag{6}$$

So, we can write the solution of the direct problem (1) in the form

$$u(x,t)=\sum_{n=1}^{\infty} c_n \exp[-n^2t]\phi_n(x) \tag{7}$$

Now by applying (3), we can write

$$f(x)=\int_0^{\pi} K(x,\zeta)g(\zeta)d\zeta \tag{8}$$

which is an integral equation of the first kind. The singular system of the integral Eq. (8) is given by

$$\{\exp[-n^2T],\phi_n(x),\phi_n(x)\} \tag{9}$$

Now by application of Picard's theorem the inverse problem can be solved if

$$\sum_{n=1}^{\infty} \exp[2n^2T]|f_n|^2<\infty \tag{10}$$

where

$$f_n=\int_0^{\pi}\phi_n(\zeta)f(\zeta)d\zeta \tag{11}$$

are the classical Fourier coefficients of f. Now again using Picard's theorem, we can recover the initial profile by the following expression

$$g(x)=\sum_{n=1}^{\infty} \exp[n^2T]f_n\phi_n(x) \tag{12}$$

Picard's theorem demonstrates the ill-posed nature of the problem considered. If we perturb the data by setting $f^{\delta}=f+\delta\phi_n$ we obtain a perturbed solution $g^{\delta}=g+\delta\phi_n\exp[n^2T]$. Hence, the ratio $\|g^{\delta}-g\|/\|f^{\delta}-f\|=\exp[n^2T]$ can be made arbitrarily large due to the fact that the singular values $\exp[-n^2T]$ decay exponentially. The influence of errors in the data f is obviously affected by the rate of this decay. So in regularizing, we will confine ourselves to lower modes by only retaining the first few terms in the series (12). This technique of truncating the series is known as truncated singular value decomposition (TSVD), see Hansen [10].

3 The Hyperbolic Model

The method we apply is similar to the quasi-inverse method of Lions [11]. The Lions' method is based on replacing the problem (1–4) by a problem for equation of higher order with a small parameter. There are several methods for solving ill-posed problems. The quasi-solution method to solve the equation of the first kind was introduced by Ivanov [12]. The essence of this method is to change the notion of solution of an ill-posed problem so that, for certain conditions, the problem of its determination will be well-posed. Tikhonov's regularization method is widely used for solving linear and nonlinear operator equations of the first kind, see Tikhonov and Arsenin [13]. Iterative methods are applied to solve different problems and particularly these methods can also be applied to solve operator equations of the first kind. Moultanovsky [14] applied such an iterative method to solve an initial inverse heat transfer problem. The projective methods for solving various ill-posed problems are based on the representation of the approximate solution as a finite linear combination of a certain functional system, see, e.g., Vasin and Ageev [15].

The methods mentioned in the previous paragraph may be applied for solving the extensive class of inverse problems. These methods do not take into account the specific character of concrete inverse problems. The Lion's method and the method we present in this paper take into account peculiarities of the inverse problem. There is an alternative approach to the inverse heat conduction problem [2,3], which consists of introducing a small damping parameter with the term $\partial^2u/\partial t^2$. So, let us consider the following hyperbolic heat equation

$$\epsilon\frac{\partial^2u}{\partial t^2}+\frac{\partial u}{\partial t}=\frac{\partial^2u}{\partial x^2}, \quad \epsilon>0, \quad 0<x<\pi, \tag{13}$$

together with conditions (2–4) and one additional condition

$$\frac{\partial u}{\partial t}(x,0)=0. \tag{14}$$

Following the same procedure as that for the parabolic heat equation and assuming the solution of the form (5), for $\epsilon\to0^+$ we get the following ordinary differential equation

$$\epsilon\frac{d^2a_n(t)}{dt^2}+\frac{da_n(t)}{dt}+n^2a_n(t)=0, \quad \epsilon>0, \quad t>0, \tag{15}$$

subject to

$$a_n(0)=c_n, \quad \text{and} \quad \frac{da_n(0)}{dt}=0. \tag{16}$$

This is a singular perturbation problem, so we seek the WKBJ solution to this problem [7]. The WKBJ solution to (15) is

$$a_n(t)=\left(\frac{\epsilon n^2-1}{2\epsilon n^2-1}\right)c_n\exp[-n^2t]+\left(\frac{\epsilon n^2c_n}{2\epsilon n^2-1}\right)\exp\left[n^2t-\frac{t}{\epsilon}\right] \tag{17}$$

Using Picard's theorem the solution exists if

$$\sum_{n=1}^{\infty}\frac{|f_n|^2}{\left\{\left(\frac{\epsilon n^2-1}{2\epsilon n^2-1}\right)\exp[-n^2T]+\left(\frac{\epsilon n^2}{2\epsilon n^2-1}\right)\exp\left[n^2T-\frac{T}{\epsilon}\right]\right\}^2}<\infty \tag{18}$$

and the solution is given by

$$g(x)=\sum_{n=1}^{\infty}\times\frac{f_n\phi_n(x)}{\left\{\left(\frac{\epsilon n^2-1}{2\epsilon n^2-1}\right)\exp[-n^2T]+\left(\frac{\epsilon n^2}{2\epsilon n^2-1}\right)\exp\left[n^2T-\frac{T}{\epsilon}\right]\right\}} \tag{19}$$

Supposing $\epsilon\to0^+$ in the expression (19), we get the solution of the heat conduction problem (12). So, the solution of the heat equation can also be treated as the limiting case of the hyperbolic heat equation.

Example. Let us consider the initial temperature distribution of the form $g(x)=\sqrt{2/\pi}\sin(mx)$, where m is some fixed integer, then the final data for (19) and (12) can be given by

$$f_m=\left(\frac{\epsilon m^2-1}{2\epsilon m^2-1}\right)\exp[-m^2T]+\left(\frac{\epsilon m^2}{2\epsilon m^2-1}\right)\exp\left[m^2T-\frac{T}{\epsilon}\right] \tag{20}$$

and

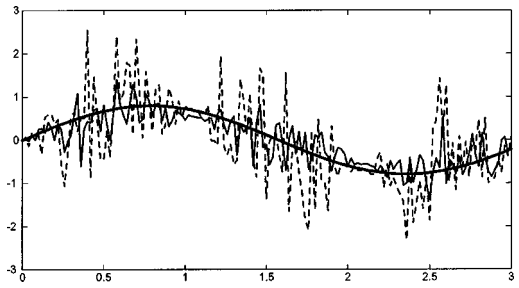

Fig. 1 The case of noisy data with SNR=50 dB, $N=3$, $m=2$, $T=1$, and $\epsilon=0.04$. The noisy data used in the heat conduction solution (12) is represented by the dotted line and in the damped wave solution (19) by the thin solid line and the noiseless temperature by the thick solid line.

$$f_m = \exp[-m^2 T]. \tag{21}$$

The expression (20) represents the final data for the hyperbolic model corresponding to the assumed initial profile $g(x)$ in the absence of the noise. Using (20) in the expression (19), the initial profile $g(x)$ can be recovered exactly. The expression (21) represents the final data for the parabolic model corresponding to the assumed initial profile $g(x)$ in the absence of the noise and the initial profile can be recovered exactly by using it in the expression (12).

Now we analyze the models by adding white Gaussian noise to the data (21). The reason to use (21) as final data is that the exact measured data would be of this form. In Figs. 1–3, we use the noisy data (white Gaussian noise+(21)) in both parabolic heat conduction and hyperbolic heat models and see the mean behavior of 100 independent realizations.

We have considered the second mode, that is, $m=2$ in Figs. 1–3 as well as retaining the first three terms ($N=3$) in series (12) and (19). In Fig. 1, the hyperbolic heat model behaves better than the parabolic heat conduction model for SNR=50 dB. We have increased the level of noise in Figs. 2–3 to SNR=20 dB. The inherent instability of the parabolic heat conduction model is clear from Fig. 3 by observing the range of the vertical axis.

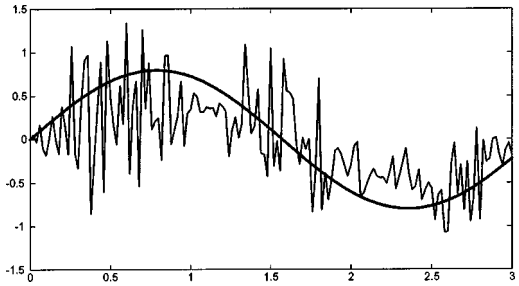

Fig. 2 Response of the damped model (19) in the case of noisy data with SNR=20 dB, $N=3$, $m=2$, $T=1$, $\epsilon=0.07$

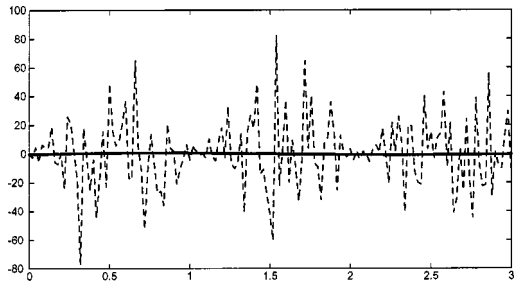

Fig. 3 Response of the classical heat model (12) in the case of noisy data with SNR=20 dB, $N=3$, $m=2$, $T=1$

Conclusions

The inverse solution of the heat conduction model is characterized by discontinuous dependence on the data. It is shown that in case of noisy data, the hyperbolic model approximates the exact initial profile better than the parabolic heat conduction model. Further, in the case of noisy data, the information about the initial profile cannot be recovered for higher modes by the parabolic heat conduction model but by the hyperbolic model some useful information may be recovered. However for higher modes the information recovered by the hyperbolic model is better than the parabolic model but it may not be good enough for a particular application.

Acknowledgment

The authors wish to acknowledge support provided by the King Fahd University of Petroleum and Minerals and the Hafr Al-Batin Community College.

Nomenclature

$|\cdot|$ = absolute value
$\|\cdot\|$ = norm
c_n = $\int_0^\pi g(x)\phi_n(\tau)d\tau$
$K(x,\zeta)$ = $\Sigma_{n=1}^{\infty} \exp[-n^2 T]\phi_n(\zeta)\phi_n(x)$
u_x = $\partial u/\partial x$
SNR = signal-to-noise ratio
WKBJ = Wentzel, Kramers, Brillouin, and Jeffreys
$\phi_n(x)$ = eigenfunctions

References

[1] Engl, H. W., Hanke, M., and Neubauer, A., 1996, *Regularization of Inverse Problems*, Kluwer, Dordrecht, pp. 31–42.
[2] Weber, C. F., 1981, "Analysis and Solution of the Ill-Posed Problem for the Heat Conduction Problem," Int. J. Heat Mass Transfer, **24**, pp. 1783–1792.
[3] Elden, L., 1987, *Inverse and Ill-Posed Problems*, Engl, H. W., and Groetsch, C. W., eds., Academic Press, Inc., pp. 345–350.
[4] Masood, K., Messaoudi, S., and Zaman, F. D., 2002, "Initial Inverse Problem in Heat Equation With Bessel Operator," Int. J. Heat Mass Transfer, **45**(14), pp. 2959–2965.
[5] Vedavarz, A., Mitra, K., and Kumar, S., 1994, "Hyperbolic Temperature Profiles for Laser Surface Interactions," J. Appl. Phys., **76**(9), pp. 5014–5021.
[6] Gratzke, U., Kapadia, P. D., and Dowden, J., 1991, "Heat Conduction in High-Speed Laser Welding," J. Appl. Phys., J. Phys. D, **24**, pp. 2125–2134.
[7] Bender, C. M., and Orszag, S. A., 1978, *Advanced Mathematical Methods for Scientists and Engineers*, McGraw Hill, New York, Chap. 10.
[8] Beck, J. V., Blackwell, B., and Clair, C. A. St., 1985, *Inverse Heat Conduction Problems*, Wiley, New York.
[9] Al-Khalidy, N., 1998, "On the Solution of Parabolic and Hyperbolic Inverse Heat Conduction Problems," Int. J. Heat Mass Transfer, **41**, pp. 3731–3740.
[10] Hansen, P. C., 1997, *Rank-Deficient and Discrete Ill-Posed Problems*, SIAM, Philadelphia, PA, Chap. 3.
[11] Lions, J.-L., and Lattes, R., 1967, *Méthode de Quasi-réversibilité et Applications*, Dunod, Paris.
[12] Ivanov, V. K., 1963, "On Ill-Posed Problems," Mat. Sb., **61**(2), pp. 211–223 (in Russian).
[13] Tikhonov, A. N., and Arsenin, V. Ya., 1977, *Solution of Ill-Posed Problems*, John Wiley, New York.
[14] Moultanovsky, A. V., 2002, "Mobile HVAC System Evaporator Optimization and Cooling Capacity Estimation by Means of Inverse Problem Solution," Inverse Problems in Engng., **10**(1), pp. 1–18.
[15] Vasin, V. V., and Ageev, A. L., 1995, *Ill-Posed Problems With a Priori Information*, VSP, Utrecht.

Effect of Double Stratification on Free Convection in a Darcian Porous Medium

P. V. S. N. Murthy
e-mail: pvsnm@maths.iitkgp.ernet.in
Department of Mathematics, Indian Institute of Technology, Kharagpur 721 302, W.B., India

D. Srinivasacharya and P. V. S. S. S. R. Krishna
Department of Mathematics and Humanities, National Institute of Technology, Warangal, 506 004, A.P., India

The problem of free convection heat and mass transfer from vertical surface embedded in a doubly stratified porous medium has been studied. The similarity solution is presented for the case of uniform heat and mass flux conditions when the thermal and solutal stratification of the medium are assumed to have the power function form $x^{1/3}$. The flow, temperature and concentration fields are effected by the complex interactions among the diffusion ratio parameter Le and buoyancy ratio parameter N in addition to the flow driving Darcy-Rayleigh number Ra_x. The temperature and concentration profiles are effected due to double stratification of the medium and its effect on the Nusselt and Sherwood numbers is discussed. [DOI: 10.1115/1.1667525]

Keywords: Boundary Layer, Heat Transfer, Mass Transfer, Natural Convection, Porous Media, Stratified

1 Introduction

Thermal and solutal transport by fluid flowing through a porous matrix is a phenomenon of great interest from both theory and application point of view. Heat transfer studies in fluid saturated porous media have given insight into understanding dynamics of hot underground springs, terrestrial heat flow through aquifer, hot fluid and ignition front displacements in reservoir engineering, heat exchange between soil and atmosphere, flow of moisture through porous industrial materials, and heat exchanges with fluidized beds. Mass transfer studies have applications in miscible displacements in oil reservoirs, spreading of solutes in fluidized beds and crystal washers and salt leaching in soils. Prevention of salt dissolution into the lake water near sea shores has become a serious topic of research.

Applications are discussed with reference to salt and heat transport in porous flows in Ludvigsen et al. [1] and in Gilman and Bear [2]. Due to the applicability of these studies in many geotechnical processes, it is vital to have good theoretical understanding of the processes occurring in double diffusive flows in porous media. Interesting effects arise as the diffusion rates of heat and solute are usually different. Free convection heat and mass transfer from a vertical flat plate embedded in an unstratified porous medium has been thoroughly investigated in the recent past by many researchers such as Cheng [3], Bejan and Khair [4], Lai and kulacki [5], and Trevisan and Bejan [6]. The book by Nield and Bejan [7] covers many of the latest developments concerning double diffusive convection in a saturated porous medium.

Contributed by the Heat Transfer Division for publication in the JOURNAL OF HEAT TRANSFER. Manuscript received by the Heat Transfer Division July 17, 2002; revision received October 14, 2003. Associate Editor: V. Prasad.

Although the effect of stratification of the medium on the heat removal process in a porous medium is important, very little work has been reported in the literature. Bejan [8], Singh and Sharma [9], and Kalpana and Singh [10] studied the problem of boundary layer free convection along an isothermal vertical flat plate immersed in a thermally stratified fluid saturated porous medium using integral and series solution techniques. The case of power law variation of wall temperature with thermal stratification of the medium was discussed at length by Nakayama and Komaya [11] and by Lai et al. [12]. Takhar and Pop [13] investigated the free convective transport from a vertical flat plate in a thermally stratified Darcian fluid where the ambient temperature varies as $x^{1/3}$ using the similarity solution technique.

In practical situations where the heat and mass transfer mechanisms run in parallel, particularly in porous media applications, it is worth analysing the effect of double stratification (stratification of the medium with respect to the thermal and concentration fields) on the free convective heat and mass transfer in porous media. In the present paper, we extend the work of Takhar and Pop [13] to uncover the effect of double stratification on free convection heat and mass transfer in a Darcian fluid saturated porous medium using the similarity solution technique.

2 Governing Equations

Free convection heat and mass transfer from an impermeable vertical flat wall in a stable and doubly stratified fluid saturated porous medium is considered for study, the schematic drawing is shown in Fig. 1. The wall is maintained at constant heat and mass flux conditions q_w and q_m respectively. The temperature and the mass concentration of the ambient medium are assumed to be in the form $T_\infty(x)=T_{\infty,0}+Ax^{1/3}$, $C_\infty=C_{\infty,0}+Bx^{1/3}$ where $T_{\infty,0}$ and $C_{\infty,0}$ are the temperature and concentration at any reference point inside the boundary layers respectively. We also assume that the flow is slow such that the Darcy law is valid. Then the governing equations for the boundary layer flow, heat and mass transfer from the wall $y=0$ into the fluid saturated stratified porous medium $x \geqslant 0$ and $y>0$ (after making use of the Boussinesq approximation) are given by (see Nield and Bejan [7])

$$\frac{\partial u}{\partial x}+\frac{\partial v}{\partial y}=0 \tag{1}$$

$$u=\frac{Kg}{\nu}\{\beta_T(T-T_\infty)+\beta_C(C-C_\infty)\} \tag{2}$$

$$u\frac{\partial T}{\partial x}+v\frac{\partial T}{\partial y}=\alpha\frac{\partial^2 T}{\partial y^2} \tag{3}$$

$$u\frac{\partial C}{\partial x}+v\frac{\partial C}{\partial y}=D\frac{\partial^2 C}{\partial y^2} \tag{4}$$

with the boundary conditions

$$\left.\begin{array}{lll} y=0: v=0, & -k\dfrac{\partial T}{\partial y}=q_w, & -D\dfrac{\partial C}{\partial y}=q_m \\ y\to\infty: u\to 0, & T=T_\infty(x), & C=C_\infty(x) \end{array}\right\}. \tag{5}$$

Here x and y are the Cartesian coordinates, u and v are the averaged velocity components in x and y directions respectively, T is the temperature, C is the concentration, β_T is the coefficient of thermal expansion, β_C is the coefficient of solutal expansion, ν is the kinematic viscosity of the fluid, K is the permeability, g is the acceleration due to gravity. The subscripts w and ∞ indicate the conditions at the wall and at the outer edge of the boundary layer, respectively.

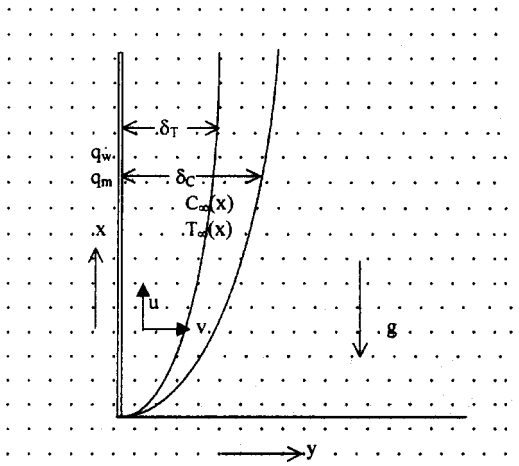

Fig. 1 Schematic drawing of the problem

Making use of the following similarity transformation

$$\eta = \frac{y}{x}\mathrm{Ra}_x^{1/3}, \quad \psi(\eta) = \alpha \mathrm{Ra}_x^{1/3} f(\eta),$$

$$T - T_\infty(x) = \frac{q_w x}{k}\mathrm{Ra}_x^{-1/3}\theta(\eta) \quad C - C_\infty(x) = \frac{q_m x}{D}\mathrm{Ra}_x^{-1/3}\phi(\eta)$$

the governing Eqs. (1–4) become,

$$f' = \theta + N\phi \tag{6}$$

$$\theta'' = \frac{1}{3}(\theta f' - 2f\theta' + \epsilon_1 f') \tag{7}$$

$$\phi'' = \frac{\mathrm{Le}}{3}(\phi f' - 2f\phi' + \epsilon_2 f') \tag{8}$$

and the boundary conditions (5) transform into

$$\left.\begin{aligned} \eta = 0 &: f = 0, \quad \theta' = -1, \quad \phi' = -1 \\ \eta \to \infty &: f' = 0, \quad \theta \to 0, \quad \phi \to 0 \end{aligned}\right\} \tag{9}$$

The important parameters involved are the local Darcy-Rayleigh number $\mathrm{Ra}_x = Kg\beta_T q_w x^2/\alpha\nu k$ which is defined with reference to the thermal conditions alone, the buoyancy ratio is $N = \beta_C q_m k/\beta_T q_w D$ and the diffusivity ratio $\mathrm{Le} = \alpha/D$. The Lewis number is the ratio of Schmidt number (ν/D) and Prandtl number (ν/α). $N>0$ indicates the aiding buoyancy and $N<0$ indicates the opposing buoyancy. The Stratification parameters are defined as $\epsilon_1 = k/q_w \mathrm{Ra}_x^{1/3}\partial T_\infty(x)/\partial x$ and $\epsilon_2 = D/q_m \mathrm{Ra}_x^{1/3}\partial C_\infty(x)/\partial x$. When $T(\infty)(x) = T_{\infty,o} + Ax^{1/3}$ and $C(\infty)(x) = C_{\infty,o} + Bx^{1/3}$, ϵ_1 and ϵ_2 will be independent of x and allows the similarity solution.

3 Results and Discussion

The resulting ordinary differential Eqs. (6–8) along with the boundary conditions (9) are integrated by giving appropriate initial guess values for $f'(0)$, $\theta(0)$, and $\phi(0)$ to match the values with the corresponding boundary conditions at $f'(\infty)$, $\theta(\infty)$, and $\phi(\infty)$, respectively. NAG software (D02HAFE routine) is used for integrating the corresponding first order system of equations and for shooting and matching the initial and boundary conditions. The integration length η_∞ varies with parameter values and it has been suitably chosen at each time such that the boundary conditions at the outer edge of the boundary layer are satisfied. The results obtained here are accurate up to fourth decimal place. Extensive calculations have been performed to obtain the flow, temperature and concentration fields for the following range of parameters: $-1 < N \leq 5$, $0.01 \leq \mathrm{Le} \leq 100$, $0 \leq \epsilon_1 \leq 5$ and $0 \leq \epsilon_2 \leq 5$. As an indication of proper formulation and accurate calculation, the results obtained here are compared with the results in Takhar and Pop [13].

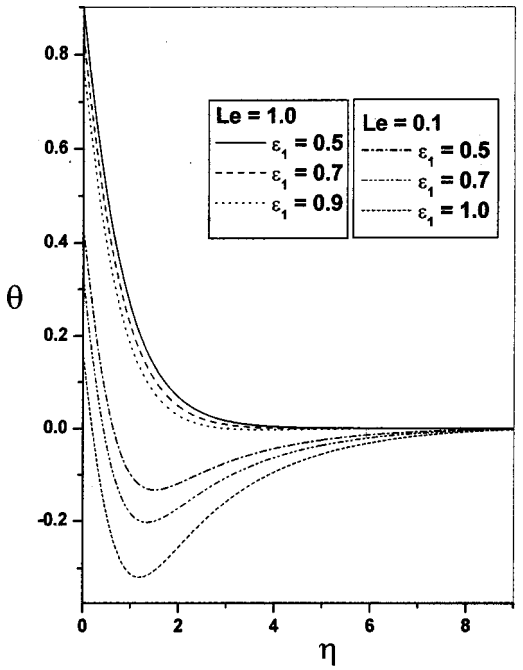

Fig. 2 Variation of temperature with η for different values of ϵ_1 when $N=1$ and $\epsilon_2=0.3$

The effect of ϵ_1 and ϵ_2 on the wall velocity, temperature and concentration fields for uniform wall heat and mass flux conditions is plotted for some selected combinations of parameter values. For fixed value of $N(=1)$ and for $\mathrm{Le}=0.1$, 1.0 variation of

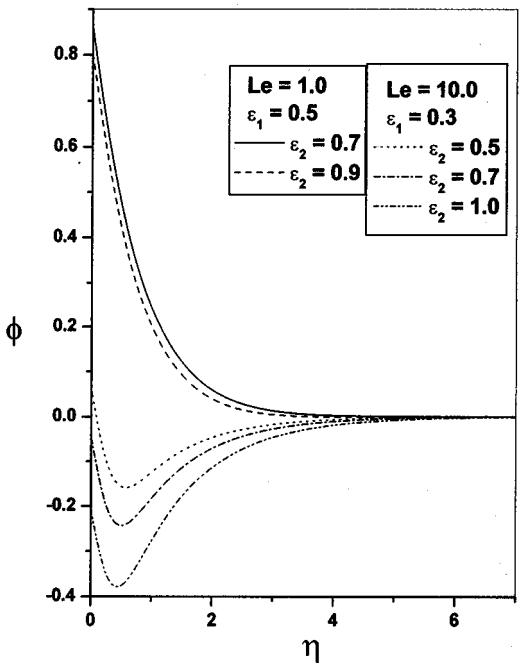

Fig. 3 Variation of concentration with η for different values of ϵ_2 when $N=1$

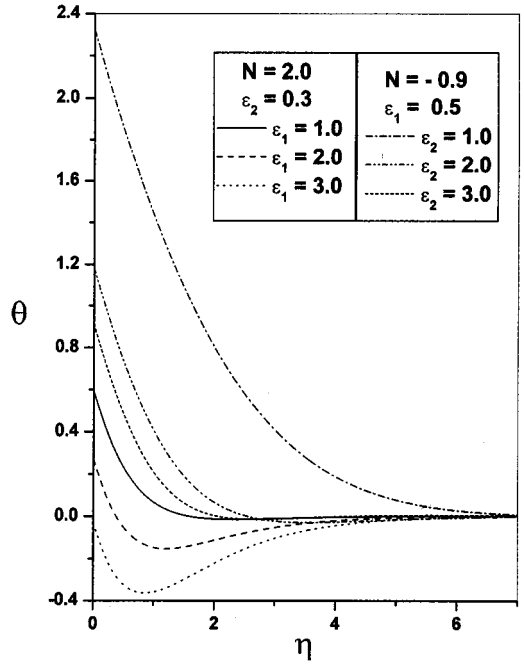

Fig. 4 Variation of temperature with η when Le=1

$\theta(\eta)$ with η is plotted in Fig. 2 for different values of ϵ_1 with $\epsilon_2=0.3$. Similarly variation of $\phi(\eta)$ with η is plotted in Fig. 3 for different values of ϵ_2 with $N=1$, Le=1.0, 10.0 and $\epsilon_1=0.3$, 0.5. The velocity and temperature at the wall decreased as the thermal stratification parameter ϵ_1 increased while the wall concentration decreased with an increase in the value of solutal stratification parameter ϵ_2. Increase in the value of solutal stratification parameter ϵ_2 further reduced the wall velocity and the wall temperature coefficients.

It is observed that the temperature and concentration profiles became negative from critical points η_T, η_C for temperature and concentration profiles, respectively, near the edge of the corresponding boundary layers before they finally attained the boundary conditions $\theta(\infty))=0$ and $\phi(\infty)=0$. Also, η_T shifts towards the wall as ϵ_1 becomes large and η_C shifts towards the wall as ϵ_2 is increased. This can be explained by the way in which the temperature and concentration fields are defined. We have

$$T-T_\infty(x)=\frac{q_w x}{k}\mathrm{Ra}_x^{-1/3}\theta(\eta)$$

and when the temperature in the medium becomes smaller than that of the stratified ambient medium, i.e., if $T-T_\infty(x)<0$, then $\theta(\eta)$ has to be negative as $q_w x/k\mathrm{Ra}_x^{-1/3}$ is positive. Similarly,

$$C-C_\infty(x)=\frac{q_m x}{D}\mathrm{Ra}_x^{-1/3}\phi(\eta),$$

$\phi(\eta)$ has to become negative when $C-C_\infty(x)<0$. In double diffusive processes in porous media, it is not unnatural to assume that different strata of the medium are at varying stratification levels and complex interactions among thermal and solutal fields can not be overruled. Also, overpowering of thermal stratification over the concentration stratification and vice versa resulted in interesting observations in the thermal and concentration profiles as discussed in this article. For fixed values of N and Le, when $\epsilon_1 \geqslant \epsilon_2$, $\theta(\eta)$ is becoming negative and when $\epsilon_2 \geqslant \epsilon_1$, $\phi(\eta)$ is becoming negative. This is also clear from the Figs. 2 and 3.

Now the effect of Le and N on the thermal and concentration profiles is as follows: Le<1 means $\alpha<D$ and mass diffusion is predominant. Hence the concentration profile decreases to zero without any change of sign in the boundary layer. In Fig. 2, the temperature profile is plotted for $N=1$, Le=0.1, $\epsilon_2=0.3$ and varying ϵ_1, in this case, the negative values are no more mild, and they creep into the boundary layer. Keeping ϵ_1 fixed at 0.3 and varying ϵ_2 is also resulting in a similar phenomena, but the temperature on the wall is increasing as ϵ_2 is increased and when $\epsilon_2 \gg \epsilon_1$ the temperature distribution is becoming free from the oscillations in the boundary layer. The temperature profile is plotted for large value of the buoyancy parameter in Fig. 4. A close observation of Figs. 2 and 4 clearly indicate that the oscillations are delayed by increasing the value of the buoyancy parameter. When $N<0$, the thermal field is stable with increasing values of

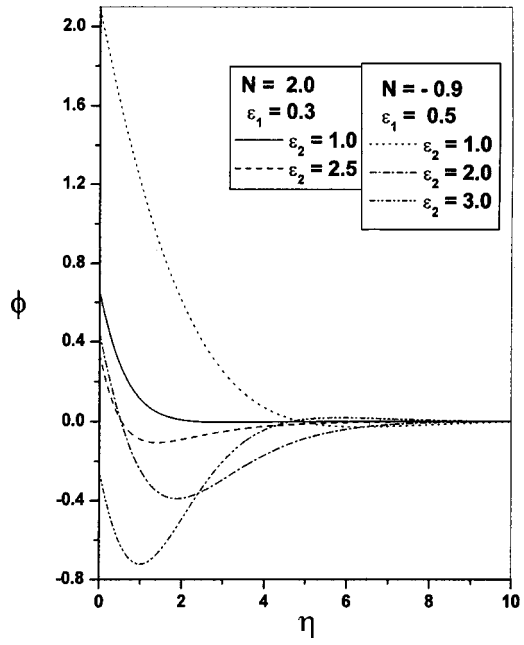

Fig. 5 Variation of concentration with η for different values of ϵ_2, when Le=1

Table 1 Nusselt number versus buoyancy parameter when Le=1 and $\epsilon_2=0.5$

	$\mathrm{Nu_x}/(\mathrm{Nu_x})_0$		
N	$\epsilon_1=0.1$	$\epsilon_1=0.3$	$\epsilon_1=0.5$
−0.5	0.9375	0.9332	0.9329
0.	0.9821	0.9484	0.9167
0.5	1.0041	0.9541	0.9059
1.0	1.0184	0.9572	0.8973
3.0	1.0507	0.9619	0.8741
5.0	1.0694	0.9635	0.8585

Table 2 Sherwood number versus buoyancy parameter when Le=1 and $\epsilon_1=0.5$

	$\mathrm{Sh_x}/(\mathrm{Sh_x})_0$		
N	$\epsilon_2=0.1$	$\epsilon_2=0.3$	$\epsilon_2=0.5$
−0.5	1.0888	1.0811	0.9329
0.	1.0469	0.9818	0.9167
0.5	1.0290	0.9671	0.9059
1.0	1.0184	0.9572	0.8973
3.0	0.9978	0.9342	0.8741
5.0	0.9878	0.9205	0.8585

Table 3 Effect of Le on mass transfer coefficient when $N=1$ and $\epsilon_1=0$

	$Sh_x/(Sh_x)_0$		
ϵ_2	Le=1	Le=5	Le=10
0	1.0000	1.0000	1.0000
0.1	1.0333	1.1179	1.2062
0.3	1.1057	1.4618	2.0488
0.5	1.1870	2.1053	6.7694

the thermal stratification parameter while the oscillations are set in when the concentration stratification parameter is increased beyond a limit. This feature can be observed from the Fig. 4.

For large value of Le, $\alpha \gg D$ and thermal diffusion is predominant, the temperature profile decreases to zero without any change of sign in the boundary layer. By increasing the solutal stratification parameter, the value of $\phi(0)$ becomes negative for large values of ϵ_2. Also, the negative values are significant and they creep into the boundary layer. This is clearly seen from Fig. 3. For large Le and fixed ϵ_2, increasing the value of ϵ_1 increased the value of $\phi(0)$ and when $\epsilon_1 \gg \epsilon_2$ the concentration distribution become free from oscillations in the boundary layer. When the buoyancy parameter N is large, both the thermal and concentration fields are normal, and the concentration profile crossed the η axis only at large value of ϵ_2. In opposing buoyancy case, large values of solutal stratification resulted in this type of abnormality in the concentration profile. These results are evident from Fig. 5.

The heat and mass transfer from the plate into the doubly stratified porous medium are expressed in terms of the local Nusselt and Sherwood numbers and are defined as

$$\frac{\mathrm{Nu}_x}{(\mathrm{Nu}_x)_0} = \frac{\theta(0)}{\theta(0,\epsilon_1)}$$

where $\mathrm{Nu}_x = q_w x/(T_w - T_\infty)k$ and

$$\frac{\mathrm{Sh}_x}{(\mathrm{Sh}_x)_0} = \frac{\phi(0)}{\phi(0,\epsilon_2)}$$

where $\mathrm{Sh}_x = q_m x/(C_w - C_\infty)D$ with $(\mathrm{Nu}_x)_0$ and $(\mathrm{Sh}_x)_0$ as the values of Nu_x and Sh_x at $\epsilon_1 = 0$ and $\epsilon_2 = 0$, respectively.

For fixed values of Le and ϵ_2, the Nusselt number and the Sherwood number results are tabulated against the buoyancy ratio parameter. The Nusselt number results are presented for three different values of the thermal stratification parameter ϵ_1 in Table 1. The results show the increase in the non-dimensional coefficient with increasing value of the parameter N. Also, increasing the value of ϵ_1 decreased the heat transfer rate into the medium. From Table 2 it is evident that the mass transfer coefficient is a maximum in the case of opposing buoyancy flow. It is also clear that the increase in the parameter N decreased the mass transfer coefficient. Similarly for fixed value of ϵ_1, increase in ϵ_2 lowered the mass transfer rate into the medium.

For fixed values of N and ϵ_1, the effect of Le is observed to favor the mass transfer into the medium. Increase in the value of Le increased the mass transfer coefficient. In the absence of thermal stratification, it further increased the mass transfer co-efficient with increasing solutal stratification parameter value. These results are tabulated in Table 3.

Acknowledgment

The authors are thankful to the journal reviewers and especially to Professor A. S. Gupta of the Department of Mathematics, IIT-Kharagpur for constructive suggestions on the manuscript.

Nomenclature

C = concentration
C_∞, o = ambient concentration at a reference point
D = molecular diffusivity
f = non-dimensional stream function
g = acceleration due to gravity
K = permeability
Le = α/D, Lewis number
k = thermal conductivity
N = $\beta_C q_m k/\beta_T q_w D$, buoyancy ratio
q_w, q_m = wall heat and mass flux constants
Ra_x = modified Rayleigh number, $K_g \beta_T q_w x^2/\alpha \nu k$
T = temperature
T_∞, o = ambient temperature at a reference point
u, v = velocity components in x and y directions respectively
x, y = Cartesian coordinates

Greek

α = thermal diffusivity constant
β_T, β_C = thermal and solutal expansion coefficients
η = similarity variable
ν = kinematic viscosity
ψ = stream function
θ, ϕ = nondimensionl temperature and concentration, respectively
ϵ_1 = $A/3(k_g \beta_T k^2/\alpha \nu q_w^2)^{1/3}$, constant, thermal stratification parameter
ϵ_2 = $B/3(K_g \beta_T D_{q_w}^3/\alpha \nu k q_m^3)^{1/3}$, constant, solutal stratification parameter

Subscripts

w = evaluated at wall
∞ = evaluated at the outer edge of the boundary layer

References

[1] Ludvigsen, A., Palm, E., and Mc Kibbin, R., 1992, "Convective Momentum and Mass Transport in Porous Sloping Layers," J. Geophys. Res. B, **97**, pp. 12315–12325.
[2] Gilman, A., and Bear, J., 1996, "The Influence of Free Convection on Soil Salinization in Arid Regions," Transp. Porous Media, **23**, pp. 275–301.
[3] Cheng, P., 1978, "Heat Transfer in Geothermal Systems," Adv. Heat Transfer, **14**, pp. 1–105.
[4] Bejan, A., and Khair, K. R., 1985, "Heat and Mass Transfer by Natural Convection in a Porous Medium," Int. J. Heat Mass Transfer, **28**, pp. 909–918.
[5] Lai, F. C., and Kulacki, F. A., 1991, "Coupled Heat and Mass Transfer by Natural Convection From Vertical Surfaces in Porous Media," Int. J. Heat Mass Transfer, **34**, pp. 1189–1194.
[6] Trevisan, O. V., and Bejan, A., 1990, "Combined Heat and Mass Transfer by Natural Convection in a Porous Medium," Adv. Heat Transfer, **28**, pp. 315–352.
[7] Nield, D. A., and Bejan, A., 1999, *Convection in Porous Media*, Springer-Verlag, New York.
[8] Bejan, A., 1984, *Convection Heat Transfer*, John-Wiley & Sons, New-York, Chpt. 10.
[9] Singh, P., and Sharma, K., 1990, "Integral Method for Free Convection in Thermally Stratified Porous Medium," Acta Mech. **83**, pp. 157–163.
[10] Kalpana, T., and Singh, P., 1992, "Natural Convection in a Thermally Stratified Fluid Saturated Porous Medium," Int. J. Eng. Sci., **30**, pp. 1003–1007.
[11] Nakayama, A., and Koyama, H., 1987, "Effect of Thermal Stratification on Free Convection With a Porous Medium," AAIA J. Thermophys. Heat Transfer, **1**, pp. 282–285.
[12] Lai, F. C., Pop, I., and Kulacki, F. A., 1990, "Natural Convection from Isothermal Plates in Thermally Stratified Porous Media," AAIA J. Thermophys. Heat Transfer, **4**, pp. 533–535.
[13] Takhar, H. S., and Pop, I., 1987, "Free Convection From a Vertical Flat Plate to a Thermally Stratified Darcian Fluid," Mechanics Research Communications, **14**, pp. 81–86.

Predicting Inlet Temperature Effects on the Pressure-Drop of Heated Porous Medium Channel Flows Using the M-HDD Model

Arunn Narasimhan
Mem. ASME
Staff Research Engineer, Microlithography Division, FSI International, Allen, TX 75013

José L. Lage
Fellow ASME
e-mail: JLL@engr.smu.edu
Laboratory for Porous Materials Applications, Mechanical Engineering Department, Southern Methodist University, Dallas, TX-75275-0337

A Modified Hazen-Dupuit-Darcy (M-HDD) model, incorporating nonlinear temperature-dependent viscosity effects, has been proposed recently for predicting the global pressure-drop of nonisothermal flows across a heated (or cooled) porous medium channel. Numerical simulations, mimicking the flow of a liquid with nonlinear temperature-dependent viscosity, are presented now for establishing the influence of inlet temperature on the pressure-drop and on the predictive capabilities of the M-HDD model. As a result, new generalized correlations for predicting the coefficients of the M-HDD model are derived. The results not only demonstrate the importance of fluid inlet temperature on predicting the global pressure-drop but they also extend the applicability of the M-HDD model. [DOI: 10.1115/1.1667526]

Keywords: Forced Convection, Heat Transfer, Porous Media, Properties, Viscous

1 Introduction

Recent studies on the variable viscosity effects in porous medium flows begin with the work of Ling and Dybbs [1]. They investigated theoretically the influence of temperature-dependent fluid viscosity on the forced convection through a semi-infinite porous medium bounded by an isothermal flat plate. For a similar flat plate configuration, Postelnicu et al. [2] considered the effect of heat generation as well. For non–Darcy flow in the same flat plate porous medium flow configuration, Kumari [3] and [4] provided similarity solutions for mixed convection with variable viscosity, under constant and variable wall heat flux.

While addressing heat transfer effects of variable viscosity porous medium flows, none of the previously cited works studied the impact of variable viscosity on the existing Hazen-Dupuit-Darcy (HDD) model, to predict the pressure-drop across porous medium channels, which was the subject of the pioneering studies in [5] and [6]. This led to the development of the Modified HDD (M-HDD) model, as proposed in [5], incorporating the temperature-dependent viscosity effects in the prediction of global pressure-drop. We shall now proceed, using fresh numerical simulations, to study the influence of changing the inlet temperature on the pressure-drop and on the correction coefficients of the M-HDD model in an effort to extend the applicability of the model.

Contributed by the Heat Transfer Division for publication in the JOURNAL OF HEAT TRANSFER. Manuscript received by the Heat Transfer Division January 31, 2003; revision received September 29, 2003. Associate Editor: V. Prasad.

2 The M-HDD Model and Inlet Temperature Influence

The HDD model (also known as the Darcy-Forchheimer equation),

$$\frac{\Delta \mathrm{P}}{\mathrm{L}} = \left(\frac{\mu_0}{\mathrm{K}_0}\right)\mathrm{U} + (\rho \mathrm{C}_0)\mathrm{U}^2 \tag{1}$$

is rigorously valid for flows of fluids with uniform and constant properties. This model has been generalized as a modified Hazen-Dupuit-Darcy model (M-HDD) in [5] for nonisothermal flows of fluids with temperature-dependent viscosity

$$\frac{\Delta \mathrm{P}}{\mathrm{L}} = \zeta_\mu \left(\frac{\mu_0}{\mathrm{K}_0}\right)\mathrm{U} + \zeta_\mathrm{C}(\rho \mathrm{C}_0)\mathrm{U}^2 \tag{2}$$

with the coefficients ζ_μ and ζ_C representing the lumped local effect of temperature dependent viscosity and the effect of viscosity on the fluid velocity profile, respectively, as,

$$\zeta_\mu = \left[1 - \left(\frac{Q''}{1+Q''}\right)^{0.325}\right]\left(\frac{1}{1+Q''}\right)^{18.2} \qquad \zeta_C = 2 + (Q'')^{0.11} - \zeta_\mu^{-0.06} \tag{3}$$

with

$$Q'' = \frac{q''}{\left(\frac{k_e}{KC}\right)\mu_0}\left|\frac{d\mu}{dT}\right|_{T_0} \tag{4}$$

Notice in Eqs. (1)–(4), the viscosity and its derivative are evaluated at a reference temperature T_0, and K_0 and C_0 are obtained from Eq. (1) using no-heat experimental results. Therefore, for a heat flux input q'', one can estimate the viscosity variation effects from the M-HDD model, Eq. (2).

The correlations to predict the coefficients of the M-HDD model, Eq. (3), were primarily obtained for poly-alpha-olefin (PAO) in [5] from numerical simulations at a single inlet temperature, i.e., $T_{in} = 21°\mathrm{C}$. PAO is a very important fluid, used as the base-stock for motor oils and lubricants and the cold-plate coolant of preference in airborne military avionics [7]. The strong temperature-dependent dynamic viscosity of PAO can be modeled [8] as

$$\mu(T) = 0.1628\mathrm{T}^{-1.0868}, \quad 5°\mathrm{C} \leqslant T \leqslant 170°\mathrm{C} \tag{5}$$

Equation (5), when the values of temperature T are given in °C, predicts the viscosity in Nsm^{-2} within 3% accuracy [10]. Although derived for PAO, Eq. (2) is recommended for fluids having their viscosity behave in a fashion similar to Eq. (5), or following the general form $\mu(T) = AT^{-B}$, where A and B are two constants.

Transport equations and their respective boundary conditions, used to model the momentum and energy transport through a parallel plate porous medium channel with surfaces heated uniformly, and all of the simulation details (e.g., channel dimensions, thermophysical properties, mesh geometry, grid independence tests and convergence criteria used) remain identical with that detailed in [5], [9], and [10].

3 Pressure-Drop Versus Fluid Speed Results

Figures 1 through 3 present results of global pressure-drop versus fluid speed for 7, 21, and 32°C PAO inlet temperature, respectively, and several heat fluxes. The top curve in each of the figures represents the no-heating pressure-drop results. Obviously, the no-heating pressure-drop results could be predicted using the global HDD model, Eq. (1), with the viscosity evaluated at the appropriate inlet temperature ($\mu_0 = \mu_{in} = \mu(T_{in})$). The bottom curve in each of the figures is the inviscid pressure-drop result that could be predicted as well by

$$\frac{\Delta P}{L} = \rho C_0 U^2 \tag{6}$$

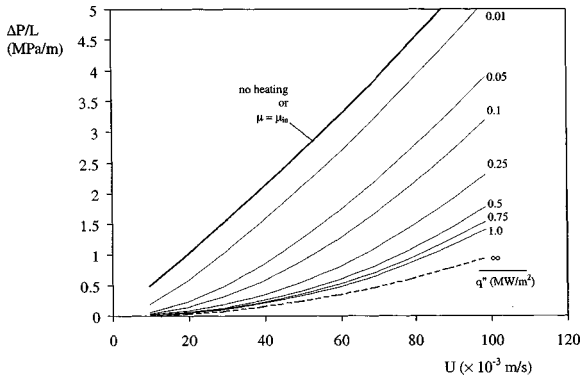

Fig. 1 Longitudinal pressure-drop versus fluid speed for several heat fluxes at $T_{in}=7°C$

the inviscid form-drag limit equation. As the density variation of PAO with temperature is very small (less than one-percent, [7]), obviously this limit can be considered invariant for any inlet temperature.

Proceeding from Figs. 1 to 3, it is apparent that for the same heat flux variation the reduction in the global pressure-drop becomes less evident. If we recall that the inviscid drag limit is the same no matter the inlet temperature (i.e., the location of the dashed line in Figs. 1, 2, and 3), we can reason that a hotter fluid (increased inlet temperature, thereby, smaller inlet viscosity) already has a weaker viscous drag term to begin with. Therefore, the pressure-drop of a stream of fluid with higher inlet temperature suffers less the heating effect on the viscosity. Moreover, heating a cold fluid stream shows a more pronounced effect on the viscous drag term because the viscosity at lower temperatures is more sensitive to heating than at a higher temperature (see viscosity Eq. (5)).

Another subtle reason is that reducing the viscosity by increasing the inlet temperature reduces the magnitude of the global viscous drag term (second term in Eq. (2)) directly, even if the channel remains isothermal. However, the global form drag (third term in Eq. (2)) is not affected for isothermal flows, even if the inlet temperature is altered. It is affected only when the flow becomes non-isothermal (here, because of heating) whereby, because of the viscosity variation, the velocity profiles are altered, leading to non-slug flow profiles. Furthermore, the hotter the flow becomes, the extent to which the velocity profiles are altered from their original slug flow like profiles is greatly reduced, leading to a reduction in global form drag variation. This is explained in detail in [9].

4 Inlet Temperature Influence on the Correction Coefficients

The behavior of the correction coefficients (ζ_μ and ζ_C) can be predicted for several heat fluxes by using the M-HDD model, Eq. (2) to curve-fit the numerical pressure-drop results.

An average deviation defined as

$$\sigma=\frac{\left[\frac{1}{N}\Sigma_1^N(\Delta P/L_\zeta-\Delta P/L_{\text{num}})^2\right]^{1/2}}{\frac{1}{N}\Sigma_1^N(\Delta P/L_{\text{num}})} \tag{7}$$

is used for analyzing the goodness of the fit. In Eq. (7), N is the sample size of the pressure-drop versus fluid speed data for each of the heat flux values, for one inlet temperature. Further, $\Delta P/L_\zeta$ is the pressure-drop results predicted through the curve-fit procedure (using Eq. (2)) while $\Delta P/L_{\text{num}}$ is the pressure-drop results (data points) from the numerical simulations.

Notice in the function defined in Eq. (7), the numerical pressure-drop results are taken as the fixed ''reference'' values as the results predicted by the curve-fitting procedure is compared to them. The curve-fitting procedure is further detailed in [7].

From the curve fitting results, a common curve-fitting function, one each for the two ζs of the M-HDD model, Eq. (2), predicting the inlet temperature influence, is proposed. The results of the curve-fit are shown in Fig. 4.

The form of the original, empirical, ζ curve-fit function (Eqs. (3) and (4)) proposed in [5] and the one to be proposed here are conceived with the standard technique discussed in detail in [11] and [12]. Notice from Eqs. (3) and (4), that, $\zeta_\mu=\zeta_C=1$ for $q''=0$ (i.e., for no heating, for any inlet temperature) and $\zeta_\mu\to 0$ and

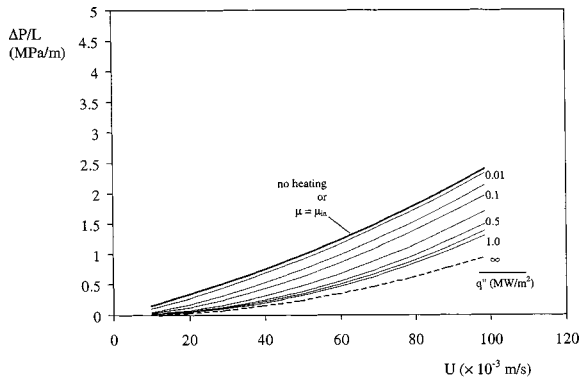

Fig. 2 Longitudinal pressure-drop versus fluid speed for several heat fluxes at $T_{in}=21°C$

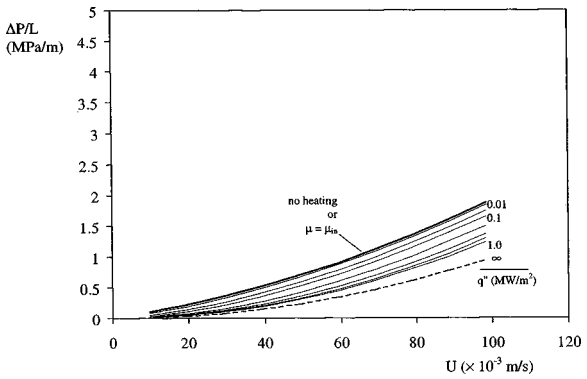

Fig. 3 Longitudinal pressure-drop versus fluid speed for several heat fluxes at $T_{in}=32°C$

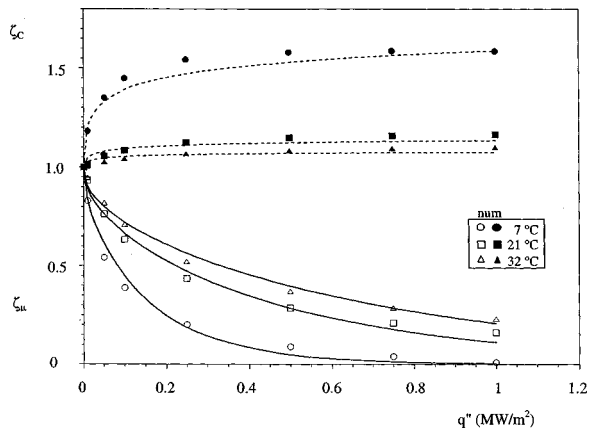

Fig. 4 ζ_μ and ζ_C versus q'', and their curve-fit for several inlet temperatures

$\zeta_C \to 1$ for $q'' \to \infty$ (again, for any/all inlet temperature), for any general porous flow configuration where predictions from the M-HDD model, Eq. (2), is sought. We also invoke the reference temperature method of accounting for viscosity variation effect—a standard practice in forced convection literature [13], to modify suitably the existing constant-viscosity correlation for the heat transfer coefficient (Nu).

Based on the above discussions, the following correlation is proposed for predicting the correction factors of the M-HDD model, Eq. (2),

$$\zeta_\mu = \left[1 - \left(\left(\frac{\mu(T_{in})}{\mu(T_r)}\right)^{0.15} \frac{Q''}{1+Q''}\right)^{0.28}\right]\left(\frac{1}{1+Q''}\right)^{45};$$

$$\zeta_C = 2 + \left(\left(\frac{\mu(T_{in})}{\mu(T_r)}\right)^{5} Q''\right)^{0.2} - (\zeta_\mu)^{-0.01} \tag{8}$$

with the non-dimensional group Q'', given as before, by Eq. (4) and T_r being a suitable reference temperature based on the particular fluid.

In the present case, where the fluid is PAO, the reference temperature $T_r = 7°C$ is chosen close to the lower bound of Eq. (5), the equation predicting the functional dependence of viscosity on temperature. Notice, by doing this, when $T_r = T_{in} = 7°C$, the group $\mu(T_{in})/\mu(T_r)$ in Eq. (8) is equal to unity.

Equation (7) is again used to analyze the goodness of the fit (done using Eq. (8)) in Fig. 4, by suitably modifying the variables. The error range of ζ_μ curve fits (i.e., the deviation of the curve-fit value of ζ_μ from that of its corresponding data point in Fig. 4, which were in turn got by using Eq. (2) to curve-fit the numerical pressure-drop data, as explained in the earlier section) for $T_{in} = 7°C$, is 40 to 60% for the last three heat flux values. Although this seems alarming, the actual ζ_μ values for these three heat fluxes is already less than 0.05, ensuring a very weak global viscous drag regime anyway (see [7] for a more elaborated discussion). The curve fitting function, Eq. (8), predicts the rest of the ζ_μ and ζ_C data with accuracy within six percent, which is considered good.

The usefulness of the empirical relations, Eq. (8), is apparent as most of the practical engineering applications involving coolants like PAO, water and ethyl alcohol, operate within the heat flux range that keeps the temperature of the convecting coolant flow within the range of application of Eq. (5). In other words, this is the range within which an engineer is interested in the M-HDD model's predictions for the thermo-hydraulic performance.

5 Summary and Conclusion

Using fresh numerical simulations, the influence of inlet temperature on the M-HDD model has been studied. For increasing heat flux, the degree of reduction in the global pressure-drop decreases with increase in inlet temperature, because of the nonlinear temperature dependence of the viscosity, Eq. (5). New empirical correlations, Eq. (8), capturing the inlet temperature influence on the correction factors of the M-HDD model, Eq. (2), have been proposed. Although obtained primarily for PAO, these correlations are recommended for fluids having their viscosity behave in a similar fashion to Eq. (5). Within this range, the correlations that are proposed in Eq. (8) are extremely relevant and practical.

Nomenclature

C = form coefficient, m^{-1}
K = permeability, m^2
L = channel length, heated section, m
U = global (cross-section averaged) longitudinal velocity, $m\,s^{-1}$
σ = deviation
ζ = coefficients

Subscripts

C = form
e = effective
f = fluid
in = inlet
r = reference
s = solid
0 = isothermal condition
μ = viscous

References

[1] Ling, J. X., and Dybbs, A., 1992, "The Effect of Variable Viscosity on Forced Convection Over a Flat Plate Submersed in a Porous Medium," ASME J. Heat Transfer, **114**, pp. 1063–1065.

[2] Postelnicu, A., Grosan, T., and Pop, I., 2001, "The Effect of Variable Viscosity on Forced Convection Flow Past a Horizontal Flat Plate in a Porous Medium With Internal Heat Generation," Mechanics Research Communications, **28**, pp. 331–337.

[3] Kumari, M., 2001, "Effect of Variable Viscosity on Non-Darcy Free or Mixed Convection Flow on a Horizontal Surface in Saturated Porous Medium," Int. J. Heat Mass Transfer, **28**(5), pp. 723–732.

[4] Kumari, M., 2001, "Variable Viscosity Effects on Free and Mixed Convection Boundary-Layer Flow From a Horizontal Surface in a Saturated Porous Medium—Variable Heat Flux," Mechanics Research Communications, **28**(3), pp. 339–348.

[5] Narasimhan, A., and Lage, J. L., 2001, "Modified Hazen-Dupuit-Darcy Model for Forced Convection of a Fluid With Temperature Dependent Viscosity," ASME J. Heat Transfer, **123**, pp. 31–38.

[6] Narasimhan, A., Lage, J. L., Nield, D. A., and Porneala, D. C., 2001, "Experimental Verification of Two New Theories for Predicting the Temperature-Dependent Viscosity Effects on the Forced Convection Through a Porous Media Channel," ASME J. Fluids Eng., **123**, pp. 948–951.

[7] Narasimhan, A., 2002, "Unraveling, Modeling and Validating the Temperature Dependent Viscosity Effects in Flow Through Porous Media," Ph.D. dissertation, Southern Methodist University, Dallas, TX.

[8] Porneala, D. C., 1998, "Experimental Tests of Microporous Enhanced Cold Plates for Cooling High Frequency Microwave Antennas," Ph.D. dissertation, Southern Methodist University, Dallas, TX.

[9] Narasimhan, A., and Lage, J. L., 2001, "Forced Convection of a Fluid With Temperature-Dependent Viscosity Through a Porous Medium Channel," Numer. Heat Transfer, **40**(8), pp. 801–820.

[10] Lage, J. L., Antohe, B. V., and Nield, D. A., 1997, "Two Types of Nonlinear Pressure-Drop Versus Flow-Rate Relation Observed for Saturated Porous Media," ASME J. Fluids Eng., **119**, pp. 700–706.

[11] Churchill, S. W., and Usagi, R., 1972, "A General Expression for the Correlation of Rates of Transfer and Other Phenomena," AIChE J., **18**(6), pp. 1121–1128.

[12] Churchill, S. W., and Ozoe, H., 1973, "Correlations for Laminar Forced Convection With Uniform Heating in Flow Over a Plate and in Developing and Fully Developed Flow in a Tube," ASME J. Heat Transfer, **95**, pp. 78–84.

[13] Kakaç, S., 1987, "The Effect of Temperature-Dependent Fluid Properties on Convective Heat Transfer," in *Handbook of Single-Phase Convective Heat Transfer*, Kakaç et al., Eds., John Wiley and Sons, New York, Chpt. 18.